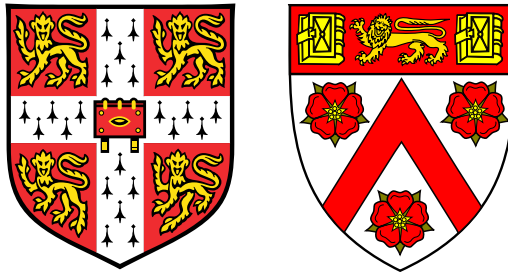# Piled Foundation Dynamics: Considering Inertial and Underground Railway Excitation

A dissertation submitted to the University of Cambridge
for the degree of Doctor of Philosophy

by

Tisal Lakshitha Edirisinghe

Trinity College

December 2021

I would like to dedicate this dissertation to

my loving parents and my brother, Lasitha

Declaration

This dissertation is the result of my own work and includes nothing which is the outcome of work done in collaboration, except as declared in the Acknowledgements and specified in the text. I further state that no substantial part of my dissertation has already been submitted before for any degree, or other qualification, at the University of Cambridge or a similar institution. This dissertation contains approximately 64,500 words and 127 figures, which does not exceed the prescribed word limit for the Engineering Degree Committee.

Tisal Laksitha Edirisinghe

Cambridge, December 2021

Abstract

Title: Piled foundation dynamics: Considering inertial and underground railway excitation

Author: Tisal Lakshitha Edirisinghe

Understanding the fundamental dynamics of piled foundations is important for practitioners, as ground-borne vibration can result in adverse disturbances, particularly in urban areas. Through the development of computationally efficient models, this dissertation examines the vibration of piles due to (1) inertial excitation at the pile heads and (2) incident waves from underground railways. The latter excitation mechanism also considers the building superstructure above the foundation. The numerical models account for the dynamic motion in three-dimensional space and are formulated in the frequency domain.

A new iterative model is developed using the boundary-element method (BEM) to study the effects due to wave scattering in inertially excited pile-groups. When different inertial loads are applied, the converged solutions of the iterative BEM model strongly agree with the interaction factors predicted using a conventional BEM model. A comprehensive parametric study on the inertial response of piles provides new insight into the wave-scattering effect and how various material and geometric parameters influence it, particularly at high excitation frequencies.

The iterative approach is then used to combine the BEM model of a piled foundation and the semi-analytical model of an underground railway tunnel. The result is an efficient coupled tunnel-foundation model, which fully accounts for the source-receiver interaction that has been neglected in existing models. It is discovered that this interaction is most significant when the separation distance between the tunnel and foundation is less than the shear wavelengths in the soil. For the first time, two counteracting mechanisms that govern the added-foundation effect, which is the modification of the ground (greenfield) response when a foundation is constructed near an underground railway, are also highlighted in a thorough parametric study.

iv

It is demonstrated that a simple dashpot model is representative of the essential dynamics of a modern tall building, with respect to its base impedance, over the frequencies associated with the perception of vibration. When the simplified building model is combined with the coupled tunnel-foundation model, the differences between the train-induced vibration of a building that is supported on deep piles and shallow footings are likely to be imperceptible by the occupants. Furthermore, the mean vibrational energy entering through the foundations of a tall building is found to be dominated by the added-foundation effect. The effectiveness of full and partial base isolation to mitigate the vibration disturbances in a building is also explored using power-flow techniques. Finally, a virtual case study concerning the construction of a building next to a pre-existing underground railway tunnel shows how the developed models can be used in practice to evaluate the performance of different designs. The conclusions are expected to establish new guidelines for designing foundations and buildings near underground railways.

Acknowledgements

The work published in this dissertation was conducted at the Department of Engineering of the University of Cambridge between October 2018 and December 2021. The research project was suggested by Dr. James Talbot, who also acted as my supervisor. It has been a great pleasure to work with James over the past few years, and I am greatly indebted to him for his enthusiastic guidance, continuous support, encouragement and interest in all aspects of the work presented herein.

My sincere thanks goes to Dr. Mohammed Hussein of Qatar University (Doha, Qatar) for securing me the funding to work as a research assistant at the College of Engineering during my winter holidays in 2018 and 2019. I am grateful for his assistance in understanding the pipe-in-pipe model, and his guidance on formulating an iterative approach to account for through-soil coupling was invaluable. I would also like to thank Prof. Hugh Hunt and Prof. Robin Langley for their interest in this project and the numerous helpful discussions we have had.

A special thanks goes to all my colleagues in the Dynamics and Vibration Group for making the research an enjoyable experience. I also give my thanks to Trinity College for providing me a pleasant environment to live in and the opportunity to meet like-minded individuals in similar research fields. For this, I am most grateful.

Last but not least, I wish to thank my mother, father, brother, and my extended family for the support and comfort they have provided throughout my studies. I would also like to express my sincerest gratitude to my friends in the UK, particularly from the vibrant Sri Lankan community in Cambridge, and all over the world. They have all brought a bright ray of sunshine to my life in an otherwise unprecedented time for the world.

Contents

List of Figures

List of Tables

Chapter 1

Introduction

Ever since the first underground railway line was opened in London in 1863, the use of the subsurface for transportation purposes has increased worldwide. Densely populated areas have benefited from underground transportation because it helps to mitigate urbanisation problems, such as road traffic congestion, land shortage, and air pollution. Recent improvements in safety and passenger capacity have also made subway systems a sustainable mode of public transport; for example, over one million passengers use the London Underground every single day. This means that the construction of new underground tunnels, and the expansion of existing lines, will continue well into the future. As of 2017, there were metro networks in 182 cities across 56 countries, carrying on average a total of 168 million passengers per day [232].
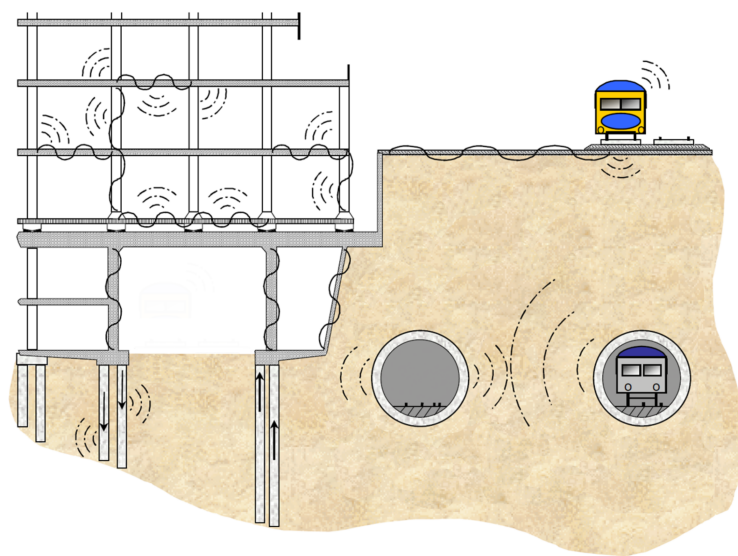
Fig. 1.1 An illustration of the problem of ground-borne vibration and re-radiated noise for a foundation-building system near surface and underground railways (based on Talbot's [221] original illustration).

The passage of trains through underground tunnels does, however, lead to the generation of ground-borne vibration and noise. The ground-borne vibration propagates through the ground as *wave-fields* and can produce environmental disturbances at the surface. When the wave-fields approach soil-embedded structures, such as the foundations shown in Fig. 1.1, the *soil-structure interaction* (SSI) can induce perceptible vibration and audible noise within buildings. This can lead to adverse mental and physical effects on people, so the problem of ground-borne vibration is an issue for urban planners. The day-to-day running of vibration-sensitive premises, such as operating theatres, recording studios, and concert halls, can also be adversely affected by low-levels of ground-borne vibration. However, the vibration induced by trains rarely results in the structural and cosmetic damage of buildings [202, 225].

1.1 Motivation for the Research

A recent study by Connolly et al. [40] analysed a database of 56 technical reports concerning the ground-borne vibration and noise due to surface, underground and elevated railway lines from nine different countries, with the US and UK representing a majority of the reports. It was found that directly perceived vibration limits and indirect re-radiated noise limits were exceeded in 44% and 31% of all cases, respectively. More importantly, it was noted that even though much of the current research is focused on computational modelling and the development of passive vibration reduction solutions, these approaches have not yet been fully embraced by practising engineers.

In general, the theoretical models that are used to solve ground-borne vibration problems can be classified into two groups. The first group consists of highly detailed numerical models that can predict the absolute vibration at specific locations of the building or ground. Rigorous numerical models, such as FemRail [203], MEFISSTO [120, 121] and FINDWAVE [47, 227], have been used to predict the ground-borne vibration near the underground railway tunnels of the London Crossrail and the Grand Paris Express. Whilst these rigorous models may be useful in practice to inform the decisions of engineers, they come with the drawbacks of significantly high model development time, computation time and cost.

In contrast, the second group consists of more computationally efficient models that capture the fundamental physics of the problem and can predict relative changes in the overall building vibration as the system's parameters are varied. Therefore, these efficient models are generally

used as scoping tools to guide the design of foundations and buildings during early construction. The numerical models developed in this dissertation will adhere to the fundamental approach because it can be difficult to verify the accuracy of rigorous models against real measurements due to modelling uncertainties and data collection errors.

Current practices suggest that the building response to ground-borne vibration is affected by the type of foundation, underlying ground conditions, building construction, and the state of repair of the building. Nevertheless, many unanswered questions remain as to how a nearby underground railway tunnel might influence the overall building vibration. For example, which foundation arrangements best mitigate the building's train-induced response, and how does the distance between the railway tunnel and foundation affect the response? The answers to these questions will have a significant impact on the design of buildings near underground railways.

Hence, there is a clear need to develop our physical understanding of how the wave-fields emanating from an underground railway can affect the vibration of foundations and the building superstructure above. It is also important to understand the *structure-soil-structure interaction* (3SI) between multiple neighbouring soil-embedded structures and how it can affect the wave-field distribution in the soil [33, 161]. In this case, 3SI accounts for the *through-soil coupling* between the tunnel and foundation, while SSI only regards the coupling between the soil and each structure in isolation.

1.2   Objectives of the Research

The primary aim of this dissertation is to develop theoretical techniques that can numerically predict the train-induced response of a piled foundation due to the ground-borne vibration from a nearby underground railway tunnel. Piled foundations typically consist of concrete piles that are embedded in the ground to transfer the weight of buildings from week strata to stiffer soil or rock at greater depth. To achieve the primary aim, the following objectives must be satisfied:

- to develop a comprehensive model of a piled foundation, which accounts for the pile-pile interaction between neighbouring piles;

- to combine the piled foundation model with an underground railway tunnel model so that the tunnel-foundation interaction is fully captured;

- to identify the factors governing the dynamic 3SI between a piled foundation and a nearby underground railway tunnel;

- to understand how constructing a building above the foundation may modify the overall vibration of the combined foundation-building system.

The programs for running all the numerical models presented in this dissertation are written using the technical computing software MATLAB [170]. The models will be generalised so that the parameters of the problem can be modified to simulate the fundamental dynamic behaviour of various test cases rather than focusing on a specific example. It will also be beneficial if the models are computationally efficient so that, in principle, consultants, engineers and designers can readily run simulations to predict the performance of various designs against ground-borne vibration. The developed models have four main uses:

- to determine the significance of different problem parameters on the vibration levels;

- to observe the general trends in the results over the frequencies associated with ground-borne vibration, and explain the observations through physics-based reasoning;

- to assess the performance of various foundation and building designs due to the vibration of underground trains;

- to help guide better design practices for foundations and buildings.

1.3   Outline of the Dissertation

This dissertation presents the following research work: (1) a review of the relevant literature; (2) the development of a piled foundation model to study the dynamic interaction between piles; (3) the development of a comprehensive tunnel-foundation model to investigate the train-induced vibration of piles; and (4) the combining of the tunnel-foundation model with simplified models of tall buildings to analyse the dynamic behaviour of the tunnel-foundation-building system.

Chapter 2 presents a review of the available literature that is relevant to this dissertation. The initial sections provide an overview of the ground-borne vibration problem and explores various countermeasures that mitigate its effects. Later sections discuss existing modelling techniques for underground railway tunnels and piled foundations while also highlighting limitations that need to be addressed.

In Chapter 3, a three-dimensional model of a piled foundation is developed, which captures the interaction between all piles in a group to predict the coupled response. Chapter 4 considers an alternative piled foundation model, whereby an iterative approach is used to approximate the

coupled response by considering the scattered wave-fields between a source and receiver sub-system in the pile-group. The effects of various parameters on the pile-group response are also investigated.

Chapter 5 considers the train-induced vibration of a piled foundation due to an underground railway tunnel, assuming that the foundation is multiple soil wavelengths away from the tunnel. Chapter 6 presents the development of a comprehensive tunnel-foundation model, which is able to capture the effects due to both tunnel-foundation and pile-pile coupling. This is achieved by applying an iterative approach to capture the waves that propagate back and forth between the tunnel and foundation sub-systems. The model is used to study the influence of various material and geometric parameters on the train-induced response of piles.

Chapter 7 couples simplified building models to the tunnel-foundation model to investigate how constructing a building, and installing base isolation, can affect the directional and overall vibration levels. Also, a virtual case study on the construction of a tall residential building near a pre-existing railway tunnel demonstrates how the models developed in the dissertation can be used in practice as scoping tools and for guiding design.

The main conclusions in this dissertation and recommendations for further work are given in Chapter 8. In its present form, the coupled tunnel-foundation-building model offers a flexible and efficient means of studying the train-induced vibration of modern buildings. It also shows significant potential for further development.

Chapter 2

Literature Review

Multiple researchers have considered the effects of ground-borne vibration. Studies on different vibration sources include the works of Hunt [108] and Ng [183] on surface roads, and that of Forrest [68], Hussein [112], Jones [125], Kuo [145] and Coulier [42] on underground railways. Studies on the vibration transmission path include the work of Lo [157] on the vibration of piled foundations, Sanitate [206] on the vibration of slab foundations, whilst the work of Cryer [48] and Talbot [221] consider the noise and vibration in buildings.

However, only a handful of studies investigate how the ground (*greenfield*) disturbance from an underground railway tunnel can be modified by piled foundations (*added-foundation effect*) and buildings (*added-building effect*). This chapter gives an overview of previous research on the response of piled foundations due to ground-borne vibration, with particular emphasis on work related to train-induced vibration. Sections 2.1 and 2.2 outline the nature of the problem and various countermeasures that can be applied to mitigate it. A critical review of a variety of techniques for modelling the soil, underground railway tunnel and piled foundation is presented in Sections 2.3–2.5. Finally, the main conclusions are summarised in Section 2.6.

2.1 The Problem of Ground-Borne Vibration

Over the past century, there has been an increase in the number of reported problems related to ground-borne disturbances as residential buildings and offices are constructed ever closer to vibration sources. This is particularly true in urban regions where rapid infrastructure projects, increased road traffic and over-demand peak railway timetables are prevalent [40]. Practising engineers are therefore concerned with minimising these disturbances.

2.1.1 Sources of Ground-Borne Vibration

There are many external sources of ground-borne vibration, which include those from above ground (e.g., construction activities and road traffic) and below ground (e.g., earthquakes and underground railways). Internal vibration sources that originate from within a building (e.g., human activity, air-conditioning equipment, and conveyance systems) will not be considered in this dissertation, as they do not significantly contribute to the source-soil-foundation-building vibration transmission path. A brief discussion on the four principal sources of ground-borne vibration is presented below; particular attention is given to the level of vibration intensity and the excitation frequencies associated with each source.

Earthquakes

Most earthquakes occur when a geological fault-plane becomes stuck, and the relative motion at the fault-plane causes an increase in the shear stresses, such that it exceeds the frictional resistance. This causes the two sides of the fault to suddenly slip past each other, releasing large amounts of stored strain energy, and generate elastodynamic waves in the process. These waves propagate through intermediate bedrock and soil layers to get to the surface, often causing structural damage to foundations and buildings. Extensive research has been done in this field [19, 49, 94] to minimise the potential of structural damage and human casualties.

Since earthquake deformation leads to large shear strains in the soil, generally above 10^{-4}, the predictive tools need to consider non-linearities [74]. When 3SI is also considered using a non-linear model, Vicencio & Alexander [233] observed that two adjacent buildings can exhibit more dynamic coupling over a broad range of frequencies.

In general, earthquakes excite low frequencies from 0 to 5 Hz, so it is adequate to consider the rigid-body modes and the first few flexural modes of a building to find its seismic response [200]. This low-frequency seismic excitation is outside the scope of this dissertation because it does not influence the high-frequency content of ground-borne vibration.

Construction Activities

There are six principal sources of ground-borne vibration from construction activities: pile driving, dynamic compaction, vibratory compaction, excavation, tunnelling, and blasting. The dominant source is from blasting, with 50 to 1000 times the energy transferred to the ground

compared to pile driving [217]. The peak particle velocity due to blasting can also range from 0.1 to 100 mm/s. Therefore, this has pushed researchers to develop robust prediction methods to assess blasting vibration levels [103, 104]. High vibration levels are likely to disturb building occupants and can potentially lead to structural damage (see Table 2.1). The frequency content of the surface waves generated from quarry and construction blasting can vary between 10 and 60 Hz [53]. In contrast, the vibration from mechanised construction activities usually produce low-frequency surface waves between 3 and 30 Hz [217].

Construction activities generally result in transient disturbances that excite the ground for short time durations, so this form of excitation will not be considered further in this dissertation. On the other hand, roads and railways result in more continuous disturbances. Even though the amplitude of these disturbances may not be significant to cause structural damage, they expose a higher proportion of people to perceptible disturbances at a much higher rate of occurrence.

Road Traffic

Road surface irregularities can be assumed to be a random, stationary roughness that interacts with vehicle tyres to produce dynamic forces at the contact patches. These forces are typically 15% higher than the corresponding static forces [4], and they predominantly generate ground-borne vibration in the form of surface waves.

The frequencies associated with road traffic vibration typically lie between 5 and 25 Hz, with amplitudes from 0.05 to 1.0 mm/s. However, this frequency range can vary significantly depending on the vehicle speed, soil type, and soil stratification [107]. An experimental study by Hunt [108] revealed that the type of road surface can also have a significant effect on the measured surface vibration spectra. Typically, these spectra contain two peaks below 20 Hz, corresponding to the natural frequencies of the vehicle's body-bounce and wheel-hop modes, as seen in measurements by Hong et al. [92].

The surface waves from roads are less likely to interact with deep foundations, such as those used for tall buildings. Hence, the vibration from road traffic is deemed to be outside the scope of this dissertation.

Railways

There are multiple excitation mechanisms by which railway trains can generate ground-borne vibration over a wide range of frequencies, as illustrated in Fig. 2.1. These can be grouped into

five fundamental mechanisms, which are detailed here in ascending order with respect to the typical frequencies they excite.

The first mechanism is a quasi-static effect due to the motion of the train's self-weight over a fixed observation point on the track. The frequency response at the observation point contains harmonics of the wheel-passing frequency, which depends on the spacing between consecutive axles in a train bogie and the train speed. Hence, a peak is present when a wheel is above a point on the track nearest the observer; a trough occurs when the same point on the track is nearer the mid-span of two axles. Typically, this effect is modelled by superposing multiple point forces along the track, which are equal to the static load applied at the wheel-rail interface [29, 124]. An experimental study by Auersch [6] found that the passage of axle loads is only significant in the localised region around the track. Sheng et al. [213] compared theoretical models with measurements to find that quasi-static loads dominate at low frequencies between 0 and 20 Hz.

A variant of the quasi-static effect is attributed to the sleepers, which are typically present in ballasted tracks to support the rails along their length. This second mechanism, referred to as parametric excitation, occurs when a wheel encounters variation in the track stiffness. The most common example of this excitation occurs at the sleeper-passing frequency (25-150 Hz), which depends on the train speed and sleeper distance [225]. When the railway track contains regularly spaced sleepers, the stiffness of the track varies periodically along its span, with a high stiffness directly above a sleeper and a low stiffness between adjacent sleepers, which results in a time-harmonic force when a moving train deflects the track. Heckl et al. [97] investigated the velocity spectra measurements that were taken in the vicinity of a suburban train and observed resonance at characteristic frequencies, which included the sleeper-passing and wheel-passing frequencies. Furthermore, a maximum resonance occurred when the wheel-passing frequency coincided with one of the harmonics of the sleeper-passing frequency. According to a study by Hawari & Murray [93], the continuous passage of trains over the sleepers can also permanently deteriorate the track ballast, which contributes to the roughness profile of the rails. However, as the average speed of underground trains is generally below 100 km/hr, which is lower than the train speed required to induce parametric excitation, this mechanism is outside the scope of this dissertation [139].

The third mechanism occurs as a result of roughness at the wheel-rail interface, and this can generate truly dynamic forces with an excitation frequency that is equal to the train speed divided by the roughness wavelength at the contact point. Numerical predictions by Nielsen

[184] showed that imperfections at the wheel-rail interface can grow from a localised region due to the continuous passage of trains. Nielsen also concluded that the growth occurs due to wear at the contact patch when non-linearities are neglected; these findings are also supported by Hawari & Murray [93]. In general, *wheel-rail roughness* can generate ground vibration over a wide range of frequencies, with longer wavelengths having higher amplitudes. An exception to this rule is corrugation: a spatially harmonic roughness profile that usually consists of short wavelengths between 25 and 50 mm. Short-wavelength corrugations can result in noise above 250 Hz at the typical speeds of metro trains [90]. These high-frequency disturbances are usually attenuated by the ground, so they rarely reach nearby infrastructure. A recent study by Ntotsios et al. [193] found that the wheel-rail roughness across two parallel rails must be treated as being uncorrelated if the roughness wavelengths are short. If both rails have the same in-phase rail correlation, the ground response would be around 3 dB higher [193].

Dynamic excitation can also occur due to height differences at the rail joints and crossings when short sections of track are welded together. Modern railway tracks contain rail joints that divide and insulate the electrical circuits, which are used to power and locate the trains [127]. In this case, non-linear track models should be used to account for the discontinuities in the track profile [226]. The track discontinuities can result in large impulse loads and transient vibration at the wheel-rail interface, thus generating rolling noise that could annoy the train passengers. Compared to linear models, non-linear models require different techniques to transform the equations of motion from the time domain to the frequency domain [136]. However, non-linear track models will not be considered further in this dissertation because it is assumed that the train travels over a well-maintained track with negligible discontinuities.

The final excitation mechanism is caused by high-speed trains, which produce a Mach cone when the train speed exceeds the ground's critical speed. Rayleigh waves, which exist near the surface, have the slowest phase speed of the elastodynamic waves that propagate through the ground (see Section 2.3.2). When the train exceeds the Rayleigh-wave speed, a high-amplitude ground vibration 'boom' occurs [142], which is similar to how a shock wave is formed when a supersonic aircraft exceeds the speed of sound. Multiple investigations into this phenomenon have been conducted by Takemiya [220] and Karlström [128] on the X-2000 train in Ledsgard, Sweden, when it approaches soft soil deposits. However, this mode of excitation rarely occurs in underground railways, and then only in highly localised areas with specific soil properties. Therefore, it can be disregarded over the remainder of this dissertation.
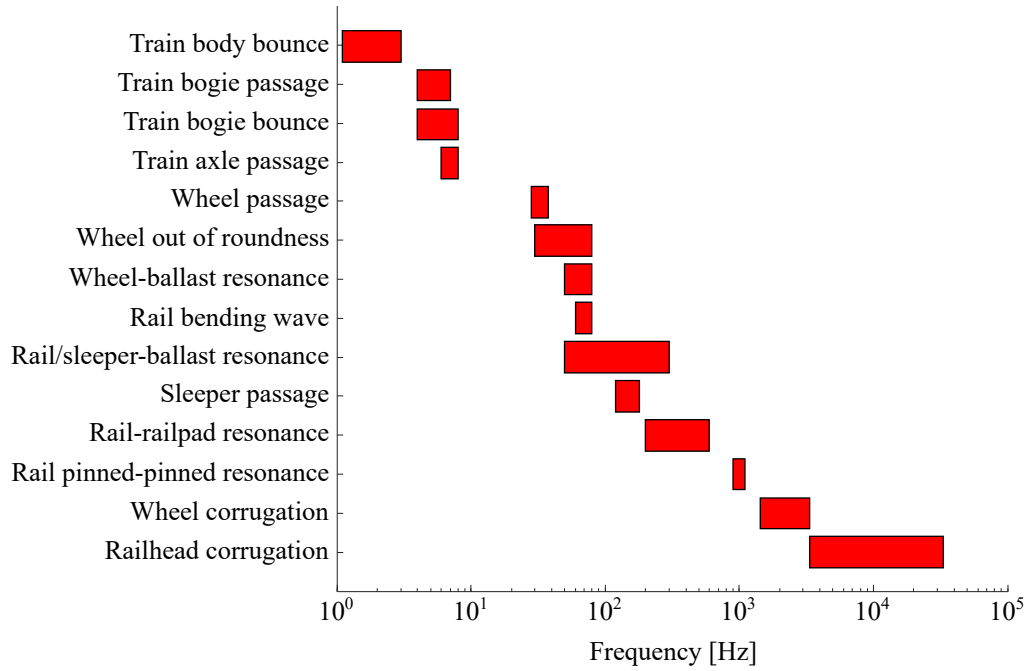
Fig. 2.1 The frequency distribution of different dynamic train-track interactions (based on the original illustration by Kouroussis et al. [139]).

2.1.2 The Impact of Ground-Borne Vibration on Buildings

The response of buildings to ground vibration can modified by the dynamic characteristics of the building, the foundation and the soil, which all affect the mode shapes, natural frequencies and damping [22]. This suggests that the best way of simulating the ground-borne vibration is by considering all the structures together in one model, especially given the intimate complexity between them. The dynamic characteristics can be altered by the design and construction of the buildings; depth, arrangement and type of foundation; and the geology of the ground, which can include soil-layers, bed-rock and the water-table [91].

The inertial forces on a structure pose the greatest threat towards structural damage. The potential for crack formation increases when the inertial forces give rise to large cyclic strains. However, ground vibration does not generally result in crack formation. The evidence gathered by Mead [172] suggests that the damage due to vibration is proportional to the inverse-square of the frequency, which is equivalent to having a dependence solely on the root-mean-square (r.m.s.) speed. This has some physical basis, as the particle speed of a propagating wave gives an indication of its vibrational energy and thus its ability to cause structural damage. Table 2.1 summarises some provisional building damage criteria, where the r.m.s. speed corresponds to the maximum of the three orthogonal velocities at various points in the structure.

Band	R.m.s. speed [mm/s]	Effect
I	< 1.75	No damage
II	2.5-5.0	Damage very improbable
III	5.0-10.0	Damage not probable
IV	> 10.0	Damage possible; check the stresses!

Table 2.1 Root-mean-square (r.m.s.) speed bands for building damage criteria (reproduced from Mead [172]).

Re-radiated noise describes vibration that first radiates through the ground and building surfaces, such as the walls and floors, and is then transmitted to the surrounding air in the form of audible sound. Although it may not be a precise term, it is in common use and is more widely accepted than the alternatives of ground-borne or structure-borne noise. Re-radiated noise can usually be heard as a low-frequency 'rumble' above 25 Hz, even after the vibration has fallen to imperceptible levels. The high-frequency energy content in propagating waves often dissipates due to damping in soft ground, which results in inaudible building vibration. In contrast, hard ground retains more of the high-frequency energy content, which can manifest as re-radiated noise within the rooms of buildings.

2.1.3 The Impact of Ground-Borne Vibration on Humans

Based on their lifestyle and environment, people can be exposed to various sources of vibration and noise. The frequencies that are typically associated with the human perception of ground-borne vibration and re-radiated noise are 1-80 Hz and 30-250 Hz, respectively [39]. The factors affecting vibration perception can be divided into two groups [21]:

1. intrinsic variables, which include the type of population (age, gender, size, fitness, etc.), experience, motivation, body posture, physical activities, financial situation, expectation, and arousal;

2. extrinsic variables, which include the vibration axis, magnitude, frequency, duration, and other environmental influences (noise, temperature, light intensity, etc.).

There are numerous metrics for measuring the annoyance levels due to vibration and noise stimuli. The main metrics suggested by the British Standards Institution (BSI) are the vibration dose value (VDV) [24] and sound exposure level L_{AE} [23]. The VDV is defined as

$$\text{VDV} = \left(\int_0^T a_w^4(t) dt \right)^{\frac{1}{4}}, \tag{2.1}$$

where $a_w(t)$ is the frequency-weighted r.m.s. acceleration over the time period T. Therefore, for a given magnitude, frequency and direction of vibration, the VDV measures the excitation levels in SI units of $\text{m/s}^{1.75}$. The VDV is often used in practice to quantify the perception of continuous and intermittent vibration stimuli by taking cumulative measurements. In contrast, the L_{AE} is used to quantify the perception re-radiated noise stimuli and is defined as

$$L_{\text{AE}} = 10 \log_{10} \left(\frac{1}{T} \int_0^T \frac{p_A^2}{p_0^2} dt \right), \tag{2.2}$$

where p_0 is the reference sound pressure of 20 μPa, and p_A is the instantaneous sound pressure measured using an A-weighted filter. The A-weighted filter accounts for the relative loudness perceived by the human ear, which varies with frequency.

Table 2.2 gives a range of VDVs, suggested by Mead [172], at which building occupants may experience some adverse reactions. However, these exposure criteria levels do not consider how the time of day could alter the perception of vibration. Peris et al. [195] conducted face-to-face interviews and railway vibration measurements in the United Kingdom to study whether human annoyance can be affected by the time of day. For similar vibration exposure levels, the overall annoyance response over a 24-hour period was found to be more closely related to the evening and night-time annoyance rather than the daytime annoyance. Therefore, it is advised that policy makers and practitioners need to consider different weighting factors, depending on the time of day, when assessing the annoyance due to railway vibration.

A survey of 565 households by Obermeyer, a German engineering firm, was reviewed by Knall [137] to investigate the perception threshold for ground-borne vibration and re-radiated noise near long-distance rail networks and suburban metro lines. Seventy-eight percent of the residents reported that they were 'considerably' affected by the noise, whereas only 57% were 'considerably' affected by the vibration. Knall suggests that the proportion of trains exceeding the human perception threshold for vibration has a more significant effect on the annoyance level than the absolute number of train passes. The study also provides evidence to suggest that once the perception threshold is exceeded, the annoyance level and the measured disturbance become independent of the stimulus.

A recent study by Smith et al. [215] looked to minimise the subjective perception of various stimuli by taking electrophysiological measurements from sleeping volunteers, while they were

Location	Vibration dose value (VDV) $[\mathrm{mm/s}^{1.75}]$		
	Low probability of adverse comment	Adverse comment possible	Adverse comment probable
Critical working areas	0.1	0.2	0.4
Residential	0.2-0.4	0.4-0.8	0.8-1.6
Office	0.4	0.8	1.6
Workshops	0.8	1.6	3.2

Table 2.2 Vibration dose values (VDVs) that may cause adverse human reactions in different locations (reproduced from Mead [172]).

exposed to railway disturbances. A majority of the sleep parameters, including the heart rate, the cardiac activation and the likelihood of arousal, were negatively impacted when the noise exposure level increased from 35 to 45 dB L_{AE}. Most of these sleep parameters also correlated positively with the self-reported annoyance levels. Therefore, to minimise the level of skewness in the results due to subjective opinions, Smith et al. recommend that nocturnal physiological readings should be recorded in future investigations instead of directly asking the participants about their annoyance levels.

All of these studies highlight the difficulties in setting human perception guidelines for acceptable vibration and noise levels due to railway induced disturbances. In summary, humans have a difficulty in differentiating between vibration and noise stimuli, and the perception of vibration can be highly subjective.

2.2 Ground-Borne Vibration Countermeasures

There are numerous approaches that can be adopted to mitigate the ground-borne vibration in buildings. The majority can be grouped into three categories: countermeasures at the vibration source, disrupting the vibration transmission path, and isolation of the building. The following sections introduce some countermeasures that are widely used in practice and also outlines techniques for measuring their effectiveness.

2.2.1 Countermeasures at the Source

Targeting the railway tracks is the most effective method of reducing ground-borne vibration because it attenuates the wave-fields that emanate directly from the source. Rail welding and

rail grinding can be used to reduce irregularities at the wheel-rail interface [202]; however, these are regarded as general maintenance rather than countermeasures. The response at frequencies near the bounce and wheel-hop modes of an individual train bogie wheel can be decreased by softening the suspension or by modifying the unsprung axle mass [102]. Soft rubber pads [202], mounted sleepers [123], and track foundation enhancements [135] have all been effective at attenuating the vibration leaking into the ground. Unfortunately, side-effects, such as increased noise radiation, may also manifest at the same time [234].

The floating slab track (FST) is another countermeasure that can isolate the train-induced vibration from the ground [109]. It is constructed by mounting the whole slab assembly on top of rubber bearings or steel springs. This prevents waves that have a higher oscillation frequency than the slab isolation (natural) frequency from propagating away from the track. Grootenhuis [83] conducted one of the first practical studies on the effectiveness of different FST designs. More recent theoretical studies, using both two-dimensional (2D) and three-dimensional (3D) models [246, 248], have also demonstrated the benefits of FSTs under various conditions.

2.2.2 Interrupting the Vibration Transmission Path

Common methods of passively interrupting the transmission path from the source to the receive include open trenches, in-filled trenches, elastic foundations, and tubular or solid pile rows. Yang & Hung [247] performed a parametric study to evaluate the effectiveness of open trenches, in-filled trenches and elastic foundations against surface train vibrations. All three approaches provided similar levels of attenuation at high frequencies, which was when the wavelengths in the soil were shorter than the corresponding structural dimensions. The attenuation level of the open and in-filled trenches was found to be governed by the trench depth, which must be of the same order of magnitude as the surface wavelength to have the greatest effect [247]. However, there are practical limitations on the excavation depth of trenches, such as the soil load-bearing capacity and the water-table depth.

In contrast, pile rows, which consist of piles arranged in a line, are not restricted by their depth or excavation location. Different methods of modelling the dynamic response of a single pile and multiple piles are detailed in Section 2.5. Nevertheless, in practice, the installation of pile rows is not a standard solution to decrease the vibration induced by railway tunnels. The main reason for this is the scale of installation required for urban railways, which raises the cost compared to cheaper isolation methods at the railway track or building. The study of piled

foundation designs, for the purpose of minimising the transmission of ground-borne vibration into buildings, is also limited.

2.2.3 Countermeasures at the Building

Vibration levels at the building can be reduced by installing countermeasures either during or after construction. Retrofitting techniques that are used to mitigate seismic vibration include material based dissipation systems, such as fluid viscous dampers in high-rise buildings [49], and tuned-mass dampers that counteract inertial forces [205]. The resonant frequencies of the building can also be shifted through localised stiffening and mass adjustments. However, post-construction procedures result in higher installation costs and are likely to provide only local protection against vibration.

Base isolation, consisting of steel springs or elastomeric bearings to de-couple the building from the ground, offers a more viable solution against ground-borne vibration. Examples exist across a broad selection of buildings, from residential to commercial, and comprises specialist buildings, such as cinemas [100], hospitals [84] and broadcasting studios [99]. A comprehensive review of base-isolated buildings by Talbot & Hunt [224] found that single degree of freedom (SDOF) models only give sensible results at low excitation frequencies – that is, near the rigid-body modes of the building. To investigate the high-frequency vibration, more complex models are required that account for flexural modes and wave propagation in the building.

Cryer [48] adopted the dynamic-stiffness method (DSM) [30] to simulate an infinite, 2D portal-framed building to study the effectiveness of different base isolation techniques. Cryer concludes that the effectiveness of the base isolation is governed by its natural frequency, with lower frequencies generally indicating better isolation. However, the damping of the isolation material does not significantly influence its effectiveness. Later, Talbot [221] connected Cryer's model to a piled foundation model via isolation bearings. Talbot agreed with Cryer's findings and notes that a comprehensive foundation model is required to predict isolation performance.

2.2.4 Measuring Vibration Performance

It is essential to have vibration performance measures to compare the effectiveness of various foundation designs. Reliable performance measures, based on robust engineering models, are also important in moving towards an evidence-based design approach [222]. This will help to

introduce better design guidelines for practising engineers, similar to how the seismic industry has made great strides in developing new procedures that produce structures with predictable seismic performances [81]. Two metrics for evaluating the vibration performance of a building are presented in this section.

Insertion Gain

The *insertion gain* (IG) is often adopted as a measure of variation in the vibration performance of a building when countermeasures, such as isolation bearings, are installed. When a building experiences steady-state, time-harmonic disturbances with angular excitation frequency ω, the IG at some location x is defined in units of decibels (dB) as the following ratio:

$$\mathrm{IG}^{(\mathrm{iso})} = 20\log_{10}\left(\frac{|u^{(\mathrm{iso})}(x,\omega)|}{|u^{(\mathrm{uniso})}(x,\omega)|}\right), \tag{2.3}$$

where $u^{(\mathrm{iso})}$ and $u^{(\mathrm{uniso})}$ are the building responses in a particular direction for the isolated and unisolated configurations, respectively. The building responses in Eq. (2.3) can be a measure of the displacement, velocity or acceleration.

While the IG is very effective at measuring the isolation performance of SDOF systems, its dependence on position and direction makes it less suitable for complex 3D buildings, which may include a combination of axial, flexural and torsional behaviour. These problems can be alleviated by adopting power-flow techniques.

Power-Flow Insertion Gain

Power-flow based approaches use the *mean vibrational power*, a scalar quantity, to evaluate the overall vibration performance of a multiple DOF structure. Recent studies have demonstrated that when the source-soil-structure system is modified, the *power-flow insertion gain* (PFIG) can be a useful metric for assessing the variation in the mean vibrational power entering across the base of the building [44, 115, 207]. PFIG is based on the principle that, assuming there are no internal sources, the mean power flow entering a building drives all the structural vibration and re-radiated noise. Compared to IG, PFIG is a better metric for characterising the changes in the overall vibration because it accounts for multi-directional inputs and is insensitive to spatial variation in the vibration levels.

By considering the mean power flow, a practising engineer can also analyse variations in the transmission of vibrational energy at different locations and excitation frequencies. A study

by Talbot & Hunt [224] found that the mean power flow into a base-isolated building can be negative over certain frequency bands due to the re-radiation of vibrational energy back into the soil. More recently, Heaton & Talbot [95] use PFIG to show that partial isolation can be as effective as full base isolation if the vibration field generated by the source is localised both in space, over the building's footprint, and in frequency. These studies highlight the value of using power-flow approaches when investigating vibration transmission paths across the soil-building interface.

When an SDOF system is excited by a steady-state, time-harmonic disturbance with angular frequency ω, the mean vibrational power $\bar{P}$ flowing into the element is

$$\bar{P} = \frac{1}{2}\mathrm{Re}\left(i\omega u S^*\right), \tag{2.4}$$

where u and S^* are the displacement and the complex $(i = \sqrt{-1})$ conjugate of the force S at the element, respectively. Note, as derived by Talbot [221], the real part of the complex expression within the brackets is considered in Eq. (2.4). If the element has multiple DOFs, the total mean power flow is the sum of the mean powers for each DOF. For example, the mean power entering an element with horizontal u, vertical w and rotational θ generalised displacements is

$$\bar{P} = \frac{1}{2}\mathrm{Re}\left(i\omega\left(u S^* + w F^* + \theta Q^*\right)\right), \tag{2.5}$$

where S^*, F^* and Q^* are the complex conjugate generalised forces corresponding to u, w and θ, respectively. Hence, the PFIG in decibels for a base-isolated building can be expressed as

$$\mathrm{PFIG}^{(\mathrm{iso})} = 10\log_{10}\left(\frac{|\bar{P}^{(\mathrm{iso})}(\mathbf{x},\omega)|}{|\bar{P}^{(\mathrm{uniso})}(\mathbf{x},\omega)|}\right), \tag{2.6}$$

where $\bar{P}^{(\mathrm{iso})}$ and $\bar{P}^{(\mathrm{uniso})}$ are the total mean power flows entering across multiple points $\mathbf{x}$ along the base of the building in the isolated and unisolated configurations, respectively.

2.3 Modes of Wave Propagation Through the Soil

A propagating wave transfers energy from a source to a receiver due to the oscillatory motion of particles in a medium. In a simple one-dimensional space domain, this can be represented using the homogeneous, hyperbolic wave equation:

$$\frac{\partial^2 u}{\partial x^2} = \frac{1}{c_0^2}\frac{\partial^2 u}{\partial t^2},\qquad(2.7)$$

where $u(x,t)$ is the particle displacement as a function of the space x-domain and time t, and c_0 is the wave phase speed. The classical D'Alembert solution to the wave equation is

$$u(x,t) = f(x - c_0 t) + g(x + c_0 t),\qquad(2.8)$$

where the arbitrary functions $f(x - c_0 t)$ and $g(x + c_0 t)$ represent propagating waves travelling at the same speed c_0 in the positive and negative x-directions, respectively. It is important to note that Eq. (2.8) describes *non-dispersive waves*: the waves propagate without distortion because c_0 is independent of the excitation frequency ω. The functions $f(x,t)$ and $g(x,t)$ can be determined by applying appropriate boundary conditions. If the differential equations contain higher order partial derivatives or external forces, such as $q(x,t)$ in Eq. (2.7), it can lead to dispersive relationships and the existence of leaky or *evanescent waves*. These are waves that do not propagate; their energy is instead spatially concentrated near the vicinity of the vibration source.

The following sections review the relevant literature on the propagation of elastodynamic waves in a full-space and a half-space.

2.3.1 Wave Propagation in a Full-Space

The governing laws satisfied by all points within a homogeneous, isotropic, linear-elastic full-space are given by Navier's coordinate-free equations [82]:

$$(\lambda + \mu)\nabla\nabla\cdot\mathbf{u} + \mu\nabla^2\mathbf{u} + \rho\mathbf{b} = \rho\ddot{\mathbf{u}},\qquad(2.9)$$

where $\mathbf{u}$ and $\mathbf{b}$ are the displacements and internal body forces per unit mass, respectively, and ρ is the density. The first and second elastic Lamé constants are λ and μ, respectively. Since the material properties of an isotropic, homogeneous medium are uniquely defined by two elastic moduli, the Lamé constants can be redefined in terms of the shear modulus G and Poisson's ratio ν: $\lambda = \frac{2G\nu}{1-2\nu}$ and $\mu = G$. Helmholtz's theorem states that $\mathbf{u}$ can be decomposed into a scalar ϕ and vector $\mathbf{H}$ potential [82]:

$$\mathbf{u} = \nabla\phi + \nabla\times\mathbf{H}\quad\text{and}\quad\nabla\cdot\mathbf{H} = 0.\qquad(2.10)$$

By considering only free waves ($\mathbf{b} = \mathbf{0}$) and substituting Eq. (2.10) into Eq. (2.9), Navier's equation will be satisfied if

$$\nabla^2 \phi = \left(\frac{\rho}{\lambda + 2\mu} \right) \ddot{\phi} = \frac{1}{c_P^2} \ddot{\phi}, \tag{2.11}$$

and

$$\nabla^2 \mathbf{H} = \left(\frac{\rho}{\mu} \right) \ddot{\mathbf{H}} = \frac{1}{c_S^2} \ddot{\mathbf{H}}. \tag{2.12}$$

Equations (2.11) and (2.12) show that freely propagating waves in a full-space can take the form of two non-dispersive body waves. The first body wave, governed by Eq. (2.11), is a dilatational or irrotational field, commonly referred to as a *pressure wave* (P-wave), which propagates at a phase speed of $c_P = \left(\frac{\lambda + 2\mu}{\rho} \right)^{1/2}$ in the direction parallel to the plane of oscillation. The other body wave, governed by Eq. (2.12), is an equivoluminal or solenoidal field, also known as a *shear wave* (S-wave). Compared to P-waves, S-waves propagate at a slower phase speed of $c_S = \left(\frac{\mu}{\rho} \right)^{1/2}$ in the direction perpendicular to the plane of oscillation. Shear waves also have an additional polarisation property, where they can either oscillate parallel to the horizontal (SH-wave) or vertical (SV-wave) plane.

As both P- and S-waves propagate away from a source through the bulk of the medium, the oscillations are attenuated due to two mechanisms: *radiation damping* and *material damping*. Radiation damping is dependent on the geometry of the soil domain when hemispherical body wave-fields spread out as the distance R from the source increases, which causes the magnitude to decrease by a factor of R^{-1}. On the other hand, material damping causes the kinetic and strain (potential) energy to be dissipated as thermal energy when a wave passes through a medium. Multiple studies on piled foundation dynamics [76, 186, 187, 191] use a frequency-independent hysteretic damping model [45] for the soil. Through experimental work, Hunt [108] observed that the soil exhibits hysteretic damping behaviour under low strains. Hunt also proposed that all the energy dissipation in the soil occurs through shear deformation, described by the shear modulus G, with no losses due to volumetric expansion, described by the bulk modulus K. Hysteretic damping in the soil can be modelled using the viscoelastic correspondence principle [18]:

$$G^* = G(1 + i\eta_G), \tag{2.13}$$

$$K^* = K, \tag{2.14}$$

where G^* is the complex shear modulus with hysteretic loss factor η_G. This form of damping model has been used for the soil in numerous railway tunnel models [42, 68, 112, 145], so it will be used again in this dissertation. It is important to note that assigning a non-zero value to η_G also converts the other elastic parameters of the material into complex variables.

2.3.2 Wave Propagation in a Half-Space

Since the majority of ground-borne vibration sources induce low shear strains in the soil, as detailed in Section 2.1.1, and if no slip occurs at the soil-structure interfaces, it is reasonable to model the soil as a homogenous, isotropic, linear-viscoelastic half-space. The presence of the ground at the top of the half-space imposes a boundary constraint, which allows a third type of wave to exist, known as a surface or *Rayleigh wave* (R-wave). These non-dispersive waves are slower than body waves and are confined to a depth usually one wavelength below the surface. The particles in the medium follow an elliptical path as the R-wave propagates. Since they are found near the surface, R-waves are the least affected by radiation damping, with an attenuation factor of $R^{-1/2}$ [82]. The velocity components of the R-waves also decay exponentially with depth, which is also a characteristic of evanescent waves.

The analytical solutions for the steady-state transfer functions of a homogeneous, isotropic half-space subjected to point and distributed forces at the surface were first derived by Lamb [151]. These solutions are expressed implicitly in the form of integral equations, which require
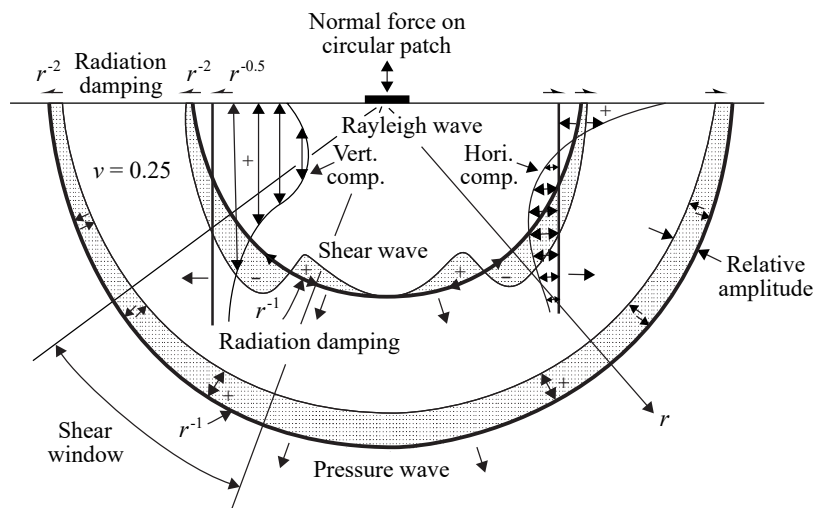
Fig. 2.2 The pressure, shear and Rayleigh waves produced when a time-harmonic point force is applied normal to the surface of a homogeneous, isotropic half-space (based on the original illustration by Woods [245]).

special convolution techniques to be solved, as detailed in a comprehensive review by Graff [82]. Miller & Pursey [175] are often cited for publishing the energy distribution when a time-harmonic, point force is applied normal to a circular region on the surface of a half-space. Of the total input energy, the radiated energy is distributed as 67% R-waves, 26% S-waves and 7% P-waves, as illustrated in Fig. 2.2.

In a layered half-space, where layers with different properties lie on top of one another, dispersive waves can propagate along the interface between each layer. These waves travel at phase speeds between the R-wave speed of the upper layer and the S-wave speed of the half-space. The behaviour of waves at the interface depends on the layer properties and boundary conditions; *Stoneley waves* appear at solid-solid interfaces that have different properties, while *Love waves* are horizontally polarised waves that propagate parallel to the interface [82].

2.4 Modelling the Dynamics of an Underground Railway

Over the past 50 years, researchers have developed models to capture the dynamic train-track and soil-tunnel interaction when an underground railway tunnel is excited. The first models of surface railways considered discrete parts of the system; for example, Winkler [240] modelled the track as an infinite beam on an elastic foundation. Simple SDOF models like this provide useful insight on the propagation or stagnation of waves at different frequencies when analysing their dispersion curves. One well-known characteristic is the *cut-on frequency* ω_c [225]: waves can only propagate along the track when the excitation frequency ω is greater than ω_c. When $\omega < \omega_c$, then localised evanescent waves only exist along the track near the wheel-rail contact points.

In recent years, computer-based models have become increasingly popular. However, even with technological advances, assumptions based on reliable engineering principles need to be made to achieve computational efficiency while, at the same time, maintaining good numerical accuracy. The following sections examine the widely cited underground railway models in the available literature. Models that use statistical energy analysis (SEA) [167] are not considered in this dissertation because they are more suitable for systems that exhibit a high modal density when excited, which does not occur at the excitation frequencies associated with underground railways.

2.4.1 Analytical Methods

Analytical approaches often provide the most insight because the governing relationships are expressed in the equations of motion. Metrikine & Vrouwenvelder [173] provide an example of a 2D analytical method, where the railway tunnel is modelled as an infinite Euler-Bernoulli beam embedded in a viscoelastic soil layer. The steady-state response of the beam is derived by moving a point force along the beam to simulate the motion of the train along the track. However, the problem with 2D analytical models is two-fold: they cannot accurately simulate the radiation damping in the soil, nor account for wave propagation perpendicular to the tunnel [121, 248]. These problems mean that the displacement wave-fields propagating from the tunnel are overestimated.

Kausel [131] published a comprehensive collection of analytical transfer functions when different dynamic loads – including point forces, line-loads, torques, and pressure pulses – are applied in a full-space and a half-space. Tadeu & Kausel [219] made a significant contribution when they derived the full-space *Green's functions* or fundamental solutions for a line-load in a 2D plane. The wavenumber domain is exploited to allow the amplitude of the line-load to vary sinusoidally with respect to the space domain perpendicular to the 2D plane. This type of formulation is known as a *two-and-a-half-dimensional* (2.5D) problem because the additional wavenumber domain enables 3D wave propagation to be captured using two space domains. Following on from this, Tadeu et al. [218] derived the 2.5D Green's functions for a half-space. These Green's functions have been used in numerical [85] and semi-analytical [113] methods to predict the ground-borne vibration from underground railway tunnels.

2.4.2 Numerical Methods

Physical vibration problems may involve soil layers, foundations or irregular railway tunnel geometries, which make it difficult to solve the wave equations analytically. Thus, numerical methods, such as the finite-difference time-domain (FDTD) method, the finite-element method (FEM), and the boundary-element method (BEM), are widely used to solve these problems.

The Finite-Difference Time Domain (FDTD) Method

The FDTD method [236] is based on a strong formulation of the dynamic problem, where the governing partial differential equations (PDEs) and boundary conditions are used to obtain

closed-form solutions. Furthermore, the finite-difference (FD) form of the wave equations are only solved between neighbouring nodes in a meshed structure. The advantage of this method, over conventional FEM and BEM, is that less effort is needed to write the computational code. However, if transient wave propagations are present in the time domain, the solution may exhibit spurious oscillations, related to the Gibbs phenomenon [28], as well as dissipation and dispersion errors in the wave propagation speed [11, 168].

Restrictions in the FD mesh can also make it challenging to satisfy the FD formulation for the governing PDEs and the boundary conditions [10]. On account of this issue, complex geometries are often difficult to model accurately, which has led to the gradual decline of the FDTD method. Nevertheless, this method has been used to simulate the ground-borne vibration near underground trains [227] and high-speed surface trains [129].

The Finite-Element Method (FEM)

The finite-element method [3] uses a weak formulation of the problem by restating the PDEs as definite integrals. FEM is widely used in railway vibration problems due to its versatility to model complex tunnel geometries. However, the traditional FEM cannot satisfy the radiation damping condition in the ground, similar to the FTDT method, and it can also generate spurious reflections at artificial edges in the discretised mesh.

Special handling is required, for instance through the application of infinite elements [15], artificial boundaries [154], or perfectly matched layers (PML) [13], to suppress the undesirable reflections in discretised infinite media. Yang et al. [248] applied the former approach to predict the response of a longitudinally invariant tunnel. In this case, the near field close to the tunnel was discretised using standard finite elements, while the far field was discretised using infinite elements with a propagation function to capture the radiation damping. Bian et al. [16] applied artificial boundary conditions in the far field by using gradually damped elements that absorbed the waves propagating from the tunnel. The damping ratios of the far-field elements increased in relation to a power law as the boundary was approached. Finally, PML is based on stretching the far-field space by means of position-dependent, complex-valued scaling functions, which cause the waves entering the PML region to attenuate exponentially. A 2.5D PML formulation was adopted by Lopes et al. [159] to prevent the waves reflected at the edges of the PML domain from entering the FEM domain of interest around an underground railway tunnel.

The Boundary-Element Method (BEM)

The boundary-element method [12, 52] is well-suited for the analysis of both infinite and semi-infinite domains. A review paper about recent BEM advances by Liu et al. [156] covers a wide range of engineering problems where it has been useful, including elastodynamics. Following extensive research over the 1970s, BEM became the most widely used numerical method for solving the strong formulation, written as a system of boundary integral equations (BIEs). BEM works by only discretising the boundaries of the domain and then uses Green's functions to find the response at given points within the domain. In contrast to FEM meshes, spurious reflections do not occur in BEM meshes, as no artificial boundaries have to be imposed. Therefore, it takes less effort to discretise a BEM mesh when modelling the soil as a half-space.

BEM models formulated in the frequency domain have been regularly used to predict the vibration of both single-tunnel [86] and twin-tunnel [87] underground railways. However, the inclusion of train-track-tunnel interaction can sometimes lead to numerical difficulties. This is because the tunnel walls can contain complex geometries, such as arched roofs, which need to be discretised in the mesh [140]. Numerical errors can also arise when thin-walled tunnels are discretised because the boundary elements, representing the inner and outer tunnel walls, are close together [214].

The MATLAB Elastodynamics Toolbox (EDT) [211], developed at KU Leuven, has been a valuable asset for researchers to model layered half-spaces. The Green's functions for layered half-spaces often contain transcendental functions, which have no closed-form solutions, so the integrals are solved using sophisticated numerical techniques, such as the dynamic-stiffness method (DSM) and the thin-layer method (TLM). A recent paper by Brookes et al. [26] used the EDT to solve the 2.5D layered Green's functions in a BEM model of the soil. The soil BEM model is coupled to a railway tunnel model to predict the disturbances from a newly constructed twin-tunnel section of the Elizabeth line beneath the Grand Central Recording Studios, London. Even though qualitative similarities are observed, the numerical model generally overpredicts the vibration levels compared to measurements taken over a year. This is most likely because the numerical model neglects the presence of other soil-embedded structures close to the tunnel, which may modify the response.

The Coupled FEM-BEM Approach

Soon after the development of FEM and BEM, researchers proposed that coupling structures, modelled using the two methods, could combine the advantages of both schemes. For example, Andersen & Jones [2] used a coupled FEM-BEM approach to compare the dynamic responses predicted from 2D and 3D models of a tunnel embedded in a half-space. Time-harmonic point forces were used to excite the FEM model of a thick-walled tunnel, while the dynamics of the soil were characterised using a BEM model. Their work re-emphasises that 2D models can, at best, only provide generalised trends at low computational cost, while a 3D model is required to make more accurate predictions.

FEM-BEM models have also been used to study 2.5D problems by assuming the tunnel is invariant along its length [70,72,214]. However, most railway tunnels are lined with concrete or cast iron segments, with circumferential stiffeners, once the tunnel is excavated using a tunnel boring machine [98]. This introduces periodicity along the length of the tunnel, which can be modelled by applying the Floquet transform in the longitudinal direction. Rigorous numerical models, based on the Floquet transform, were developed by Clouteau et al. [31,34]. Degrande et al. [50] also adopt the Floquet transform to simulate a tunnel embedded in inhomogeneous soil, with the use of periodic, layered Green's functions. The periodic formulation offers more flexibility to model a tunnel because the approach overcomes some of the problems associated with 3D and 2.5D models [50]. Jin et al. [122] present an alternative periodic model that uses the mode shapes of an equivalent isotropic cylinder for the tunnel, and the predicted responses show reasonably good agreement with the measured train-induced vibration.

2.4.3 Semi-Analytical Methods

Even though the numerical methods in the previous section have become more efficient with advances in computer processing power and storage capacity, it is common for a coupled FEM-BEM model to take tens of hours to run. If engineers need to run multiple iterations of models during the design stage of a project, these methods make the process economically unfeasible. Semi-analytical methods improve computational efficiency while sacrificing some accuracy, as they use simple tunnel geometries and numerical algorithms.

The pipe-in-pipe (PiP) model, which was initially developed by Forrest [68], is an efficient semi-analytical tool for predicting the steady-state response of a railway tunnel embedded in a

homogenous full-space. The PiP model represents the tunnel and the soil as concentric, hollow, cylindrical shells, or 'pipes', which are coupled together at the soil-tunnel interface. A detailed description of the PiP model, including the equations of motion, is presented in Appendix C. Hussein et al. [113] extended the full-space PiP model so that it can simulate a tunnel embedded in a homogeneous half-space by using the half-space Green's functions [218] and the fictitious-force method. When the half-space PiP model is compared against a rigorous, 2.5D FEM-BEM model developed by François et al. [70], the predicted results show good agreement between 1 and 80 Hz [113].

A recent paper by Yuan et al. [250] presented a semi-analytical solution for the vibration induced by a moving, time-harmonic point force in a tunnel. It implemented the superposition principle by treating the wave-field as a summation of analytical expressions that correspond to downward-travelling and upward-travelling waves. The displacement responses at the ground surface showed good agreement with the predictions from a 2.5D FEM-BEM model [70] for a shallow tunnel (5 m depth) and a deep tunnel (20 m depth). Since the half-space PiP model uses the fictitious-force method, which assumes that the traction-free surface does not influence the near field around the tunnel, it does not accurately predict the surface response for shallow tunnels [250].

2.5 Modelling the Dynamics of a Piled Foundation

The foundation is the lower part of a building in direct contact with the ground. Foundations fall into two main groups: shallow foundations (e.g., pad foundations, strip foundations, raft foundations, and footings) and deep foundations (e.g., piled foundations, piers, and caissons). Shallow foundations are often embedded less than 3 m in the ground and are used when the surface soil is sufficiently stiff to support the static loads of the building. Deep foundations are embedded at greater depths and help transmit static loads to stable soil strata, which are beyond the reach of shallow foundations.

This dissertation will focus on piled foundations because piles are widely used during the construction of tall buildings, and they are embedded at roughly the same depth as underground railway tunnels. In practice, a foundation is described as being 'piled' when the depth is three times greater than the breadth [5]. The top of a pile is called the pile head, while the bottom is referred to as the pile toe. There are many types of piles, but the two main sub-groups are end-

bearing piles and friction or floating piles. End-bearing piles are embedded through soft, upper soil layers until they terminate on top of bedrock; the piles support the building predominantly through the end-bearing resistance of the firmer bedrock at the pile toe [229]. Friction piles do not reach down to bedrock and, hence, carry most of the load through skin-friction or adhesion at the soil-pile interface [229].

Current building design codes for practitioners are given in the EN 1990 [61] and BS 8004 [25]. The two codes complement each other by following a limit-state design approach, where potential problems are identified and subdivided into three limit-states to minimise the overall risk. These include the ultimate, serviceability and durability limit-states. The ultimate limit-state reduces the critical failure risk of the foundation and building, the serviceability limit-state ensures the structure remains fit for purpose, and the durability limit-state ensures the structure can resist attack from environmental conditions.

When piled foundations are located near a ground-borne vibration source, the two systems will interact due to 3SI. One important aspect of 3SI is the study of how multiple soil-embedded structures can cause waves to scatter or diffract around them. Therefore, the design of a piled foundation could have a significant influence on the vibration transmission path from a railway tunnel to a building. The current design practices for piled foundations provide no evidence that the design is optimised to minimise this issue, which will affect the durability and serviceably limit-states.

The following sections outline the scattered-field problem and review the relevant literature on modelling the dynamics of a piled foundation.

2.5.1 The Scattered Wave-Field Problem

In general, the interaction of a propagating wave-field with discontinuities, or obstacles, in a medium can result in two principal wave phenomena: diffraction and scattering. Diffraction is defined as the bending or deflection of waves around the edge of an obstacle, while scattering occurs when waves radiate outwards due to the interaction at an obstacle's interface, primarily through reflections. In the case of elastodynamic waves, the interaction of an incoming *incident wave-field* with an embedded foundation or an underground tunnel is generally classified as a scattered wave-field problem.

In most wave applications, finding the *scattered wave-field* at an obstacle is straightforward because the wave-field remains either solenoidal (e.g., electromagnetic waves) or irrotational

(e.g., acoustic waves) throughout the interaction process. However, an elastodynamic wave can be decomposed into a scalar and vector potential by applying Helmholtz's theorem, as detailed in Section 2.3.1. This makes computing the scattered wave-field rather difficult, such as when mode conversion occurs. A classic example of mode conversion in a homogeneous half-space is when upward-travelling oblique P-waves are reflected as downward-travelling P-waves and SV-waves by the traction-free surface [82].

A wave scattering problem with multiple obstacles in the soil can be divided into two types: independent and multiple scattering [169]. The simplest approximation for the scattered wave-field is independent scattering, which occurs when the distances between nearby obstacles are large compared to the wavelengths in the soil. In this case, the obstacles can be assumed to be dynamically uncoupled from each other. This simplification is often used in seismic analysis, as the distance between the source and receiver is significantly large [17, 249]. However, if the distances between obstacles is around the same order of magnitude as the soil wavelengths, the waves can travel back and forth between the obstacles. This is regarded as a multiple scattering problem because the obstacles interact with each other due to through-soil coupling.

Various techniques can be applied to solve problems involving multiple scatterers: integral equation methods, iterative orders-of-scatter methods, transfer matrix (T-matrix) methods, and the separation of variables. The latter two techniques are outside the scope of this dissertation because the T-matrix method requires all the equations of the sub-systems to be formulated in the same domain (e.g., the space-frequency domain), and the separation of variables can only be applied to solve problems with closed-form solutions. For more details on all four approaches, the reader can refer to Martin [169].

As reviewed in Section 2.4.2, the BEM is an integral equation method that can derive the displacement frequency-response function (FRF), which is the matrix describing the dynamic response of the system. The off-diagonal components of the FRF matrix relate to the coupling between multiple structures. However, the computer memory required to store a large matrix that accounts for the coupling between many structures can be unfeasible.

In comparison, the iterative wave-scattering approach is advantageous because the coupled response between multiple structures can be approximated using a series of calculations. That is to say, the scattered wave-field induced by an obstacle induces scattered wave-fields at other obstacles, which in turn induce more scattered wave-fields, and so forth. During each iteration, or order-of-scatter, the scattered wave-field induced at each obstacle is calculated in isolation.

Convergence is achieved when the difference in the scattered wave-fields, between successive iterations, falls below a threshold value. The iterative approach has been applied to approximate the coupling between multiple obstacles in problems involving electromagnetic waves [65, 89], acoustic waves [64] and elastodynamic waves [54, 152]. However, the iterative approach has not been applied to solve elastodynamic problems with 3D soil-embedded structures.

2.5.2 Modelling the Dynamics of a Single Pile

To understand the dynamic response of piled foundations, one must first consider the response of a single pile. As the earliest models of piles are extensions of models for embedded footings, this section begins with a brief description of some footing models.

The first studies on foundation dynamics considered simple footings resting on the soil, for which analytical solutions exist. For example, Wong & Luco [243] present the expressions of the dynamic impedances of a 3D rigid, rectangular footing due to force and moment excitation. This was later extended to model embedded square footings and pad foundations by Mita & Luco [176].

A landmark was achieved when Novak [188] derived the steady-state solution of a floating pile subjected to a time-harmonic point load at the pile head. The motion of the pile is evaluated in the vertical, horizontal and rotational directions. Unlike previous models, the Novak model is able to account for both SSI and radiation damping in the soil. The model assumes plane-strain conditions, so the soil is modelled as an infinite number of infinitesimally thin, horizontal layers [9]. These layers extend to infinity from the soil-pile interface, where the pile is perfectly bonded to the soil. Each soil layer along the soil-pile interface is represented as a spring with a frequency-dependent stiffness and damping factor. The pile is modelled as an elastic bar and an Euler-Bernoulli beam to account for axial and flexural vibration, respectively. Novak concludes that while piles can be used to minimise permanent settlement in the soil, they cannot eliminate vibration.

Togami & Novak [187] derived the analytical expressions for the response of an end-bearing pile excited at the head by a vertical, point force. The dynamic stiffness and damping at the pile head are compared to Novak's plane-strain solution; the analytical model captured the dynamic response reasonably well for slender piles and soft soils when the excitation frequency was less than 80 Hz. Following on, the same researchers [191] derived the analytical expressions for the response of an end-bearing pile when it is excited by a horizontal, point force. The comparison

with Novak's solution again showed reasonably good agreement over the same frequency range. The experiments conducted by Novak & Grigg [189] and Cryer [48] also showed that Novak's solution predicted the response of single piles fairly well at very low frequencies below 10 Hz.

Kuhlemeyer is credited with developing the first rigorous, numerical solution for a single pile subjected to static and dynamic forces in the lateral [143] and vertical [144] directions. It uses a FEM model for the pile with the aid of non-reflecting boundaries. Good agreement is observed between Kuhlemeyer's and Novak's [188] solutions for the vertical response when the soil-pile stiffness ratio (or Young's Modulus ratio) is $E_s/E_p = 10^{-2}$, but shows poor agreement when E_s/E_p is decreased. Hence, Kuhlemeyer [144] concludes that Novak's model accurately captures the vertical motion of floating piles made of wood or concrete.

2.5.3 Modelling the Dynamics of a Pile-Group

In general, the piles in a piled foundation are placed close together to form a pile-group, which results in *pile-soil-pile interaction* (PSPI). The presence of neighbouring piles can cause two prominent effects: the *soil-stiffening effect* occurs at low frequencies when the piles constrain the motion of the surrounding soil; and the *wave-scattering effect* dominates at high frequencies when the soil wavelengths are around the same order of magnitude as the pile diameter.

This section describes the techniques that are most widely used in pile-group modelling, some of which are illustrated in Table 2.3. Two excitation mechanisms are considered: *inertial excitation* is when a pile head is excited by a harmonic force; and *kinematic excitation* is when each pile is excited by the incident wave-fields from a vibration source.

Inertial Excitation

Poulos was one of the first researchers to derive the static response of floating pile-groups that are subjected to vertical [196] and lateral [197] forces at the pile heads. First, the response of two piles within the group is computed when one of the piles is loaded. Then the response of the whole pile-group is approximated by applying the linear superposition principle to superpose the responses due to multiple sub-groups that consist of two piles. This approach is referred to as the *sub-system technique* because each sub-system of two piles is regarded in isolation (i.e., the effect of PSPI on the soil displacement is not fully captured). In order to analyse the static PSPI between two piles, Poulos [196] introduces the concept of an *interaction factor*, which defines the displacement of an adjacent pile as a function of the displacement of a loaded pile.

However, the static interaction factor is rarely used to study the steady-state behaviour of pile-groups, as the dynamic response is highly dependent on the frequency of excitation. Wolf & von Arx [242] and Nogami [185] discovered that pile-groups exhibit a frequency-dependent response, which varies significantly from the static response. Hence, the frequency-dependent interaction between two neighbouring piles, when one pile is excited by a time-harmonic load, needs to be characterised by a dynamic interaction factor. Kaynia & Kausel [132, 134] explored the dynamic behaviour of pile-groups embedded in an isotropic, homogeneous medium using the superposition principle. A semi-analytical, boundary-integral-type formulation, which uses the layered Green's functions for dynamic barrel loads and circular patch loads, is adopted to calculate the soil's dynamic stiffness matrix. In order to minimise computing power, the model does not explicitly account for the presence of cavities around each embedded pile in the soil. The dynamic interaction factors show good agreement with those obtained when the piles are explicitly coupled together; both models exhibit frequency-dependent behaviour due to the constructive and destructive interference between the individual piles. An extensive parametric study by Mamoon et al. [166] on the response of single piles and pile-groups highlighted that, even though Kaynia does not explicitly account for the cavities, only the responses of the single piles show pronounced effects at high excitation frequencies due to the cavities.

Approximate and closed-form solutions for dynamic interaction factors continue to be of interest to researchers because they are more computationally efficient than rigorous, numerical solutions. Dobry & Gazetas [51] derived the approximate dynamic interaction factors for a pile-group in a homogeneous half-space by considering the interference of cylindrical wave-fields that originate from each pile. Mylonakis & Gazetas [177] idealised the soil-pile interface as a dynamic Winkler foundation: a system of closely spaced linear-elastic springs and dashpots. By considering how the incident wave-field from an oscillating 'source' pile is scattered by an adjacent 'receiver' pile, closed-form solutions for the interaction factors are obtained. These analytical solutions agree reasonably well with numerical solutions and also give further insight into the nature of PSPI.

Talbot [221] adopted a 3D BEM model to simulate an infinitely long row of piles embedded in a homogeneous half-space. Each pile was modelled as an elastic bar and an Euler-Bernoulli beam to account for axial and flexural motion, respectively. The BEM model used smooth, constant boundary elements, with four elements approximating the circumference of each pile as a square. When compared against the static and dynamic compliances of a single pile [143,
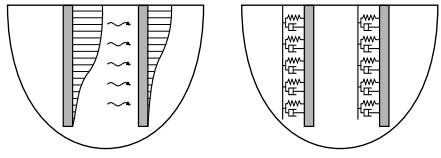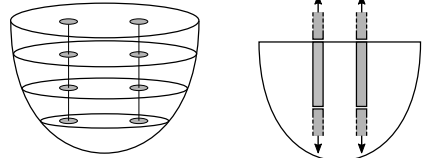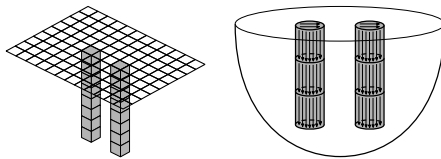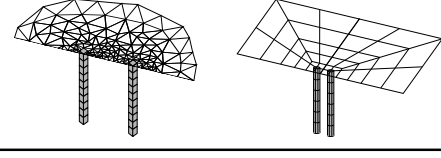
Type of model	Pile-group schematic diagrams		Author(s)
Analytical			Dobry & Gazetas [51] (L) Makris & Gazetas [164] Mylonakis & Gazetas [177] (R)
Semi-analytical			Hamad et al. [88] (L) Kuo [145] (R)
BEM			Coulier [42] (L) Kaynia [132] (R) Talbot [221]
Coupled BEM-FEM			Àlamo et al. [1] (L) Millán & Domínguez [174] (R)

Table 2.3 Summary of different pile-group models that illustrate the increase in complexity from analytical to coupled BEM-FEM solutions. The left (L) and right (R) diagrams for each type of model illustrates a schematic representation of the pile-group for some of the authored examples.

144, 212], the BEM model shows very good agreement. At the time, limitations in computing power prevented Talbot from producing multiple soil-pile interface meshes to model a pile-group. Instead, he modified a single pile to represent a repeating unit. In order to account for the PSPI, an infinite number of these repeating units are coupled to either side of a centrally loaded pile using periodic structure theory. Thereby, the interaction factors between the central pile and an adjacent pile can be computed. There is very good agreement between the dynamic interaction factors predicted using Talbot's model and Kaynia's model [132, 133]. Later, Talbot coupled the piles to a 2D portal-framed structure via springs to represent a building resting on isolation bearings. It is shown that if PSPI is neglected in a base-isolated building, it could lead to an overprediction of 7 dB in the PFIG [221].

Recently, Millán & Domínguez [174] developed a coupled BEM-FEM model to analyse the interaction of a pile-group in either viscoelastic or poroelastic soils. The cavities around the embedded piles were represented using cylindrical boundary elements that were developed by Coda et al. [36, 37] to represent axisymmetric piles. Since the node of each cylindrical element is located along the pile's centroidal axis, no singularities are present when integrating over the

cylindrical surface [174]. Good agreement is seen when the results are compared to dynamic stiffness coefficients published by Kaynia & Kausel [134] for a single pile and a pile-group.

Other researchers have investigated the behaviour of pile-groups embedded in layered soil media because it represents a more realistic situation. Hamad et al. [88] used a semi-analytical approximation to capture the PSPI between two piles embedded in a multi-layered half-space and compares the responses against a BEM model. The semi-analytical model adopted a hybrid formulation, which combined the thin-layer method (TLM) with the dynamic-stiffness method (DSM) through the use of the layered Green's functions for circular patch loads [130]. At low frequencies, under 35 Hz, there is reasonably good agreement between the two models when predicting the driving-point displacement and the dynamic interaction factors. Nonetheless, the semi-analytical model does not capture the far-field displacements at high frequencies, as the patch loads do not account for cavities in the soil [88]. This means that the scattered wave-fields at each pile do not fully account for the SSI around the pile's circumferential boundary. It is believed that this underpredicts the dynamic stiffness of the soil, resulting in notable differences between the far-field displacements of the hybrid formulation and the BEM model [192].

Kinematic Excitation

Fan et al. [62] analysed the seismic response of a pile-group due to upward-travelling S-waves by adopting the boundary-integral-type formulation developed by Kaynia & Kausel [134]. The SSI within the pile-group is decomposed into two components: incident wave-field interaction at a single pile and kinematic interaction between neighbouring piles. Their results show that the response of the pile-group follows the low-frequency components of the incident wave-field, while filtering out the high-frequency components. This shows that piled foundations can be used to minimise the transmission of seismic vibration into buildings.

Mamoon & Ahmad [165] investigated the response of a single pile due to obliquely incident SH-waves, SV-waves and P-waves using a hybrid BEM model. Their results also show the presence of high-frequency filtering in the pile response, which reduces the pile displacement amplitude as a function of frequency. More intermediate frequencies are filtered out when a rigid pile is used compared to a flexible one. Pile length also influences the results, with longer piles being more susceptible to vibration.

Makris & Gazetas [164] developed an analytical approach, based on a Winkler foundation, to predict the dynamic response of various pile-groups that were excited by the same seismic

incident wave-field used by Fan et al. [62]. The kinematic interaction between nearby piles was insignificant, even when the piles were close together, so the PSPI can be neglected. Makris & Badoni [163] reached a similar conclusion when they investigated the seismic response of pile-groups due to R-waves and obliquely incident SH-waves.

Àlamo et al. [1] used a coupled FEM-BEM model to investigate how the presence of rigid bedrock alters the performance of pile barriers when a time-harmonic point force is applied at the surface of a layered elastic half-space. Appreciable differences between the responses with and without the pile barrier were found when the piles touched the rigid bedrock. Increasing the pile slenderness ratio also improved the barrier's performance at low soil-pile stiffness ratios, and decreasing the pile spacing had the greatest positive influence on the bedrock profile. These conclusions indicate that end-bearing piles in contact with rigid bedrock provide a vibration transmission path into the bedrock, which isolates the soil region behind the pile barrier against vibration. An earlier parametric study by Gao et al. [73] also supports the conclusions made by Àlamo et al. [1], as the study highlights that pile stiffness and separation can influence vibration isolation performance.

2.5.4 The Train-Induced Response Due to a Railway Tunnel

The vibration generated by railway tunnels can also result in the kinematic excitation of a piled foundation. A number of empirical techniques are available that can evaluate the train-induced vibration of a building based on a statistical set of measurement data. Two empirical methods are presented by Hood et al. [106] for predicting the response of buildings in the vicinity of railway tunnels. Both approaches start with track measurement data, which is combined with a series of factors or transfer functions obtained through statistical analysis. A similar approach is also followed by Kuppelwieser & Ziegler [149], the difference being that some of the transfer functions are obtained from theoretical models or database analysis.

While empirical techniques may be useful as scoping methods for predicting the vibration and noise levels within a building, they should be used alongside rigorous, theoretical methods that account for the physics of the dynamic problem. Empirical methods are restricted by the following limitations: the difficulty for a compiled database of measurements to be statistically significant for multiple sources, propagation paths and building typologies; and the transfer functions for the source, propagation path and receiver are assumed to be independent, while they are in fact interconnected.

Kuo et al. [146] published one of the first papers that propose a semi-analytical method for predicting the train-induced response of a pile-group. The piles, which are modelled as purely elastic bars to capture the axial behaviour, are directly coupled to the soil along a series of nodal points using the displacement FRF for an infinitesimal dipole in a viscoelastic full-space [204]. The use infinitesimal dipoles alleviates the problem of dealing with a stress singularity when a point force is applied within an elastic solid. The incident wave-fields from the underground railway are calculated using the PiP model for a half-space [114]. The paper concludes that the foundation model should not neglect train-induced excitation, as it can cause the displacement at the pile head to deviate by $\pm 10 \, \text{dB}$ [146]. However, PSPI and cavities in the soil are neglected in the model, so the scattered wave-field is not accurately predicted.

Coulier [42] extended the BEM single-pile model developed by Talbot [221] to analyse the motion of a pile-group, which takes PSPI and the cavities into account. The numerical model captures the axial and flexural behaviour of the piles by using the governing equations for an elastic bar and a Timoshenko beam [228], respectively. There is good agreement between the dynamic interaction factors calculated using Coulier's model and those published by Kaynia [132] for two neighbouring piles. Coulier extends the pile-group model so that it can be excited by the incident wave-fields from a railway tunnel using the half-space PiP formulation [114]. The PiP model is solved first, and then the incident wave-fields from the underground railway are applied as input loads onto the boundary-element mesh using the sub-system technique. The train-induced response of a row of four piles (a 1×4 pile-group) beside a railway tunnel is compared against the greenfield response (i.e., the soil motion prior to adding the piles). The difference in the responses is significant, with a variation between $\pm 15 \, \text{dB}$ at high frequencies. This shows that the added-foundation effect can markedly modify the ground vibration.

A semi-analytical approach developed by Kuo [145] takes inspiration from the PiP [68, 112] approach to model the pile as an infinite elastic cylinder within a viscoelastic full-space. The axial and flexural waves in the infinite pile are approximated using specific circumferential ring modes. The infinite pile is then transformed into a finite pile using the mirror-image theorem. To find the train-induced response of a single pile, the finite pile is excited by the incident wave-fields from a railway tunnel, which are calculated using the half-space PiP model [114]. When modelling a pile-group, each pile is treated as an isolated sub-system and the superposition principle is applied to couple neighbouring piles together. The train-induced response of a 1×4 pile-group, with and without PSPI, is compared between Coulier's and Kuo's models. The

vertical pile-head displacement varies as much as 10 dB between the two models when PSPI is included. In some cases, when PSPI is neglected in Kuo's model, there is better agreement with Coulier's BEM model at certain frequencies. This shows that the superposition method does not accurately capture the PSPI between piles [145]. Furthermore, the mirror-image theorem causes residual tractions to appear at the surface [212], which can lead to errors.

In their models, Coulier [42] and Kuo [145, 146] assumed that the wheel-rail roughness was spatially harmonic. However, in reality, the excitation due to the wheel-rail roughness exhibits random characteristics, as the wheel and rail profiles are irregular. Hussein et al. [117] account for this by approximating the irregularities at the wheel-rail interface as a white-noise power-spectral density (PSD). The sub-system technique is adopted to model the tunnel-foundation system, whereby the incident wave-fields, predicted using the PiP model, excite a collection of piles, which are modelled using the semi-analytical approach developed by Hamad et al. [88]. However, this semi-analytical approach is unable to accurately capture the scattered wave-fields at the soil-pile interface because the soil cavities are neglected. Nevertheless, the results show that coupling a 2D building to the piles causes significant attenuation, of around 15 dB, in the vertical displacement PSD, which suggests that the added-building effect may be significant.

The semi-analytical [117, 145, 146] and numerical [42] methods presented in this section model the tunnel and foundation as an uncoupled source-receiver system. In order words, the waves propagating from the tunnel are able to excite the piles, but the waves that are scattered by the piles are unable to re-excite the tunnel. Therefore, the through-soil coupling between the two sub-systems is neglected, which is only applicable if the source-receiver distance is greater than the wavelengths in the soil because, in this case, the scattered wave-fields from the piles do not significantly influence the tunnel vibration. However, buildings and foundations are often constructed close together in densely populated cities. Surveys conducted along sections of the Channel Tunnel Rail Link (CTRL), London [119] and the Metropolitan Rapid Transit (MRT), Singapore [194] found railway tunnels that are about 1 to 1.6 m clear of structural foundations. In such cases, wave scattering must be considered at both the soil-tunnel and soil-foundation interfaces in order to accurately account for through-soil coupling. Therefore, there is a need to develop computationally efficient models that do not neglect the through-soil coupling between soil-embedded structures.

2.6 Conclusions

Section 2.1 highlighted that railways, roads, earthquakes and construction work are all sources of ground-borne vibration that can cause structural problems and environmental disturbances in buildings. In particular, the vibration from underground railways rarely results in structural damage, but building occupants often complain about being adversely affected, both mentally and physically. Section 2.2 showed that modifying the railway track (source), the transmission path, or the foundation and building design (receiver) can mitigate the overall vibration induced in a building.

Since transient disturbances do not generally cause prolonged vibration levels, the analysis is restricted to steady-state excitation in three-dimensional space, so all the numerical models in this dissertation will be formulated in the frequency domain. Unless specified otherwise, the frequency range of interest will be between 1 and 80 Hz since these frequencies are associated with the perception of ground-borne vibration. The ground will be modelled as a homogeneous, isotropic half-space, as described in Section 2.3. Although this may not be fully realistic (soil layers, voids, etc., are disregarded), the half-space accounts for the P-, S- and R-waves that are widely found in the ground. It is recommended that the effects due to soil layering should be considered in further work to account for inhomogeneity in the ground (see Chapter 8).

Based on the railway models discussed in Section 2.4, the tunnel in this dissertation will be modelled as a longitudinally invariant, cylindrical shell, which is representative of the geometry of a typical subway tunnel. It also means that computationally efficient techniques can be used to calculate the tunnel vibration in the wavenumber-frequency domain. The train-track model will consider the wheel-rail roughness as the primary excitation mechanism due to the passage of an average-speed metro train along a well-maintained track. Random vibration due to track irregularities are neglected in this dissertation because they tend to skew the results, making it difficult to ascertain the physics governing the response.

Section 2.5 emphasised that the foundation model in this dissertation needs to account for the presence of soil cavities, the PSPI between neighbouring piles, and the axial and flexural vibration of the piles themselves. Even though existing piled foundation models have captured the dynamics of piles under inertial loading and kinematic loading due to seismic waves, only a limited number of models have attempted to partially study the added-foundation effect when a piled foundation modifies the vibration field from a railway tunnel. No extensive parametric

studies have been conducted to understand the parameters governing the train-induced vibration of the piles. Furthermore, the through-soil coupling between a railway tunnel and nearby piles is neglected in existing tunnel-foundation models. These gaps in the literature originate due to complexities in the problem, particularly in modelling the 3SI, as the wave-fields interact with multiple soil-embedded structures. Hence, a comprehensive generalised model is required that captures the essential dynamic behaviour of the entire tunnel-foundation system while, at the same time, remaining computationally efficient.

Chapter 3

Development of a Piled Foundation Model

The models discussed in Section 2.5 highlight the importance of capturing the dynamics of a foundation when considering the interaction with other soil-embedded structures, such as railway tunnels. Therefore, a comprehensive model of the piled foundation (or pile-group) is required that accounts for the following dynamic behaviour:

1. axial and flexural motion of the pile as forces and moments are applied at the pile head;

2. pile-soil-pile interaction (PSPI), which captures the wave interaction between multiple neighbouring piles in the surrounding soil.

This chapter describes the development of a piled foundation model that satisfies the above requirements by using the BEM detailed in Appendix B.6. Sections 3.1 and 3.2 describe the pile and soil models, while the coupling between the two models is detailed in Section 3.3. In Section 3.4, the BEM pile-group model is compared against Kaynia's model [132], and some concluding remarks are given in Section 3.5.

The BEM pile-group model is based on the single-pile and pile-group models developed by Talbot [221] and Coulier [42], respectively. The following changes are applied to Talbot's and Coulier's models to improve the computational efficiency of the new pile-group model.

1. In this dissertation, the dynamic-stiffness method (DSM) [30] is adopted to calculate the pile's dynamic-stiffness matrix, which is then inverted to compute the displacement FRF matrix (see Section 3.1). This makes the application of different boundary conditions at the head and toe of the pile into a straightforward process: the rows and columns in the dynamic-stiffness matrix, corresponding to the respective forces and displacements that are constrained by the boundary conditions, can be simply deleted.

2. The algebraic expressions in Coulier's model are more involved; the equations need to be extensively reformulated each time a new pile is added. Therefore, in this dissertation, a different approach involving block-diagonal matrices is used instead (see Section 3.1.2). This makes the addition of new piles a simple procedure, and the equations can also be generalised for any pile-group configuration.

To solve the steady-state response of a pile-group due to inertial excitation, the loads applied at a pile head are assumed to be time-harmonic. Thus, the governing equations of motion can be solved in the space-frequency $(\mathbf{x}, \omega)$-domain, where $\mathbf{x}$ is a position vector and ω is the angular excitation frequency. For example, the displacement vector $\bar{\mathbf{u}}$ in the space-time $(\mathbf{x}, t)$-domain can be written as

$$\bar{\mathbf{u}}(\mathbf{x}, t) = \text{Re}\left(\mathbf{u}(\mathbf{x}, \omega) \cdot e^{i\omega t}\right),\tag{3.1}$$

where $\mathbf{u}$ is the complex $\left(i = \sqrt{-1}\right)$ displacement vector in the $(\mathbf{x}, \omega)$-domain. For clarity, the exponential term is omitted from the remainder of this chapter. Note that only the real part of a complex displacement or force accounts for the physical behaviour of a system.

3.1 The Pile Model

The DSM is used to capture the response of each cylindrical pile along its centroidal axis. It is assumed that the pile's axial and flexural motion are uncoupled because the axial forces are not significant enough to influence the pile's flexural response. Analytical expressions for the uncoupled axial-flexural motion can be derived by modelling the pile as an elastic bar and an Euler-Bernoulli beam. Since the pile response is dominated by radiation damping in the soil, it is unnecessary to account for material damping in the pile, which would normally be achieved through a hysteretic loss factor [18].

Talbot [221] tests if Euler's assumptions are valid for a typical pile in comparison to using Timoshenko beam theory, where rotational inertia and shear deformation are considered [228]. At the frequencies associated with ground-borne vibration, Talbot concludes that the errors due to Euler's assumptions are negligible. Thus, it is unnecessary to model the pile as a Timoshenko beam. The pile's cross-section is represented using four elements, as detailed in Section 3.2.

The following sections derive the governing equations of motion for a single pile and a pile-group with N piles.

3.1.1 The Single-Pile Case

A single pile is discretised into $n_P - 1$ equally spaced nodes and a further two nodes are added for the pile head and toe, giving a total of n_P bar-beam elements. The pile is defined by the following parameters: length L, mass density ρ_p, cross-sectional area A_p, Young's modulus E_p and second moment of inertia I_p. The pile head is free to rotate about the x- and y-axes, so the pile is unconstrained. Bar-beam element j, as illustrated in Fig. 3.1, contains five degrees of freedom (DOFs) at each node and is defined by the following parameters: L_j, $\rho_j = \rho_p$, $A_j = A_p$, $E_j = E_p$, $I_j = I_p$. The lengths of all elements in a pile must satisfy $L = \sum_{j=1}^{n_P} L_j$.

For the axial motion $\bar{u}_z(l,t)$ of an elastic bar in the z-direction, the governing undamped, free-vibration equation is given by Newland [181]:

$$\frac{\partial^2 \bar{u}_z}{\partial t^2} - \frac{E_p}{\rho_p} \frac{\partial^2 \bar{u}_z}{\partial l^2} = 0. \tag{3.2}$$

At a point l along the element, the general steady-state solution for the vertical displacement in the z-direction is

$$u_z(l,\omega) = c_1 e^{i\alpha l} + c_2 e^{-i\alpha l}, \tag{3.3}$$

where $\alpha = \omega \left(\frac{\rho_p}{E_p}\right)^{1/2}$ is the wavenumber of axial waves, ω is the excitation frequency, and c_1 and c_2 are the complex coefficients. The force due to axial motion in the z-direction is

(a)

(b)
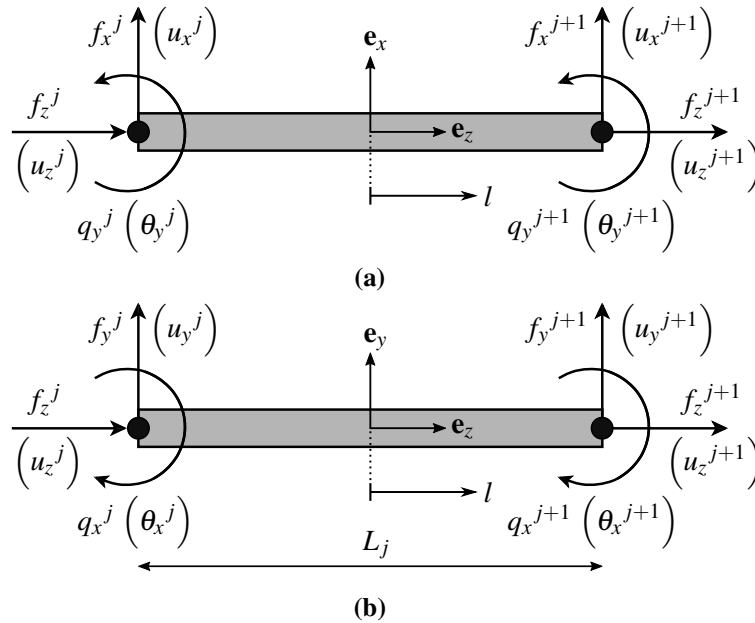
Fig. 3.1 Representation of a pile as a bar-beam element of length L_j in the **(a)** xz- and **(b)** yz-planes. The superscripts 'j' and '$j+1$' are used to denote the generalised forces $\left(f_x, f_y, f_z, q_x, q_y\right)$ and displacements $\left(u_x, u_y, u_z, \theta_x, \theta_y\right)$ at the left- and right-hand nodes, respectively.

$$f_z(l, \omega) = E_p A_p \frac{\partial u_z}{\partial l}. \tag{3.4}$$

For the flexural motion $\bar{u}_x(l, t)$ of an Euler-Bernoulli beam in the x-direction, the governing undamped, free-vibration equation is given by Newland [181]:

$$\frac{\partial^2 \bar{u}_x}{\partial t^2} + \frac{E_p I_p}{\rho_p A_p} \frac{\partial^4 \bar{u}_x}{\partial l^4} = 0. \tag{3.5}$$

At a point l along the element, the general steady-state solution for the lateral displacement in the x-direction is

$$u_x(l, \omega) = c_3 e^{\beta l} + c_4 e^{-\beta l} + c_5 e^{i\beta l} + c_6 e^{-i\beta l}, \tag{3.6}$$

where $\beta = \sqrt{\omega} \left(\frac{\rho_p A_p}{E_p I_p} \right)^{1/4}$ is the wavenumber of flexural waves, and c_3, c_4, c_5 and c_6 are the complex coefficients. The rotation θ_y and moment q_y about the y-axis, and the force f_x in the x-direction are

$$\theta_y(l, \omega) = \frac{\partial u_x}{\partial l}, \quad q_y(l, \omega) = E_p I_p \frac{\partial^2 u_x}{\partial l^2} \quad \text{and} \quad f_x(l, \omega) = E_p I_p \frac{\partial^3 u_x}{\partial l^3}. \tag{3.7}$$

The generalised forces and displacements expressed in Eqs. (3.3), (3.4), (3.6) and (3.7) are related through the following boundary conditions:

$$u_x = u_x{}^j, u_z = u_z{}^j, \theta_y = \theta_y{}^j, f_x = f_x{}^j, f_z = -f_z{}^j, q_y = -q_y{}^j \text{ at } l = -\frac{L_j}{2}, \tag{3.8a}$$

$$u_x = u_x{}^{j+1}, u_z = u_z{}^{j+1}, \theta_y = \theta_y{}^{j+1}, f_x = -f_x{}^{j+1}, f_z = f_z{}^{j+1}, q_y = q_y{}^{j+1} \text{ at } l = \frac{L_j}{2}, \tag{3.8b}$$

where the superscripts 'j' and '$j+1$' denote the variables at the left- and right-hand nodes of each bar-beam element j.

At the nodes of element j, the following two matrix equations can be assembled for the generalised displacements and forces due to axial motion in the z-direction:

$$\left\{ \begin{array}{c} u_z{}^j \\ u_z{}^{j+1} \end{array} \right\} = \left[\begin{array}{cc} e^{-i\alpha L_j/2} & e^{i\alpha L_j/2} \\ e^{i\alpha L_j/2} & e^{-i\alpha L_j/2} \end{array} \right] \left\{ \begin{array}{c} c_1 \\ c_2 \end{array} \right\}, \tag{3.9}$$

$$\left\{ \begin{array}{c} f_z{}^j \\ f_z{}^{j+1} \end{array} \right\} = E_p A_p \left[\begin{array}{cc} -i\alpha e^{-i\alpha L_j/2} & i\alpha e^{i\alpha L_j/2} \\ i\alpha e^{i\alpha L_j/2} & -i\alpha e^{-i\alpha L_j/2} \end{array} \right] \left\{ \begin{array}{c} c_1 \\ c_2 \end{array} \right\}. \tag{3.10}$$

44

Likewise, the following matrix equations denote the generalised displacements and forces due to flexural motion in the *x*-direction:

$$
\left\{
\begin{array}{c}
u_x{}^j \\
\theta_y{}^j \\
u_x{}^{j+1} \\
\theta_y{}^{j+1}
\end{array}
\right\}
=
\begin{bmatrix}
e^{-\beta L_j/2} & e^{\beta L_j/2} & e^{-i\beta L_j/2} & e^{i\beta L_j/2} \\
\beta e^{-\beta L_j/2} & -\beta e^{\beta L_j/2} & i\beta e^{-i\beta L_j/2} & -i\beta e^{i\beta L_j/2} \\
e^{\beta L_j/2} & e^{-\beta L_j/2} & e^{i\beta L_j/2} & e^{-i\beta L_j/2} \\
\beta e^{\beta L_j/2} & -\beta e^{-\beta L_j/2} & i\beta e^{i\beta L_j/2} & -i\beta e^{-i\beta L_j/2}
\end{bmatrix}
\left\{
\begin{array}{c}
c_3 \\
c_4 \\
c_5 \\
c_6
\end{array}
\right\},
\qquad (3.11)
$$

$$
\left\{
\begin{array}{c}
f_x{}^j \\
q_y{}^j \\
f_x{}^{j+1} \\
q_y{}^{j+1}
\end{array}
\right\}
= E_p I_p
\begin{bmatrix}
\beta^3 e^{-\beta L_j/2} & -\beta^3 e^{\beta L_j/2} & -i\beta^3 e^{-i\beta L_j/2} & i\beta^3 e^{i\beta L_j/2} \\
-\beta^2 e^{-\beta L_j/2} & -\beta^2 e^{\beta L_j/2} & \beta^2 e^{-i\beta L_j/2} & \beta^2 e^{i\beta L_j/2} \\
-\beta^3 e^{\beta L_j/2} & \beta^3 e^{-\beta L_j/2} & i\beta^3 e^{i\beta L_j/2} & -i\beta^3 e^{-i\beta L_j/2} \\
\beta^2 e^{\beta L_j/2} & \beta^2 e^{-\beta L_j/2} & -\beta^2 e^{i\beta L_j/2} & -\beta^2 e^{-i\beta L_j/2}
\end{bmatrix}
\left\{
\begin{array}{c}
c_3 \\
c_4 \\
c_5 \\
c_6
\end{array}
\right\}.
\quad (3.12)
$$

Similar matrix equations to Eqs. (3.11) and (3.12) also exist for the vectors of generalised displacements $\left\{ u_y{}^j, \theta_x{}^j, u_y{}^{j+1}, \theta_x{}^{j+1} \right\}^{\mathrm{T}}$ and generalised forces $\left\{ f_y{}^j, q_x{}^j, f_y{}^{j+1}, q_x{}^{j+1} \right\}^{\mathrm{T}}$ due to flexural motion in the *y*-direction, where the superscript 'T' denotes the vector transpose. In this case, the complex coefficients are denoted as c_7, c_8, c_9 and c_{10}.

By combining all the equations of motion for element *j*, the following two matrix equations can be obtained:

$$
\mathbf{u}_j =
\left\{
\begin{array}{c}
u_x{}^j \\
u_y{}^j \\
u_z{}^j \\
\theta_x{}^j \\
\theta_y{}^j \\
u_x{}^{j+1} \\
u_y{}^{j+1} \\
u_z{}^{j+1} \\
\phi_x{}^{j+1} \\
\phi_y{}^{j+1}
\end{array}
\right\}
= \mathbf{M}_j \mathbf{c}
\quad \text{and} \quad
\mathbf{f}_j =
\left\{
\begin{array}{c}
f_x{}^j \\
f_y{}^j \\
f_z{}^j \\
q_x{}^j \\
q_y{}^j \\
f_x{}^{j+1} \\
f_y{}^{j+1} \\
f_z{}^{j+1} \\
q_x{}^{j+1} \\
q_y{}^{j+1}
\end{array}
\right\}
= \mathbf{N}_j \mathbf{c},
\qquad (3.13)
$$

where the vectors $\mathbf{u}_j$ and $\mathbf{f}_j$ contain all ten generalised displacements and forces at the nodes, $\mathbf{c} = \{c_1, c_2, c_3, c_4, c_5, c_6, c_7, c_8, c_9, c_{10}\}^{\mathrm{T}}$ is the complex coefficient vector, and both $\mathbf{M}_j$ and $\mathbf{N}_j$

are 10×10 matrices. After rearranging Eq. (3.13), the dynamic-stiffness matrix $\mathbf{K}_j$ [199] for element j can be expressed as

$$\mathbf{f}_j = \mathbf{K}_j \mathbf{u}_j. \tag{3.14}$$

The boundary conditions for the generalised displacements and forces in Eq. (3.8) are used to attach consecutive bar-beam elements from end-to-end until the dynamic-stiffness matrix $\mathbf{K}$ for the entire pile is assembled:

$$\mathbf{f} = \mathbf{K}\mathbf{u}, \tag{3.15}$$

where the vectors $\mathbf{u}$ and $\mathbf{f}$ denote the displacements and forces along the pile's centroidal axis. Equation (3.15) can be rearranged as follows:

$$\mathbf{u} = \mathbf{K}^{-1}\mathbf{f} = \mathbf{H}\mathbf{f}, \tag{3.16}$$

where $\mathbf{H}$ is the displacement FRF matrix of a free-free pile. The dimensions of matrices $\mathbf{H}$ and $\mathbf{K}$ are the same: $5\,(n_\mathrm{P}+1) \times 5\,(n_\mathrm{P}+1)$.

The nodes below the pile head are not excited by external moments at the soil-pile interface, so these particular nodes only have three DOFs due to translation. Therefore, Eq. (3.16) can be rewritten as

$$\begin{Bmatrix} u_x{}^1 \\ u_y{}^1 \\ u_z{}^1 \\ \theta_x{}^1 \\ \theta_y{}^1 \\ u_x{}^2 \\ u_y{}^2 \\ u_z{}^2 \\ \vdots \\ u_x{}^{n_\mathrm{P}+1} \\ u_y{}^{n_\mathrm{P}+1} \\ u_z{}^{n_\mathrm{P}+1} \end{Bmatrix} = \mathbf{H}_\mathrm{P}^{(i)} \begin{Bmatrix} f_x{}^1 \\ f_y{}^1 \\ f_z{}^1 \\ q_x{}^1 \\ q_y{}^1 \\ f_x{}^2 \\ f_y{}^2 \\ f_z{}^2 \\ \vdots \\ f_x{}^{n_\mathrm{P}+1} \\ f_y{}^{n_\mathrm{P}+1} \\ f_z{}^{n_\mathrm{P}+1} \end{Bmatrix}, \tag{3.17a}$$

or simplified:

$$\mathbf{u}^{(k)} = \mathbf{H}_\mathrm{P}^{(k)} \mathbf{f}^{(k)}, \tag{3.17b}$$

where $\mathbf{H}_P^{(k)}$ is the displacement FRF matrix of pile k. Note that the node at the pile head contains five DOFs in Eq. (3.17). Torsional rotation about the pile's longitudinal axis is excluded, as the net contribution of the torsion of each pile on the torsional response of the entire pile-group is negligible [190].

By partitioning $\mathbf{H}_P^{(k)}$ into four sub-matrices, Eq. (3.17) can be rewritten as the following matrix equation:

$$\begin{Bmatrix} \mathbf{u}_{PH}^{(k)} \\ \mathbf{u}_P^{(k)} \end{Bmatrix} = \begin{bmatrix} \mathbf{H}_{P11}^{(k)} & \mathbf{H}_{P12}^{(k)} \\ \mathbf{H}_{P21}^{(k)} & \mathbf{H}_{P22}^{(k)} \end{bmatrix} \begin{Bmatrix} \mathbf{f}_{PH}^{(k)} \\ \mathbf{f}_P^{(k)} \end{Bmatrix}, \tag{3.18}$$

where the vector subscripts 'PH' and 'P' denote the field variables at the pile-head node and all other pile nodes, respectively. Equation (3.18) can be separated into the following two matrix equations:

$$\mathbf{u}_{PH}^{(k)} = \mathbf{H}_{P11}^{(k)} \mathbf{f}_{PH}^{(k)} + \mathbf{H}_{P12}^{(k)} \mathbf{f}_P^{(k)}, \tag{3.19}$$

$$\mathbf{u}_P^{(k)} = \mathbf{H}_{P21}^{(k)} \mathbf{f}_{PH}^{(k)} + \mathbf{H}_{P22}^{(k)} \mathbf{f}_P^{(k)}. \tag{3.20}$$

In the subsequent section, it is shown how expressing Eqs. (3.19) and (3.20) in this form makes it convenient to assemble the block-diagonal matrices, which describe the dynamic behaviour of multiple piles.

3.1.2 The Pile-Group Case

Now, consider when there are N piles arranged as a pile-group. The total number of bar-beam elements in the group is $N_P = \sum_{k=1}^{N} n_P^{(k)}$. By generalising Eq. (3.19) for N piles, the pile-head displacement of each pile can be written as the following matrix equations:

$$\begin{aligned} \mathbf{u}_{PH}^1 &= \mathbf{H}_{P11}^1 \mathbf{f}_{PH}^1 + \mathbf{H}_{P12}^1 \mathbf{f}_P^1, \\ \mathbf{u}_{PH}^2 &= \mathbf{H}_{P11}^2 \mathbf{f}_{PH}^2 + \mathbf{H}_{P12}^2 \mathbf{f}_P^2, \\ \vdots &= \qquad \vdots \\ \mathbf{u}_{PH}^N &= \mathbf{H}_{P11}^N \mathbf{f}_{PH}^N + \mathbf{H}_{P12}^N \mathbf{f}_P^N. \end{aligned} \tag{3.21}$$

The N matrix equations in Eq. (3.21) can be combined into a single matrix equation:

$$
\begin{Bmatrix} \mathbf{u}_{\text{PH}}^1 \\ \mathbf{u}_{\text{PH}}^2 \\ \vdots \\ \mathbf{u}_{\text{PH}}^N \end{Bmatrix} = \begin{bmatrix} \mathbf{H}_{\text{P11}}^1 & \mathbf{0} & \cdots & \mathbf{0} \\ \mathbf{0} & \mathbf{H}_{\text{P11}}^2 & & \mathbf{0} \\ \vdots & & \ddots & \vdots \\ \mathbf{0} & \mathbf{0} & \cdots & \mathbf{H}_{\text{P11}}^N \end{bmatrix} \begin{Bmatrix} \mathbf{f}_{\text{PH}}^1 \\ \mathbf{f}_{\text{PH}}^2 \\ \vdots \\ \mathbf{f}_{\text{PH}}^N \end{Bmatrix} + \begin{bmatrix} \mathbf{H}_{\text{P12}}^1 & \mathbf{0} & \cdots & \mathbf{0} \\ \mathbf{0} & \mathbf{H}_{\text{P12}}^2 & & \mathbf{0} \\ \vdots & & \ddots & \vdots \\ \mathbf{0} & \mathbf{0} & \cdots & \mathbf{H}_{\text{P12}}^N \end{bmatrix} \begin{Bmatrix} \mathbf{f}_{\text{P}}^1 \\ \mathbf{f}_{\text{P}}^2 \\ \vdots \\ \mathbf{f}_{\text{P}}^N \end{Bmatrix}, \quad (3.22a)
$$

or simplified:

$$
\mathbf{u}_{\text{PH}} = \mathbf{H}_{\text{P11}}\mathbf{f}_{\text{PH}} + \mathbf{H}_{\text{P12}}\mathbf{f}_{\text{P}}, \qquad (3.22b)
$$

where the vectors $\mathbf{u}_{\text{PH}}$, $\mathbf{f}_{\text{PH}}$ and $\mathbf{f}_{\text{P}}$ describe the displacements and forces of all N piles. The block-diagonal matrices $\mathbf{H}_{\text{P11}}$ and $\mathbf{H}_{\text{P12}}$ of the piles have dimensions of $5N \times 5N$ and $5N \times 3N_{\text{P}}$, respectively.

A similar matrix equation can be derived by generalising Eq. (3.20) for a pile-group:

$$
\mathbf{u}_{\text{P}} = \mathbf{H}_{\text{P21}}\mathbf{f}_{\text{PH}} + \mathbf{H}_{\text{P22}}\mathbf{f}_{\text{P}}, \qquad (3.23)
$$

where the block-diagonal matrices $\mathbf{H}_{\text{P21}}$ and $\mathbf{H}_{\text{P22}}$ have dimensions of $3N_p \times 5N$ and $3N_p \times 3N_p$, respectively. Both Eqs. (3.22) and (3.23) are expressed in a form that makes it easier to couple the pile and soil models at the soil-pile interface (see Section 3.3).

3.2 The Soil Model

In order to account for the PSPI in a piled foundation, an appropriate model of the soil must be used that simulates the dynamic behaviour of the ground. Similar to previous papers that have investigated the dynamics of pile-groups [43, 165, 166, 223], the BEM is used to model the soil domain in this dissertation. Since no artificial boundaries are imposed in this method, spurious reflections are avoided and radiation damping is inherently accounted for in the soil, as presented in Section 2.4.2. The BEM model, described here, uses the Green's functions for a homogeneous, isentropic full-space (see Appendix B.4). Note, alternative Green's functions could also be used in this BEM formulation, such as those for a 3D layered half-space [31] so that the ground is representative of realistic soil profiles (see Section 2.5).

By applying the viscoelastic correspondence principle [18], material damping is included in the soil via a hysteretic loss factor η_G for the shear modulus, as discussed in Section 2.3.1. However, Talbot [221] finds that radiation damping in the soil dominates any material damping, so the precise value of η_G is not very important.

(a)   (b)
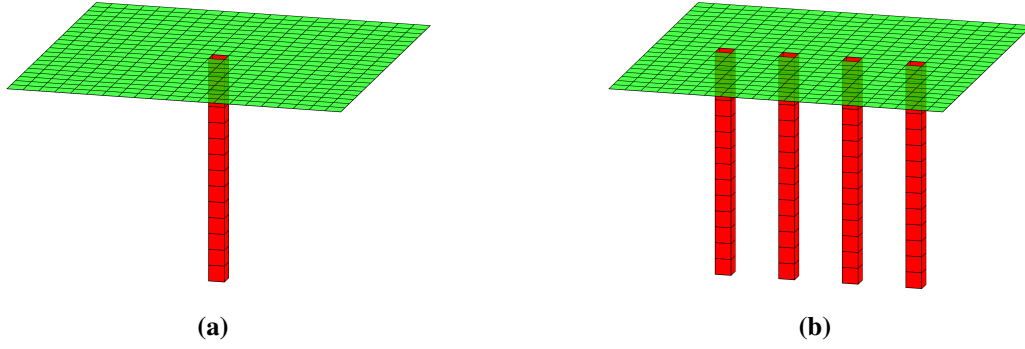
Fig. 3.2 Examples of the unbounded boundary-element meshes for the soil domain around **(a)** a single pile and **(b)** a 1×4 pile-group. The coloured elements identify the free surface (green) and the soil-pile interface (red).

The 3D half-space domain for the soil consists of two main boundaries: the free surface and the soil-pile interface. The free surface needs to be discretised to account for the zero traction boundary condition at the ground surface, otherwise the full-space Green's functions cannot accurately capture the wave interaction within a semi-infinite domain. The dynamic coupling between piles is achieved at the soil-pile interface, which is formed by discretising the soil cavities around the circumference of each embedded pile.

Special consideration must be given to the number of boundary elements around each pile's circumference so that numerical accuracy and computational efficiency is maintained by the solver. Talbot [221] examines how the number of circumferential boundary elements around a rigid cylindrical cavity influences the dynamic stiffness of an infinite, viscoelastic medium by comparing a two-dimensional BEM model, constrained under plain-strain conditions, with analytical solutions for the non-dimensional transverse stiffness K_t and longitudinal stiffness K_l. As the number of circumferential elements is increased from 4 to 16, the numerical results tend to converge with the analytical solutions. However, the errors in the numerical results increase as the excitation frequency is increased. This is because, at high frequencies, the wavelengths in the soil approach the same order of magnitude as the cavity diameter, which means that the wave interaction at the cavity is not fully captured by the discretised elements. Nevertheless, Talbot concludes that the advantages in using 4 circumferential elements, which include lower computation time and faster mesh discretisation, outweigh the numerical errors. Hence, square elements are adopted in this dissertation to discretise the boundary-element mesh for the soil, which forms a 4-element square section at the free surface when 4 elements are placed around the circumference of each pile.

The unbounded boundary-element mesh for the soil domain, as illustrated in Fig. 3.2 for a single pile and a 1×4 pile-group, contains a total of N_T elements. The sides of the free surface are represented using N_1 and N_2 elements. Smooth, constant boundary elements are used in the mesh, so the displacement and traction wave-fields are assumed to be uniform over each element and equal to the central node value.

3.2.1 The Single-Pile Case

For a single pile, the boundary-element mesh is represented by $N_{FS} = N_1 N_2 - 1$ elements at the free surface and n_{SP} elements at the soil-pile interface. In Appendix B.6, the relationship between the displacement and traction wave-fields at the N_T boundary element nodes is derived, which is repeated here for convenience:

$$\mathbf{H u} = \mathbf{G p}, \tag{3.24}$$

where $\mathbf{H}$ and $\mathbf{G}$ are the $3N_T \times 3N_T$ frequency-dependent collocation matrices, which inherently account for the through-soil coupling between all discretised boundary surfaces in the domain. This means that the soil and pile models can be fully coupled together at the soil-pile interface.

The vector $\mathbf{u}$ in Eq. (3.24) denotes the displacement wave-field at the N_T nodes:

$$\mathbf{u} = \left\{ u_x{}^1, u_y{}^1, u_z{}^1 \mid u_x{}^2, u_y{}^2, u_z{}^2 \mid \ldots \mid u_x{}^{N_T}, u_y{}^{N_T}, u_z{}^{N_T} \right\}^T, \tag{3.25}$$

where $\mathbf{u}^j = \left\{ u_x{}^j, u_y{}^j, u_z{}^j \right\}^T$ is the displacement wave-field at node j in the global Cartesian (x, y, z) coordinate system. Likewise, the vector $\mathbf{p}$ corresponds to the traction wave-field at the N_T nodes:

$$\mathbf{p} = \left\{ p_x{}^1, p_y{}^1, p_z{}^1 \mid p_x{}^2, p_y{}^2, p_z{}^2 \mid \ldots \mid p_x{}^{N_T}, p_y{}^{N_T}, p_z{}^{N_T} \right\}^T. \tag{3.26}$$

Rearranging Eq. (3.24) gives

$$\mathbf{u} = \mathbf{H}^{-1} \mathbf{G p} = \mathbf{H}_S \mathbf{p}, \tag{3.27}$$

where $\mathbf{H}_S$ is the soil displacement FRF matrix that relates the displacement and traction wave-fields across different nodes.

By partitioning $\mathbf{H}_S$ into four sub-matrices, Eq. (3.27) can be rewritten as the following matrix equation:

$$\left\{ \begin{matrix} \mathbf{u}_{FS} \\ \mathbf{u}_{SP}^{(k)} \end{matrix} \right\} = \begin{bmatrix} \mathbf{H}_{S11} & \mathbf{H}_{S12} \\ \mathbf{H}_{S21} & \mathbf{H}_{S22} \end{bmatrix} \left\{ \begin{matrix} \mathbf{p}_{FS} \\ \mathbf{p}_{SP}^{(k)} \end{matrix} \right\}, \tag{3.28}$$

where the vector subscripts 'SP' and 'FS' denote the response at the soil-pile interface of pile k and the free surface, respectively.

3.2.2 The Pile-Group Case

For a pile-group with N piles, there are $N_{FS} = N_1 N_2 - N$ free surface elements and $N_{SP} = \sum_{k=1}^{N} n_{SP}^{(k)}$ soil-pile interface elements. The respective soil displacement FRF matrix $\mathbf{H}_S$ for the pile-group can be partitioned, similar to Eq. (3.28), into four sub-matrices:

$$\left\{ \begin{matrix} \mathbf{u}_{FS} \\ \mathbf{u}_{SP}^1 \\ \mathbf{u}_{SP}^2 \\ \vdots \\ \mathbf{u}_{SP}^N \end{matrix} \right\} = \begin{bmatrix} \mathbf{H}_{S11} & \mathbf{H}_{S12} \\ \mathbf{H}_{S21} & \mathbf{H}_{S22} \end{bmatrix} \left\{ \begin{matrix} \mathbf{p}_{FS} \\ \mathbf{p}_{SP}^1 \\ \mathbf{p}_{SP}^2 \\ \vdots \\ \mathbf{p}_{SP}^N \end{matrix} \right\}. \tag{3.29}$$

In this case, the dimensions of sub-matrices $\mathbf{H}_{S11}$, $\mathbf{H}_{S12}$, $\mathbf{H}_{S21}$ and $\mathbf{H}_{S22}$ are $3N_{FS} \times 3N_{FS}$, $3N_{FS} \times 3N_{SP}$, $3N_{SP} \times 3N_{FS}$ and $3N_{SP} \times 3N_{SP}$, respectively. Equation (3.29) can be separated into the following two matrix equations:

$$\mathbf{u}_{FS} = \mathbf{H}_{S11}\mathbf{p}_{FS} + \mathbf{H}_{S12}\mathbf{p}_{SP}, \tag{3.30}$$

$$\mathbf{u}_{SP} = \mathbf{H}_{S21}\mathbf{p}_{FS} + \mathbf{H}_{S22}\mathbf{p}_{SP}, \tag{3.31}$$

where the vectors $\mathbf{u}_{SP} = \left\{ \mathbf{u}_{SP}^1, \mathbf{u}_{SP}^2, \ldots, \mathbf{u}_{SP}^N \right\}^T$ and $\mathbf{p}_{SP} = \left\{ \mathbf{p}_{SP}^1, \mathbf{p}_{SP}^2, \ldots, \mathbf{p}_{SP}^N \right\}^T$ denote the displacement and traction wave-fields, respectively, at the soil-pile interfaces of all N piles.

3.3 The BEM Pile-Group Model

In this section, the coupling equations at the soil-pile interface are first derived for the single-pile case and are then extended for the pile-group case by re-expressing the equations in terms of block-diagonal matrices. These equations are later used to couple the pile (see Section 3.1)

and soil (see Section 3.2) models together so that the dynamic response of a pile-group can be evaluated due to inertial excitation.

3.3.1 The Single-Pile Case

Each pile is assumed to be perfectly bonded to the soil at the soil-pile interface, such that no voids are present, which is justified given the low-strain amplitudes associated with the ground-borne vibration of interest. Therefore, each node along the pile's centroidal axis, except for the pile-head node, is coupled to the corresponding central nodes of four boundary elements at the soil-pile interface. Each group of four boundary elements at the soil-pile interface is assumed to deflect as a rigid structure, as local deformation around the pile due to Poisson's ratio effects is neglected. Thus, compatibility between the displacements along the pile's centroidal axis and the displacement wave-field at the soil-pile interface requires

$$\mathbf{u}_{\mathrm{SP}}{}^{4j-3} = \mathbf{u}_{\mathrm{SP}}{}^{4j-2} = \mathbf{u}_{\mathrm{SP}}{}^{4j-1} = \mathbf{u}_{\mathrm{SP}}{}^{4j} = \mathbf{u}_{\mathrm{P}}{}^{j} \quad \text{for } j = 1, 2, \ldots, n_{\mathrm{P}} - 1 \,, \tag{3.32a}$$

at intermediate nodes (i.e., between the pile head and toe), and

$$\mathbf{u}_{\mathrm{SP}}{}^{4n_{\mathrm{P}}-3} = \mathbf{u}_{\mathrm{P}}{}^{n_{\mathrm{P}}} \,, \tag{3.32b}$$

at the pile toe, where $4n_{\mathrm{P}} - 3 = n_{\mathrm{SP}}$. Each pile node j is numbered starting from the first node below the pile head towards the toe.

For pile k in a pile-group, Eq. (3.32) simplifies to the following matrix equation:

$$\mathbf{u}_{\mathrm{SP}}^{(k)} = \mathbf{Q}_1^{(k)} \mathbf{u}_{\mathrm{P}}^{(k)} \,, \tag{3.33}$$

where $\mathbf{Q}_1^{(k)}$ is a transformation matrix expressed in terms of the 3×3 identity matrix $\mathbf{I}$ as

$$\mathbf{Q}_1^{(k)} = \begin{bmatrix} \mathbf{I} & \mathbf{I} & \mathbf{I} & \mathbf{I} & & & & & \\ & & & & \mathbf{I} & \mathbf{I} & \mathbf{I} & \mathbf{I} & \\ & & & & & & \ddots & & \\ & & & & & \mathbf{I} & \mathbf{I} & \mathbf{I} & \mathbf{I} \\ & & & & & & & & \mathbf{I} \end{bmatrix}^{\mathrm{T}} \,. \tag{3.34}$$

Satisfying equilibrium between the traction wave-field on the soil-pile interface and the forces on the pile's centroidal axis leads to

$$\mathbf{f_P}^j = -b^2 \left(\mathbf{p_{SP}}^{4j-3} + \mathbf{p_{SP}}^{4j-2} + \mathbf{p_{SP}}^{4j-1} + \mathbf{p_{SP}}^{4j} \right) \quad \text{for } j = 1, 2, \ldots, n_P - 1, \quad (3.35a)$$

at intermediate nodes, and

$$\mathbf{f_P}^{n_P} = -b^2 \mathbf{p_{SP}}^{4n_P - 3}, \quad (3.35b)$$

at the pile toe, where the side length of each square boundary-element is b.

For pile k in a pile-group, Eq. (3.34) simplifies to the following matrix equation:

$$\mathbf{f}_P^{(k)} = -b^2 \left[\mathbf{Q}_1^{(k)} \right]^T \mathbf{p}_{SP}^{(k)} = -\mathbf{Q}_2^{(k)} \mathbf{p}_{SP}^{(k)}, \quad (3.36)$$

where $\mathbf{Q}_2^{(k)}$ is a transformation matrix.

3.3.2 The Pile-Group Case

Similar to Eq. (3.22), Eq. (3.33) can be generalised to apply for N piles by combining the N equations into a single matrix equation:

$$\begin{Bmatrix} \mathbf{u}_{SP}^1 \\ \mathbf{u}_{SP}^2 \\ \vdots \\ \mathbf{u}_{SP}^N \end{Bmatrix} = \begin{bmatrix} \mathbf{Q}_1^1 & \mathbf{0} & \cdots & \mathbf{0} \\ \mathbf{0} & \mathbf{Q}_1^2 & & \mathbf{0} \\ \vdots & & \ddots & \vdots \\ \mathbf{0} & \mathbf{0} & \cdots & \mathbf{Q}_1^N \end{bmatrix} \begin{Bmatrix} \mathbf{u}_P^1 \\ \mathbf{u}_P^2 \\ \vdots \\ \mathbf{u}_P^N \end{Bmatrix}, \quad (3.37a)$$

or simplified:

$$\mathbf{u}_{SP} = \mathbf{Q}_1 \mathbf{u}_P, \quad (3.37b)$$

where $\mathbf{Q}_1$ is a $3N_{SP} \times 3N_P$ block-diagonal transformation matrix. Applying the same pile-group generalisation to Eq. (3.36) results in the following matrix equation:

$$\mathbf{f}_P = -\mathbf{Q}_2 \mathbf{p}_{SP}, \quad (3.38)$$

where $\mathbf{Q}_2$ is a $3N_P \times 3N_{SP}$ block-diagonal transformation matrix.

3.3.3 The Coupled Response of a Pile-Group

By using the coupling equations derived in the previous section and the governing equations for the pile and soil models, the response of a pile-group can be derived when one or multiple

pile heads are driven by a generalised load $\mathbf{f}_{PH}$. The following governing equations are used in the derivation: Eqs. (3.22), (3.23), (3.30), (3.31), (3.37) and (3.38).

Pre-multiplying Eq. (3.23) by $\mathbf{Q}_1$ and substituting in Eqs. (3.37) and (3.38) gives

$$\mathbf{u}_{SP} = \mathbf{Q}_1 \mathbf{H}_{P21} \mathbf{f}_{PH} - \mathbf{Q}_1 \mathbf{H}_{P22} \mathbf{Q}_2 \mathbf{p}_{SP}. \tag{3.39}$$

Substituting Eq. (3.31) into Eq. (3.39) gives

$$\mathbf{H}_{S21} \mathbf{p}_{FS} + \mathbf{H}_{S22} \mathbf{p}_{SP} = \mathbf{Q}_1 \mathbf{H}_{P21} \mathbf{f}_{PH} - \mathbf{Q}_1 \mathbf{H}_{P22} \mathbf{Q}_2 \mathbf{p}_{SP}. \tag{3.40}$$

Equation (3.40) is rearranged as follows:

$$\left(\mathbf{H}_{S22} + \mathbf{Q}_1 \mathbf{H}_{P22} \mathbf{Q}_2 \right) \mathbf{p}_{SP} = \mathbf{Q}_1 \mathbf{H}_{P21} \mathbf{f}_{PH} - \mathbf{H}_{S21} \mathbf{p}_{FS}. \tag{3.41}$$

Hence, the matrix equation for the traction wave-field $\mathbf{p}_{SP}$ at the soil-pile interface, as a function of the pile-head forces $\mathbf{f}_{PH}$ and free surface tractions $\mathbf{p}_{FS}$, is

$$\mathbf{p}_{SP}(\mathbf{x}, \omega) = \mathbf{A} \left(\mathbf{Q}_1 \mathbf{H}_{P21} \mathbf{f}_{PH} - \mathbf{H}_{S21} \mathbf{p}_{FS} \right), \tag{3.42}$$

where

$$\mathbf{A} = \left(\mathbf{H}_{S22} + \mathbf{Q}_1 \mathbf{H}_{P22} \mathbf{Q}_2 \right)^{-1}. \tag{3.43}$$

The traction-free boundary condition at the free surface is satisfied by setting $\mathbf{p}_{FS} = \mathbf{0}$, which simplifies Eq. (3.42) to

$$\mathbf{p}_{SP}(\mathbf{x}, \omega) = \mathbf{A} \mathbf{Q}_1 \mathbf{H}_{P21} \mathbf{f}_{PH}. \tag{3.44}$$

By substituting Eq. (3.44) back into the governing equations, the following matrix equations are derived for the other variables:

$$\mathbf{f}_{P}(\mathbf{x}, \omega) = -\mathbf{Q}_2 \mathbf{A} \mathbf{Q}_1 \mathbf{H}_{P21} \mathbf{f}_{PH}, \tag{3.45}$$

$$\mathbf{u}_{P}(\mathbf{x}, \omega) = \left(\mathbf{H}_{P21} - \mathbf{H}_{P22} \mathbf{Q}_2 \mathbf{A} \mathbf{Q}_1 \mathbf{H}_{P21} \right) \mathbf{f}_{PH}, \tag{3.46}$$

$$\mathbf{u}_{PH}(\mathbf{x}, \omega) = \left(\mathbf{H}_{P11} - \mathbf{H}_{P12} \mathbf{Q}_2 \mathbf{A} \mathbf{Q}_1 \mathbf{H}_{P21} \right) \mathbf{f}_{PH}, \tag{3.47}$$

$$\mathbf{u}_{SP}(\mathbf{x}, \omega) = \mathbf{H}_{S22} \mathbf{A} \mathbf{Q}_1 \mathbf{H}_{P21} \mathbf{f}_{PH}, \tag{3.48}$$

$$\mathbf{u}_{FS}(\mathbf{x}, \omega) = \mathbf{H}_{S12} \mathbf{A} \mathbf{Q}_1 \mathbf{H}_{P21} \mathbf{f}_{PH}. \tag{3.49}$$

3.4 Validating the BEM Pile-Group Model

Talbot [221] shows there is good agreement over the frequency range of interest between the responses predicted using the BEM single-pile model and the static and dynamic compliance results published by Kuhlemeyer [143, 144] and Sen et al. [212]. Moreover, Talbot notes that although the square elements around the soil-pile interface do not directly account for the pile's axisymmetry, disturbances at the free surface appear as circular wavefronts around the pile. Coulier [42] also observes good agreement in his pile-group model by performing similar validation tests to Talbot for a single pile. Therefore, to avoid repetition, the BEM pile-group model developed in this chapter will not be validated for the case of a single pile.

Before the BEM pile-group model can be used to simulate the dynamics of a general piled foundation, the model has to be validated to check whether the equations of motion derived in Sections 3.1–3.3 can predict the inertial response of the simplest pile-group configuration: two neighbouring piles. Figure 3.3 shows two piles (1 and 2) that are embedded in a homogeneous half-space. Both piles have the same material and geometric parameters. By applying different unit-magnitude loads at the head of pile 1, the dynamic interaction factors α_{ij} that characterise the PSPI between piles 1 and 2 can be calculated [132]:

$$\alpha_{ij} = \frac{\text{Dynamic displacement } i \text{ at pile-head 2 due to load } j \text{ applied to pile-head 1}}{\text{Static displacement } i \text{ at pile-head 1 due to load } j \text{ applied to pile-head 1}}. \quad (3.50)$$

The time-harmonic pile-head displacement $\mathbf{u}_{\text{PH}}$ can be expressed as a function of the pile length L, the pile diameter d, the pile spacing s, the Young's modulus E, the mass density ρ, the Poisson's ratio ν, and the soil's shear modulus loss factor η_G:

$$\mathbf{u}_{\text{PH}} = f\left(L, d, s, \omega, E_p, E_s, \rho_p, \rho_s, \nu_p, \nu_s, \eta_G\right), \quad (3.51)$$

where the subscripts 'p' and 's' denote the respective material parameters for the pile and soil. Note, the soil's bulk modulus loss factor is not included in Eq. (3.51) because it is assumed that material damping only occurs through shear motion, as discussed in Section 2.3.1. After performing dimensional analysis on Eq. (3.51), the non-dimensional pile-head displacement, or α_{ij}, can be expressed as a function of eight non-dimensional groups:

$$\alpha_{ij} = g_{ij}\left(a_0, \frac{L}{d}, \frac{s}{d}, \frac{E_s}{E_p}, \frac{\rho_s}{\rho_p}, \nu_p, \nu_s, \eta_G\right), \quad (3.52)$$
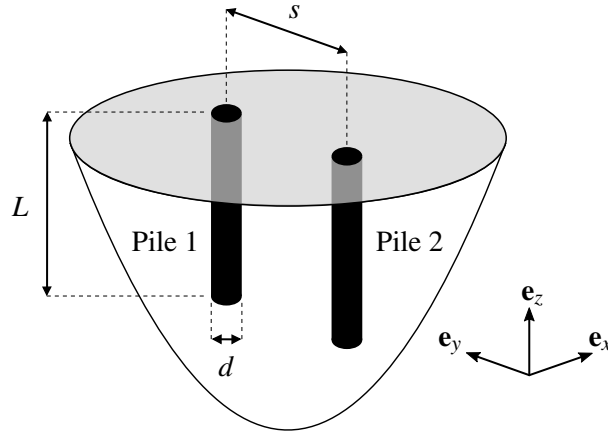
Fig. 3.3 Schematic diagram of two neighbouring piles embedded in a homogeneous half-space. The two piles are described by their length L, centre-to-centre spacing s, and diameter d.

where $a_0 = \omega d/c_S$ is the non-dimensional frequency, and $c_S = \left(\frac{E_s}{2(1+\nu_s)\rho_s}\right)^{1/2}$ is the phase speed of S-waves in the soil.

The dynamic interaction factors, predicted using the BEM pile-group model, are compared against the results published by Kaynia [132] for the following non-dimensional soil and pile parameters: $L/d = 15$, $s/d = 2$, $E_s/E_p = 10^{-3}$, $\rho_s/\rho_p = 0.7$, $\nu_p = 0.4$, $\nu_s = 0.25$, $\eta_G = 0.05$. In order to achieve the same non-dimensional parameters in the BEM model, the parameter values summarised in Table 3.1 are used to describe the soil and the piles. Based on the soil parameter values, the phase speeds of P- and S-waves in the soil are $c_P = 548$ m/s and $c_S = 224$ m/s, respectively.

The real and imaginary parts of nine dynamic interaction factors are plotted against a_0 in Fig. 3.4. Note that Kaynia's results are only available until $a_0 = 1.0$ (≈ 50 Hz), while the results for the BEM model are plotted up to $a_0 = 1.6$ (≈ 80 Hz) to ensure there are no irregularities over the entire frequency range of interest for ground-borne vibration (1-80 Hz).

Parameters [Units]	Soil	Piles
Young's modulus [Pa]	$E_s = 280 \times 10^6$	$E_p = 280 \times 10^9$
Poisson's ratio [$-$]	$\nu_s = 0.40$	$\nu_p = 0.25$
Density [kg/m^3]	$\rho_s = 2000$	$\rho_p = 2857$
Shear modulus loss factor [$-$]	$\eta_G = 0.05$	$-$
Length [m]	$-$	$L = 10.5$
Diameter [m]	$-$	$d = 0.71$

Table 3.1 Soil and pile parameter values used to validate the BEM pile-group model.

Mesh configuration	N_{FS}	N_{SP}	$N_T = N_{FS} + N_{SP}$	Run time [min]
1	88	170	258	5.7
2	238	170	408	12.5
3	460	170	630	30.1

Table 3.2 Mesh parameters of three different configurations used to validate the BEM pile-group model. The number of elements at the free surface and soil-pile interface are N_{FS} and N_{SP}, respectively. The run times correspond to a quadcore Intel i7-8550U (1.80 GHz) processor with 12 GB of RAM.

Table 3.2 shows the number of elements in three different mesh configurations, which are used in the BEM model to predict the dynamic interaction factors. The number of elements at the free surface and soil-pile interface are N_{FS} and N_{SP}, respectively. All three meshes contain the same square elements of size 0.5 m $\times$ 0.5 m to ensure that at least six elements per shear wavelength (S-wavelength) are used, as recommended by Domínguez [52].

In general, there is very good agreement between Kaynia's model and the BEM model in Fig. 3.4. This shows that the square elements in the boundary-element mesh are able to capture the PSPI and the circular wavefronts radiating outwards from the pile-group. The reciprocity relationships $\alpha_{u_x q_y} = \alpha_{\theta_y f_x}$ and $\alpha_{u_y q_x} = \alpha_{\theta_x f_y}$ are also satisfied [132]; however, there are small distortions between these dynamic interaction factors, which are most likely due to numerical errors when computing the soil displacement FRF matrix $\mathbf{H}_S$. Note that when $a_0 \approx 0$, all the interaction factors are purely real because the motion of the two piles are in-phase; this is expected when static pile-head loads are applied.

As the mesh configuration is varied, the largest differences in the interaction factors occur when $a_0 < 0.6$. This is because the long-wavelength waves at these low frequencies can leak around the sides of the unbounded mesh and radiate out to infinity if the number of free surface elements N_{FS} is low. The waves have a tendency to escape the half-space domain since the full-space Green's functions in the soil model are defined in an infinite domain. However, Table 3.2 shows that using more elements will cause the run time to significantly increase because more time is taken to compute the fully populated $\mathbf{H}_S$ matrix. Thus, it is recommended to initially run the model using a low value for N_{FS}, and then increase N_{FS} over multiple successive runs until a desired level of convergence is achieved in the interaction factors. This will ensure that a compromise is reached between two competing factors: the model's run time is minimised without limiting its numerical accuracy.
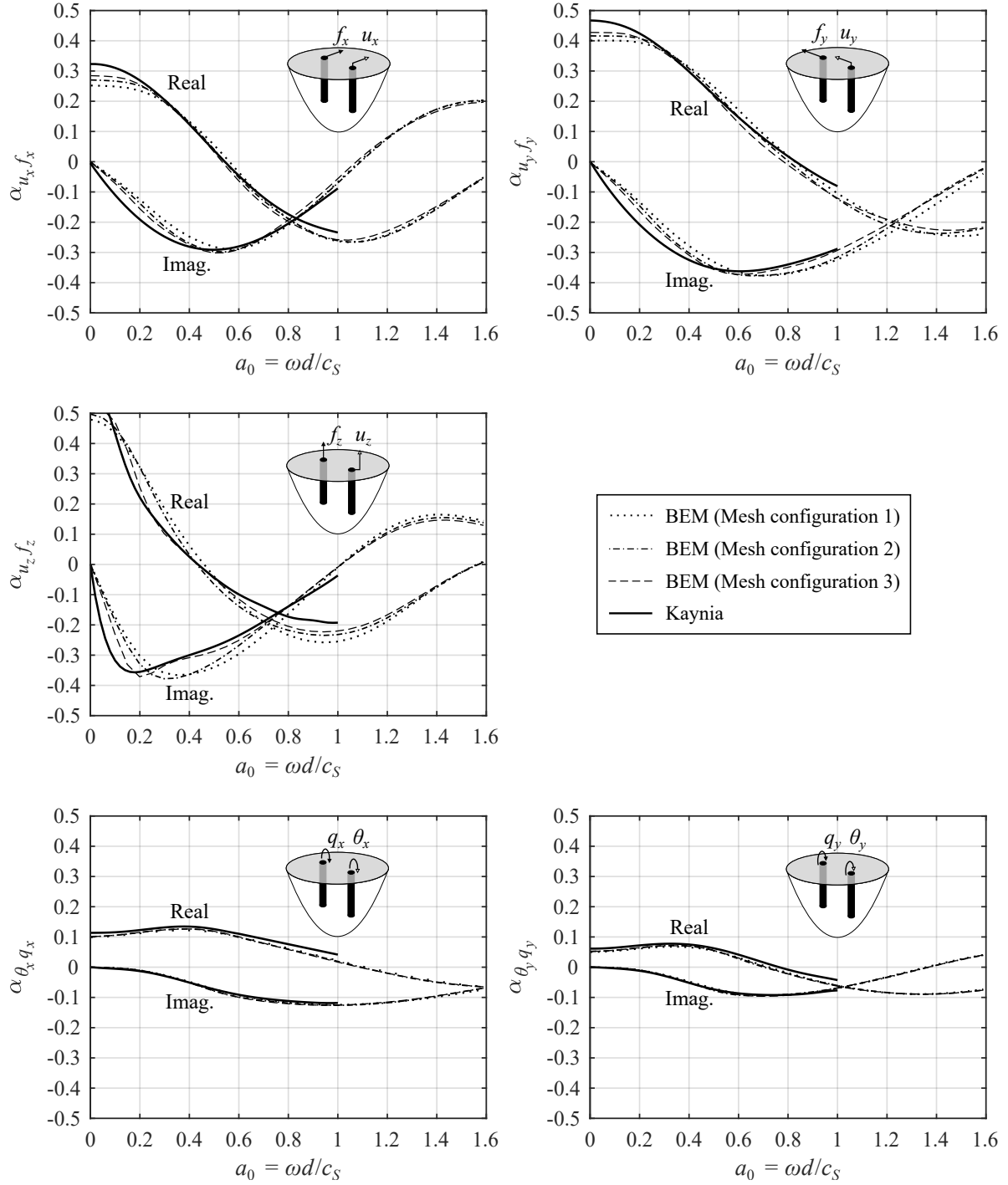
Fig. 3.4 Continues over page.
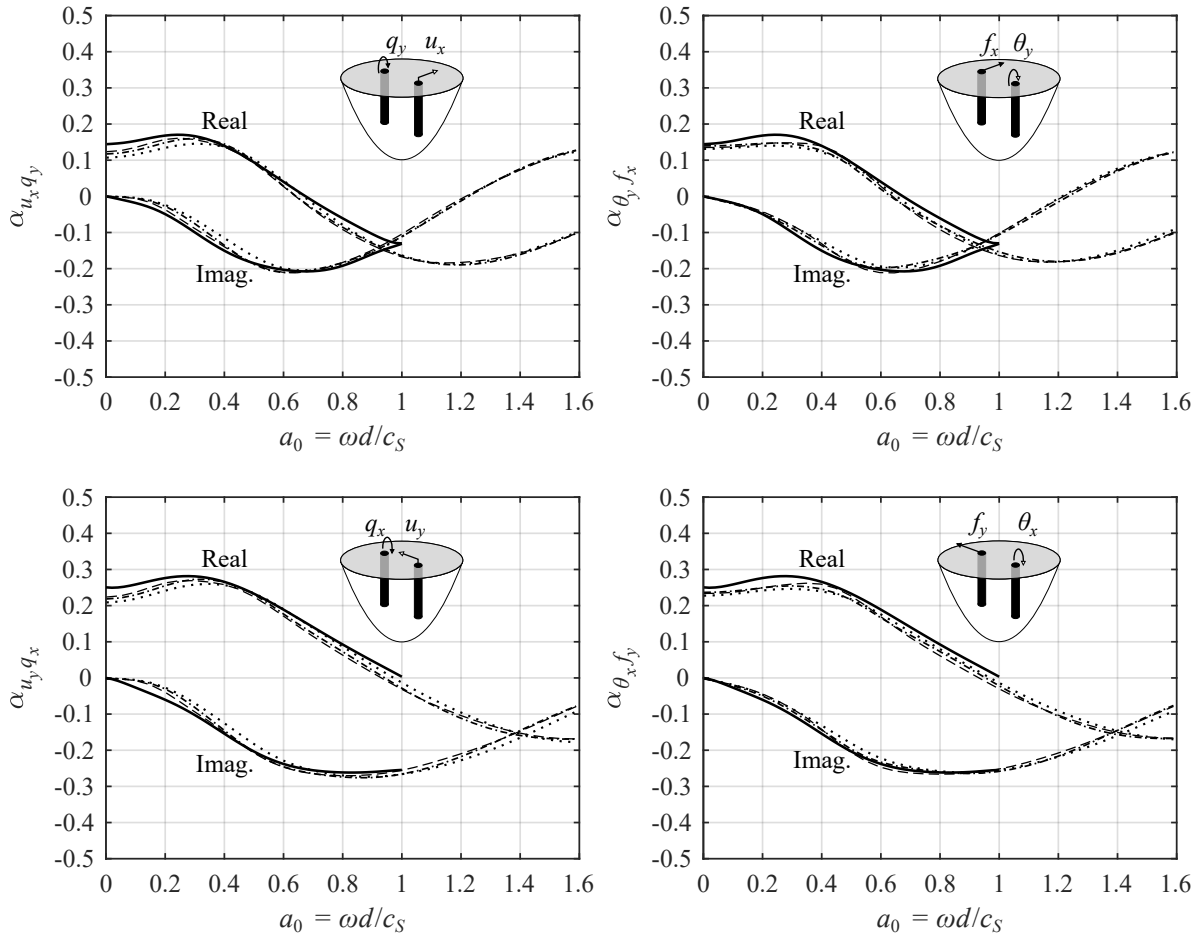
Fig. 3.4 The complex dynamic interaction factors α_{ij} of two neighbouring piles, plotted against non-dimensional frequency a_0. The responses are predicted using the BEM model, with mesh configurations 1, 2 and 3 in Table 3.2, and Kaynia's model. The non-dimensional soil and pile parameters are $L/d = 15$, $s/d = 2$, $E_s/E_p = 10^{-3}$, $\rho_s/\rho_p = 0.7$, $\nu_p = 0.4$, $\nu_s = 0.25$, and $\eta_G = 0.05$.

Figure 3.5 plots the real and imaginary parts of the lateral ($\alpha_{u_x f_x}$, $\alpha_{u_y f_y}$) and vertical ($\alpha_{u_z f_z}$) dynamic interaction factors published by Kaynia [132] against those calculated using the BEM model at different pile spacing ratios ($s/d = 2, 5, 10$). The same parameter values for the soil and pile, as given in Table 3.1, are used along with mesh configuration 3 from Table 3.2. Again, there is good agreement between the BEM model and Kaynia's model over the frequency range $0 < a_0 < 1$. Note that, as s/d is increased, there is a decrease in the magnitude of the interaction factors because there is more wave attenuation due to radiation damping in the soil when the piles are spaced further apart.
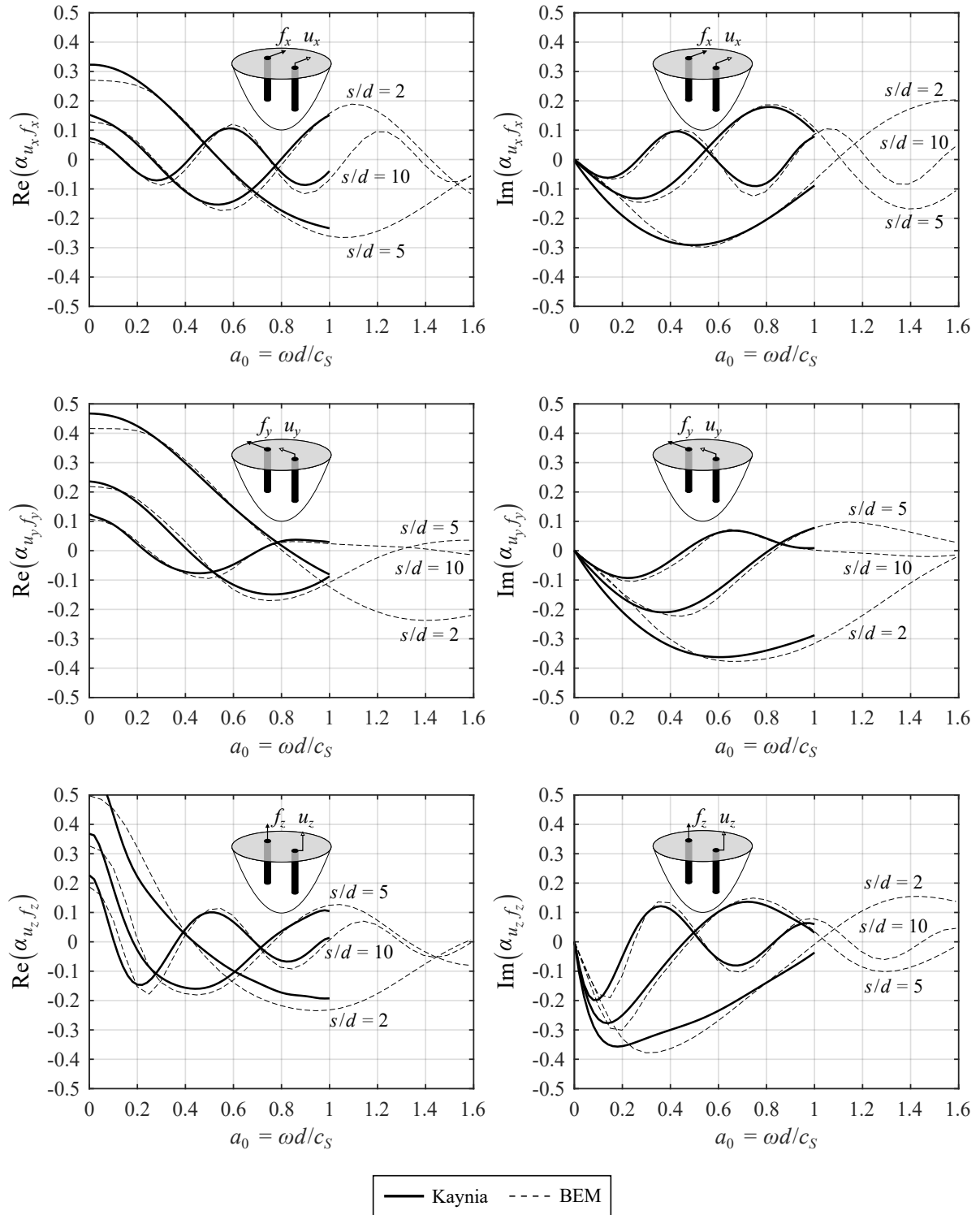
Fig. 3.5 The real (left) and imaginary (right) parts of the lateral $(\alpha_{u_x f_x}, \alpha_{u_y f_y})$ and vertical $(\alpha_{u_z f_z})$ dynamic interaction factors of two neighbouring piles, plotted against non-dimensional frequency a_0. The influence of the pile spacing ratio s/d on the response, predicted using Kaynia's model and the BEM model, is illustrated. The non-dimensional soil and pile parameters are $L/d = 15$, $E_s/E_p = 10^{-3}$, $\rho_s/\rho_p = 0.7$, $\nu_p = 0.4$, $\nu_s = 0.25$, and $\eta_G = 0.05$.

3.5 Conclusions

A piled foundation model has been developed in Sections 3.1–3.3 that can account for both the dynamics of each pile and the PSPI between multiple piles. Each pile was discretised into bar-beam elements along its centroidal axis to analytically compute the pile displacement FRF matrix. The soil displacement FRF matrix was calculated numerically using the BEM once the soil-pile interface and free surface were discretised into constant, square elements in the mesh. Each pile was then coupled to the soil by extending Talbot's single-pile model [221] so that the governing matrix equations for a pile embedded in a homogeneous half-space were rewritten in terms of block-diagonal matrices. Hence, the governing matrix equations for a pile-group with N embedded piles can be computed using a generalised set of algebraic expressions.

The BEM pile-group model was validated against Kaynia's model [132] in Section 3.4 by comparing the complex dynamic interaction factors of two neighbouring piles, plotted against the non-dimensional frequency a_0. Over the non-dimensional frequency range used by Kaynia, there was very good agreement between the two models, and the interaction factors predicted using the BEM model did not exhibit any frequency-dependent irregularities. Furthermore, the results for the different mesh configurations showed that the number of free-surface elements in the BEM model must be appropriately selected to ensure that the model's accuracy, over the frequency range of interest, is not compromised by its computational efficiency.

Throughout the remainder of this dissertation, the validated BEM pile-group model is used to predict the fundamental dynamics of a piled foundation due to ground-borne vibration.

Chapter 4

The Wave-Scattering Effect of a Pile-Group

When a pile-group experiences inertial excitation, dynamic interaction factors are often used to characterise the PSPI between pairs of piles, as detailed in Section 2.5.3. In most studies, these interaction factors are found using uncoupled source-receiver models and coupled models.

Dobry & Gazetas [51], Gazetas & Makris [78], and Makris & Gazetas [164] derived semi-analytical solutions for the interaction factors by representing a pair of piles as an uncoupled source-receiver system. By applying the sub-system technique, each pile in the pair is regarded as an isolated sub-system. The source sub-system only simulates the excited pile and calculates the response of the surrounding soil in the absence of the second pile (the receiver). The wave-field propagating away from the source, assuming the receiver does not influence the waves, is applied as an incident excitation on the receiver sub-system. However, this approach cannot capture the wave scattering at high frequencies when the receiver is able to scatter the incident wave-field, which, in turn, can propagate back to excite the source. The receiver can also affect the wave-field propagating away from the source if the piles are closer together. This can even occur at low frequencies if the pressure bulb of the source, where the soil stresses (and strains) are significant, also encloses the receiver.

The alternative approach is to model the entire pile-group as a fully coupled system, which directly accounts for the PSPI. Kaynia & Kausel [132, 134] developed a boundary-integral-type formulation to derive the pile-group response. Generally, there is good agreement between this model and uncoupled source-receiver models. However, the interaction factors are presented over non-dimensional frequencies that do not extend to the high-frequency content of ground-borne vibration. Another concern is that the soil's flexibility matrix is computed by superposing a 'fictitious' column onto the soil at the location of each pile, such that the flexural and inertial

properties of the composite solid (i.e., the column and soil) are equivalent to the pile. Thus, the soil cavity around the pile is not represented, and this can lead to inaccuracies in the results at high frequencies, as concluded by Mamoon et al. [166].

The main objective of this chapter is to investigate whether dynamic interaction factors can effectively characterise the PSPI caused by the wave-scattering effect at high frequencies. Two different techniques are used to account for the PSPI: (1) the coupled BEM pile-group model developed in Chapter 3, and (2) an iterative BEM model. The pile-group in the iterative model is divided into two isolated sub-systems (the source and the receiver), which are then coupled together using the iterative wave-scattering approach. Compared to Chapter 3, the results in this chapter are presented over a broader range of non-dimensional frequencies, which correspond to ground-borne vibration between 1 and 160 Hz in London Clay. Although the iterative model does not offer additional computational benefits compared to the coupled model, this chapter serves as an initial study to explore if the iterative approach can solve a manageable problem involving multiple piles. Later, in Chapter 6, the iterative approach is used to solve the more complex problem of wave interaction between an underground railway tunnel and a foundation.

Most of the work in this chapter has been published in a journal paper by Edirisinghe & Talbot [56]. The chapter begins with Section 4.1, which outlines the wave-scattering approach adopted in the iterative BEM model to capture the coupling between the source and receiver sub-systems in a pile-group. Sections 4.2 and 4.3 use the BEM described in Appendix B.7 to derive the equations of motion for the two sub-systems under inertial excitation. A convergence study is conducted in Section 4.4 so as to determine the mesh resolution required to maintain accuracy at frequencies above 80 Hz. Then, the iterative BEM model is validated against the coupled BEM model in Section 4.5. Section 4.6 presents an extensive parametric study, where the influence of various material and geometric parameters on the wave-scattering effect of pile-groups is explored. Finally, the main conclusions of the chapter are given in Section 4.7.

4.1 The Iterative Wave-Scattering Approach

The iterative wave-scattering approach, detailed in Section 2.5.1, can account for the interaction between the scattered wave-fields induced around a source and a receiver. For a general pile-group, the excited pile is referred to as the source sub-system, while all the other piles in the group are collectively referred to as the receiver sub-system.

The first iteration only accounts for the initial 'outgoing' wave-field from the source that interacts with the receiver; this is equivalent to using an uncoupled source-receiver model. In the second iteration, the 'incoming' wave-field that propagates back towards the source, due to the scattered wave-field at the receiver, is computed. The motion of the source, due to both the pile-head load and the incident wave-field from the receiver, causes another incident wave-field to propagate towards the receiver, which revises the response of the two piles compared to the first iteration. During each iteration, the source and receiver are thus 'weakly' coupled. When this process is repeated for multiple iterations, the response converges to the solution for when the source and receiver are fully coupled. An advantage of this approach, compared to a coupled system, is that it gives further insight into the wave-scattering behaviour. That is to say, if multiple iterations are required to converge to the coupled solution, then the wave-scattering effect is clearly more significant than if only one iteration is required.
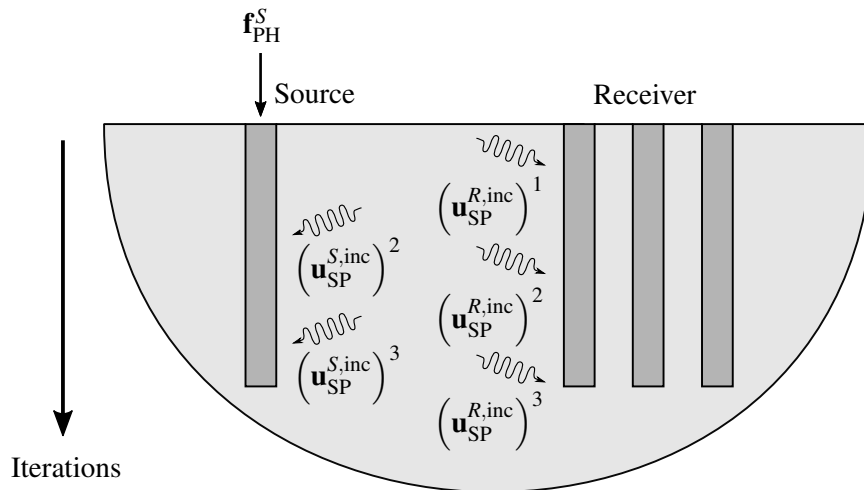
Fig. 4.1 Schematic diagram illustrating the implementation of the iterative wave-scattering approach for a pile-group with four piles. The pile-group is divided into a source and receiver sub-system.
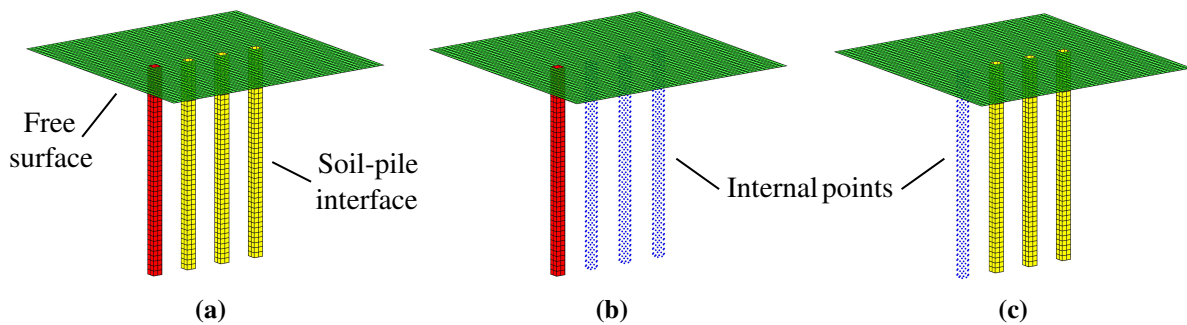
Fig. 4.2 The pile-group in Fig. 4.1 can be modelled using the following meshes: **(a)** the complete pile-group in the coupled BEM model, and **(b)** the source and **(c)** the receiver sub-systems in the iterative BEM model. The coloured elements represent the free surface (green), and the soil-pile interfaces of the source (red) and receiver (yellow). The blue dots represent internal points within each sub-system.

The schematic diagram in Fig. 4.1 illustrates the incident displacement wave-fields at the source $\left(\mathbf{u}_{\mathrm{SP}}^{S,\mathrm{inc}}\right)^{i}$ and receiver $\left(\mathbf{u}_{\mathrm{SP}}^{R,\mathrm{inc}}\right)^{i}$ sub-systems for a pile-group with four piles, which are computed during each iteration i. The incident traction wave-fields at the source $\left(\mathbf{p}_{\mathrm{SP}}^{S,\mathrm{inc}}\right)^{i}$ and receiver $\left(\mathbf{p}_{\mathrm{SP}}^{R,\mathrm{inc}}\right)^{i}$ sub-systems are computed using a similar approach. The meshes used in the coupled and iterative BEM models are shown in Fig. 4.2. The mesh for the source sub-system (Fig. 4.2b) contains N_{FS}^{S} free surface elements and N_{SP}^{S} soil-pile interface elements, while the receiver sub-system's mesh (Fig. 4.2c) contains N_{FS}^{R} and N_{SP}^{S} elements for the free surface and soil-pile interface, respectively. Internal points within the mesh of a sub-system are used to evaluate the incident wave-fields that approach the soil-pile interface of the other sub-system. Note that the free surface in the source and receiver meshes is discretised to the same extent to account for the zero traction boundary condition.

The following two sections derive the incident wave-fields at the receiver and source for each iteration. For clarity, the superscript 'i', which denotes the iteration of the revised wave-fields, is omitted.

4.2 The Source Sub-System of the Iterative BEM Model

This section derives the equations for the scattered wave-fields at the source sub-system, when it is excited in isolation, and the incident wave-fields that arrive, as a consequence, at the soil-pile interface of the receiver. Figure 4.3 shows the meshes for the source sub-system in a 1×2 pile-group, where mesh 1 is used to perturb the source (pile 1) and mesh 2 is used to evaluate the incident wave-fields at the soil-pile interface of the receiver (pile 2). The free surface and soil-pile interface of pile 1 are discretised in meshes 1 and 2. Mesh 2 also discretises the soil-pile interface of pile 2 as internal points within the unbounded domain of the source sub-system.

By applying the superposition principle, the total displacement wave-field at pile 1's soil-pile interface $\mathbf{u}_{\mathrm{SP}}^{1}$ can be decomposed into a scattered wave-field $\mathbf{u}_{\mathrm{SP}}^{1,\mathrm{sca}}$ and an incident wave-field $\mathbf{u}_{\mathrm{SP}}^{1,\mathrm{inc}}$, such that $\mathbf{u}_{\mathrm{SP}}^{1} = \mathbf{u}_{\mathrm{SP}}^{1,\mathrm{sca}} + \mathbf{u}_{\mathrm{SP}}^{1,\mathrm{inc}}$. Likewise, the traction wave-field at pile 1's soil-pile interface can be decomposed as follows: $\mathbf{p}_{\mathrm{SP}}^{1} = \mathbf{p}_{\mathrm{SP}}^{1,\mathrm{sca}} + \mathbf{p}_{\mathrm{SP}}^{1,\mathrm{inc}}$. This decomposition allows the scattered wave-field at pile 1 to be computed when an incident wave-field approaches pile 1.

When the BEM is applied by using mesh 1 for the unbounded domain's surface, the soil displacement FRF matrix $\mathbf{H}_{\mathrm{S}}^{1}$ around pile 1 can be derived, as detailed in Section 3.2.1. Thus, the scattered displacement and traction wave-fields at the mesh boundaries can be expressed as
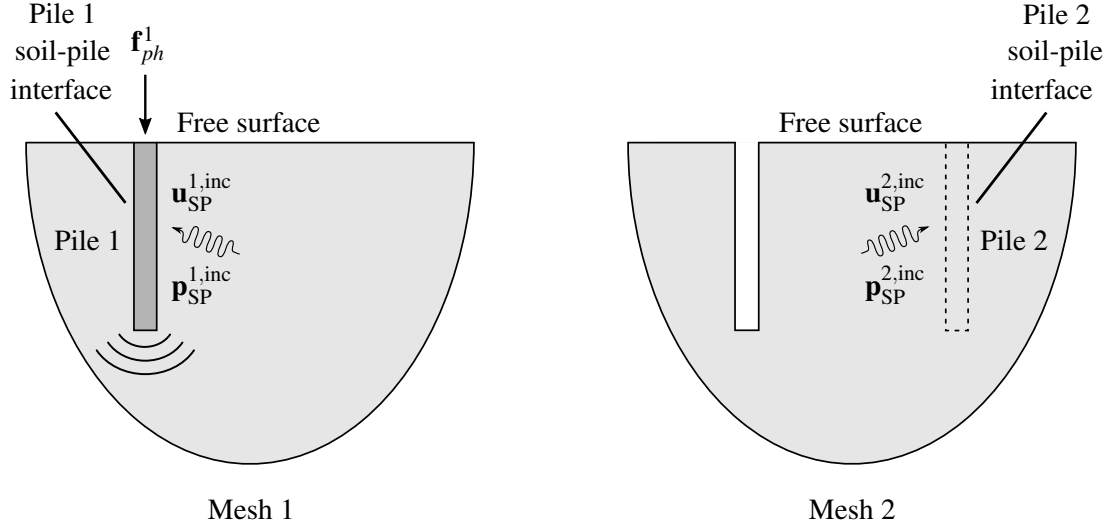
Fig. 4.3 An example of the meshes used for the unbounded domain of the isolated source sub-system in a 1×2 pile-group. Internal points within the source's domain lie along the dashed line in mesh 2. The darker and lighter shaded regions represent pile and soil material, respectively.

$$\left\{ \begin{array}{c} \mathbf{u}_{FS}^1 \\ \mathbf{u}_{SP}^1 - \mathbf{u}_{SP}^{1,inc} \end{array} \right\} = \mathbf{H}_S^1 \left\{ \begin{array}{c} \mathbf{p}_{FS}^1 \\ \mathbf{p}_{SP}^1 - \mathbf{p}_{SP}^{1,inc} \end{array} \right\}, \tag{4.1}$$

where $\mathbf{u}_{FS}^1$ and $\mathbf{p}_{FS}^1 = \mathbf{0}$ denote the displacement wave-field and the traction-free boundary condition, respectively, at the free surface surrounding pile 1. There are no incident wave-fields at the free surface because the same extent of the free surface is discretised in both meshes. The $\mathbf{H}_S^1$ matrix can be partitioned into four sub-matrices:

$$\left\{ \begin{array}{c} \mathbf{u}_{FS}^1 \\ \mathbf{u}_{SP}^1 - \mathbf{u}_{SP}^{1,inc} \end{array} \right\} = \begin{bmatrix} \mathbf{H}_{S11}^1 & \mathbf{H}_{S12}^1 \\ \mathbf{H}_{S21}^1 & \mathbf{H}_{S22}^1 \end{bmatrix} \left\{ \begin{array}{c} \mathbf{0} \\ \mathbf{p}_{SP}^1 - \mathbf{p}_{SP}^{1,inc} \end{array} \right\}. \tag{4.2}$$

Since pile 1 represents the source in a general pile-group, the superscript '1' can be replaced by 'S' to denote this. Equation (4.2) can be separated into the following two governing matrix equations for the soil surrounding the isolated source:

$$\mathbf{u}_{FS}^S = \mathbf{H}_{S12}^S \left(\mathbf{p}_{SP}^S - \mathbf{p}_{SP}^{S,inc} \right), \tag{4.3}$$

$$\mathbf{u}_{SP}^S - \mathbf{u}_{SP}^{S,inc} = \mathbf{H}_{S22}^S \left(\mathbf{p}_{SP}^S - \mathbf{p}_{SP}^{S,inc} \right). \tag{4.4}$$

The soil is coupled to the source pile at the soil-pile interface by satisfying equilibrium and compatibility conditions at the respective boundary, as described in Section 3.3. Hence,

the displacement and traction wave-fields at the discretised boundary surface of the isolated source can be found, which are referred to as the boundary values. The matrix equation for the boundary value $\mathbf{p}_{SP}^S$, as a function of the excitation $\left(\mathbf{f}_{PH}^S, \mathbf{u}_{SP}^{S,inc}, \mathbf{p}_{SP}^{S,inc} \right)$ at the source, is

$$\mathbf{p}_{SP}^S(\mathbf{x}, \omega) = \mathbf{A}^S \left(\mathbf{Q}_1^S \mathbf{H}_{P21}^S \mathbf{f}_{PH}^S + \mathbf{H}_{S22}^S \mathbf{p}_{SP}^{S,inc} - \mathbf{u}_{SP}^{S,inc} \right), \tag{4.5}$$

where the block-diagonal matrices $\mathbf{A}^S$, $\mathbf{Q}_1^S$ and $\mathbf{H}_{P21}^S$ for the isolated source are of a similar form to the block-diagonal matrices defined in Chapter 3. The other boundary values, $\mathbf{u}_{FS}^S$ and $\mathbf{u}_{SP}^S$, can be computed by substituting Eq. (4.5) into Eqs. (4.3) and (4.4), respectively:

$$\mathbf{u}_{FS}^S(\mathbf{x}, \omega) = \mathbf{H}_{S12}^S \mathbf{A}^S \left(\mathbf{Q}_1^S \mathbf{H}_{P21}^S \mathbf{f}_{PH}^S - \mathbf{u}_{SP}^{S,inc} \right) + \mathbf{H}_{S12}^S \left(\mathbf{A}^S \mathbf{H}_{S22}^S - \mathbf{I} \right) \mathbf{p}_{SP}^{S,inc}, \tag{4.6}$$

$$\mathbf{u}_{SP}^S(\mathbf{x}, \omega) = \mathbf{H}_{S22}^S \mathbf{A}^S \mathbf{Q}_1^S \mathbf{H}_{P21}^S \mathbf{f}_{PH}^S + \left(\mathbf{H}_{S22}^S \mathbf{A}^S - \mathbf{I} \right) \left(\mathbf{H}_{S22}^S \mathbf{p}_{SP}^{S,inc} - \mathbf{u}_{SP}^{S,inc} \right), \tag{4.7}$$

where $\mathbf{I}$ is the identity matrix.

It is important to note that, for the first iteration, there are no incident wave-fields at the soil-pile interface of the source ($\mathbf{u}_{SP}^{S,inc} = \mathbf{p}_{SP}^{S,inc} = \mathbf{0}$) because the receiver has not yet been excited. For all subsequent iterations, the expressions for $\mathbf{u}_{SP}^{S,inc}$ and $\mathbf{p}_{SP}^{S,inc}$ are derived later in Section 4.3, as shown in Eqs. (4.19) and (4.20), respectively.

Once the boundary values are known for the source excited in isolation, the incident wave-fields that propagate through the soil towards the soil-pile interface of the receiver need to be evaluated. The BEM described in Appendix B.7 is used to compute these incident wave-fields, with the receiver's soil-pile interface regarded as a group of internal points within the domain of the source sub-system.

It is worth noting that the internal points are regarded solely as integration points, and only the boundary surface of the source sub-system is discretised as collocation points in the integral formulation (see Appendix B.7). The number of integration and collocation points are also not constrained to be equal, so it is possible to obtain non-square matrices. In contrast, the BEM that is used to solve the boundary values at the domain's surface (see Appendix B.6), uses the same elements for both the collocation and integration points, so the resulting FRF matrices are always square.

The general relationship between the displacement wave-field $\mathbf{u}^{int}$ at internal points and the boundary values $\mathbf{u}$ and $\mathbf{p}$ is derived in Appendix B.7, which is repeated here for convenience:

$$\mathbf{u}^{int} = \mathbf{G}_u \mathbf{p} - \mathbf{H}_u \mathbf{u}, \tag{4.8}$$

where $\mathbf{G}_u$ and $\mathbf{H}_u$ are the displacement-state matrices. The relationship between the traction wave-field $\mathbf{p}^{\text{int}}$ at internal points and the boundary values is also derived in Appendix B.7:

$$\mathbf{p}^{\text{int}} = \mathbf{G}_p \mathbf{p} - \mathbf{H}_p \mathbf{u}, \tag{4.9}$$

where $\mathbf{G}_p$ and $\mathbf{H}_p$ are the traction-state matrices. After discretising the boundary surface of the source sub-system into elements and the receiver's soil-pile interface into internal points, Eqs. (4.8) and (4.9) can be used to calculate the incident displacement $\mathbf{u}_{\text{SP}}^{R,\text{inc}}$ and traction $\mathbf{p}_{\text{SP}}^{R,\text{inc}}$ wave-fields arriving at all $N-1$ piles in the receiver:

$$\mathbf{u}_{\text{SP}}^{R,\text{inc}}(\mathbf{x}, \omega) = \begin{Bmatrix} \mathbf{u}_{\text{SP}}^{2,\text{inc}} \\ \mathbf{u}_{\text{SP}}^{3,\text{inc}} \\ \vdots \\ \mathbf{u}_{\text{SP}}^{N,\text{inc}} \end{Bmatrix} = \mathbf{G}_u^{RS} \begin{Bmatrix} \mathbf{0} \\ \mathbf{p}_{\text{SP}}^{S} \end{Bmatrix} - \mathbf{H}_u^{RS} \begin{Bmatrix} \mathbf{u}_{\text{FS}}^{S} \\ \mathbf{u}_{\text{SP}}^{S} \end{Bmatrix}, \tag{4.10}$$

$$\mathbf{p}_{\text{SP}}^{R,\text{inc}}(\mathbf{x}, \omega) = \begin{Bmatrix} \mathbf{p}_{\text{SP}}^{2,\text{inc}} \\ \mathbf{p}_{\text{SP}}^{3,\text{inc}} \\ \vdots \\ \mathbf{p}_{\text{SP}}^{N,\text{inc}} \end{Bmatrix} = \mathbf{G}_p^{RS} \begin{Bmatrix} \mathbf{0} \\ \mathbf{p}_{\text{SP}}^{S} \end{Bmatrix} - \mathbf{H}_p^{RS} \begin{Bmatrix} \mathbf{u}_{\text{FS}}^{S} \\ \mathbf{u}_{\text{SP}}^{S} \end{Bmatrix}, \tag{4.11}$$

where the superscript 'RS' denotes that the transfer functions in the displacement-state and traction-state matrices relate to the propagation of wave-fields from the source to the receiver. The dimensions of all matrices in Eqs. (4.10) and (4.11) are $3N_{\text{SP}}^{R} \times 3\left(N_{\text{FS}}^{S} + N_{\text{SP}}^{S}\right)$.

4.3 The Receiver Sub-System of the Iterative BEM Model

This section derives the equations for the scattered wave-fields at the receiver sub-system, when it is excited in isolation by the source, and the resulting incident wave-fields that arrive at the soil-pile interface of the source. Figure 4.4 shows the meshes used for the receiver sub-system in a pile-group containing two piles, where mesh 3 is used to perturb the receiver (pile 2) and mesh 4 is used to find the incident wave-fields at the soil-pile interface of the source (pile 1). The free surface and soil-pile interface of pile 2 are discretised in meshes 3 and 4. Mesh 4 also discretises the soil-pile interface of pile 1 as internal points within the unbounded domain of the receiver sub-system.
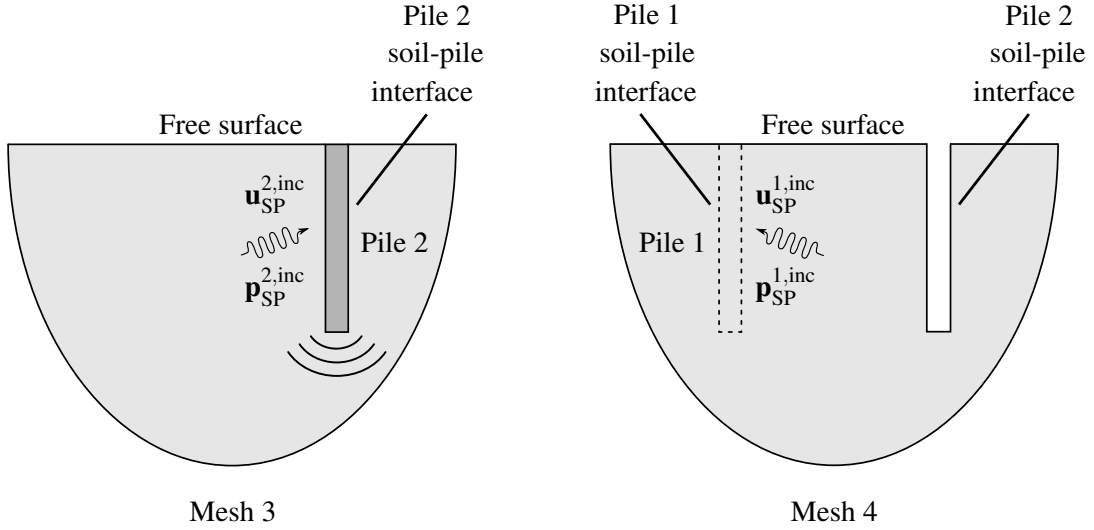
Fig. 4.4 An example of the meshes used for the unbounded domain of the isolated receiver sub-system in a 1×2 pile-group. Internal points within the receiver's domain lie along the dashed line in mesh 4. The darker and lighter shaded regions represent pile and soil material, respectively.

When the BEM is applied by using mesh 3 for the unbounded domain's surface, the soil displacement FRF matrix $\mathbf{H}_\mathrm{S}^2$ around pile 2 can be derived. Similar to Eqs. (4.1) and (4.2), $\mathbf{H}_\mathrm{S}^2$ can be partitioned into four sub-matrices:

$$\left\{ \begin{array}{c} \mathbf{u}_\mathrm{FS}^2 \\ \mathbf{u}_\mathrm{SP}^2 - \mathbf{u}_\mathrm{SP}^{2,\mathrm{inc}} \end{array} \right\} = \begin{bmatrix} \mathbf{H}_\mathrm{S11}^2 & \mathbf{H}_\mathrm{S12}^2 \\ \mathbf{H}_\mathrm{S21}^2 & \mathbf{H}_\mathrm{S22}^2 \end{bmatrix} \left\{ \begin{array}{c} \mathbf{p}_\mathrm{FS}^2 \\ \mathbf{p}_\mathrm{SP}^2 - \mathbf{p}_\mathrm{SP}^{2,\mathrm{inc}} \end{array} \right\}, \tag{4.12}$$

where $\mathbf{u}_\mathrm{FS}^2$ and $\mathbf{p}_\mathrm{FS}^2 = \mathbf{0}$ denote the displacement wave-field and the traction-free boundary condition, respectively, at the free surface surrounding pile 2. Based on the reasoning given in the previous section, there are again no incident wave-fields at the free surface.

When Eq. (4.12) is extended for a pile-group receiver with $N-1$ cavities, the resulting soil displacement FRF matrix $\mathbf{H}_\mathrm{S}^R$ around the receiver can be partitioned into four sub-matrices:

$$\left\{ \begin{array}{c} \mathbf{u}_\mathrm{FS}^R \\ \mathbf{u}_\mathrm{SP}^2 - \mathbf{u}_\mathrm{SP}^{2,\mathrm{inc}} \\ \vdots \\ \mathbf{u}_\mathrm{SP}^N - \mathbf{u}_\mathrm{SP}^{N,\mathrm{inc}} \end{array} \right\} = \begin{bmatrix} \mathbf{H}_\mathrm{S11}^R & \mathbf{H}_\mathrm{S12}^R \\ \mathbf{H}_\mathrm{S21}^R & \mathbf{H}_\mathrm{S22}^R \end{bmatrix} \left\{ \begin{array}{c} \mathbf{p}_\mathrm{FS}^R \\ \mathbf{p}_\mathrm{SP}^2 - \mathbf{p}_\mathrm{SP}^{2,\mathrm{inc}} \\ \vdots \\ \mathbf{p}_\mathrm{SP}^N - \mathbf{p}_\mathrm{SP}^{N,\mathrm{inc}} \end{array} \right\}. \tag{4.13}$$

Equation (4.13) can be separated into the following two governing matrix equations for the soil surrounding the isolated receiver:

$$\mathbf{u}_{FS}^{R} = \mathbf{H}_{S12}^{R} \left(\mathbf{p}_{SP}^{R} - \mathbf{p}_{SP}^{R,\text{inc}} \right), \tag{4.14}$$

$$\mathbf{u}_{SP}^{R} - \mathbf{u}_{SP}^{R,\text{inc}} = \mathbf{H}_{S22}^{R} \left(\mathbf{p}_{SP}^{R} - \mathbf{p}_{SP}^{R,\text{inc}} \right), \tag{4.15}$$

where the wave-fields at the receiver's soil-pile interface are denoted by the following four vectors: $\mathbf{u}_{SP}^{R,\text{inc}} = \left\{ \mathbf{u}_{SP}^{2,\text{inc}}, \ldots, \mathbf{u}_{SP}^{N,\text{inc}} \right\}^{\text{T}}$, $\mathbf{p}_{SP}^{R,\text{inc}} = \left\{ \mathbf{p}_{SP}^{2,\text{inc}}, \ldots, \mathbf{p}_{SP}^{N,\text{inc}} \right\}^{\text{T}}$, $\mathbf{u}_{SP}^{R} = \left\{ \mathbf{u}_{SP}^{2}, \ldots, \mathbf{u}_{SP}^{N} \right\}^{\text{T}}$, and $\mathbf{p}_{SP}^{R} = \left\{ \mathbf{p}_{SP}^{2}, \ldots, \mathbf{p}_{SP}^{N} \right\}^{\text{T}}$.

The soil is coupled to the pile-group receiver at its soil-pile interface by applying the same approach detailed in Section 3.3. Note that the off-diagonal components in the sub-matrix $\mathbf{H}_{S22}^{R}$ inherently account for the PSPI within the pile-group receiver when the soil is coupled to the piles. Once the soil and piles are coupled together, the boundary values at the isolated receiver can be found. The matrix equation for the boundary value $\mathbf{p}_{SP}^{R}$, as a function of the excitation $\left(\mathbf{u}_{SP}^{R,\text{inc}}, \mathbf{p}_{SP}^{R,\text{inc}} \right)$ at the receiver, is

$$\mathbf{p}_{SP}^{R}(\mathbf{x}, \omega) = \mathbf{A}^{R} \left(\mathbf{H}_{S22}^{R} \mathbf{p}_{SP}^{R,\text{inc}} - \mathbf{u}_{SP}^{R,\text{inc}} \right), \tag{4.16}$$

where the matrix $\mathbf{A}^{R}$ for the isolated receiver is of a similar form to $\mathbf{A}$ in Eq. (3.43). The other boundary values, $\mathbf{u}_{FS}^{R}$ and $\mathbf{u}_{SP}^{R}$, are found by substituting Eq. (4.16) into Eqs. (4.14) and (4.15), respectively:

$$\mathbf{u}_{FS}^{R}(\mathbf{x}, \omega) = \mathbf{H}_{S12}^{R} \mathbf{A}^{R} \left(\mathbf{u}_{SP}^{R,\text{inc}} \right) + \mathbf{H}_{S12}^{R} \left(\mathbf{A}^{R} \mathbf{H}_{S22}^{R} - \mathbf{I} \right) \mathbf{p}_{SP}^{R,\text{inc}}, \tag{4.17}$$

$$\mathbf{u}_{SP}^{R}(\mathbf{x}, \omega) = \left(\mathbf{H}_{S22}^{R} \mathbf{A}^{R} - \mathbf{I} \right) \left(\mathbf{H}_{S22}^{R} \mathbf{p}_{SP}^{R,\text{inc}} - \mathbf{u}_{SP}^{R,\text{inc}} \right), \tag{4.18}$$

where $\mathbf{I}$ is the identity matrix.

Once the boundary values at the isolated receiver are known, the BEM is used to find the incident wave-fields within the receiver's domain. This is achieved by discretising the boundary surface of the receiver sub-system into boundary elements and the source's soil-pile interface into internal points. Therefore, the same relationships in Eqs. (4.8) and (4.9) can be applied to find the incident displacement $\mathbf{u}_{SP}^{S,\text{inc}}$ and traction $\mathbf{p}_{SP}^{S,\text{inc}}$ wave-fields, respectively, at the soil-pile interface of the source pile:

$$\mathbf{u}_{SP}^{S,\text{inc}}(\mathbf{x}, \omega) = \mathbf{u}_{SP}^{1,\text{inc}} = \mathbf{G}_{u}^{SR} \begin{Bmatrix} \mathbf{0} \\ \mathbf{p}_{SP}^{R} \end{Bmatrix} - \mathbf{H}_{u}^{SR} \begin{Bmatrix} \mathbf{u}_{FS}^{R} \\ \mathbf{u}_{SP}^{R} \end{Bmatrix}, \tag{4.19}$$

$$\mathbf{p}_{\text{SP}}^{S,\text{inc}}(\mathbf{x},\omega) = \mathbf{p}_{\text{SP}}^{1,\text{inc}} = \mathbf{G}_p^{SR} \begin{Bmatrix} \mathbf{0} \\ \mathbf{p}_{\text{SP}}^R \end{Bmatrix} - \mathbf{H}_p^{SR} \begin{Bmatrix} \mathbf{u}_{\text{FS}}^R \\ \mathbf{u}_{\text{SP}}^R \end{Bmatrix}, \tag{4.20}$$

where the superscript 'SR' denotes that the transfer functions in the displacement-state and traction-state matrices relate to the propagation of wave-fields from the receiver to the source. The dimensions of all matrices in Eqs. (4.19) and (4.20) are $3N_{\text{SP}}^S \times 3\left(N_{\text{FS}}^R + N_{\text{SP}}^R\right)$.

4.4 A Convergence Study of the Boundary-Element Mesh

In order to simulate the pile-group dynamics over a broader range of frequencies (from 1 to 160 Hz), the boundary-element mesh of the soil model must be discretised to an appropriate level of resolution. Therefore, a convergence study is conducted in this section to identify the mesh resolution required to maintain accuracy over the entire frequency range of interest. The mesh must satisfy the following two conditions: (1) the elements at the soil-pile interface can accurately account for soil-pile interaction; and (2) the elements at the free surface can capture the concentric, circular wavefronts that appear around the pile.

The first condition can be investigated by comparing the compliance functions of a single pile. In the available literature, dynamic compliance functions are obtained by normalising the driving-point displacement FRFs at the pile head with respect to their static values:

$$F_{ij} = \frac{\text{Dynamic driving-point displacement } i \text{ at the pile-head due to load } j}{\text{Static driving-point displacement } i \text{ at the pile-head due to load } j}. \tag{4.21}$$

8-element square section   8-element octagonal section   16-element section
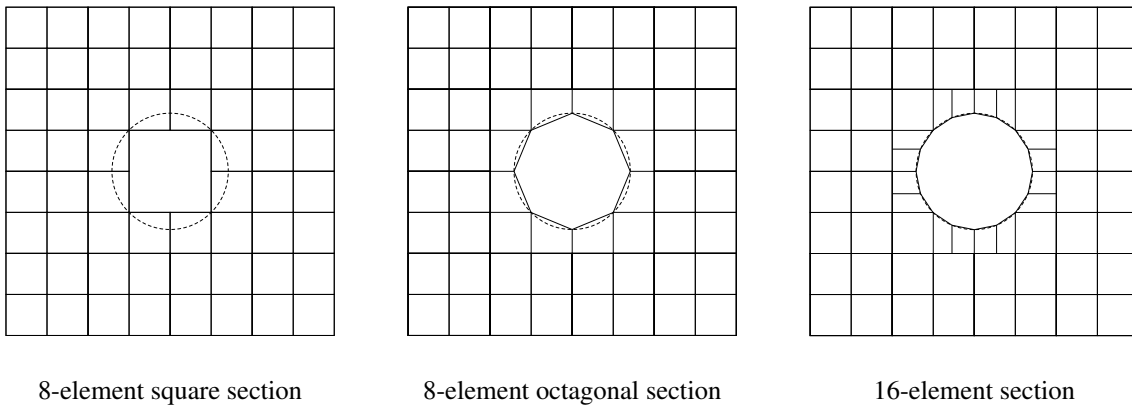
Fig. 4.5 Boundary-element meshes of varying resolution used for the free surface in the piled foundation model. The pile's circumference (dashed circle) needs to be represented by non-rectangular elements if the soil-pile interface is not approximated to be square.
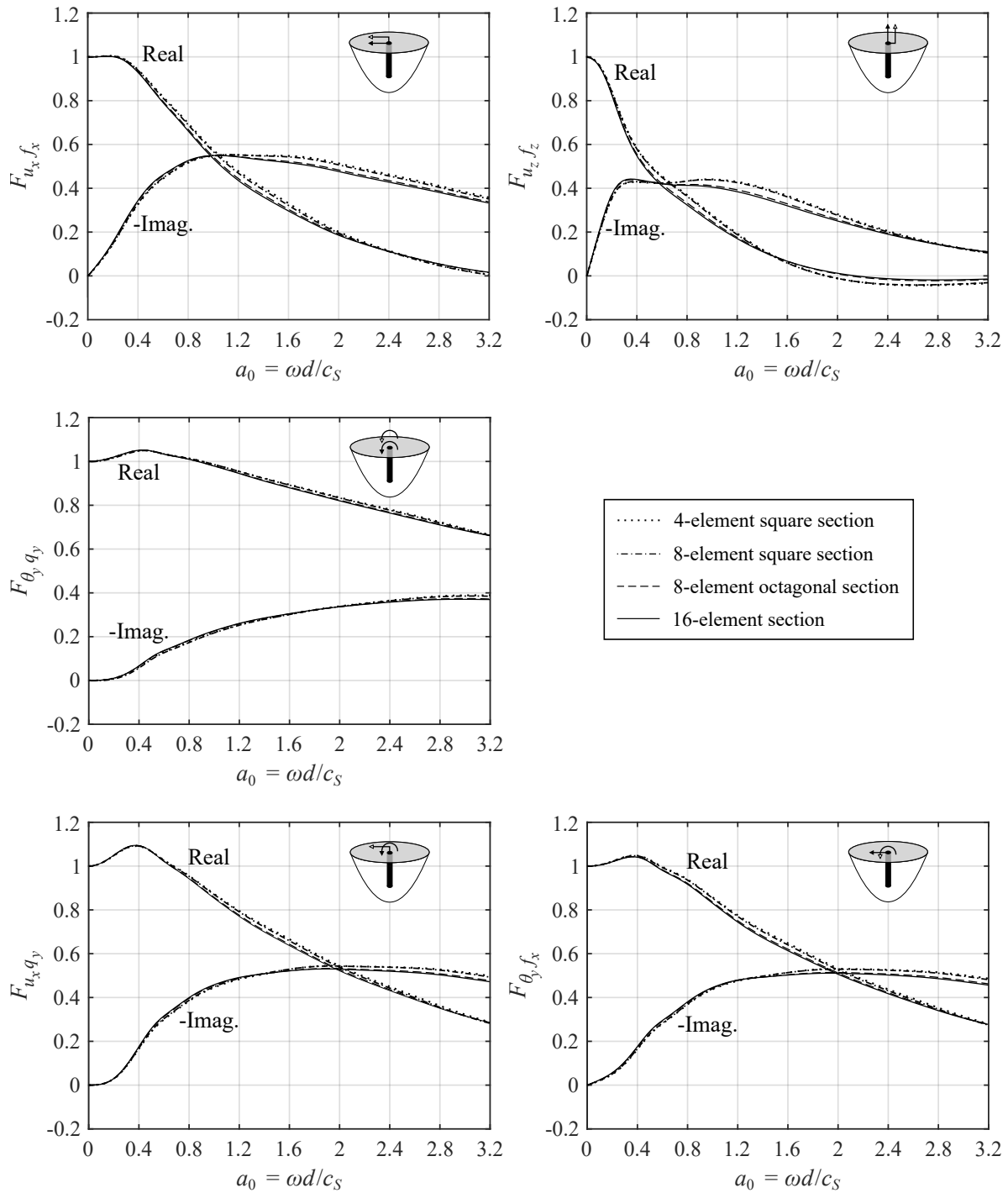
Fig. 4.6 The complex dynamic compliance functions F_{ij} of a single pile, plotted against non-dimensional frequency a_0. The effect of changing the boundary-element section around the pile's circumference on the responses, predicted using the coupled BEM model, is illustrated. The non-dimensional soil and pile parameters are $L/d = 15$, $E_s/E_p = 10^{-3}$, $\rho_s/\rho_p = 0.7$, $\nu_p = 0.4$, $\nu_s = 0.25$, and $\eta_G = 0.05$.

Figure 4.5 illustrates three possible boundary-element meshes, with increasing resolution at the soil-pile interface. The square elements at the free surface are similar to the ones used in Section 3.4, but they now have a smaller side-length of $b = 0.25$ m. At the higher excitation frequencies, in order to better capture the pile's circumference at the soil-pile interface, non-rectangular elements are used in the 8-element octagonal section and the 16-element section. It is worth noting that the numerical integration steps in the BEM become more involved when non-rectangular elements are used, as discussed in Appendix B.6.

The real and imaginary parts of the dynamic compliance functions against non-dimensional frequency $a_0 = \omega d / c_S$ are presented in Fig. 4.6 when a single pile is excited in the xz-plane. The results are plotted up to $a_0 = 3.2$ (≈ 160 Hz), using four different meshes in the coupled BEM model, in order to include the frequency range of interest. The four meshes include the three shown in Fig. 4.5 and the 4-element square section ($b = 0.5$ m) described in Section 3.2. For all cases, the soil and pile are modelled using the parameter values in Table 3.1. Note that, due to symmetry, the lateral, rocking and coupled lateral-rocking compliance functions in the yz-plane are equivalent to the respective functions in Fig. 4.6.

The compliance functions, predicted using all four meshes, show very good agreement up to $a_0 = 3.2$. As the resolution of the soil-pile interface is increased from a 4-element square section to a 16-element section, the compliance functions converge. However, the use of non-rectangular elements will increase the complexity of discretising the mesh for multiple piles, and will also increase the computation time required for numerical integration. Therefore, it is recommended to use the 8-element square section mesh at high excitation frequencies above $a_0 = 1.6$, as this mesh uses rectangular elements and it ensures that there are at least six constant elements per S-wavelength [52].

Figure 4.7 clearly shows that concentric wavefronts appear at the free surface when using the 8-element square section mesh, thereby satisfying the second condition of the convergence study. For additional verification, the predicted wavelengths at the free surface can be compared against the theoretical Rayleigh wavelength λ_R in an isotropic half-space [160]. Vinh & Ogden [235] derived λ_R as a function of the excitation frequency f and the elastic material parameters:

$$\lambda_R = \frac{1}{f} \sqrt{ \frac{4\mu}{\rho} (1 - \gamma) \left(2 - \frac{4}{3}\gamma + \sqrt[3]{R + \sqrt{D}} + \sqrt[3]{R - \sqrt{D}} \right)^{-1} }, \qquad (4.22)$$

where

$$\gamma = \frac{\mu}{\lambda + 2\mu}, \tag{4.23}$$

$$R = \frac{2}{27}\left(27 - 90\gamma + 99\gamma^2 - 32\gamma^3\right), \tag{4.24}$$

$$D = \frac{4}{27}(1 - \gamma)^2 \left(11 - 62\gamma + 107\gamma^2 - 64\gamma^3\right), \tag{4.25}$$

and λ and μ are the first and second elastic Lamé constants, respectively. By using Eq. (4.22), the expected Rayleigh wavelengths at 80 Hz and 160 Hz are 2.63 m and 1.32 m, respectively, which are approximately equal to the predicted values shown in Fig. 4.7. However, due to the coarseness of the mesh, the agreement between the observed and theoretical wavelengths is not perfect.
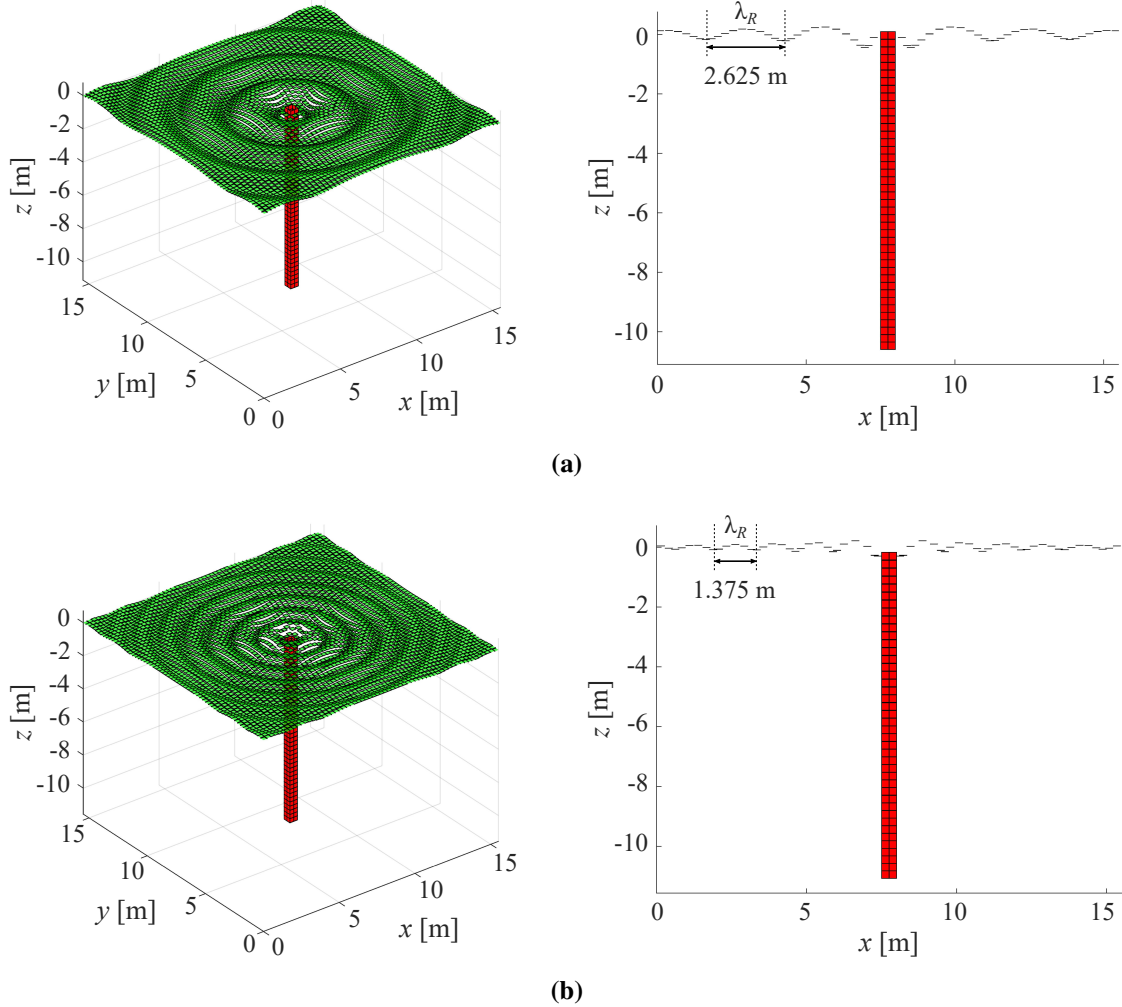
Fig. 4.7 Three-dimensional (left) and two-dimensional (right) views of the free surface waves generated when a pile is excited by a vertically applied pile-head force at a frequency of **(a)** 80 Hz (multiplied by a factor of 4×10^9) and **(b)** 160 Hz (multiplied by a factor of 8×10^9). Predicted using the coupled BEM model with an 8-element square section.

In summary, to improve the BEM model's computational efficiency, the mesh resolution is varied depending on the frequency; the 4-element square section is used at frequencies below 80 Hz, while the 8-element square section is used at higher frequencies. This type of frequency-dependent mesh is beneficial when working with large pile-groups, as shown in Section 4.6.4.

4.5 Validating the Iterative BEM Model

In this section, the iterative BEM model is validated against the coupled BEM model developed in Chapter 3. The dynamic interaction factors of two neighbouring piles, as shown in Fig. 4.8, are used to validate the two models. In the iterative model, pile 1 is the source, while pile 2 is the receiver.

Figure 4.9 presents the real and imaginary parts of the dynamic interaction factors, predicted using the coupled and iterative models for different pile spacing ratios ($s/d = 2$, 5, 10). The non-dimensional soil and pile parameters are $L/d = 15$, $E_s/E_p = 10^{-3}$, $\rho_s/\rho_p = 0.7$, $v_p = 0.25$, $v_s = 0.4$, $\eta_G = 0.05$. The interaction factors are plotted up to a non-dimensional frequency of $a_0 = 3.2$ (≈ 160 Hz).

In general, there is very good agreement between the interaction factors predicted using the two models. For closely spaced piles ($s/d = 2$), two iterations are required when $a_0 > 1.2$ for the iterative BEM model to converge with the coupled BEM model when the lateral force f_y is applied at the pile head. For all other interaction factors, one iteration, which is equivalent to the uncoupled source-receiver model, is enough for convergence. Since the force f_y results in pile deformation that is parallel to the direction of wave propagation between the piles, the incident wave-fields are more likely to be influenced by the presence of the receiver.

(a)   **(b)**
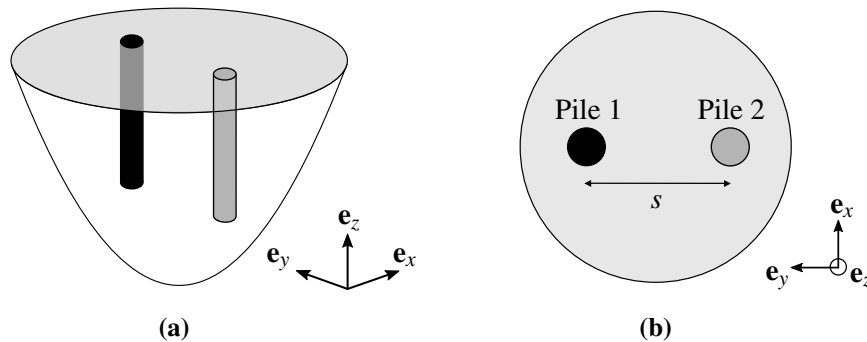
Fig. 4.8 (a) Three-dimensional and **(b)** plan views of two neighbouring piles. Pile 1 (shaded black) is the source, while pile 2 (shaded grey) is the receiver.

As expected, the influence of the receiver pile on the pile-group response decreases with increasing pile spacing: one iteration is sufficient to converge with the coupled BEM solution when $s/d \geq 5$. At high frequencies ($a_0 > 2$), the amplitude of the interaction factors is close to zero when the force f_y is applied at the pile head; this implies that the PSPI is negligible for high-frequency waves that oscillate parallel to the orientation of the piles. Furthermore, the number of peaks and troughs in the results increases as the number of half-wavelengths between the piles increases, leading to a greater degree of constructive and destructive interference in the soil.
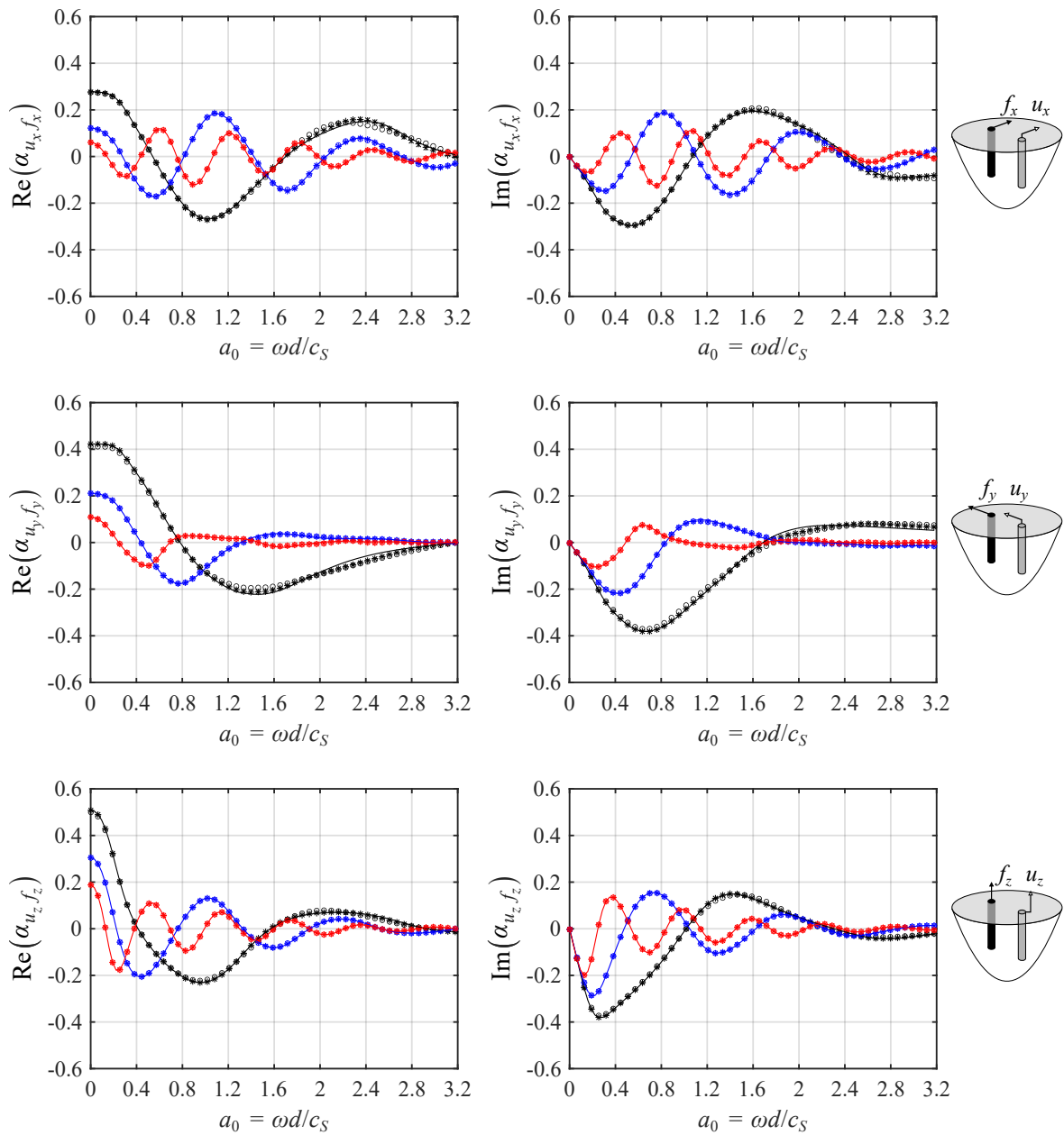
Fig. 4.9 Continues over page.
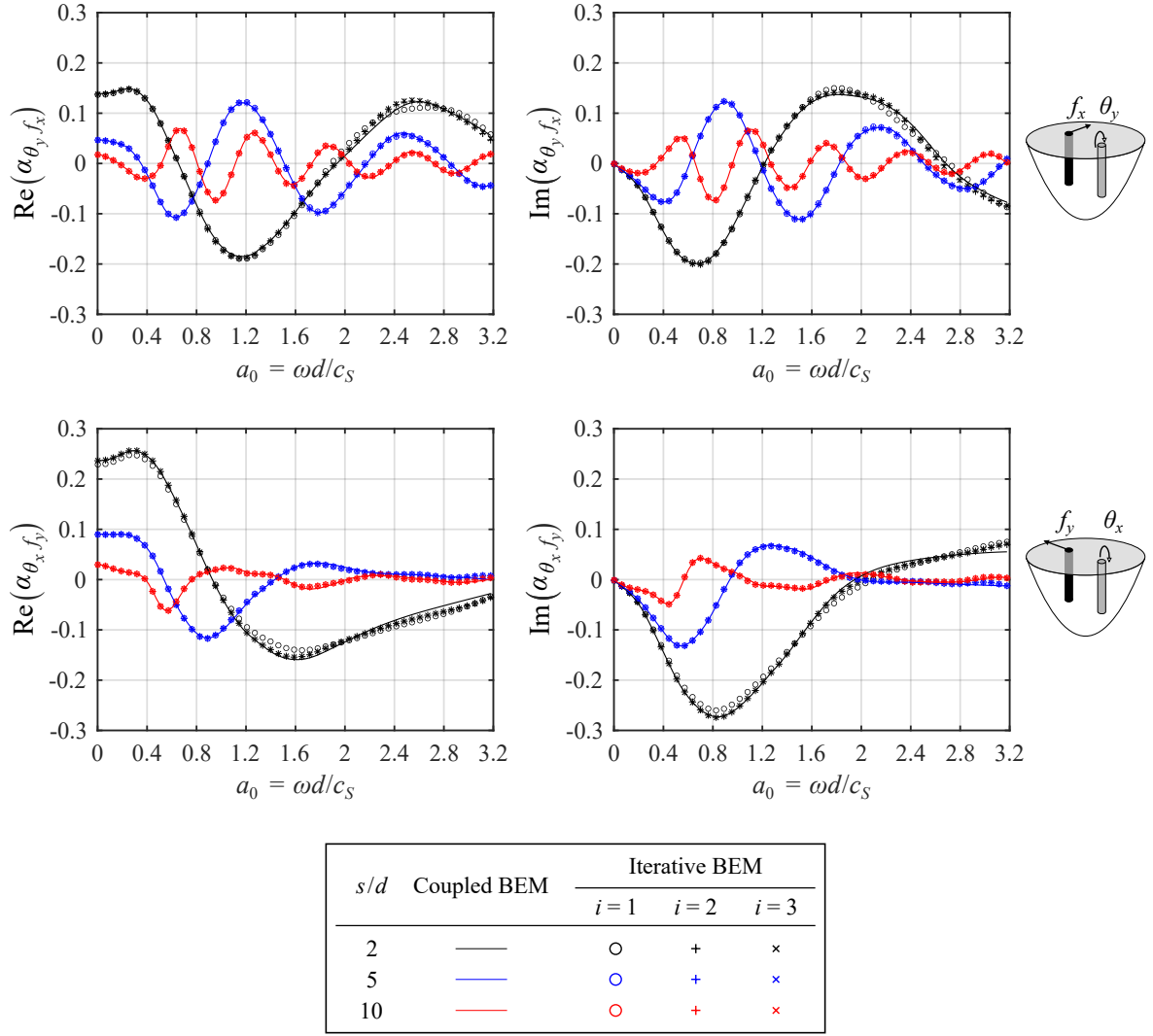
Fig. 4.9 The real (left) and imaginary (right) parts of the dynamic interaction factors of two neighbouring piles, plotted against non-dimensional frequency a_0. The influence of the pile spacing ratio s/d on the response, predicted using the coupled BEM model and the iterative BEM model for the first three iterations ($i = 3$), are shown. The non-dimensional soil and pile parameters are $L/d = 15$, $E_s/E_p = 10^{-3}$, $\rho_s/\rho_p = 0.7$, $\nu_p = 0.4$, $\nu_s = 0.25$, and $\eta_G = 0.05$.

4.6 A Parametric Study of the Inertial Pile-Group Response

This section investigates the influence of different material and geometric parameters on the wave-scattering effect between two neighbouring piles by focusing on the lateral $(\alpha_{u_x f_x}, \alpha_{u_y f_y})$ and vertical $(\alpha_{u_z f_z})$ interaction factors. The inclusion of neighbouring and intermediate piles in larger pile-groups is also analysed.

Unless stated otherwise, the pile spacing ratio between all piles is $s/d = 2$. The dynamic interaction factors of the pile-groups, as presented in Figs. 4.10–4.14, are predicted using the coupled and iterative BEM models.

4.6.1 The Effect of the Soil-Pile Density Ratio

The interaction factors of two neighbouring piles with different soil-pile density ratios, which correspond to light ($\rho_s/\rho_p = 1$) and dense ($\rho_s/\rho_p = 0.7, 0.4$) piles, are plotted in Fig. 4.10. As expected, the static and low-frequency ($a_0 < 0.8$) amplitudes of all interaction factors are independent of ρ_s/ρ_p because inertial effects are insignificant at these frequencies. When ρ_s/ρ_p is decreased from 1 to 0.7, there is no discernible effect on the interaction factors over the frequency range of interest, which is in agreement with the study by Gazetas et al. [77] on the dynamic response of floating pile-groups.

Reducing the soil-pile density ratio to $\rho_s/\rho_p = 0.4$ causes two effects at higher frequencies: (1) an increase in the interaction factor amplitudes; and (2) a decrease in the frequency at which the peaks and troughs of the interaction factors occur. In physical terms, lighter soils offer less resistance to the motion of the piles, leading to higher amplitude waves in the soil. For the densest piles ($\rho_s/\rho_p = 0.4$), two iterations of the iterative model are required for convergence at high frequencies ($a_0 > 1.2$), which is consistent with the wave-scattering effect: the amplitude of the scattered wave-field increases when there is a large difference in mechanical impedance between the soil and piles.

4.6.2 The Effect of the Soil-Pile Stiffness Ratio

Figure 4.11 plots the dynamic interaction factors of two neighbouring piles for a broad range of soil-pile stiffness ratios, corresponding to flexible ($E_s/E_p = 10^{-2}, 10^{-3}$) and relatively rigid ($E_s/E_p = 10^{-4}, 10^{-5}$) piles. In all cases, the first iteration of the iterative BEM model provides a good approximation for the solution of the coupled BEM model, even at high frequencies. This suggests that varying the stiffness ratio does not significantly influence the wave-scattering effect.

Furthermore, the effect of the stiffness ratio on the lateral factors, $\alpha_{u_x f_x}$ and $\alpha_{u_y f_y}$, is found to be two-fold. First, the pseudo-static and low-frequency ($a_0 < 0.8$) amplitudes decrease as the piles become more flexible (or as E_s/E_p increases). Second, the decrease in amplitude becomes less significant when $a_0 > 0.8$. In contrast, there is almost no change in the vertical factor $\alpha_{u_z f_z}$ over the frequency range of interest when E_s/E_p is varied, except for very flexible pile ($E_s/E_p = 10^{-2}$). In this case, the increased flexibility reduces the amplitude across the entire frequency range.
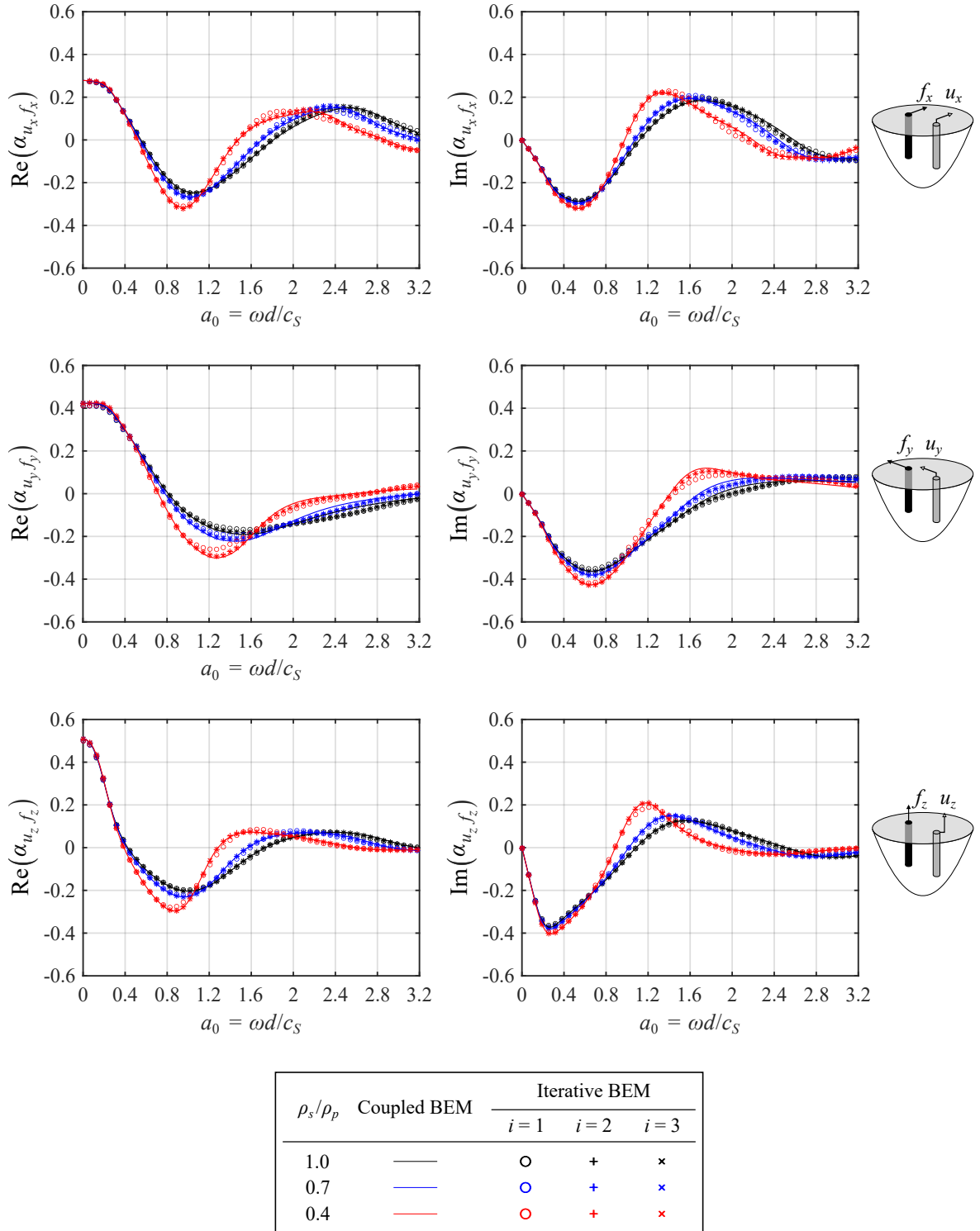
Fig. 4.10 The real (left) and imaginary (right) parts of the lateral $(\alpha_{u_x f_x}, \alpha_{u_y f_y})$ and vertical $(\alpha_{u_z f_z})$ dynamic interaction factors of two neighbouring piles, plotted against non-dimensional frequency a_0. The influence of the soil-pile density ratio ρ_s/ρ_p on the response, predicted using the coupled BEM model and the iterative BEM model for the first three iterations $(i = 3)$, is shown. The non-dimensional soil and pile parameters are $L/d = 15$, $s/d = 2$, $E_s/E_p = 10^{-3}$, $\nu_p = 0.4$, $\nu_s = 0.25$, and $\eta_G = 0.05$.
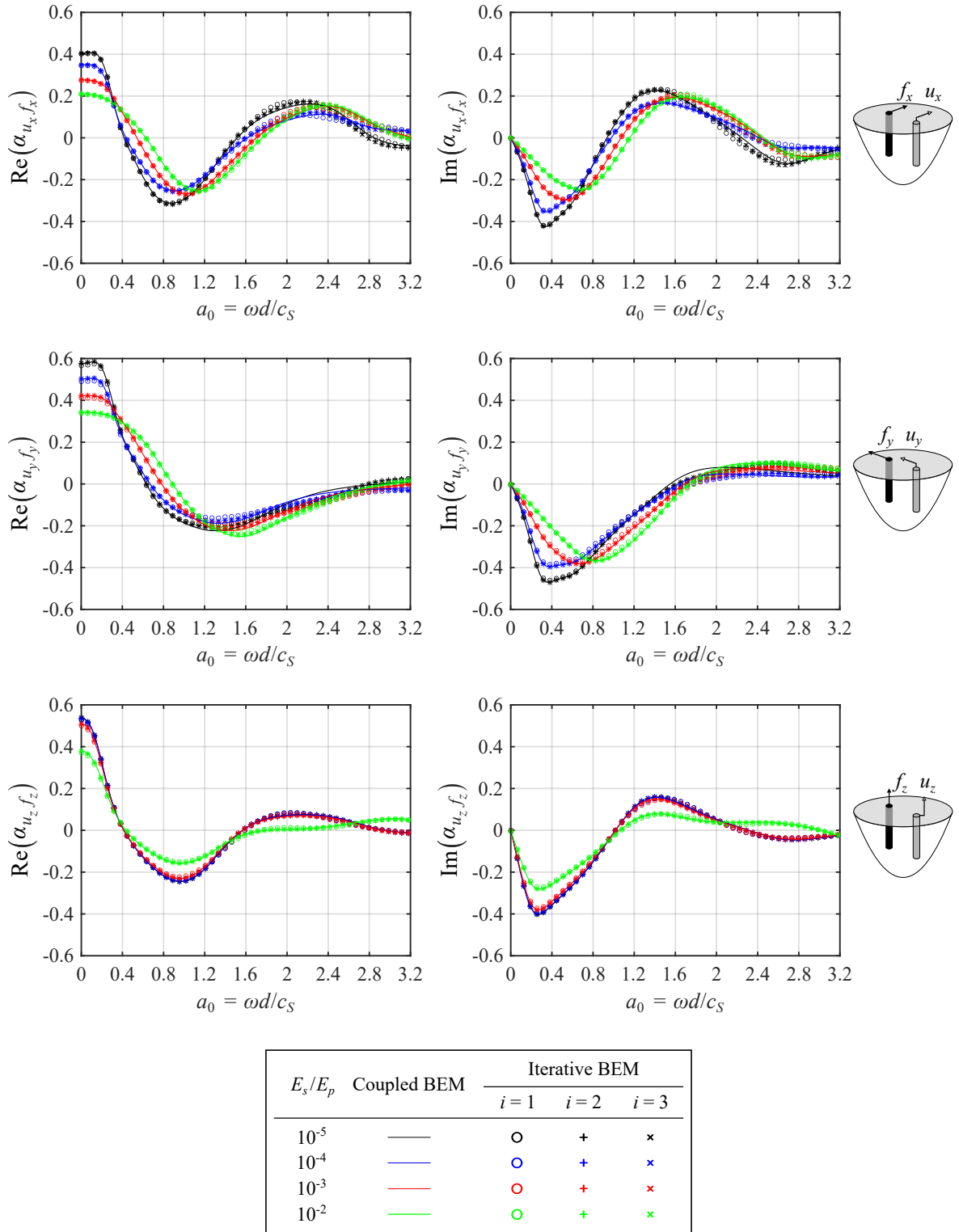
Fig. 4.11 The real (left) and imaginary (right) parts of the lateral $(\alpha_{u_x f_x}, \alpha_{u_y f_y})$ and vertical $(\alpha_{u_z f_z})$ dynamic interaction factors of two neighbouring piles, plotted against non-dimensional frequency a_0. The influence of the soil-pile stiffness ratio E_s/E_p on the response, predicted using the coupled BEM model and the iterative BEM model for the first three iterations $(i=3)$, is shown. The non-dimensional soil and pile parameters are $L/d = 15$, $s/d = 2$, $\rho_s/\rho_p = 0.7$, $\nu_p = 0.4$, $\nu_s = 0.25$, and $\eta_G = 0.05$.

L/d	Coupled BEM	Iterative BEM		
		$i=1$	$i=2$	$i=3$
5	——	○	+	×
15	——	○	+	×
45	——	○	+	×
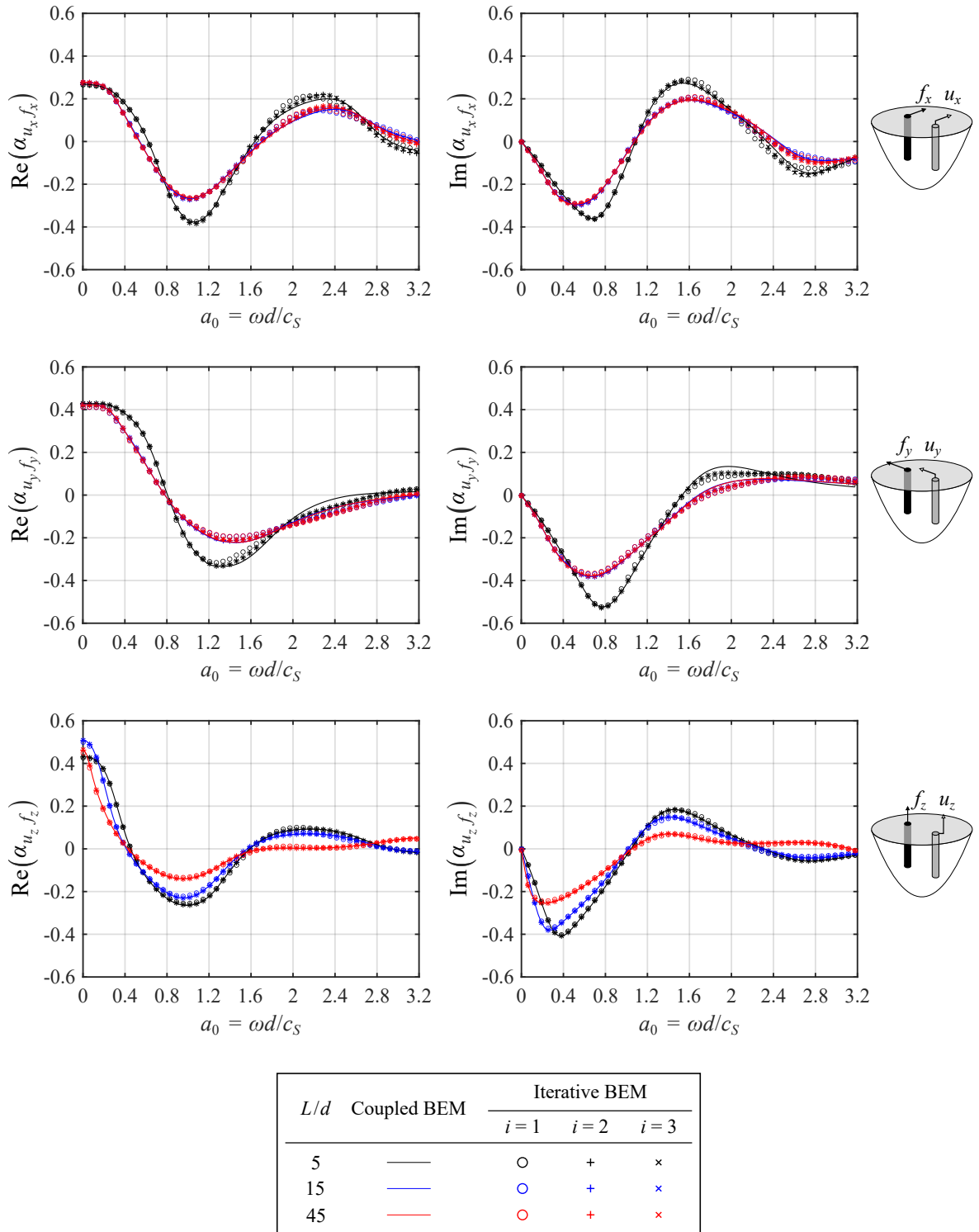
Fig. 4.12 The real (left) and imaginary (right) parts of the lateral $(\alpha_{u_x f_x}, \alpha_{u_y f_y})$ and vertical $(\alpha_{u_z f_z})$ dynamic interaction factors of two neighbouring piles, plotted against non-dimensional frequency a_0. The influence of the pile slenderness ratio L/d on the response, predicted using the coupled BEM model and the iterative BEM model for the first three iterations $(i=3)$, is shown. The non-dimensional soil and pile parameters are $s/d = 2$, $E_s/E_p = 10^{-3}$, $\rho_s/\rho_p = 0.7$, $\nu_p = 0.4$, $\nu_s = 0.25$, and $\eta_G = 0.05$.

4.6.3 The Effect of the Pile Slenderness Ratio

Figure 4.12 presents the dynamic interaction factors of two neighbouring piles for a range of pile slenderness ratios ($L/d = 5, 15, 45$). The shortest piles ($L/d = 5$) require two iterations to converge using the iterative model at high frequencies ($a_0 > 1.2$), while the longer piles only require one iteration. Hence, increasing the slenderness ratio reduces the wave-scattering effect. This is because the longer piles are able to constrain the motion of the soil due to the soil-stiffening effect, resulting in a decrease in the amplitude of the scattered wave-fields.

Gazetas [75] suggests that when the pile length L exceeds the active pile length L' there is negligible variation in the pile's lateral response. The active pile length is approximated by the following empirical relationship for homogeneous soil:

$$
L' \approx 2d \left(\frac{E_s}{E_p} \right)^{-1/4},
\tag{4.26}
$$

which has been found by fitting curves to numerical solutions. Since $E_s/E_p = 10^{-3}$ in Fig. 4.12, the non-dimensional active pile length is $L'/d \approx 11.2$. The lateral interaction factors of the two longer piles ($L/d = 15, 45$), which satisfy $L/d > L'/d$, are equivalent over the entire frequency range. Furthermore, the amplitude of the lateral factors of the shortest piles ($L/d = 5$) is higher than the longer piles. Therefore, these observations support the presence of an active pile length for the inertial response of a pile-group.

It is important to note that the real part of the static lateral factors is independent of L/d. In contrast, the real part of the static vertical factor changes as L/d is varied. As the frequency is increased above $a_0 = 0.4$, the two shorter piles ($L/d = 5, 15$) exhibit similar variations in $\alpha_{u_z f_z}$, whereas the $\alpha_{u_z f_z}$ values of the longest piles ($L/d = 45$) deviate from those of the shorter piles.

4.6.4 The Effect of Neighbouring and Intermediate Piles

In order to identify if neighbouring and intermediate piles can influence the wave-scattering effect, the definition in Eq. (3.51), referring to the dynamic interaction factors of two isolated piles, needs to be extended to a general pile-group. The corresponding interaction factors α_{ij}^{ab} between any two piles, namely a and b, in a large, general pile-group can be defined as

$$
\alpha_{ij}^{ab} = \frac{\text{Dynamic displacement } i \text{ at pile-head } a \text{ due to load } j \text{ applied at pile-head } b}{\text{Static displacement } i \text{ at pile-head } b \text{ due to load } j \text{ applied at pile-head } b}.
\tag{4.27}
$$

It is expected that the wave-scattering effect will have a greater influence on the PSPI between any two piles as the number of piles increases. This is because there will be an increase in the distribution of waves propagating back and forth between piles in the group to create regions of constructive and destructive interference in the soil.

Figure 4.13 plots the interaction factors for two adjacent piles, namely piles 1 and 2, when the number of neighbouring piles is increased from a 1×2 pile-group to a 3×3 pile-group. Slight changes are observed, especially at high frequencies ($a_0 > 1.6$), and these coincide with an increase in the number of iterations required for the iterative model's solution to converge, which is consistent with the expected increase in wave scattering. For example, when $a_0 > 1.4$, the vertical interaction factor $\alpha^{21}_{u_z f_z}$ requires two iterations for convergence when there are more than two piles in the group. Nevertheless, these changes are not significant, and it is clear that an isolated two-pile model provides a good approximation, across the frequency range, for the interaction factors of larger pile-groups.

In contrast, the influence of intermediate piles is more significant. Figure 4.14 plots the interaction factors for two diagonally opposite piles, namely piles 1 and 9, in a 3×3 pile-group when the intermediate piles are either included or omitted. The pile spacing ratio between piles 1 and 9 is $s/d = 6$ when the intermediate piles are omitted. Note that the lateral interaction factors, $\alpha^{91}_{u_x f_x}$ and $\alpha^{91}_{u_y f_y}$, are equivalent because piles 1 and 9 are positioned at $45°$ to the lateral x- and y-axes. There is no discernible difference between the two sets of results at low and intermediate frequencies ($a_0 < 1.2$). At higher frequencies, when the intermediate piles are included, the peaks and troughs in the interaction factors shift to lower frequencies and increase in number. In physical terms, when pile 1 is excited, the wave-fields that eventually arrive at pile 9 are scattered by the intermediate piles with a different phase shift. Note that, in this case, the wave-scattering effect is captured well with just one iteration because all the piles in the receiver sub-system, which include the intermediate piles and pile 9, are fully coupled together.

Based on these observations, it is clear that the PSPI between two piles in a large group can indeed be approximated by ignoring the presence of neighbouring piles, even at the higher frequencies associated with ground-borne vibration (1-160 Hz), provided the two piles are adjacent to each other. This approximation is also valid when intermediate piles are present, but only at frequencies below 60 Hz. At higher frequencies, when the soil wavelengths approach the same order of magnitude as the pile diameter, the scattered wave-fields generated at the intermediate piles are more significant and influence the PSPI to a greater extent.
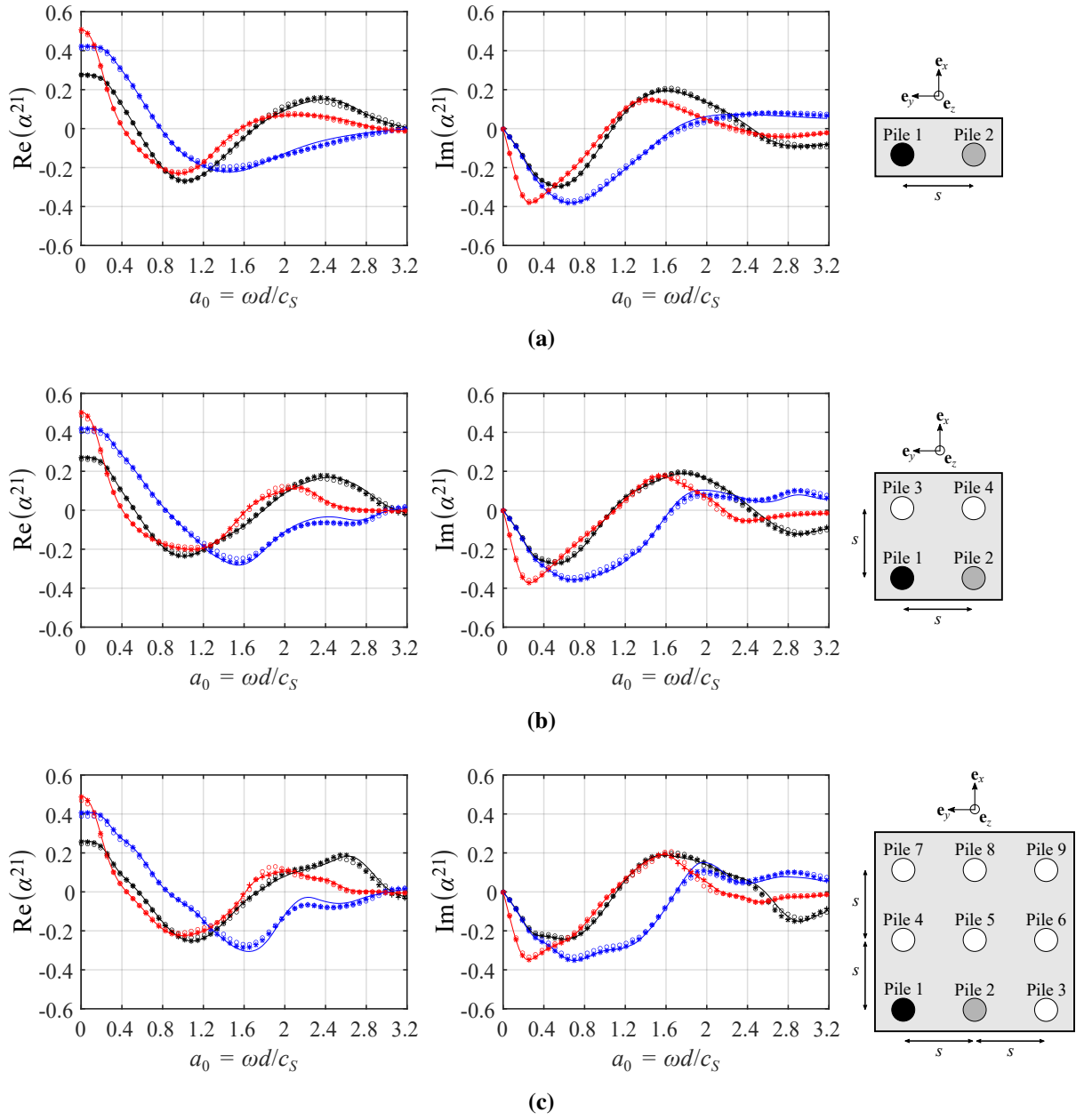
Fig. 4.13 The real (left) and imaginary (right) parts of the lateral $(\alpha_{u_x f_x}, \alpha_{u_y f_y})$ and vertical $(\alpha_{u_z f_z})$ dynamic interaction factors of two adjacent piles in a **(a)** 1×2, **(b)** 2×2 and **(c)** 3×3 pile-group. In each pile-group, pile 1 (shaded black) is excited and the displacement is measured at pile 2 (shaded grey). The results, predicted using the coupled BEM model and the iterative BEM model for the first three iterations ($i = 3$), are plotted against non-dimensional frequency a_0. The non-dimensional soil and pile parameters are $L/d = 15$, $s/d = 2$, $E_s/E_p = 10^{-3}$, $\rho_s/\rho_p = 0.7$, $\nu_p = 0.4$, $\nu_s = 0.25$, and $\eta_G = 0.05$.
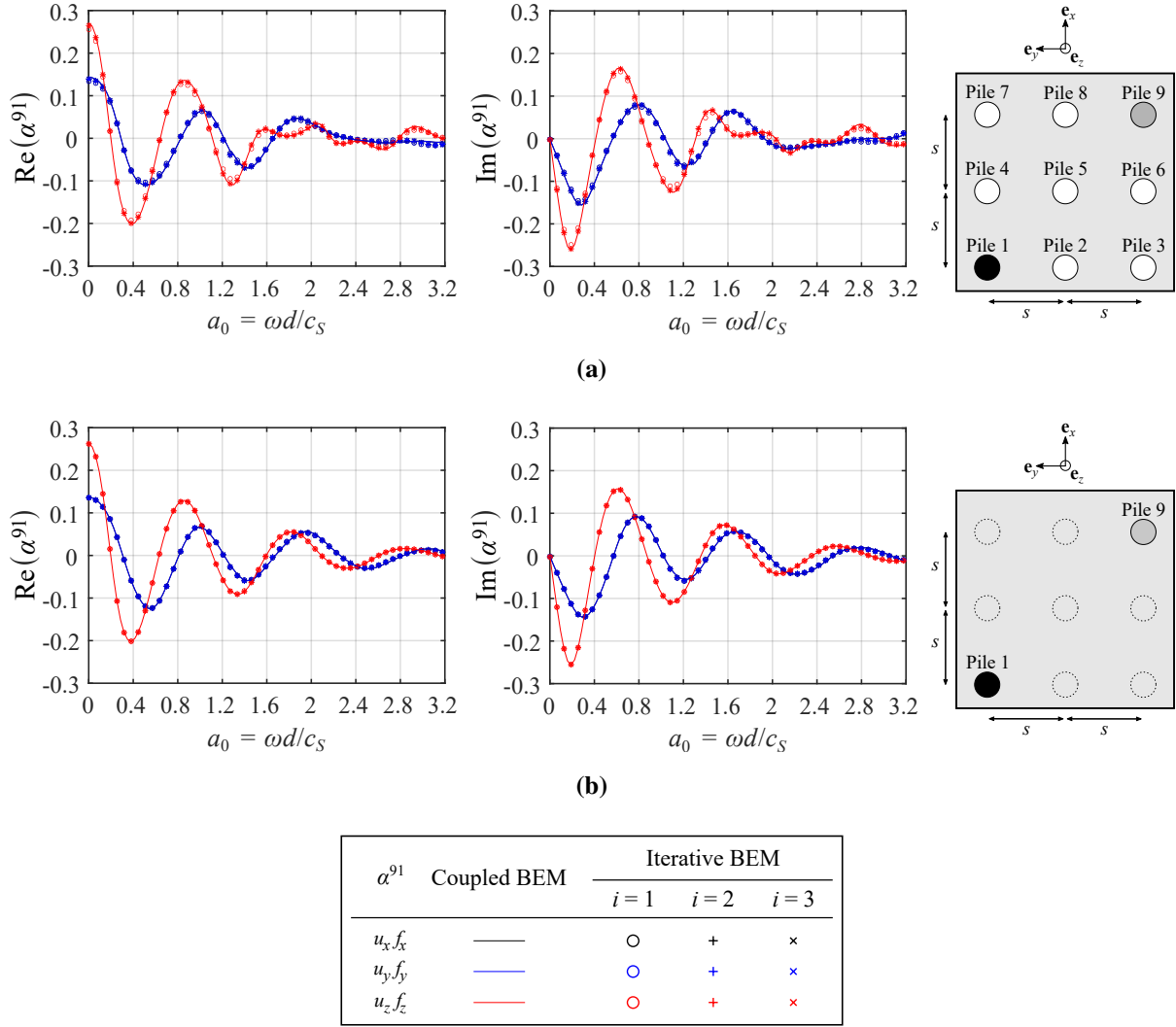
Fig. 4.14 The real (left) and imaginary (right) parts of the lateral $(\alpha_{u_x f_x}, \alpha_{u_y f_y})$ and vertical $(\alpha_{u_z f_z})$ dynamic interaction factors of two diagonally opposite piles in a 3×3 pile-group, when the intermediate piles are **(a)** included and **(b)** omitted. In each case, pile 1 (shaded black) is excited and the displacement is measured at pile 9 (shaded grey). The results, predicted using the coupled BEM model and the iterative BEM model for the first three iterations ($i = 3$), are plotted against non-dimensional frequency a_0. The non-dimensional soil and pile parameters are $L/d = 15$, $s/d = 2$, $E_s/E_p = 10^{-3}$, $\rho_s/\rho_p = 0.7$, $\nu_p = 0.4$, $\nu_s = 0.25$, and $\eta_G = 0.05$.

4.7 Conclusions

The iterative wave-scattering approach has been applied to develop an iterative BEM model in Sections 4.1–4.3 that couples the piles as a source-receiver system. The iterative model uses the scattered wave-fields at the source and receiver sub-systems to revise the response of the pile-group during each iteration. The pile-group response after the first iteration is equivalent to the uncoupled source-receiver response because the first iteration disregards the scattered

wave-field at the receiver. The iterative model has been shown to offer an effective alternative to the fully coupled BEM model developed in Chapter 3 and provides additional insight into the wave-scattering effect of a pile-group. Wave scattering is most prominent at high frequencies, as the soil wavelengths approach the same order of magnitude as the pile diameter.

Based on the convergence study in Section 4.4, a frequency-dependent mesh was used in the BEM models to capture the pile-group dynamics over a broad range of non-dimensional frequencies a_0, corresponding to ground-borne vibration between 1 and 160 Hz in London Clay. By comparing the dynamic interaction factors of two neighbouring piles, Section 4.5 showed that the standard and iterative models agree very well over the frequency range of interest. In general, as the pile spacing ratio s/d was varied, the first iteration (uncoupled response) was a good approximation for the coupled response over most frequencies. However, the level of wave scattering increased when the piles were closer together ($s/d = 2$) because two iterations were required for convergence at high frequencies ($a_0 > 1.2$).

The parametric study in Section 4.6 again showed that, in general, the first iteration was a good approximation for the coupled response as the soil-pile density ratio ρ_s/ρ_p, the soil-pile stiffness ratio E_s/E_p, and the pile slenderness ratio L/d were all varied – even at frequencies well above those of previous publications. Furthermore, the study highlighted that the dynamic interaction factors predicted using uncoupled source-receiver models can effectively account for the PSPI between piles without resorting to fully coupled models. Over the entire frequency range, an isolated two-pile model provided a good approximation for the interaction factors of adjacent piles in larger pile-groups, although the presence of intermediate piles may need to be considered at high frequencies ($a_0 > 1.2$) because of the increased influence of wave scattering that these introduce.

Chapter 5

Uncoupled Tunnel-Foundation Systems

The previous two chapters considered a piled foundation subjected to inertial excitation at an individual pile head. In this chapter, a numerical method is developed to predict the response induced in a piled foundation due to the kinematic excitation from an underground railway tunnel. Together, the railway tunnel and the piled foundation form a tunnel-foundation system.

It is assumed that the separation distance between the tunnel and foundation is greater than the wavelengths in the soil. Therefore, an uncoupled source-receiver model can be used to characterise the train-induced dynamics of an uncoupled tunnel-foundation system. In this case, the excited tunnel (source) can influence the response of the piles (receiver), but the excited piles cannot in turn influence the tunnel response. The sub-system technique is adopted to model the tunnel and foundation as isolated sub-systems, which are then 'weakly' coupled by accounting for the waves that propagate from the tunnel. The response of the tunnel sub-system is captured using the half-space pipe-in-pipe (PiP) model, which is a computationally efficient semi-analytical method (see Section 2.4.3), while the response of the foundation sub-system is captured using the BEM pile-group model developed in Chapter 3.

Section 5.1 gives an overview of the half-space PiP model, developed by Forrest [68] and Hussein [112, 114], and Section 5.2 describes the development of the PiP-BEM model for an uncoupled tunnel-foundation system. A convergence study is conducted in Section 5.3 to find the recommended level of discretisation for the discrete PiP parameters in order to accurately simulate the waves propagating away from the tunnel. In Section 5.4, the uncoupled PiP-BEM model is validated by comparing the train-induced responses of two tunnel-pile systems against the predictions from a similar model developed by Coulier [42], and some concluding remarks are given in Section 5.5.

5.1 The Half-Space Pipe-in-Pipe (PiP) Model

The PiP model can be used to compute the far-field response in the soil around a tunnel. The far-field displacement and traction wave-fields at the piled foundation (i.e., the incident waves) are used to excite the BEM mesh surrounding the piles. This is done by rewriting Eq. (3.24) for the BEM pile-group model as

$$\mathbf{H}\left(\mathbf{u} - \mathbf{u}^{\text{inc}}\right) = \mathbf{G}\left(\mathbf{p} - \mathbf{p}^{\text{inc}}\right), \tag{5.1}$$

where the two vectors $\mathbf{u}^{\text{inc}}$ and $\mathbf{p}^{\text{inc}}$ denote the incident displacement and traction wave-fields, respectively. The vectors $\mathbf{u} - \mathbf{u}^{\text{inc}}$ and $\mathbf{p} - \mathbf{p}^{\text{inc}}$ denote the respective scattered wave-fields that are induced when the incident waves interact with the soil cavities around the piles.

Appendix C provides a detailed outline of the components, assumptions and equations that are used in the standard PiP model for a tunnel embedded in a homogeneous, isotropic half-space. For convenience, the main assumptions and equations are summarised in this section.

The half-space PiP model described in this dissertation can predict the far-field response in the soil when two different time-harmonic modes of excitation are applied within the tunnel. The first mode of excitation is a time-harmonic point force at the tunnel invert, which is at the base of the inner tunnel wall. The second mode of excitation is a spatially harmonic roughness, which is applied at the wheel-rail interface when a train-track system is coupled to the tunnel invert. This chapter focusses on the latter excitation mechanism, where dynamic axle loads are generated by a train travelling over a floating slab track (FST). Alternative train-track systems may also be used in the PiP model, such as a standard (fixed) slab track.

The tunnel is modelled as an infinitely long, thick-walled, cylindrical shell with inner radius r_{ti} and outer radius r_{to}. The soil is modelled as an infinitely long, cylindrical cavity with inner radius $r_{si} = r_{to}$ and an infinite outer radius, and the tunnel is assumed to be perfectly bonded to the soil. The train-track system is modelled as an infinite number of point masses, representing the unsprung axles, on an FST with in-phase rail correlation. Based on these assumptions, the model can only account for a tunnel embedded in a full-space. To account for when the tunnel is embedded in a half-space, the fictitious-force method [113] is applied, which assumes that the free surface does not influence the near field around the tunnel.

The fictitious-force method involves calculating an equivalent set of fictitious line-loads that, when applied in a full-space where the tunnel cavity is filled in with soil material, produce

the same displacements at the soil-tunnel interface as when the cavity was present. Then, these line-loads are used to excite a half-space, and the resulting far-field displacements are computed using the 2.5D Green's functions derived by Tadeu et al. [218]. Note, these Green's functions are formulated in a left-handed Cartesian coordinate system, whereas the equations in the PiP model are defined in a right-handed Cartesian coordinate system, as shown in Table 5.1.

Consider when M fictitious line-loads are evenly distributed around the outer tunnel wall. In this case, each line-load $\widehat{\mathbf{f}}_{(p)}$ can be expressed in the double-wavenumber-frequency (ξ, γ, ω)-domain as the following vector:

$$\widehat{\mathbf{f}}_{(p)}(\xi, \gamma, z, \omega) = \left\{ \widehat{f}_x, \widehat{f}_y, \widehat{f}_z \right\}^{\mathrm{T}} \quad \text{for } p = 1, 2, \ldots, M, \tag{5.2}$$

where ξ and γ are the wavenumbers with respect to the space x- and y-domains, respectively. By using the half-space Green's functions to relate the fictitious line-loads to displacements in the soil, the incident displacement wave-field $\widehat{\mathbf{u}}^{\mathrm{inc}}$ is derived in Appendix C.7, which is repeated here for convenience:

$$\widehat{\mathbf{u}}^{\mathrm{inc}}(\xi, \gamma, z, \omega) = \left\{ \widehat{u}_x^{\mathrm{inc}}, \widehat{u}_y^{\mathrm{inc}}, \widehat{u}_z^{\mathrm{inc}} \right\}^{\mathrm{T}} = \sum_{p=1}^{M} \widehat{\mathbf{G}}_{u(p)}^{\mathrm{half}} \, \widehat{\mathbf{f}}_{(p)}, \tag{5.3}$$

where $\widehat{\mathbf{G}}_{u(p)}^{\mathrm{half}}$ is the 3×3 displacement Green's function matrix for a half-space.

The incident stress wave-field in the soil is also derived in Appendix C.7 by applying the linear-elastic kinematic relationship and the generalised Hooke's Law to the Green's functions. The resulting symmetric Cauchy stress tensor $\widehat{\sigma}^{\mathrm{inc}}$ represents each component of the incident stress wave-field as

Coordinate system	Half-space Green's functions (Left-handed) [218]	The PiP model (Right-handed)
Longitudinal coordinate	x'	x
Transverse coordinate	z'	y
Vertical coordinate	y'	z
Longitudinal wavenumber	$-k_n$	ξ
Transverse wavenumber	$-k_z$	γ

Table 5.1 The respective coordinates and wavenumbers used in the half-space Green's functions and the PiP model.

$$\widehat{\boldsymbol{\sigma}}^{\text{inc}}(\xi,\gamma,z,\omega) = \begin{bmatrix} \widehat{\sigma}_{xx}^{\text{inc}} & \widehat{\sigma}_{xy}^{\text{inc}} & \widehat{\sigma}_{xz}^{\text{inc}} \\ \widehat{\sigma}_{xy}^{\text{inc}} & \widehat{\sigma}_{yy}^{\text{inc}} & \widehat{\sigma}_{yz}^{\text{inc}} \\ \widehat{\sigma}_{xz}^{\text{inc}} & \widehat{\sigma}_{yz}^{\text{inc}} & \widehat{\sigma}_{zz}^{\text{inc}} \end{bmatrix}, \tag{5.4}$$

where

$$\left\{ \widehat{\sigma}_{xx}^{\text{inc}}, \widehat{\sigma}_{xy}^{\text{inc}}, \widehat{\sigma}_{xz}^{\text{inc}}, \widehat{\sigma}_{yy}^{\text{inc}}, \widehat{\sigma}_{yz}^{\text{inc}}, \widehat{\sigma}_{zz}^{\text{inc}} \right\}^{\text{T}} = \sum_{p=1}^{M} \widehat{\mathbf{G}}_{\sigma(p)}^{\text{half}} \, \widehat{\mathbf{f}}_{(p)}, \tag{5.5}$$

and $\widehat{\mathbf{G}}_{\sigma(p)}^{\text{half}}$ is the 6×3 stress Green's function matrix for a half-space.

For illustrative purposes, the first elements of both the $\widehat{\mathbf{G}}_{u(p)}^{\text{half}}$ and $\widehat{\mathbf{G}}_{\sigma(p)}^{\text{half}}$ matrices are written below as closed-form expressions, with respect to the k_n and k_z wavenumbers in the left-handed coordinate system (see Table 5.1):

$$\widehat{G}_{u_{xx}}^{\text{half}}(k_n,k_z,\omega) = \frac{-i}{2\rho\omega^2} \left[\frac{k_n^2}{\nu_n}\left(E_b + A_n^x E_{b0}\right) + \frac{k_z^2}{\gamma_n}\left(E_c + B_n^x E_{c0}\right) + \gamma_n\left(E_c + C_n^x E_{c0}\right) \right], \tag{5.6}$$

$$\widehat{G}_{\sigma_{xx,x}}^{\text{half}}(k_n,k_z,\omega) = \frac{-k_n}{2\rho\omega^2} \left[\lambda\left(E_b + A_n^x E_{b0}\right)\left(\frac{k_n^2}{\nu_n} + \frac{k_z^2}{\nu_n} + \nu_n\right) + \ldots \right.$$
$$\left. 2\mu\left(\frac{k_n^2}{\nu_n}\left(E_b + A_n^x E_{b0}\right) + \frac{k_z^2}{\gamma_n}\left(E_c + B_n^x E_{c0}\right) + \gamma_n\left(E_c + C_n^x E_{c0}\right)\right) \right], \tag{5.7}$$

where ρ is the density, λ and μ are the elastic Lamé constants, and the variables $\nu_n, \gamma_n, E_b, E_{b0}, E_c, E_{c0}, A_n^x, B_n^x, C_n^x$ are defined by Tadeu et al. [218].

The incident traction wave-field $\widehat{\mathbf{p}}^{\text{inc}}$ is then computed by applying Cauchy's formula:

$$\widehat{\mathbf{p}}^{\text{inc}}(\xi,\gamma,z,\omega) = \left\{ \widehat{p}_x^{\text{inc}}, \widehat{p}_y^{\text{inc}}, \widehat{p}_z^{\text{inc}} \right\}^{\text{T}} = \widehat{\boldsymbol{\sigma}}^{\text{inc}}\mathbf{n}(\mathbf{x}), \tag{5.8}$$

where $\mathbf{n}$ is the normal unit-vector at a position vector $\mathbf{x} = \{x,y,z\}^{\text{T}}$ when the traction wave-field is evaluated in the space-frequency $(\mathbf{x},\omega)$-domain.

Both $\widehat{\mathbf{u}}^{\text{inc}}$ and $\widehat{\mathbf{p}}^{\text{inc}}$ are transformed into the $(\mathbf{x},\omega)$-domain by applying the inverse discrete Fourier transform (IDFT) twice, with respect to each wavenumber (see Appendix A.2.1). The resulting $\mathbf{u}^{\text{inc}}(\mathbf{x},\omega)$ and $\mathbf{p}^{\text{inc}}(\mathbf{x},\omega)$ incident wave-fields are computed at the central node $\mathbf{x}$ of each boundary element in the mesh of the pile-group. It should be noted that the vector $\mathbf{n}$ at a node $\mathbf{x}$ is normal to the element's surface and points into the domain representing the soil.

5.2 The Uncoupled PiP-BEM Model

The incident displacement and traction wave-fields, computed using the PiP model, are applied as the external excitation at the boundary-element mesh of the piled foundation. To accomplish this, the relationship between the displacement and traction wave-fields at the free surface and the soil-pile interface of the foundation, as stated in Eq. (3.29), is modified to account for wave scattering due to the incident wave-fields:

$$
\begin{Bmatrix}
\mathbf{u}_{FS} - \mathbf{u}_{FS}^{inc} \\
\mathbf{u}_{SP}^{1} - \mathbf{u}_{SP}^{1,inc} \\
\mathbf{u}_{SP}^{2} - \mathbf{u}_{SP}^{2,inc} \\
\vdots \\
\mathbf{u}_{SP}^{N} - \mathbf{u}_{SP}^{N,inc}
\end{Bmatrix}
=
\begin{bmatrix}
\mathbf{H}_{S11} & \mathbf{H}_{S12} \\
\mathbf{H}_{S21} & \mathbf{H}_{S22}
\end{bmatrix}
\begin{Bmatrix}
\mathbf{p}_{FS} - \mathbf{p}_{FS}^{inc} \\
\mathbf{p}_{SP}^{1} - \mathbf{p}_{SP}^{1,inc} \\
\mathbf{p}_{SP}^{2} - \mathbf{p}_{SP}^{2,inc} \\
\vdots \\
\mathbf{p}_{SP}^{N} - \mathbf{p}_{SP}^{N,inc}
\end{Bmatrix},
\tag{5.9}
$$

where $\mathbf{u}_{FS}^{inc}$ and $\mathbf{p}_{FS}^{inc}$ are the incident wave-fields at the free surface, and $\mathbf{u}_{SP}^{(k),inc}$ and $\mathbf{p}_{SP}^{(k),inc}$ are the incident wave-fields at the soil-pile interface of pile k. Equation (5.9) can be separated into the following two matrix equations:

$$
\mathbf{u}_{FS} - \mathbf{u}_{FS}^{inc} = \mathbf{H}_{S12}\left(\mathbf{p}_{SP} - \mathbf{p}_{SP}^{inc}\right),
\tag{5.10}
$$

$$
\mathbf{u}_{SP} - \mathbf{u}_{SP}^{inc} = \mathbf{H}_{S22}\left(\mathbf{p}_{SP} - \mathbf{p}_{SP}^{inc}\right),
\tag{5.11}
$$

where the vectors $\mathbf{u}_{SP} = \left\{\mathbf{u}_{SP}^{1}, \mathbf{u}_{SP}^{2}, \ldots, \mathbf{u}_{SP}^{N}\right\}^{T}$ and $\mathbf{p}_{SP} = \left\{\mathbf{p}_{SP}^{1}, \mathbf{p}_{SP}^{2}, \ldots, \mathbf{p}_{SP}^{N}\right\}^{T}$ define the total displacement and traction wave-fields, respectively, at the soil-pile interface of all N piles in the foundation. The incident wave-fields $\left(\mathbf{u}_{SP}^{inc}, \mathbf{p}_{SP}^{inc}\right)$ are similarly defined at the N piles. Note that the traction-free boundary condition $(\mathbf{p}_{FS} = \mathbf{p}_{FS}^{inc} = \mathbf{0})$ is applied at the ground surface in Eqs. (5.10) and (5.11).

The other governing equations for the foundation remain the same as Eqs. (3.22), (3.23), (3.37) and (3.38), but $\mathbf{f}_{PH} = \mathbf{0}$ because inertial excitation is not considered at the pile head. The pile-head displacement $\mathbf{u}_{PH}$ of the foundation can be derived by rearranging the governing equations. The matrix equation for $\mathbf{u}_{PH}$, as a function of the incident wave-fields $\left(\mathbf{u}_{SP}^{inc}, \mathbf{p}_{SP}^{inc}\right)$ from an excited tunnel, is

$$
\mathbf{u}_{PH}(\mathbf{x}, \omega) = \mathbf{H}_{P12}\mathbf{Q}_{2}\mathbf{A}\left(\mathbf{u}_{SP}^{inc} - \mathbf{H}_{S22}\mathbf{p}_{SP}^{inc}\right),
\tag{5.12}
$$

where the matrices $\mathbf{H}_{P12}$, $\mathbf{Q}_2$ and $\mathbf{A}$ are defined in Eqs. (3.22), (3.38) and (3.43), respectively. Similar matrix equations can also be derived for the displacement wave-fields at the free surface $\mathbf{u}_{FS}(\mathbf{x}, \omega)$ and soil-pile interface $\mathbf{u}_{SP}(\mathbf{x}, \omega)$, and the traction wave-field at the soil-pile interface $\mathbf{p}_{SP}(\mathbf{x}, \omega)$ by substituting Eq. (5.12) into the governing equations.

Assuming all N piles in the group are the same length, the soil FRF sub-matrix $\mathbf{H}_{S22}$ can be sub-divided further into N^2 square matrices that account for the kinematic interaction between piles: the N matrices along the leading diagonal of $\mathbf{H}_{S22}$ account for the kinematic response of each individual pile, while the remaining $N^2 - N$ matrices account for the kinematic pile-soil-pile interaction (k-PSPI) between neighbouring piles. This has the benefit of enabling the pile-group response to be predicted with and without the inclusion of k-PSPI, the latter being achieved simply by setting all elements outside the matrices along the leading diagonal of $\mathbf{H}_{S22}$ to zero.

5.3 A Convergence Study of the Discretised PiP Parameters

The PiP model contains multiple parameters that need to be discretised within a finite domain in the semi-analytical formulation. Therefore, it is important to perform a convergence study to find the level of discretisation required for each of these parameters so that a compromise is reached between the numerical accuracy and computational efficiency of the uncoupled PiP-BEM model.

In this section, a convergence study is conducted on the following discretised parameters: the wavenumbers, the circumferential ring modes, the fictitious-force points and the train axles. Further details on these PiP parameters can be found in Appendix C.
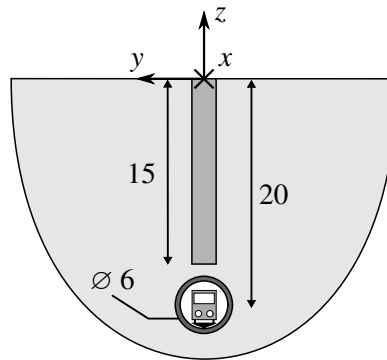
Fig. 5.1 Schematic diagram of a centred pile directly above an underground railway tunnel. Dimensions in [m]. Not drawn to scale.

Parameters [Units]	Soil (London Clay)	Tunnel (Concrete)	Pile (Concrete)
Young's modulus [Pa]	$E_s = 286 \times 10^6$	$E_t = 50 \times 10^9$	$E_p = 30 \times 10^9$
Poisson's ratio[−]	$\nu_s = 0.49$	$\nu_t = 0.30$	$\nu_p = 0.25$
Density [kg/m³]	$\rho_s = 1980$	$\rho_t = 2500$	$\rho_p = 2500$
Shear modulus loss factor [−]	$\eta_G = 0.08$	−	−
Outer wall radius [m]	−	$r_{to} = 3.00$	−
Inner wall radius [m]	−	$r_{ti} = 2.75$	−
Diameter [m]	−	−	$d = 0.71$

Table 5.2 Soil, tunnel and pile parameter values.

FST beam parameters [Units]	Each rail beam	Slab beam
Mass per unit length [kg/m]	$m_r = 50$	$m_s = 3500$
Bending stiffness [Nm²]	$K_r = 5.00 \times 10^6$	$K_s = 1.43 \times 10^9$
FST support parameters [Units]	**Each rail pad**	**Slab bearing**
Stiffness per unit length [N/m/m]	$k_r = 200 \times 10^6$	$k_s = 221 \times 10^6$
Loss factor [−]	$\eta_r = 0.3$	$\eta_s = 0.5$
Train parameters [Units]	**Axles**	
Unsprung mass [kg]	$M_a = 500$	
Spacing [m]	$L_a = 20$	

Table 5.3 Floating slab track (FST) and train parameter values.

In the convergence study, the tunnel-pile system, shown in Fig. 5.1, is used to calculate the train-induced vibration of a centred pile. The pile length and tunnel depth are fixed at $L = 15$ m and $D = 20$ m, respectively. Note that the pile will only deform in the vertical direction because it is located directly above the tunnel centre-line and the wave-field distribution is symmetric on either side of the pile. The pile toe is located 2 m away from the tunnel crown (i.e., the top of the outer tunnel wall). This ensures that the recommended discretisation for the parameters will accurately predict the waves approaching the soil-pile interface of any pile positioned close to a tunnel with similar dimensions. Since the distributed force due to the wheel-rail roughness is an extension of the point force applied at the tunnel invert, as described in Appendix C, the recommended discretisation parameters from this study will apply for both modes of excitation.

The respective parameter values summarised in Table 5.2 are used to model the piles and the railway tunnel, which are both constructed out of concrete. In order to produce results that are representative of physical soil, it is modelled as London Clay using the parameter values given in Table 5.2. The phase speeds of P- and S-waves in London Clay are $c_P = 1572$ m/s and $c_S = 220$ m/s, respectively. These soil parameter values are based on seismic cone penetration tests made close to the London Underground's Bakerloo Line, beneath Regent's Park, London [105], and are consistent with small-strain geotechnical properties reported elsewhere [101]. The train and the FST are modelled using the data in Table 5.3. Based on the parameter values for the slab beam and bearing, the isolation frequency of the FST is $f_s = \frac{1}{2\pi}\sqrt{k_s/m_s} = 40$ Hz.

The vertical (w_{ph}/Δ) displacement FRF at the pile head, which is the vertical displacement w_{ph} at the pile head due to a spatially harmonic roughness Δ at the wheel-rail interface, is used to find the recommended discretisation for the four parameters analysed in this section. The real and imaginary parts of the vertical displacement FRFs are plotted in Fig. 5.2 as the excitation frequency is swept from 1 to 80 Hz.

5.3.1 Wavenumbers

Two wavenumber domains are required to find the wave-field distribution around the tunnel: (1) the wavenumber ξ, with respect to the longitudinal x-domain, describes the variation in the force applied along the tunnel invert; and (2) the wavenumber γ, with respect to the transverse y-domain, describes the variation in the fictitious line-loads around the tunnel's circumference. Since exciting the tunnel leads to a force distribution that is (anti-)symmetric in the longitudinal and circumferential directions, arguments based on symmetry can be applied to restrict the ξ- and γ-domains to positive wavenumbers ($0 \leq \xi < \infty$ and $0 \leq \gamma < \infty$), which improves the model's computational efficiency. In order to compute the incident wave-fields in the $(\mathbf{x}, \omega)$-domain, the wavenumbers need to be discretised so that the IDFT can be performed with respect to the ξ- and γ-domains. Both domains contain the same number of discrete wavenumber points N_ξ and the same maximum wavenumber component ξ_{max}. The discrete components of the ξ and γ wavenumbers are defined as

$$\xi_m = \gamma_m = m\xi_{max}/(N_\xi - 1) \quad \text{for } m = 0, 1, \ldots, (N_\xi - 1). \tag{5.13}$$

The wavenumbers associated with P- and S-waves in the soil are denoted as ξ_S and ξ_P, respectively. Therefore, at a given excitation frequency ω, the largest wavenumber in the soil

is $\xi_S = \omega/c_S$. In order to ensure that all the broad wavenumber information is captured for waves travelling through the soil, the maximum wavenumber component is set to $\xi_{max} = 5\xi_S$ so that ξ_m and γ_m vary with frequency. Also, the 2.5D Green's functions for a half-space contain exponential terms of the form $e^{-i\nu_P|D-D_0|}$ and $e^{-i\nu_S|D-D_0|}$, where $\nu_{P,S} = \left(\xi_{P,S}^2 - \xi^2 - \gamma^2\right)^{1/2}$ are wavenumbers in the vertical direction that satisfy $\text{Im}(\nu_{P,S} \leq 0)$, and $|D-D_0|$ is the difference in height between the tunnel depth D and the depth D_0 at which the response is measured [218]. Since the imaginary parts of ν_P and ν_S are negative, the magnitude of the waves propagating from the tunnel tend to decrease exponentially as ξ_m and γ_m increase, similar to the behaviour of evanescent waves. That is, at high wavenumbers, the magnitude of the incident displacement and traction wave-fields will be too low to influence the response of the centred pile. Hence, the maximum wavenumber component ξ_{max} can be limited to an upper bound value at high frequencies when the wavenumbers are also large.

The convergence process used to find appropriate values for N_ξ and the upper bound for ξ_{max} is illustrated in Figs. 5.2a and 5.2b. These sub-figures show that the solution obtained using $\xi_{max} = \min(5\xi_S, 2\pi)$, with 401 points, is comparable in accuracy to the solution when $\xi_{max} = \min(5\xi_S, \pi)$ and just 201 points are used, which means that the upper bound for ξ_{max} can be lowered at high frequencies. Therefore, it is recommended that the ξ- and γ-domains of an incident wave-field should be discretised using 201 points with a frequency-dependent $\xi_{max} = \min(5\xi_S, \pi)$ to accurately model the train-induced response of a piled foundation. Note, if (anti-)symmetric arguments are not applied to restrict the wavenumber domains to $0 \leq \xi < \infty$ and $0 \leq \gamma < \infty$, both positive and negative wavenumbers need to be discretised using 401 points, and the minimum wavenumber component is then $\xi_{min} = -\xi_{max}$.

5.3.2   Circumferential Ring Modes

In the PiP model, a Fourier series expansion, with respect to the circumferential direction, is used to evaluate the response in terms of circumferential ring modes (see Appendix C.3.1). The nth mode, where $n \geq 0$, is associated with a natural frequency. Note that $n = 0$ accounts for the rigid-body vibration modes of the tunnel [67]. If the excitation frequency is greater than the natural frequency of a particular mode, the modal tunnel displacement, associated with that mode, transitions from a localised disturbance into propagating waves [67]. It is expected that the magnitude of these waves, some distance from the tunnel, will only depend on the modal displacements that have begun to propagate (i.e., have natural frequencies below the excitation

frequency). Modes with natural frequencies that are greater than the frequency range of interest will also have a negligible effect on the waves propagating away from the tunnel. Figure 5.2c shows the variation in the FRFs as the largest mode n_{max} is increased. When the first 6 modes ($n_{max} = 5$) are used, the corresponding FRF agrees well with the other FRFs ($n_{max} > 5$) when the frequency is below 60 Hz. At frequencies above 60 Hz, the FRFs diverge because the higher mode numbers, which result in propagating waves at these high frequencies, are omitted when $n_{max} = 5$. When n_{max} is increased to 10 and 20, there is good agreement between the FRFs over the entire frequency range. This means that at least the first 11 circumferential ring modes need to be discretised to maintain numerical accuracy.

5.3.3 Fictitious-Force Points

In the fictitious-force method, the line-loads at M equidistant points around the tunnel's outer circumference need to be calculated in the (ξ, γ, ω)-domain, as mentioned in Section 5.1. The pile-head displacement FRFs in Fig. 5.2d clearly show that the FRF when $M = 10$ quickly diverges as the excitation frequency increases because the soil displacement around the tunnel is not fully captured when fewer line-loads are used. As M is increased, there is good agreement between the FRFs when using more than 20 points. The distance between the 20 fictitious-force points around the outer tunnel wall in Fig. 5.1 is 0.939 m $\approx \lambda_S/3$, where $\lambda_S = 2.75$ m is the high-frequency S-wavelength in the soil. Therefore, it is recommended to ensure there are at least 3 fictitious-force points per S-wavelength in the soil to accurately simulate the propagating waves from an excited tunnel.

5.3.4 Train Axles

When a train-track system is coupled to the tunnel invert, it is assumed that the train, track and tunnel are infinitely long in the longitudinal direction. Although it is possible to model an infinite track and tunnel by working in the wavenumber-frequency (ξ, ω)-domain, only a finite number of axle masses can be included in the numerical model for the train. The pile-head displacement FRFs plotted in Fig. 5.2e are used to find the least possible number of axle masses N_a required to obtain convergence. For frequencies under 70 Hz, all the FRFs with different N_a are comparable with each other, but the FRF when $N_a = 7$ diverges slightly from the other FRFs at higher frequencies. Hence, 11 axle masses should be used to accurately capture the train-induced excitation of the tunnel due to a spatially harmonic wheel-rail roughness.
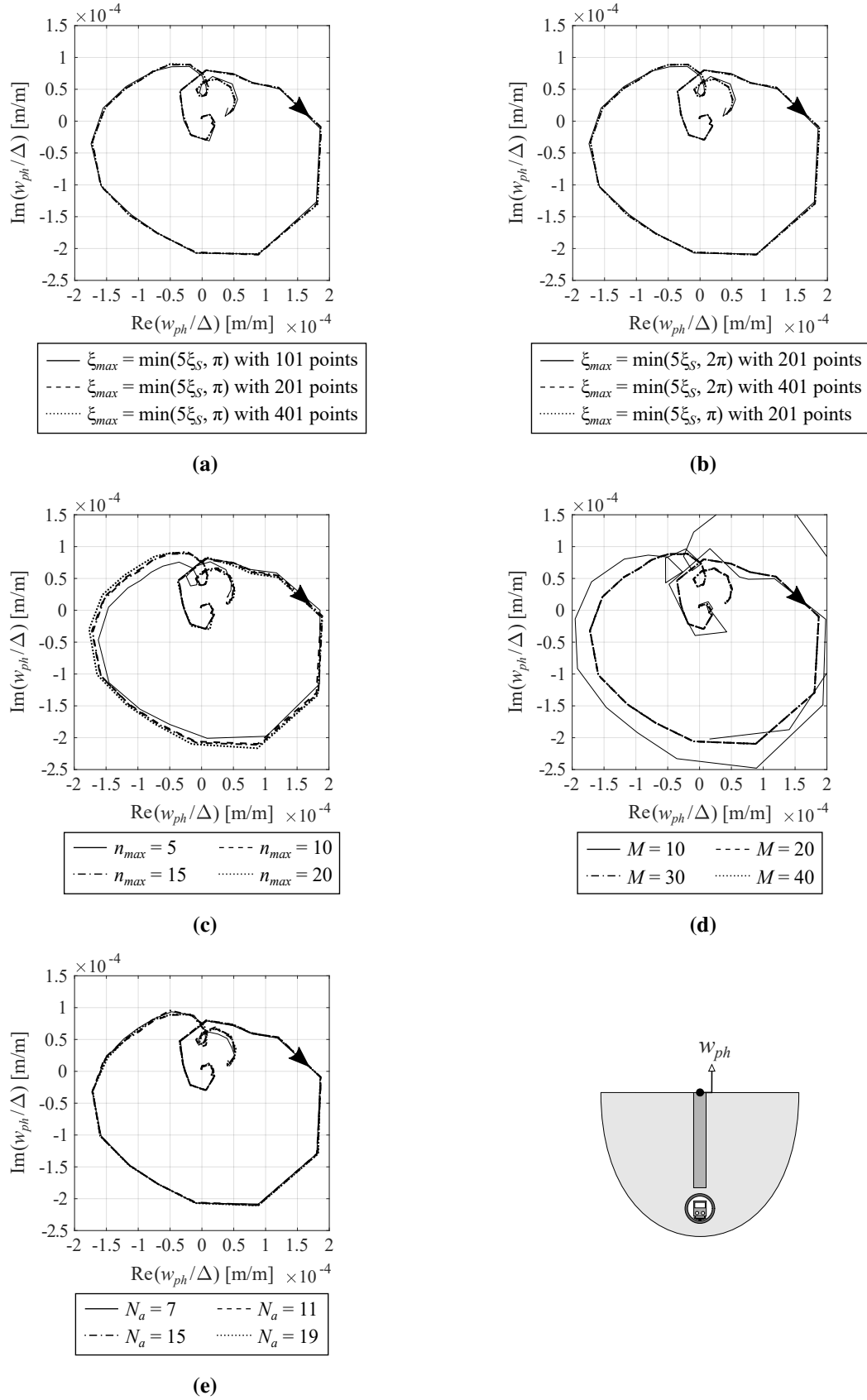
Fig. 5.2 The real and imaginary parts of the vertical displacement FRFs at the head of a centred pile above an underground railway tunnel. The influence in varying the following PiP parameters is shown: **(a)** the number of wavenumber points, **(b)** the maximum wavenumber ξ_{max}, **(c)** the maximum circumferential ring mode n_{max}, **(d)** the number of fictitious-force points M and **(e)** the number of train axles N_a. The arrows in the sub-figures represent the direction of increasing excitation frequency.

5.4   Validating the Uncoupled PiP-BEM Model

The uncoupled PiP-BEM model is validated against results published by Coulier [42] for two different tunnel-pile systems, as illustrated in Fig. 5.3; the pile configuration in each system represents an off-centred pile and a centred 1×4 pile-group. Since, in both cases, the piled foundation is far from the tunnel, the source and receiver can be assumed to be uncoupled. Coulier adopts the BEM to capture the dynamics of the soil and uses the PiP model to compute the far-field waves from a railway tunnel. Unlike the uncoupled PiP-BEM model, Coulier uses Timoshenko beam theory [228] to characterise the flexural motion of the piles. Moreover, one of the main disadvantages in Coulier's equivalent model is that the algebraic expressions need to be extensively reformulated when the pile configuration is changed.

The response of each tunnel-pile system is computed using the parameter values in Table 5.4 for the soil, tunnel and piles. Based on these values, the phase speeds of P- and S-waves in the soil are $c_P = 944$ m/s and $c_S = 309$ m/s, respectively. However, Coulier does not explicitly state the parameter values of the FST and the train, so the train-track parameters in Table 5.3, which are the default values in the free licenced PiP software [116], are used in the PiP-BEM model

For each pile configuration, a comparison is made when the heads are fixed and when they are free to rotate about the *x*- and *y*-axes. The pile heads can be constrained against rotation when they are bonded to a concrete slab, such as in a piled-raft foundation [198]. The pile-head constraint can be applied by removing the two columns and rows in the dynamic-stiffness matrix **K** in Eq. (3.15) that correspond to the pile-head rotations and moments, respectively.
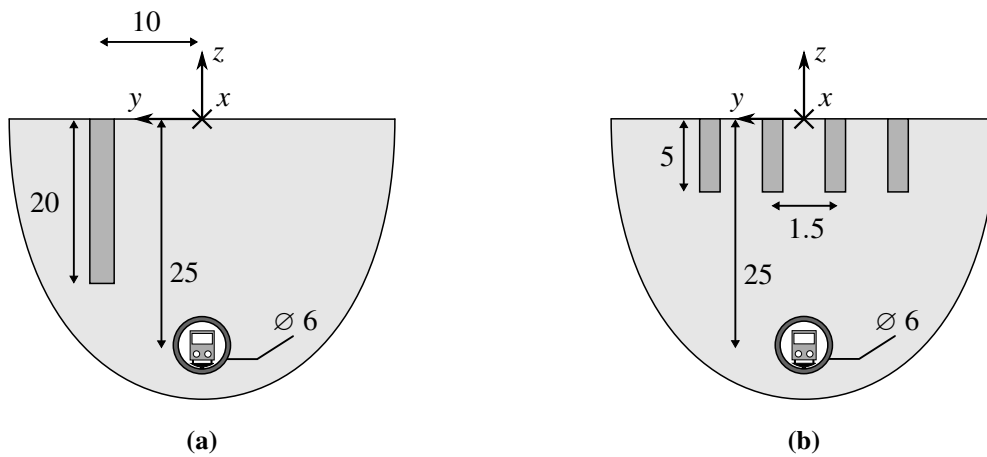
Fig. 5.3 Schematic diagrams of **(a)** the off-centred pile and **(b)** the centred 1×4 pile-group near their respective underground railway tunnels. Dimensions in [m]. Not drawn to scale.

Material parameters [Units]	Soil	Tunnel	Piles
Young's modulus [Pa]	$E_s = 550 \times 10^6$	$E_t = 50 \times 10^9$	$E_p = 30 \times 10^9$
Poisson's ratio [−]	$v_s = 0.44$	$v_t = 0.30$	$v_p = 0.25$
Density [kg/m³]	$\rho_s = 2000$	$\rho_t = 2500$	$\rho_p = 2500$
Shear modulus loss factor [−]	$\eta_G = 0.06$	−	−
Outer wall radius [m]	−	$r_{to} = 3.00$	−
Inner wall radius [m]	−	$r_{ti} = 2.75$	−
Diameter [m]	−	−	$d = 0.71$

Table 5.4 Soil, tunnel and pile parameter values used to validate the uncoupled PiP-BEM model.

By inverting the condensed **K** matrix, the displacement FRF matrix for a pile with a fixed head can be computed.

The magnitude and phase of the pile-head displacement FRFs in the transverse (v_{ph}/Δ) and vertical (w_{ph}/Δ) directions are presented in Figs. 5.4–5.9 for the two tunnel-pile configurations. The vertical displacements of the inner and outer piles of the 1×4 pile-group are equivalent on the left- and right-hand sides due to symmetry. Note, Coulier does not publish the results for the transverse displacement and the phase of the free pile-heads in the 1×4 pile-group, so they are not included in Figs. 5.8 and 5.9. Figures 5.6–5.9 also plot the pile-head displacement FRFs when k-PSPI is neglected in the 1×4 pile-group – the PiP-BEM formulation provides an opportunity to study this using the approach detailed in Section 5.2. The greenfield FRFs (i.e., displacement at the free surface before adding the piles) are included in Figs. 5.4–5.9, which are calculated using three different formulations: the half-space PiP model detailed in Section 5.1, Coulier's model [42], and the PiP software [116]. The three formulations should give the same greenfield displacements if the same parameter values are used.

The results show reasonably good agreement between Coulier's model and the uncoupled PiP-BEM model. In particular, there is almost perfect agreement in the transverse responses of the two tunnel-pile configurations. This shows that a simple, analytical pile model based on Euler-Bernoulli beam theory can accurately capture the transverse pile motion, over the entire frequency range, instead of adopting Timoshenko beam theory as Coulier does. The differences in the vertical responses, evident between approximately 50 to 70 Hz and 50 to 60 Hz for the off-centred pile (Figs. 5.4 and 5.5) and 1×4 pile-group (Figs. 5.6–5.9), respectively, are likely to be due to Coulier using different parameter values for the train-track system.

(a)

(b)
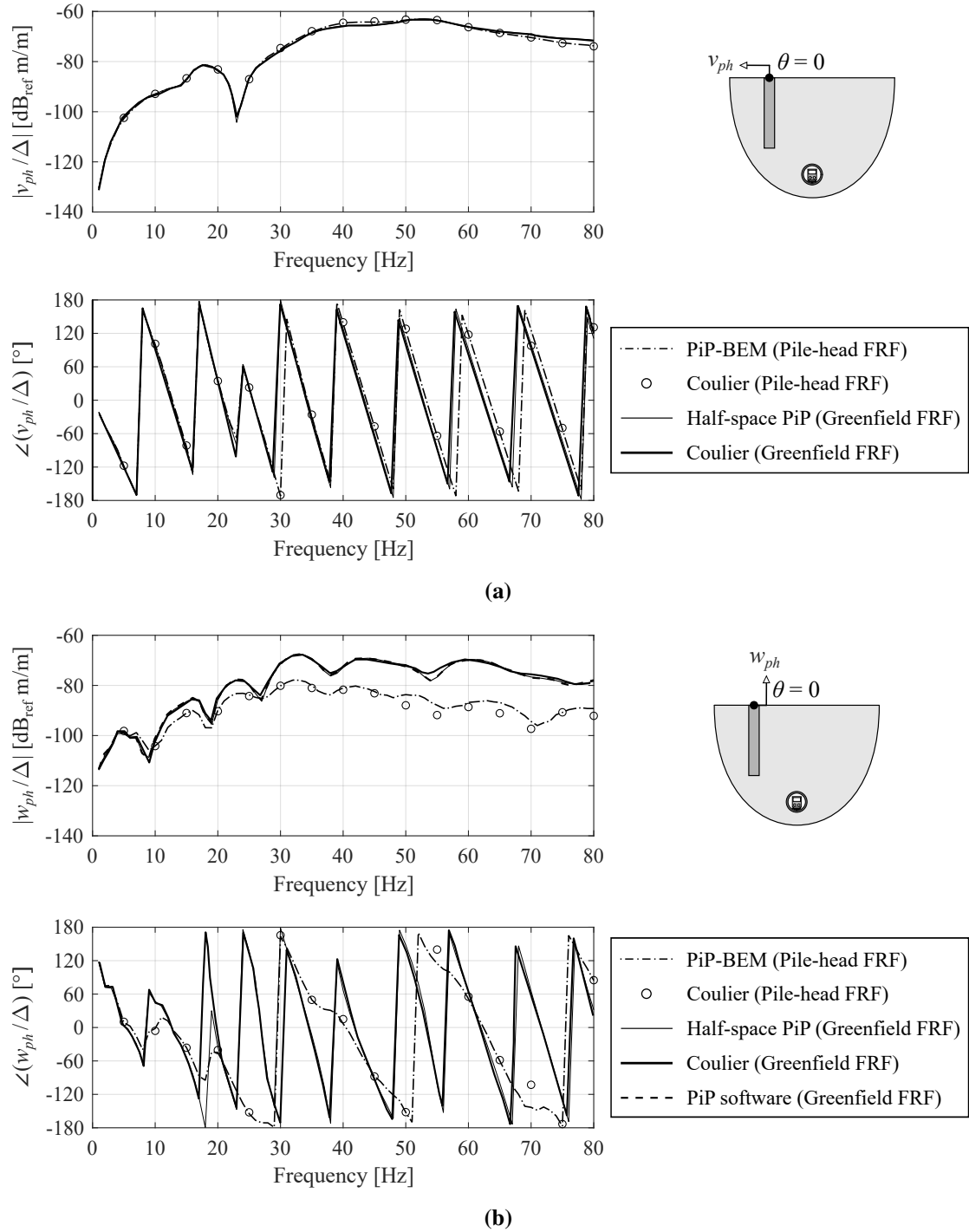
Fig. 5.4 The magnitude and phase of the **(a)** transverse and **(b)** vertical displacement FRFs at the fixed head of the off-centred pile near an underground railway tunnel. The pile-head FRFs are predicted using the PiP-BEM model and Coulier's equivalent model. The greenfield FRFs are predicted using three PiP formulations: the half-space PiP model, Coulier's model and the PiP software.
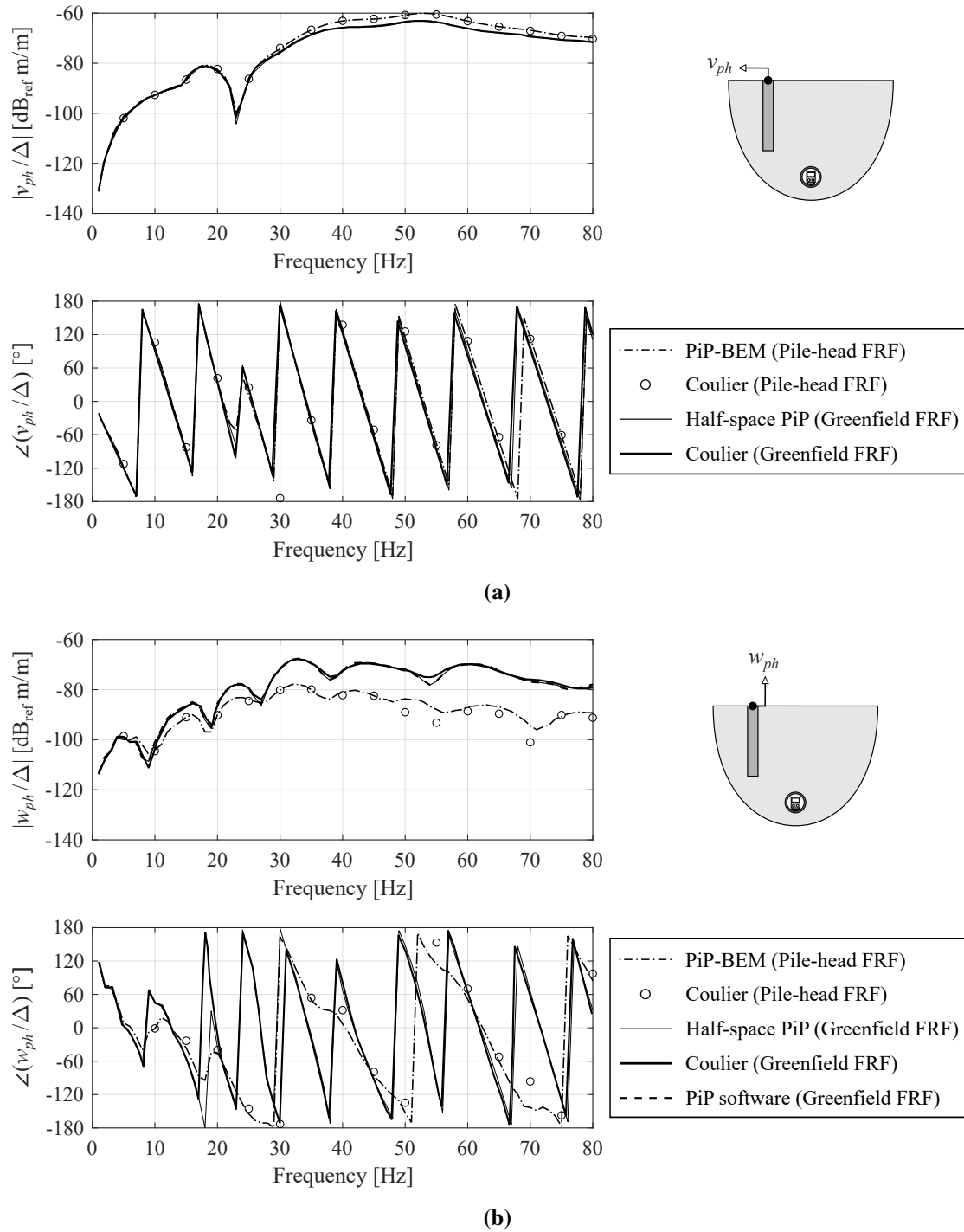
Fig. 5.5 The magnitude and phase of the **(a)** transverse and **(b)** vertical displacement FRFs at the free head of the off-centred pile near an underground railway tunnel. The pile-head FRFs are predicted using the PiP-BEM model and Coulier's equivalent model. The greenfield FRFs are predicted using three PiP formulations: the half-space PiP model, Coulier's model and the PiP software.
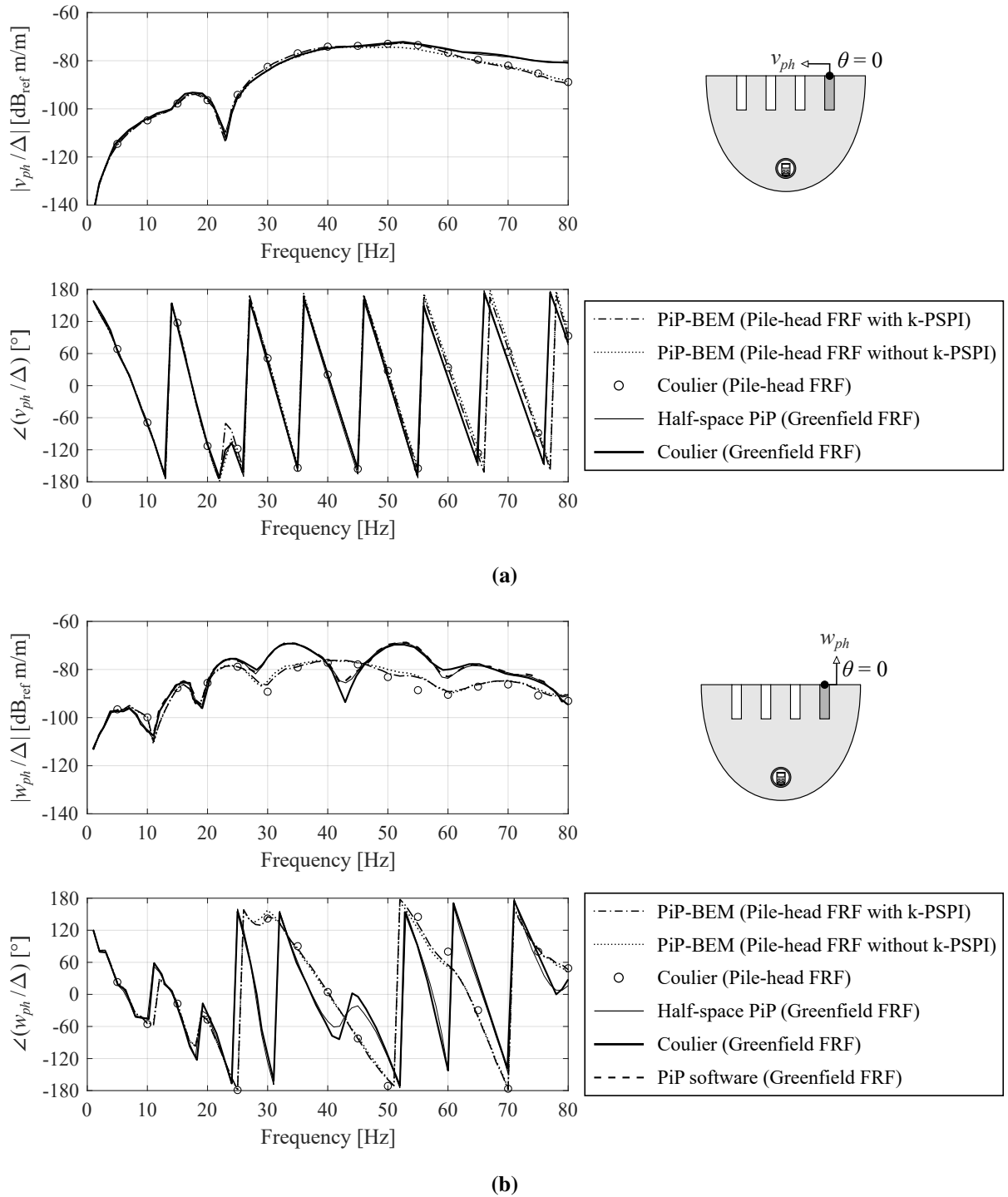
Fig. 5.6 The magnitude and phase of the **(a)** transverse and **(b)** vertical displacement FRFs at the fixed, outer pile head (shaded) of the centred 1×4 pile-group near an underground railway tunnel. The pile-head FRFs are predicted using the PiP-BEM model, with and without k-PSPI, and Coulier's equivalent model. The greenfield FRFs are predicted using three PiP formulations: the half-space PiP model, Coulier's model and the PiP software.
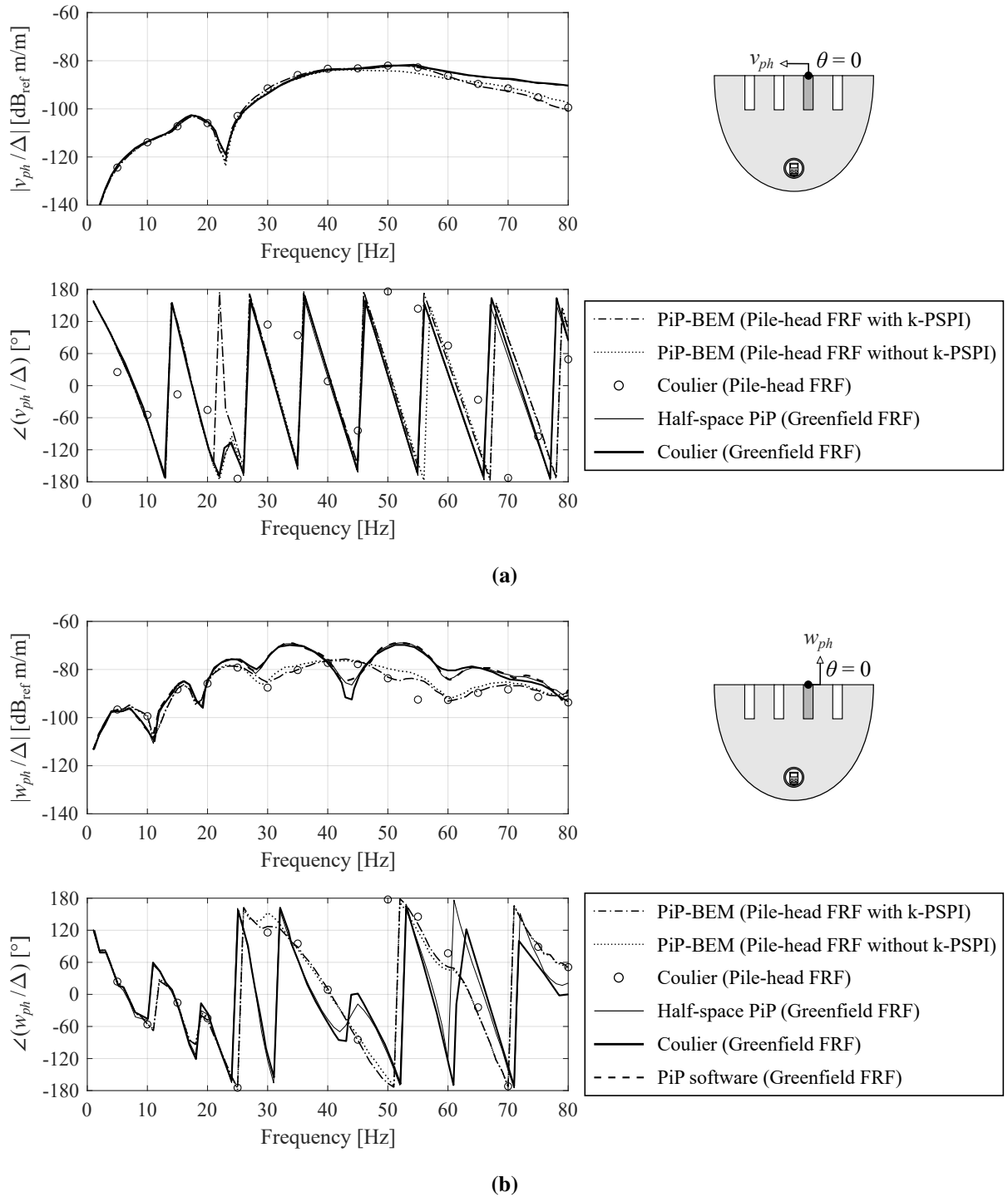
Fig. 5.7 The magnitude and phase of the **(a)** transverse and **(b)** vertical displacement FRFs at the fixed, inner pile head (shaded) of the centred 1×4 pile-group near an underground railway tunnel. The pile-head FRFs are predicted using the PiP-BEM model, with and without k-PSPI, and Coulier's equivalent model. The greenfield FRFs are predicted using three PiP formulations: the half-space PiP model, Coulier's model and the PiP software.

(a)

(b)
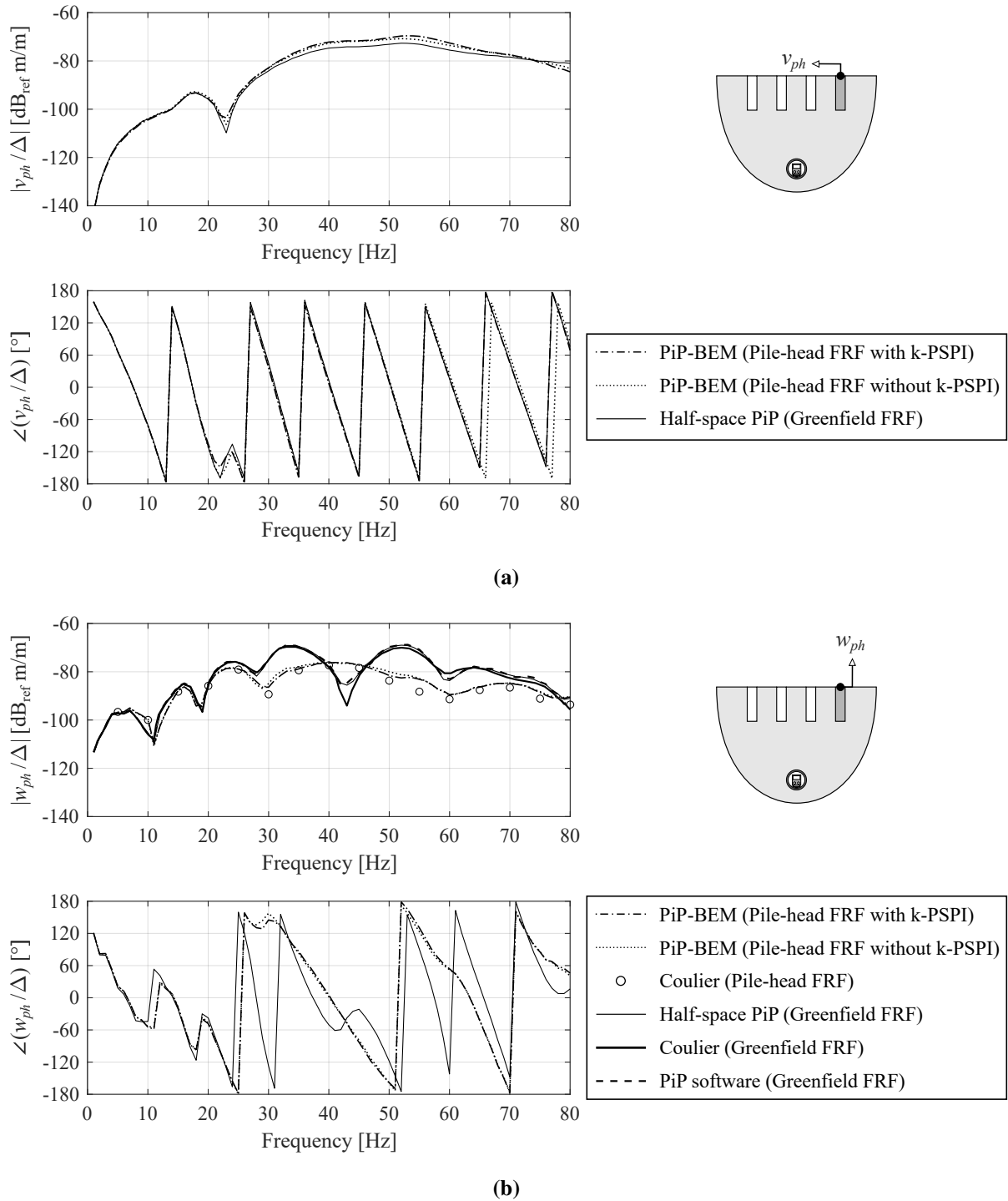
Fig. 5.8 The magnitude and phase of the **(a)** transverse and **(b)** vertical displacement FRFs at the free, outer pile head (shaded) of the centred 1×4 pile-group near an underground railway tunnel. The pile-head FRFs are predicted using the PiP-BEM model, with and without k-PSPI, and Coulier's equivalent model. The greenfield FRFs are predicted using three PiP formulations: the half-space PiP model, Coulier's model and the PiP software.

(a)

(b)
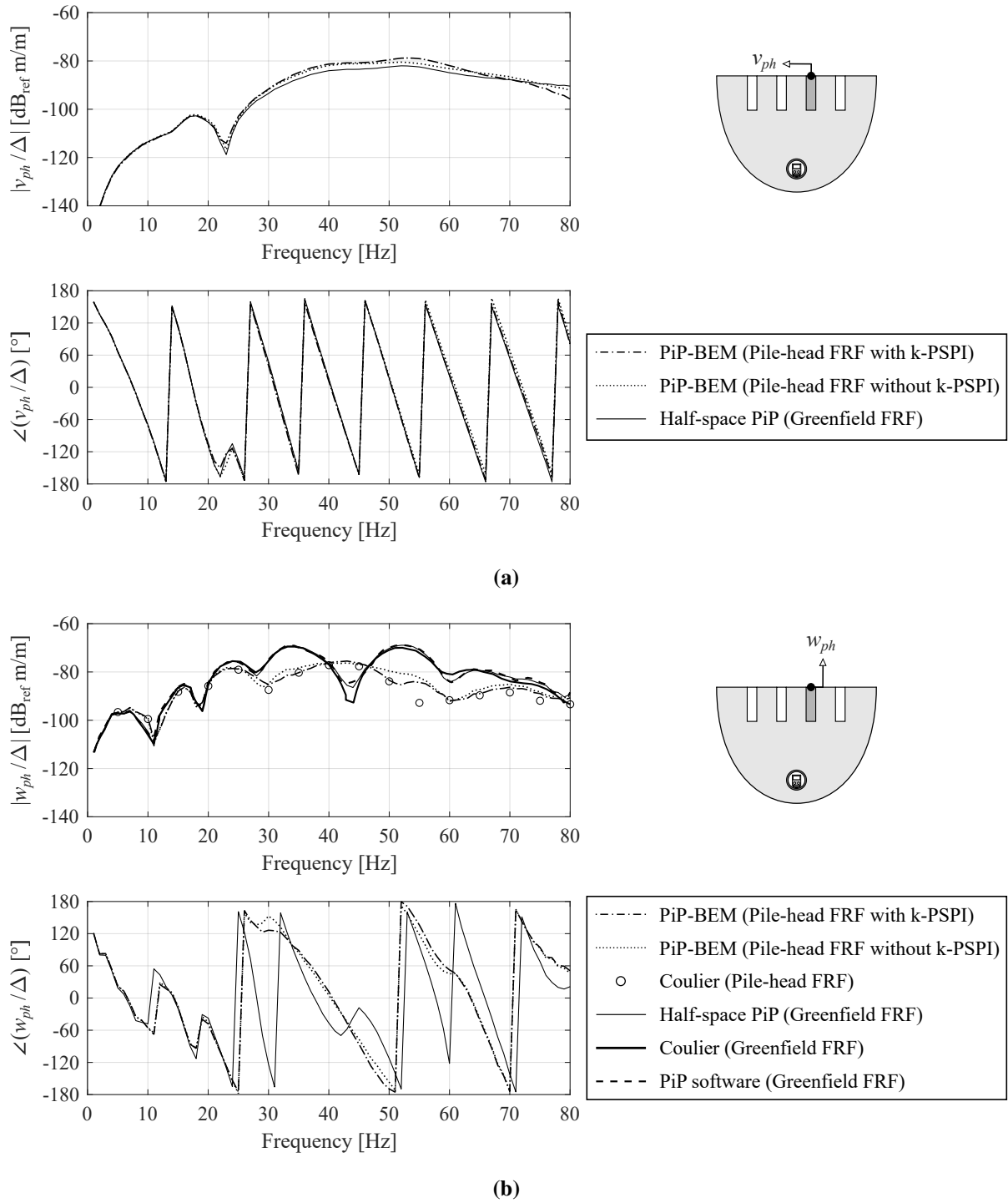
Fig. 5.9 The magnitude and phase of the (a) transverse and (b) vertical displacement FRFs at the free, inner pile head (shaded) of the centred 1×4 pile-group near an underground railway tunnel. The pile-head FRFs are predicted using the PiP-BEM model, with and without k-PSPI, and Coulier's equivalent model. The greenfield FRFs are predicted using three PiP formulations: the half-space PiP model, Coulier's model and the PiP software.

107

A key point to address from the results is the modification in ground vibration levels once a piled foundation is constructed, which, in this case, is referred to as the *added-pile effect*. The transverse displacement at the heads of both pile configuration closely follow that of the soil (i.e., the greenfield displacement) over the full frequency range of interest, which means that the added-pile effect in the transverse direction is negligible. Likewise, the same negligible difference is observed in the vertical displacement, but only below 20 Hz. This is because the piles undergo rigid-body motion at low frequencies by closely following the long-wavelength deformation of the soil. At higher frequencies, the vertical displacement at each pile head differs considerably from that of the soil: at certain frequencies the pile-head displacement is approximately 15 dB lower than the greenfield displacement, and the well-defined undulations in the greenfield response, which arise due to wave interference in the soil [85], are smoothed out by embedding the piles. This occurs due to the soil-stiffening effect, as the piles constrain the soil's motion, which was observed earlier in Section 4.6 when considering PSPI. A similar effect is also observed by Makris and Fan et al. when considering the response of a single pile to R-waves [162] and upward-travelling S-waves [62], respectively. Thus, the addition of piles tends to attenuate the wave-field in the soil, albeit with occasional 'amplification', as observed in Figs. 5.6–5.9 between 40 and 46 Hz. A comprehensive analysis on how the soil-stiffening effect influences the pile-head response, as the pile length is varied, is presented in Section 6.6.

When the pile heads are unconstrained, Figs. 5.4, 5.5, 5.8 and 5.9 show that the transverse displacements of the off-centred pile and the centred 1×4 pile-group increase by around 3 dB between 40 and 60 Hz, compared to when the heads are fixed. This is possibly due to in-phase rocking motion induced at the free pile-head, which causes the net transverse displacement to increase. In contrast, the same figures exhibit no differences between the vertical displacements when the pile heads are fixed and free. This is expected given that the pile's axial and flexural modes of vibration are uncoupled, as described in Section 3.1, so constraining the rotation does not affect the vertical response.

A further observation is that the response of the 1×4 pile-group is essentially the same whether or not k-PSPI is included. The negligible effect of k-PSPI may be surprising given the close spacing between the piles and the soil wavelengths involved (approximately 3 m at 80 Hz), which is in stark contrast to the response of piles to inertial excitation (see Chapter 3), where it is necessary to account for PSPI. However, this insensitivity to k-PSPI may be due to the orientation of the tunnel – orthogonal to, and deep below, the row of piles – and the shortness

of the piles, which reduces the surface area of the soil-pile interface. Since the tunnel is located beneath the centre-line of the pile-group, a large proportion of the scattered wave-field from each pile propagates vertically downwards, instead of interacting with adjacent piles. Similar observations of low k-PSPI have been made in various seismic studies involving the response of piles to upward-travelling S- and P-waves [62, 164, 178], as well as R-waves and obliquely incident SH-waves [163].

5.5 Conclusions

In Sections 5.1 and 5.2, the BEM pile-group model developed in Chapter 3 has been combined with the pipe-in-pipe (PiP) model, which captures the dynamics of a tunnel in a half-space, to predict the train-induced response of a piled foundation due to an underground railway tunnel. The separation distance between the tunnel and foundation was assumed to be greater than the soil wavelengths, which means that the two structures can be treated as isolated sub-systems in the uncoupled PiP-BEM model.

The convergence study in Section 5.3 highlighted the compromises that need to be made between numerical accuracy and computational efficiency when discretising the parameters in the PiP model. For the frequency range of interest (1-80 Hz), appropriate levels of discretisation were recommended for the wavenumbers, the circumferential ring modes, the fictitious-force points and the train axles. By adopting the recommended values for these PiP parameters, the uncoupled PiP-BEM model was used in Section 5.4 to predict the train-induced vibration of two tunnel-pile systems and compare the responses against the predictions made by Coulier's equivalent model [42]. In general, there was reasonably good agreement between both models. However, there were some discrepancies in the vertical pile-head responses, which were likely due to Coulier using different parameter values for the floating slab track (FST) and the train axle mass.

The added-pile effect, which is the modification of the ground (greenfield) response when a piled foundation is constructed, was found for the transverse and vertical responses of the two tunnel-pile systems. At low excitation frequencies, both the transverse and vertical pile-head responses followed the long-wavelength deformation of the soil. The same general trend was observed in the transverse response at high frequencies. In contrast, the added-pile effect had a greater influence on the vertical response at high frequencies: at certain frequencies the pile-

head displacement was approximately 15 dB lower than the greenfield displacement, and the well-defined undulations in the greenfield response were smoothed out by the addition of piles. The soil-stiffening effect due to the addition of piles tends to attenuate the vertical greenfield response, albeit with occasional 'amplification' due to undulation smoothing. Furthermore, it was found that constraining the pile heads against rotation only reduced the transverse pile-head response at high frequencies, whereas the vertical response was unaffected.

Interestingly, the effect of kinematic pile-soil-pile interaction (k-PSPI) on the response of the centred 1×4 pile-group was found to be negligible. This insensitivity to k-PSPI is possibly caused by both the orientation of the tunnel relative to the pile-group and the shortness of the individual piles. The result is that a large proportion of the scattered wave-field from each pile propagates vertically downwards, instead of interacting with adjacent piles.

Chapter 6

Coupled Tunnel-Foundation Systems

In Chapter 5, the tunnel-foundation model only captures the dynamics of an uncoupled source-receiver system because the separation distance between the tunnel and foundation is assumed to span multiple wavelengths in the soil. However, site surveys have found instances where the separation distance is around the same order of magnitude as the soil wavelengths [119, 194], which may increase the prevalence of source-receiver interaction due to through-soil coupling.

A study by Clouteau et al. [32] on the structure-soil-structure interaction (3SI) between multiple buildings found that through-soil coupling has a greater effect on the response when deep embedded foundations, rather than surface foundations, are used. In a recent paper, Kuo et al. [147] assess the differences between the uncoupled and coupled responses of a building near a surface railway as the source-receiver separation distance is varied. The railway and building are coupled using a 2.5D FEM-BEM model by assuming that both structures are infinitely long. They conclude that the separation distance has a negligible effect on the coupled response, as the two structures are resting on top of the ground instead of being embedded in it. Coulier et al. [44] use a similar 2.5D FEM-BEM model to analyse the source-receiver interaction between a building, supported on embedded strip foundations, and an underground tunnel excited via a time-harmonic point load. They observe that the source-receiver interaction mainly affects the train-induced response if the separation distance is less than the pressure wavelength in the soil. At particular locations, the insertion gain (IG) between the coupled and uncoupled responses can be as high as 10 dB, which re-emphasises that through-soil coupling can have a significant effect on the response when either the source or receiver is fully embedded in the ground [32].

In this chapter, the iterative wave-scattering approach described in Chapter 4 is applied to the tunnel-foundation system to develop an iterative PiP-BEM model, which can approximate

the through-soil coupling between a finite piled foundation and an infinitely long underground railway tunnel. Section 6.1 provides a detailed overview of the new iterative PiP-BEM model. Section 6.2 examines whether the new model can account for wave scattering at the free surface. A convergence study is performed in Section 6.3 to identify the level of discretisation required at the soil-tunnel interface when a piled foundation is positioned next to a tunnel. The iterative PiP-BEM model is then used to investigate the significance of source-receiver interaction in some test cases of tunnel-foundation systems in Section 6.4. Section 6.5 describes the changes in the soil response when a standard slab, instead of a floating slab, is used in the railway track. A parametric study is conducted in Section 6.6 for the case of a single pile next to a railway tunnel with a standard slab track, and some concluding remarks are given in Section 6.7.

6.1   The Iterative PiP-BEM Model

In principle, the iterative wave-scattering approach presented in Section 4.1 can approximate the coupling between multiple soil-embedded structures that can be divided into a source sub-system and a receiver sub-system. The result is a coupled source-receiver model that accounts for the wave-fields that propagate back and forth between the two isolated sub-systems, thereby capturing the source-receiver interaction. For the case of a tunnel-foundation system, the sub-systems are represented by the underground tunnel (source) and the piled foundation (receiver), both of which are embedded in their own respective homogeneous half-space.

The iterative approach consists of the four main steps that are illustrated in Fig. 6.1, which are repeated for each iteration. During the first iteration, the full-space PiP model is used in the first step (Fig. 6.1a) to calculate the tunnel response when it is only driven by modal tractions $\widetilde{\mathbf{q}}_n$ at the tunnel invert. In the second step (Fig. 6.1b), the fictitious-force method and the 2.5D, half-space Green's functions are used to find the far-field displacements $\widetilde{\mathbf{u}}^{\text{inc}}$ and tractions $\widetilde{\mathbf{p}}^{\text{inc}}$ induced in a half-space by the fictitious line-loads $\widetilde{\mathbf{f}}$ around the soil-tunnel interface. For further details on applying the second step, the reader can refer to Appendices C.6 and C.7. In the third step (Fig. 6.1c), the far-field displacements and tractions that propagate towards the soil-pile interface ($\mathbf{u}_{\text{SP}}^{\text{inc}}, \mathbf{p}_{\text{SP}}^{\text{inc}}$) and the free surface ($\mathbf{u}_{\text{FS}}^{\text{inc}}, \mathbf{p}_{\text{FS}}^{\text{inc}} = \mathbf{0}$) are used to excite the boundary-element mesh of the pile-group model developed in Chapter 3. Finally, the BEM is used in the fourth step (Fig. 6.1d) to calculate the incident wave-fields that propagate back towards the soil-tunnel interface ($\mathbf{u}_{\text{ST}}^{\text{inc}}, \mathbf{p}_{\text{ST}}^{\text{inc}}$) once the foundation is excited.

(a) Step 1: Full-space PiP model

(b) Step 2: Fictitious-force method

(c) Step 3: BEM pile-group model

(d) Step 4: BEM at internal points
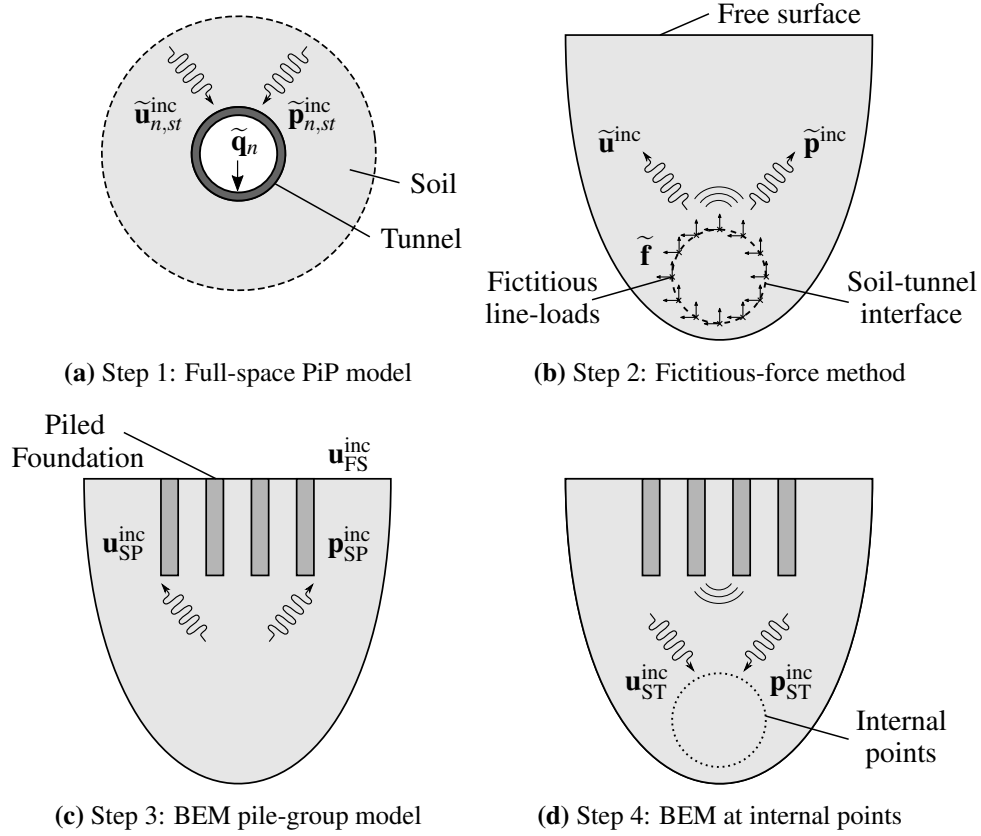
Fig. 6.1 Summary of the four steps during each iteration of the iterative PiP-BEM model, which is used to approximate the tunnel-pile coupling in a tunnel-foundation system.

In all subsequent iterations, the modal components of the incident displacement $\widetilde{\mathbf{u}}_{n,st}^{\text{inc}}$ and traction $\widetilde{\mathbf{p}}_{n,st}^{\text{inc}}$ wave-fields at the soil-tunnel interface are applied as additional excitation loads on the outer tunnel wall during the first step, which revises the tunnel response. These four steps are repeated until convergence is observed. Convergence is deemed to have been achieved when the change, between successive iterations, in the Euclidean norm of the pile-head displacement vector is less than 1%. During each iteration, the tunnel and piled foundation sub-systems are 'weakly' coupled together, thereby giving a better approximation for the fully coupled train-induced response.

Note, the first three steps in the first iteration are identical to the method described in the uncoupled tunnel-foundation model (see Sections 5.1 and 5.2). The remainder of this section outlines: the fourth step, which is used to compute the incident wave-fields at the soil-tunnel interface; and the first step that is used in subsequent iterations to revise the tunnel response.

Once the displacement and traction wave-fields at the free surface ($\mathbf{u}_{\text{FS}}, \mathbf{p}_{\text{FS}} = \mathbf{0}$) and soil-pile interface ($\mathbf{u}_{\text{SP}}, \mathbf{p}_{\text{SP}}$) are computed using the BEM pile-group model, the BEM at internal points in the domain (see Appendix B.7) is used to calculate the wave-fields that propagate
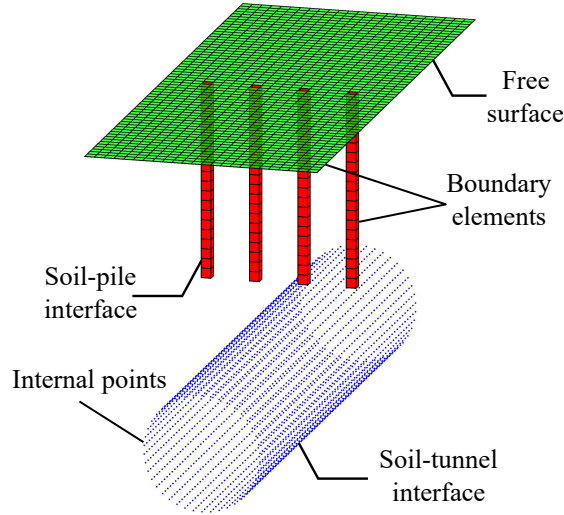
Fig. 6.2 An example of the unbounded 3D mesh for a tunnel-foundation system. Boundary elements are included at the free surface and soil-pile interface, while internal points are included at the soil-tunnel interface.

towards the soil-tunnel interface. The equations in the BEM are derived using the full-space Green's functions in the space-frequency $(\mathbf{x}, \omega)$-domain. As shown in Fig. 6.2, an unbounded 3D mesh is used to discretise the free surface, soil-pile interface and soil-tunnel interface. The free surface and soil-pile interface consists of square boundary elements, whereas the soil-tunnel interface is discretised as a collection of internal points within the soil domain. By using the general relationships between the boundary values and the wave-fields at the internal points, which are expressed in Eqs. (4.8) and (4.9), the incident wave-fields at the soil-tunnel interface $(\mathbf{u}_{\text{ST}}^{\text{inc}}, \mathbf{p}_{\text{ST}}^{\text{inc}})$ can be expressed as the following matrix equations:

$$\mathbf{u}_{\text{ST}}^{\text{inc}} = \mathbf{G}_u \left\{ \begin{matrix} \mathbf{0} \\ \mathbf{p}_{\text{SP}} \end{matrix} \right\} - \mathbf{H}_u \left\{ \begin{matrix} \mathbf{u}_{\text{FS}} \\ \mathbf{u}_{\text{SP}} \end{matrix} \right\}, \tag{6.1}$$

$$\mathbf{p}_{\text{ST}}^{\text{inc}} = \mathbf{G}_p \left\{ \begin{matrix} \mathbf{0} \\ \mathbf{p}_{\text{SP}} \end{matrix} \right\} - \mathbf{H}_p \left\{ \begin{matrix} \mathbf{u}_{\text{FS}} \\ \mathbf{u}_{\text{SP}} \end{matrix} \right\}, \tag{6.2}$$

where the matrices $\mathbf{G}_u$, $\mathbf{H}_u$, $\mathbf{G}_p$ and $\mathbf{H}_p$ are defined in Appendix B.7. The extent of the free surface mesh and the number of internal points that is required at the soil-tunnel interface to achieve convergence in the response are explored in Sections 6.2 and 6.3, respectively.

In subsequent iterations, the incident wave-fields at the soil-tunnel interface need to be applied as external excitation on the outer tunnel wall in the full-space PiP model. Thus, these

wave-fields must first be transformed from the $(\mathbf{x}, \omega)$-domain into the modal-wavenumber-frequency (n, ξ, ω)-domain that is used in the PiP model.

The discrete Fourier transform (DFT), as detailed in Appendix A.2.1, is applied with respect to the longitudinal x-domain to transform the incident wave-fields $(\mathbf{u}_{ST}^{inc}, \mathbf{p}_{ST}^{inc})$ into the wavenumber ξ-domain $(\widetilde{\mathbf{u}}_{ST}^{inc}, \widetilde{\mathbf{p}}_{ST}^{inc})$. Note that the discretised ξ-components in the transformed wave-fields and those used the PiP model must be equivalent. In order to avoid artefacts due to aliasing when computing the DFT, the Nyquist sampling criterion must be met: the sampling wavenumber $2\pi/\Delta x$ must at least be twice the maximum ξ-component ξ_{max}. The longitudinal spacing Δx between internal points will at most be 0.5 m to ensure that at least six points per S-wavelength are used [52]. Based on the Nyquist criterion, the largest ξ-component that can be captured using $\Delta x = 0.5$ m is $\xi_{max} = 2\pi$. In Section 5.3.1, the convergence study on the wavenumbers shows that using the ξ-components up to $\xi_{max} = \pi$ in the half-space PiP model can accurately predict the high-frequency waves that propagate away from the tunnel. Thus, a spacing of at least 0.5 m will be able to capture the large ξ-components of the incident waves at the soil-tunnel interface over the frequency range of interest (1-80 Hz).

Since the distribution of incident wave-fields around the soil-tunnel interface is periodic in the circumferential θ-direction, the wave-fields can be transformed into n circumferential ring modes by finding the discrete Fourier series coefficients. For more details on computing these coefficients for a sampled data set, the reader can refer to Appendix A.3. Therefore, the modal displacement and traction wave-fields can be decomposed into their symmetric $(\widetilde{\mathbf{u}}_{n1,st}^{inc}, \widetilde{\mathbf{p}}_{n1,st}^{inc})$ and anti-symmetric $(\widetilde{\mathbf{u}}_{n2,st}^{inc}, \widetilde{\mathbf{p}}_{n2,st}^{inc})$ components. Since the data is discretely sampled, a sampling criterion, similar to Nyquist's theorem, must be satisfied to avoid errors:

$$N_\theta > 2n_{max} + 1, \tag{6.3}$$

where N_θ is the number of internal points in the θ-direction, and n_{max} is the largest harmonic mode of the incident wave-fields. Numerical errors that could arise due to under-sampling are shown in Fig. A.3. In Section 5.3.2, it is observed that convergence is achieved when the first 11 circumferential ring modes ($n_{max} = 10$) are used in the half-space PiP model. Therefore, at least $N_\theta = 22$ internal elements should be used around the soil-tunnel interface to accurately capture the modal distribution of the incident waves.

Now that the incident waves have been transformed into the (n, ξ, ω)-domain, the excitation due to these waves at the tunnel wall can be expressed in terms of the scattered field in the PiP model. For example, the scattered displacement wave-field at an interface can be written as

$\widetilde{\mathbf{u}}_n - \widetilde{\mathbf{u}}_n^{\text{inc}}$, where $\widetilde{\mathbf{u}}_n$ is the revised displacement wave-field. The tunnel response is expressed in terms of the coefficient vectors $\widetilde{\mathbf{c}}$ and $\overline{\mathbf{b}}$, which describe the propagation of waves in a full-space. In Appendix C.5, the coefficient vectors that describe the revised tunnel motion due to the incident waves at the soil-tunnel interface and the tunnel invert tractions $\widetilde{\mathbf{q}}_n$ are derived, which are repeated here for convenience. The revised coefficients due to symmetric loading are

$$\widetilde{\mathbf{c}}_1 = \begin{bmatrix} \widetilde{\mathbf{C}}_{11} & \widetilde{\mathbf{C}}_{12} \end{bmatrix} \left\{ \begin{array}{c} \widetilde{\mathbf{q}}_n \\ \widetilde{\mathbf{p}}_{n1,st}^{\text{inc}} \big|_{r=r_{to}} - \widetilde{\mathbf{T}}_{m1} \big|_{r=r_{to}} \widetilde{\mathbf{U}}_{m1}^{-1} \big|_{r=r_{to}} \widetilde{\mathbf{u}}_{n1,st}^{\text{inc}} \end{array} \right\}, \tag{6.4}$$

$$\overline{\mathbf{b}}_1 = \widetilde{\mathbf{U}}_{m1}^{-1} \big|_{r=r_{to}} \left(\widetilde{\mathbf{U}}_1 \big|_{r=r_{to}} \widetilde{\mathbf{c}}_1 - \widetilde{\mathbf{u}}_{n1,st}^{\text{inc}} \right), \tag{6.5}$$

and the revised coefficients due to anti-symmetric loading are

$$\widetilde{\mathbf{c}}_2 = \begin{bmatrix} \widetilde{\mathbf{C}}_{21} & \widetilde{\mathbf{C}}_{22} \end{bmatrix} \left\{ \begin{array}{c} \mathbf{0} \\ \widetilde{\mathbf{p}}_{n2,st}^{\text{inc}} \big|_{r=r_{to}} - \widetilde{\mathbf{T}}_{m2} \big|_{r=r_{to}} \widetilde{\mathbf{U}}_{m2}^{-1} \big|_{r=r_{to}} \widetilde{\mathbf{u}}_{n2,st}^{\text{inc}} \end{array} \right\}, \tag{6.6}$$

$$\overline{\mathbf{b}}_2 = \widetilde{\mathbf{U}}_{m2}^{-1} \big|_{r=r_{to}} \left(\widetilde{\mathbf{U}}_2 \big|_{r=r_{to}} \widetilde{\mathbf{c}}_2 - \widetilde{\mathbf{u}}_{n2,st}^{\text{inc}} \right), \tag{6.7}$$

where the matrices are defined in Appendix C. The revised displacements and tractions at the soil-tunnel interface are found by substituting the coefficient vectors into Eqs. (C.69)–(C.72).

6.2 The Effect of the Free Surface on the Tunnel Response

Over the frequency range from 1 to 80 Hz, multiple studies have demonstrated that there is good agreement between the PiP model and coupled FEM-BEM models when a tunnel is embedded in either a homogeneous [110,114] or layered [118] half-space. To reiterate, the PiP model uses the fictitious-force method to find an equivalent set of line-loads that, when applied in a full-space where the tunnel cavity is filled in with soil material, produce the same displacements at the soil-tunnel interface as when the cavity was present. These fictitious line-loads are then used to excite a homogeneous half-space. One of the key assumptions in this step is that the free surface does not influence the near field around the tunnel; that is, the response at the soil cavity is the same whether the tunnel is embedded in a full-space or a half-space. This assumption is valid when the distance between the tunnel crown and the free surface (the tunnel-ground separation distance) spans multiple wavelengths in the soil. However, when the tunnel is closer

to the free surface, the response between the tunnel and free surface becomes coupled. Hence, the near field around the tunnel is likely to be modified by waves that reflect off the free surface.

Hussein et al. [113] use the PiP model and a periodic, coupled FEM-BEM model [50] to compare the greenfield FRFs induced by an excited tunnel in a homogeneous half-space as the tunnel depth D is varied between 5 m and 20 m. In all cases, the tunnel is excited by exerting a time-harmonic point force at the invert. When the tunnel depth is greater than 10 m, there is very good agreement between the two models because the tunnel-ground separation distance is sufficiently large. However, when the tunnel depth is decreased to 5 m, significant differences begin to appear in the displacement magnitudes, which are sometimes in excess of 15 dB at certain frequencies.

In a separate study, Galvín et al. [72] compare the greenfield FRFs predicted by a rigorous, coupled FEM-BEM model [70] and the PiP model when a very shallow tunnel ($D = 5.5$ m) is embedded in a single-layered half-space. This time, the tunnel is driven via a time-harmonic point force at the top of a floating slab track (FST), which is directly coupled to the tunnel invert. The difference in the greenfield response is roughly 10 dB or higher over most frequencies, which is similar to the observations made by Hussein et al. [113]. In both studies, significant differences are present between the PiP and FEM-BEM models because the waves reflected by the ground, which can influence soil-tunnel interaction of shallow tunnels, are not evaluated in the PiP model.

Therefore, this section explores whether the iterative PiP-BEM model (see Section 6.1) can capture the effect of the free surface on the coupled soil-tunnel response of shallow tunnels. For all cases, the tunnel is embedded in a half-space while it is driven by two modes of excitation at the invert: (1) a time-harmonic point force; and (2) a spatially harmonic wheel-rail roughness along the train-track system. Additional information on the excitation mechanisms is available in Appendix C. Most of the work presented in Section 6.2.1 has been published in a conference paper by Edirisinghe et al. [58].

6.2.1 The Response Due to a Time-Harmonic Point Force

Here, the greenfield displacement FRFs are evaluated at three receiver points $(0\text{ m}, 0\text{ m}, 0\text{ m})$, $(0\text{ m}, 20\text{ m}, 0\text{ m})$ and $(20\text{ m}, 20\text{ m}, 0\text{ m})$ on the free surface using the iterative PiP-BEM model when a time-harmonic point force F_0 is applied at the tunnel invert, as illustrated in Fig. 6.3. These FRFs are then compared against the coupled solutions, which are computed using the
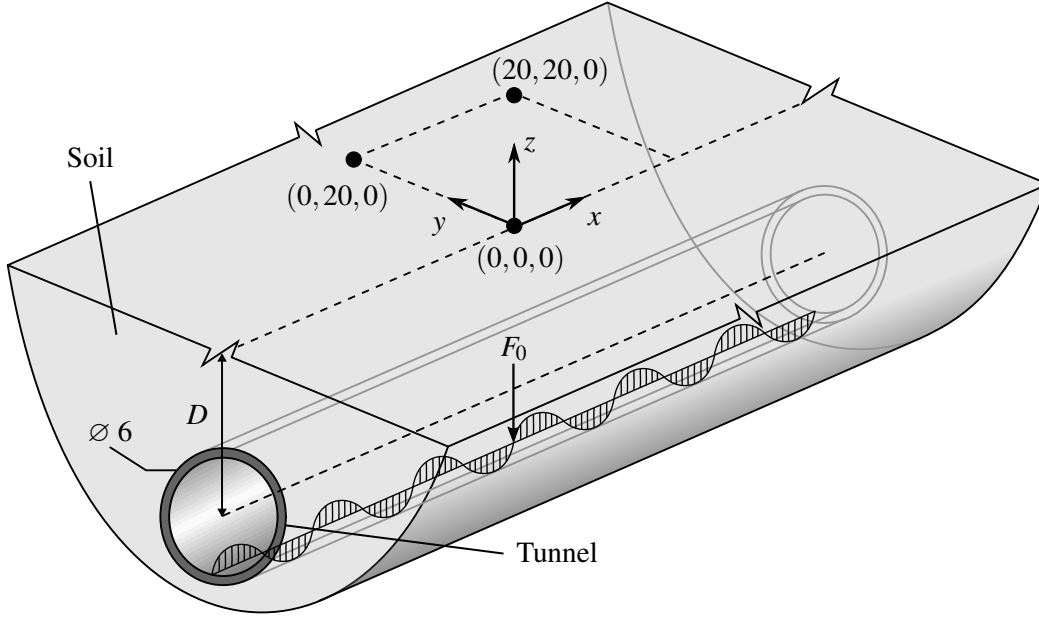
Fig. 6.3 The three receiver points $(0 \, \text{m}, 0 \, \text{m}, 0 \, \text{m})$, $(0 \, \text{m}, 20 \, \text{m}, 0 \, \text{m})$ and $(20 \, \text{m}, 20 \, \text{m}, 0 \, \text{m})$ on the free surface where the greenfield displacement FRFs are predicted for a tunnel embedded in a homogeneous half-space at depth D. The tunnel is excited at the tunnel invert by a time-harmonic point force F_0. Dimensions in [m].

rigorous FEM-BEM model developed by Degrande et al. [50], to validate if the iterative PiP-BEM model can account for the coupled soil-tunnel response.

Three different values of D are considered: very shallow (5 m), shallow (10 m) and medium depth (20 m). For all cases, the tunnel has an inner radius of $r_{ti} = 2.75$ m and an outer radius of $r_{to} = 3.0$ m, and it is constructed out of concrete with a Young's modulus of $E_t = 50$ GPa, a Poisson's ratio of $\nu_t = 0.3$ and a density of $\rho_t = 2500 \, \text{kg/m}^3$. Material damping in the tunnel is accounted for by using a hysteretic loss factor of $\eta_t = 0.03$ associated with both elastic Lamé constants. The half-space consists of a homogeneous soil with P- and S-wave phase speeds of $c_P = 400$ m/s and $c_S = 200$ m/s, respectively, a density of $\rho_s = 1800 \, \text{kg/m}^3$ and a hysteretic loss factor of $\eta_s = 0.04$ associated with both elastic Lamé constants.

The resolution of the mesh is $0.4 \, \text{m} \times 0.4 \, \text{m}$ at the free surface. The longitudinal spacing Δx between internal points at the soil-tunnel interface is 0.4 m, which satisfies the Nyquist criterion when computing the DFT of the incident wave-fields at the outer tunnel wall. In order to satisfy the sampling criterion in Eq. (6.3) when computing the discrete Fourier series coefficients, the number of circumferential points around the soil-tunnel interface is set as $N_\theta = 42$, resulting in a spacing $\Delta \theta$ of 0.448 m.

It is important to find out whether the free surface in the boundary-element mesh needs to be discretised above the tunnel or around the receiver points, where the displacement FRFs are measured. If the response, based on the former discretisation approach, agrees better with the FEM-BEM solution, it will suggest that the coupled soil-tunnel response is predominantly influenced by the reflected waves at the local free surface near the tunnel. The two discretisation approaches for the free surface are investigated in the following sub-sections.

Discretising the Local Free Surface Above the Tunnel

In order to find the greenfield displacement at the receiver point $(0\text{ m}, 0\text{ m}, 0\text{ m})$, the local free surface above the tunnel centre-line needs to be discretised because the response is measured directly above the excitation point at the tunnel invert. An unbounded 3D mesh, similar to the example shown in Fig. 6.4, can be used to discretise the free surface and the soil-tunnel interface in the soil domain. The number of elements at the free surface (N_1, N_2) and the number of longitudinal points N_x at the soil-tunnel interface are constrained by setting $N_1 = N_2 = N_x$, so that the extent of the mesh can be changed by varying a single parameter. In this sub-section, the extent of the mesh is varied between $N_1 = 26$ and $N_1 = 101$ to observe the effect this may have on the greenfield response.

The magnitude of the vertical (w_s/F_0) greenfield displacement FRFs at $(0\text{ m}, 0\text{ m}, 0\text{ m})$ are plotted in Fig. 6.5 for the first six iterations of the PiP-BEM model as both D and N_1 are varied.
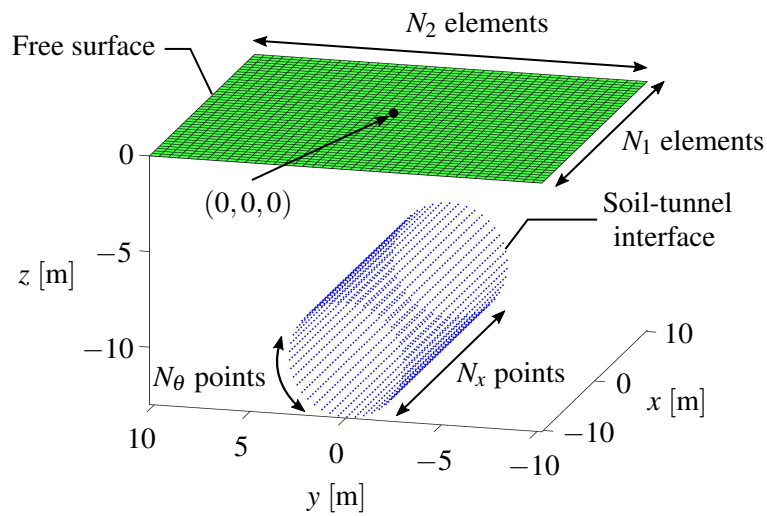
Fig. 6.4 An example of the unbounded 3D mesh, which discretises a finite region of the free surface (green) and soil-tunnel interface (blue), for a tunnel of depth $D = 10$ m. The mesh is used to find the greenfield displacement at a receiver point by only accounting for the waves reflected by the local free surface above the tunnel. $N_1 = N_2 = N_x$ and $N_\theta = 42$.

The responses using the coupled FEM-BEM model are also plotted. Note, for the first iteration of the iterative PiP-BEM model, the FRFs are equivalent to those predicted by the standard PiP model because the tunnel response has not yet been revised by the reflected waves at the free surface. By computing more successive iterations, the response converges towards the coupled solution.
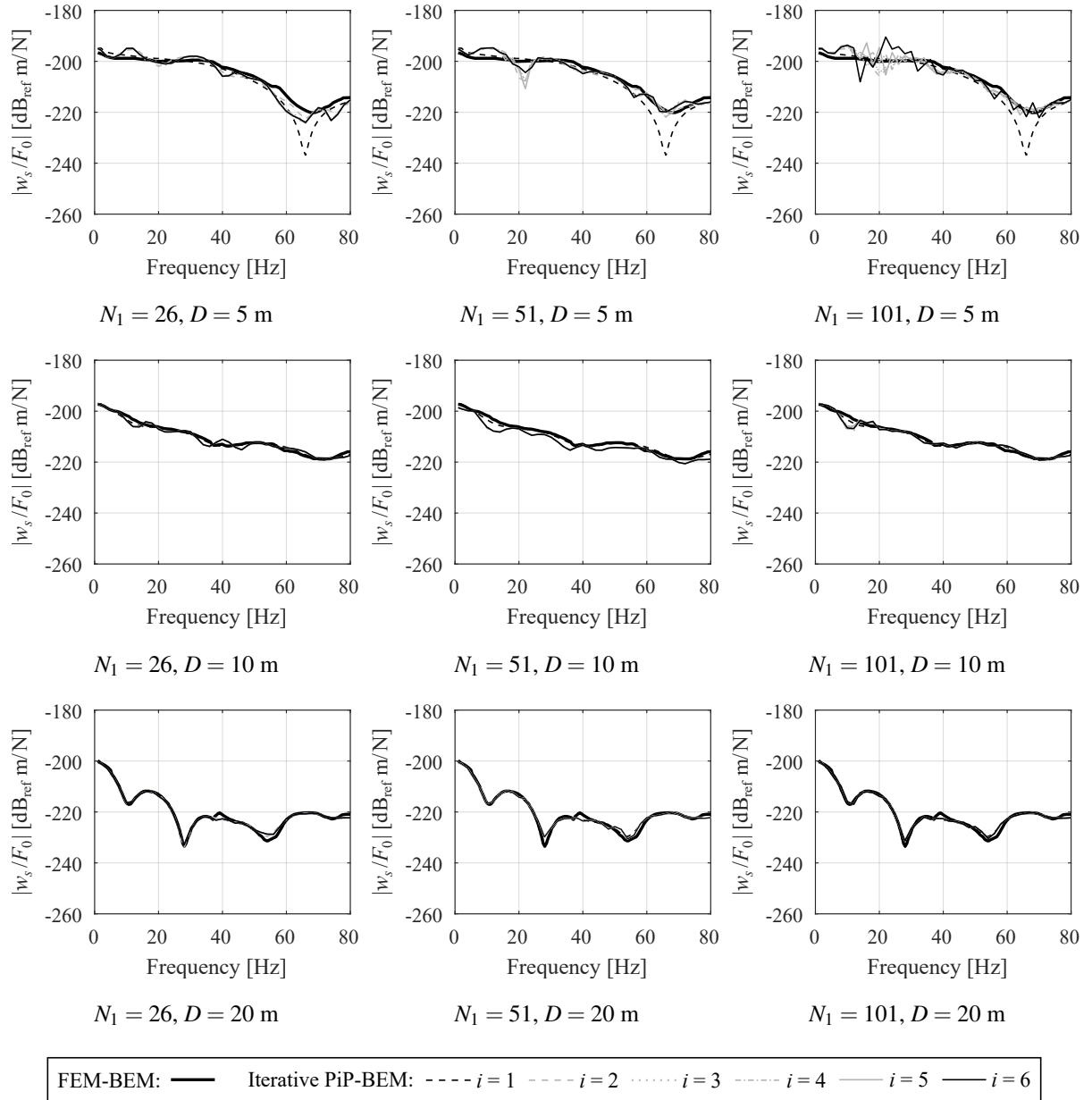
Fig. 6.5 The magnitude of the vertical greenfield displacement FRFs at the point $(0\,\text{m}, 0\,\text{m}, 0\,\text{m})$ when a time-harmonic point force is applied within an underground tunnel. The influence of the tunnel depth D on the response, predicted using the FEM-BEM model and the iterative PiP-BEM model for the first six iterations $(i = 6)$, is illustrated. For the iterative PiP-BEM model, the extent of the mesh shown in Fig. 6.4 is varied by adjusting the number of elements N_1.

When $D \geq 10$ m, there is good agreement between the iterative PiP-BEM model and the FEM-BEM model. At these depths, the FRFs also converge after just one iteration ($i = 1$), which is expected because the tunnel-ground separation distance spans multiple wavelengths. In contrast, when $D = 5$ m, there is a greater difference between the first iteration of the PiP-BEM model (uncoupled response) and the FEM-BEM model (coupled response), particularly at high frequencies above 60 Hz. A distinct anti-resonance is visible in the first iteration's FRF at around 64 Hz, which corresponds to an S-wavelength of approximately 3.1 m in the soil. For a dynamic system, an anti-resonance can be interpreted as a resonance of the system when it is fixed at the excitation point [239]. At 64 Hz, the distance between the excitation point at the tunnel invert and the free surface at $(0 \text{ m}, 0 \text{ m}, 0 \text{ m})$ spans approximately 2.5 S-wavelengths. This suggests that when wave-scattering effects are neglected during the first iteration, the anti-resonance is caused by the destructive interference of S-waves. The anti-resonance at 64 Hz is absent in the FEM-BEM solution and when more iterations are applied to revise the PiP-BEM solution.

In addition, for the very shallow tunnel ($D = 5$ m), there is better agreement between the two models as the number of elements is increased from $N_1 = 26$ to $N_1 = 51$. This is expected because the waves are prevented from leaking around the edges of the mesh when a larger extent of the free surface is discretised. However, as the number of elements is increased further from $N_1 = 51$ to $N_1 = 101$, fluctuating artefacts begin to appear in the greenfield FRFs.

Discretising the Local Free Surface Around the Receiver Points

In this sub-section, the greenfield responses at the points $(0 \text{ m}, 20 \text{ m}, 0 \text{ m})$ and $(0 \text{ m}, 20 \text{ m}, 0 \text{ m})$, which are located far from the tunnel, are predicted using the iterative PiP-BEM model. The local free surface around these points are discretised in the unbounded 3D mesh, as illustrated in Fig. 6.6, to revise the coupled soil-tunnel response.

Figure 6.7 plots the magnitude of the longitudinal (u_s/F_0), transverse (v_s/F_0), and vertical (w_s/F_0) greenfield displacement FRFs at the two receiver points for the first three iterations of the PiP-BEM model when $D = 5$ m. The corresponding results for the coupled FEM-BEM model are also plotted. Note, the longitudinal displacement at the point $(0 \text{ m}, 20 \text{ m}, 0 \text{ m})$ is zero due to symmetry. In general, there are no significant changes in the responses at both points as the number of iterations is increased, implying that the reflected waves at the local free surface around the receiver points do not influence the coupled soil-tunnel response.
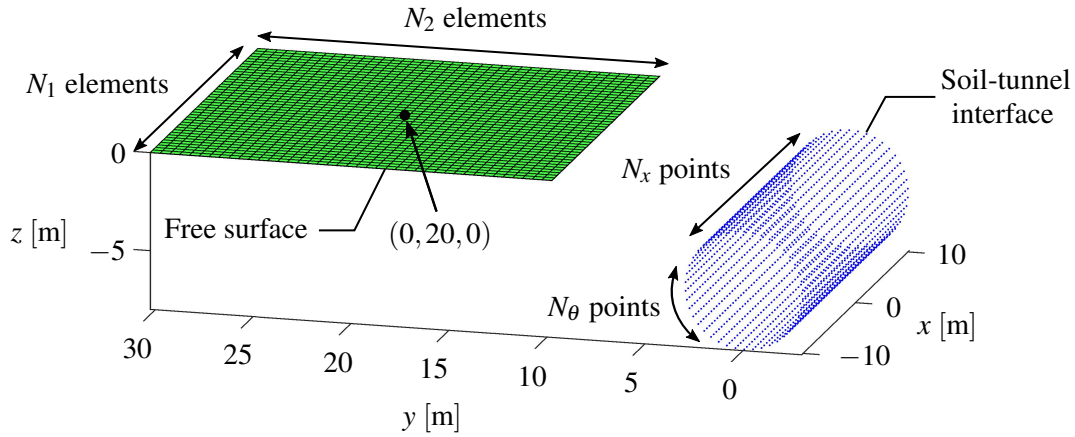
Fig. 6.6 An example of the unbounded 3D mesh, which discretises a finite region of the free surface (green) and soil-tunnel interface (blue), for a tunnel of depth $D = 5$ m. The mesh is used to find the greenfield displacement at a receiver point by only accounting for the waves reflected by the local free surface around that point. $N_1 = N_2 = N_x = 51$ and $N_\theta = 42$.
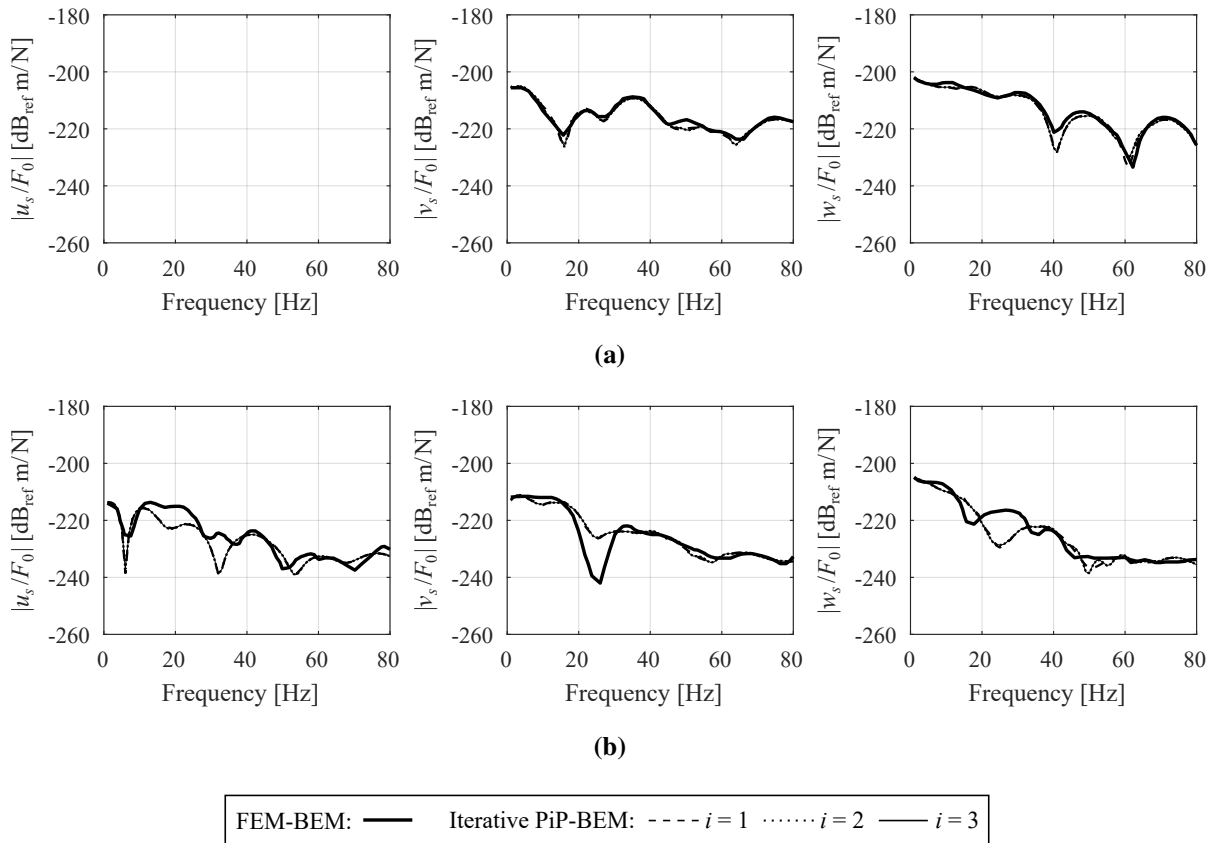
Fig. 6.7 The magnitude of the longitudinal, transverse and vertical greenfield displacement FRFs at the points **(a)** $(0 \text{ m}, 20 \text{ m}, 0 \text{ m})$ and **(b)** $(20 \text{ m}, 20 \text{ m}, 0 \text{ m})$ (bottom) when a time-harmonic point force is applied within an underground tunnel at depth $D = 5$ m. The FRFs are predicted using the FEM-BEM model and the iterative PiP-BEM model for the first three iterations ($i = 3$). A mesh similar to Fig. 6.6 is used in the iterative PiP-BEM model.

In comparison with the FEM-BEM solutions, the greenfield displacement FRFs predicted using the iterative PiP-BEM model deviate by at most 15 dB at some frequencies, which is very significant. This is because, unlike in the previous sub-section, the waves reflected by the local free surface directly above the tunnel centre-line are not captured by the mesh in the iterative PiP-BEM model. Thus, the mesh should be modified to capture the waves reflected by the local free surface near the tunnel, as they predominantly affect the coupled soil-tunnel interaction.

The Free Surface Displacement in the Far Field

Based on the observations made in the previous sub-section, a mesh that is similar to the one illustrated in Fig. 6.4, where the local free surface above the tunnel centre-line is discretised, is used to obtain better estimates for the coupled soil-tunnel response at the two points furthest from the tunnel. The extent of the mesh is also fixed by setting $N_1 = 51$ in order to minimise the amplitude of the fluctuating artefacts, which previously appeared in the FRF plots in Fig. 6.5.
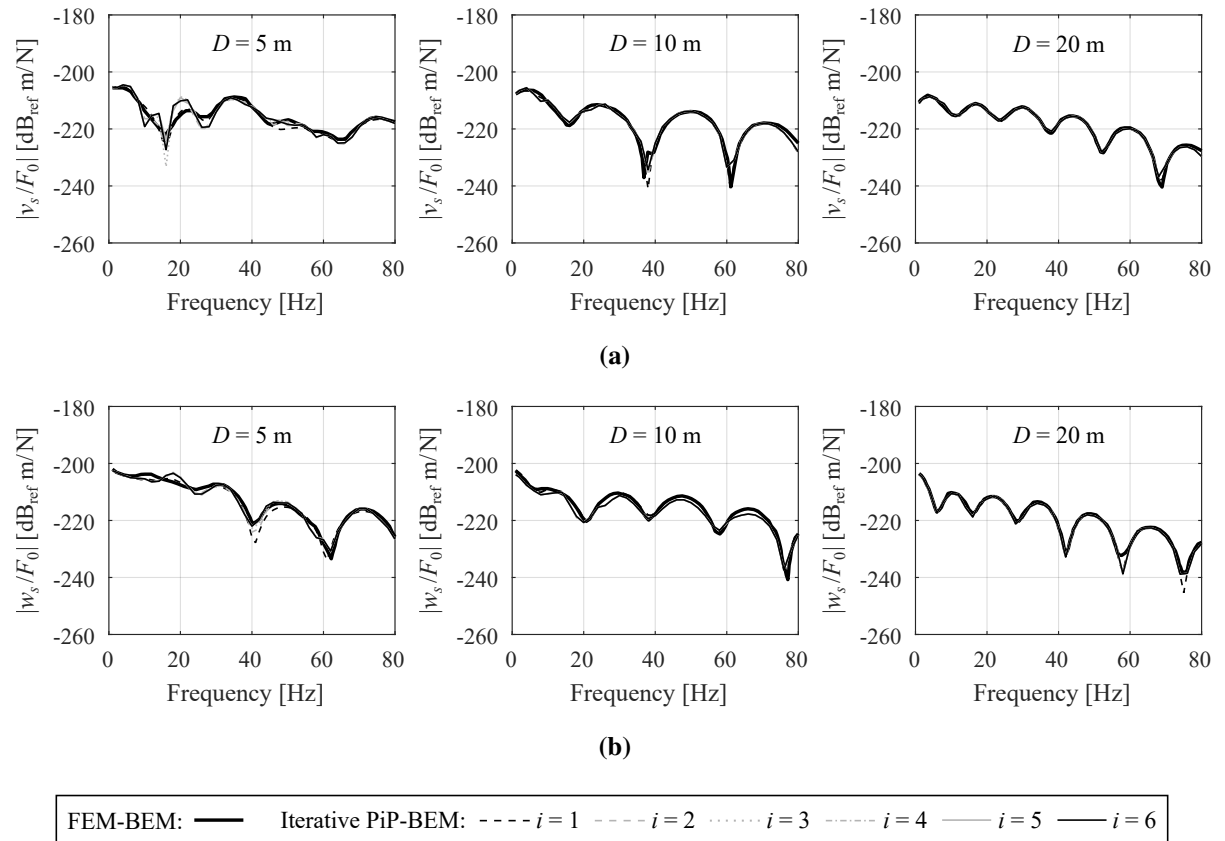
Fig. 6.8 The magnitude of the **(a)** transverse and **(b)** vertical greenfield displacement FRFs at the point $(0 \text{ m}, 20 \text{ m}, 0 \text{ m})$ when a time-harmonic point force is applied within an underground tunnel. The influence of the tunnel depth D on the response, predicted using the FEM-BEM model and the iterative PiP-BEM model for the first six iterations ($i = 6$), is illustrated. A mesh similar to Fig. 6.4 is used in the iterative PiP-BEM model with $N_1 = 51$ elements.

Figures 6.8 and 6.9 plot the magnitude of the longitudinal (u_s/F_0), transverse (v_s/F_0), and vertical (w_s/F_0) greenfield displacement FRFs at $(0\text{ m}, 20\text{ m}, 0\text{ m})$ and $(20\text{ m}, 20\text{ m}, 0\text{ m})$, respectively, for the first six iterations of the iterative PiP-BEM model. The influence on the FRFs, when varying D, is also shown. As expected, there is good agreement between the FEM-BEM model and the first iteration of the PiP-BEM model when $D \geq 10$ m. When the tunnel depth is lowered to $D = 5$ m, the FRFs predicted using the sixth iteration $(i = 6)$ agree better
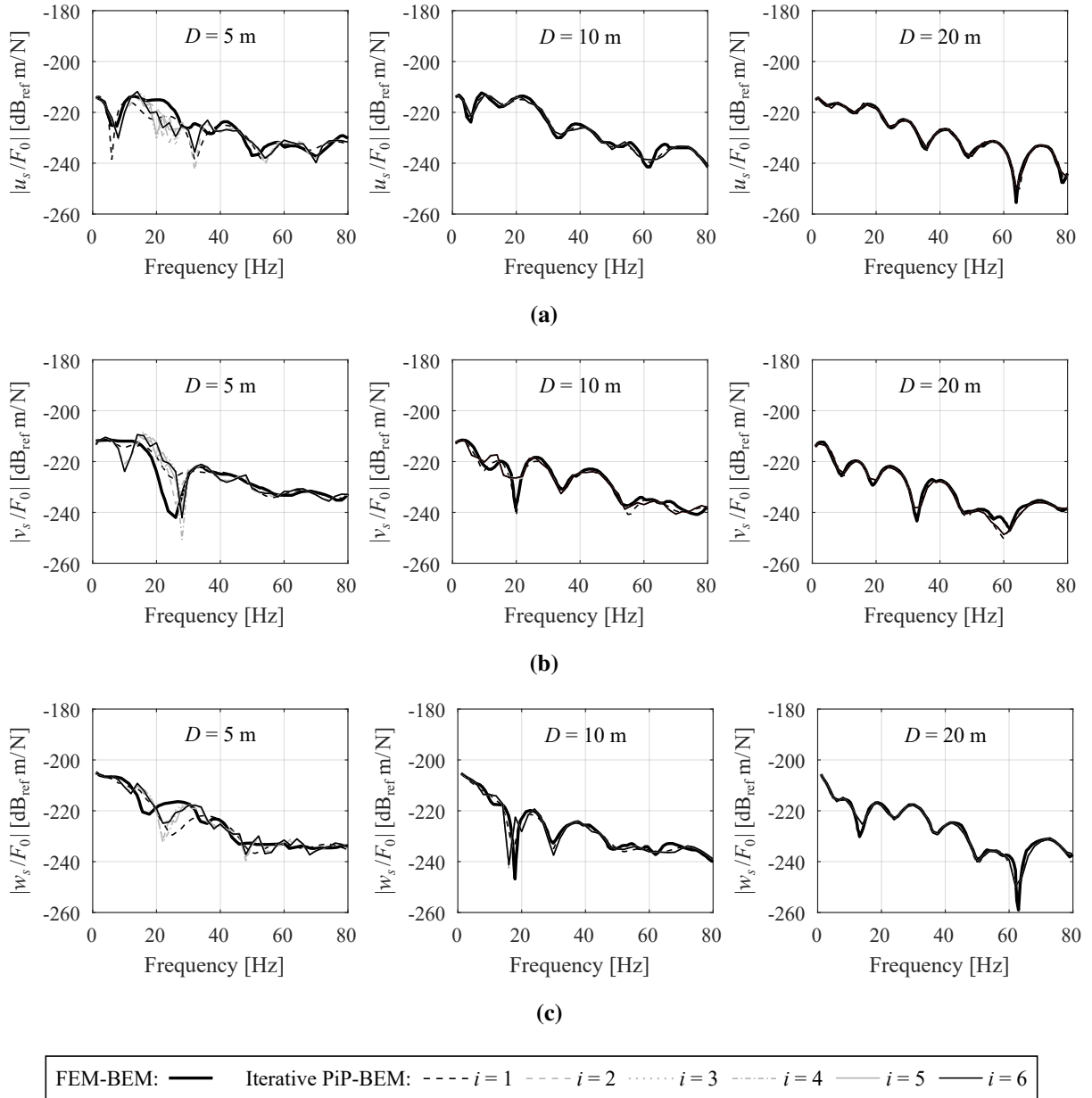
Fig. 6.9 The magnitude of the **(a)** longitudinal, **(b)** transverse and **(c)** vertical greenfield displacement FRFs at the point $(20\text{ m}, 20\text{ m}, 0\text{ m})$ when a time-harmonic point force is applied within an underground tunnel. The influence of the tunnel depth D on the response, predicted using the FEM-BEM model and the iterative PiP-BEM model for the first six iterations $(i = 6)$, is illustrated. A mesh similar to Fig. 6.4 is used in the iterative PiP-BEM model with $N_1 = 51$ elements.

with the FEM-BEM solutions in comparison to the first iteration. In particular, the maximum difference in the transverse response between the models decreased from about 20 dB to 10 dB as the number of iterations is increased. This demonstrates that the iterative PiP-BEM model can capture the coupled soil-tunnel response by revising the response based on the reflected waves at the free surface above the tunnel.

However, fluctuating artefacts are still prevalent in the responses of the very shallow tunnels in Figs. 6.5, 6.8 and 6.9. One possibility for this phenomenon is that when $D = 5$ m, the tunnel crown is positioned very close to the free surface over a large extent of the mesh. Therefore, the unbounded mesh can closely resemble a bounded domain, which may cause the solutions of the boundary-integral equations to lose their uniqueness at certain frequencies, which are known as *fictitious eigenfrequencies* [52] (see Appendix B.8).

Another possibility for the fluctuations is based on the fact that applying a time-harmonic point force at the tunnel invert equally excites all the wavenumbers between $-\infty$ and ∞. This could lead to numerical errors in the revised response at the soil-tunnel interface, as the waves that propagate towards the tunnel can only be transformed into a finite range of the wavenumber ξ-domain when computing the DFT. However, as seen later in Section 6.2.2, these fluctuations becomes less of an issue when a train-track system is coupled to the invert.

6.2.2 The Response Due to Train-Induced Excitation

This section explores the effect of the free surface on the tunnel response when the train-track system coupled to the tunnel invert is excited by a spatially harmonic wheel-rail roughness Δ. The iterative PiP-BEM model is used to evaluate the greenfield displacement FRFs at three receiver points on the free surface: $(0 \text{ m}, 0 \text{ m}, 0 \text{ m})$, $(0 \text{ m}, 5 \text{ m}, 0 \text{ m})$ and $(5 \text{ m}, 5 \text{ m}, 0 \text{ m})$. Note that these points are spaced closer together than those in Section 6.2.1 to ensure that the extent of the discretised free-surface mesh is kept to a computationally manageable size. The influence of varying D on the greenfield response is also analysed by considering the same three tunnel depths $(D = 5 \text{ m}, 10 \text{ m}, 20 \text{ m})$ that were studied in the previous section.

For all cases, the railway tunnel has the same geometry and material parameter values as the concrete tunnel in Section 6.2.1. The train-track system, which is represented by equally spaced train axles on top of an FST, is modelled using the same parameter values that are summarised in Table 5.3. The homogenous half-space around the tunnel is modelled as London Clay so that it is representative of physical soil. The same material parameter values that are summarised in

Table 5.2 are used to characterise the London Clay, resulting in phase speeds of $c_P = 1572$ m/s and $c_S = 220$ m/s for the P- and S-waves. Based on the soil wavelengths between 1 and 80 Hz, the mesh resolution at the free surface and the soil-tunnel interface need to be 0.5 m × 0.5 m and 0.5 m × 0.448 m, respectively, to maintain numerical accuracy. The local free surface above the tunnel centre-line is discretised in the mesh, similar to Fig. 6.4, and the extent of the mesh in the longitudinal and transverse directions can be adjusted by varying the number of elements N_1, as outlined in Section 6.2.1.
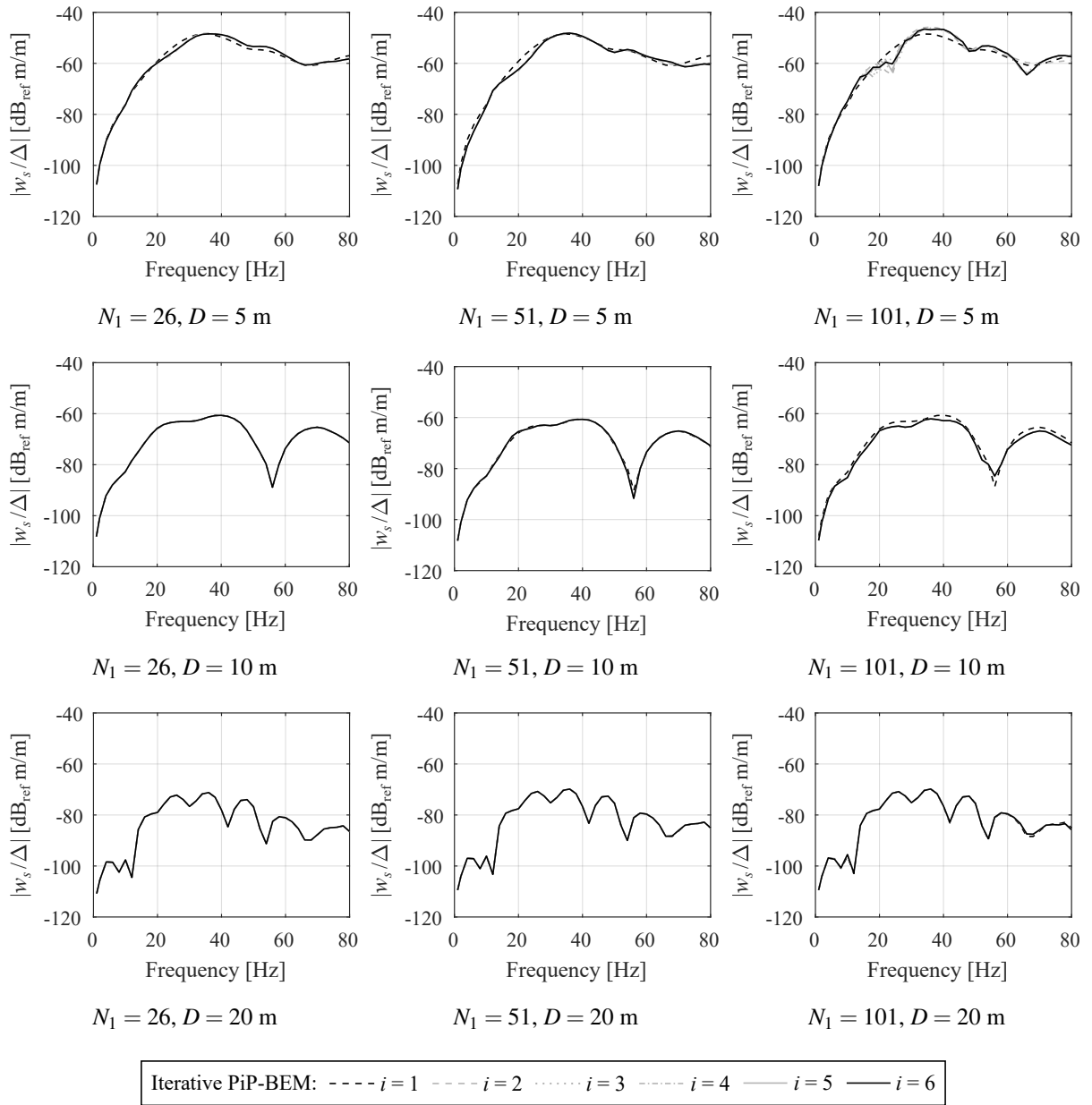
Fig. 6.10 The magnitude of the vertical greenfield displacement FRFs at the point $(0\text{ m}, 0\text{ m}, 0\text{ m})$ due to the ground-borne vibration from an underground railway tunnel. The influence of the tunnel depth D on the response, predicted using the iterative PiP-BEM model for the first six iterations $(i = 6)$, is illustrated. The extent of the mesh shown in Fig. 6.4 is varied by adjusting the number of elements N_1.

Figure 6.10 plots the magnitude of the vertical (w_s/Δ) greenfield displacement FRFs at the point $(0\text{ m}, 0\text{ m}, 0\text{ m})$ for the first six iterations of the PiP-BEM model. The sub-figures also illustrate the variations in the responses as both D and N_1 are varied. Similar to the results in Section 6.2.1, when $D \geq 10$ m, convergence is observed in the free surface response after one iteration. As D is decreased to 5 m, the difference in magnitude between the FRFs of the first (uncoupled) and sixth (coupled) iterations increases, but, on average, it is within 5 dB over the whole frequency range. Furthermore, when the extent of the mesh is increased for a very shallow tunnel ($D = 5$ m), there are fewer fluctuating artefacts visible in Fig. 6.10 compared to Fig. 6.5. A possible reason for this is that, theoretically, a narrower band of wavenumbers is excited when the train-track system exerts a distributed force, rather than a single point force, along the infinitely long tunnel invert. Therefore, when the wavenumber domain is discretised in the iterative model, there are likely to be fewer numerical errors that cause the artefacts to appear.
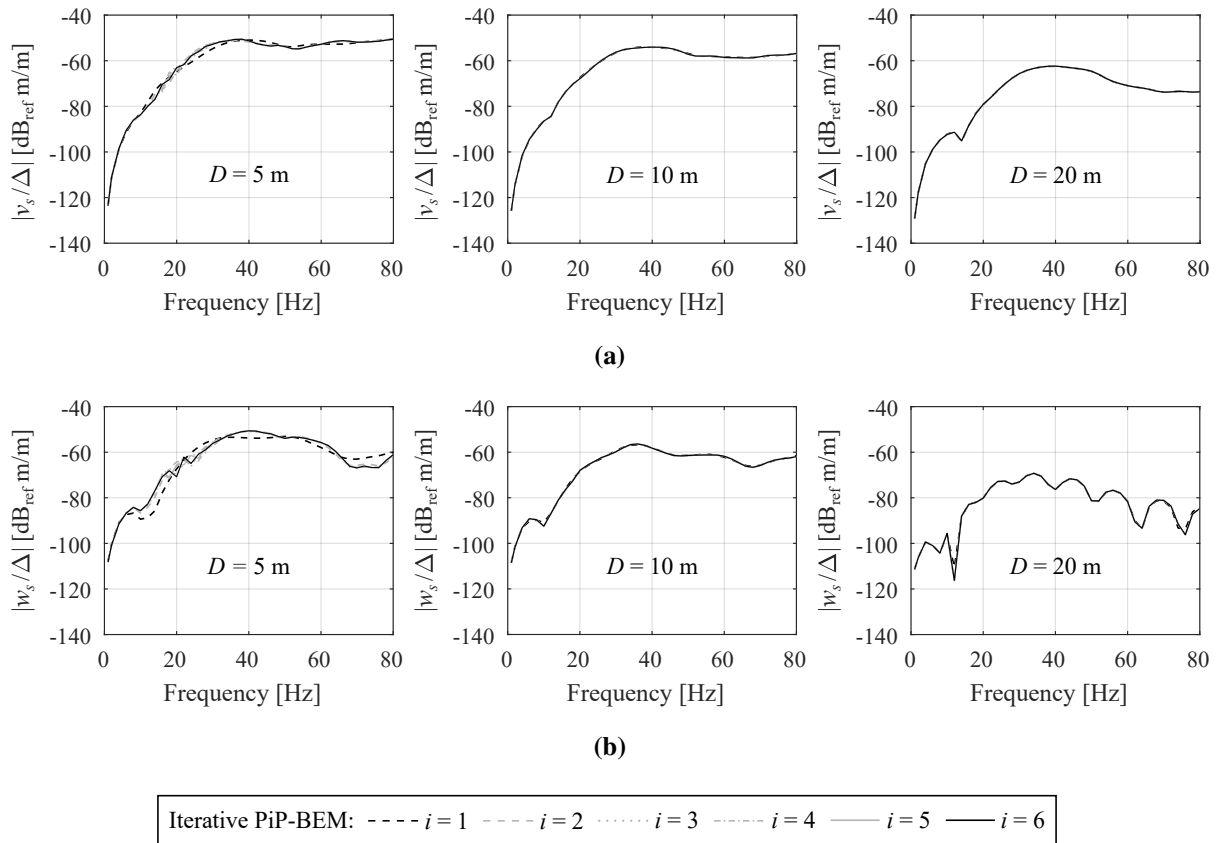
Fig. 6.11 The magnitude of the **(a)** transverse and **(b))** vertical greenfield displacement FRFs at the point $(0\text{ m}, 5\text{ m}, 0\text{ m})$ due to the ground-borne vibration from an underground railway tunnel. The influence of the tunnel depth D on the response, predicted using the iterative PiP-BEM model for the first six iterations ($i = 6$), is illustrated. A mesh similar to Fig. 6.4 is used with $N_1 = 51$ elements.

Figures 6.11 and 6.12 plot the longitudinal (u_s/Δ), transverse (v_s/Δ), and vertical (w_s/Δ) greenfield displacement FRFs at the points $(0 \text{ m}, 5 \text{ m}, 0 \text{ m})$ and $(5 \text{ m}, 5 \text{ m}, 0 \text{ m})$, respectively, for the first six iterations of the PiP-BEM model as D is varied. In both figures, the extent of the mesh is fixed by using $N_1 = 51$ elements. When $D = 5$ m, the free surface has a more significant effect on soil-tunnel interaction in the longitudinal direction, where the difference in the response between the first and sixth iterations can be as high as 10 dB; the corresponding
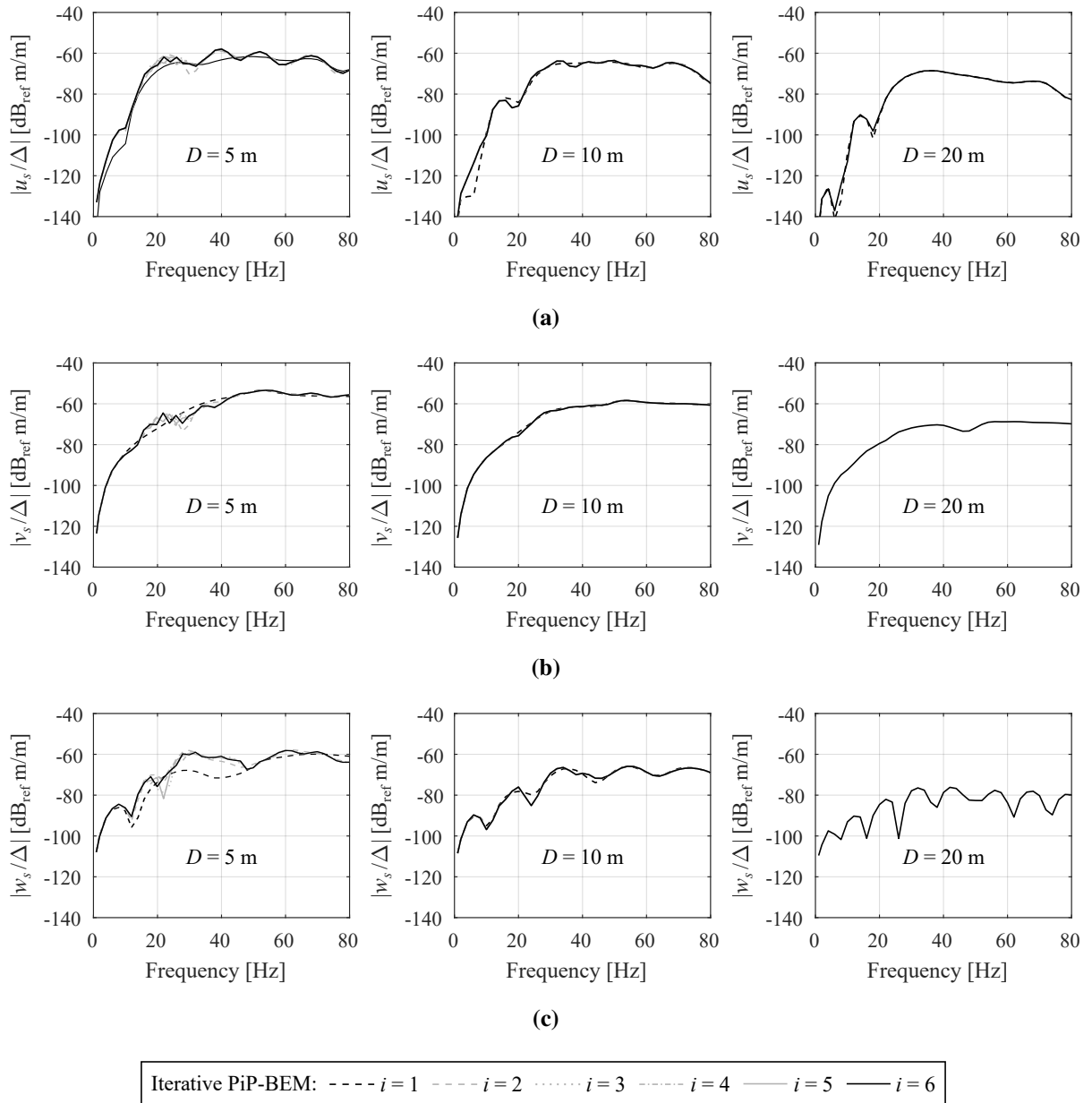
Fig. 6.12 The magnitude of the **(a)** longitudinal, **(b)** transverse and **(c)** vertical greenfield displacement FRFs at the point $(5 \text{ m}, 5 \text{ m}, 0 \text{ m})$ due to the ground-borne vibration from an underground railway tunnel. The influence of the tunnel depth D on the response, predicted using the iterative PiP-BEM model for the first six iterations ($i = 6$), is illustrated. A mesh similar to Fig. 6.4 is used with $N_1 = 51$ elements.

differences in the other two directions are at most 5 dB. In contrast, when $D \geq 10$ m, the effect of the free surface on the soil-tunnel interaction becomes negligible.

In conclusion, the two modes of tunnel excitation studied in Section 6.2 show that waves reflected by the free surface can significantly modify the near field around the tunnel when the tunnel-ground separation distance is less than the tunnel diameter. In this case, the iterative PiP-BEM model is effective at capturing the interaction between the free surface and the shallow tunnel. However, when the separation distance is greater than the tunnel diameter, the effect of the free surface on the tunnel response becomes insignificant, meaning that the PiP model for a homogeneous half-space provides a good solution for the greenfield response.

6.3 A Convergence Study of the Iterative PiP-BEM Model

One of the main conclusions from Section 6.2 is that when the tunnel depth D is greater than the tunnel diameter $2r_{to}$, the free surface has a negligible effect on the tunnel response. Hussein et al. [113] reach a similar conclusion for a tunnel embedded in a multi-layered half-space. Based on these conclusions, the extent of the mesh in the iterative PiP-BEM model can be reduced for specific cases. For example, a large extent of the free surface above the tunnel centre-line does not have to discretised in the mesh for a tunnel with $D \geq 10$ m and an outer radius of $r_{to} = 3$ m because the waves reflected by the ground will not significantly modify the tunnel's near field. Thus, all tunnels considered henceforth in this dissertation will have $D \geq 10$ m.

If a piled foundation is now positioned close to the tunnel, only the local free surface near the piles must be discretised in the mesh to capture the dynamic interaction between the soil-pile interface and the ground. The extent of the free surface, to avoid numerical errors, can be found by following the approach described in Section 3.4, whereby the number of elements (N_1, N_2) is increased until the inertial response of the pile-group converges. Examples of the unbounded meshes for a centred and an off-centred 1×4 pile-group near their respective railway tunnels are illustrated in Fig. 6.13.

To accurately capture the incident waves that propagate towards the tunnel from the excited piled foundation, the number of internal points across the soil-tunnel interface also needs to be determined. This is achieved by using the iterative PiP-BEM model to predict the train-induced displacement at the pile heads of a foundation and then varying the number of points until the response convergences over the frequency range of interest. To demonstrate this approach, the number of longitudinal N_x and circumferential N_θ points at the soil-tunnel interface are found

for the two tunnel-foundation configurations illustrated in Fig. 6.14, which represent a centred 1×2 and 2×2 pile-group directly above their respective railway tunnels.

In both configurations, the pile-group is positioned above the tunnel centre-line, and the transverse distance from the centre of each pile to the outer tunnel wall is 1 m. Therefore, the source-receiver distance is around the same order of magnitude as the soil wavelengths. This means that the tunnel-pile coupling, due to the interaction between the tunnel and foundation, can affect the pile-head response.

Both the railway tunnel and the piles are constructed out of concrete; the respective material parameters values of each structure are equivalent to those in Table 5.2. Table 5.3 summarises the parameter values of the train and FST. The soil is modelled as London Clay using the same material parameter values in Table 5.2, and the mesh is discretised to the same resolution that was recommended in Section 6.2.2.

Figures 6.15 and 6.16 plot the real and imaginary parts of the displacement FRFs at the shaded pile head in the 1×2 and 2×2 pile-groups, respectively. The figures also illustrate the variation in the FRFs as N_x and N_θ are varied. The lines representing the FRFs spiral outwards from the origin as the excitation frequency is increased from 1 to 80 Hz. For each configuration, note that the displacement magnitude at any pile head will be the same due to symmetry. Only the phase of the transverse and longitudinal displacements may vary based on the pile location

(a)   **(b)**
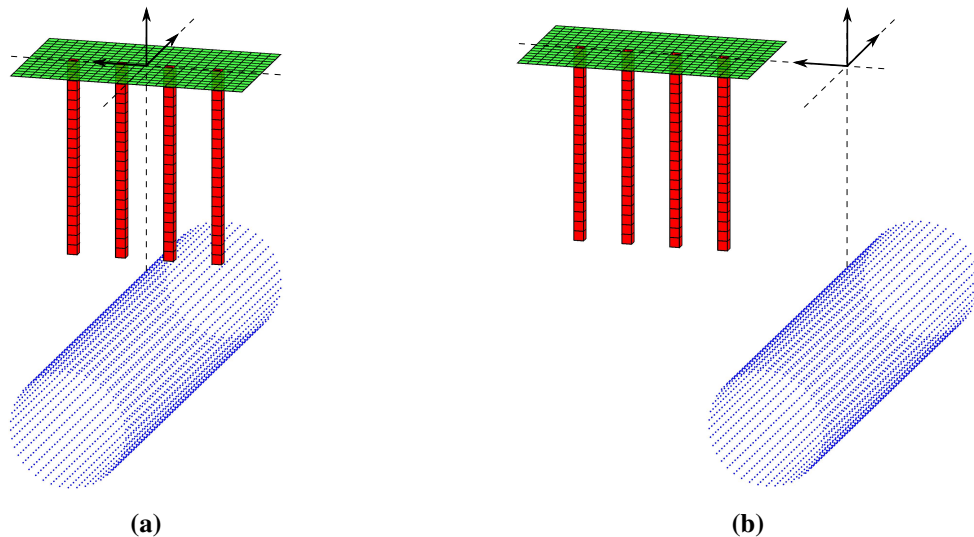
Fig. 6.13 Examples of the unbounded 3D meshes used in the iterative PiP-BEM model, where only the local free surface near the piles is discretised. The two tunnel-foundation meshes represent **(a)** a centred and **(b)** an off-centred 1×4 pile-group near their respective underground railway tunnels. The coloured elements represent the free surface (green) and the soil-pile interface (red), and the blue dotes represent internal points at the soil-tunnel interface.

relative to the tunnel. Also, note that the first iteration $(i = 1)$ of the PiP-BEM model captures the response of an uncoupled source-receiver system, which neglects the interaction between the tunnel and foundation.

In general, the results show that convergence in the coupled tunnel-foundation response is achieved after just the second iteration $(i = 2)$. Furthermore, The difference in the FRFs of the uncoupled and coupled responses tends to increase as the frequency increases. This is expected given that the soil wavelengths approach the same order of magnitude as the source-receiver distance when the frequency increases, thus increasing the effect of source-receiver interaction on the pile-head response.

Figure 6.15a shows that $N_\theta = 42$ circumferential points are sufficient to cause both the transverse and vertical pile-head displacements to converge. Having this many circumferential points also satisfies the sampling criterion in Eq. (6.3) for the discrete Fourier series. Since the 1×2 pile-group contains only one row of piles along the tunnel, at least $N_x = 21$ longitudinal
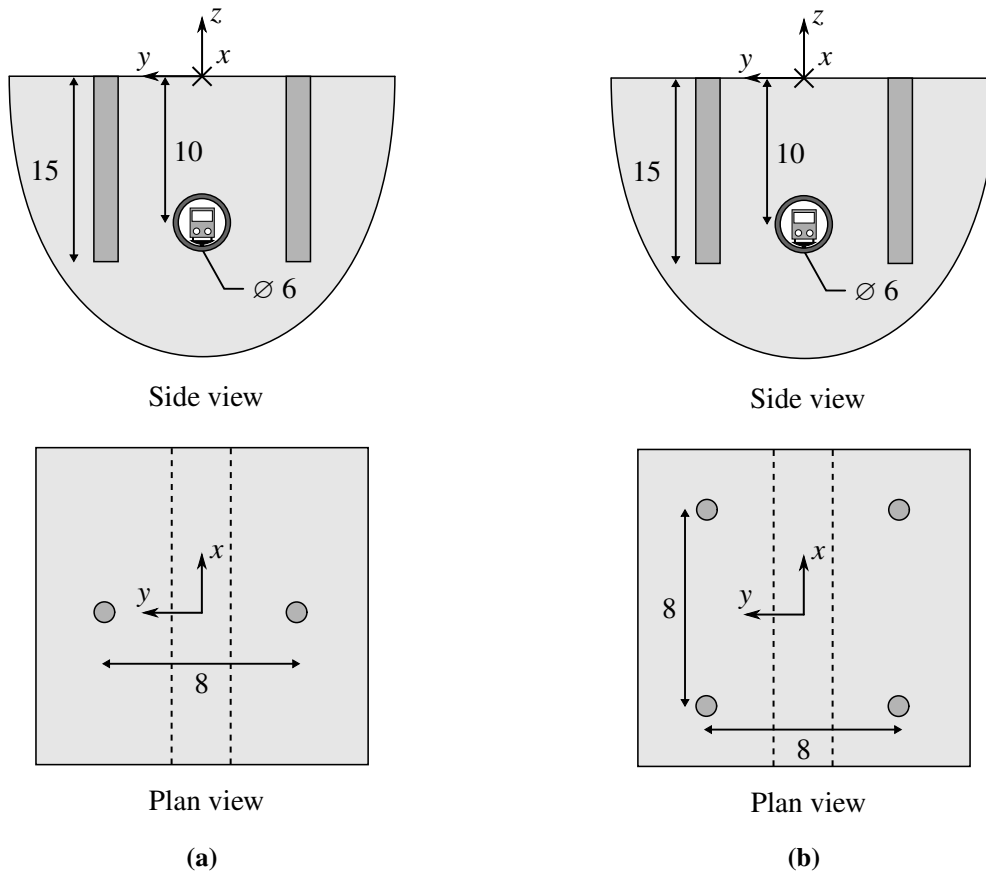
Fig. 6.14 Schematic diagrams of a centred **(a)** 1×2 and **(b)** 2×2 pile-group directly above their respective underground railway tunnels. The plan views show the tunnel's outline below the free surface (dashed lines). Dimensions in [m]. Not drawn to scale.
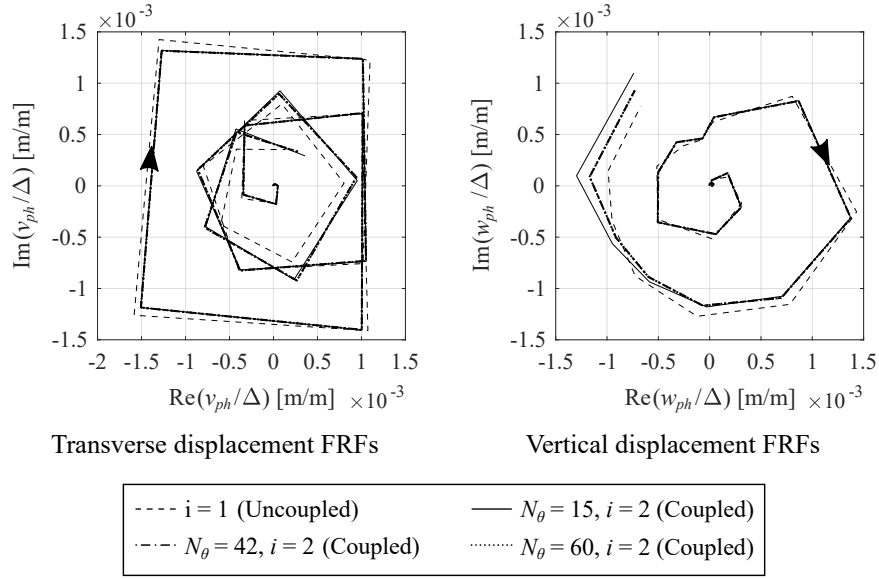
(a)
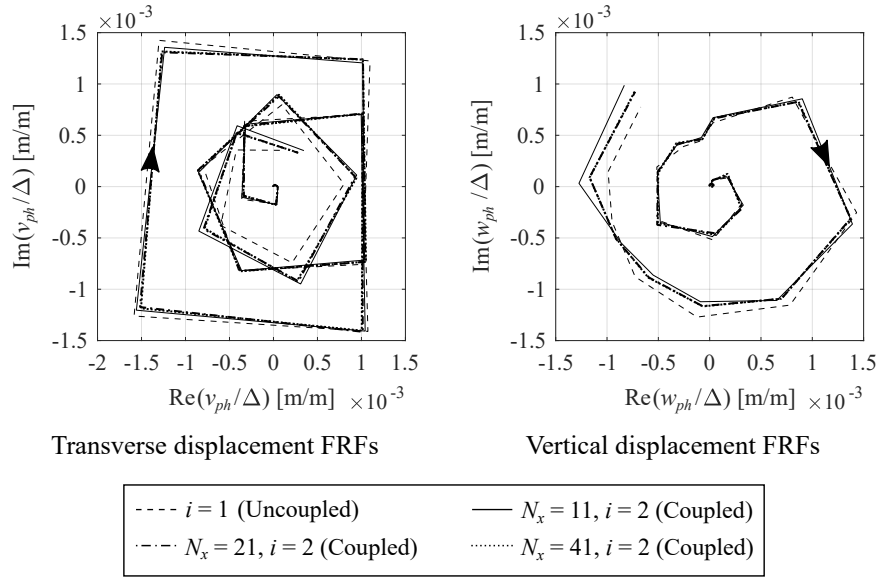
(b)
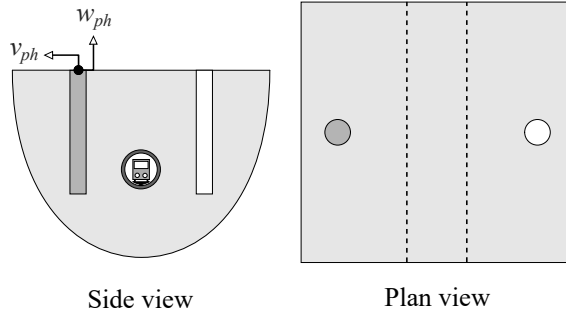
Fig. 6.15 The real and imaginary parts of the transverse and vertical displacement FRFs at the shaded pile head in a centred 1×2 pile-group near an underground railway tunnel. The FRFs are predicted using the first two iterations ($i = 2$) of the iterative PiP-BEM model as the number of **(a)** circumferential N_θ and **(b)** longitudinal N_x points at the soil-tunnel interface is varied. The arrows in the sub-figures represent the direction of increasing excitation frequency.
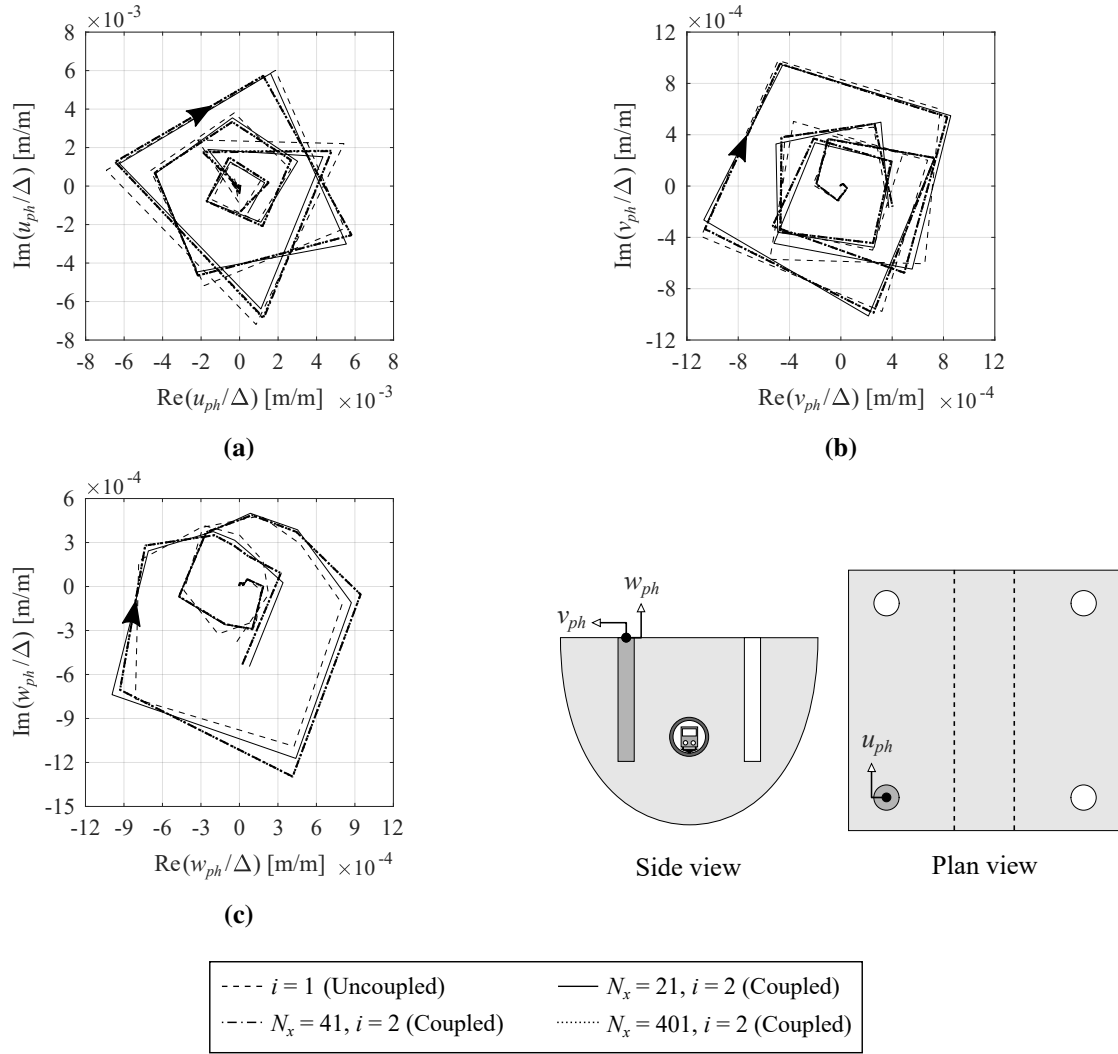
Fig. 6.16 The real and imaginary parts of the **(a)** longitudinal, **(b)** transverse and **(c)** vertical displacement FRFs at the shaded pile head in a centred 2×2 pile-group near an underground railway tunnel. The FRFs are predicted using the first two iterations $(i = 2)$ of the iterative PiP-BEM model as the number of longitudinal N_x points at the soil-tunnel interface is varied. The arrows in the sub-figures represent the direction of increasing excitation frequency.

points are required to achieve convergence in the pile-head response, as shown in Fig. 6.15b. When the number of pile rows is increased, as in the 2×2 pile-group, Fig. 6.16 shows that the number of longitudinal points required for convergence increases to $N_x = 41$, so the longitudinal length of the soil-tunnel interface must be at least 20.5 m. This implies that the reflected waves from a nearby piled foundation only influence a localised region of the idealised infinitely long tunnel. Hence, to accurately capture the source-receiver interaction over the frequency range of interest, the longitudinal length of the soil-tunnel interface must be at least twice the footprint of the foundation itself.

6.4 The Significance of Source-Receiver Interaction

The inclusion of tunnel-pile coupling in the iterative PiP-BEM model enables the significance of source-receiver interaction between a railway tunnel and a piled foundation to be investigated for the first time. This section presents the results, first published by Edirisinghe & Talbot [57], for some initial test cases where the tunnel and foundation are located close together.

Building designers are often interested in predicting the difference in the ground vibration levels before and after a foundation is constructed. For the case of a pile, this is regarded as the added-pile effect. The insertion gain (IG) at the pile head is used to characterise the added-pile effect in a particular direction and to compare the vibration performance of different tunnel-pile systems. For example, the insertion gain in the vertical direction is defined as

$$\mathrm{IG}_z^{(\mathrm{ap})} = 20 \log_{10} \left(\frac{|w_{ph}|}{|w_s|} \right), \tag{6.8}$$

where the superscript '(ap)' refers to the added-pile effect, w_{ph} is the vertical displacement at the pile head, and w_s is the vertical greenfield displacement at the same location in the soil before embedding the pile.

For all test cases, the parameter values in Table 5.2 for the tunnel (concrete), soil (London Clay) and piles (concrete) are fixed. Likewise, the parameter values in Table 5.3 for the train-track system with an FST are also fixed. The following five geometric parameters can be varied

(a)   **(b)**
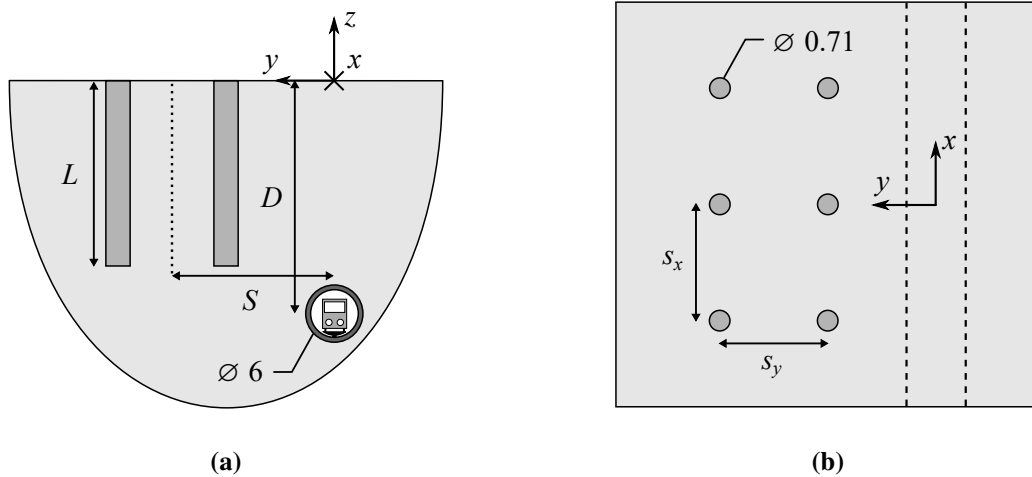
Fig. 6.17 The **(a)** side (yz-plane) and **(b)** plan (xy-plane) views of an off-centred 3×2 pile-group near a railway tunnel, illustrating the five geometric parameters (D, S, L, s_x, s_y) that can be varied. For all cases, the pile diameter, and the parameter values of the tunnel and the train-track system are fixed. The dotted line in **(a)** and the dashed lines in **(b)** represent the pile-group centre-line and the tunnel's outline below the free surface, respectively. Dimensions in [m]. Not drawn to scale.

in the tunnel-foundation system: the tunnel depth D, the tunnel-foundation separation distance S, the pile length L, and the pile spacings s_x and s_y in the respective x- and y-directions. These parameters are shown in Fig. 6.17 for an off-centred 3×2 pile-group near a railway tunnel.

6.4.1   A Single Pile Directly Above an Underground Railway Tunnel

Figure 6.18 plots the vertical insertion gain $\text{IG}_z^{(\text{ap})}$ and the piled-head and greenfield FRFs of a single centred pile, directly above the tunnel crown. The IG responses are calculated using the first three iterations ($i = 3$) of the iterative PiP-BEM model. Convergence is achieved following just the first iteration, which is equivalent to the uncoupled response of the tunnel-pile system and implies that the effects of wave scattering between the pile and tunnel are negligible. Thus, although the pile toe is just 2 m above the tunnel crown, source-receiver interaction is negligible for the case of a single pile.

(a)

(b)
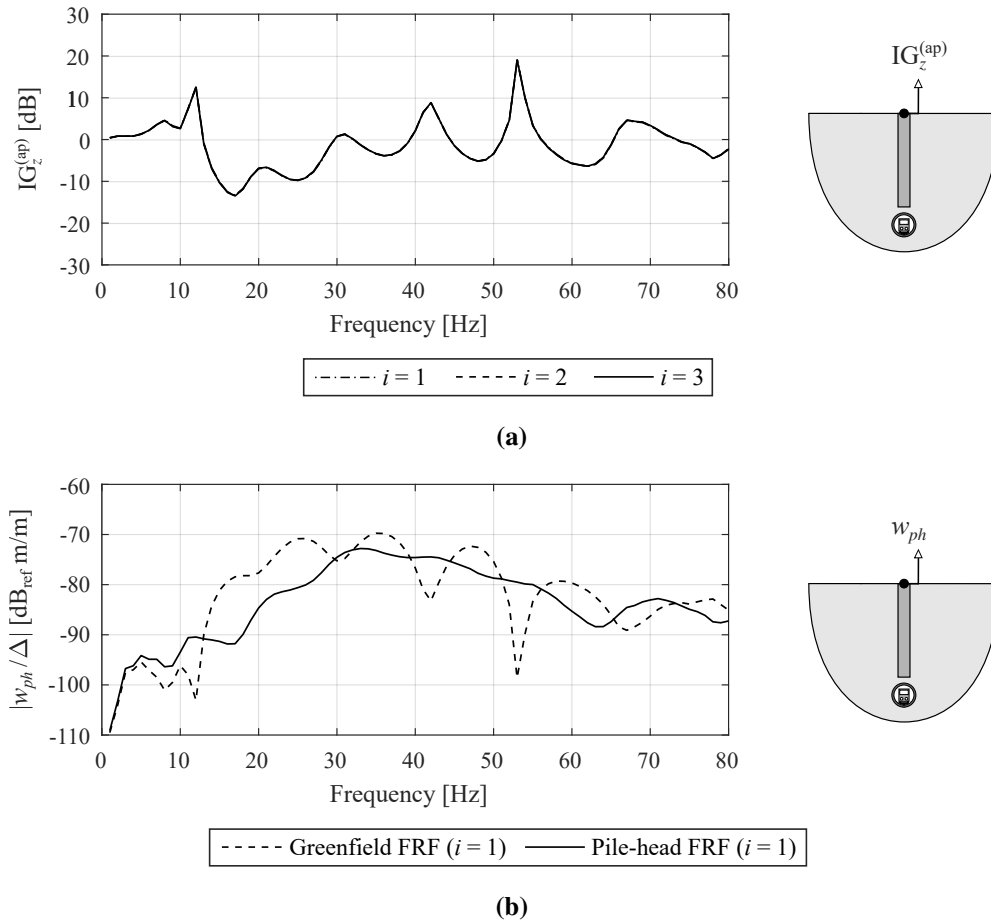
Fig. 6.18 The **(a)** vertical insertion gain and the **(b)** vertical pile-head and greenfield FRFs of a centred pile directly above an underground railway tunnel. The insertion gain is predicted using the first three iterations ($i = 3$) of the iterative PiP-BEM model, while the FRFs are only predicted using the converged first iteration. Pile length $L = 15$ m and tunnel depth $D = 20$ m.

The insertion gain is approximately 0 dB at very low frequencies, below 5 Hz, with the pile undergoing rigid-body motion. At higher frequencies, $\mathrm{IG}_z^{(ap)}$ becomes dependent on frequency because the soil wavelengths approach the same orders of magnitude as the pile's dimensions, leading to more significant effects of local wave scattering near the pile.

The $\mathrm{IG}_z^{(ap)}$ also exhibits some 'amplification' over the frequency range of interest. However, it is important to note that these peaks do not directly correspond to the eigenfrequencies of the pile itself. Since the pile is only excited axially due to its placement above the tunnel, the only eigenmode of the pile that could be excited over the frequency of interest is the fixed-free axial mode at 58 Hz. By comparing the responses in Fig. 6.18, it becomes evident that the peaks of the insertion gain occur at the same frequencies as the troughs of the greenfield FRF when the pile is not present. The troughs in the greenfield response appear as peaks in the $\mathrm{IG}_z^{(ap)}$ because the insertion gain, by definition, divides the pile-head FRF by the greenfield FRF. This means that the peaks in the IG primarily occur as a result of smoothing the troughs of the greenfield FRF, as observed in Section 5.4. In this sense, positive values of $\mathrm{IG}_z^{(ap)}$ should not be regarded as amplification because, due to natural inhomogeneity in the soil, the distinct troughs of the greenfield response are unlikely to be observed so strongly in practice.

6.4.2 The Effect of the Pile Length

When piles are offset from the tunnel centre-line, the transverse response becomes significant and changes the nature of wave scattering around the piles. The effect is analysed in this section by considering a centred 1×2 pile-group and varying L, whilst D is fixed at 20 m. Figure 6.19 shows the transverse $\mathrm{IG}_y^{(ap)}$ and vertical $\mathrm{IG}_z^{(ap)}$ insertion gains at an individual pile head for both an uncoupled (the first iteration) and coupled (the converged solution) tunnel-pile system as L is incrementally increased from 10 to 30 m.

When comparing the transverse and vertical displacements of the piles, the added-pile effect in the transverse direction is significantly smaller than that in the vertical direction, as, over the frequency range of interest, the variation in $\mathrm{IG}_y^{(ap)}$ is about 10 dB, compared to 50 dB for $\mathrm{IG}_z^{(ap)}$. It is important to note that the frequencies of the four distinct peaks in $\mathrm{IG}_z^{(ap)}$ – at 12, 52, 64 and 76 Hz – are unchanged when L is increased. Hence, the peaks of the vertical response do not correspond to the eigenfrequencies of the piles, as increasing L decreases the eigenfrequencies, which in turn would have shifted the peaks, but this is not observed. The two peaks at around 14 and 70 Hz in $\mathrm{IG}_y^{(ap)}$ also remain unchanged when L is increased. This means that, similar to

the observations in Section 6.4.1, the peaks in the insertion gains appear due to the smoothing of the troughs of the greenfield response.

In general, the added-pile effect is affected by a combination of wave scattering and soil stiffening – the stiffening effect was also observed in Section 5.4 when the uncoupled model was used. Given the relative flexibility of the piles in bending, compared to axial deformation, the relatively low values of $IG_y^{(ap)}$ may be expected, even as the soil wavelengths become shorter than the pile length. The increased pile flexibility in bending renders the added-pile effect in the transverse direction largely insensitive to pile length; this has a more significant effect in the vertical direction. When $L < D$ (i.e., the tunnel lies below the pile-group), the vertical response is, in general, attenuated by the presence of the pile-group; the frequency-averaged $IG_z^{(ap)}$ is less than 0 dB, again due to the stiffening effect. In contrast, when $L \geq D$ and the frequency is greater than 50 Hz, $IG_z^{(ap)}$ increases above 0 dB, indicating an amplification of the pile-head response. The piles appear to be providing a more efficient vibration transmission path than the

(a)

(b)
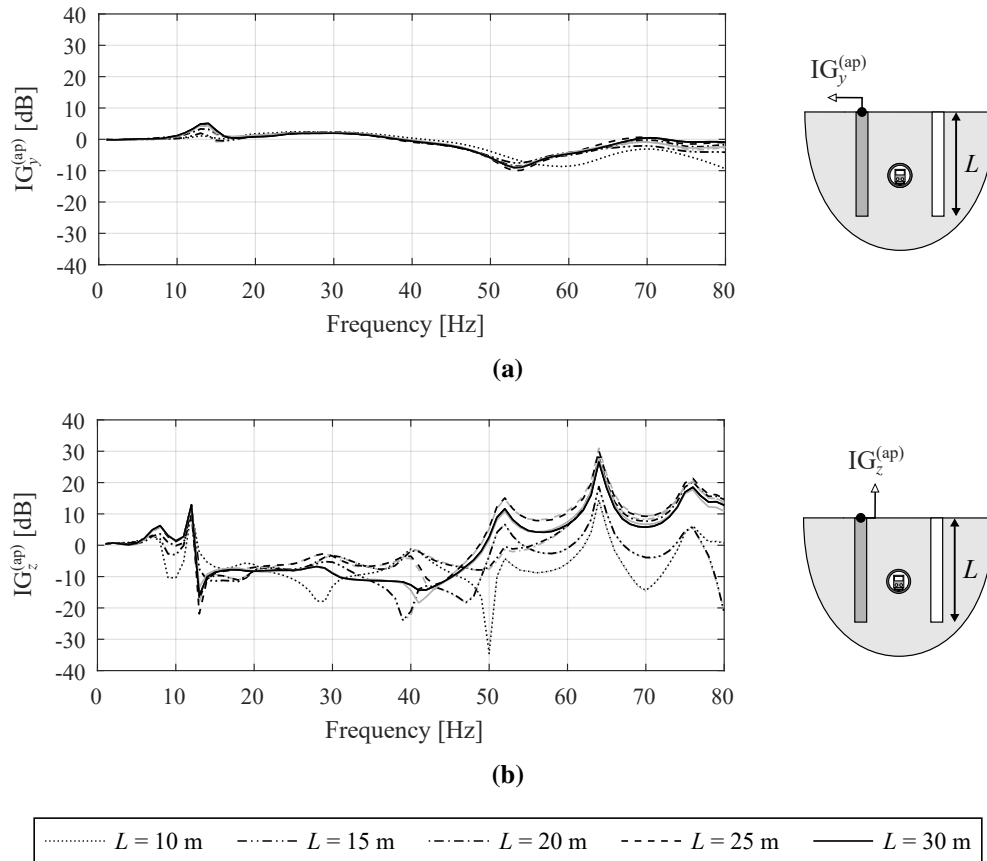
Fig. 6.19 The **(a)** transverse and **(b)** vertical insertion gains at the shaded pile in a centred 1×2 pile-group near an underground railway tunnel. The influence of the pile length L on the response, predicted with (black lines) and without (grey lines) tunnel-pile coupling, is illustrated. Tunnel depth $D = 20$ m and pile spacing $s_y = 8$ m.

soil when the piles are closer to the tunnel wall. This enhanced transmission effect is explored in more detail in Section 6.6.2.

As observed in Section 6.4.1, the responses of the coupled and uncoupled approaches are equivalent when $L < D$. When $L \geq D$, there are small differences (within ± 2 dB) between the two approaches, although these are negligible compared to the variations that generally arise due to uncertainties in the numerical model [126]. Thus, an uncoupled approach can at least be used to model the train-induced vibration of a 1×2 pile-group, as the waves scattered by the piles have a negligible effect on the tunnel response. Later, in Section 6.4.4, it is found that the effect of tunnel-pile coupling increases as more rows of piles are embedded along the tunnel.

6.4.3 The Effect of the Kinematic Pile-Soil-Pile Interaction (k-PSPI)

In this section, the effect of kinematic pile-soil-pile interaction (k-PSPI) on the train-induced vibration of a 1×5 pile-group is examined by considering the three configurations shown in Fig. 6.20. Configuration 1 is equivalent to the (single pile) tunnel-pile system investigated in Section 6.4.1, and represents the response if k-PSPI is neglected. The two other configurations model all five piles explicitly but at different positions relative to the tunnel. In each case, the vertical insertion gain $IG_z^{(ap)}$ is calculated at the pile head directly above the tunnel (shaded in Fig. 6.20), and this is presented in Fig. 6.21. As the tunnel is positioned below the piles in each configuration, convergence is achieved after just one iteration of the coupled approach.

At frequencies under 55 Hz, the differences in $IG_z^{(ap)}$ between the three configurations is within 2 dB, with the exception of the frequency range from 10 to 20 Hz, where the difference between Configurations 1 and 2 is up to 7 dB. Above 55 Hz, the difference between the three configurations is greater, resulting in more wave scattering between adjacent piles, as observed in similar pile-groups [56]. The maximum difference exists between Configurations 1 and 2, which might be expected given that the latter involves piles on both sides of the observed pile, and this reaches approximately 10 dB between 68 and 74 Hz. At this level, the difference is becoming significant and suggests that k-PSPI could be important to consider when predicting the train-induced response over certain frequency ranges. It is worth highlighting that these results contrast with those of the 1×4 pile-group ($L = 5$ m) considered in Section 5.4, where k-PSPI is insignificant. The longer piles in the 1×5 pile-group ($L = 15$ m), considered in this section, provide a larger surface area for a greater proportion of the wave-field to be scattered between adjacent piles, which is expected to contribute to the observed differences in k-PSPI.

Configuration 1
(Centred pile)

Configuration 2
(Centred 1×5 pile-group)

Configuration 3
(Off-centred 1×5 pile-group)
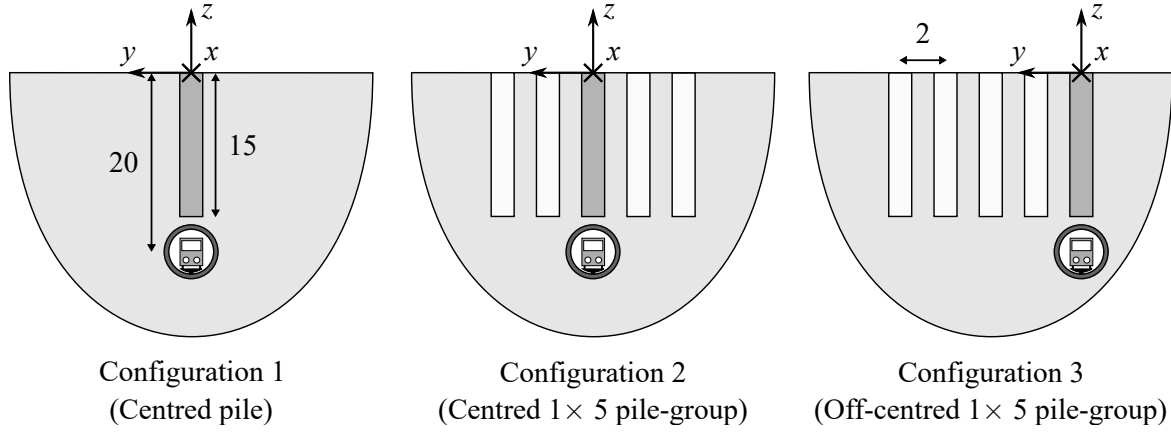
Fig. 6.20 Schematic diagrams of the three tunnel-pile configurations used to analyse the influence of kinematic PSPI (k-PSPI) on the train-induced response of a 1×5 pile-group. Dimensions in [m]. Not drawn to scale.
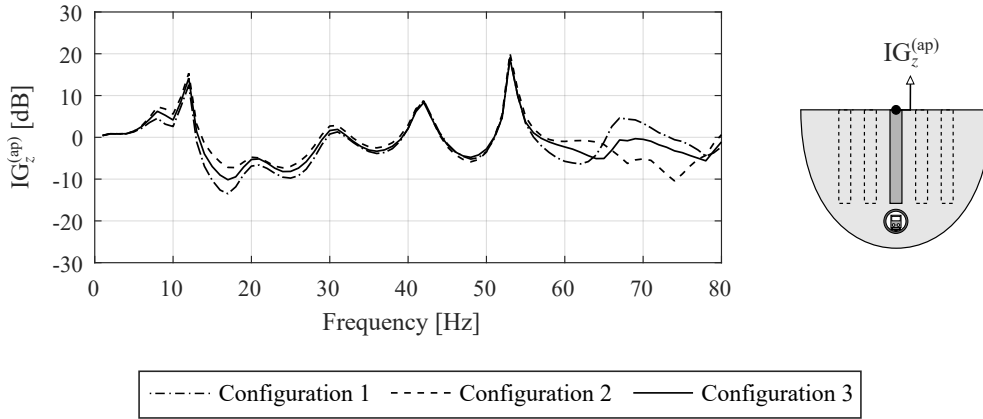
Fig. 6.21 The vertical insertion gain at the shaded pile directly above the underground railway tunnel for the three tunnel-pile configurations in Fig. 6.21. Just the first (converged) iteration of the coupled approach is plotted. Pile length $L = 15$ m, tunnel depth $D = 20$ m, and pile spacing $s_y = 2$ m.

6.4.4 Piles Arranged Along the Tunnel's Longitudinal Axis

Previous studies on the dynamic interaction in a tunnel-foundation system have only considered individual rows of piles arranged perpendicular to the tunnel cross-section [42, 117, 145]. In reality, piles are typically constructed in groups and, thus, also contain rows of piles arranged parallel to the tunnel. The influence of additional piles along the longitudinal x-axis is explored in this section. Figure 6.22 shows the three centred pile-groups considered, in which the number of rows along the x-axis is incrementally increased.

The transverse IG_y and vertical IG_z insertion gain at an outer pile head in each pile-group, represented by the shaded pile in Fig. 6.22, are plotted in Fig. 6.23 when the tunnel-foundation

model is uncoupled (grey lines) and coupled (black lines). The frequency-averaged difference between the uncoupled and coupled insertion gains of the 1×2 pile-group is less than 1 dB, in both the transverse and vertical directions. This again shows that, as in Sections 6.4.2 and 6.4.3, tunnel-pile coupling can be neglected when the pile-group consists of only one row of piles.

The difference between the coupled and uncoupled responses increases with the number of piles along the tunnel. This becomes more noticeable above 20 Hz, as the soil wavelength approaches the same order of magnitude as the tunnel diameter and the pile length. Increasing the number of piles along the x-axis positions more of them close to the tunnel; this increases the level of tunnel-pile coupling and increases the tunnel length affected by the pile-scattered wave-field. The difference in $\mathrm{IG}_y^{(\mathrm{ap})}$ between the coupled and uncoupled responses lies within 3 dB for all three pile-groups; considering $\mathrm{IG}_z^{(\mathrm{ap})}$, the 2×2 and 3×2 pile-groups have maximum differences of 4 and 14 dB, respectively. While the latter difference appears to be significant, it should be noted that this occurs at the troughs in the response and, as mentioned earlier, such differences are unlikely to be observed so strongly in practice due to the soil's inhomogeneity.
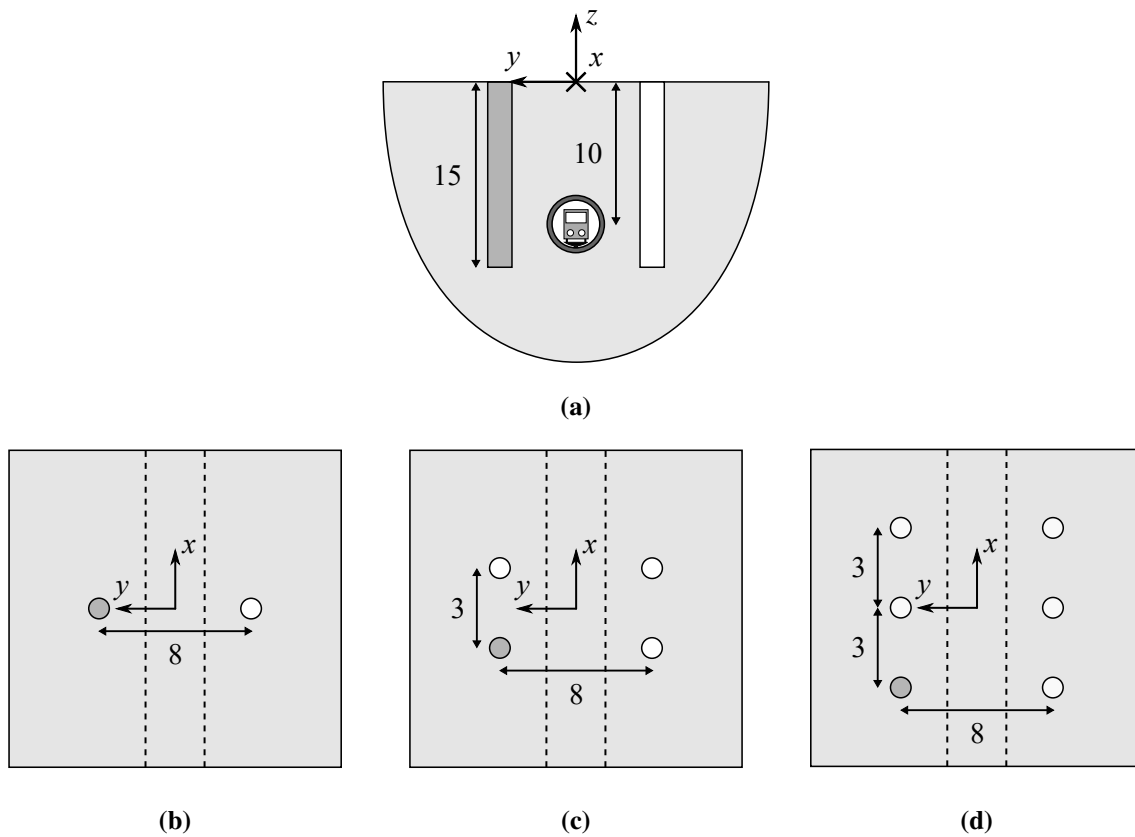
Fig. 6.22 Schematic diagrams of the **(a)** common side view (yz-plane) and the plan views (xy-plane) of a centred **(b)** 1×2 **(c)** 2×2 and **(d)** 3×2 pile-group near their respective underground railway tunnels. The dashed lines in the plan views represent the tunnel's outline below the free surface. Dimensions in [m]. Not drawn to scale.
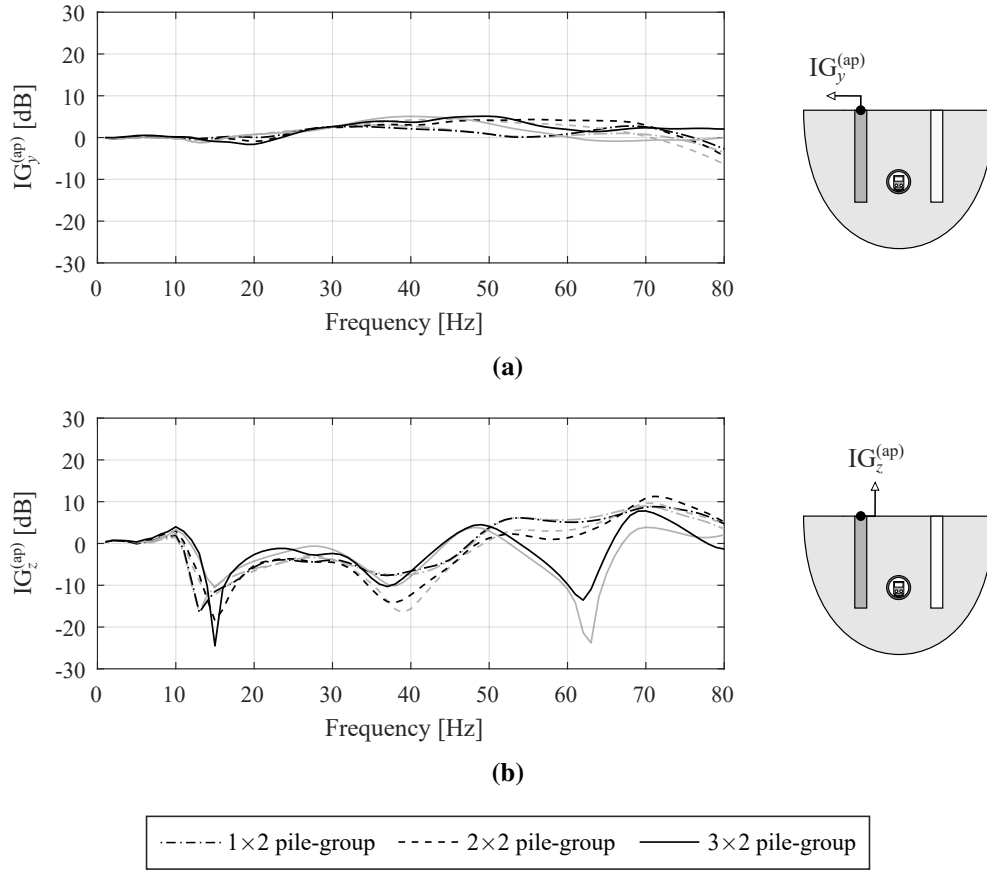
Fig. 6.23 The (a) transverse and (b) vertical insertion gains at the shaded pile for the three tunnel-pile configurations of Fig. 6.22, as predicted using the uncoupled (grey lines) and coupled (black lines) approaches. Pile length $L = 15$ m, tunnel depth $D = 10$ m, and pile spacing $s_x = 3$ m and $s_y = 8$ m.

6.4.5 The Effect of the Source-Receiver Distance

In this section, the 3×2 pile-group in Section 6.4.4 is used to extensively explore how the distance between a tunnel and foundation can influence the tunnel-pile coupling. To assist with this, the insertion gain is redefined to illustrate the effect of either including or omitting the tunnel-pile coupling. For vibration in the vertical direction, the coupling insertion gain is

$$\text{IG}_z^{(c)} = 20 \log_{10} \left(\frac{|w_{ph}^{(c)}|}{|w_{ph}^{(uc)}|} \right), \tag{6.9}$$

where $w_{ph}^{(c)}$ and $w_{ph}^{(uc)}$ are the vertical pile-head displacements calculated using the coupled and uncoupled approaches – likewise for vibration in the transverse and longitudinal directions. Furthermore, rather than computing the insertion gain at a single pile head, the mean insertion gain $\overline{\text{IG}}^{(c)}$ due to coupling is computed across all six piles in an attempt to quantify the overall response of the foundation.

141

Figures 6.24–6.26 plot the variation in the source-receiver insertion gain as the location of the tunnel, relative to the foundation, is varied. It is reasonable to expect the source–receiver interaction to be insignificant if the soil wavelengths are small compared to the source–receiver distance $\mathcal{D}$, based on the prior use of uncoupled approaches in the seismic analysis of buildings [17, 249]. Lines are therefore superimposed on the figures to indicate the frequencies at which the distance $\mathcal{D}$ is equal to the S-wavelength λ_S (solid) and $2\lambda_S$ (dashed) in the soil.

Figure 6.24 plots the results for a centred pile-group as the vertical distance $\mathcal{D}_z$ between the tunnel crown and the pile toes is varied. This is achieved by increasing the tunnel depth D from 10 to 34 m. In each direction, the source-receiver insertion gain is greatest when the piles extend below the tunnel crown ($\mathcal{D}_z < 0$), which is consistent with the tunnel-pile interaction observed in Section 6.4.4. When the tunnel lies underneath the pile-group ($\mathcal{D}_z > 0$), $\overline{\mathrm{IG}}^{(c)}$ is less than 1 dB over the full frequency range of interest, and the tunnel-pile system may reasonably be treated as being uncoupled. Note, $\overline{\mathrm{IG}}^{(c)}$ tends to 0 dB outside the region bounded by the solid line, indicating negligible coupling for frequencies at which the tunnel-foundation separation exceeds the soil S-wavelength.

Figures 6.25 and 6.26 plot the respective results for a centred and an off-centred pile-group, this time as the transverse distance $\mathcal{D}_y$ between the railway tunnel and the nearest pile is varied. This is achieved, for the centred pile-group, by changing the transverse pile spacing s_y, and for the off-centred pile-group, by keeping the pile spacing fixed ($s_x = 3$ m, $s_y = 8$ m) and varying the distance between the pile-group centre-line and the tunnel. These results support the general conclusion, that tunnel-pile interaction is greatest when the tunnel is close to the foundation – in particular, when the piles extend below the tunnel crown – and that this becomes negligible when the separation exceeds the soil S-wavelength. The interaction is most significant in the longitudinal direction, where $\overline{\mathrm{IG}}^{(c)}$ can vary as much as ± 10 dB – compared to ± 2 dB in both the transverse and vertical directions. At this level, the tunnel-pile coupling is again likely to be significant, being comparable with other sources of uncertainty in the system [126].

In a similar study, Coulier et al. [44] investigate the source-receiver interaction between a building supported on embedded strip foundations and an underground railway tunnel excited by a time-harmonic point force. In this case, the tunnel and building are coupled in the 2.5D wavenumber-frequency domain by assuming that both structures are infinitely long. They find that the vertical insertion gain, quantifying the tunnel-building coupling, at certain locations can be as high as 10 dB, which is of a similar order of magnitude to the $\overline{\mathrm{IG}}$ observed in this section.
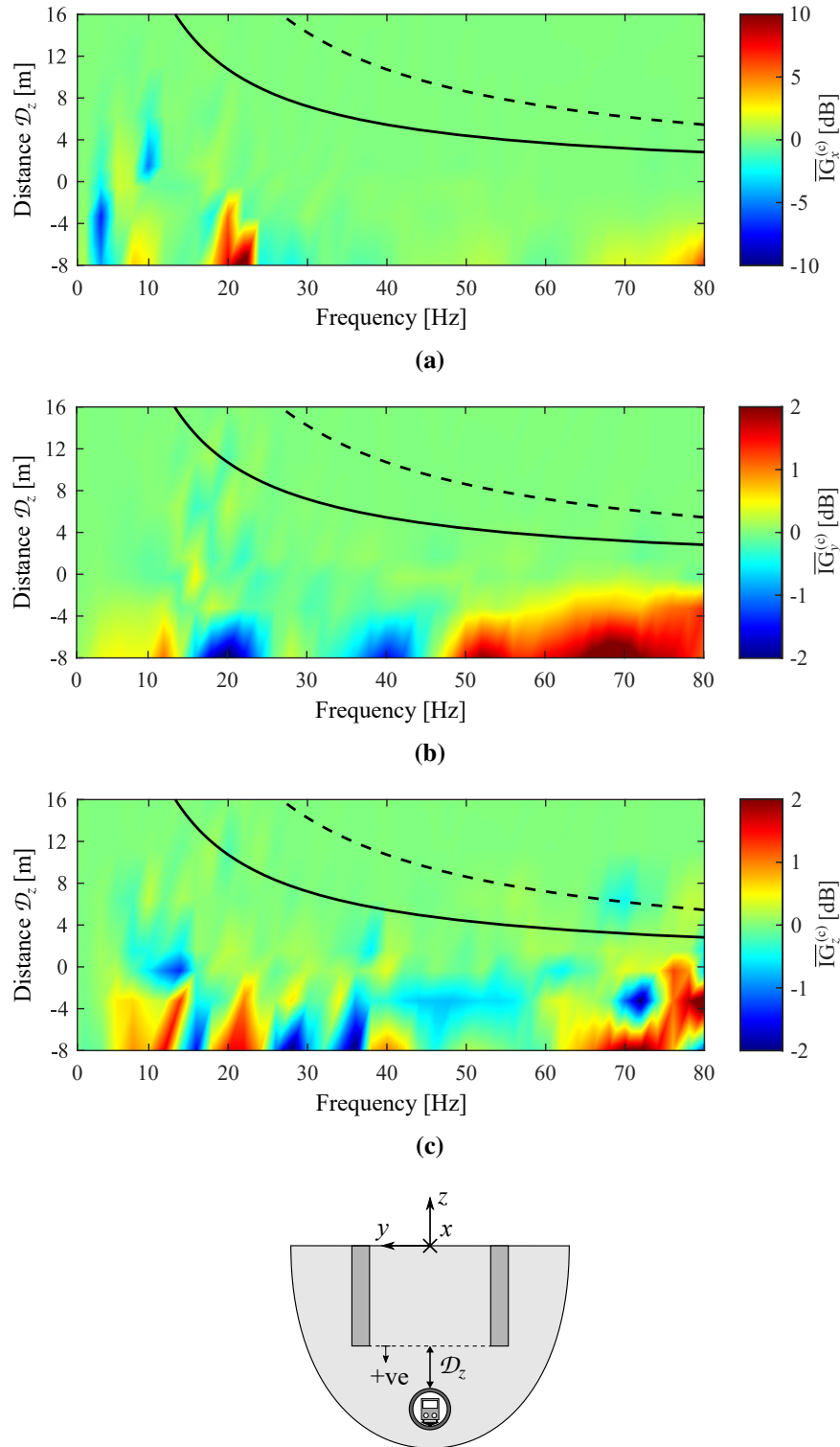
Fig. 6.24 The **(a)** longitudinal, **(b)** transverse and **(c)** vertical mean, source-receiver insertion gains of a centred 3×2 pile-group near an underground railway tunnel, illustrating the influence of the vertical source-receiver distance $\mathcal{D}_z$. The superimposed lines indicate the frequencies at which $\mathcal{D}_z = \lambda_S$ (solid) and $\mathcal{D}_z = 2\lambda_S$ (dashed), where λ_S is the soil's shear wavelength. Pile length $L = 15$ m, and pile spacing $s_x = 3$ m and $s_y = 8$ m. Note that the piles extend below the tunnel crown when $\mathcal{D}_z < 0$.
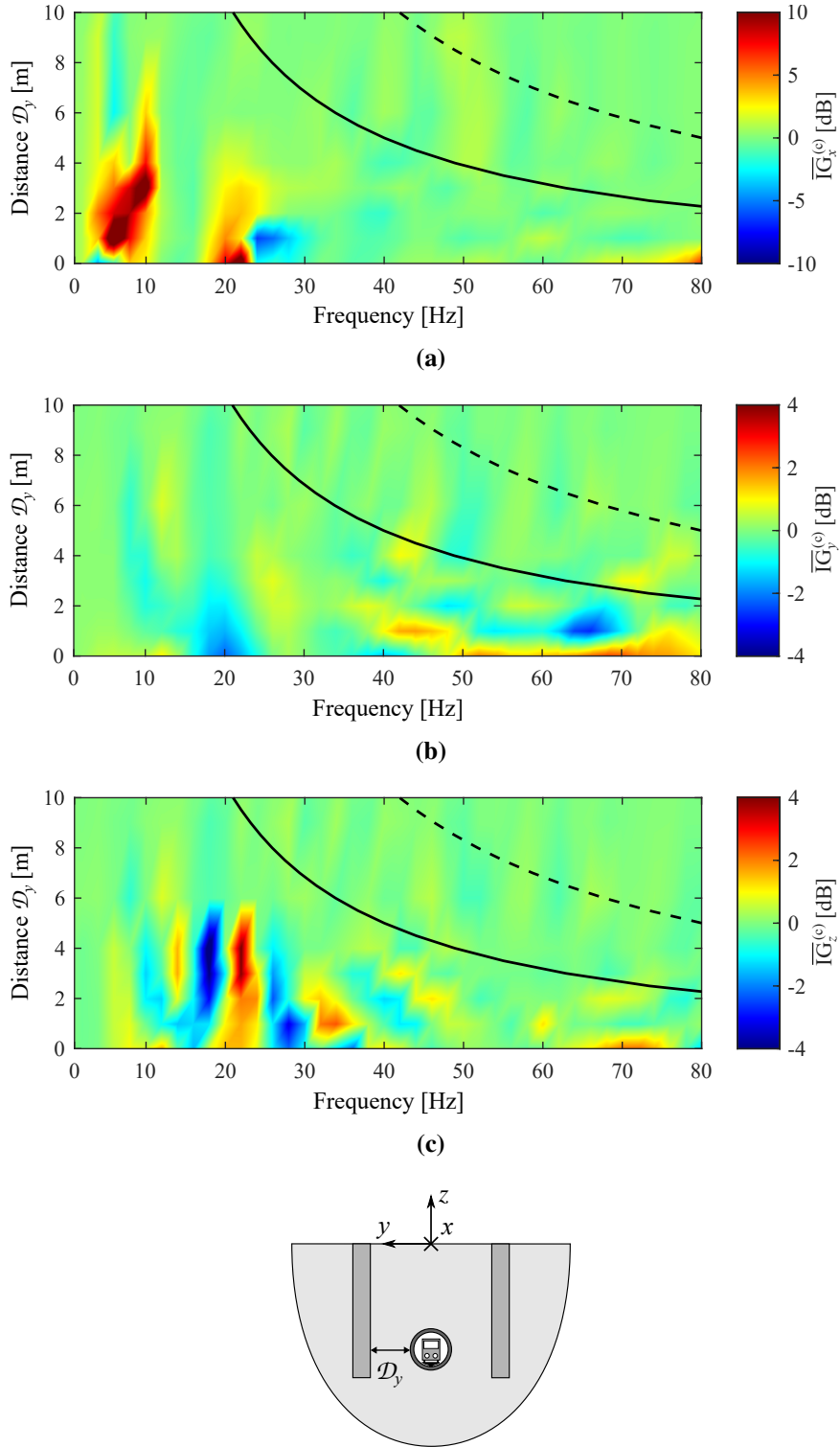
Fig. 6.25 The (a) longitudinal, (b) transverse and (c) vertical mean, source-receiver insertion gains of a centred 3×2 pile-group near an underground railway tunnel, illustrating the influence of the transverse source-receiver distance $\mathcal{D}_y$. The superimposed lines indicate the frequencies at which $\mathcal{D}_y = \lambda_S$ (solid) and $\mathcal{D}_y = 2\lambda_S$ (dashed), where λ_S is the soil's shear wavelength. Pile length $L = 15$ m, tunnel depth $D = 10$ m, and pile spacing $s_x = 3$ m.
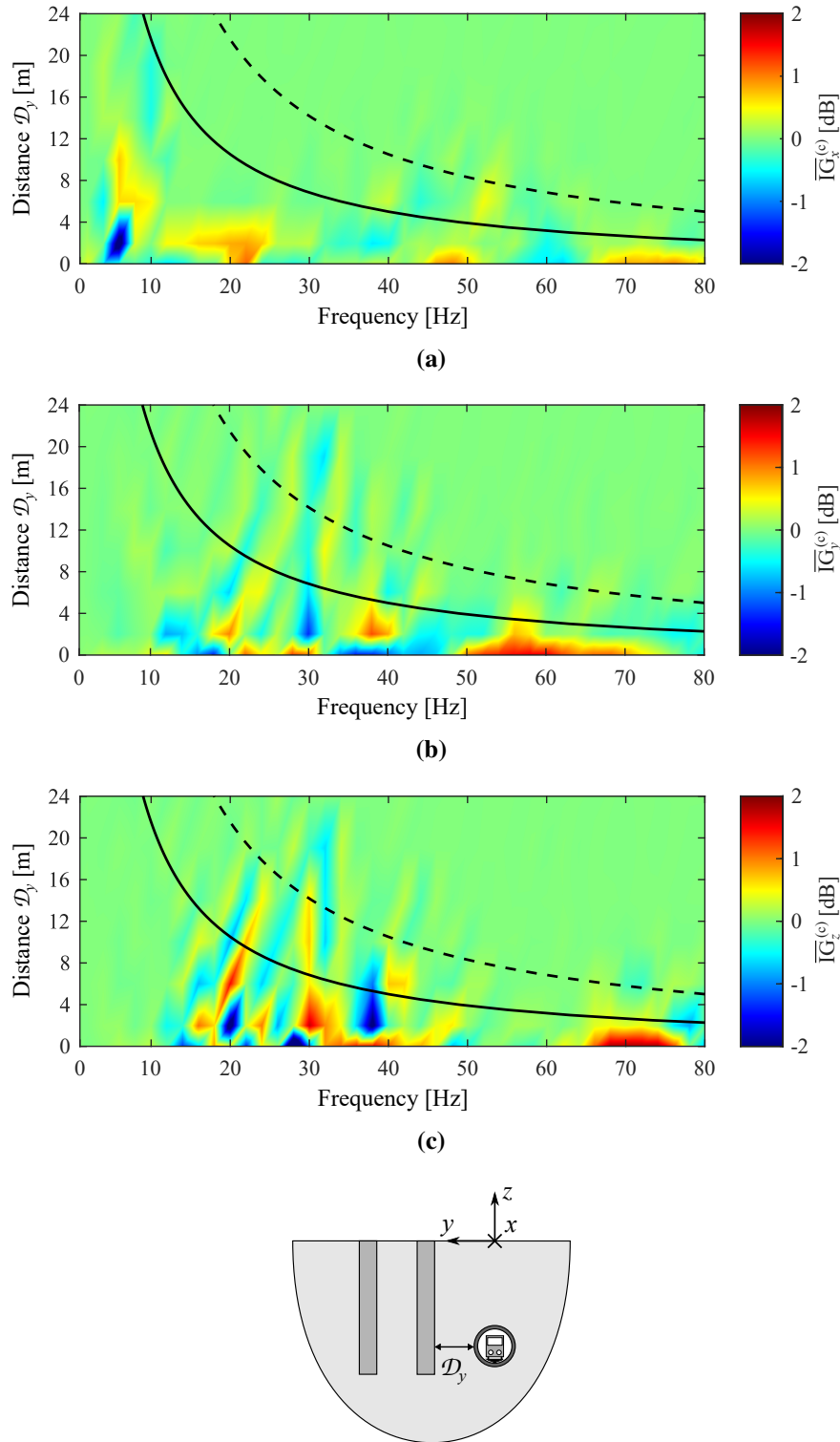
Fig. 6.26 The **(a)** longitudinal, **(b)** transverse and **(c)** vertical mean, source-receiver insertion gains of an off-centred 3×2 pile-group near an underground railway tunnel, illustrating the influence of the transverse source-receiver distance $\mathcal{D}_y$. The superimposed lines indicate the frequencies at which $\mathcal{D}_y = \lambda_S$ (solid) and $\mathcal{D}_y = 2\lambda_S$ (dashed), where λ_S is the soil's shear wavelength. Pile length $L = 15$ m, tunnel depth $D = 10$ m, and pile spacing $s_x = 3$ m and $s_y = 8$ m.

Furthermore, by varying the tunnel depth between 5 and 25 m, they observe that the power-flow insertion gain of the building varies by ± 2 dB when the source-receiver distance is less than the pressure wavelength (P-wavelength) in the soil. In contrast, the source-receiver distance in this section correlates with the S-wavelength, which is shorter than the P-wavelength. One possible explanation for this is that the 3D foundation model, unlike the 2.5D model, captures the shorter length scales along the longitudinal direction, such as the pile spacing. These shorter lengths are likely to induce more interaction due to S-waves compared to P-waves. Nevertheless, the observations discussed in this section, and those made by Coulier et al., signify the importance of accounting for dynamic coupling when the source-receiver distance is around the same order of magnitude as the soil wavelengths.

6.5 The Response from a Standard and Floating Slab Track

Although a floating slab track (FST), such as the one used in Sections 5.4 and 6.2–6.4, can, in practice, isolate the tunnel from noise and vibration, there are some constraints that limit its use over long spans of railway line. In addition to having high installation costs, more space is sometimes required inside the tunnel to house the slabs and bearings of the FST [225]. Further construction limitations arise due to the finite length of the pre-cast concrete slabs.

Compared to the FST, a typical standard (fixed) slab track consists of a lighter, continuous concrete slab, which is supported above the tunnel invert by a bonding layer of self-compacting concrete (SCC). The SCC is also much stiffer than the FST bearings. This type of trackform

Track beam parameters [Units]	Each rail beam	Slab beam
Mass per unit length [kg/m]	$m_r = 50$	$m_s = 3500$
Bending stiffness [Nm^2]	$K_r = 5.00 \times 10^6$	$K_s = 1.43 \times 10^9$
Track support parameters [Units]	Each rail pad	Slab support
Stiffness per unit length [N/m/m]	$k_r = 0.2 \times 10^9$	$k_s = 17.0 \times 10^9$
Loss factor [$-$]	$\eta_r = 0.3$	$\eta_s = 0.5$
Train parameters [Units]	Axles	
Unsprung mass [kg]	$M_a = 500$	
Spacing [m]	$L_a = 20$	

Table 6.1 Standard (fixed) slab track and train parameter values.

Parameters [Units]	Soil (London Clay)	Tunnel (Concrete)
Young's modulus [Pa]	$E_s = 286 \times 10^6$	$E_t = 50 \times 10^9$
Poisson's ratio[−]	$v_s = 0.49$	$v_t = 0.30$
Density [kg/m^3]	$\rho_s = 1980$	$\rho_t = 2500$
Shear modulus loss factor [−]	$\eta_G = 0.08$	−
Outer wall radius [m]	−	$r_{to} = 3.00$
Inner wall radius [m]	−	$r_{ti} = 2.75$

Table 6.2 Soil and tunnel parameter values.

is often used in underground metros due to the cost and construction benefits; it approximately accounts for 80% of the railway lines on London Crossrail's central section [35]. Hence, over the remainder of this dissertation, a standard slab track, with the parameter values presented in Table 6.1, is used in the PiP model.

In order to demonstrate the different vibration profiles produced by a standard and floating slab track, this section compares the soil response around an underground railway tunnel with these two track configurations. For both configurations, the parameter values in Table 6.2 are used to model the soil and tunnel. The parameter values of the FST are presented in Table 5.3. Based on these values, the isolation frequency of the FST is 40 Hz. For all the cases investigated in this section, the tunnel depth D is fixed at 25 m.

Figure 6.27 plots the vertical (w_s/Δ) soil displacement FRFs at the point $(0\,\text{m}, 0\,\text{m}, z\,\text{m})$ on the tunnel centre-line for the two track configurations. By varying the vertical z-coordinate, the change in the soil response at different depths is illustrated. Likewise, Fig. 6.28 illustrates the variation in the longitudinal (u_s/Δ), transverse (v_s/Δ), and vertical (w_s/Δ) soil displacement FRFs as the z-coordinate is varied at the point $(5\,\text{m}, 5\,\text{m}, z\,\text{m})$ beside the tunnel centre-line.

In general, the soil response decreases in magnitude as the measuring point moves further away from the tunnel due to the radiation damping in a half-space (see Section 2.3). When the excitation frequency is below the FST's isolation frequency (40 Hz), the soil responses of both track configurations are relatively similar in Figs. 6.27 and 6.28. However, when the frequency is greater than 40 Hz, the soil response due to the FST is about 10 dB lower compared to that of the standard slab track. This is because the transfer of vibrational energy from the train axles to the slab becomes inefficient when the excitation frequency is greater than the FST's isolation frequency, thereby leading to a decrease in the distributed force along the tunnel invert [153].
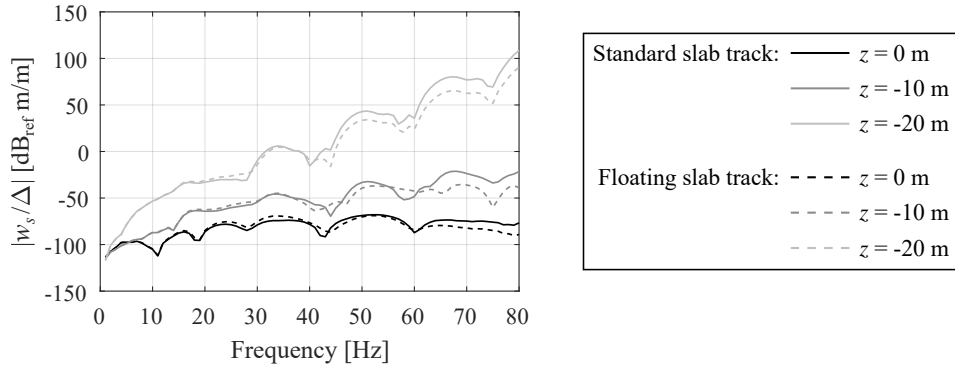
Fig. 6.27 The magnitude of the vertical soil displacement FRFs at the point $(0 \text{ m}, 0 \text{ m}, z \text{ m})$ due to the ground-borne vibration from an underground railway tunnel. The influences of the vertical z-coordinate and the type of slab track (standard or floating) on the response, predicted using the PiP model, are illustrated. Tunnel depth $D = 25$ m.
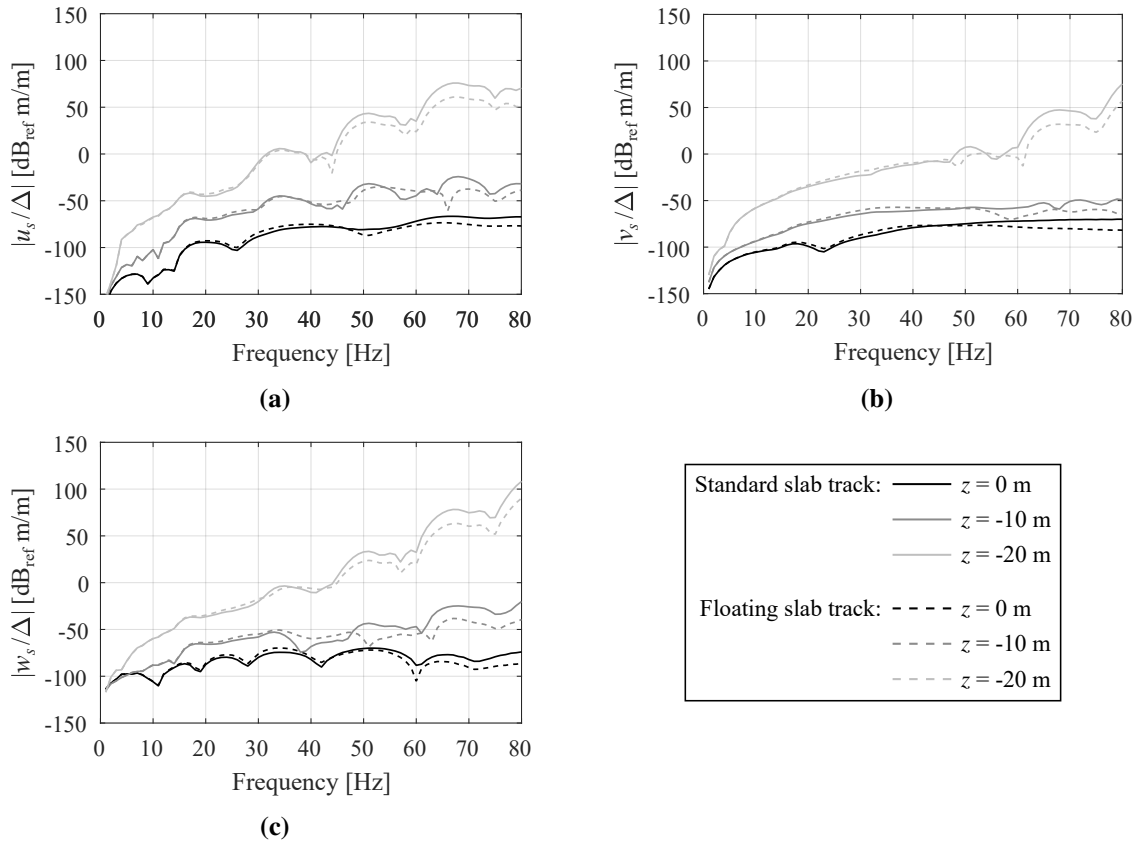
Fig. 6.28 The magnitude of the **(a)** longitudinal, **(b)** transverse and **(c)** vertical soil displacement FRFs at the point $(5 \text{ m}, 5 \text{ m}, z \text{ m})$ due to the ground-borne vibration from an underground railway tunnel. The influences of the vertical z-coordinate and the type of slab track (standard or floating) on the response, predicted using the PiP model, are illustrated. Tunnel depth $D = 25$ m.
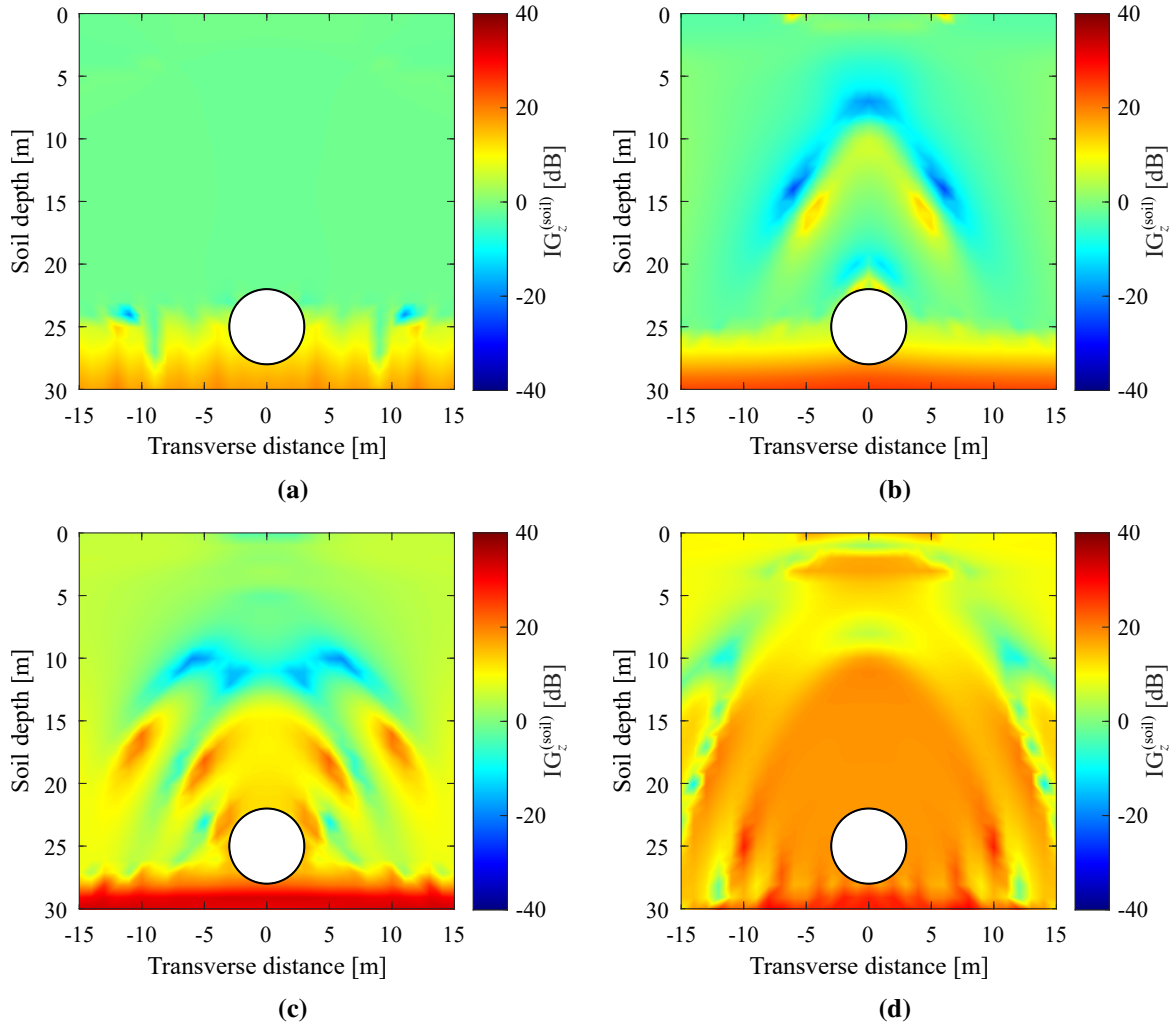
Fig. 6.29 The vertical insertion gain, at excitation frequencies of **(a)** 20 Hz, **(b)** 40 Hz **(c)** 60 Hz and **(d)** 80 Hz, comparing the soil responses due to a standard and floating slab track within an underground railway tunnel. The responses are predicted using the PiP model. The tunnel, at a depth of $D = 25$ m, is represented as a white circle in the plane of the tunnel cross-section.

The difference in isolation performance between the two railway track configurations can be evaluated using the vertical insertion gain in the soil, which is defined as

$$\mathrm{IG}_z^{(\mathrm{soil})} = 20 \log_{10} \left(\frac{\left| w_s^{(\mathrm{stand})} \right|}{\left| w_s^{(\mathrm{float})} \right|} \right), \tag{6.10}$$

where $w_s^{(\mathrm{stand})}$ and $w_s^{(\mathrm{float})}$ are the vertical soil displacements using the standard and floating slab track configurations, respectively. Figure 6.29 illustrates the spatial variation of $\mathrm{IG}_z^{(\mathrm{soil})}$ in the plane of the tunnel cross-section at four excitation frequencies (20, 40, 60 and 80 Hz). Note that the variation of $\mathrm{IG}_z^{(\mathrm{soil})}$ is symmetric about the vertical axis due to the inherent symmetry of the problem.

At excitation frequencies below 40 Hz, the $IG_z^{(soil)}$ is approximately 0 dB in the soil above the tunnel, so there is a negligible difference in the soil response due to each track configuration. However, when the frequency is increased above 40 Hz, the standard configuration produces larger vertical displacements in the soil, which is similar to the observations made in Figs. 6.27 and 6.28. At certain locations above the tunnel, the $IG_z^{(soil)}$ is as high as 20 dB at 60 and 80 Hz. It is also worth noting that, at all four frequencies, the $IG_z^{(soil)}$ is generally positive in the soil underneath the tunnel.

6.6 A Parametric Study of the Train-Induced Vibration of a Single Pile

Works of literature that investigate the parameters governing the level of vibration attenuation or amplification associated with the presence of a foundation near a source of ground vibration are few and far between. Exceptions include numerical studies by Auersch [7] and Sanitate & Talbot [209], who analysed the effects of concrete slab foundations subjected to incident waves in the ground; both papers made highly useful progress in identifying dimensionless parameters that can influence slab design.

With the aim of making similar progress in understanding the parameters that govern the train-induced vibration of piled foundations, this section presents a parametric study undertaken using the iterative PiP-BEM model. The results deliver new insight on the added-pile effect for the benefit of both academics and practitioners. A journal article covering the main results that are presented in this section has been accepted for publication [55].

The parametric study concerns the pile-head response of just a single pile, rather than a pile-group. This limits the number of parameters so that the study can focus on the general trends associated with the fundamental unit of a piled foundation, which may then be extrapolated to inform the design of an entire pile-group. It also mirrors the practice of embedding a test pile in the ground so that foundation designers can assess the added-pile effect on a construction site [171].

It should be noted that only interaction in the vertical direction is considered in this study. That is, the vertical insertion gain $IG_z^{(ap)}$, which characterises the added-pile effect, is analysed. Section 6.4 highlights that the added-pile effect is significantly lower in the transverse direction compared to the vertical direction due to the relative flexibility of the piles in bending. It may

also be argued that the axial motion of a pile couples most effectively to the axial motion of a subsequent building column, and propagates more efficiently to higher floors. Nevertheless, it is acknowledged that there is some evidence of additional vibration transmission at specific frequencies due to pile-head motion in the lateral and rocking DOFs [224].

The parameter values in Tables 6.1 and 6.2, to model the trackform (standard slab track), soil (London Clay), and tunnel (concrete), are fixed; the focus will be on how the added-pile effect depends on the properties of the pile and its position relative to the tunnel. The effect of the pile Poisson's ratio is judged to be minor based on the kinematic response of single piles to seismic waves [155], so it is fixed at $\nu_p = 0.25$. The pile diameter is also fixed at $d = 0.71$ m.

The influence of the following six parameters on the added-pile effect are investigated: the non-dimensional frequency $a_0 = \omega d / c_S$, the soil-pile density ratio ρ_s / ρ_p, the soil-pile stiffness ratio E_s / E_p, the pile length L, the tunnel depth D, and the tunnel-pile separation distance S. The results are plotted over the non-dimensional frequency range $0 < a_0 < 1.6$, which corresponds to excitation frequencies between 1 and 80 Hz for piles embedded in London Clay.

As noted in Section 6.2, the iterative PiP-BEM model is only valid when the circular tunnel is located at least one diameter ($2r_{to}$) below the free surface. Therefore, four different values of D that satisfy this condition are explored in this parametric study: 10 m (shallow), 25 m, 40 m and 60 m (deep). This range accounts for both the average (25 m) and deepest (60 m) railway tunnels in the London Underground.

6.6.1 The Effect of the Soil-Pile Density Ratio

Each sub-figure in Fig. 6.30 plots the $\mathrm{IG}_z^{(\mathrm{ap})}$ of a centred pile as the soil-pile density ratio ρ_s / ρ_p is increased incrementally from 0.4 (dense piles) to 1.2 (light piles). For reference, the density ratio of a concrete pile in London Clay is approximately 0.8. The soil-pile stiffness ratio is fixed at 10^{-2} (representative of a solid concrete pile in London Clay). The sub-figures also illustrate the variation in $\mathrm{IG}_z^{(\mathrm{ap})}$ as the pile length L is increased from 10 m (left) to 20 m (right) and as the tunnel depth D is increased from 25 m (top) to 60 m (bottom).

It is clear that the IG is largely insensitive to the density ratio, which is in broad agreement with the seismic study of Liu et al. [155] on the response of piles to vertically incident P-waves. As ρ_s / ρ_p is increased in each sub-figure, the $\mathrm{IG}_z^{(\mathrm{ap})}$ decreases by only a few decibels, with the exception of Fig. 6.30b, where $\mathrm{IG}_z^{(\mathrm{ap})}$ decreases by up to 10 dB at high frequencies. In this case, the pile is relatively long and the pile toe is close the tunnel crown. However, the underlying

mechanism is not entirely clear. In general, increasing the density ratio corresponds to lighter piles and, therefore, the observed decrease in IG is not a direct effect of the pile's inertia. This contrasts with the response of slab foundations, where the density ratio has been found to have a similarly weak influence on the IG but in the opposite sense, and which is indeed attributed to the slab's inertia [7, 209]. In the case of piles, wave scattering, due to differences in impedance with the soil, plays a more significant role. It is suspected that this is the underlying mechanism responsible for the high-frequency sensitivity to density observed here.

In conclusion, the results clearly demonstrate that the added-pile effect under train-induced excitation is not governed by density. Realistically, any variations in the pile-head motion due to differences in pile or soil density are expected to be negligible in comparison to those that generally arise from system uncertainties and modelling inaccuracies [126].

Before leaving Fig. 6.30, there is a second observation that is worth mentioning. In general, as observed previously in Section 5.4, the greenfield response of an isolated railway tunnel, remote from any neighbouring structures, contains distinct troughs at certain frequencies due to wave interference in the soil. An embedded pile acts to smooth out these undulations over the frequency range [57]. When the pile-head response is divided by the greenfield response to calculate the IG, the troughs appear as distinct peaks, as evident in Fig. 6.30. Based on the observations in Section 6.4, it is important to note that these undulations in the response are due to wave interaction between the pile and soil, and not caused by the dynamics of the pile itself. That is, the frequency spacing between the undulations in $\mathrm{IG}_z^{(\mathrm{ap})}$ is independent of the pile parameters. Gupta et al. [85] demonstrate that the spacing Δf, in units of hertz, between the undulations in the wave-field from an excited tunnel is approximately the same as that from a time-harmonic point force applied in a full-space:

$$\Delta f = \frac{c_P c_S}{R(c_P - c_S)}, \tag{6.11}$$

where R is the shortest distance between the centre of the tunnel and the response point, and c_P and c_S are the phase speeds of P- and S-waves in the soil. In this case, taking R as the distance between the centre of the tunnel and the pile head, the non-dimensional frequency spacing can be expressed as

$$\Delta a_0 = \frac{2\pi d c_P}{R(c_P - c_S)}. \tag{6.12}$$

(a) $L = 10$ m, $D = 25$ m

(b) $L = 20$ m, $D = 25$ m

(c) $L = 10$ m, $D = 40$ m

(d) $L = 20$ m, $D = 40$ m

(e) $L = 10$ m, $D = 60$ m

(f) $L = 20$ m, $D = 60$ m

Fig. 6.30 The vertical insertion gains of a centred pile above an underground railway tunnel, plotted against non-dimensional frequency a_0. In each sub-figure, the influence of the soil-pile density ratio ρ_s/ρ_p on the pile-head response is illustrated. The pile length L is increased from 10 m (left) to 20 m (right), and the tunnel depth D is increased from 25 m (top) to 60 m (bottom). Soil-pile stiffness ratio $E_s/E_p = 10^{-2}$.

The tunnel depths of 25 m, 40 m and 60 m yield Δa_0 values of 0.23, 0.14 and 0.09, respectively, which agree closely with those observed in Fig. 6.30.

It is important to be mindful of these undulations when interpreting the IG results presented in Sections 6.6.2 and 6.6.3. Positive values of $\text{IG}_z^{(ap)}$ at the peaks of the undulations should not be regarded as true amplification, in the sense that constructing a pile will significantly amplify the vibration, since the distinct troughs in the predicted greenfield response will unlikely be so pronounced in practice due to the natural inhomogeneity of the soil. In general, the main focus should be on identifying the underlying trends in the results when they are averaged over the full frequency range of interest.

6.6.2   The Effects of the Pile Length and Soil-Pile Stiffness Ratio

The effects of the pile length L and soil-pile stiffness ratio E_s/E_p on the pile-head response are found to be interlinked, so both parameters are considered together in this section with reference to Figs. 6.31–6.37. The soil-pile density ratio is fixed at $\rho_s/\rho_p = 0.8$ (representative of a concrete pile in London Clay). Note that Figs. 6.31–6.33 and 6.35–6.37 present the same results but in two different ways: the sub-figures in the former set are arranged to illustrate the effect of varying L, while the sub-figures in the latter set illustrate the effect of varying E_s/E_p. For the cases when $D \geq 25$ m (relatively deep tunnels), it is worth noting that the frequency spacing Δa_0 evident in Figs. 6.31–6.33 and 6.35–6.37 is approximately equal to that predicted by Eq. (6.12). Since the influence of the free surface on the greenfield response becomes more significant as D decreases, Δa_0 cannot be accurately predicted in Fig. 6.34, corresponding to the shallow tunnel ($D = 10$ m), because the full-space assumption applied in Eq. (6.12) is no longer valid.

The effect of varying L is investigated first. Figures 6.31–6.33 plot the $\text{IG}_z^{(ap)}$ of a centred pile, for tunnel depths of 25 m, 40 m and 60 m, respectively. In each sub-figure, E_s/E_p is held constant while L is increased from 5 m until the pile toe is just 2 m above the tunnel crown. Therefore, the length of the shortest pile remains fixed at $L = 5$ m in Figures 6.31–6.33, whereas the length of the longest pile varies with the tunnel depth considered in the respective figures, such that $D - L = 5$ m. By comparing between the sub-figures, the effect of decreasing E_s/E_p from 10^{-1} (flexible piles) to 10^{-5} (relatively rigid piles) is also illustrated. For reference, the soil-pile stiffness ratios of a solid concrete and steel pile in London Clay are of the order of 10^{-2} and 10^{-3}, respectively.

(a) $E_s/E_p = 10^{-1}$

(b) $E_s/E_p = 10^{-2}$

(c) $E_s/E_p = 10^{-3}$

(d) $E_s/E_p = 10^{-4}$

(e) $E_s/E_p = 10^{-5}$
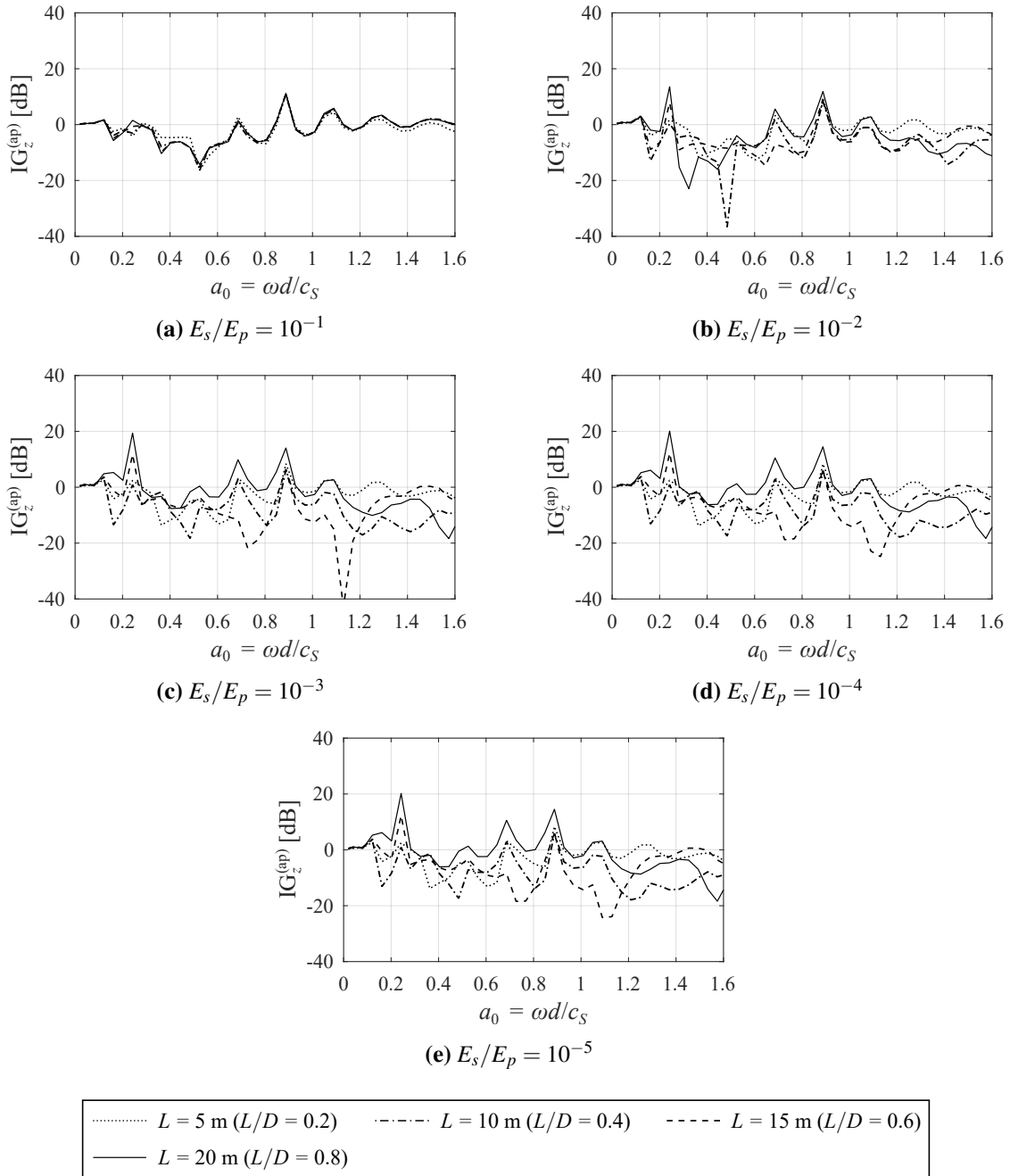
Fig. 6.31 The vertical insertion gains of a centred pile above an underground railway tunnel, plotted against non-dimensional frequency a_0. In each sub-figure, the influence of the pile length L on the pile-head response is illustrated. The soil-pile stiffness ratio E_s/E_p is decreased from **(a)** 10^{-1} to **(e)** 10^{-5}. Soil-pile density ratio $\rho_s/\rho_p = 0.8$ and tunnel depth $D = 25$ m.
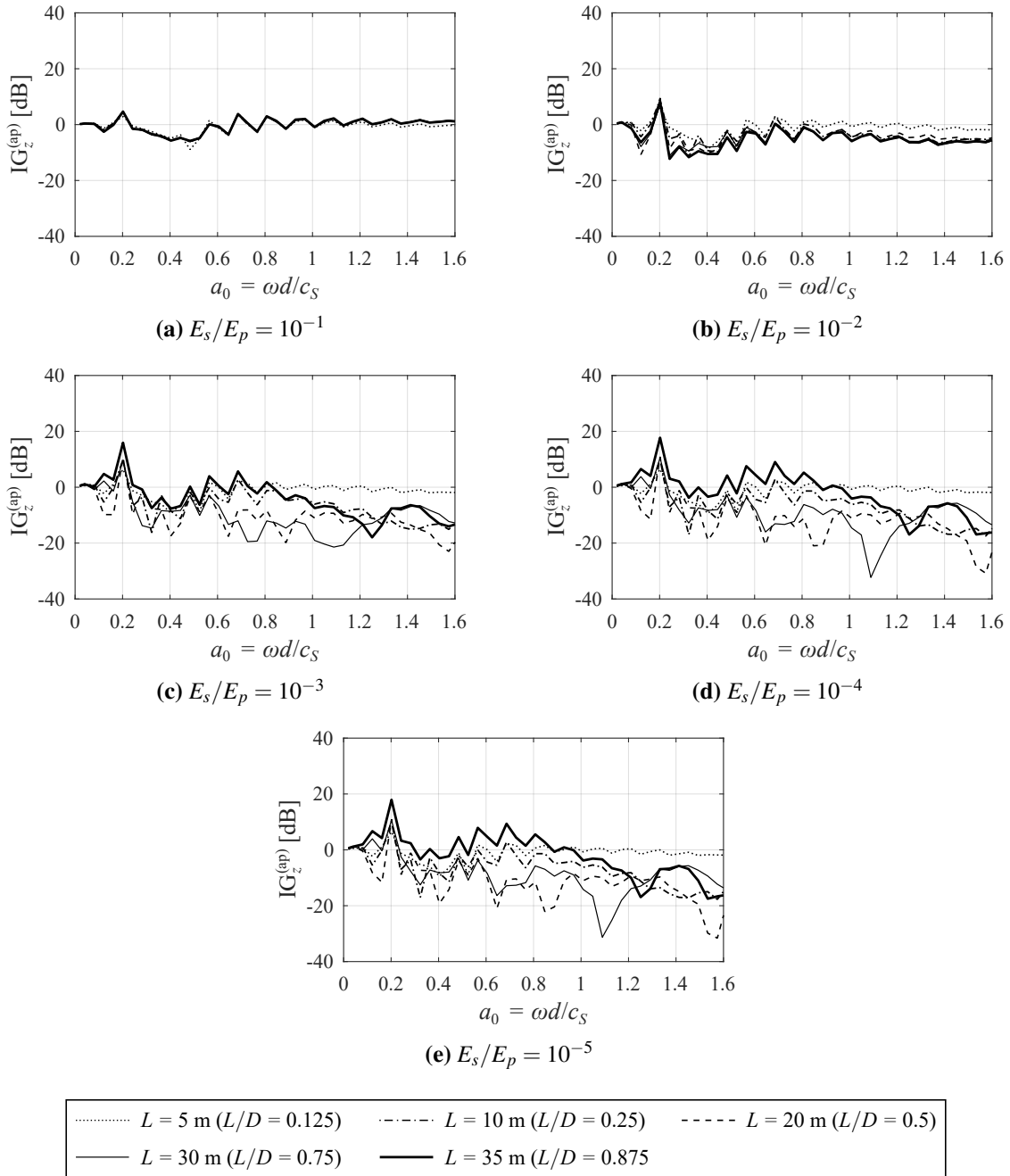
Fig. 6.32 The vertical insertion gains of a centred pile above an underground railway tunnel, plotted against non-dimensional frequency a_0. In each sub-figure, the influence of the pile length L on the pile-head response is illustrated. The soil-pile stiffness ratio E_s/E_p is decreased from **(a)** 10^{-1} to **(e)** 10^{-5}. Soil-pile density ratio $\rho_s/\rho_p = 0.8$ and tunnel depth $D = 40$ m.
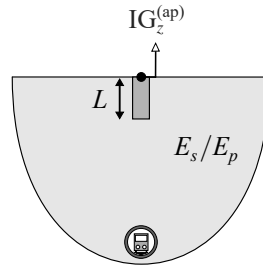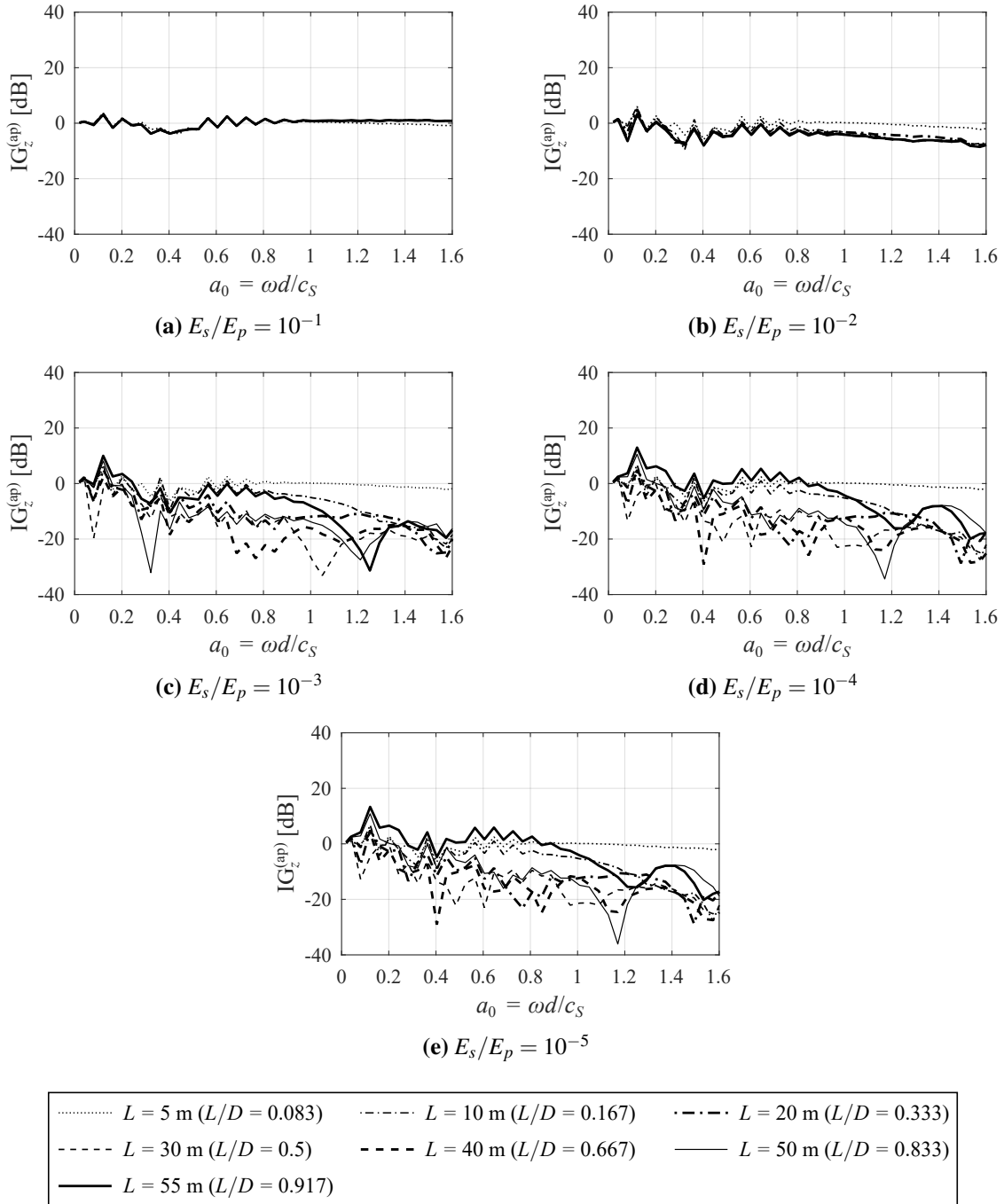
Fig. 6.33 The vertical insertion gains of a centred pile above an underground railway tunnel, plotted against non-dimensional frequency a_0. In each sub-figure, the influence of the pile length L on the pile-head response is illustrated. The soil-pile stiffness ratio E_s/E_p is decreased from **(a)** 10^{-1} to **(e)** 10^{-5}. Soil-pile density ratio $\rho_s/\rho_p = 0.8$ and tunnel depth $D = 60$ m.

When $E_s/E_p \geq 10^{-2}$, there are two counteracting mechanisms that influence the IG as L is increased. Firstly, the pile constrains the motion of the local soil, which tends to decrease the pile-head response. Secondly, the pile offers a more efficient transmission path than the soil for vibration propagating from the tunnel to the free surface, thereby increasing the response. Figures 6.31–6.33 illustrate how the soil-stiffening effect dominates in piles that are relatively far from the tunnel crown, with the IG decreasing as L is increased from the shortest ($L = 5$ m) to the second-longest ($D - L = 10$ m) pile in each case. Any amplification due to the enhanced transmission effect along these piles remains negligible because the waves propagating from the tunnel must travel a significant distance through the soil before reaching the pile. On average, over the frequency range of interest, the decrease in $IG_z^{(ap)}$ is approximately 20 dB between the shortest and the second-longest pile.

In contrast, the IG of the longest piles ($D - L = 5$ m) is approximately 10 dB greater than the second-longest piles, particularly when $a_0 < 1$, when $IG_z^{(ap)}$ typically becomes positive and the overall result is an amplification of the greenfield response. This occurs because the enhanced transmission effect overcomes the attenuation caused by the soil-stiffening effect. With regard to the longest piles, the gap, consisting of soil material, between the tunnel crown and the pile
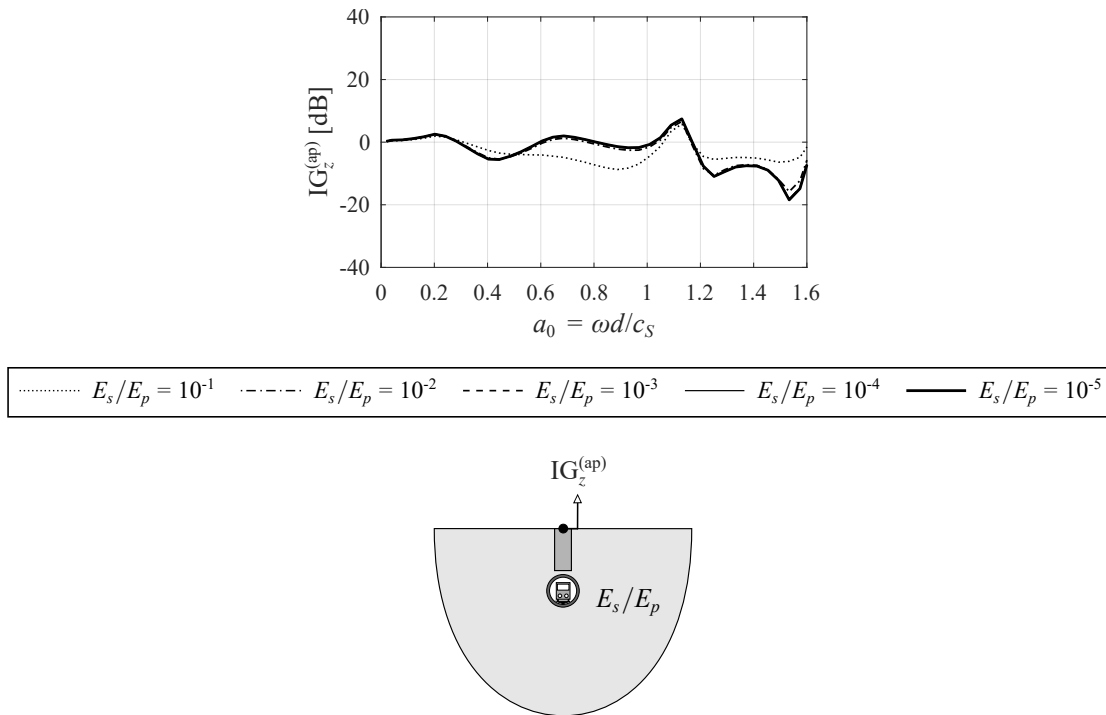
Fig. 6.34 The vertical insertion gains of a centred pile above an underground railway tunnel, plotted against non-dimensional frequency a_0. The influence of the soil-pile stiffness ratio E_s/E_p on the pile-head response is illustrated. Pile length $L = 5$ m, soil-pile density ratio $\rho_s/\rho_p = 0.8$, and tunnel depth $D = 10$ m.
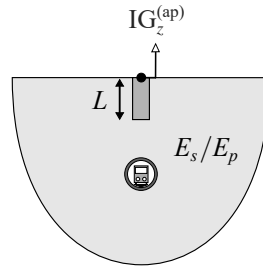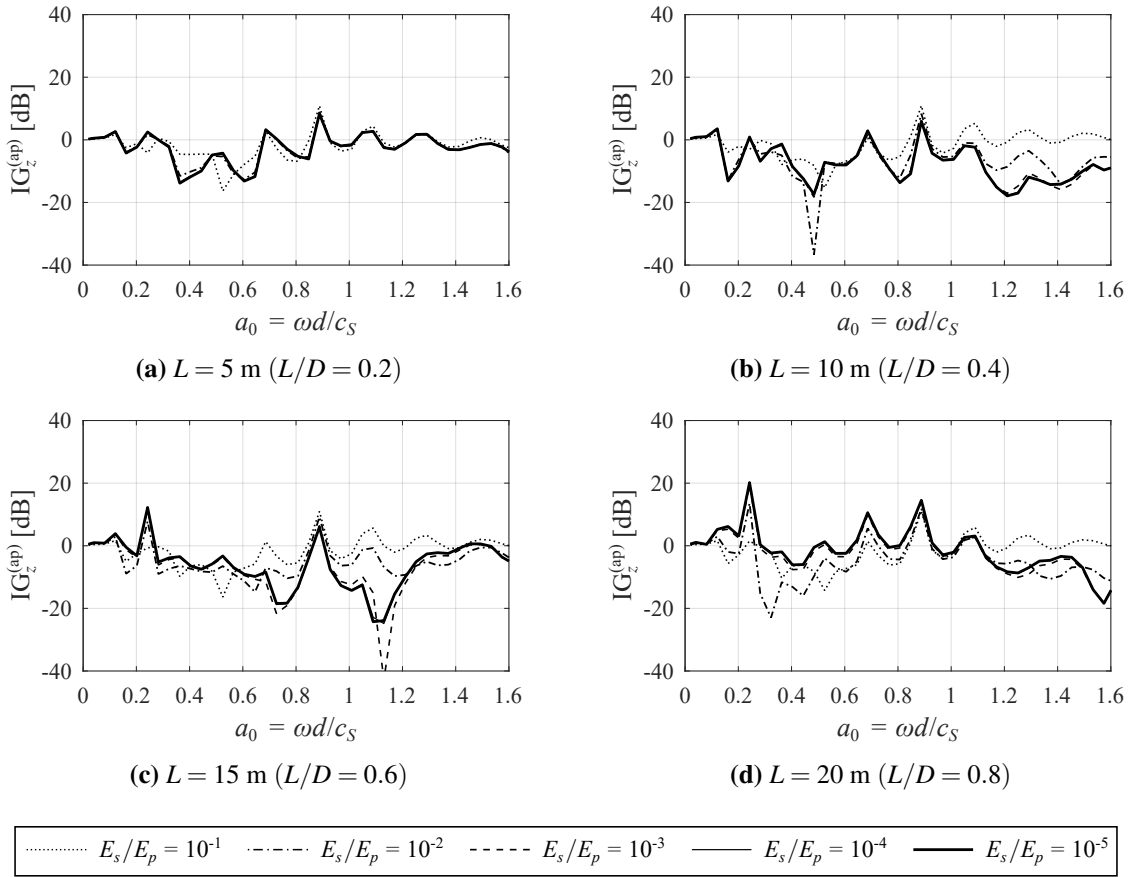
Fig. 6.35 The vertical insertion gains of a centred pile above an underground railway tunnel, plotted against non-dimensional frequency a_0. In each sub-figure, the influence of the soil-pile stiffness ratio E_s/E_p on the pile-head response is illustrated. The pile length L is increased from **(a)** 5 m to **(d)** 20 m. Soil-pile density ratio $\rho_s/\rho_p = 0.8$ and tunnel depth $D = 25$ m.

toe is reduced to 2 m, which is sufficiently less than the soil wavelengths – the S-wavelength at $a_0 = 1$ is $\lambda_S = 2\pi d/a_0 = 4.44$ m. This means that the incident waves at the piles are attenuated less by the soil. Furthermore, when $a_0 < 1$, the $\mathrm{IG}_z^{(\mathrm{ap})}$ of the longest pile is observed to be as high as that of the shortest pile.

Another significant observation is that when the pile is relatively flexible, there is negligible variation in $\mathrm{IG}_z^{(\mathrm{ap})}$ as L is increased. This is noticeable in Fig. 6.31 for a medium depth tunnel ($D = 25$ m), when $E_s/E_p = 10^{-1}$, and in Figs. 6.32 and 6.33 for deep tunnels ($D \geq 40$ m), when

(a) $L = 5$ m ($L/D = 0.125$)

(b) $L = 10$ m ($L/D = 0.25$)

(c) $L = 20$ m ($L/D = 0.5$)

(d) $L = 30$ m ($L/D = 0.75$)

(e) $L = 35$ m ($L/D = 0.875$)

$\cdots\cdots$ $E_s/E_p = 10^{-1}$ $\quad$ $-\cdot-\cdot-$ $E_s/E_p = 10^{-2}$ $\quad$ $-----$ $E_s/E_p = 10^{-3}$ $\quad$ ——— $E_s/E_p = 10^{-4}$ $\quad$ **———** $E_s/E_p = 10^{-5}$
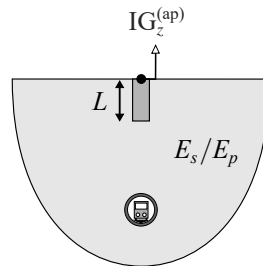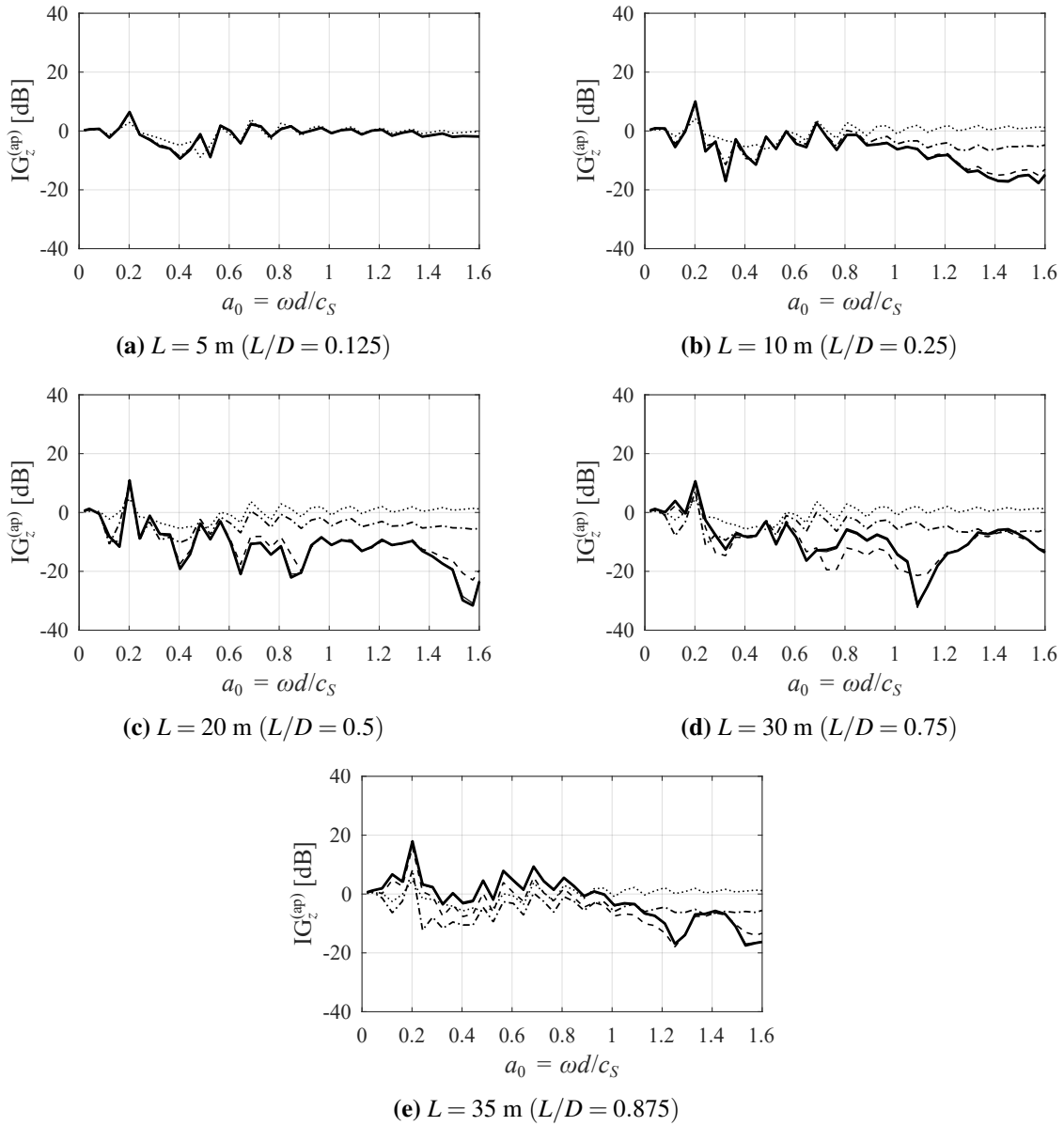
Fig. 6.36 The vertical insertion gains of a centred pile above an underground railway tunnel, plotted against non-dimensional frequency a_0. In each sub-figure, the influence of the soil-pile stiffness ratio E_s/E_p on the pile-head response is illustrated. The pile length L is increased from **(a)** 5 m to **(e)** 35 m. Soil-pile density ratio $\rho_s/\rho_p = 0.8$ and tunnel depth $D = 40$ m.
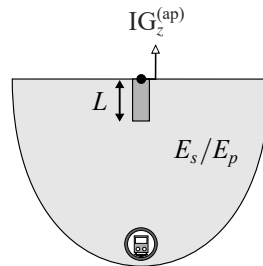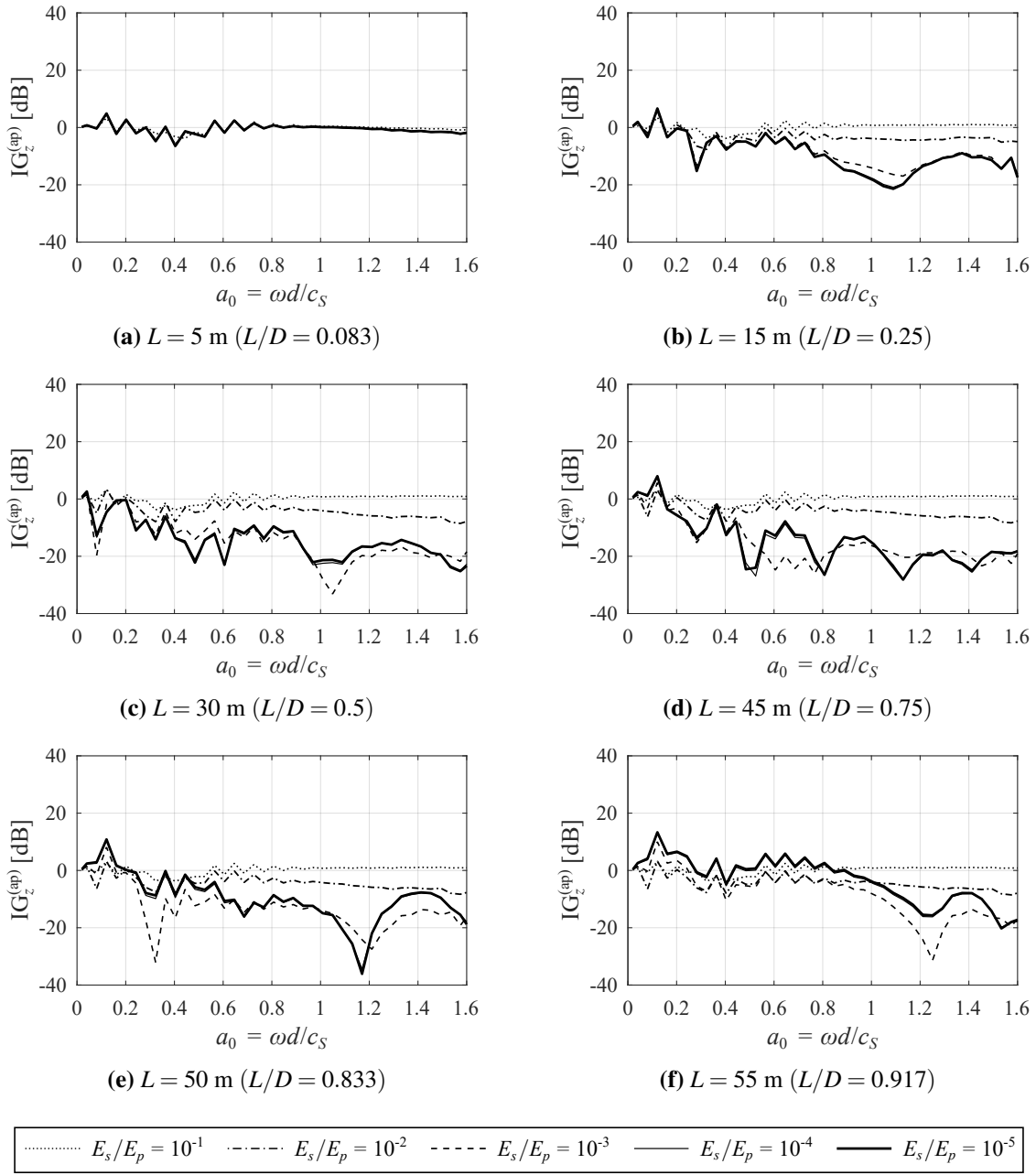
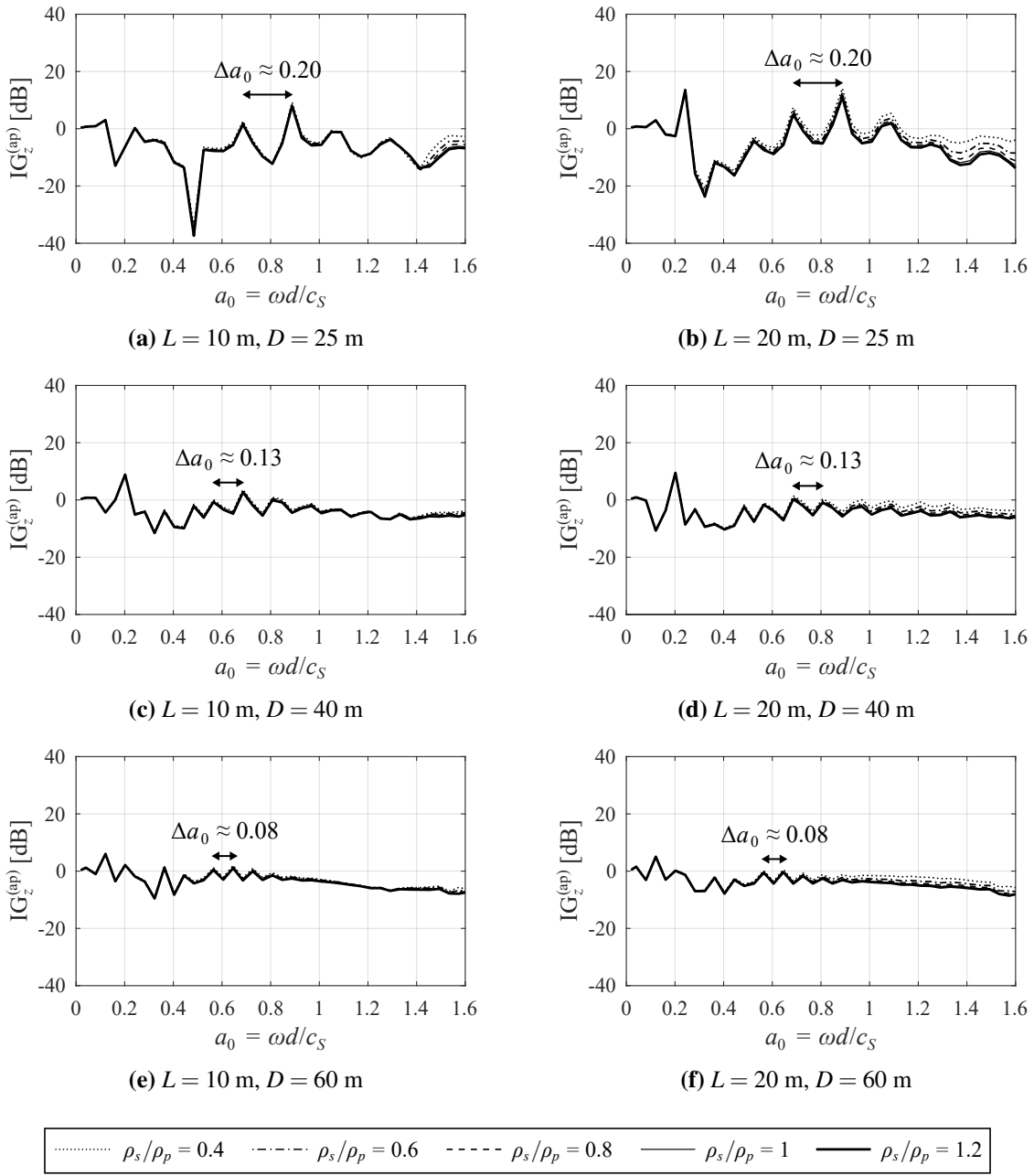**Fig. 6.37** The vertical insertion gains of a centred pile above an underground railway tunnel, plotted against non-dimensional frequency a_0. In each sub-figure, the influence of the soil-pile stiffness ratio E_s/E_p on the pile-head response is illustrated. The pile length L is increased from **(a)** 5 m to **(f)** 55 m. Soil-pile density ratio $\rho_s/\rho_p = 0.8$ and tunnel depth $D = 60$ m.

$E_s/E_p \leq 10^{-2}$. In these cases, it appears that the piles are sufficiently flexible that the added-pile effect is negligible, with the underlying IG being close to zero. Section 6.6.4 explores why varying L at these values of E_s/E_p and D does not influence the pile-head response.

Now, consider the effect of varying E_s/E_p as L is fixed. Figures 6.34–6.37 plot the $\mathrm{IG}_z^{(\mathrm{ap})}$ of a centred pile, for tunnel depths of 10 m, 25 m, 40 m and 60 m, respectively. In each sub-figure, L is held constant while E_s/E_p is decreased from 10^{-1} (flexible piles) to 10^{-5} (relatively rigid piles). By comparing between the sub-figures of Figures 6.35–6.37, the effect of increasing L is also shown, in increments of 5 or 10 m, until the pile toe is just above the tunnel crown. Note, the length of the pile is restricted to $L = 5$ m when it is above the shallowest tunnel ($D = 10$ m).

It is clear that, for a pile length of $L = 5$ m, there is no significant variation in IG as E_s/E_p is decreased below 10^{-2}. For a very short pile, the soil-stiffening effect is insignificant because its length does not span multiple wavelengths of the incident wave-field from the tunnel. Varying the pile stiffness, therefore, has a negligible effect on the response of very short piles.

For the longer piles ($D - L \geq 10$ m), it is clear that as E_s/E_p is decreased from 10^{-1}, the IG decreases until convergence is achieved when $E_s/E_p = 10^{-4}$. Although the reduction level varies with the excitation frequency, Figs. 6.35–6.37 show that the general decrease in $\mathrm{IG}_z^{(\mathrm{ap})}$ lies between 5 and 20 dB. The largest decreases in IG occur at higher frequencies because the pile spans more wavelengths of the incident wave-field, thereby increasing the soil-stiffening effect. Therefore, these results illustrate that the added-pile effect is clearly governed by the pile stiffness, which is consistent with previous studies on the response of piles due to seismic P-waves [155, 178]. Stiffness, rather than density, has also been found to have a similar governing influence on the IG of slab foundations [7, 209].

In contrast, the results for the longest piles ($D - L = 5$ m) show that decreasing E_s/E_p from 10^{-2} to 10^{-4} increases $\mathrm{IG}_z^{(\mathrm{ap})}$ by approximately 10 dB when $a_0 < 1$. This occurs due to the enhanced transmission effect observed earlier, which overcomes the soil-stiffening effect when the distance between the tunnel crown and pile toe is sufficiently less than the soil wavelength.

6.6.3 The Effect of the Tunnel-Pile Separation Distance

In this section, the IG of off-centred piles ($S > 0$ m) is investigated, in contrast to the centred piles ($S = 0$ m) analysed in Sections 6.6.1 and 6.6.2. Figures 6.38–6.40 plot the $\mathrm{IG}_z^{(\mathrm{ap})}$ of an off-centred pile, for tunnel depths of 10 m, 25 m and 40 m, respectively, with each sub-figure illustrating the variation in the IG as L is increased beyond the tunnel depth. By comparing

(a) $S = 5$ m, $E_s/E_p = 10^{-2}$

(b) $S = 5$ m, $E_s/E_p = 10^{-3}$

(c) $S = 10$ m, $E_s/E_p = 10^{-2}$

(d) $S = 10$ m, $E_s/E_p = 10^{-3}$

(e) $S = 20$ m, $E_s/E_p = 10^{-2}$

(f) $S = 20$ m, $E_s/E_p = 10^{-3}$

$\cdots\cdots$ $L = 5$ m $(L/D = 0.5)$ $-\cdot-\cdot-$ $L = 10$ m $(L/D = 1)$ $----$ $L = 15$ m $(L/D = 1.5)$

—— $L = 25$ m $(L/D = 2.5)$
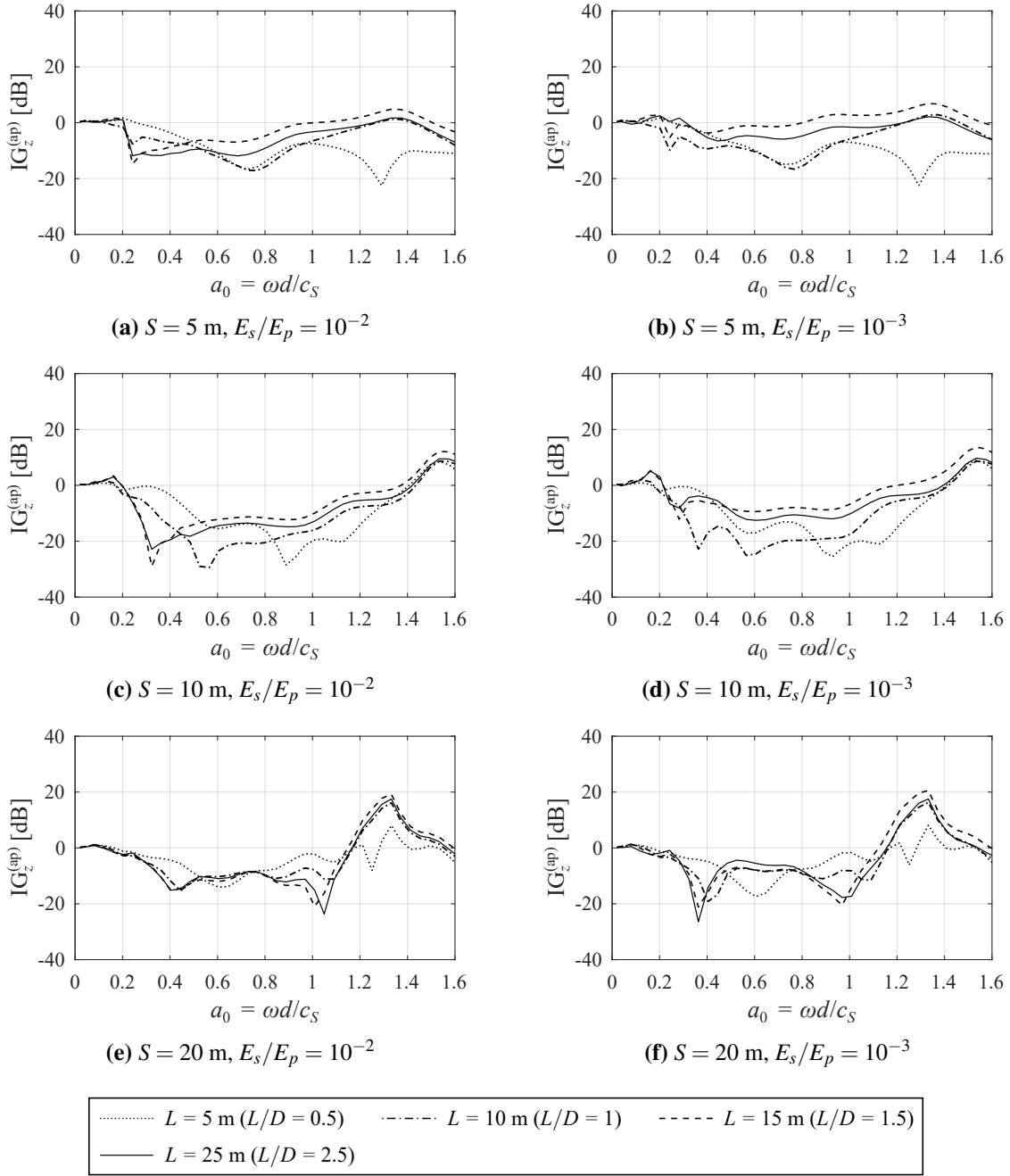
Fig. 6.38 The vertical insertion gains of an off-centred pile near an underground railway tunnel, plotted against non-dimensional frequency a_0. In each sub-figure, the influence of the pile length L on the pile-head response is illustrated. The soil-pile stiffness ratio E_s/E_p is decreased from 10^{-2} (left) to 10^{-3} (right), and the tunnel-pile separation distance S is increased from 5 m (top) to 20 m (bottom). Soil-pile density ratio $\rho_s/\rho_p = 0.8$ and tunnel depth $D = 10$ m.

Fig. 6.39 The vertical insertion gains of an off-centred pile near an underground railway tunnel, plotted against non-dimensional frequency a_0. In each sub-figure, the influence of the pile length L on the pile-head response is illustrated. The soil-pile stiffness ratio E_s/E_p is decreased from 10^{-2} (left) to 10^{-3} (right), and the tunnel-pile separation distance S is increased from 5 m (top) to 20 m (bottom). Soil-pile density ratio $\rho_s/\rho_p = 0.8$ and tunnel depth $D = 25$ m.

(a) $S = 5$ m, $E_s/E_p = 10^{-2}$

(b) $S = 5$ m, $E_s/E_p = 10^{-3}$

(c) $S = 10$ m, $E_s/E_p = 10^{-2}$

(d) $S = 10$ m, $E_s/E_p = 10^{-3}$

(e) $S = 20$ m, $E_s/E_p = 10^{-2}$

(f) $S = 20$ m, $E_s/E_p = 10^{-3}$

|		
$L = 10$ m ($L/D = 0.25$)	$L = 20$ m ($L/D = 0.5$)	$L = 30$ m ($L/D = 0.75$)
$L = 35$ m ($L/D = 0.875$)	$L = 40$ m ($L/D = 1$)	$L = 50$ m ($L/D = 1.25$)
$L = 60$ m ($L/D = 1.5$)		
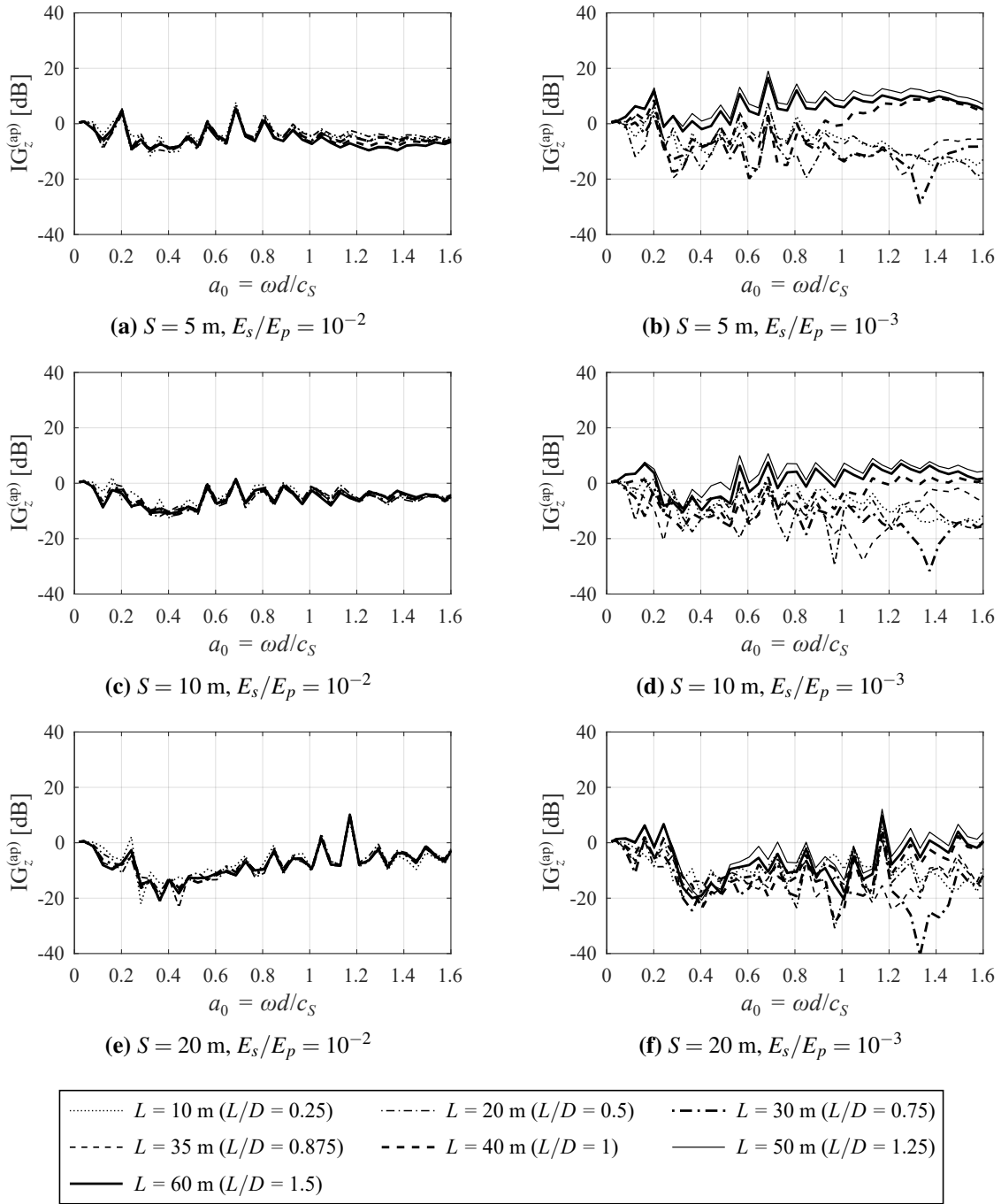
Fig. 6.40 The vertical insertion gains of an off-centred pile near an underground railway tunnel, plotted against non-dimensional frequency a_0. In each sub-figure, the influence of the pile length L on the pile-head response is illustrated. The soil-pile stiffness ratio E_s/E_p is decreased from 10^{-2} (left) to 10^{-3} (right), and the tunnel-pile separation distance S is increased from 5 m (top) to 20 m (bottom). Soil-pile density ratio $\rho_s/\rho_p = 0.8$ and tunnel depth $D = 40$ m.

between the sub-figures, the effect of decreasing E_s/E_p from 10^{-2} (left) to 10^{-3} (right) and increasing S from 5 m (top) to 20 m (bottom) is also illustrated. Similar to Section 6.6.2, the soil-pile density ratio is again fixed at $\rho_s/\rho_p = 0.8$.

Although varying S does influence the added-pile effect, no general trend in the results can be observed over the full frequency range of interest. Nonetheless, some of the trends discussed previously on the influence of L and E_s/E_p remain evident, including the same counteracting effects noted in Section 6.6.2 for a centred pile.

A key parameter to consider is the pile-tunnel depth ratio L/D. When $L/D < 1$ (i.e., the pile toe remains above the depth of the tunnel centre), the IG tends to decrease as L is increased due to the soil-stiffening effect. In general, the enhanced transmission effect takes over as the dominant mechanism once the pile toe reaches the depth of the tunnel centre, leading to positive values of IG and a net amplification of the greenfield response. When $L/D = 1$, the IG can be as high as 15 dB at high frequencies ($a_0 > 1$). As L is increased further ($L/D > 1$), so does the IG, but this never exceeds approximately 20 dB. There appears to be a point at which further increases in L produce negligible changes in IG as the pile toe descends below the tunnel.

When E_s/E_p is decreased from 10^{-2} to 10^{-3} for a shallow tunnel ($D = 10$ m, Fig. 6.38), there is negligible variation in the IG of equal-length piles. As for a deeper tunnel ($D = 25$ m, Fig. 6.39), provided $L/D < 1$, the same decrease in E_s/E_p tends to cause the IG to decrease due to the soil-stiffening effect, as seen in Figures 6.34–6.37 for a centred pile. In contrast, when $L/D \geq 1$, the decrease in E_s/E_p causes the IG to increase over the frequency range of interest.

Note also that, for the deepest tunnel ($D = 40$ m, Fig. 6.40), when the off-centred pile is flexible ($E_s/E_p = 10^{-2}$), the IG is largely insensitive to pile length, as observed in Figs. 6.32 and 6.33 for a centred pile.

6.6.4 A Note on the Displacement Along the Length of Flexible Piles

Sections 6.6.2 and 6.6.3 highlight that when the pile is relatively flexible with a high E_s/E_p, increasing L does very little to change the pile-head response. In an attempt to explain why, this section compares the displacement w_p along centred piles of varying length against the soil displacement w_s^{inc} solely due to the incident wave-field from the railway tunnel.

For a medium depth tunnel ($D = 25$ m), Figs. 6.41 and 6.42 illustrate the variation in these displacements along different lengths of piles (L is increased from 5 to 20 m) when E_s/E_p is 10^{-1} and 10^{-2}, respectively. Likewise, for a deep tunnel ($D = 40$ m), Figs. 6.43 and 6.44 show
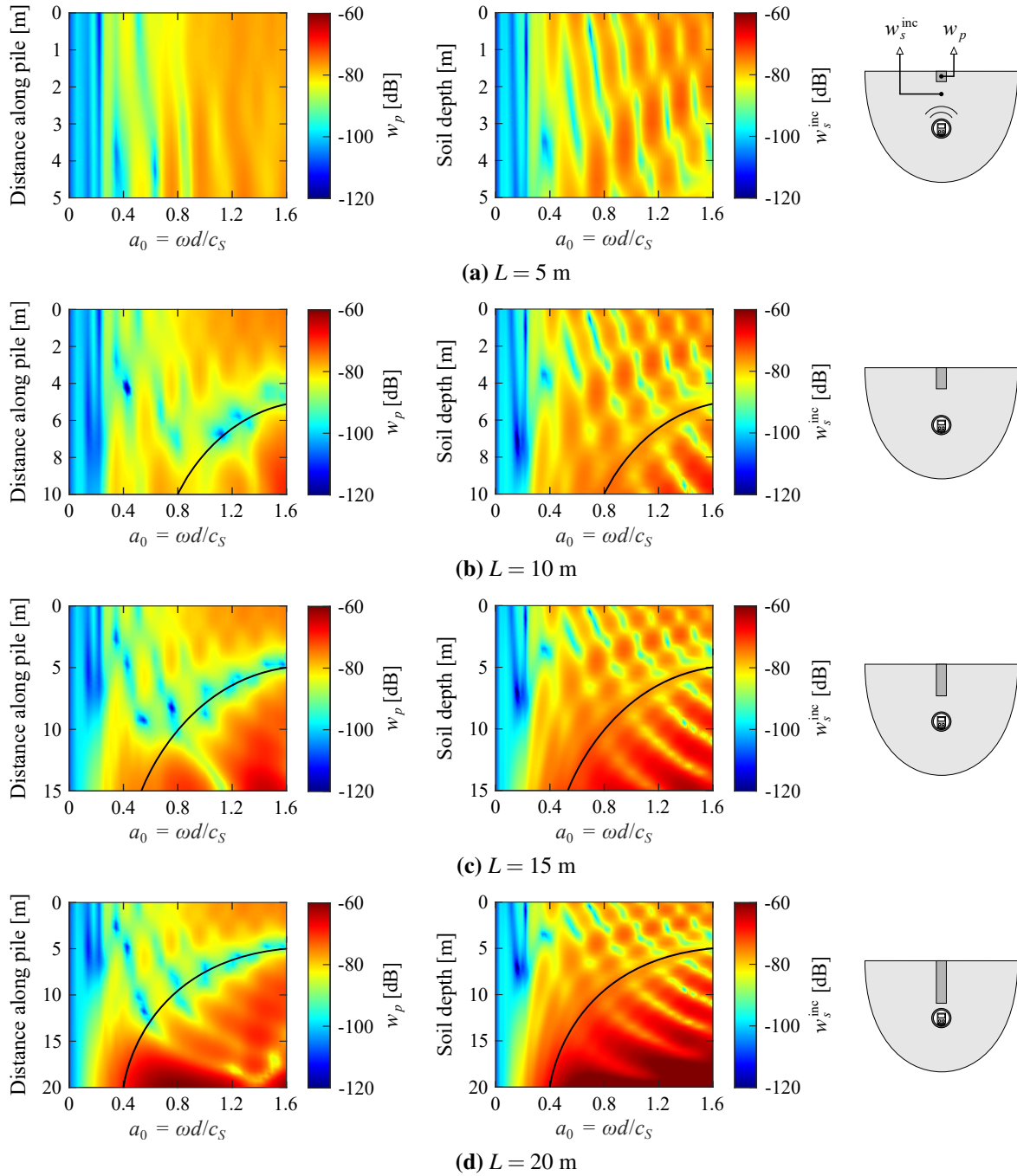
Fig. 6.41 The magnitude of the train-induced displacements along the pile (left) and the incident wave-fields in the soil (right), plotted against non-dimensional frequency a_0. The length of the pile L above the underground railway tunnel is increased from **(a)** 5 m to **(d)** 20 m. The superimposed black lines highlight similarities in the pile and soil displacements. Soil-pile stiffness ratio $E_s/E_p = 10^{-1}$, soil-pile density ratio $\rho_s/\rho_p = 0.8$, and tunnel depth $D = 25$ m.

(a) $L = 5$ m

(b) $L = 10$ m

(c) $L = 15$ m

(d) $L = 20$ m
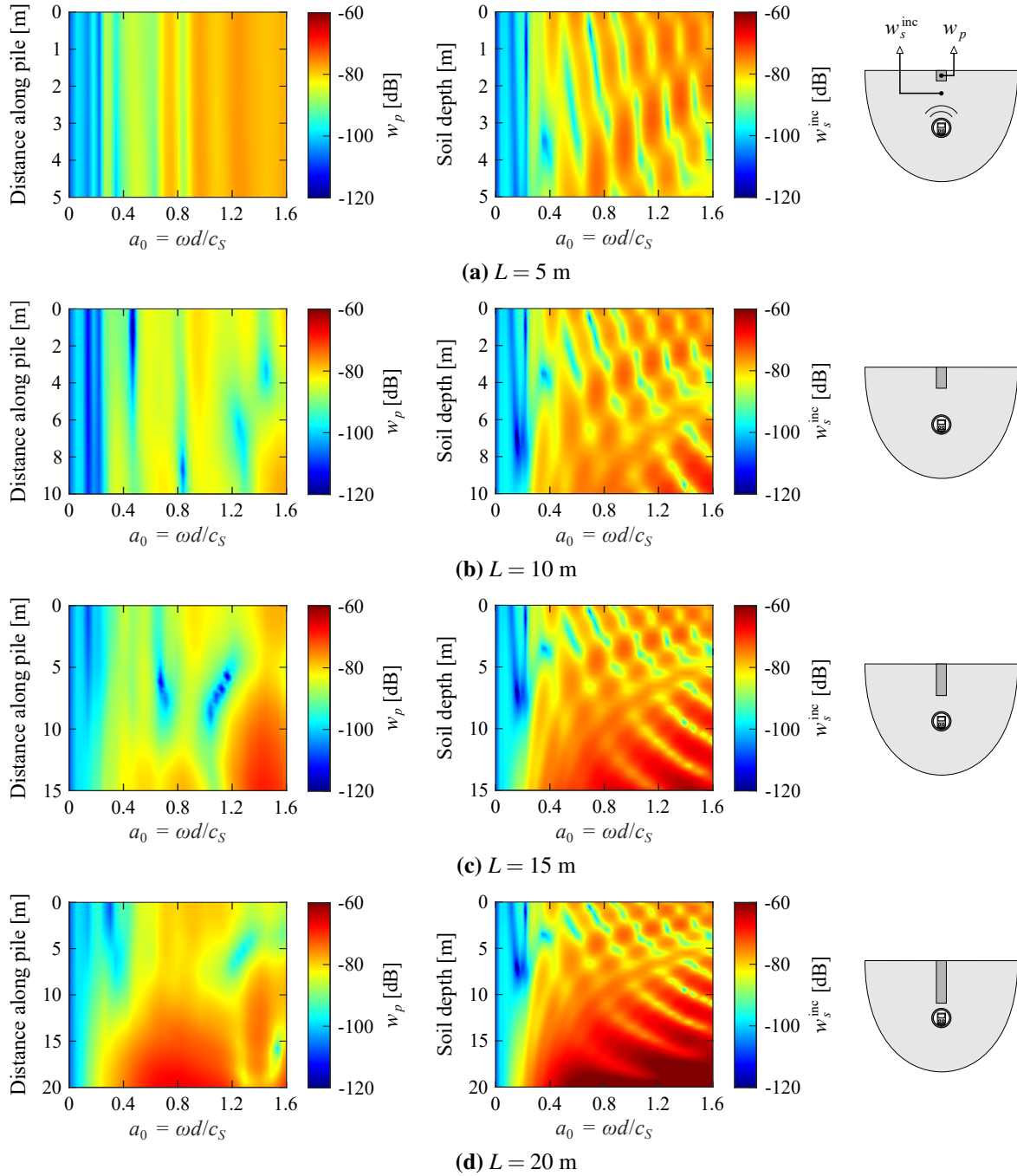
Fig. 6.42 The magnitude of the train-induced displacements along the pile (left) and the incident wave-fields in the soil (right), plotted against non-dimensional frequency a_0. The length L of the centred pile above the underground railway tunnel is increased from **(a)** 5 m to **(d)** 20 m. Soil-pile stiffness ratio $E_s/E_p = 10^{-2}$, soil-pile density ratio $\rho_s/\rho_p = 0.8$, and tunnel depth $D = 25$ m.
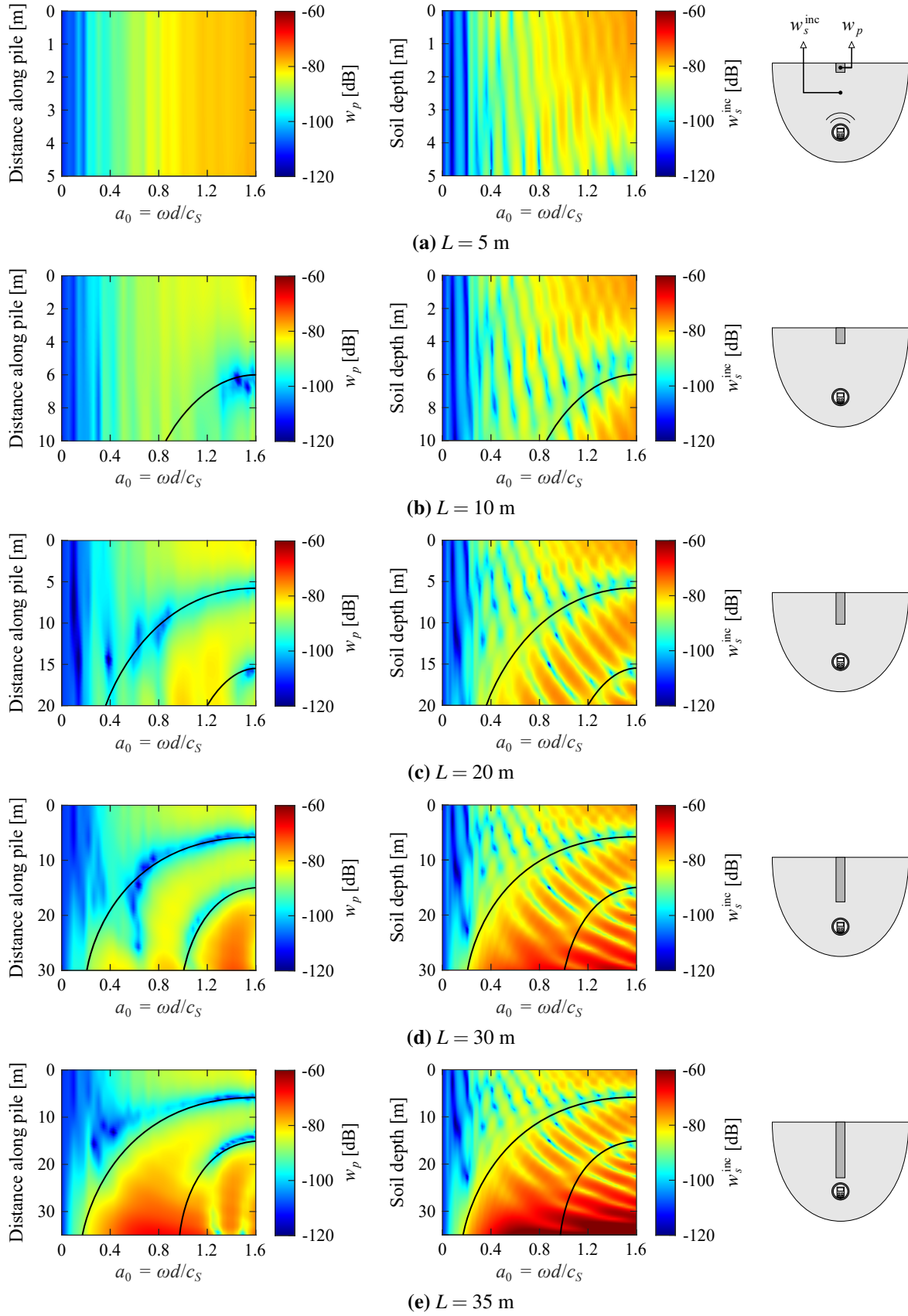
Fig. 6.43 The magnitude of the train-induced displacements along the pile (left) and the incident wave-fields in the soil (right), plotted against non-dimensional frequency a_0. The length L of the centred pile above the underground railway tunnel is increased from **(a)** 5 m to **(e)** 35 m. The superimposed black lines highlight similarities in the pile and soil displacements. Soil-pile stiffness ratio $E_s/E_p = 10^{-2}$, soil-pile density ratio $\rho_s/\rho_p = 0.8$, and tunnel depth $D = 40$ m.

(a) $L = 5$ m

(b) $L = 10$ m

(c) $L = 20$ m

(d) $L = 30$ m

(e) $L = 35$ m
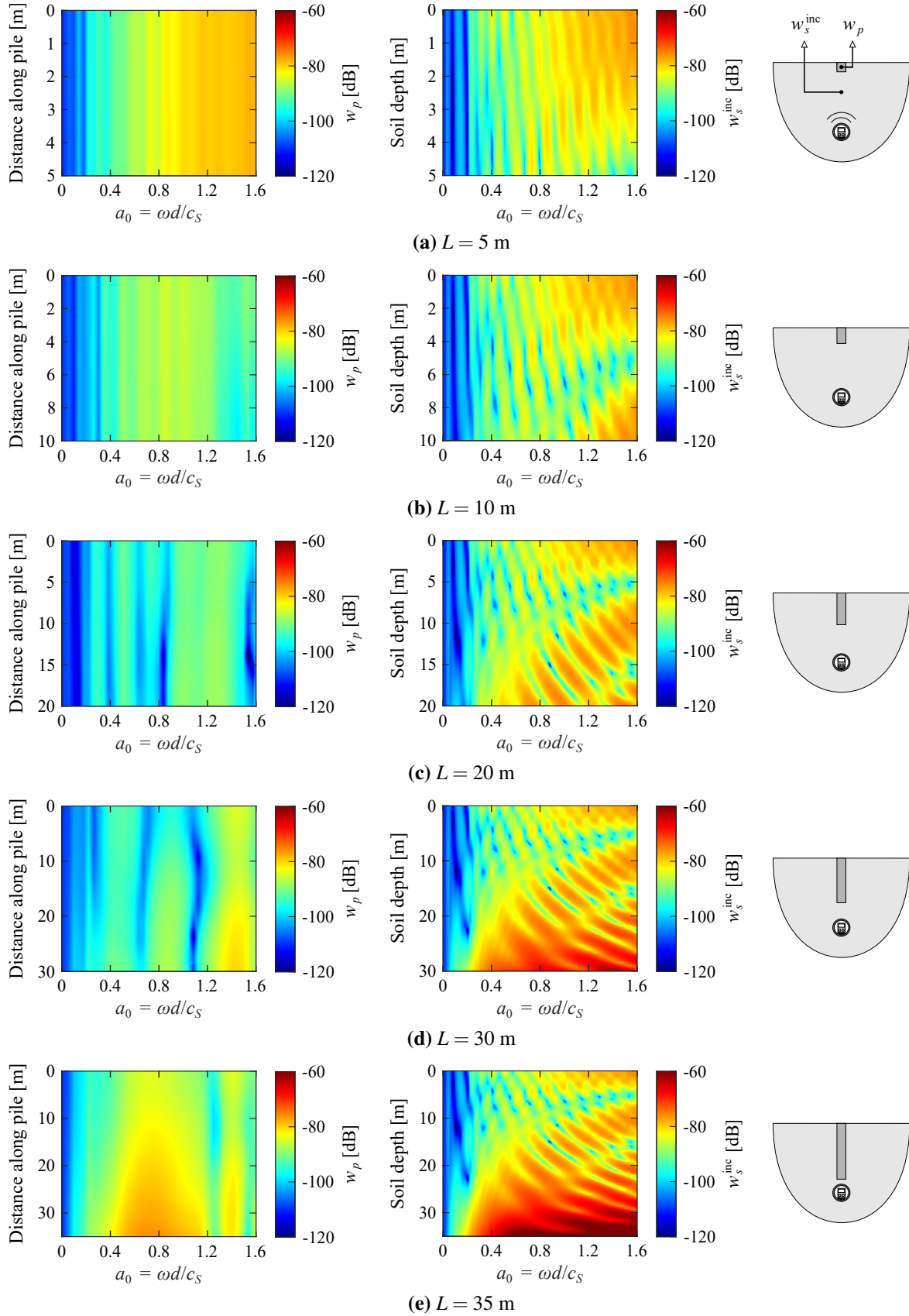
Fig. 6.44 The magnitude of the train-induced displacements along the pile (left) and the incident wave-fields in the soil (right), plotted against non-dimensional frequency a_0. The length L of the centred pile above the underground railway tunnel is increased from **(a)** 5 m to **(e)** 35 m. Soil-pile stiffness ratio $E_s/E_p = 10^{-3}$, soil-pile density ratio $\rho_s/\rho_p = 0.8$, and tunnel depth $D = 40$ m.

the variation in the pile and soil displacements when E_s/E_p is 10^{-2} and 10^{-3}, respectively, as L is increased from 5 to 35 m. The black lines superimposed over the sub-figures in Figs. 6.41 and 6.43, relating to the more flexible piles at each tunnel depth, highlight similarities in the distribution of the pile and soil displacements, both spatially along the pile and in frequency.

The similarities between the pile and soil responses in Figs. 6.41 and 6.43 indicate that, for these particular values of D and E_s/E_p, the mechanical impedances of the pile and soil are similar. Therefore, there is little or no difference in the pile and soil displacements at the soil-pile interface. It is also worth noting that the displacement distribution over the same distance along piles of different lengths, for example from 0 to 10 m in Figs. 6.41b–6.41d and from 0 to 20 m in Figs. 6.43c–6.43e, remains approximately identical.

On the other hand, Figs. 6.42 and 6.44 illustrate how the distribution of the pile and soil displacements can vary considerably when E_s/E_p is decreased so that the piles are no longer relatively flexible. Here, the greater impedance mismatch between the pile and soil causes the pile-head response to vary as the pile length is increased.

In conclusion, the two counteracting mechanisms that have been identified in Section 6.6.2 – the soil-stiffening effect and the enhanced transmission effect – become more pronounced when there are large differences in the relative characteristics of the soil-pile system, resulting in a mismatch in the soil-pile impedance. This mismatch can occur by either varying the soil-pile stiffness ratio or the pile length.

6.7 Conclusions

An iterative PiP-BEM model was developed in Section 6.1 to simulate the 3SI due to tunnel-pile and pile-pile interaction in a coupled tunnel-foundation system. Section 6.2 demonstrated that the dynamic interaction between the ground surface and very shallow tunnels can be captured by the iterative PiP-BEM model. When the tunnel-ground separation distance is greater than the tunnel diameter, only the local free surface around the piled foundation needs to be discretised in the mesh. The mesh also contains internal points along the soil-tunnel interface. Based on the convergence study in Section 6.3, the soil-tunnel mesh must contain at least 42 circumferential points and its longitudinal length must be at least twice the footprint of the foundation itself to maintain numerical accuracy over the frequency range of interest (1-80 Hz).

The results in Section 6.4 support the general conclusion that source-receiver interaction is greatest when the tunnel is close to the foundation, particularly when the piles descend below

the crown of the tunnel. Increasing the number of rows of piles along the tunnel also increased the effect of tunnel-pile coupling. In the large 3×2 pile-group, the coupling became negligible when the distance between the tunnel and the nearest pile exceeded the S-wavelength in the soil. Moreover, the significance of kinematic interaction between neighbouring piles (k-PSPI) depended on the length of the piles and their location and orientation relative to the tunnel. Wave scattering was also more significant at relatively high frequencies (short wavelengths), to the extent that k-PSPI could be important to consider when predicting the response, particularly when long piles provide a large surface for scattering.

Section 6.6 used the standard slab track described in Section 6.5 to conduct a parametric study on the train-induced vibration of a single pile in the vertical direction. The insertion gain (IG) at the pile head was used to characterise the added-pile effect. The results clearly showed that variations in density had an insignificant effect on the added-pile effect. In contrast, both the pile length L and the soil-pile stiffness ratio E_s/E_p can influence the added-pile effect. Two counteracting mechanisms were identified when L was increased: (1) the soil-stiffening effect, which was particularly significant at high frequencies; and (2) the enhanced transmission effect when the pile was close to the railway tunnel. Provided the pile length was less than the tunnel depth, the soil-stiffening effect dominated the pile-head response, meaning that increasing L or decreasing E_s/E_p decreased the IG, as long as the pile was not too short or flexible that it failed to constrain sufficient wavelengths in the soil. If the soil gap between the tunnel crown and the pile toe was small in comparison to the soil S-wavelength, the amplification due to the enhanced transmission effect overcomes the attenuation due to the soil stiffening effect, thereby causing the IG to increase and become positive at some frequencies. For off-centred piles, increasing L beyond the tunnel depth led to further increases in IG, but at a diminishing rate.

Chapter 7

Coupled Tunnel-Foundation-Building Systems

In circumstances where it is necessary to construct a building near a pre-existing underground railway tunnel, numerical models that can predict the vibration performance of the building are very desirable for practising engineers. If the vibration levels exceed the frequency-dependent thresholds for human annoyance, countermeasures, such as base isolation (see Section 2.2.3), may have to be implemented to attenuate the vibration. However, in practice, existing models are either computationally intensive or do not fully capture the fundamental physics [39].

A better option is to use computationally efficient models for the tunnel, ground, foundation and building that capture the essential dynamics of the entire system. This allows practitioners to compare the performance of different designs before the important features of the building are finalised during pre-construction. In this chapter, the BEM model is used for the foundation (see Chapter 3) and the PiP model is used for the railway tunnel (see Appendix C), henceforth denoted as the Fb and Tp models, respectively. The resulting Tp-Fb model for the fully coupled tunnel-foundation system (see Chapter 6) accounts for the 3SI due to tunnel-pile coupling and k-PSPI. A similarly comprehensive model of a building needs to be used in this chapter.

Section 7.1 introduces a generalised model that can assess the vibration performance of a building that is directly coupled to the Tp-Fb model. The added-building effect, predicted using three different models for a modern tall building, is investigated in Section 7.2. These building models are then used to examine the overall vibration of different foundation-building systems in Section 7.3. To minimise the train-induced vibration of a building, Section 7.4 explores the effect of installing base isolation. Section 7.5 presents a virtual case study that shows how the techniques developed in this dissertation can be used to help guide the design of buildings near pre-existing railway tunnels. Finally, some concluding remarks are presented in Section 7.6.

7.1 The Generalised Model of a Foundation-Building System

By adapting the work of Sanitate [206], this section describes how the ground-borne vibration problem of a generalised building can be evaluated. While Sanitate only considered the effect of planar incident waves on the response of 2D portal-framed buildings, this chapter models the buildings as 3D portal frames, as a first approximation, in order to fully capture the effect of the 3D wave-fields from an underground railway tunnel on the entire 3D foundation-building system. Further simplifications to the building model are introduced later in Section 7.2. Non-structural components (floor slabs, walls, façade, etc.) are neglected in the building model.

7.1.1 Variation in the Response During Building Construction

Consider when an existing underground railway tunnel generates steady-state, time-harmonic excitation with angular frequency ω. Prior to building construction, the vibration that reaches a position vector $\mathbf{x} = \{x, y, z\}^{\mathrm{T}}$ on the free surface is the greenfield displacement vector $\mathbf{u}_{\mathrm{S}}(\mathbf{x}, \omega)$. Adding the foundation modifies the greenfield displacement due to wave interaction at the soil-foundation interface (added-foundation effect), which results in the displacement wave-field $\mathbf{u}_{\mathrm{F}}(\mathbf{x}, \omega)$ at the top of the foundation. Constructing the building modifies the wave-field further due to coupling between the building and soil-foundation systems (added-building effect), with the resulting displacement wave-field $\mathbf{u}_{\mathrm{B}}(\mathbf{x}, \omega)$ at the base of the building. The displacement at different floors in the building will depend on the distribution of $\mathbf{u}_{\mathrm{B}}(\mathbf{x}, \omega)$ across the foundation-building interface. An overview of these effects is illustrated in Fig. 7.1.

Sanitate & Talbot [208] observed that the inclusion of soil-foundation-building interaction for a 2D portal-framed building supported on rigid, surface footings attenuated the greenfield
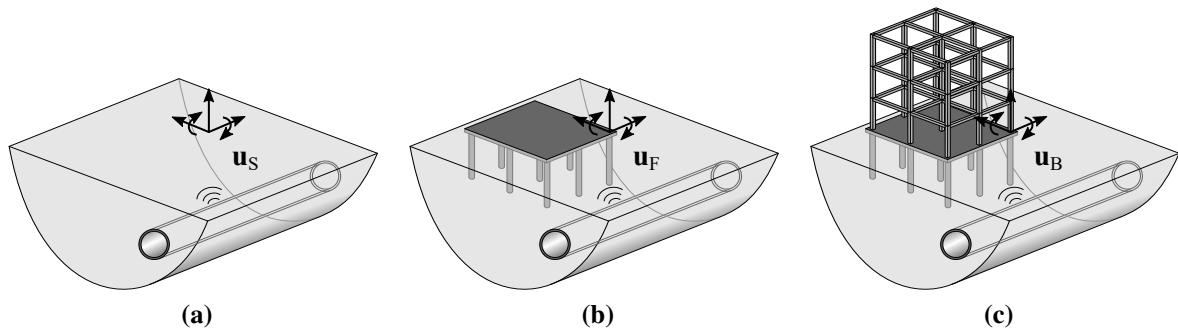
Fig. 7.1 An overview of the ground-borne vibration problem of a tunnel-foundation-building system: **(a)** greenfield displacement $\mathbf{u}_{\mathrm{S}}$ generated by an underground railway tunnel; **(b)** displacement wave-field $\mathbf{u}_{\mathrm{F}}$ at the top of the foundation, accounting for tunnel-foundation interaction; and **(c)** displacement wave-field $\mathbf{u}_{\mathrm{B}}$ at the base of the building, accounting for soil-foundation-building interaction.

response. In particular, when the frequency was greater than 40 Hz, the added-building effect in the vertical direction resulted in attenuation around the order of 10 dB. A more recent study by Kuo et al. [148], which used a 2.5D, coupled FEM-BEM model to predict the vibration of a building next to a surface railway, observed similar attenuation in the vertical direction when the building was supported on embedded strip and raft foundations. Furthermore, increasing the soil stiffness generally decreased the added-building effect at high frequencies. These studies highlight the significance of the interaction between the soil, foundation and building systems.

7.1.2   Coupling at the Foundation-Building Interface

The added-building effect can be analysed by assuming that the base of each building column is directly coupled at a single point to the head of a corresponding foundation pile. Figure 7.2 illustrates the coupling model for the fundamental unit of a general foundation-building system, which can capture any changes in the response during each construction stage of the building. The notation is generalised so that it is applicable for any foundation-building model.

The semi-infinite, 3D soil system is denoted by $\mathcal{S}$, the 3D foundation system by $\mathcal{F}$ and the 3D building system by $\mathcal{B}$. As far as the building response is concerned, the added-foundation effect is represented by the difference between $\mathbf{u}_S$ and $\mathbf{u}_F$ without the presence of the building. When the building is coupled to the foundation at the coupling point O, the added-building effect is similarly represented by the difference between $\mathbf{u}_F$ and $\mathbf{u}_B$. The modification in $\mathbf{u}_F$ can
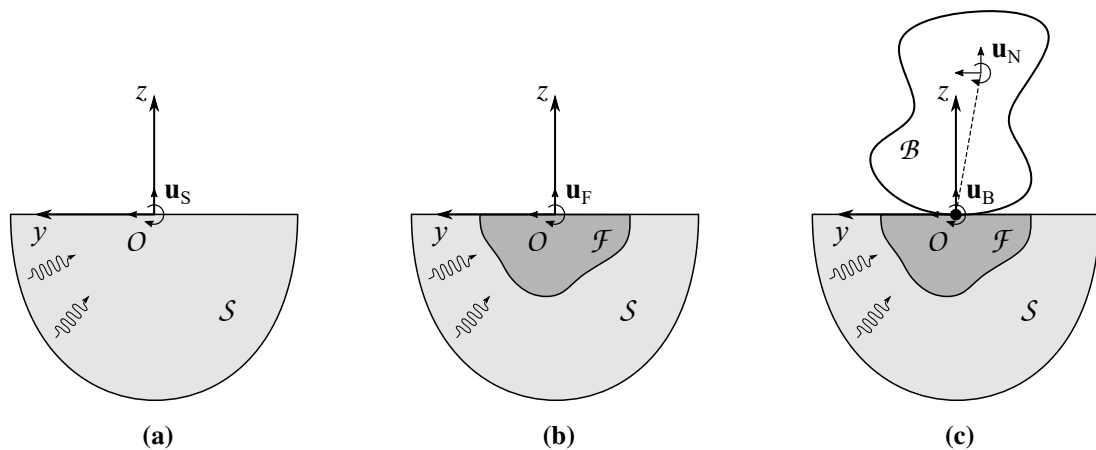
Fig. 7.2 Schematic diagrams illustrating the coupling model for the fundamental unit of a foundation-building system. **(a)** The incident waves-fields from a vibration source in the 3D soil system $\mathcal{S}$ leads to the greenfield displacement $\mathbf{u}_S$ at a point O on the free surface. **(b)** The presence of a 3D foundation system $\mathcal{F}$ is then considered, with the resulting displacement $\mathbf{u}_F$ at the top of $\mathcal{F}$. **(c)** A 3D building system $\mathcal{B}$ is coupled to the soil-foundation system, with the resulting displacements $\mathbf{u}_B$ and $\mathbf{u}_N$ at the base and remainder of $\mathcal{B}$, respectively.

be approached as a wave-scattering problem in its generalised form:

$$\mathbf{u}_B(\mathbf{x}_0, \omega) = \mathbf{u}_F(\mathbf{x}_0, \omega) + \mathbf{H}_F(\mathbf{x}_0, \mathbf{x}_0, \omega)\mathbf{f}_F(\mathbf{x}_0, \omega), \qquad (7.1)$$

where the vector $\mathbf{f}_F$ is the force exerted by the building on the foundation at O, and $\mathbf{H}_F$ is the driving-point displacement FRF matrix of the coupled soil-foundation system. The directional components of the vectors in Eq. (7.1) correspond to the five DOFs at the foundation-building interface: three translations in the x-, y- and z-axes; and two rotations about the x- and y-axes. In general, the displacement and force vectors can be expressed as follows:

$$\mathbf{u}(\mathbf{x}_0, \omega) = \left\{ u_{x0}, u_{y0}, u_{z0}, \theta_{x0}, \theta_{y0} \right\}^T = \left\{ u_0, v_0, w_0, \phi_0, \theta_0 \right\}^T, \qquad (7.2)$$

$$\mathbf{f}(\mathbf{x}_0, \omega) = \left\{ f_{x0}, f_{y0}, f_{z0}, q_{x0}, q_{y0} \right\}^T = \left\{ s_0, t_0, f_0, p_0, q_0 \right\}^T. \qquad (7.3)$$

Torsion due to rotation about the z-axis of individual building columns is neglected because it has a negligible effect on the overall building structure.

Equilibrium of forces is satisfied by letting $\mathbf{f}_F = -\mathbf{f}_B$, where $\mathbf{f}_B$ is the force exerted on the building at O. In general, the global displacement-force relationship within $\mathcal{B}$ can be written in the form:

$$\mathbf{u}_{BG}(\mathbf{x}_G, \omega) = \left\{ \begin{array}{c} \mathbf{u}_B(\mathbf{x}_0, \omega) \\ \mathbf{u}_N(\mathbf{x}_N, \omega) \end{array} \right\} = \left[\begin{array}{cc} \mathbf{H}_{BB}(\mathbf{x}_0, \mathbf{x}_0, \omega) & \mathbf{H}_{BN}(\mathbf{x}_0, \mathbf{x}_N, \omega) \\ \mathbf{H}_{NB}(\mathbf{x}_N, \mathbf{x}_0, \omega) & \mathbf{H}_{NN}(\mathbf{x}_N, \mathbf{x}_N, \omega) \end{array} \right] \left\{ \begin{array}{c} \mathbf{f}_B(\mathbf{x}_0, \omega) \\ \mathbf{f}_N(\mathbf{x}_N, \omega) \end{array} \right\} \qquad (7.4)$$

$$= \mathbf{H}_{BG}(\mathbf{x}_G, \mathbf{x}_G, \omega)\mathbf{f}_{BG}(\mathbf{x}_G, \omega),$$

where $\mathbf{x}_G = \mathbf{x}_0 \bigcup \mathbf{x}_N$ is the collection of position vectors $\mathbf{x}_0$ and $\mathbf{x}_N$ at the base and remainder of $\mathcal{B}$, respectively. Given there are no external forces within the building ($\mathbf{f}_N = \mathbf{0}$), Eq. (7.4) can be rewritten in terms of the displacement-force relationship at the coupling point:

$$\mathbf{f}_B(\mathbf{x}_0, \omega) = \mathbf{H}_{BB}^{-1}(\mathbf{x}_0, \mathbf{x}_0, \omega)\mathbf{u}_B(\mathbf{x}_0, \omega) = \mathbf{H}_B^{-1}(\mathbf{x}_0, \mathbf{x}_0, \omega)\mathbf{u}_B(\mathbf{x}_0, \omega), \qquad (7.5)$$

where $\mathbf{H}_B$ is the driving-point displacement FRF matrix of the building at O. Alternatively, $\mathbf{K}_B = \mathbf{H}_B^{-1}$ is defined as the condensed dynamic-stiffness matrix [199] of the building. Note that the FRF matrices $\mathbf{H}_F$ and $\mathbf{H}_B$ are symmetric. By eliminating the forces in Eqs. (7.1) and (7.5), the relationship characterising the change in the displacement wave-field at the foundation-building interface, once the building is constructed, can be derived [222]:

$$\mathbf{u}_B = (\mathbf{I} + \mathbf{H}_F\mathbf{K}_B)^{-1}\mathbf{u}_F = \mathbf{T}_B\mathbf{u}_F, \qquad (7.6)$$

where $\mathbf{I}$ is the identity matrix, and $\mathbf{T_B}$ is the foundation-building transfer matrix describing the added-building effect. In general, $\mathbf{T_B}$ is a fully populated, non-symmetric matrix. The response of the building at $\mathbf{x_N}$ can be retrieved from Eqs. (7.4) and (7.6):

$$\mathbf{u_N} = \mathbf{H_{NB}K_B u_B} = \mathbf{H_{NB}K_B T_B u_F}. \tag{7.7}$$

It is worth noting that the added-building effect depends on the dynamics of both the foundation and building, as Eqs. (7.6) and (7.7) are expressed in terms of $\mathbf{H_F}$ and $\mathbf{K_B}$.

7.1.3 Assessing the Performance of Different Building Configurations

It is yet relatively unclear how effective deep piled foundations (typically, where the length is more than 3 m) are at mitigating the vibration transmitted into a building compared to shallow foundations, such as soil-embedded footings. Although they are unlikely to be used in practice to support tall buildings, footings provide a useful reference against which the effect of piles on the vibration may be compared. In this chapter, the circular footings are assumed to exhibit elastic behaviour, so the Fb model can be used to characterise their motion by considering each footing as equivalent to a very short pile with a fixed length of 0.5 m and a diameter of 0.71 m.

The insertion gain (IG) can be used as a measure of variation in the vibration performance between two different configurations of the foundation-building system. In order to compare the response between buildings supported on piles and footings, the IG can be defined as

$$\mathrm{IG}^{(\mathrm{pf})} = 20\log_{10}\left(\frac{|u_N^{(\mathrm{pile})}|}{|u_N^{(\mathrm{foot})}|}\right), \tag{7.8}$$

where $u_N^{(\mathrm{pile})}$ and $u_N^{(\mathrm{foot})}$ are the displacements at a single point within the foundation-building system in the pile and footing configurations, respectively, and the superscript '(pf)' denotes that the IG measures changes in the displacement of the pile and footing configurations.

However, the effectiveness of IG is limited, as it only captures the performance of a single point with respect to a particular direction. Section 6.4 shows how the IG can characterise the added-pile effect of a single pile, but it is unable to describe the performance of the entire piled foundation. The mean source-receiver insertion gain in Section 6.4.5 was an attempt to find the overall response of a piled foundation by computing the average response across the pile heads.

Instead of measuring the displacement, the mean vibrational power is a more effective scalar measure of the building's multi-directional response, as described in Section 2.2.4. Based on

the notation defined in Section 7.1.2, the mean vibrational power flow entering the building can be evaluated by taking the dot product of the force $\mathbf{f}_B$ and velocity $i\omega\mathbf{u}_B$ vectors at the base of the building:

$$\bar{P} = \frac{1}{2}\mathrm{Re}\left(\mathbf{f}_B^* \cdot i\omega\mathbf{u}_B\right) = \frac{1}{2}\mathrm{Re}\left(i\omega\left[\mathbf{f}_B^*\right]^T\mathbf{u}_B\right) = \frac{1}{2}\mathrm{Re}\left(i\omega\mathbf{f}_B^\dagger\mathbf{u}_B\right), \tag{7.9}$$

where the superscripts '$*$' and '$\dagger$' denote the complex conjugate and the Hermitian transpose, respectively. Based on the sign convention adopted in Eq. (7.9), positive values represent power flow entering the building. By using Eqs. (7.5) and (7.6) to eliminate $\mathbf{f}_B$ and $\mathbf{u}_B$, Eq. (7.9) can be rewritten in terms of the displacement $\mathbf{u}_F$ before the building is constructed:

$$\bar{P} = \frac{1}{2}\mathrm{Re}\left(i\omega\mathbf{u}_F^\dagger\mathbf{T}_B^\dagger\mathbf{K}_B^\dagger\mathbf{T}_B\mathbf{u}_F\right). \tag{7.10}$$

To compare the overall vibration performance between the pile and footing configurations, the power-flow insertion gain (PFIG) can be defined as

$$\mathrm{PFIG}^{(\mathrm{pf})} = 10\log_{10}\left(\frac{|\bar{P}^{(\mathrm{pile})}|}{|\bar{P}^{(\mathrm{foot})}|}\right), \tag{7.11}$$

where $\bar{P}^{(\mathrm{pile})}$ and $\bar{P}^{(\mathrm{foot})}$ define the mean power flows entering the building when it is supported on piles and footings, respectively.

7.2 Modelling a Building

This section discusses three possible approaches in which a building can be modelled, using a benchmark building design as a generic example. The three building models are used to study the similarities and differences in the added-building effect and the mean power flow entering the benchmark building when it is supported on either piles or embedded footings.

7.2.1 The Benchmark Building

The benchmark building is represented by the 10-storey, 2-by-2-bay frame illustrated in Fig. 7.3 because it is not too computationally demanding to solve, yet it is sufficiently comprehensive enough to capture the fundamental dynamic behaviour of a modern tall building. In total, there are $N = 9$ coupling points at the foundation-building interface. At each coupling point, the base of a building column is directly coupled to the top of a corresponding pile or footing by using

the coupling model presented in Section 7.1.2. The steady-state motion of an elastic bar and an Euler-Bernoulli beam are used to characterise the propagation of axial and flexural waves, respectively, through the individual building columns and beams.

Table 7.1 presents the parameter values of the building and foundation, both of which are constructed out of concrete. The parameter values in Table 6.1 are used to model the concrete tunnel and the London Clay soil. The train-track system is modelled using the parameter values in Table 6.2 that represent a standard slab track.

Typically, two principal mechanisms cause damping in the dynamic response of a building: material damping and boundary damping. The former is related to energy dissipation within the bulk building material, while the latter is due to energy dissipation at the connections between various elements (columns, floors, windows, etc.). When the damping is measured in a built-up
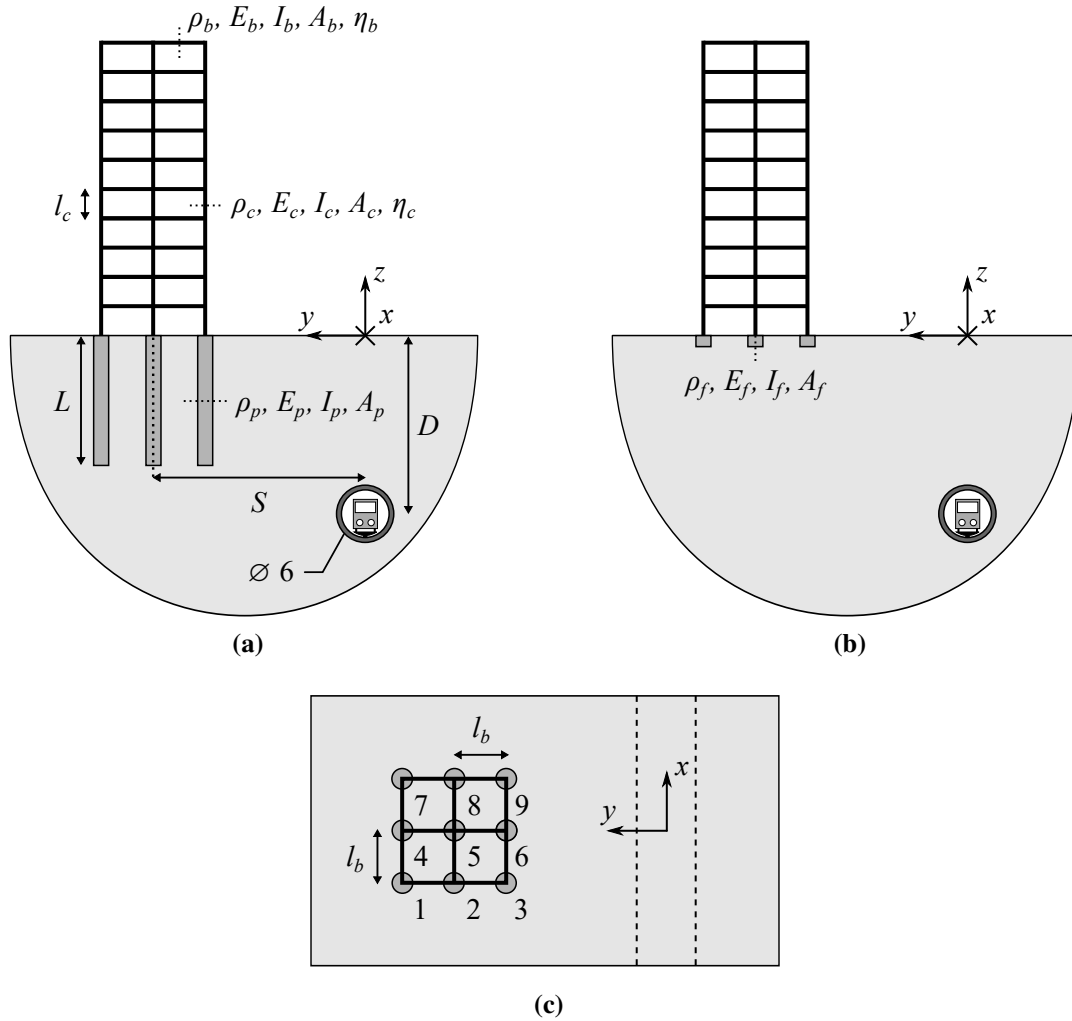
Fig. 7.3 Schematic diagrams of the benchmark building, represented as a 10-storey, 2-by-2-bay frame supported on a foundation of **(a)** piles and **(b)** embedded footings, near an underground railway tunnel. **(c)** Common plan view shows the $N = 9$ coupling points (numbered) at the foundation-building interface and the tunnel's outline below the free surface (dashed lines).

Building parameters [Units]	Columns	Beams
Young's modulus [Pa]	$E_c = 30 \times 10^9$	$E_b = 30 \times 10^9$
Density [kg/m^3]	$\rho_c = 2500$	$\rho_b = 2500$
Cross-section area [m^2]	$A_c = 0.25$	$A_b = 1.25$
Second moment of area [m^4]	$I_c = 5.2 \times 10^{-3}$	$I_b = 6.5 \times 10^{-3}$
Length [m]	$l_c = 3$	$l_b = 4$
Loss factor [−]	$\eta_c = 0.1$	$\eta_b = 0.1$
Foundation parameters [Units]	Piles	Footings
Young's modulus [Pa]	$E_p = 30 \times 10^9$	$E_f = 30 \times 10^9$
Density [kg/m^3]	$\rho_p = 2500$	$\rho_f = 2500$
Cross-section area [m^2]	$A_p = 0.39$	$A_f = 0.39$
Second moment of area [m^4]	$I_p = 12.3 \times 10^{-3}$	$I_f = 12.3 \times 10^{-3}$

Table 7.1 Building and foundation parameter values for the benchmark foundation-building system.

structure, such as a building, it is usually found to be at least an order of magnitude higher than the intrinsic material damping of the structural components [244]. This difference is attributed to effects such as frictional micro-slipping at bolted joints [46, 96], which make it difficult to accurately simulate the boundary damping. Hence, the contribution due to boundary damping in the building is assumed to be captured by a model that accounts for the material damping.

Experimental evidence suggests that the damping in concrete columns does not strongly depend on the frequency, and different reinforcement configurations can cause small variations in the damping. Based on this, Newland & Hunt [182] state that a hysteretic damping model, as mentioned in Section 2.3.1, with loss factors in the order of $\eta = 0.01$ can be representative of the material damping in a concrete column. Moreover, they highlight the difficulty in modelling the damping in a complete building, suggesting a tenfold value of η in such a case. This order of magnitude is in agreement with the typical damping values assigned to equivalent SDOF models of concrete buildings, when analysing design spectra in earthquake engineering [216]. Therefore, a hysteretic loss factor of $\eta = 0.1$ is used in this dissertation to account for both material and boundary damping in the overall building.

7.2.2 The Portal-Frame (Bp) Model

In order to explicitly capture the influence of through-floor coupling and modal behaviour, the building can be modelled as a portal frame (Bp model). This is an 'exact' model because the

frame is divided into bar-beam elements, which are then coupled together using appropriate boundary conditions. However, although the Bp model is useful in many applications, such as predicting the absolute isolation performance of a building [206], it requires more resources to develop and run compared to the other two models presented in Sections 7.2.3 and 7.2.4.

For the element shown in Fig. 7.4, the generalised displacements and forces at the nodes are represented by the following vectors:

$$\mathbf{u}'_e = \left\{ u'_1, v'_1, w'_1, \phi'_1, \theta'_1, u'_2, v'_2, w'_2, \phi'_2, \theta'_2 \right\}^T, \tag{7.12}$$

$$\mathbf{f}'_e = \left\{ s'_1, t'_1, f'_1, p'_1, q'_1, s'_2, t'_2, f'_2, p'_2, q'_2 \right\}^T. \tag{7.13}$$

The dynamic-stiffness method (DSM) [30] is applied, as presented in Section 3.1.1 for a pile, to obtain a force-displacement relationship between the nodes of the element:
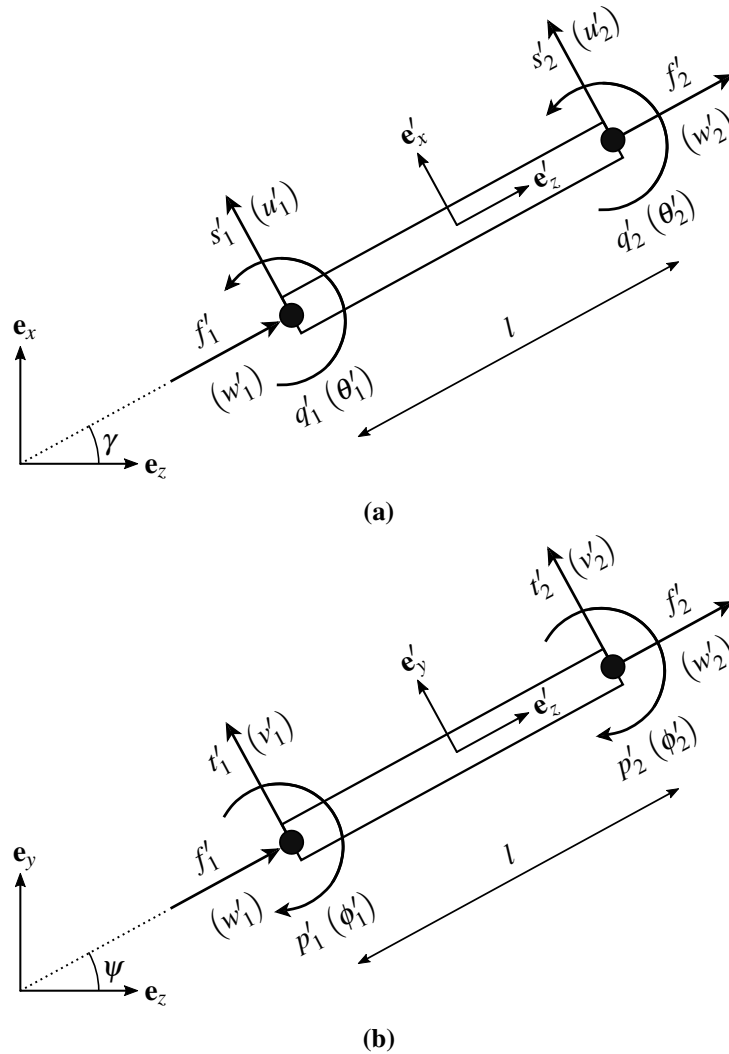
Fig. 7.4 Representation of a bar-beam element of length l in the global (x,y,z) coordinate system due to rotations of γ and ψ about the **(a)** y- and **(b)** x-axes. The generalised displacements (u',v',z',ϕ',θ') and forces (s',t',f',p',q') at the element's nodes are defined in the local (x',y',z') coordinate system.

$$\mathbf{f}'_e = \mathbf{K}'_e \mathbf{u}'_e, \tag{7.14}$$

where $\mathbf{K}'_e$ is the element's dynamic-stiffness matrix in the local (x', y', z') coordinate system.

In the portal frame, multiple elements are coupled together in the global (x, y, z) coordinate system. A transformation matrix $\mathbf{R}$ is needed to refer to the displacements $\mathbf{u}$ and forces $\mathbf{f}$ in the global coordinate system when each element is rotated by the angles of ψ and γ about the x- and y-axes, as illustrated in Fig. 7.4. These transformations can be expressed as

$$\mathbf{u}_e = \mathbf{R}\mathbf{u}'_e, \quad \mathbf{f}_e = \mathbf{R}\mathbf{f}'_e, \quad \text{and} \quad \mathbf{R} = \begin{bmatrix} \mathbf{S} & \mathbf{0} \\ \mathbf{0} & \mathbf{S} \end{bmatrix}, \tag{7.15}$$

where

$$\mathbf{S} = \begin{bmatrix} \cos\gamma & -\sin\gamma\sin\psi & \sin\gamma\cos\psi & 0 & 0 \\ 0 & \cos\psi & \sin\psi & 0 & 0 \\ -\sin\gamma & -\cos\gamma\sin\psi & \cos\gamma\cos\psi & 0 & 0 \\ 0 & 0 & 0 & \cos\gamma & 0 \\ 0 & 0 & 0 & 0 & \cos\psi \end{bmatrix}. \tag{7.16}$$

Note, $\mathbf{R}$ does not transform torsional rotation about the element's local z'-axis. By substituting Eq. (7.14) into Eq. (7.15), the global dynamic-stiffness matrix $\mathbf{K}_e$ of the element can be found:

$$\mathbf{f}_e = \mathbf{R}\mathbf{f}'_e = \mathbf{R}\mathbf{K}'_e \mathbf{u}'_e = \mathbf{R}\mathbf{K}'_e \mathbf{R}^{-1} \mathbf{u}_e = \mathbf{K}_e \mathbf{u}_e, \tag{7.17}$$

Once multiple elements are coupled together in the portal frame, by satisfying equilibrium and compatibility at the nodes, the global dynamic-stiffness matrix $\mathbf{K}_{BGp}$ of the entire frame can be calculated. By partitioning the inverse of $\mathbf{K}_{BGp}$, the fully populated displacement FRF matrix $\mathbf{H}_{Bp}$ at the base of the portal frame can be determined. The $H_{Bpij}^{(m,n)}$ components in $\mathbf{H}_{Bp}$ that relate the displacement i at coupling point m, when a force j is applied at coupling point n, can be expressed as the following matrix:

$$\mathbf{H}_{Bp}^{(m,n)} = \begin{bmatrix} H_{Bpxx}^{(m,n)} & H_{Bpxy}^{(m,n)} & H_{Bpxz}^{(m,n)} & H_{Bpx\phi}^{(m,n)} & H_{Bpx\theta}^{(m,n)} \\ H_{Bpyx}^{(m,n)} & H_{Bpyy}^{(m,n)} & H_{Bpyz}^{(m,n)} & H_{Bpy\phi}^{(m,n)} & H_{Bpy\theta}^{(m,n)} \\ H_{Bpzx}^{(m,n)} & H_{Bpzy}^{(m,n)} & H_{Bpzz}^{(m,n)} & H_{Bpz\phi}^{(m,n)} & H_{Bpz\theta}^{(m,n)} \\ H_{Bp\phi x}^{(m,n)} & H_{Bp\phi y}^{(m,n)} & H_{Bp\phi z}^{(m,n)} & H_{Bp\phi\phi}^{(m,n)} & H_{Bp\phi\theta}^{(m,n)} \\ H_{Bp\theta x}^{(m,n)} & H_{Bp\theta y}^{(m,n)} & H_{Bp\theta z}^{(m,n)} & H_{Bp\theta\phi}^{(m,n)} & H_{Bp\theta\theta}^{(m,n)} \end{bmatrix}. \tag{7.18}$$

Note, reciprocity between the coupling points $\left(\mathbf{H}_{\text{Bp}}^{(m,n)} = \mathbf{H}_{\text{Bp}}^{(n,m)} \right)$ and the force-displacement components $\left(H_{Bpij}^{(m,n)} = H_{Bpji}^{(m,n)} \right)$ is considered in $\mathbf{H}_{\text{Bp}}$.

7.2.3 The Column (Bc) Model

In circumstances where the added-building effect, or the isolation performance of a building, has to be evaluated, it is important to explore if simplified models, which can predict the base impedance, are as effective as the Bp model at capturing the essential dynamics of the building. This section derives the equations of motion at the base of a simplified building model, where the building is represented as a series of independent columns (Bc model) because the through-floor coupling between adjacent columns is neglected.

The mass and stiffness of each column is assumed to be uniformly distributed along its height of $L_c = n_{\text{storeys}} l_c$, where n_{storeys} is the number of storeys. The columns are described by their Young's modulus E_c, density ρ_c, cross-section area A_c, second moment of area I_c, and loss factor η_c, as presented in Table 7.1. From these parameters, the mass per unit length $m_c = \rho_c A_c$ and the bending stiffness $K_c = E_c I_c$ of each column are used to derive the equations of motion for the Bc model.

Consider the column shown in Fig. 7.5, with generalised forces applied at the coupling point O. The displacement FRF matrix $\mathbf{H}_{\text{Bc}}$ of the column at O is derived by assuming that the axial and flexural motion are uncoupled. In this section, the equations are derived for the undamped case; the equations for the damped case can be found by substituting $E_c^* = E_c(1 + i\eta_c)$ for E_c.

In the space-time (z,t)-domain, the general solution describing the undamped, steady-state axial motion of an elastic bar in the z-direction is

$$\bar{w}(z,t) = w(z,\omega) \cdot e^{i\omega t} = \left(a_1 e^{i\alpha z} + a_2 e^{-i\alpha z} \right) \cdot e^{i\omega t} \quad \text{for } z \geq 0, \tag{7.19}$$

where ω is the angular frequency and $\alpha = \omega \left(\frac{\rho_c}{E_c} \right)^{1/2}$ is the wavenumber of axial waves in the column. Note, only the real part of Eq. (7.19) represents the column's physical motion. When

Fig. 7.5 The generalised forces at the coupling point O of a finite column. Note that only the forces in the xz-plane are represented.

a time-harmonic axial force $(f_0 \cdot e^{i\omega t})$ is applied at O, the following boundary conditions need to be satisfied:

$$\frac{E_c m_c}{\rho_c} \frac{\partial \bar{w}}{\partial z}\bigg|_{z=0} = -f_0 \cdot e^{i\omega t}, \quad \text{and} \quad \frac{\partial \bar{w}}{\partial z}\bigg|_{z=L_c} = 0. \tag{7.20}$$

By substituting Eq. (7.19) into Eq. (7.20), the complex coefficients a_1 and a_2 can be found:

$$\begin{Bmatrix} a_1 \\ a_2 \end{Bmatrix} = \begin{bmatrix} 1 & -1 \\ e^{i\alpha L_c} & -e^{-i\alpha L_c} \end{bmatrix}^{-1} \begin{Bmatrix} \frac{i\rho_c}{\alpha E_c m_c} f_0 \\ 0 \end{Bmatrix}. \tag{7.21}$$

The general solution in the (z,t)-domain that describes the undamped, steady-state flexural motion of an Euler-Bernoulli beam in the x-direction is

$$\bar{u}(z,t) = u(z,\omega) \cdot e^{i\omega t} = \left(b_1 e^{\beta z} + b_2 e^{-\beta z} + b_3 e^{i\beta z} + b_4 e^{-i\beta z} \right) \cdot e^{i\omega t} \quad \text{for } z \geq 0, \tag{7.22}$$

where $\beta = \sqrt{\omega} \left(\frac{m_c}{K_c} \right)^{1/4}$ is the wavenumber of flexural waves. The complex coefficients b_1, b_2, b_3 and b_4 can be determined by applying appropriate boundary conditions. Since excitation due to both shear forces and bending moments can generate flexural waves, the overall motion of the column needs to be considered by applying the superposition principle.

When a time-harmonic shear force $(s_0 \cdot e^{i\omega t})$ is applied at point O, the following boundary conditions need to be satisfied:

$$\frac{\partial^2 \bar{u}}{\partial z^2}\bigg|_{z=0} = \frac{\partial^2 \bar{u}}{\partial z^2}\bigg|_{z=L_c} = \frac{\partial^3 \bar{u}}{\partial z^3}\bigg|_{z=L_c} = 0, \quad \text{and} \quad K_c \frac{\partial^3 \bar{u}}{\partial z^3}\bigg|_{z=0} = s_0 \cdot e^{i\omega t}. \tag{7.23}$$

By substituting Eq. (7.22) into Eq. (7.23), the complex coefficients due to the shear force can be found:

$$\begin{Bmatrix} b_{1s} \\ b_{2s} \\ b_{3s} \\ b_{4s} \end{Bmatrix} = \begin{bmatrix} 1 & 1 & -1 & -1 \\ 1 & -1 & -i & i \\ e^{\beta L_c} & e^{-\beta L_c} & -e^{i\beta L_c} & -e^{-i\beta L_c} \\ e^{\beta L_c} & -e^{-\beta L_c} & -ie^{i\beta L_c} & ie^{-i\beta L_c} \end{bmatrix}^{-1} \begin{Bmatrix} 0 \\ \frac{1}{K_c \beta^3} s_0 \\ 0 \\ 0 \end{Bmatrix}. \tag{7.24}$$

When a time-harmonic bending moment $(q_0 \cdot e^{i\omega t})$ is applied at O, the following boundary conditions need to be satisfied:

$$K_c \left. \frac{\partial^2 \bar{u}}{\partial z^2} \right|_{z=0} = -q_0 \cdot e^{i\omega t}, \quad \text{and} \quad \left. \frac{\partial^3 \bar{u}}{\partial z^3} \right|_{z=0} = \left. \frac{\partial^2 \bar{u}}{\partial z^2} \right|_{z=L_c} = \left. \frac{\partial^3 \bar{u}}{\partial z^3} \right|_{z=L_c} = 0. \tag{7.25}$$

By substituting Eq. (7.22) into Eq. (7.25), the complex coefficients due to the bending moment can be found:

$$\begin{Bmatrix} b_{1q} \\ b_{2q} \\ b_{3q} \\ b_{4q} \end{Bmatrix} = \begin{bmatrix} 1 & 1 & -1 & -1 \\ 1 & -1 & -i & i \\ e^{\beta L_c} & e^{-\beta L_c} & -e^{i\beta L_c} & -e^{-i\beta L_c} \\ e^{\beta L_c} & -e^{-\beta L_c} & -ie^{i\beta L_c} & ie^{-i\beta L_c} \end{bmatrix}^{-1} \begin{Bmatrix} \frac{-1}{K_c \beta^2} q_0 \\ 0 \\ 0 \\ 0 \end{Bmatrix}. \tag{7.26}$$

Note, the equations that describe the flexural motion of the column in the y-direction are similar to Eqs. (7.22)–(7.26).

By evaluating all the equations describing the axial and flexural motion at O, the following displacement-force relationship in the space-frequency (z, ω)-domain can be derived for the Bc model:

$$\begin{Bmatrix} u_0 \\ v_0 \\ w_0 \\ \phi_0 \\ \theta_0 \end{Bmatrix} = \begin{bmatrix} H_{Bcxx} & 0 & 0 & 0 & H_{Bcx\theta} \\ 0 & H_{Bcyy} & 0 & H_{Bcy\phi} & 0 \\ 0 & 0 & H_{Bczz} & 0 & 0 \\ 0 & H_{Bc\phi y} & 0 & H_{Bc\phi\phi} & 0 \\ H_{Bc\theta x} & 0 & 0 & 0 & H_{Bc\theta\theta} \end{bmatrix} \begin{Bmatrix} s_0 \\ t_0 \\ f_0 \\ p_0 \\ q_0 \end{Bmatrix}, \tag{7.27}$$

or simplified:

$$\mathbf{u}_B = \mathbf{H}_{Bc} \mathbf{f}_B. \tag{7.28}$$

7.2.4 The Dashpot (Bd) Model

A further simplification can be applied to the Bc model by assuming that each building column is semi-infinite, which is the extreme case for very tall buildings. In this case, vibrational energy entering at the base of each semi-infinite column is completely dissipated along its height. It is assumed that all waves propagate up the column without being reflected downwards; that is, the waves are damped out before they reach any boundaries, so the building's modal behaviour is neglected. Thus, the benchmark building, although having finite dimensions, can be assumed to be infinitely tall from the perspective of wave propagation, as viewed from the base.
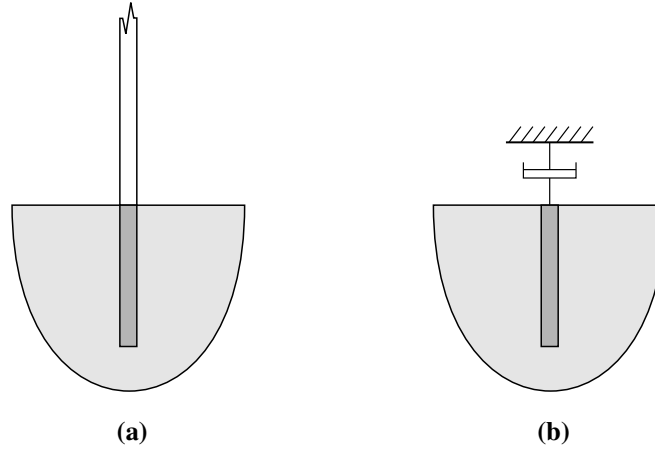
Fig. 7.6 Representation of **(a)** a semi-infinite column as **(b)** an equivalent viscous dashpot. Note that the dashpot represented here accounts for motion in the five DOFs at the base of the semi-infinite column.

In principle, the response at the base of each semi-infinite column can be idealised using the equations of motion for an equivalent viscous dashpot, as represented in Fig. 7.6. A dashpot is a type of mechanical element that dissipates the kinetic energy supplied to it by producing a resistive force that is proportional to the driving velocity. Thus, the benchmark building can be modelled as a series of independent, viscous dashpots (Bd model), with each dashpot coupled to either a pile or footing at a single point.

Consider the semi-infinite column illustrated in Fig. 7.7, with generalised forces applied at the coupling point O. The dynamic behaviour of a dashpot is characterised by its impedance function Z, which is defined as the generalised force divided by the driving-point velocity [181]. Therefore, the displacement FRF matrix $\mathbf{H}_{\mathrm{Bd}}$ at the base of each semi-infinite column can be expressed in terms of the impedance functions for an equivalent dashpot. It is worth noting that the impedance functions for axial and flexural motion of the semi-infinite column are different.

Since the column is semi-infinite, the general solution for the undamped axial motion of a semi-infinite bar is similar to Eq. (7.19), but the complex coefficient $a_1 = 0$, as only forward-travelling axial waves are able to propagate in the positive z-direction. When a time-harmonic axial force $(f_0 \cdot e^{i\omega t})$ is applied at O, only the boundary condition at $z = 0$ needs to be satisfied in Eq. (7.20). By substituting Eq. (7.19) into Eq. (7.20), the motion in the (z, ω)-domain due to the axial force can be derived:

$$w(z, \omega) = \frac{-i\rho_c}{E_c m_c \alpha} f_0 e^{-i\alpha z} \quad \text{for } z \geq 0. \tag{7.29}$$

The complex impedance Z_A due to the axial response at O is defined as [46]

$$Z_A = \frac{f_0}{\dot{w}_0} = c_A m_c \,, \tag{7.30}$$

where $\dot{w}_0 = i\omega w_0$ is the driving-point velocity, and $c_A = \left(\frac{E_c}{\rho_c}\right)^{1/2}$ is the phase speed of axial waves.

The general solution for the undamped flexural motion of a semi-infinite beam is similar to Eq. (7.22), but the complex coefficients must satisfy $b_1 = b_3 = 0$ so that only forward-travelling flexural waves propagate in the positive z-direction. Again, similar to the axial response, only the boundary conditions at $z = 0$ need to be satisfied in Eqs. (7.23) and (7.25) when a time-harmonic shear force $(s_0 \cdot e^{i\omega t})$ and bending moment $(q_0 \cdot e^{i\omega t})$, respectively, is applied at point O. By substituting Eq. (7.22) into Eqs. (7.23) and (7.25), the following equations in the (z, ω)-domain describe the flexural motion of the semi-infinite column due to the shear force:

$$u_s(z, \omega) = \frac{-(i+1)}{2K_c \beta^3} s_0 \left(e^{-\beta z} + e^{-i\beta z}\right) \quad \text{for } z \geq 0\,, \tag{7.31}$$

and the bending moment:

$$u_q(z, \omega) = \frac{(i+1)}{2K_c \beta^2} q_0 \left(i e^{-\beta z} + e^{-i\beta z}\right) \quad \text{for } z \geq 0\,. \tag{7.32}$$

The complex impedances Z_S, Z_Q and Z_C due to the lateral, rocking and coupled lateral-rocking responses, respectively, at O are defined by the following equations [46]:

$$Z_S = \frac{s_0}{\dot{u}_s(0, \omega)} = \frac{s_0}{\dot{u}_{s0}} = \frac{i+1}{2} c_B m_c \,, \tag{7.33}$$

$$Z_Q = \frac{q_0}{\frac{\partial \dot{u}_q}{\partial z}(0, \omega)} = \frac{q_0}{\dot{\theta}_{q0}} = \frac{1-i}{2\omega} c_B \sqrt{K_c m_c} \,, \tag{7.34}$$

$$Z_C = \frac{s_0}{\frac{\partial \dot{u}_s}{\partial z}(0, \omega)} = \frac{s_0}{\dot{\theta}_{s0}} = \frac{q_0}{\dot{u}_q(0, \omega)} = \frac{q_0}{\dot{u}_{q0}} = -\sqrt{K_c m_c} \,, \tag{7.35}$$

where $c_B = \sqrt{\omega} \left(\frac{K_c}{m_c}\right)^{1/4}$ is the phase speed of flexural waves. By adding Eqs. (7.33) and (7.35) through superposition, the net lateral driving-point velocity $\dot{u}_0$ due to both shear and bending
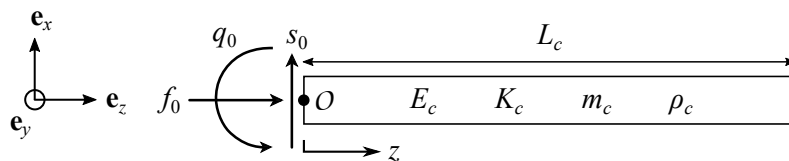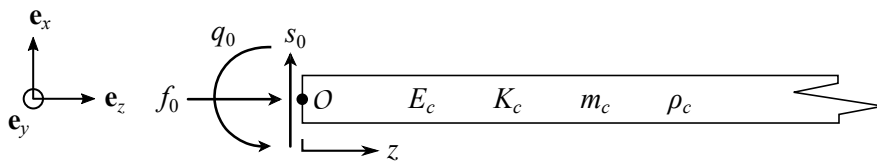

Fig. 7.7 The generalised forces at the coupling point O of a semi-infinite column. Note, only the forces in the xz-plane are represented.

can be expressed as

$$\dot{u}_0 = i\omega u_0 = \dot{u}_{s0} + \dot{u}_{q0} = \frac{s_0}{Z_S} + \frac{q_0}{Z_C}. \tag{7.36}$$

Likewise, the superposition of Eqs. (7.34) and (7.35) expresses the net angular driving-point velocity $\dot{\theta}_0$ as

$$\dot{\theta}_0 = i\omega\theta_0 = \dot{\theta}_{s0} + \dot{\theta}_{q0} = \frac{s_0}{Z_C} + \frac{q_0}{Z_Q}. \tag{7.37}$$

Equations (7.30), (7.36) and (7.37) can be combined into the following displacement-force relationship in the (z, ω)-domain that describes the axial and flexural motion of the equivalent dashpot model:

$$\begin{Bmatrix} u_0 \\ v_0 \\ w_0 \\ \phi_0 \\ \theta_0 \end{Bmatrix} = \frac{1}{i\omega} \begin{bmatrix} 1/Z_S & 0 & 0 & 0 & 1/Z_C \\ 0 & 1/Z_S & 0 & -1/Z_C & 0 \\ 0 & 0 & 1/Z_A & 0 & 0 \\ 0 & -1/Z_C & 0 & 1/Z_Q & 0 \\ 1/Z_C & 0 & 0 & 0 & 1/Z_Q \end{bmatrix} \begin{Bmatrix} s_0 \\ t_0 \\ f_0 \\ p_0 \\ q_0 \end{Bmatrix}, \tag{7.38}$$

or simplified:

$$\mathbf{u}_B = \mathbf{H}_{Bd}\mathbf{f}_B. \tag{7.39}$$

Note, reciprocity is considered between the lateral-rocking components in $\mathbf{H}_{Bd}$. The negative components in Eq. (7.38) are present as a result of the sign convention used for the generalised displacements and forces.

7.2.5 The Added-Building Effect of the Benchmark Building

When the Fb (BEM) model of the foundation system is coupled to the three building models in Sections 7.2.2–7.2.4, the following models for the foundation-building system are produced: Fb-Bp (portal frame), Fb-Bc (columns) and Fb-Bd (dashpots). Even though the latter model is limited because it neglects the through-floor coupling and modal behaviour of the building, it is important to explore whether the simplified Fb-Bd model can account for the fundamental physics that are associated with the added-building effect when a tall building is supported on either piles or embedded footings. The significance of these assumptions on the added-building effect is analysed in this section.

Equation (7.6), which is representative of the added-building effect, can be rewritten in terms of the displacements i and j at coupling points m (base of the building) and n (top of the foundation), respectively:

$$u_{Bi}^{(m)} = \sum_{n=1}^{N} \sum_{j=1}^{5} T_{Bij}^{(m,n)} u_{Fj}^{(n)}. \tag{7.40}$$

Figures 7.8 and 7.9 plot the components in the $\mathbf{T}_{B}^{(1,n)}$ sub-matrices of the benchmark building supported on footings and piles (of equal length $L = 20$ m), respectively. The response of the foundation-building system is predicted using three models: Fb-Bp, Fb-Bc and Fb-Bd. For the Fb-Bp model, the coupling points at $n = 1, 2, 5$ are used to compare between components of the diagonal $\mathbf{T}_{B}^{(1,1)}$ and off-diagonal $\mathbf{T}_{B}^{(1,n)}$ sub-matrices. In contrast, components of the diagonal $\mathbf{T}_{B}^{(1,1)}$ sub-matrix are only shown in Figs. 7.8 and 7.9 for the Fb-Bc and Fb-Bd models; the off-diagonal $\mathbf{T}_{B}^{(1,n)}$ sub-matrices are null, as there is no coupling between the columns or dashpots.

Whether the building is supported on piles or footings, there is good agreement between the three models for the components of $T_{Bxx}^{(1,1)}$, $T_{Bx\theta}^{(1,1)}$, $T_{B\theta x}^{(1,1)}$, $T_{Bzz}^{(1,1)}$ and $T_{B\theta\theta}^{(1,1)}$, which relate to lateral, lateral-rocking, vertical and rocking motion at the foundation-building interface. Over most frequencies between 1 and 80 Hz, the predicted magnitudes of these components, using the Fb-Bp and Fb-Bc models, remain within ± 5 dB of the Fb-Bd model. Therefore, the Fb-Bd model is able to capture these components, as the variation is less than those that generally arise due to system uncertainties and inaccuracies in the model [126]. When $n = 2$ or $n = 5$ for the Fb-Bp model, the off-diagonal counterparts of these diagonal components are, on average, at least 10 dB less than when $n = 1$. In order words, at the base of the portal frame, the interaction between columns, due to through-floor coupling, is less than the interaction at an individual column. For a 2D portal-framed building supported on five surface footings, Sanitate & Talbot [208] made similar observations about the coupling between neighbouring columns, which in their case was at least 20 dB less than the interaction at an individual column.

In Figs. 7.8 and 7.9, the diagonal components of $T_{Bxz}^{(1,1)}$, $T_{Byx}^{(1,1)}$, $T_{By\theta}^{(1,1)}$, $T_{Bzx}^{(1,1)}$, $T_{Bz\theta}^{(1,1)}$, $T_{B\theta y}^{(1,1)}$, $T_{B\theta x}^{(1,1)}$ and $T_{B\theta\phi}^{(1,1)}$ are null when using the Fb-Bc and Fb-Bd models. The same is also true for the remaining twelve components of the diagonal $\mathbf{T}_{B}^{(1,1)}$ sub-matrix, which are not shown in these figures for convenience. This is because the $\mathbf{H}_{B}$ matrix for the column and dashpot models, as expressed in Eqs. (7.27) and (7.38), are not fully populated, unlike Eq. (7.18) for the portal-frame model. These latter diagonal components, obtained using the Fb-Bp model, are often less
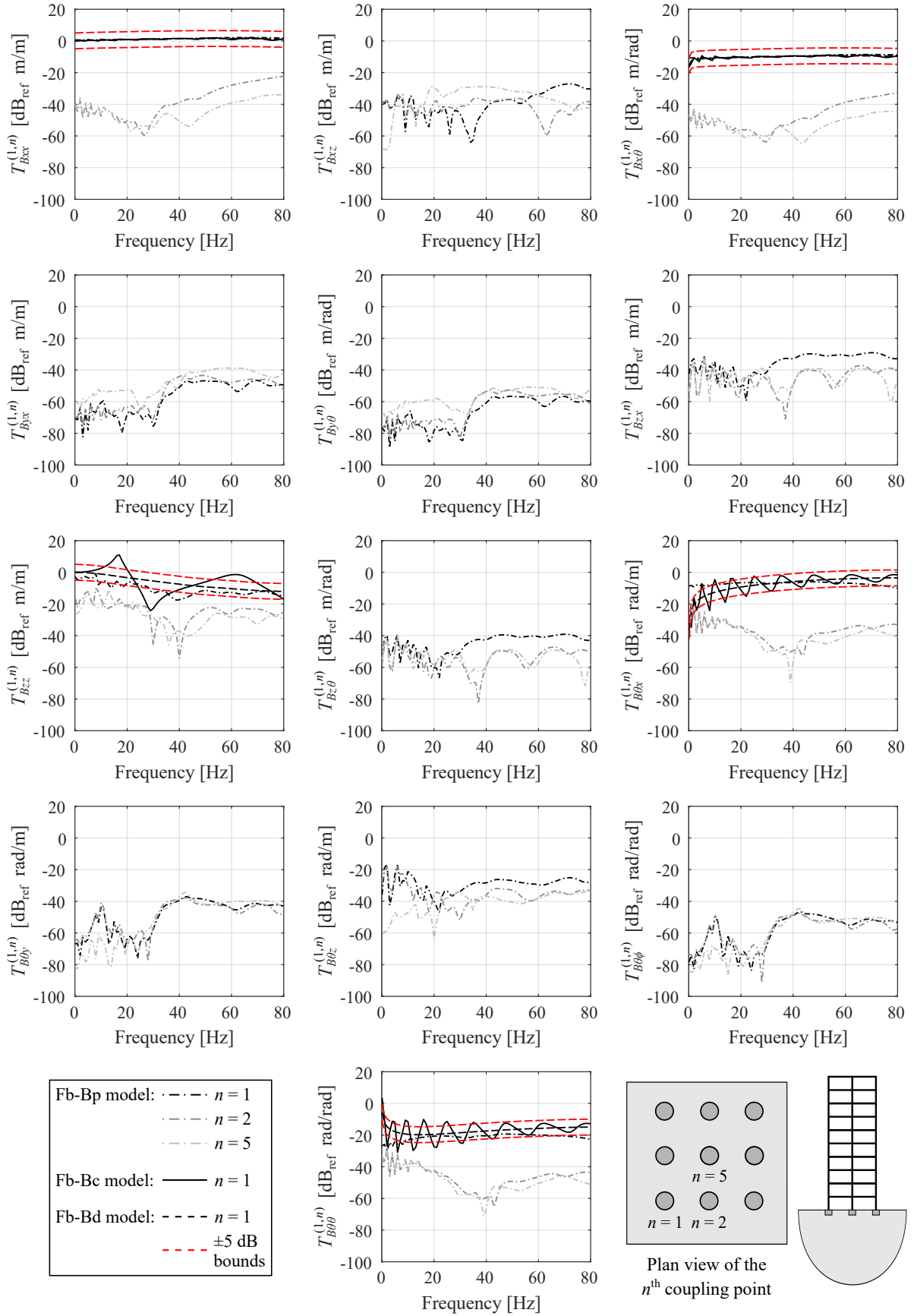
Fig. 7.8 Magnitude of the components in the $\mathbf{T}_B^{(1,n)}$ transfer matrix of the benchmark building supported on embedded footings. The results are predicted using the Fb-Bp, Fb-Bc and Fb-Bd models, and ± 5 dB uncertainty bounds are superimposed for the Fb-Bd model predictions.
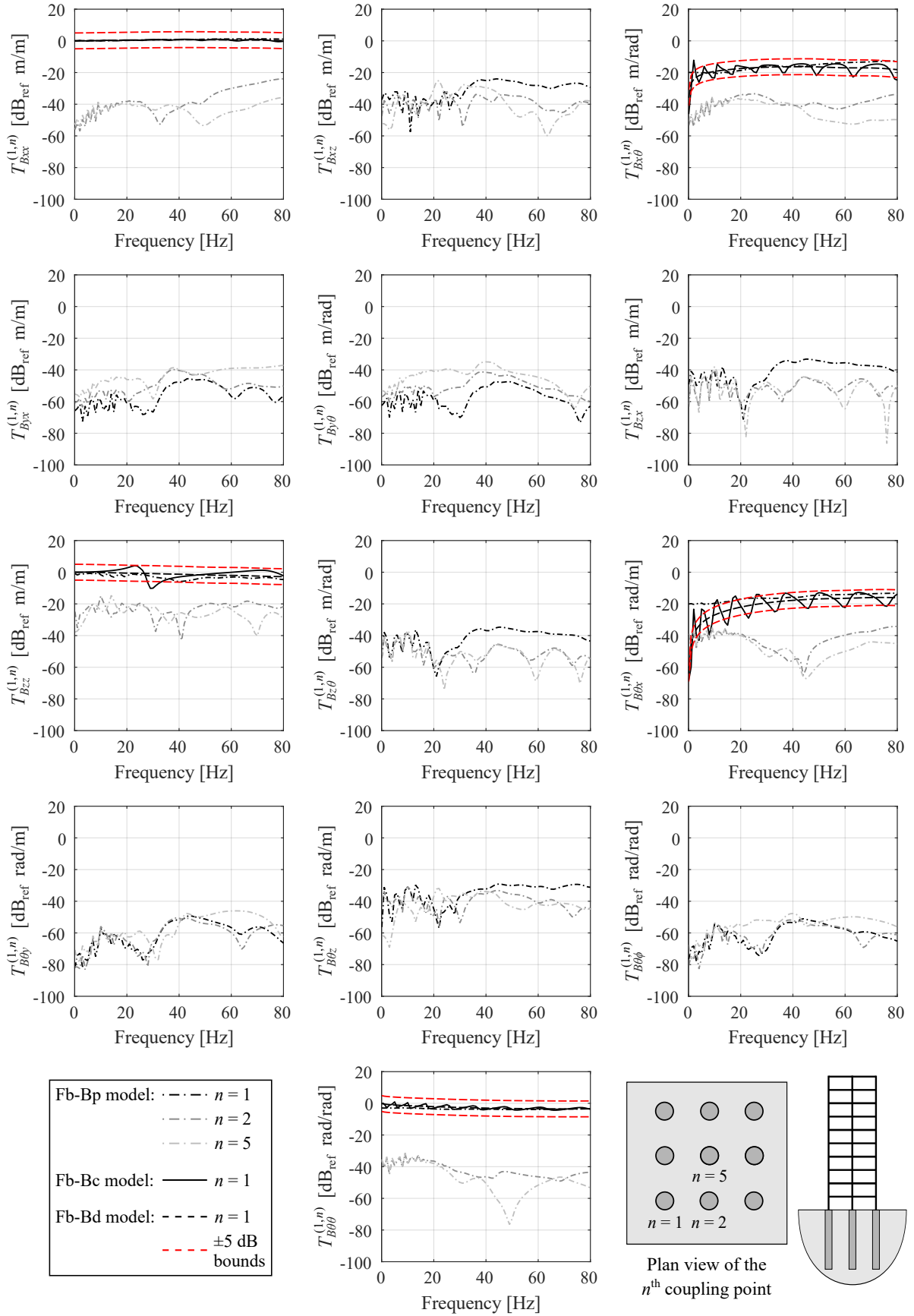
Fig. 7.9 Magnitude of the components in the $\mathbf{T}_B^{(1,n)}$ transfer matrix of the benchmark building supported on piles of length $L = 20$ m. The results are predicted using the Fb-Bp, Fb-Bc and Fb-Bd models, and ± 5 dB uncertainty bounds are superimposed for the Fb-Bd model predictions.

than -20 dB over the frequency range of interest and are of the same order of magnitude as their respective off-diagonal components ($n = 2, 5$). In contrast, the former diagonal components, obtained using all three models, are greater than -20 dB, particularly for the case of $T_{Bxx}^{(1,1)}$, $T_{Bzz}^{(1,1)}$ and $T_{B\theta\theta}^{(1,1)}$. Based on the results, the influence of these latter components on the overall vibration of the benchmark building is likely to be limited, and the use of a simplified dashpot model can be representative of the added-building effect.

Note that, regardless of whether the building is supported on piles or embedded footings, the lateral $T_{Bxx}^{(1,1)}$ component is close to 0 dB over the full frequency range of interest. In other words, constructing a building above a pre-existing foundation does not significantly modify the lateral response at the top of the foundation. Likewise, when the building is supported on piles (Fig. 7.9), the vertical $T_{Bzz}^{(1,1)}$ and rocking $T_{B\theta\theta}^{(1,1)}$ components, evaluated using the Fb-Bd model, do not deviate significantly from 0 dB as the frequency is increased. In contrast, when the building is instead supported on embedded footings (Fig. 7.8), both $T_{Bzz}^{(1,1)}$ and $T_{B\theta\theta}^{(1,1)}$ tend to decrease from 0 dB at 1 Hz to approximately -15 dB at 80 Hz. Sanitate & Talbot [208] also observed a similar steady decrease from 0 dB to around -10 dB in both the vertical and rocking components when the frequency was increased from 1 to 80 Hz. These results suggest that the vertical impedance of the footings and the building differ significantly, which constrains the foundation's vertical motion when the building is constructed. The same can also be said about the difference in rocking impedance. On the other hand, the piles and the building have similar lateral, vertical and rocking impedances, so constructing the building has a negligible effect on constraining the vibration of the piled foundation.

7.2.6 The Mean Power Flow due to Base Excitation

The previous section explored the $\mathbf{T_B}$ transfer matrix in detail to better understand the dynamic behaviour of a foundation-building system. However, engineers are interested in predicting the overall building vibration, which is transmitted into the building due to base excitation, because it can help guide design-based decisions on vibration mitigation methods. Thus, in this section, the three foundation-building models are used to analyse the mean vibrational power entering the benchmark building due to excitation at the base of a single column.

Figure 7.10 plots the mean power flows when a unit-magnitude shear force, an axial force, and a bending moment is independently applied at coupling points $n = 1, 2, 5$. The building is supported above two different foundation configurations: embedded footings (Fig. 7.10a) and

20 m piles (Fig. 7.10b). Bounds of ± 5 dB, which correspond to the typical uncertainty levels associated with numerical models of ground-borne vibration problems [126], are superimposed on Fig. 7.10 for the Fb-Bd model predictions.

The resonant peaks in the mean power flows show that the Fb-Bp and Fb-Bc models capture the building's modal behaviour. In contrast, these peaks are absent when using the Fb-Bd model because the waves in the building are damped out. Furthermore, as both the Fb-Bc and Fb-Bd models neglect through-floor coupling between the columns, the power flow is independent of which coupling point is excited. Only the Fb-Bp model produces varying power flows when the
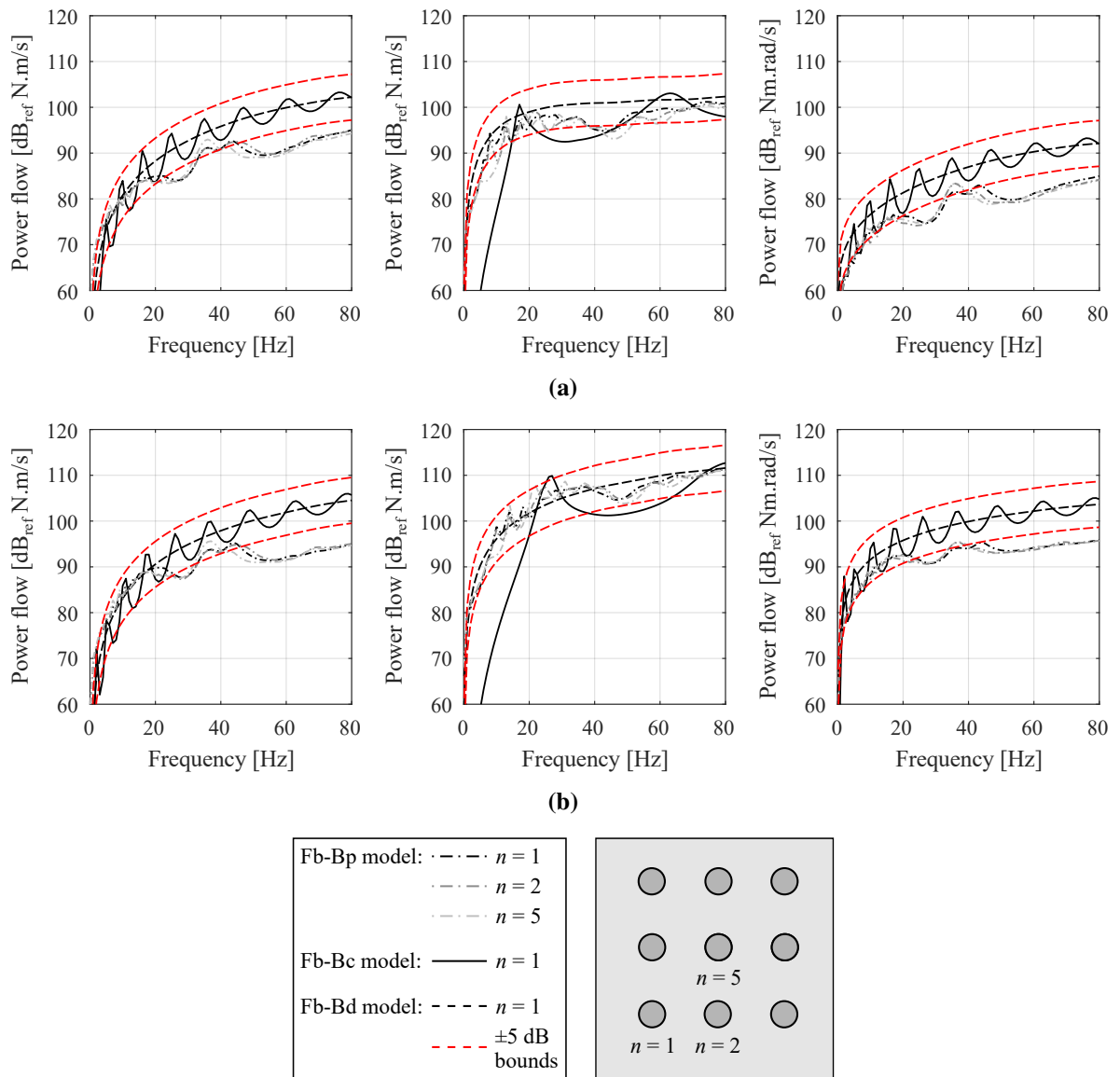
Fig. 7.10 Magnitude of the mean power flows entering the benchmark building supported on **(a)** embedded footings and **(b)** piles of length $L = 20$ m when a unit-magnitude, time-harmonic shear force (left), axial force (centre), and bending moment (right) is applied at coupling point n on the foundation-building interface. The results are predicted using the Fb-Bp, Fb-Bc and Fb-Bd models, and ± 5 dB uncertainty bounds are superimposed for the Fb-Bd model predictions.

generalised forces are applied at different coupling points. Even so, the average difference, over the full frequency range, between the power flows at the three coupling points ($n = 1, 2, 5$) is within ± 2 dB, which shows that the influence of through-floor coupling on the mean vibrational power is rather small compared to uncertainties in the Fb-Bp model.

It is worth noting that the footing configuration generally causes less power to flow into the building than the pile configuration; in particular, applying either an axial force or bending moment causes the mean power flow to decrease by about 10 dB at frequencies over 40 Hz. This decrease in power flow, when the building is supported on footings, correlates with the decrease in the transfer matrix components that relate to vertical and rocking motion in Section 7.2.5.

In conclusion, the results presented in this section and Section 7.2.5 suggest that the dashpot (Bd) model, where a tall building is assumed to behave as a collection of semi-infinite columns, is effective at capturing the frequency-averaged variation in both the added-building effect and the mean vibrational power entering the building. Moreover, the modal behaviour of the column (Bc) and portal-frame (Bp) models, as well as the through-floor coupling captured in the latter model, does not significantly influence the overall building vibration. However, the difference in impedance between the foundation and building may contribute to the added-building effect, particularly when using footings.

7.3 Vibration in the Presence of an Underground Railway

By using the generalised equations in Section 7.1 and the portal-frame (Bp), column (Bc) and dashpot (Bd) models presented in Section 7.2, this section analyses the vibration performance of a building when it is next to an underground railway tunnel. Firstly, the analysis focuses on the significance of the added-foundation and added-building effects on the fundamental unit of a foundation-building system. Later, for the purpose of analysing any differences in the train-induced vibration of a realistic building supported on piles and footings, the mean power flow entering the benchmark building in each foundation configuration is predicted.

7.3.1 A Note on the Equivalence of the Vertical and Power-Flow Insertion Gains of a Centred Fundamental Unit

Suppose that a fundamental unit is positioned directly above the centre-line of an underground railway tunnel. In this particular arrangement, the fundamental unit only experiences vibration

in the vertical direction due to symmetry, so the entire structure can be represented as a single-input, single-output system. For the special case of a single-input, single-output system, it has been proven that the insertion gain (IG) and the power-flow insertion gain (PFIG) are directly equivalent when they are used to characterise the system's isolation performance [206, 221]. This section shows that a similar equivalence relationship can be derived for the vertical IG and the PFIG that measure the change in the displacement and the vibrational power, respectively, between the pile and footing configurations.

By substituting Eq. (7.7) into Eq. (7.8), the vertical IG between the displacements of the pile and footing configurations can be computed for a centred fundamental unit:

$$
\begin{aligned}
\mathrm{IG}_z^{(\mathrm{pf})} &= 20\log_{10}\left(\frac{\left|H_{NBzz}K_{Bzz}T_{Bzz}^{(\mathrm{pile})}w_F^{(\mathrm{pile})}\right|}{\left|H_{NBzz}K_{Bzz}T_{Bzz}^{(\mathrm{foot})}w_F^{(\mathrm{foot})}\right|}\right) \\
&= 20\log_{10}\left(\frac{\left|T_{Bzz}^{(\mathrm{pile})}w_F^{(\mathrm{pile})}\right|}{\left|T_{Bzz}^{(\mathrm{foot})}w_F^{(\mathrm{foot})}\right|}\right),
\end{aligned}
\tag{7.41}
$$

where $w_F^{(\mathrm{pile})}$ and $w_F^{(\mathrm{foot})}$ are the displacements at the top of the pile and footing, respectively, before the building column is constructed. Equation (7.41) highlights that $\mathrm{IG}_z^{(\mathrm{pf})}$ is independent of position.

Similarly, the PFIG between the mean vibrational power that gets transmitted into the pile and footing configurations can be computed by substituting Eq. (7.10) into Eq. (7.11) and then simplifying the resulting equation:

$$
\begin{aligned}
\mathrm{PFIG}^{(\mathrm{pf})} &= 10\log_{10}\left(\frac{\frac{1}{2}\left|\mathrm{Re}\left(i\omega\left[w_F^{(\mathrm{pile})}\right]^*\left[T_{Bzz}^{(\mathrm{pile})}\right]^*K_{Bzz}^*T_{Bzz}^{(\mathrm{pile})}w_F^{(\mathrm{pile})}\right)\right|}{\frac{1}{2}\left|\mathrm{Re}\left(i\omega\left[w_F^{(\mathrm{foot})}\right]^*\left[T_{Bzz}^{(\mathrm{foot})}\right]^*K_{Bzz}^*T_{Bzz}^{(\mathrm{foot})}w_F^{(\mathrm{foot})}\right)\right|}\right) \\
&= 10\log_{10}\left(\frac{\left|\mathrm{Re}\left(i\omega\left|T_{Bzz}^{(\mathrm{pile})}w_F^{(\mathrm{pile})}\right|^2 K_{Bzz}^*\right)\right|}{\left|\mathrm{Re}\left(i\omega\left|T_{Bzz}^{(\mathrm{foot})}w_F^{(\mathrm{foot})}\right|^2 K_{Bzz}^*\right)\right|}\right) \\
&= 10\log_{10}\left(\frac{\mathrm{Im}\left(\omega K_{Bzz}^*\right)\left|T_{Bzz}^{(\mathrm{pile})}w_F^{(\mathrm{pile})}\right|^2}{\mathrm{Im}\left(\omega K_{Bzz}^*\right)\left|T_{Bzz}^{(\mathrm{foot})}w_F^{(\mathrm{foot})}\right|^2}\right) \\
&= 20\log_{10}\left(\frac{\left|T_{Bzz}^{(\mathrm{pile})}w_F^{(\mathrm{pile})}\right|}{\left|T_{Bzz}^{(\mathrm{foot})}w_F^{(\mathrm{foot})}\right|}\right).
\end{aligned}
\tag{7.42}
$$
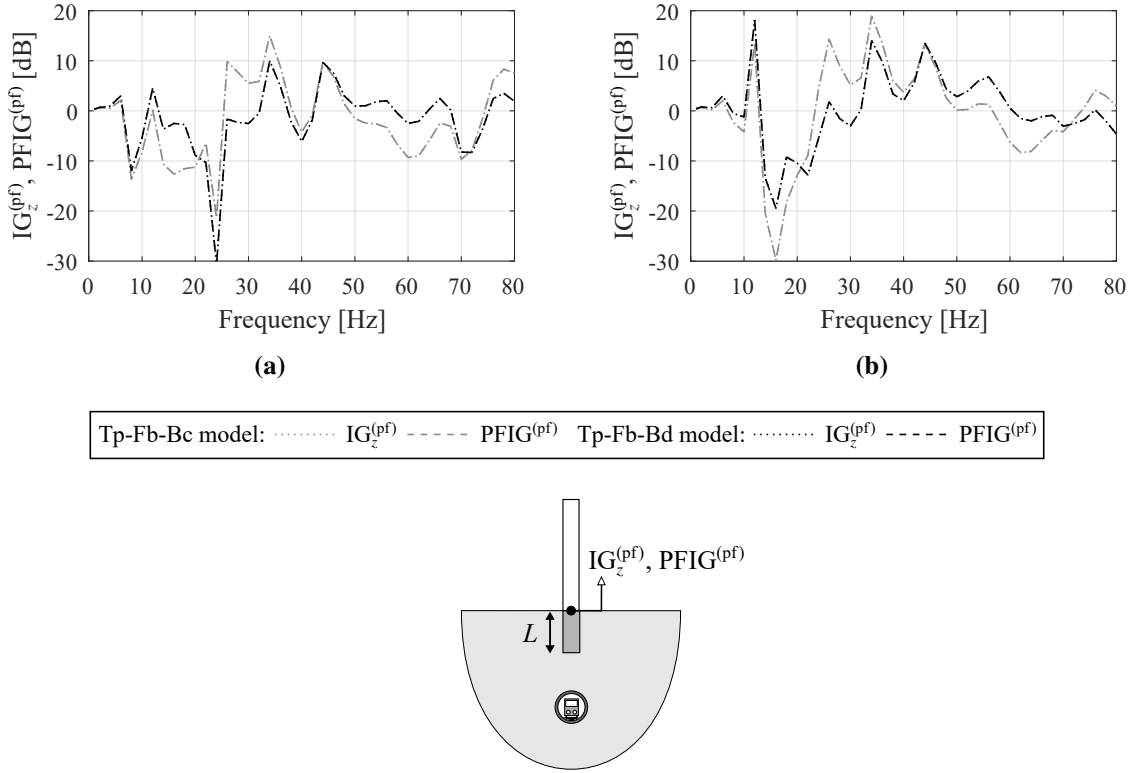
Fig. 7.11 The vertical and power-flow insertion gains of a centred foundation-building fundamental unit above an underground railway tunnel, predicted using the Tp-Fb-Bc and Tp-Fb-Bd models. The insertion gains compare the vibration responses of the pile and footing configurations when the pile length L is **(a)** 10 m and **(b)** 20 m. Tunnel-foundation separation distance $S = 0$ m and tunnel depth $D = 25$ m.

Note, Eqs. (7.41) and (7.42) show that $\text{IG}_z^{(\text{pf})}$ and $\text{PFIG}^{(\text{pf})}$ are equivalent when evaluating the vibration performance of a centred fundamental unit above an underground railway tunnel. Although this equivalence relationship is only true when there is a single coupling point at the foundation-building interface, it suggests that PFIG is a feasible scalar metric for characterising the overall vibration performance of a general building with multiple columns.

In order to validate the equivalence in $\text{IG}_z^{(\text{pf})}$ and $\text{PFIG}^{(\text{pf})}$, Fig. 7.11 presents the respective insertion gains of a centred fundamental unit above a 25 m depth tunnel. The insertion gains, predicted using the Tp-Fb-Bc and Tp-Fb-Bd models, compare the responses of the pile and footing configurations when the pile length is 10 and 20 m. In both cases, the parameter values in Section 7.2.1, for the soil, tunnel, foundation and building, are used to model the system.

As expected, $\text{IG}_z^{(\text{pf})}$ and $\text{PFIG}^{(\text{pf})}$ are equal over the entire frequency range of interest for both pile lengths. Furthermore, although the Bc and Bd models for the building column predict slightly different insertion gains, the undulations in the responses are consistent with each other.

7.3.2 The Added-Column Effect of a Fundamental Unit

When a building is constructed above a pre-existing foundation, being able to predict the added-building effect as a result of its own mass, stiffness and damping is considered to be particularly important in deciding whether or not some form of vibration isolation is necessary [222]. The combination of both the added-foundation effect and the added-building effect accounts for the overall modification in the ground vibration field when an entire foundation-building system is constructed, which, in this section, is referred to as the 'added-foundation-building effect'.

The work presented here examines the insertion gains that capture these three effects due to the construction of an off-centred fundamental unit near a railway tunnel. Differences in the responses when the column is supported on either a footing or pile are also investigated. Since the fundamental unit is off-centred from the tunnel centre-line, the footing-column and pile-column systems will experience motion in both the transverse and vertical directions. Thus, the analysis is an extension to the parametric study presented in Section 6.6, which only focused on the vertical added-pile effect of a pile near an underground railway tunnel.

For the particular case of a pile-column system, the added-foundation effect is referred to as the added-pile effect, which was previously considered in Sections 6.4 and 6.6. The vertical IG characterising the added-pile effect in the vertical direction is defined as

$$\text{IG}_z^{(\text{ap})} = 20\log_{10}\left(\frac{|w_F^{(\text{pile})}|}{|w_S|}\right), \tag{7.43}$$

where w_S is the vertical displacement at the free surface before a pile is embedded in the ground. In order to measure the added-building effect when a column is constructed above the pile, the following additional IG definitions are introduced:

$$\text{IG}_z^{(\text{ac})} = 20\log_{10}\left(\frac{|w_B^{(\text{pile})}|}{|w_F^{(\text{pile})}|}\right), \tag{7.44}$$

where the superscript '(ac)' refers to the added-column effect when the column is constructed, and $w_B^{(\text{pile})}$ is the vertical displacement at the column-pile interface; and

$$\text{IG}_z^{(\text{apc})} = \text{IG}_z^{(\text{ap})} + \text{IG}_z^{(\text{ac})} = 20\log_{10}\left(\frac{|w_B^{(\text{pile})}|}{|w_S|}\right), \tag{7.45}$$

where the superscript '(apc)' refers to the added-pile-column effect of the overall pile-column

system. The comparable terms of the added-foundation and added-foundation-building effects for a footing-column system are referred to as the added-footing (af) and added-footing-column (afc) effects, respectively.

Figures 7.12 and 7.13 plot the transverse (IG_y) and vertical (IG_z) insertion gains of an off-centred footing-column and pile-column system, respectively. Figure 7.13 also shows the influence of increasing the pile length L from 10 to 30 m on the insertion gains. For both the footing-column and pile-column systems, the tunnel depth D is 25 m and the tunnel-foundation separation distance S is 5 m. Note, when the column is present, the Tp-Fb-Bc and Tp-Fb-Bd models are used to predict the response of the fundamental unit. In the absence of the column, the added-pile and added-footing effects are predicted using the Tp-Fb model.

First, consider the transverse IG, with respect to frequency, of the fundamental unit. The $IG_y^{(ac)}$ for the footing-column system remains close to 0 dB as the frequency is increased up to 50 Hz, and then decreases to a minimum of -3 dB at 80 Hz. Even more so, the $IG_y^{(ac)}$ for the pile-column system remains close to 0 dB over the entire frequency range. These observations highlight that, for both the footing and pile configurations, the added-column effect is negligible
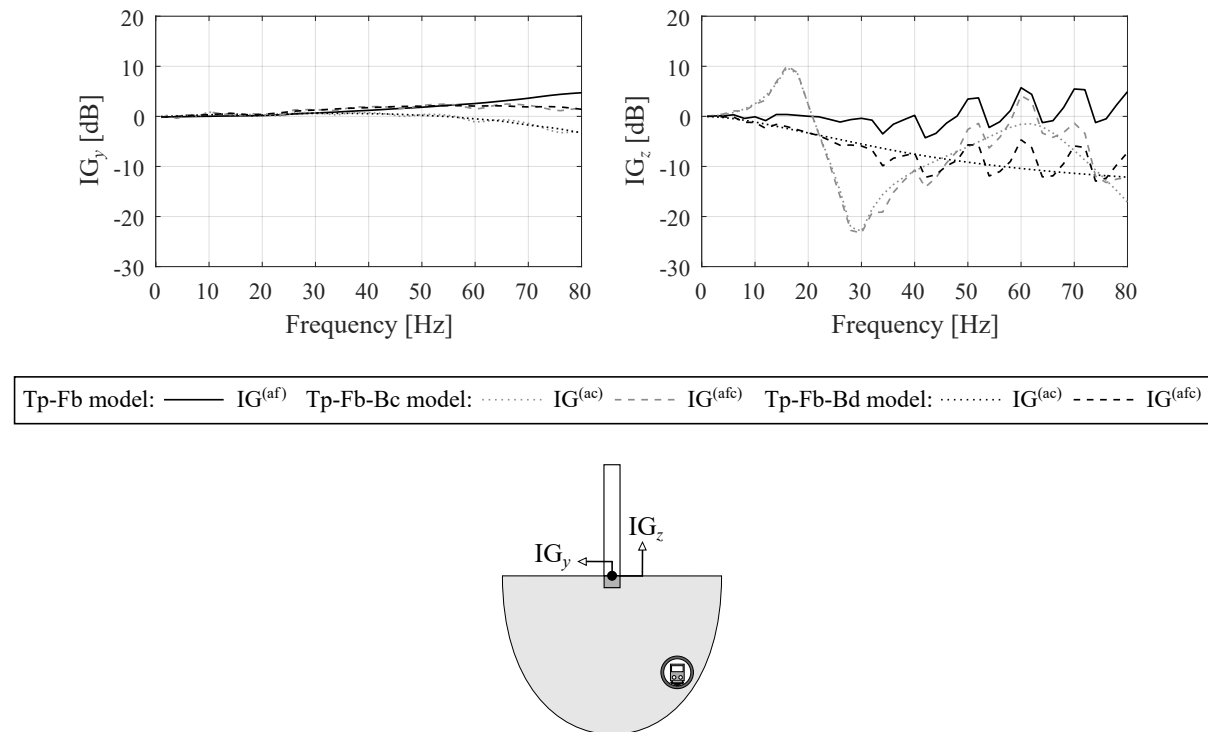
Fig. 7.12 The transverse (left) and vertical (right) insertion gains of an off-centred footing-column system near an underground railway tunnel, predicted using the Tp-Fb-Bc and Tp-Fb-Bd models. The footing response without a column is predicted using the Tp-Fb model. In each sub-figure, the insertion gains corresponding to the added-footing (af), added-column (ac) and added-footing-column (afc) effects are shown. Tunnel-foundation separation distance $S = 5$ m and tunnel depth $D = 25$ m.
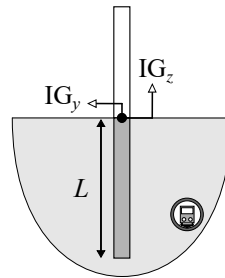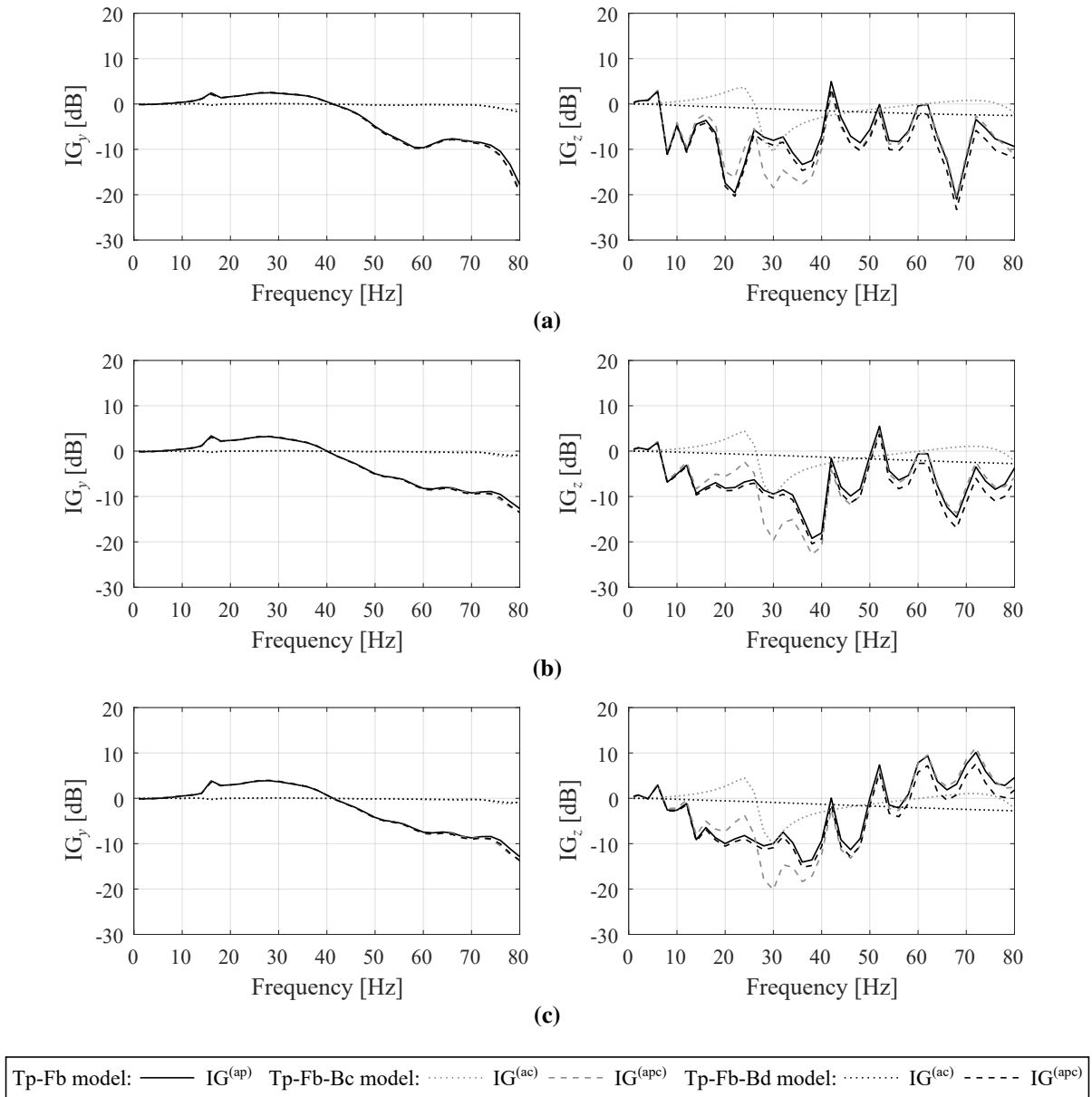
Fig. 7.13 The transverse (left) and vertical (right) insertion gains of an off-centred pile-column system near an underground railway tunnel, predicted using the Tp-Fb-Bc and Tp-Fb-Bd models. The pile-head response without a column is predicted using the Tp-Fb model. In each sub-figure, the insertion gains corresponding to the added-pile (ap), added-column (ac) and added-pile-column (apc) effects are shown. The influence of the pile length L on the response is also illustrated: **(a)** 10 m, **(b)** 20 m and **(c)** 30 m. Tunnel-foundation separation distance $S = 5$ m and tunnel depth $D = 25$ m.

in the transverse direction because the long, slender column is flexible under bending. Hence, constructing a column does not significantly modify the transverse displacement at the top of the foundation.

There is also excellent agreement between the transverse responses predicted using the Bc and Bd models over the whole frequency range of interest. This demonstrates that the lateral and coupled lateral-rocking motion at the foundation-building interface is captured well by an equivalent dashpot model.

Now, consider the vertical IG of the footing-column and pile-column systems. In general, as the excitation frequency is increased, both fundamental units exhibit attenuation in the vertical added-column effect, which is similar to the vertical component of the foundation-building transfer matrix (see Section 7.2.5). However, the attenuation is more significant in the footing-column system, as the $\text{IG}_z^{(\text{ac})}$ is roughly -10 dB at 80 Hz. Furthermore, the Tp-Fb-Bc model prediction for the footing-column system exhibits large-magnitude undulations in the $\text{IG}_z^{(\text{ac})}$ that vary between 10 dB and -20 dB. In contrast, the $\text{IG}_z^{(\text{ac})}$ of the pile-column system remains close to 0 dB over most frequencies, particularly when predictions are made using the Tp-Fb-Bd model. Therefore, the vertical added-column effect is negligible for the pile-column system, meaning that the overall $\text{IG}_z^{(\text{apc})}$ of the whole fundamental unit is approximately equal to the $\text{IG}_z^{(\text{ap})}$ of the pile alone.

Sanitate & Talbot [208] observed that, for a 2D portal-framed building supported on surface footings, the added-building effect in the vertical direction decreased steadily from 0 dB to roughly -10 dB, as the frequency was increased from 1 to 80 Hz. At higher frequencies, up to 250 Hz, the added-building effect remained constant at -10 dB. This decrease in the response is similar, in order of magnitude, to the attenuation in $\text{IG}_z^{(\text{ac})}$ for the footing-column system in the present study. Since both studies consider shallow footings that are coupled to long columns, the large difference in axial impedance between the two components causes the addition of the building to greatly constrain the vertical vibration of the foundation. In the present study, when piles are used instead of footings, the difference in axial impedance between the foundation and building is not as great, resulting in significantly less attenuation.

A few observations can be made about the undulations between 10 and 40 Hz when the Tp-Fb-Bc model is used to predict the $\text{IG}_z^{(\text{ac})}$ in Figs. 7.12 and 7.13. These undulations contain distinct peaks and troughs because the column (Bc) model accounts for modal behaviour in the finite-length column (see Section 7.2.3). The trough at around 30 Hz is present in the responses

of the footing-column and pile-column systems, with the former system causing twice as much attenuation as the latter due to the greater difference in axial impedance between the footing and column. The attenuation at 30 Hz is found to be caused by the first anti-resonance of the free-free column under axial vibration. The first anti-resonant frequency, when the base of the column is excited, can be approximated by assuming that the base is fixed, and then calculating the natural frequency of the column's fixed-free axial mode:

$$f_0 = \frac{1}{4L_c}\left(\frac{E_c}{\rho_c}\right)^{1/2} = 29\,\mathrm{Hz}\,. \tag{7.46}$$

In contrast to the trough at 30 Hz, the frequency of the peak increases from 16 to 24 Hz when the foundation is changed from a shallow (0.5 m) footing to a deep (30 m) pile. In order to explain this phenomenon, assume that the first axial vibration mode of the entire fundamental unit can be modelled as an SDOF system, where the inertial mass of the column is coupled to a spring corresponding to the dynamic stiffness of the soil-foundation system. The parametric study in Section 6.6 found that the soil-stiffening effect dominates as the pile length is increased, which increases the stiffness of the soil-foundation system. Therefore, using a deep pile instead of a footing will increase the spring stiffness, and indeed the natural frequency, of the SDOF system, thereby increasing the frequency of the peak.

It is also worth noting that when the pile length is increased from 20 to 30 m in Fig. 7.13, the overall $\mathrm{IG}_z^{(\mathrm{apc})}$ tends to increase above 0 dB at frequencies greater than 50 Hz. This occurs because of the efficient vibration transmission path along the pile when the pile toe descends below the tunnel. The amplification of the response due to the enhanced transmission effect was discussed previously in Section 6.6.3 when the vertical added-pile effect of off-centred piles was investigated.

In summary, if the observations from the fundamental unit can be extrapolated to apply for a multi-storey building with multiple columns, the added-foundation effect will likely be more significant than the added-building effect over the range of frequencies associated with ground-borne vibration. That is to say, the dynamics associated with the building will be dominated by that of the piled foundation. Furthermore, the addition of a column itself does not significantly alter the general trends observed in Section 6.6 for a single pile, so the added-column effect is negligible. Nevertheless, it is important to note that the added-building effect of a more realistic building could be significant if it is supported on footings or when the excitation frequency is close to the resonant frequencies of the building itself.

7.3.3 The Effect of the Foundation-Building System on the Greenfield

Rather than analysing the train-induced vibration of a single fundamental unit, the following sections focus on the response of the benchmark building because it is more representative of the fundamental dynamic motion of modern buildings. This section explores how constructing the entire foundation-building system directly above a pre-existing underground railway tunnel modifies the greenfield displacement near the foundation. To simply the analysis of the results, only the vertical displacement of the soil will be considered.

The modification in the vertical greenfield displacement can be evaluated using the vertical insertion gain in the soil, which is defined as

$$\text{IG}_z^{(\text{soil})} = 20 \log_{10} \left(\frac{\left| w_S^{(\text{found})} \right|}{\left| w_S \right|} \right), \tag{7.47}$$
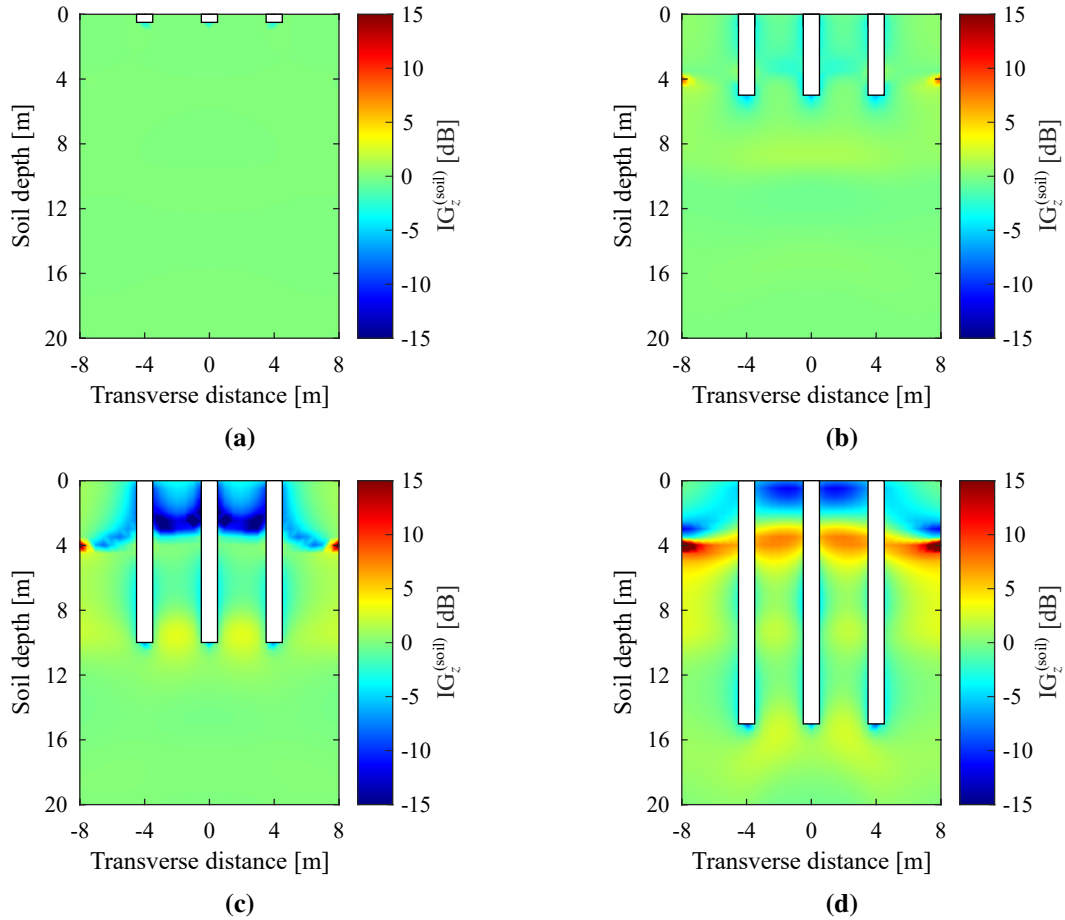
Fig. 7.14 The vertical insertion gain of the soil near the building's foundation at an excitation frequency of 20 Hz. The insertion gain characterises the modification of the greenfield displacement before and after a centred benchmark building is constructed above an underground railway tunnel. The influence of using **(a)** footings and piles of length **(b)** 5 m, **(c)** 10 m and **(d)** 15 m on the soil response, predicted using the Tp-Fb-Bp model, is also illustrated. Tunnel depth $D = 25$ m.

where w_S and $w_S^{(\text{found})}$ are the vertical displacements of the soil before and after the foundation-building system is constructed, respectively. For a fixed tunnel depth of 25 m, Figs. 7.14–7.17 plot the spatial variation of $\text{IG}_z^{(\text{soil})}$ in the plane perpendicular to the tunnel's longitudinal axis as the excitation frequency is incrementally increased from 20 to 80 Hz. The sub-figures also show the changes in the soil displacements when footings and piles, of varying length, are used.

At the four different excitation frequencies, Figs. 7.14–7.17 clearly show that embedding shallow footings near a pre-existing underground railway tunnel does not modify the greenfield displacements significantly, as the vertical insertion gain of the local soil around the footings is close to 0 dB. This is expected because the length of each footing is much shorter than the wavelengths in the soil, even when the excitation frequency is 80 Hz. Therefore, there will be insignificant wave scattering at the footings, and the resulting scattered waves have a negligible effect on the incident waves from the excited railway tunnel.
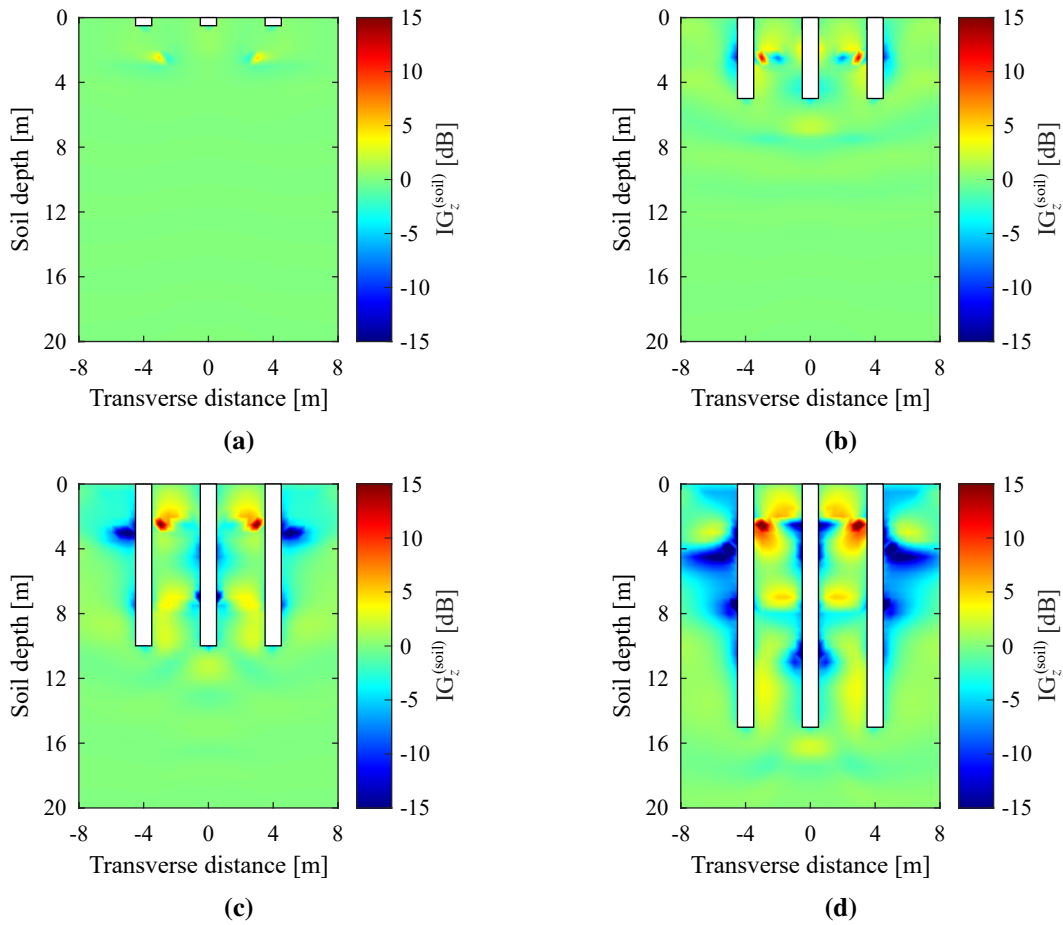
Fig. 7.15 The vertical insertion gain of the soil near the building's foundation at an excitation frequency of 40 Hz. The insertion gain characterises the modification of the greenfield displacement before and after a centred benchmark building is constructed above an underground railway tunnel. The influence of using **(a)** footings and piles of length **(b)** 5 m, **(c)** 10 m and **(d)** 15 m on the soil response, predicted using the Tp-Fb-Bp model, is also illustrated. Tunnel depth $D = 25$ m.

Now, consider the case when the building is supported on piles. At an excitation frequency of 20 Hz, the short (5 m) piles have a negligible effect on the vertical greenfield displacement, whereas the longer (10 and 15 m) piles cause significant attenuation near the free surface, as shown in Fig. 7.14. This is because the scattered waves at the soil-pile interface have a greater effect on modifying the greenfield displacement when the S-wavelength in the soil is less than the lengths of the longer piles. Furthermore, when the longest (15 m) piles are embedded in the soil, the vertical insertion gain exhibits an additional amplification band at a soil depth of 4 m. Therefore, at low excitation frequencies, a large proportion of the scattered waves at the piles tend to propagate downwards rather than interacting with adjacent piles, as the soil wavelengths are longer than the pile spacing. The superposition of the downward-travelling scattered waves with the upward-travelling incident waves from the tunnel produces the stratified amplification and attenuation bands observed in Fig. 7.14d.
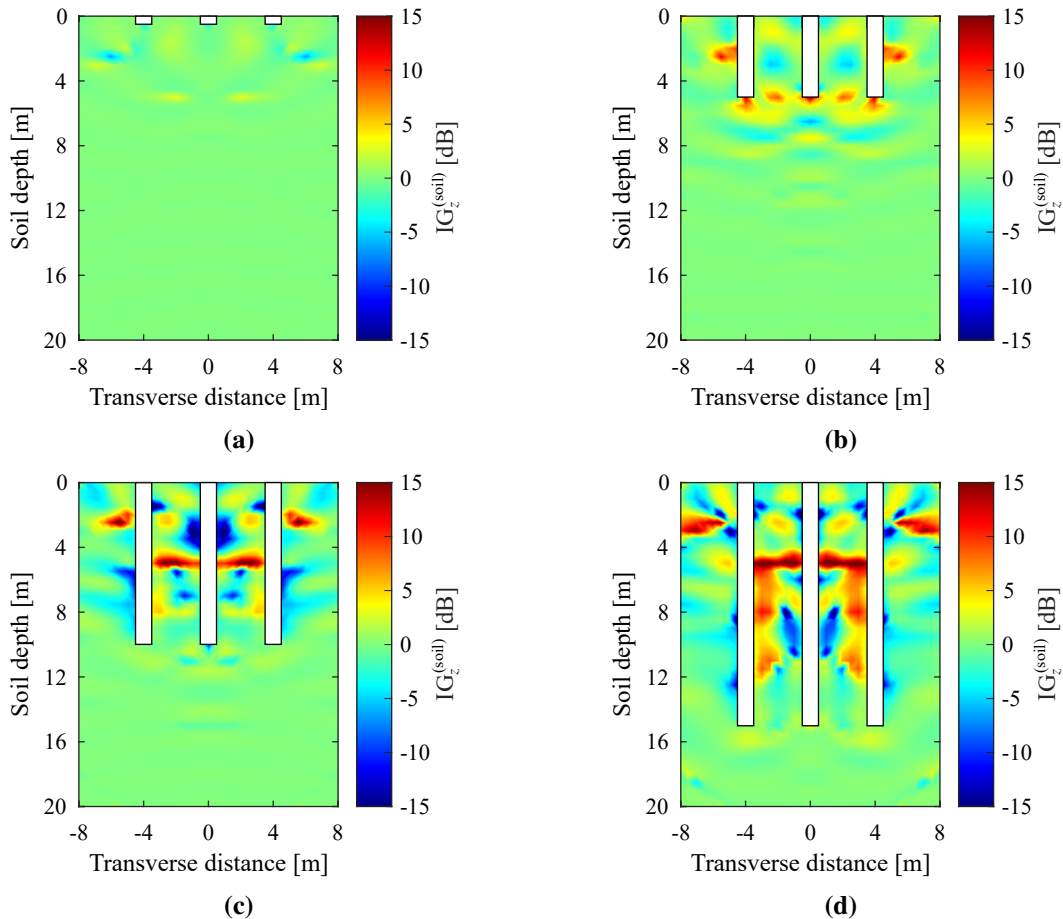
Fig. 7.16 The vertical insertion gain of the soil near the building's foundation at an excitation frequency of 60 Hz. The insertion gain characterises the modification of the greenfield displacement before and after a centred benchmark building is constructed above an underground railway tunnel. The influence of using (**a**) footings and piles of length (**b**) 5 m, (**c**) 10 m and (**d**) 15 m on the soil response, predicted using the Tp-Fb-Bp model, is also illustrated. Tunnel depth $D = 25$ m.

At the high excitation frequencies above 40 Hz, the PSPI becomes more significant because the S-wavelengths in the soil are now less than the pile spacing. Therefore, there is more wave scattering between adjacent piles, which causes the amplification and attenuation zones of the insertion gains to be interspersed near the piles, as illustrated in Figs. 7.15–7.17. Note that these insertion gain plots are highly intricate due to the short wavelengths of the interfering waves.

In conclusion, this section highlights the complexity of the 3SI in ground-borne vibration problems, which makes it difficult to discern the nature of the interfering waves, particularly when the deep piles of a foundation-building system modify the greenfield at the high excitation frequencies. However, measuring the insertion gain of the soil does not help in understanding the factors that influence the vibration entering the building. These factors are highly important for vibration consultants to recognise. Therefore, the mean power flow is used in the following two sections to study how different factors affect the vibrational energy entering the building.

(a)

(b)

(c)

(d)
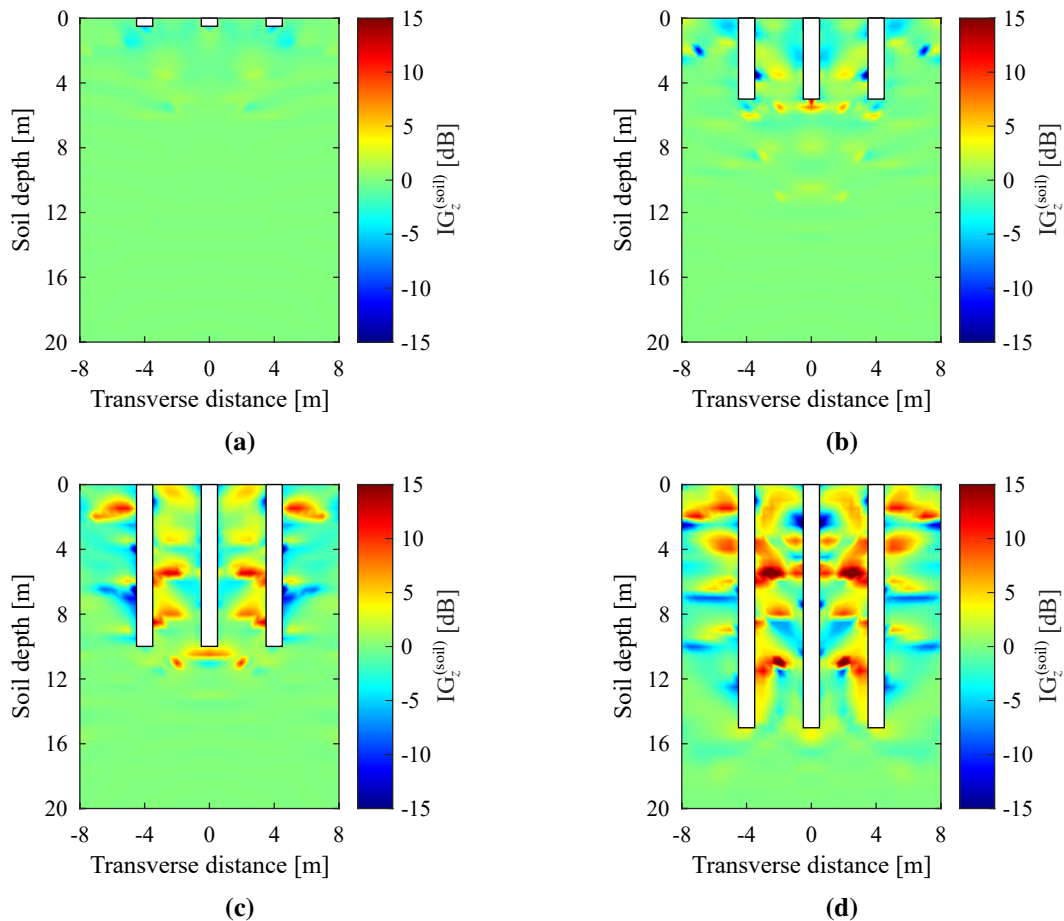
Fig. 7.17 The vertical insertion gain of the soil near the building's foundation at an excitation frequency of 80 Hz. The insertion gain characterises the modification of the greenfield displacement before and after a centred benchmark building is constructed above an underground railway tunnel. The influence of using (a) footings and piles of length (b) 5 m, (c) 10 m and (d) 15 m on the soil response, predicted using the Tp-Fb-Bp model, is also illustrated. Tunnel depth $D = 25$ m.

7.3.4 The Effect of Piles and Footings on the Directional Power Flow

In this section, the vibration performance of different tunnel-foundation-building systems is investigated by varying features of the foundation and analysing the directional components of the mean power flow entering each configuration. The effects due to the following three features are explored: (1) the presence of footings, (2) the pile length *L*, and (3) the tunnel-foundation separation distance *S*. For all configurations, the foundation supports the benchmark building.
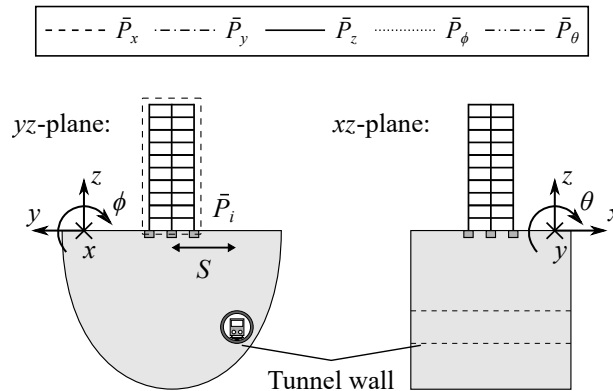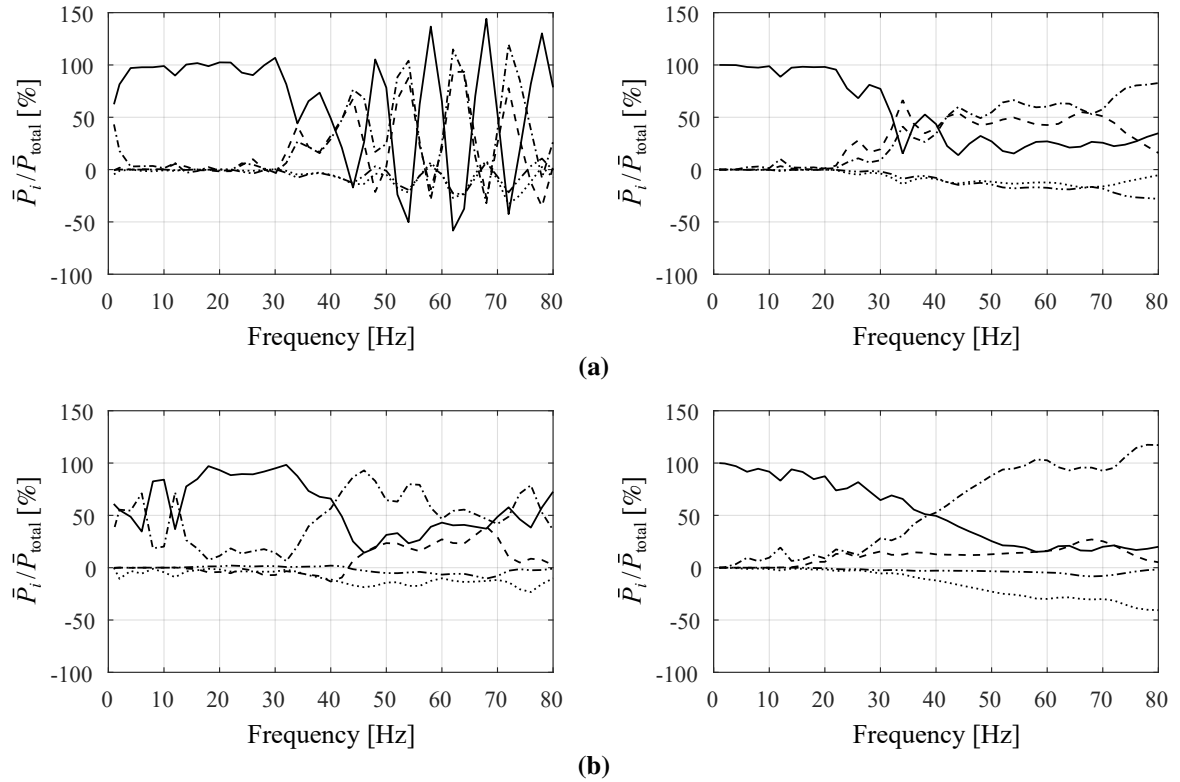
Fig. 7.18 The directional components of the mean power flows entering **(a)** a centred ($S = 0$ m) and **(b)** an off-centred ($S = 15$ m) footing-building system near their respective underground railway tunnels, presented as percentages of the total mean power flow. The responses are predicted using the Tp-Fb-Bp (left) and Tp-Fb-Bd (right) models. Note that a negative value signifies vibrational power leaving the building. Tunnel depth $D = 25$ m.

The effect of using footings on the vibrational power transmitted into the building is studied first. Figure 7.18 plots the directional components of the mean power flow entering a centred ($S = 0$ m) and an off-centred ($S = 15$ m) footing-building system. The responses are predicted using the Tp-Fb-Bp and Tp-Fb-Bd models. The total mean power flow $\bar{P}_{\text{total}}$ can be decomposed into five directional components $(\bar{P}_x, \bar{P}_y, \bar{P}_z, \bar{P}_\phi, \bar{P}_\theta)$, which correspond to the five DOFs at the foundation-building interface, as denoted in Section 7.1.2. Each mean power flow component

(a) $L = 5$ m ($L/D = 0.2$)

(b) $L = 10$ m ($L/D = 0.4$)

(c) $L = 15$ m ($L/D = 0.6$)

(d) $L = 20$ m ($L/D = 0.8$)
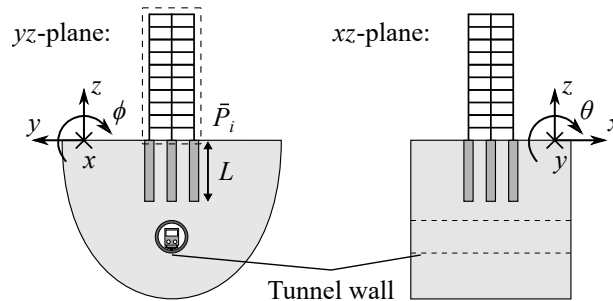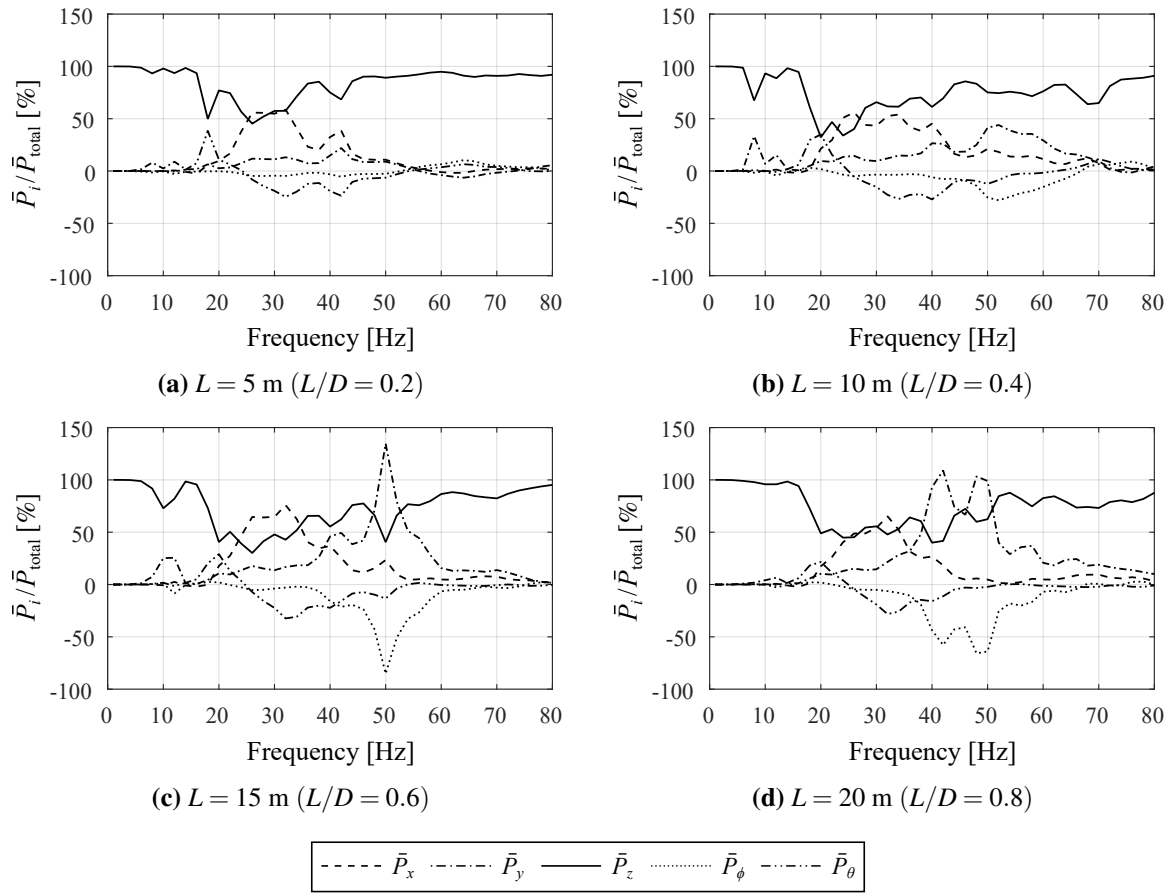
Fig. 7.19 The directional components of the mean power flows entering a centred pile-building system above an underground railway tunnel, presented as percentages of the total mean power flow. The effect of increasing the pile length L from **(a)** 5 m to **(d)** 20 m is illustrated. The responses are predicted using the Tp-Fb-Bd model. Note that a negative value signifies vibrational power leaving the building. Tunnel-foundation separation distance $S = 0$ m and tunnel depth $D = 25$ m.

(a) $L = 5$ m $(L/D = 0.2)$

(b) $L = 10$ m $(L/D = 0.4)$

(c) $L = 20$ m $(L/D = 0.8)$

(d) $L = 25$ m $(L/D = 1)$

(e) $L = 30$ m $(L/D = 1.2)$

(f) $L = 40$ m $(L/D = 1.6)$
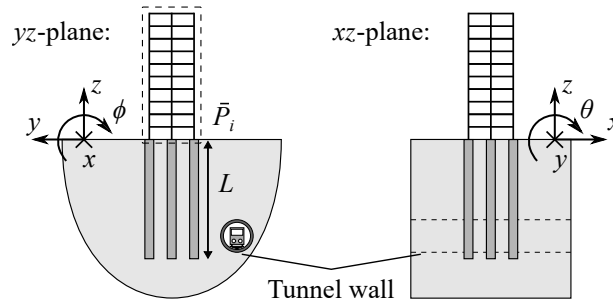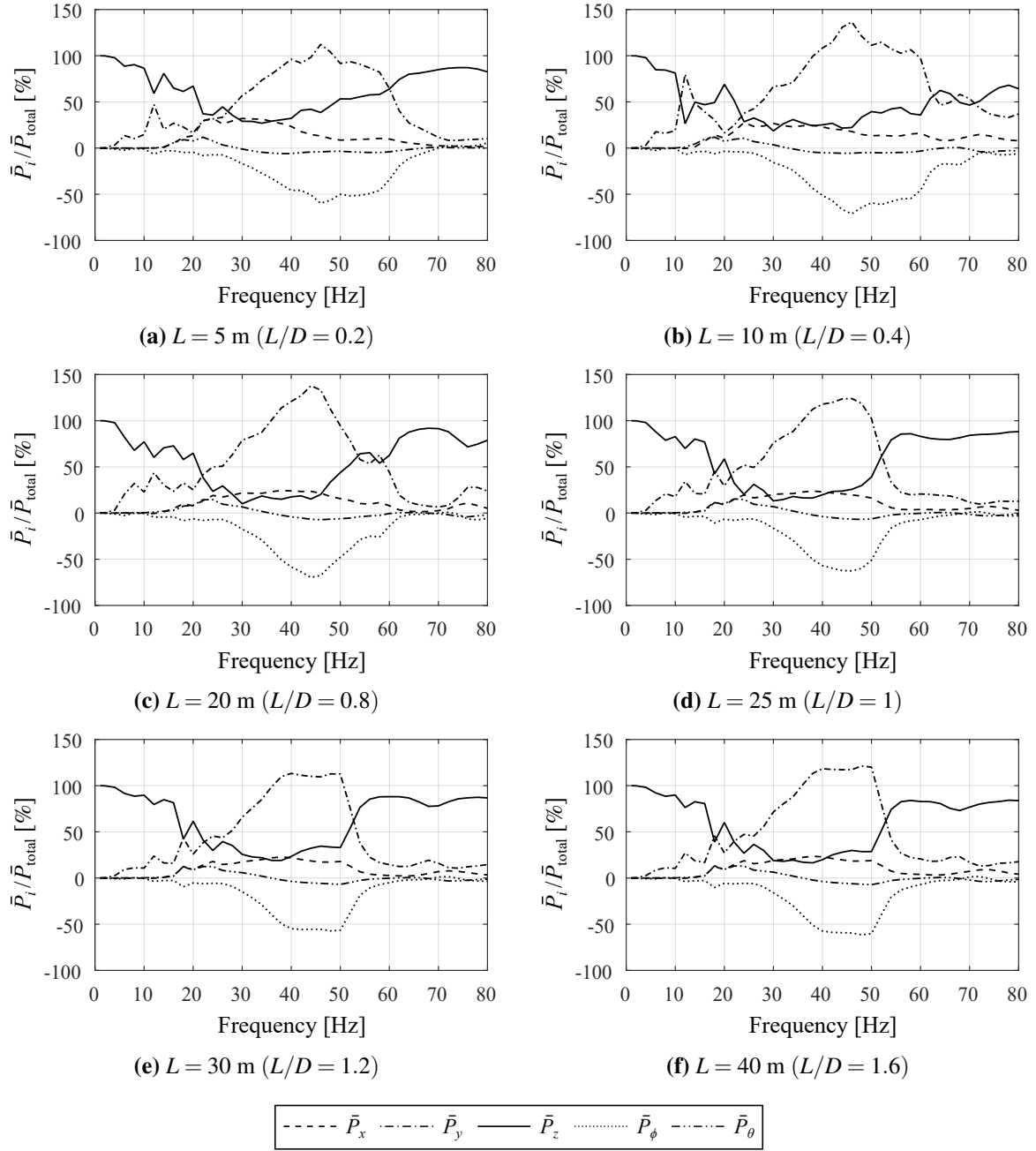
Fig. 7.20 The directional components of the mean power flows entering an off-centred pile-building system near an underground railway tunnel, presented as percentages of the total mean power flow. The effect of increasing the pile length L from **(a)** 5 m to **(f)** 40 m is illustrated. The responses are predicted using the Tp-Fb-Bd model. Note that a negative value signifies vibrational power leaving the building. Tunnel-foundation separation distance $S = 15$ m and tunnel depth $D = 25$ m.

is presented as a percentage of the total power flow entering the building. Note that, based on the power flow definition in Eq. (7.9), positive values correspond to vibrational energy entering the building, whereas negative values mean that the energy is re-radiated back into the soil and the foundation.

When the Tp-Fb-Bp model is used, there are distinctive undulations that appear in the mean power flow components. In particular, the undulations in Fig. 7.18a cause the longitudinal $(\bar{P}_x)$, transverse $(\bar{P}_y)$, and vertical $(\bar{P}_z)$ mean power flows to oscillate between positive and negative values at high frequencies above 40 Hz. Based on Eq. (7.9), these undulations arise as a result of shifts in the phase difference between the displacement and force wave-fields at the foundation-building interface. The phase is likely to shift due to the superposition of wave-fields that are reflected by the boundaries of the portal-framed building.

On the other hand, the Tp-Fb-Bd model is able to approximately capture the same general variation in the mean power flow components as the Tp-Fb-Bp model over the entire frequency range of interest, but without the undulations. This makes it easier to analyse the trends in the responses. Therefore, based on the results of the Tp-Fb-Bd model, the following observations can be made about the footing-building system.

In general, the vibrational power entering the building is mainly in the vertical direction when the frequency is below 30 Hz. At higher frequencies, the mean power flow is more or less equally distributed between the $\bar{P}_x$, $\bar{P}_y$ and $\bar{P}_z$ components for the centred system. In contrast, the dominant component of power flow switches from $\bar{P}_z$ to $\bar{P}_y$ for the off-centred system at frequencies above 30 Hz. Some of the power flow also leaves the building due to rocking about the x-axis $(\bar{P}_\phi)$. This variation in the vibration of the centred and off-centred systems can be explained as follows. Due to symmetry in the centred system, the net displacement at the four corner footings will be of equal magnitude, resulting in almost equivalent power transmission in these respective directions. When the building is instead located beside the tunnel, a greater proportion of the propagating wave-fields from the tunnel will reach the footings at an oblique angle, thereby inducing more transverse and rocking motion in the building.

Now, consider the effect of varying the pile length L on the vibrational performance of a pile-building system. Figures 7.19 and 7.20 plot the power flow components entering a centred $(S = 0 \text{ m})$ and an off-centred $(S = 15 \text{ m})$ pile-building system, respectively, as L is increased and the tunnel depth D is fixed at 25 m. The responses are predicted using the Tp-Fb-Bd model in order to better observe the general trends in the results.

For the centred system, $\bar{P}_z$ is clearly the dominant component of vibrational power entering the building, with the proportion being greater than 50% over the frequency range of interest. This demonstrates that when the piled foundation is directly above the tunnel centre-line, the piles provide a vibration transmission path in the vertical direction for waves to propagate into the building. Nonetheless, for long piles ($L \geq 15$ m), there are certain frequencies between 25 and 50 Hz where $\bar{P}_y$ is greater than $\bar{P}_z$.

In contrast, Fig. 7.20 shows that, regardless of the pile length, the proportion of $\bar{P}_y$ and $\bar{P}_\phi$ is greater than $\bar{P}_z$ between 20 and 55 Hz for the off-centred pile-building system. Furthermore, when the toe of the piled foundation descends below the tunnel ($L/D > 1$), increasing L has a negligible effect on the variation of the power flow components with respect to frequency. This is similar to the observation made in Section 6.6.3, where the insertion gain, characterising the added-pile effect of a single off-centred pile, is insensitive to changes in L once $L/D > 1$.

It is worth noting that Figs. 7.18–7.20 show that the transmission of vibrational power due to translational motion in the x- and y-directions ($\bar{P}_x, \bar{P}_y$) acts in the opposite direction to rocking motion about the y- and x-axes ($\bar{P}_\theta, \bar{P}_\phi$), respectively. That is to say, if $\bar{P}_x$ is positive, then $\bar{P}_\theta$ will be around the same order of magnitude but negative, and vice versa. Also, at most frequencies, rocking causes the vibrational power to radiate out of the building. Talbot & Hunt [224] make a similar observation when analysing the horizontal and rocking components of the power flow entering a 2D portal-framed building due to vertical excitation at the centre pile head.

In summary, this section highlights the importance of considering vibration transmission in multiple DOFs when investigating the overall vibration of a 3D building. Furthermore, as some vibrational power can be re-radiated into the foundation, it raises an interesting point: not all vibration transmission paths across the foundation-building interface are undesirable.

7.3.5 The Effect of Piles and Footings on the Power-Flow Insertion Gain

Although the previous section has highlighted some new interesting features on the directional components of the mean power flow, it does not clearly indicate whether there are noticeable differences between the overall vibration of the pile and footing configurations. The analysis of these differences is particularly important on a building construction site because vibration consultants need to ensure that the foundation design prevents undesirable noise and vibration from being transmitted into the building. Since piles and footings are widely used in foundation structures, building designers would need to understand if deep piles, which could be embedded

closer to the tunnel walls, significantly compromise the vibration performance of the building compared to using shallow footings.

To compare the mean vibrational power entering a typical pile-building system against the baseline case of a footing-building system, this section evaluates the PFIG$^{(pf)}$, which is defined in Eq. (7.11), of different test cases of the benchmark building. The effect of the pile length L on the overall vibration of centred and off-centred arrangements of the benchmark building is also explored. Figures 7.21 and 7.22 plot the PFIG$^{(pf)}$ of a centred ($S = 0$ m) and an off-centred ($S = 15$ m) building, respectively, near an underground railway tunnel of depth $D = 25$ m. The mean vibrational power is predicted using the Tp-Fb-Bp and Tp-Fb-Bd models.

In general, the undulations in the PFIG, predicted using the Tp-Fb-Bd model, agree well with those of the Tp-Fb-Bp model, albeit with slightly more attenuation of around 5 dB. Note that the Tp-Fb-Bp model predicts peaks at 8 and 10 Hz for the centred and off-centred buildings,
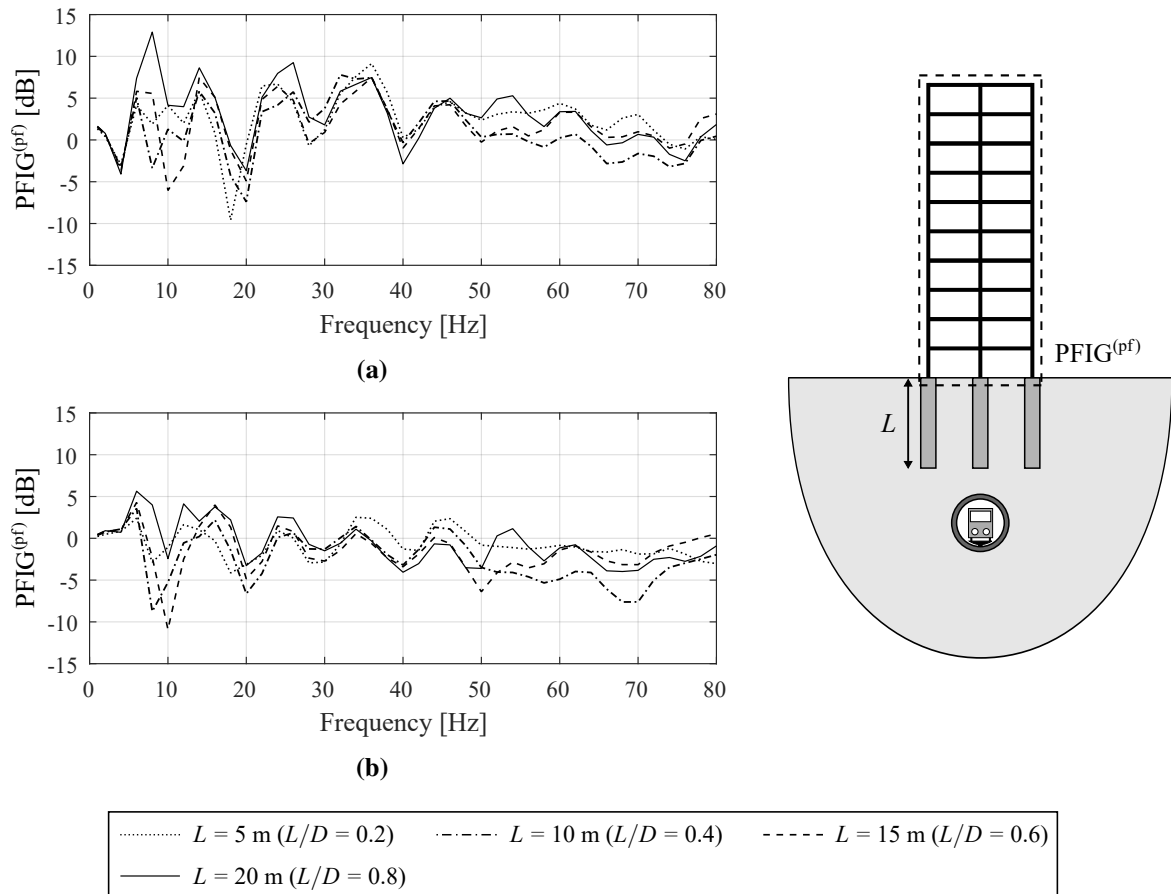
Fig. 7.21 The power-flow insertion gains of a centred foundation-building system above an underground railway tunnel, predicted using the **(a)** Tp-Fb-Bp and **(b)** Tp-Fb-Bd models. The insertion gain compares the overall vibration of the pile and footing configurations. The influence of the pile length L on the response is illustrated. Tunnel-foundation separation distance $S = 0$ m and tunnel depth $D = 25$ m.
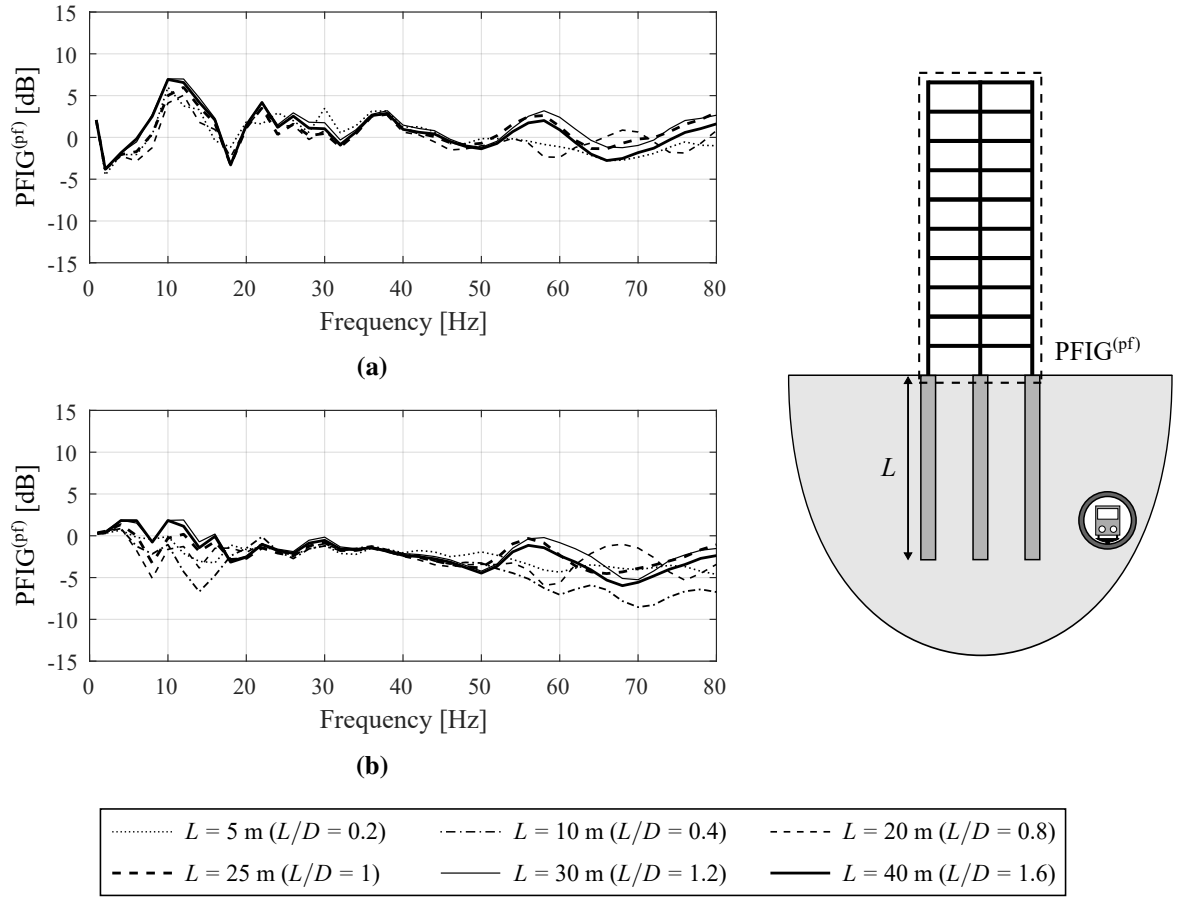
Fig. 7.22 The power-flow insertion gains of an off-centred foundation-building system near an underground railway tunnel, predicted using the **(a)** Tp-Fb-Bp and **(b)** Tp-Fb-Bd models. The insertion gain compares the overall vibration of the pile and footing configurations (pf). The influence of the pile length L on the response is illustrated. Tunnel-foundation separation distance $S = 15$ m and tunnel depth $D = 25$ m.

respectively, which are absent when using the Tp-Fb-Bd model. These low-frequency peaks are close to 12 Hz, corresponding to the eigenfrequency of the portal frame's first mode in which all the columns deformed axially. When the building is coupled to the piled foundation, the new eigenfrequencies of the entire structure will tend to decrease compared to those of the building itself. Hence, the frequencies of the peaks at 8 and 10 Hz are slightly less than 12 Hz.

For both the centred and off-centred buildings, as L is increased from 5 to 10 m, PFIG$^{(pf)}$ tends to decrease by approximately 5 dB, on average, over the frequency range of interest. In contrast, when L is increased from 10 to 20 m, PFIG$^{(pf)}$ increases by around 3 dB. For the off-centred building in particular, increasing L from 20 to 25 m, such that $L = D$, causes the PFIG to increase by only a few decibels. Increasing L further ($L/D > 1$) has a negligible effect on the PFIG. It is worth noting that these observations are similar to those observed in Section 6.6

for single piles. That is, the trends in the PFIG results can be explained using the soil-stiffening effect, which decreases the PFIG as L is increased for piles that satisfy $L < D$, and the enhanced transmission effect, which increases the PFIG when $L > D$.

Finally, the variation in $\text{PFIG}^{(\text{pf})}$ over the entire frequency range is roughly ± 5 dB, which is around the same order of magnitude as the generally regarded uncertainty in numerical models [126]. Therefore, for the cases explored in this section, there is little to no difference between the overall vibration of buildings supported on deep piles or shallow footings. In conclusion, if practitioners are required to embed piles rather than footings near a railway tunnel, they can be reasonably confident that the piles will not adversely compromise the vibration of the building.

7.4 Base-Isolated Buildings

Section 7.3 has highlighted that the added-foundation effect can often be more significant than the added-building effect when the overall vibration of the entire foundation-building system is considered. However, in situations when the vibration attenuation, due to the added-foundation effect, is insufficient to prevent the absolute vibration levels of the building from exceeding the guideline values set by standards [21,22,24], steps need to be taken to mitigate the disturbances.

Base isolation, as reviewed in Section 2.2.3, is a commonly used countermeasure against excessive vibration and re-radiated noise. To a certain extent, the base isolation de-couples the building from the soil-foundation system. Most isolation systems consist of either elastomeric bearings or helical steel springs. This section presents the model used for the isolation system and derives the power-flow insertion gain for characterising the isolation performance of a base-isolated building. The isolation model is then used to analyse the performance of a base-isolated design of the benchmark building near an underground railway tunnel.

7.4.1 Modelling the Isolation

Each isolator is modelled as a linear, massless spring that accounts for motion in the vertical, lateral and rocking DOFs. The stiffnesses of the springs, with respect to the two lateral (x, y) and rocking (ϕ, θ) DOFs, are assumed to be equivalent. In most applications, lateral-rocking coupling due to flexural deformation of the isolator is negligible, so it is not considered in this dissertation. Hence, each isolator is associated with three independent modes of deformation (vertical, lateral and rocking), as illustrated in Fig. 7.23 for an elastomeric bearing.

In practice, the main design parameter of an isolated system is the isolation frequency f_{iso}. This parameter is derived by assuming that the base-isolated building can be modelled as an equivalent SDOF system, whereby the rigid mass of the building is coupled to a single isolator that is vertically excited at its base. Therefore, the performance of the system can be described by the transmissibility, which is defined as the frequency-dependent ratio of the building and ground displacements. The essential features of the simplified isolated system, as illustrated in the transmissibility plot in Fig. 7.24, are as follows: (1) the isolator amplifies the low-frequency vibration; (2) maximum transmissibility is observed when the excitation frequency equals f_{iso}; and (3) the isolator is only effective when the frequency is more than $f_{\text{iso}}\sqrt{2}$, above which the isolation improves with increasing frequency. It should be mentioned that although the SDOF system neglects the multi-directional input at the base, it does provide a convenient method for characterising the vertical stiffness of an isolator:

$$k_{vv} = (2\pi f_{\text{iso}})^2 M_T \,, \tag{7.48}$$

where M_T is the building mass that is supported by each isolator. In this chapter, M_T is found by only considering the individual building columns with mass $M_T = M_c = m_c L_c$, where these parameters are defined in Section 7.2. This is because including the additional floor mass in the portal-frame (Bp) model (see Section 7.2.2) does not significantly change the dynamics of the building compared to the column (Bc) model (see Section 7.2.3), as presented in Section 7.2.5.

Natural rubber exhibits elastomeric properties that vary with strain amplitude and frequency due to material non-linearities [210]. Nevertheless, it is reasonable to assume that these effects are negligible when considering base-isolated buildings since the strain amplitudes associated with ground-borne vibration are around the order of 10^{-4} [74]. At these strain levels, the rubber may be assumed to behave linearly, provided that an appropriate dynamic stiffness is used, as expressed in Eq. (7.48). In contrast, given the inherent small-strain elastic behaviour of steel,
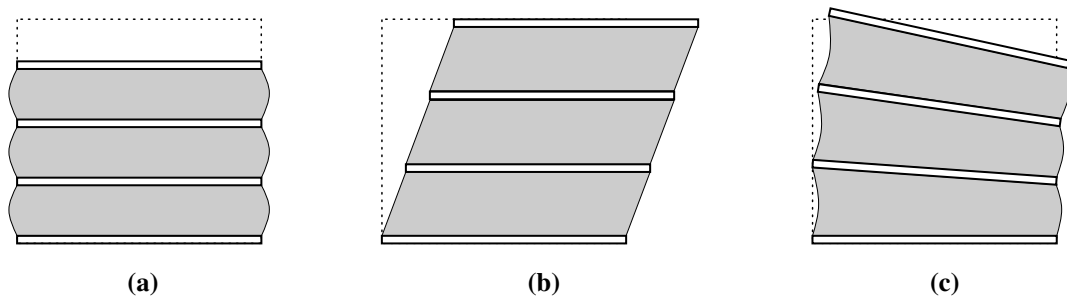
Fig. 7.23 The **(a)** vertical, **(b)** lateral and **(c)** rocking deformation of an elastomeric bearing (reproduced from Talbot [219]).

the assumption of linearity is more easily justified for helical steel springs. Furthermore, the dynamic stiffness of steel springs can be assumed to be equal to its static stiffness because there is no significant variation with frequency; the stiffness only depends on the spring's geometry and properties [238].

The lateral k_{ll} and rocking $k_{\theta\theta}$ stiffnesses of the isolator are assigned as

$$k_{ll} = k_{\theta\theta} = 0.5k_{vv}. \tag{7.49}$$

In general, for laminated rubber bearings, the k_{ll}/k_{vv} and $k_{\theta\theta}/k_{vv}$ ratios depend on the shape factor of constituent pads, which is inversely proportional to the square of the pad thickness [179]. For the case of steel springs, the same ratios depend on its length and diameter [238]. Nonetheless, based on the comprehensive investigations by Talbot [221] and Sanitate [206], the ratios in Eq. (7.49) are considered to be appropriate for most isolation bearings. If more precise values for k_{vv}, k_{ll} and $k_{\theta\theta}$ do become available, or a different isolation model altogether, they may be implemented in future work without affecting the conclusions drawn in this dissertation.

A hysteretic damping model is used to account for damping in the isolators. Loss factors of $\eta_k = 0.01$ and $\eta_k = 0.1$ are representative of the approximate limiting values for undamped steel springs and high-hysteresis rubber bearings, respectively [221]. For an equivalent SDOF system of a base-isolated building, increasing the loss factor only attenuates the transmissibility when the excitation frequency is close to f_{iso}, as shown in Fig. 7.24.

In practice, depending on the region of the building being isolated (single column, structural core, etc.), the base isolation can either be installed individually or as a cluster of isolators. The former is assumed here by using a two-point connection O'–O to isolate the building from the foundation at each coupling point. The points O' and O refer to the base and top of an isolator,
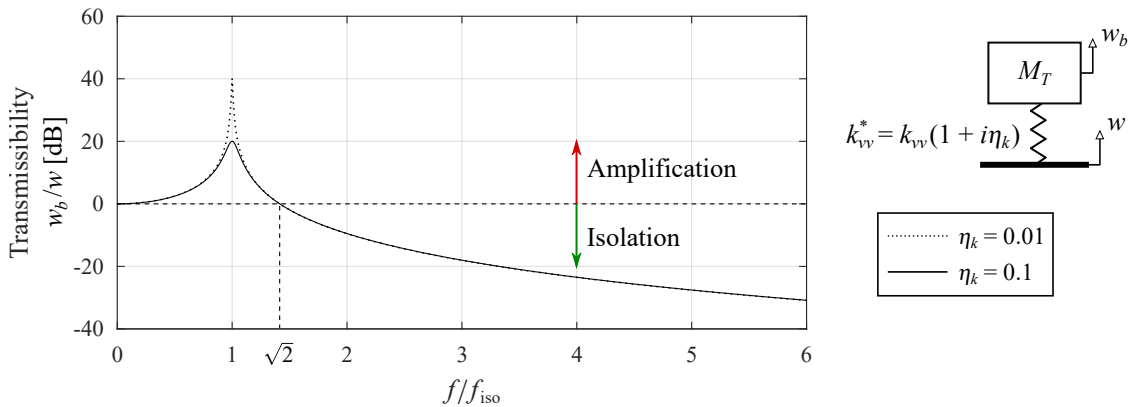
Fig. 7.24 The transmissibility, plotted with respect to the excitation frequency f, of an SDOF system representing a simplified base-isolated building with mass M_T, stiffness k_{vv}, and isolation frequency $f_{\mathrm{iso}} = 1/2\pi\sqrt{k_{vv}/M_T}$. The influence of the hysteretic loss factor η_k on the response is illustrated.

respectively. Given no external forces at O, the force-displacement relationship at the ends of an isolator can be expressed as

$$\mathbf{f}(\mathbf{x}_0) = -\mathbf{f}(\mathbf{x}_{0'}) = \mathbf{K}_\mathrm{I} \left(\mathbf{u}(\mathbf{x}_0) - \mathbf{u}(\mathbf{x}_{0'}) \right). \tag{7.50}$$

where the isolator's dynamic stiffness matrix $\mathbf{K}_\mathrm{I}$, with respect to the five DOFs at the coupling point, is

$$\mathbf{K}_\mathrm{I} = \begin{bmatrix} k_{ll} & 0 & 0 & 0 & 0 \\ 0 & k_{ll} & 0 & 0 & 0 \\ 0 & 0 & k_{vv} & 0 & 0 \\ 0 & 0 & 0 & k_{\theta\theta} & 0 \\ 0 & 0 & 0 & 0 & k_{\theta\theta} \end{bmatrix}. \tag{7.51}$$

7.4.2 Coupling at the Isolation Interface of a Base-Isolated Building

In this section, Eq. (7.50) is used to augment the coupling model in Section 7.1.2 so that, now, the dynamics of a base-isolated building can be simulated. The variation in the displacement, when an isolator is connected between the foundation $\mathcal{F}$ and building $\mathcal{B}$ systems, is illustrated by the coupling model in Fig. 7.25. Given that there are no external forces at the isolation-building
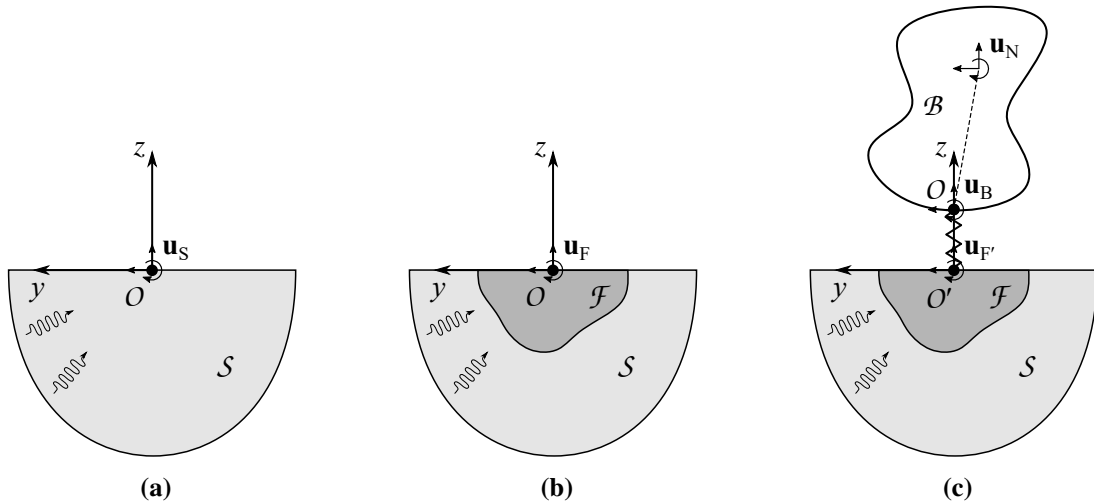
Fig. 7.25 Schematic diagrams illustrating the coupling model for the fundamental unit of a base-isolated foundation-building system. **(a)** The incident wave-fields from a vibration source in the 3D soil system $\mathcal{S}$ leads to the greenfield displacement $\mathbf{u}_\mathrm{S}$ at a point O on the free surface. **(b)** The presence of a 3D foundation system $\mathcal{F}$ is then considered, with the resulting displacement $\mathbf{u}_\mathrm{F}$ at the top of $\mathcal{F}$. **(c)** A base-isolated 3D building system $\mathcal{B}$ is coupled to the soil-foundation system using a two-point connection O'–O, with the resulting displacements $\mathbf{u}_{\mathrm{F}'}$ and $\mathbf{u}_\mathrm{B}$ at the base of the isolator and $\mathcal{B}$, and $\mathbf{u}_\mathrm{N}$ in the remainder of $\mathcal{B}$.

interface, the equilibrium of forces at the base of the building (point O) can be expressed as

$$\mathbf{f}_B = \mathbf{f}_{F'} = \mathbf{K}_I(\mathbf{u}_{F'} - \mathbf{u}_B) = \mathbf{K}_B\mathbf{u}_B, \tag{7.52}$$

where the vectors $\mathbf{u}_{F'}$ and $\mathbf{f}_{F'}$ are the respective displacement and force at the base of the isolator (point O'). By rearranging Eq. (7.52), the displacement-force relationship at O' can be written as

$$\mathbf{u}_{F'} = (\mathbf{K}_B^{-1} + \mathbf{K}_I^{-1})\mathbf{f}_B = \mathbf{H}_C\mathbf{f}_{F'}, \tag{7.53}$$

where $\mathbf{H}_C$ is the driving-point displacement FRF matrix of the isolation-building system at O'. Rearranging Eqs. (7.52) and (7.53) gives the following matrix equation:

$$\mathbf{u}_{F'} = \mathbf{H}_C\mathbf{K}_B\mathbf{u}_B. \tag{7.54}$$

Following the same method used in Section 7.1.2 to derive Eq. (7.6), the displacement $\mathbf{u}_{F'}$ can be related to the displacement $\mathbf{u}_F$ at the top of the foundation prior to building construction:

$$\mathbf{u}_{F'} = (\mathbf{I} + \mathbf{H}_F\mathbf{K}_C)^{-1}\mathbf{u}_F = \mathbf{T}_C^{iso}\mathbf{u}_F, \tag{7.55}$$

where $\mathbf{K}_C = \mathbf{H}_C^{-1}$ is the dynamic stiffness matrix of the isolation-building system. Rearranging Eqs. (7.54) and (7.55) gives the following matrix equation:

$$\mathbf{u}_B = \mathbf{K}_B^{-1}\mathbf{K}_C\mathbf{T}_C^{iso}\mathbf{u}_F = \mathbf{T}_B^{iso}\mathbf{u}_F, \tag{7.56}$$

where $\mathbf{T}_B^{iso}$ is the foundation-building transfer matrix for the isolated case. Similar to Eq. (7.7) for the unisolated case, the displacement $\mathbf{u}_N$ at a point within the building can be obtained:

$$\mathbf{u}_N = \mathbf{H}_{NB}\mathbf{K}_B\mathbf{u}_B = \mathbf{H}_{NB}\mathbf{K}_B\mathbf{T}_B^{iso}\mathbf{u}_F, \tag{7.57}$$

where $\mathbf{H}_{NB}$ is a sub-matrix of the building's global displacement FRF matrix $\mathbf{H}_{BG}$ in Eq. (7.4).

7.4.3 The Isolation Performance of the Benchmark Building

The IG and PFIG have been discussed in Section 2.2.4 as two metrics that can offer insight into the isolation performance of a base-isolated building. In this section, the PFIG is used to evaluate the isolation performance of the benchmark building when different isolation systems are installed. However, Section 7.1.3 has shown that IG is not an effective performance metric for structures with multiple DOFs, so it will not be considered in this section. Unless specified otherwise, only the dashpot (Bd) model is used to simulate the motion of tall buildings over the

remainder of this chapter because Sections 7.2 and 7.3 have demonstrated that the simplified model can account for the essential building dynamics between 1 and 80 Hz.

For the unisolated case, the mean power flow entering a building has already been derived in Section 7.1.3, which is repeated here for convenience:

$$\bar{P}^{(\mathrm{uniso})} = \frac{1}{2}\mathrm{Re}\left(i\omega\mathbf{u}_{\mathrm{F}}^{\dagger}\mathbf{T}_{\mathrm{B}}^{\dagger}\mathbf{K}_{\mathrm{B}}^{\dagger}\mathbf{T}_{\mathrm{B}}\mathbf{u}_{\mathrm{F}}\right). \tag{7.58}$$

By substituting Eqs. (7.52) and (7.56) into Eq. (7.9), a similar expression can be derived for the mean power flow entering an isolated building:

$$\bar{P}^{(\mathrm{iso})} = \frac{1}{2}\mathrm{Re}\left(i\omega\mathbf{u}_{\mathrm{F}}^{\dagger}\mathbf{T}_{\mathrm{B}}^{\mathrm{iso}\,\dagger}\mathbf{K}_{\mathrm{B}}^{\dagger}\mathbf{T}_{\mathrm{B}}^{\mathrm{iso}}\mathbf{u}_{\mathrm{F}}\right). \tag{7.59}$$

Given Eqs. (7.58) and (7.59), the isolation performance can be evaluated using the PFIG:

$$\mathrm{PFIG}^{(\mathrm{iso})} = 10\log_{10}\left(\frac{|\bar{P}^{(\mathrm{iso})}|}{|\bar{P}^{(\mathrm{uniso})}|}\right). \tag{7.60}$$

In practice, a building isolation system is classified on its designed isolation performance: 'very high' ($f_{\mathrm{iso}} = $ 2-4 Hz), 'high' ($f_{\mathrm{iso}} = $ 5-12 Hz) and 'medium' ($f_{\mathrm{iso}} = $ 13-20 Hz) [63]. The parameter values in Table 7.2 are used to study the performance of four isolation systems that span a wide range of isolation frequencies. Figure 7.26 plots the PFIGs of a centred ($S = 0$ m) and an off-centred ($S = 15$ m) pile-building system when the four isolation systems are installed at the base of every column in the benchmark building.

In general, the performance of the base isolation improves as the excitation frequency is increased, which is similar to the performance of the SDOF system in Fig. 7.24. The isolation becomes more significant when the isolation frequency is low. For example, isolation system 1, which has the lowest isolation frequency of 2.5 Hz, exhibits the lowest frequency-averaged $\mathrm{PFIG}^{(\mathrm{iso})}$ of around -20 dB. Increasing the isolation frequency from 2.5 to 5 Hz causes the

System	Material	Classification	Isolation frequency [Hz]	Loss factor [−]
1	Steel springs	Very high	$f_{\mathrm{iso}} = 2.5$	$\eta_k = 0.01$
2	Steel springs	High	$f_{\mathrm{iso}} = 5$	$\eta_k = 0.01$
3	Rubber bearings	High	$f_{\mathrm{iso}} = 10$	$\eta_k = 0.1$
4	Rubber bearings	Medium	$f_{\mathrm{iso}} = 15$	$\eta_k = 0.1$

Table 7.2 Parameter values of four isolation systems, classified based on their isolation performance.

PFIG$^{(iso)}$ to increase by approximately 12 dB. Further increasing the isolation frequency by increments of 5 Hz, from 5 to 15 Hz, causes the marginal increase in PFIG$^{(iso)}$ to significantly decrease from 10 dB to around 3 dB.

Since the columns in the centred and off-centred configurations undergo flexural and axial vibration, due to the tunnel position relative to each column, the performances of the identical isolation systems in both configurations are similar to within ± 5 dB over the frequency range. However, between 70 and 80 Hz, there is a significant decrease of 10 dB in the PFIG$^{(iso)}$ of all four isolation systems when the centred configuration is used, while there is lower decrease of 5 dB for the off-centred configuration. This suggests that the isolation performance might be dependent on the location of the building relative to the tunnel at certain frequencies.

Figures 7.27 and 7.28 plot the directional components of the mean power flows entering the centred and off-centred buildings, respectively, when the four isolation systems are installed. From these figures, any variation in the overall vibration, with respect to the five DOFs, can be observed between the unisolated and isolated building configurations.
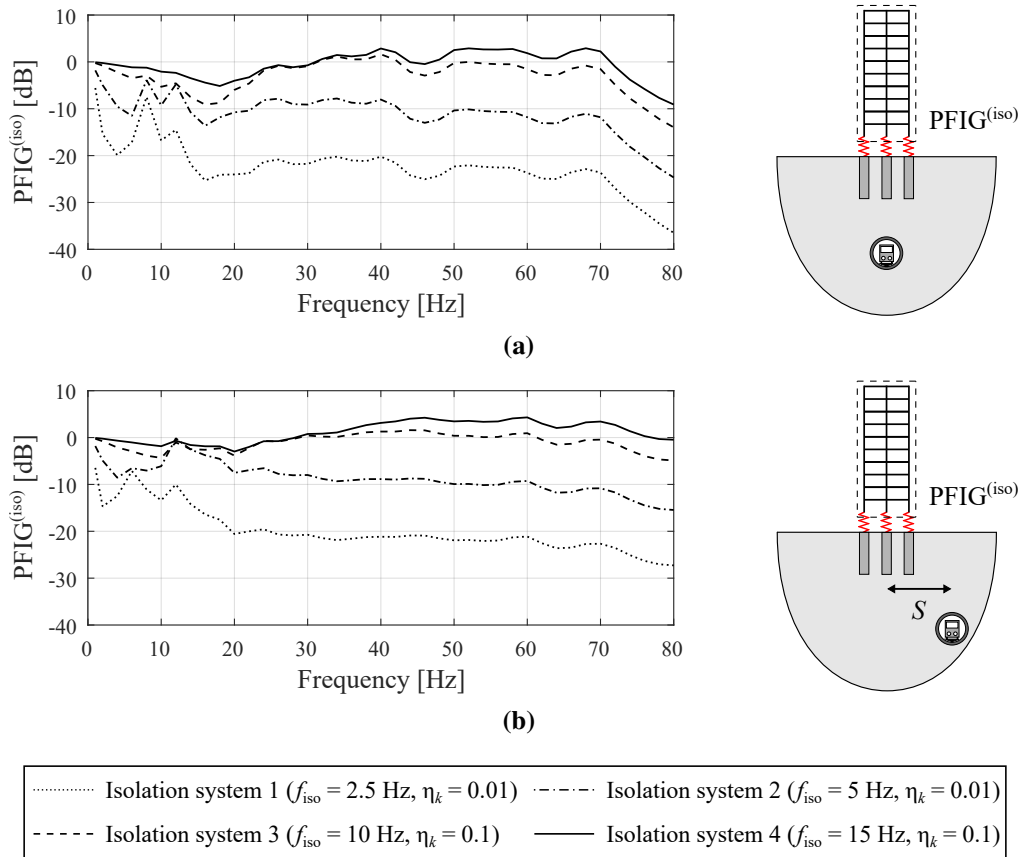
Fig. 7.26 The isolation power-flow insertion gains of **(a)** a centred ($S = 0$ m) and **(b)** an off-centred ($S = 15$ m) pile-building system near their respective underground railway tunnels. The effect of varying the isolation system on the response is illustrated. Pile length $L = 10$ m and tunnel depth $D = 25$ m.

(a) Unisolated

(b) Isolation system 1 ($f_{\text{iso}} = 2.5$ Hz, $\eta_k = 0.01$)

(c) Isolation system 2 ($f_{\text{iso}} = 5$ Hz, $\eta_k = 0.01$)

(d) Isolation system 3 ($f_{\text{iso}} = 10$ Hz, $\eta_k = 0.1$)

(e) Isolation system 4 ($f_{\text{iso}} = 15$ Hz, $\eta_k = 0.1$)
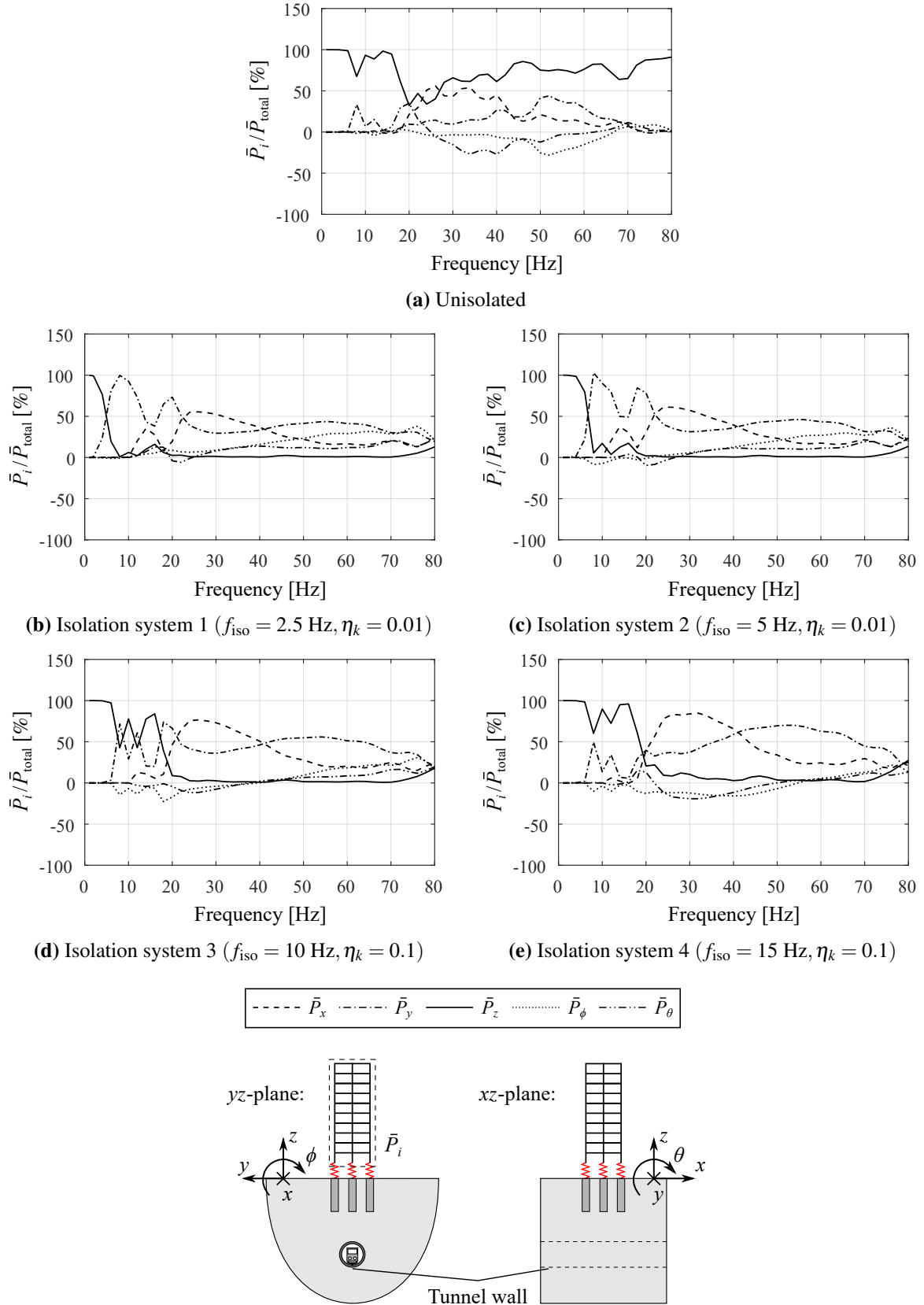
Fig. 7.27 The directional components of the mean power flows entering a centred, base-isolated pile-building system above an underground railway tunnel, presented as percentages of the total mean power flow. The sub-figures illustrate the effect of varying the isolation system on the response. Note that a negative value signifies vibrational power leaving the building. Pile length $L = 10$ m, tunnel-foundation separation distance $S = 0$ m, and tunnel depth $D = 25$ m.

(a) Unisolated

(b) Isolation system 1 ($f_{\text{iso}} = 2.5$ Hz, $\eta_k = 0.01$)

(c) Isolation system 2 ($f_{\text{iso}} = 5$ Hz, $\eta_k = 0.01$)

(d) Isolation system 3 ($f_{\text{iso}} = 10$ Hz, $\eta_k = 0.1$)

(e) Isolation system 4 ($f_{\text{iso}} = 15$ Hz, $\eta_k = 0.1$)
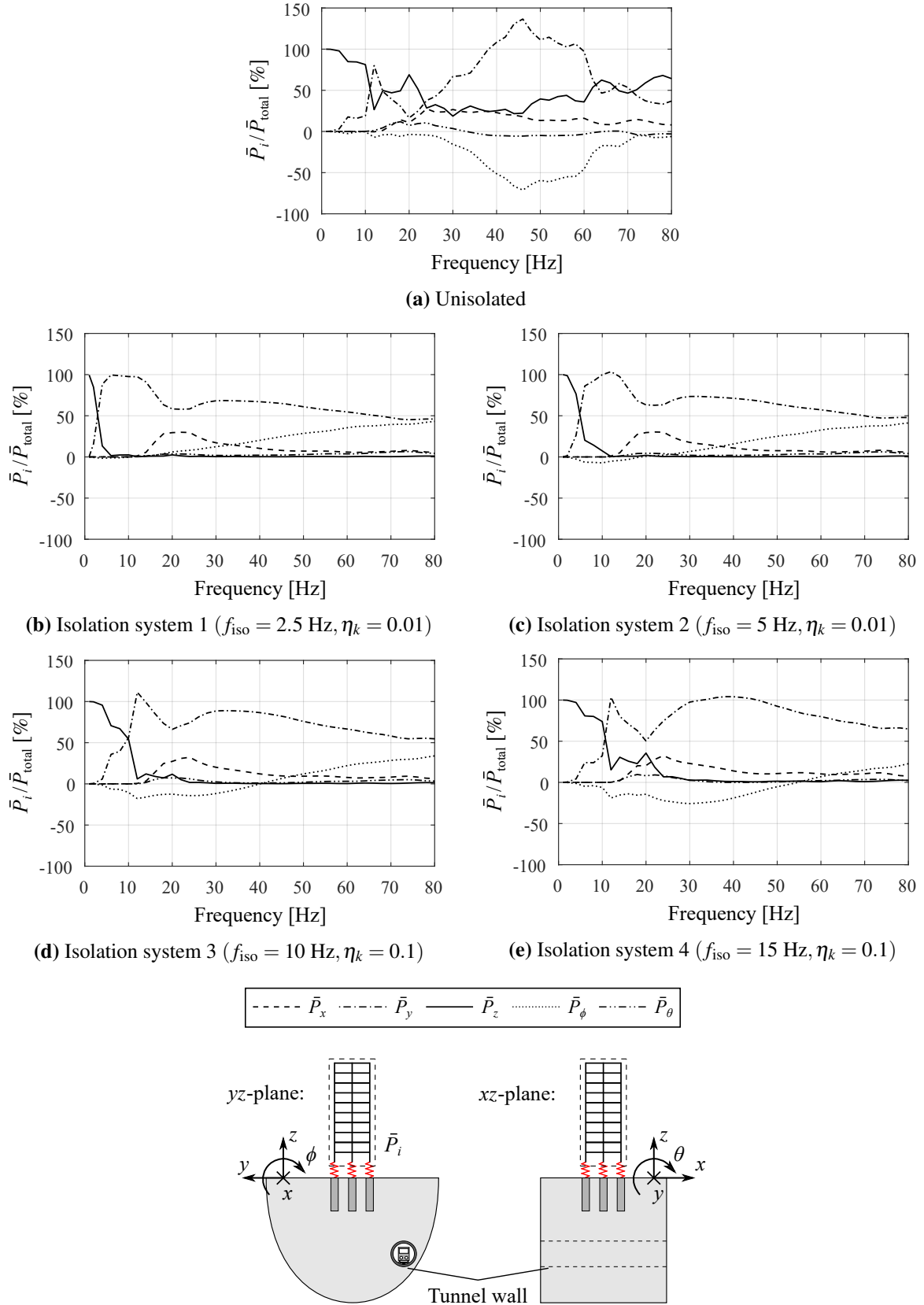
Fig. 7.28 The directional components of the mean power flows entering an off-centred, base-isolated pile-building system near an underground railway tunnel, presented as percentages of the total mean power flow. The sub-figures illustrate the effect of varying the isolation system on the response. Note that a negative value signifies vibrational power leaving the building. Pile length $L = 10$ m, tunnel-foundation separation distance $S = 15$ m, and tunnel depth $D = 25$ m.

It is clearly evident from Figs. 7.27 and 7.28 that all four isolation systems are very good at mitigating the vibrational power in the vertical direction. When the excitation frequency is less than the isolation frequency of the respective isolation system, the proportion of the vertical power flow entering a base-isolated building is generally greater than 50%, whereas it is under 10% at higher excitation frequencies. This shows that the isolation frequency can be used to determine the frequencies at which the isolation system is most effective at mitigating the axial vibration in the building.

At frequencies above 20 Hz, the summation of the longitudinal and transverse power flows is significantly higher than the vertical power flow entering a base-isolated building. That is, a greater proportion of the mean power is transmitted into the building via flexural vibration than axial vibration when the excitation frequency is higher than the isolation frequency. This occurs because the lateral stiffness of a tall, narrow-based building, such as the benchmark building, is much lower than its axial stiffness. Therefore, when lateral excitation is applied to the base of the isolators, flexural vibration is more efficiently transmitted into the base-isolated building, which is not the desired effect of the isolation system.

Going back to Fig. 7.26, it is important to recognise that isolation system 4, which has the highest isolation frequency of 20 Hz, is the only system that exhibits amplification over a large frequency range from 30 to 70 Hz, with a maximum $\text{PFIG}^{(\text{iso})}$ of 4 dB. An explanation for the amplification can be found by also analysing Figs. 7.27 and 7.28. Based on the isolation model, Eqs. (7.48) and (7.49) indicate that a high isolation frequency will increase the lateral stiffness of the isolators. Therefore, the high lateral stiffness of isolation system 4 lowers the difference in lateral impedance at the isolation-building interface, thereby increasing the flexural vibration that enters the building, as observed in Figs. 7.27 and 7.28. When the amplification of flexural vibration overcomes the isolation of axial vibration, the base-isolated building will experience an overall amplification in the PFIG with respect to all five DOFs.

In summary, this study reiterates that base isolation can be effective at mitigating the overall building vibration induced by railway tunnels, which is in agreement with other similar studies on base-isolated buildings [206, 222]. However, using the isolation frequency, which is based on the vibration of an SDOF system, to guide design might produce misleading results because it only accounts for axial vibration in the building. It is therefore recommended to account for vibration isolation in multiple DOFs by using the PFIG as a viable performance metric.

7.5 A Virtual Case Study

A virtual case study on the construction of a tall building near a pre-existing railway tunnel is presented in this section to demonstrate how the models developed in this dissertation can be used in practice to mitigate the perceptible vibration. Suppose that the project architect has produced the design for a 10-storey, 4-by-4-bay residential building, as shown in Fig. 7.29, but the location of the foundation, relative to the tunnel, and the lengths of the 25 piles have not yet been finalised. In this situation, the role of a vibration consultant would be to use the models to help guide the foundation design and the installation of base isolation so that the vibration limits for a residential building are not exceeded. The IG and PFIG are used as vibration performance metrics to evaluate the designs.

The Tp-Fb and Tp-Fb-Bd models are used to capture the dynamics of the foundation alone and the entire building, respectively, due to train-induced vibration. The parameter values and reference data for the concrete foundation and building are summarised in Tables 7.3 and 7.4,

Parameters [*Units*]	Columns	Beams	Piles
Young's modulus [Pa]	$E_c = 30 \times 10^9$	$E_b = 30 \times 10^9$	$E_p = 30 \times 10^9$
Density [kg/m^3]	$\rho_c = 2500$	$\rho_b = 2500$	$\rho_p = 2500$
Cross-section area [m^2]	$A_c = 0.25$	$A_b = 1.25$	$A_p = 0.39$
Second moment of area [m^4]	$I_c = 5.2 \times 10^{-3}$	$I_b = 6.5 \times 10^{-3}$	$I_p = 12.3 \times 10^{-3}$
Length [m]	$l_c = 3$	$l_b = 5$	L
Loss factor [$-$]	$\eta_c = 0.1$	$\eta_b = 0.1$	$-$

Table 7.3 Building and piled foundation parameter values for the virtual case study. Note, the length L of piles in the foundation is not fixed, so it can be varied to produce different foundation designs.

Building and foundation	Number of storeys	10
	Number of bays	4 by 4
	Number of piles	25
Non-structural dead load	Building category	A - residential
	Partition category	1 - weight ≤ 1 kN/m
	Floor density	1600 kN/m
	Floor thickness	0.1 m

Table 7.4 Building and piled foundation reference data for the virtual case study.

(a)   **(b)**
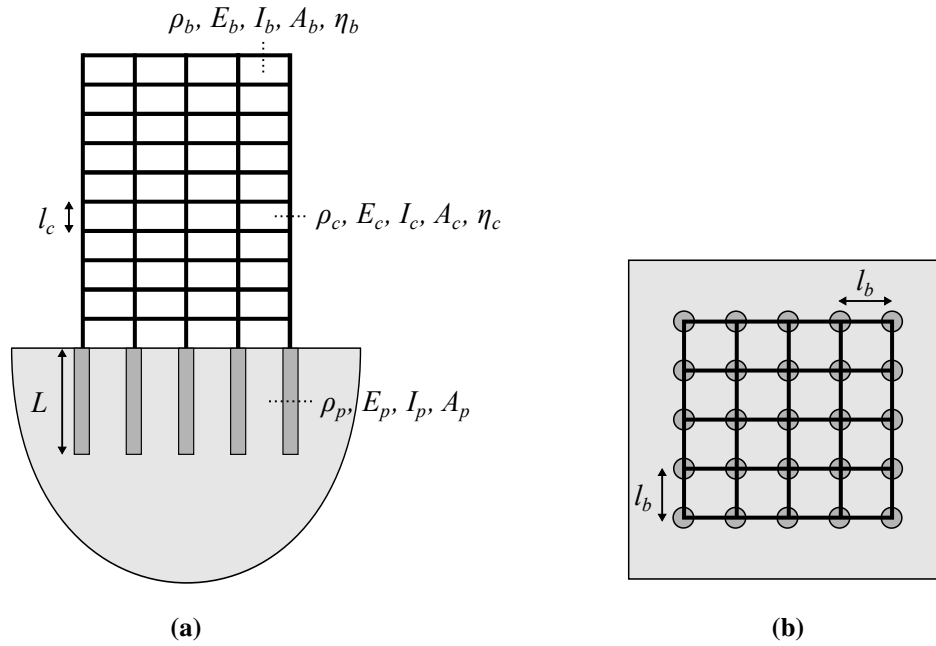
Fig. 7.29 Schematic diagrams of the **(a)** side and **(b)** plan views of the pile-building system in the virtual case study. The residential building is represented by a 10-storey, 4-by-4-bay frame.

while Table 6.1 presents the parameter values of the concrete tunnel and the London Clay soil. For the train excitation to be representative of a typical subway line, the parameter values in Table 6.2 are used to model the train-track system within the tunnel. In all cases, the depth of the tunnel is fixed at $D = 25$ m, which is around the average depth of the London Underground.

7.5.1   The Tunnel-Foundation-Building Configurations

The four tunnel-foundation-building configurations shown in Fig. 7.30 are considered in this study. The centred piled foundation in Configuration 1 can be regarded as a conservative design, as the lengths of all 25 piles is 20 m. Given the total mass of the residential building, as based on Tables 7.3 and 7.4, the foundation of Configuration 1 meets the criteria of the EN 1991-1-1 [60] and EN 1990 [59] design codes, where the actions on the building and their combination, with respect to the serviceability state, are considered using static analysis.

However, a practical drawback with Configuration 1 is that the foundation is located directly above the railway tunnel, thereby limiting the vertical clearance between the central piles and the tunnel to just 2 m. Configuration 2 resolves this issue, as the shorter inner piles nearer the tunnel are 10 m in length, while the ten outermost piles are 30 m in length. The dimensions of the piles in Configuration 3 are the same as in Configuration 2, but the longer 30 m piles are instead positioned beside the tunnel. Since tunnel-pile coupling has a significant effect on the
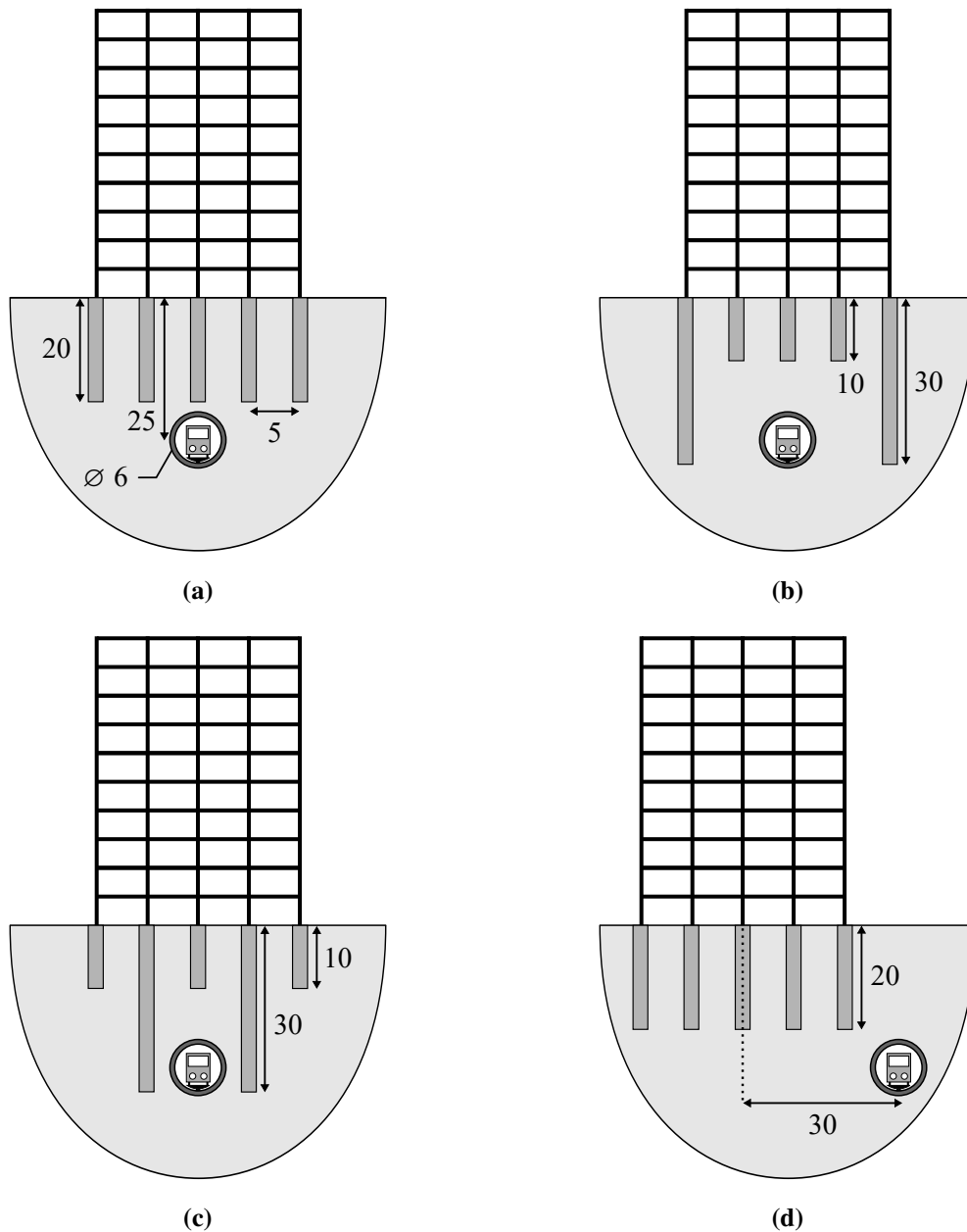
Fig. 7.30 Schematic diagrams of Configurations **(a)** 1, **(b)** 2, **(c)** 3 and **(d)** 4 for the tunnel-foundation-building system. Dimensions in [m]. Not drawn to scale.

response when the pile toes descend below an adjacent tunnel, as observed in Section 6.4.5, the source-receiver interaction is expected to be more significant in Configuration 3. The respective foundations of Configurations 2 and 3 also comply with the aforementioned design codes.

Configuration 4 contains the same piles as Configuration 1, but the foundation is off-centred from the tunnel by a separation distance of 30 m. At first glance, it is reasonable to assume that Configuration 4 will produce the lowest vibration levels in the building because the foundation is furthest from the tunnel. Nevertheless, a thorough technical analysis should be conducted

on all four configurations to decide which designs are most effective at mitigating the overall vibration of the building.

7.5.2 The Added-Foundation and Added-Building Effects

This section studies the added-foundation and added-building effects of the four configurations. In order to characterise the overall modification in the vibration, the mean insertion gain $\overline{\text{IG}}$ is calculated over all 25 piles in each configuration. Hence, the added-foundation effect $\overline{\text{IG}}^{(\text{aF})}$ and the added-building effect $\overline{\text{IG}}^{(\text{aB})}$ are described by the respective means of Eqs. (7.43) and (7.44), taken across all pile heads. Figures 7.31 and 7.32 plot the directional components of the former and latter effects, respectively.

First, consider the added-foundation effect of Configurations 1, 2 and 3, where the piles are above the railway tunnel. In general, attenuation is observed in both the transverse and vertical directions, while amplification is observed in the longitudinal direction. Over most frequencies, the variation in $\overline{\text{IG}}^{(\text{aF})}$ between these centred configurations is similar in the three orthogonal
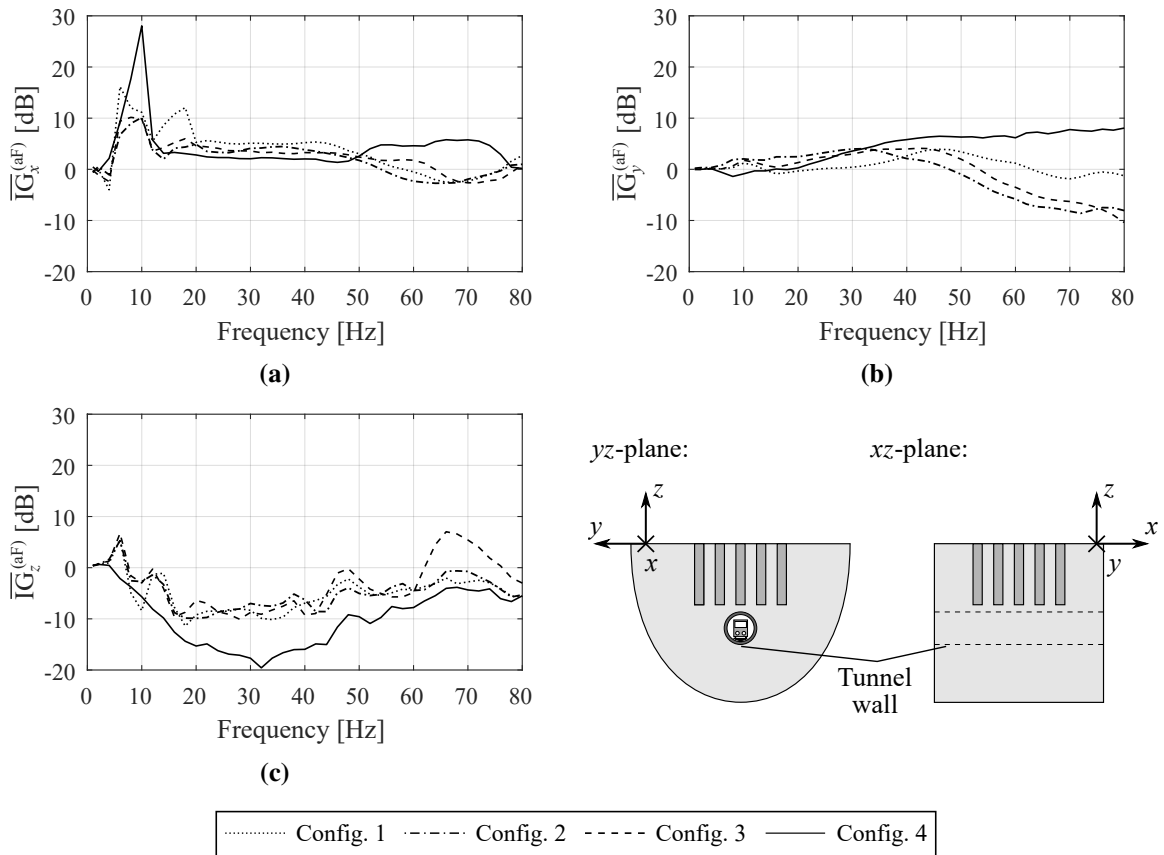
Fig. 7.31 The **(a)** longitudinal, **(b)** transverse and **(c)** vertical mean insertion gains of Configurations 1, 2, 3 and 4, characterising the added-foundation effect before building construction. The responses are predicted using the Tp-Fb model.

directions. However, when the frequency is above 60 Hz, the differences in $\overline{\mathrm{IG}}_y^{(\mathrm{aF})}$ and $\overline{\mathrm{IG}}_z^{(\mathrm{aF})}$ between the centred configurations can be as high as 10 dB, which is significant. At these high frequencies, the S-wavelengths in the soil are less than the 5 m pile spacing of the foundations. This can thereby increase the effect of k-PSPI due to the wave scattering between neighbouring piles, as observed in Section 6.4.3. Furthermore, when the lengths of adjacent piles positioned along the y-direction are different, as in Configurations 2 and 3, the resulting k-PSPI is likely to differ from that in Configuration 1, where all the piles are equivalent. Therefore, variations in the k-PSPI of the centred foundations can lead to the differences observed in $\overline{\mathrm{IG}}_y^{(\mathrm{aF})}$ and $\overline{\mathrm{IG}}_z^{(\mathrm{aF})}$, particularly at the high frequencies.

In addition to k-PSPI, the differences in $\overline{\mathrm{IG}}_z^{(\mathrm{aF})}$ between Configurations 2 and 3, when the frequency is greater than 60 Hz, are partly due to the greater effect of tunnel-pile coupling in Configuration 3. This is because the distance from the 30 m piles to the sides of the tunnel in Configuration 3 is only 2 m, whereas the same respective distance in Configuration 2 is 7 m. Thus, based on the conclusions drawn in Section 6.4.5, tunnel-pile coupling is more significant in Configuration 3, as the tunnel-foundation separation distance is less than the S-wavelengths.

Now, consider the added-foundation effect of Configuration 4. Compared to the three other configurations, Configuration 4 causes significantly more attenuation in the vertical response between 15 and 60 Hz, with a minimum $\overline{\mathrm{IG}}_z^{(\mathrm{aF})}$ of -20 dB at 32 Hz. The results in Section 6.6 show that when the pile toe lies below or a few metres above the tunnel crown, a more efficient vibration transmission path along the pile increases the vertical pile-head response. As the pile toes in Configuration 1 are just above the tunnel crown and the outer piles in Configurations 2 and 3 descend below the tunnel, the transmission path will be more effective at increasing the vertical response of the centred configurations rather than Configuration 4. This helps explain the attenuation in the vertical response of Configuration 4.

Moreover, Configuration 4 is the only design that produces noticeable amplification in the transverse foundation response, as $\overline{\mathrm{IG}}_y^{(\mathrm{aF})}$ is roughly 10 dB at 80 Hz. Due to the slender nature of each pile, the entire piled foundation is more flexible under bending than axial deformation in the vertical direction. Consequently, when all the piles are located on one side of the tunnel, as in Configuration 4, more flexural motion will be induced in the off-centred foundation rather than the centred foundations and, as a result, will increase the transverse foundation response.

In summary, it is clearly evident from Fig. 7.31 that constructing a piled foundation near a pre-existing railway tunnel can significantly modify the vibration field over the frequency range

of interest. This emphasises that the added-foundation effect, with the inclusion of k-PSPI and tunnel-pile coupling, should not be neglected in prediction tools for ground-borne vibration.

In contrast, Fig. 7.32 shows that the added-building effect of all four configurations is close to 0 dB throughout the entire frequency range. This is in agreement with the conclusions drawn in Section 7.3.2 for a fundamental unit of the foundation-building system. Thus, over the range of frequencies associated with vibration perception, the added-building effect is negligible due to similarities in the impedances of the piles and building.
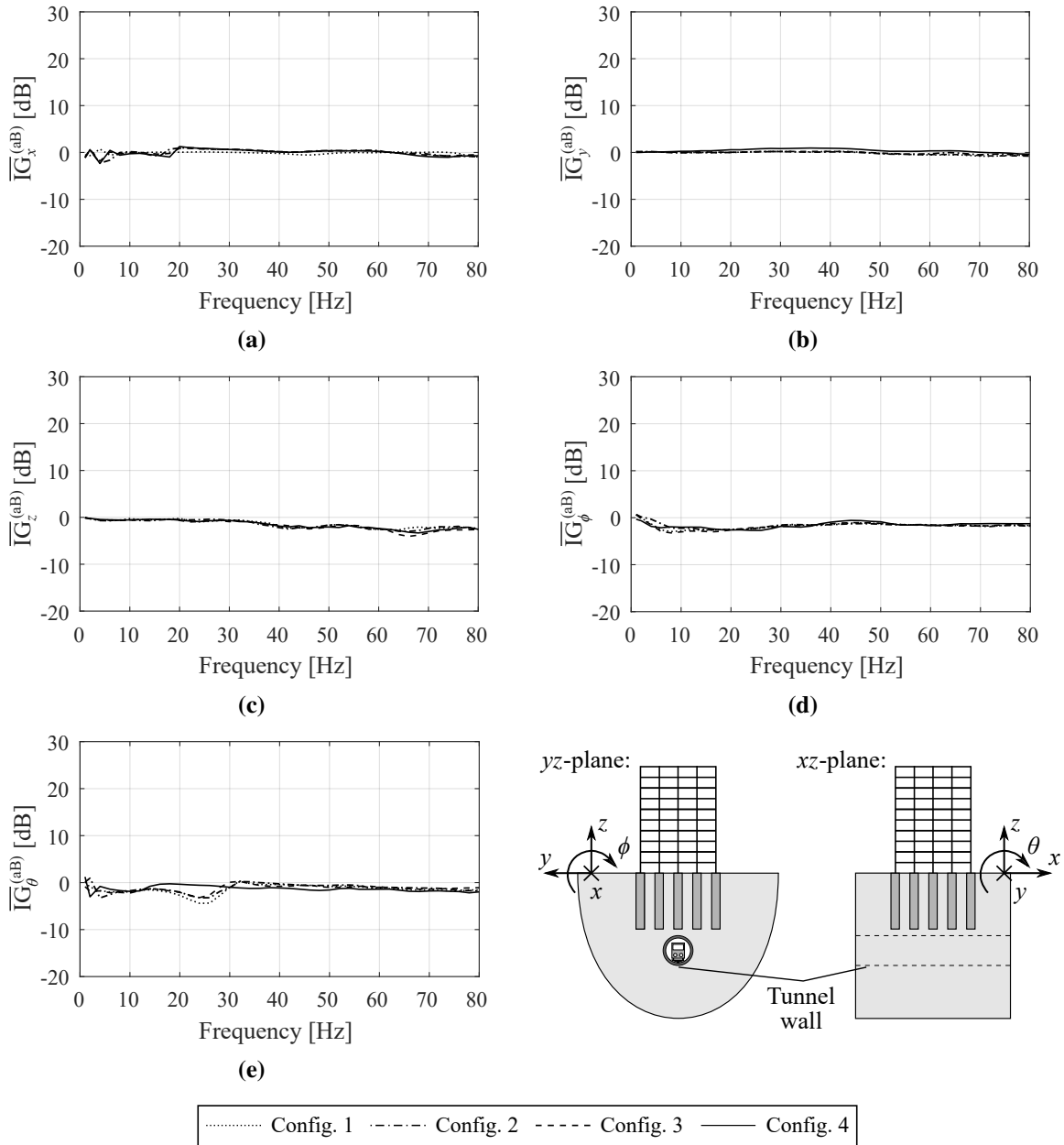
Fig. 7.32 The **(a)** longitudinal, **(b)** transverse, **(c)** vertical and **(d,e)** two rocking mean insertion gains of Configurations 1, 2, 3 and 4, characterising the added-building effect after building construction. The responses are predicted using the Tp-Fb-Bd model.

The results in Fig. 7.32 differ considerably in comparison to the insertion gains predicted by Hussein et al. [117], where the added-building effect of a 2D portal-framed building supported on 10 m piles was around -15 dB at 80 Hz. This discrepancy arises because the semi-analytical approach used by Hussein et al. neglects the presence of soil cavities at the soil-pile interface, so the dynamics of the foundation may not be captured effectively. Note that the $\mathbf{T}_B$ matrix in Eq. (7.6), which characterises the added-building effect, depends on the foundation dynamics.

7.5.3 Comparing the Overall Building Vibration of the Configurations

This section uses the PFIG to compare the overall building vibration of the four configurations by considering Configuration 1 as the baseline design. Since Section 7.5.2 highlighted that the added-building effect is negligible, the mean vibrational power entering the base of the building will be predominantly affected by the added-foundation effect. The PFIG comparing between the train-induced vibration of Configuration i and Configuration 1 is defined as

$$\text{PFIG}^{(\text{config})} = 10\log_{10}\left(\frac{|\bar{P}^{(\text{Config. } i)}|}{|\bar{P}^{(\text{Config. 1})}|}\right), \tag{7.61}$$

where $\bar{P}^{(\text{Config. } i)}$ is the mean power flow entering the building of Configuration i. Figure 7.33 plots the PFIGs comparing the vibration of Configurations 2, 3 and 4 with Configuration 1.

Based on the results, the best design is clearly Configuration 4 because it causes the largest attenuation in the overall building vibration, particularly at the high frequencies. Reassuringly, this is in agreement with the common-sense approach, where a practitioner with a basic grasp of ground-borne vibration might expect the vibration levels to be lowest in the building furthest
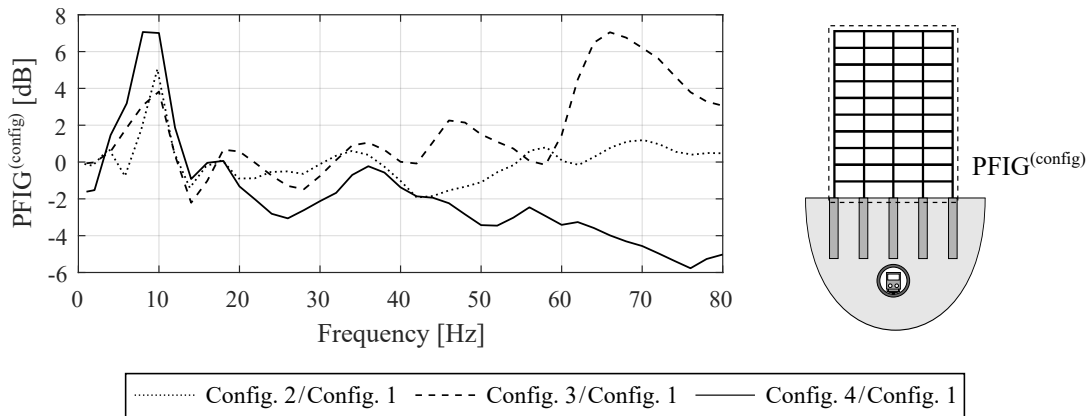
Fig. 7.33 The power-flow insertion gains comparing the overall building vibration in Configurations 2, 3 and 4 with Configuration 1. The responses are predicted using the Tp-Fb-Bd model.

from the underground tunnel due to the effect of radiation damping in the ground. Nevertheless, between 4 and 14 Hz, there is more vibration transmission into the building in Configuration 4 compared to the others, with a maximum PFIG$^{(\text{config})}$ of around 7 dB. Note that the peaks do not directly correspond to the eigenfrequencies of the system, as the PFIG$^{(\text{config})}$, defined in Eq. (7.61), evaluates the differences in the mean power flow entering the respective buildings in two different configurations. Figure 7.33 does not exhibit any eigenfrequencies of the building because it is simulated using the dashpot model, which does not consider the modal behaviour of the building (see Section 7.2.4).

If, however, site regulations constrain the building so that it can only be constructed directly above the pre-existing tunnel, a different design will need to be approved from the three centred configurations. Out of these, the worst design is clearly Configuration 3, as there is significant amplification greater than 5 dB at the high frequencies. This increase in PFIG is brought about by a combination of k-PSPI and tunnel-pile coupling effects. In contrast, Configurations 1 and 2 produce relatively similar vibration responses; on average, the PFIG remains relatively close to 0 dB over the entire frequency range of both designs. In this case, additional factors, other than building vibration, will need to be reviewed before Configurations 1 or 2 is approved.

One factor that is important to consider when constructing close to underground railways is the tunnel exclusion zone, which is defined as an area around the tunnel perimeter that cannot be encroached by planned developments. The size of the exclusion zone can vary depending on the tunnel's location and its diameter, but, in general, it includes the area that is 3 m away from each side of the tunnel and 6 m above the tunnel crown [230, 231]. Thus, based on the response of the buildings and the subterranean clearance between the piles and the tunnel, Configuration 2 is the only design that can be approved out of the three centred configurations.

7.5.4 The Effects of Partial and Full Base Isolation in Configuration 4

The effect of installing full base isolation to mitigate the building vibration was investigated in Section 7.4.3, where isolators were fitted to the base of every column in the benchmark building. However, the installation cost for full isolation can be expensive when the building footprint covers a large area, such as the residential building in the present study. In this case, partial base isolation could be a potential solution, where only particular columns that contribute heavily to the transmission of vibration are isolated to cut costs. An initial numerical study by Heaton & Talbot [95], which looked at isolating a 2D portal-framed building supported on footings from

incident R-waves, has shown that partial base isolation can be as effective as full base isolation, provided the ground vibration is localised near a particular region of the wide building footprint.

In this section, the effectiveness of using partial and full base isolation in Configuration 4 is analysed. Configuration 4 is chosen because the foundation is positioned on the left-hand side of the railway tunnel, as illustrated in Figure 7.30, so the building can be partially isolated by installing isolation at the base of the columns near the tunnel. Figure 7.34 shows the different isolation layouts that are investigated in this section. Firstly, Layout 1 provides partial isolation at the right-most row of columns parallel to the tunnel. Then, from Layouts 2 to 4, the number of rows of base-isolated columns is incrementally increased to isolate a greater footprint of the building's right-hand side. Finally, Layout 5 presents the fully base-isolated building.

By comparing against the unisolated case, the isolation PFIGs of the five different layouts are plotted in Fig. 7.35. The effect of using the 'very high' and 'high' isolation steel springs in Table 7.2 on the isolation performance is also illustrated. These springs are used in this section because they were effective at isolating the benchmark building in Section 7.4.3.

Considering the partial isolation in Layouts 1 and 2, both are ineffective at mitigating the building vibration, as only the right-side columns are isolated. Therefore, the vibration induced in the left-side piles can be freely transmitted across the greater number of unisolated columns. Furthermore, in both layouts, there is no significant difference in the performance of the 'very high' and 'high' isolation cases, as the vibration transmission across the unisolated columns significantly outweighs the attenuation provided by the springs.

When the number of base-isolated columns is incrementally increased, from Layouts 2 to 4, the performance of the partial isolation improves, with Layout 4 providing an acceptable PFIG
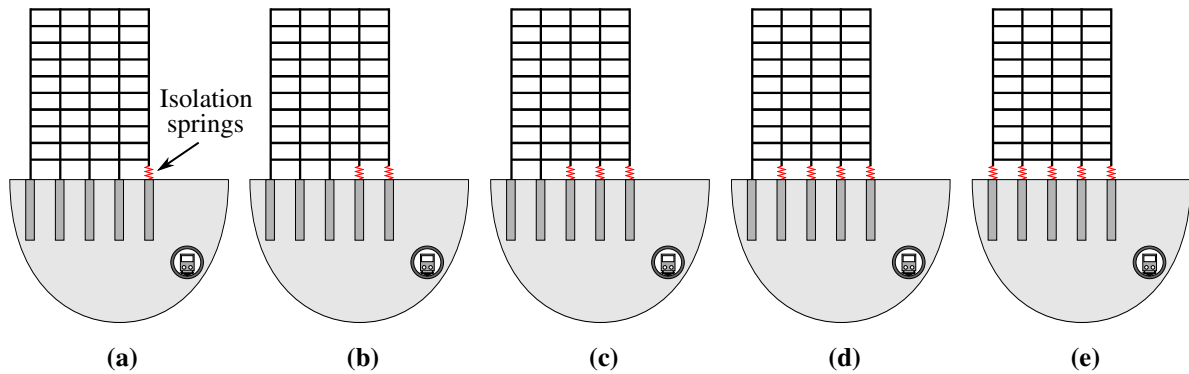
Fig. 7.34 Schematic diagrams of five different base isolation layouts for the building in Configuration 4. Layouts **(a)** 1, **(b)** 2, **(c)** 3 and **(d)** 4 represent different forms of partial base isolation as the number of base-isolated columns is incrementally increased, while **(e)** Layout 5 represents full base isolation.

of -10 dB at 80 Hz. As the frequency is initially increased, the use of 'very high' isolation in Layouts 3 and 4 is more effective at mitigating the building vibration than the 'high' isolation. This is consistent with Fig. 7.26, where the performance of a fully isolated building is studied. However, at frequencies above 50 Hz, the PFIGs of the two spring systems in each layout tend to converge and remain approximately constant, without further improving the isolation as the frequency is increased. This means that any additional isolation provided by the springs at the high frequencies is balanced by increased vibration transmission across the unisolated left-side
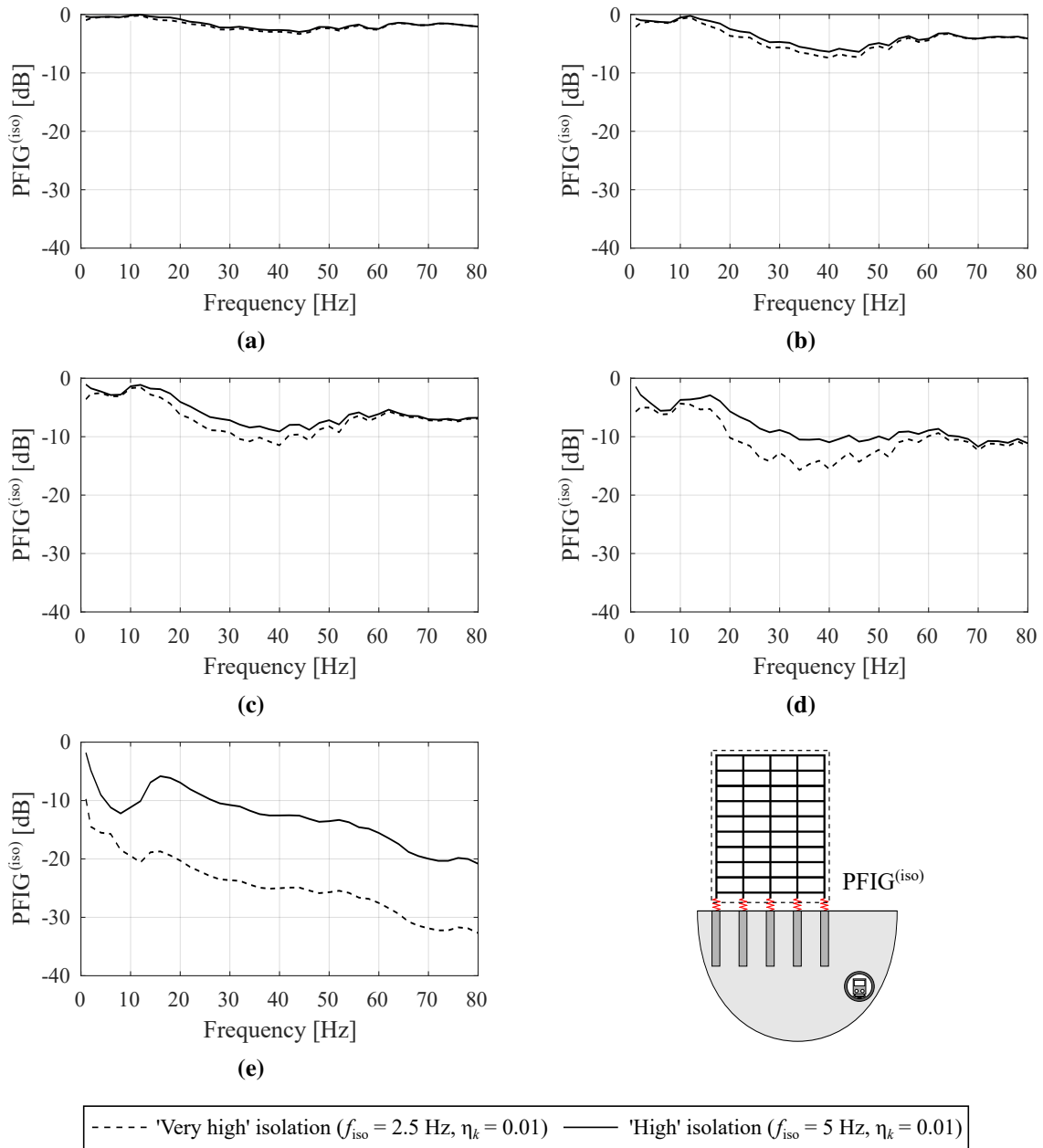
Fig. 7.35 The isolation power-flow insertion gains of Layouts (a) 1, (b) 2, (c) 3, (d) 4 and (e) 5 of the respective base-isolated buildings in Fig. 7.34. The effect of installing 'very high' and 'high' isolation springs on the responses, predicted using the Tp-Fb-Bd model, is also illustrated.

columns, which diminishes the performance of the partially base-isolated buildings compared to the fully isolated case.

In summary, with regards to mitigating the overall vibration of an entire building supported on piles, it is found that partial isolation is not as effective as full isolation. Nevertheless, it is conceivable that the former could be used to isolate specific areas of the building, such as rooms containing vibration-sensitive equipment [95]. In addition to the isolation performance, other factors have to be considered in practice before selecting a base isolation system. These include the system's static and dynamic load capacities; the ambient temperature, which is particularly relevant for elastomeric systems; the cost of installation and maintenance; and the service life.

7.6 Conclusions

In order to capture the fundamental dynamics of a coupled tunnel-foundation-building system, the generalised model presented in Section 7.1 has been used to combine the iterative PiP-BEM model of a tunnel-foundation system with simplified building models. Section 7.2 highlighted that the dashpot model, which simulates the entire building as a collection of independent semi-infinite columns, successfully captured the frequency-averaged variation of the added-building effect and the mean vibrational power entering the benchmark building. This is because, across the range of frequencies associated with the perception of ground-borne vibration (1-80 Hz), the modal behaviour and through-floor coupling of the building have a negligible effect on the vibration at its base.

Section 7.3 emphasised that the transverse added-column effects of both the footing-column and pile-column systems were negligible. In contrast, the vertical added-column effect resulted in a significantly greater decrease in the train-induced vibration of the footing-column system than the pile-column system because of differences in axial impedance between the footings and columns. However, in the context of the entire foundation-building system, the differences between the power-flow insertion gain (PFIG) of a tall building supported on deep piles and shallow footings were not very significant. As the length of the piles was increased, the general frequency-dependent trends in the PFIG of the centred and the off-centred tunnel-foundation-building systems were similar to the trends observed in the parametric study in Section 6.6.

Through the use of power-flow techniques, Section 7.4 demonstrated that full base isolation could effectively mitigate the vibration induced in a tall building due to an underground railway, provided that the isolation frequency was below 10 Hz. The isolation system was most effective

at attenuating the axial vibration of the building. However, there was notably less attenuation in the flexural vibration due to the high lateral flexibility of tall buildings. Furthermore, when the isolation frequency was greater than 10 Hz, the resulting increase in the lateral stiffness of the isolation system adversely amplified the overall vibration of the building at certain excitation frequencies. Hence, it is recommended to evaluate the isolation performance of a base-isolated building against train-induced vibration by considering the mean vibrational power entering the building at different excitation frequencies.

The virtual case study presented in Section 7.5 showed that the added-building effect due to constructing a foundation-building system near a pre-existing railway tunnel was negligible. The overall train-induced vibration of the building was instead significantly dominated by the added-foundation effect due to 3SI in the ground. By using the PFIG to compare between the mean vibrational power entering the building of four different configurations, Configuration 4 was found to be the best at attenuating the train-induced response. Moreover, the use of partial base isolation in Configuration 4 was not as effective as using full base isolation at mitigating the overall vibration of the building.

Chapter 8

Conclusions and Further Work Recommendations

This chapter reviews the original objectives of the research and considers the extent to which they have been met. The conclusions from the work of previous chapters are summarised and, based on these, recommendations are then made for further work.

8.1   Conclusions

The main aim of this research has been to develop efficient, numerical models that account for the essential dynamic interaction between piled foundations and nearby underground railway tunnels as a means of predicting the train-induced vibration in three-dimensional space. To this end, a number of specific objectives were set, as stated in Section 1.2. These are now reviewed, and consideration is given to the extent to which they have been met.

A comprehensive, coupled model of a general piled foundation has been developed using the boundary-element method (BEM) in Chapter 3 that considers the behaviour of each pile due to inertial excitation at the pile heads and pile-soil-pile interaction (PSPI) between neighbouring piles. Furthermore, a novel iterative approach has been developed in Chapter 4 using a source-receiver BEM model to account for the wave-scattering effect of pile-groups that becomes more significant at high frequencies. The coupled and iterative BEM models were formulated in the space-frequency (x, ω)-domain, and the head of each pile accounted for motion in five degrees of freedom: three translations in the x-, y- and z-axes; and two rotations about the lateral x- and y-axes. Both models showed good agreement in predicting the pile-group response over a broad range of non-dimensional frequencies a_0, corresponding to ground-borne vibration between 1 and 160 Hz – well above existing models. An extensive parametric study highlighted that the dynamic interaction factors, predicted using uncoupled source-receiver models, can effectively

account for the PSPI without resorting to fully coupled models. Furthermore, an isolated two-pile model provided a good approximation for the interaction factors of adjacent piles in large pile-groups, although the presence of intermediate piles might need to be considered at high frequencies due to wave scattering.

In order to predict the essential dynamic behaviour of a coupled tunnel-foundation system, the iterative approach has been used in Chapter 6 to combine the BEM foundation model with the pipe-in-pipe (PiP) model of an underground tunnel. Since the PiP model is formulated in the wavenumber-frequency (ξ, ω)-domain to account for the longitudinally-invariant nature of the tunnel, Fourier techniques have been utilised to appropriately couple the tunnel and foundation models. The excitation due to a train was simulated by a spatially harmonic roughness applied onto the train-track system at the tunnel invert. By comparison with the results from a rigorous FEM-BEM model, the accuracy of the iterative PiP-BEM model has been shown to be good at capturing the interaction between the ground surface and shallow tunnels over the excitation frequencies between 1 and 80 Hz, which is the frequency range associated with the perception of ground-borne vibration. For the first time in the available literature, the iterative PiP-BEM model also efficiently captured the structure-soil-structure interaction (3SI) due to tunnel-pile interaction between the source and receiver, as well as pile-pile interaction within the receiver itself.

The change in the greenfield vibration when a pile is embedded in the ground is known as the added-pile effect, which can be evaluated using the insertion gain. The initial test cases in Chapter 6, involving the construction of single piles and pile-groups near underground railways, highlighted new features of the added-pile effect that will give valuable insight to practitioners. It was observed that the significance of kinematic PSPI depended on the length of the piles and their location and orientation relative to the tunnel. For example, when multiple rows of piles were positioned parallel to the tunnel, significant differences of up to 14 dB were observed in the insertion gain at high frequencies. Furthermore, when the separation distance between the tunnel and the piles was less than the shear wavelengths in the soil, tunnel-pile coupling caused the mean insertion gain of the entire foundation to vary by as much as ± 10 dB, particularly in the longitudinal direction. Moreover, the novel parametric study of the train-induced vibration of a single pile clearly showed that the soil-pile density ratio ρ_s/ρ_p has an insignificant impact on the added-pile effect, while the pile length L, the tunnel depth D, and the soil-pile stiffness ratio E_s/E_p can significantly influence the response. Two counteracting mechanisms governing

the pile-head displacement were also identified: (1) the soil-stiffening effect, which attenuated the response as the pile length was initially increased; and (2) the enhanced transmission effect, which amplified the response when the pile toe was just above the tunnel crown or descended below it.

Finally, in Chapter 7, simplified building models were combined with the iterative PiP-BEM model to simulate the essential dynamics of the entire tunnel-foundation-building system. The dashpot model, which assumes that the building behaves as a collection of independent semi-infinite columns, effectively captured the frequency-averaged variation in the mean vibrational power entering a tall benchmark building. It was also highlighted that the added-building effect, defined as the change in the piled foundation response when the building is constructed, was negligible over the entire frequency range of interest (1-80 Hz). Therefore, the general trends of the building response were similar to the trends observed in the response of the foundation itself. This emphasises that the model used for the foundation-building system needs to capture the wave interaction in the ground due to soil-embedded structures, as it dominates the overall vibration response of the building. In terms of vibration mitigation, initial tests have shown that full base isolation is more effective than partial base isolation at mitigating the overall building vibration, particularly at the high frequencies. A virtual case study concerning the construction of a residential building near a pre-existing railway tunnel also demonstrated how the models developed in this dissertation could be used in practice to mitigate the ground-borne vibration. These conclusions are expected to help establish new guidelines for designing buildings, and their foundations, near underground railway tunnels.

8.2   Further Work Recommendations

The coupled tunnel-foundation-building model, as it stands, provides an efficient and versatile means of analysing the ground-borne vibration of the entire system. There are several valuable studies, in addition to those presented in Chapter 7, which may be undertaken with little further development. These include, but are not limited to, the following studies: the effect of different foundation and building arrangements on their respective responses; the significance of adding pile caps and ground beams on the piled foundation response; and the effect of side-restraint bearings on the performance of base-isolated buildings.

In their present form, the numerical models developed in this dissertation assume that the soil behaves as a homogeneous half-space. While this assumption accounts for the main body

(pressure and shear) waves and surface (Rayleigh) waves, it does not capture the elastodynamic waves due to layering, as described in Section 2.3.2. In reality, the soil is stratified, with each soil layer defined by different material properties. Layering is expected to introduce additional wave reflections and mode conversions at the soil-layer interfaces, and this is likely to affect the pile-pile and tunnel-pile interactions at the high frequencies associated with ground-borne vibration. The ElastoDynamics Toolbox [211], developed at KU Leuven, provides an extensive set of MATLAB functions for computing the Green's functions that simulate wave propagation in a layered half-space. Using these layered Green's functions in the iterative PiP-BEM model, additional wave-scattering effects at the soil-layer interfaces may be captured.

Further work is required to improve the boundary-element mesh used for the soil-structure interfaces of the foundation and tunnel, so that accurate predictions can be made at excitation frequencies above 80 Hz. There are two possibilities worth exploring. Firstly, the use of higher-order elements could reduce the total number of elements required to achieve the same accuracy as the constant elements used in the current formulation. Secondly, while the author made every effort to write computationally efficient code that executes the BEM in the numerical models, better performance could be achieved using commercially available boundary-element code.

There also remains a need to experimentally validate the piled foundation model, the tunnel-foundation model, and the final tunnel-foundation-building model for the entire fully coupled system. To this end, future construction projects should be identified, and attempts made to gain access for taking measurements from real buildings near underground railway tunnels.

In general, this dissertation has shown that the newly developed iterative wave-scattering approach can capture the dynamic coupling between a source sub-system and a receiver sub-system for the case of pile-pile and tunnel-pile interaction. Therefore, the iterative approach is worthy of further development to solve more complex problems in the field of elastodynamics. One such problem is the ground-borne vibration near underground basements, for which there is no evidence-based guidance on vibration mitigation. The iterative approach may be extended to account for the through-soil coupling between basements and various subterranean structures (foundations, sewers, water pipes, railway tunnels, etc.) when modelling this problem.

References

[1] G. M. Álamo, J. D. R. Bordón, J. J. Aznárez, & G. Lombaert, "The effectiveness of a pile barrier for vibration transmission in a soil stratum over a rigid bedrock," *Comput. Geotech.*, vol. 110, pp. 274–286, 2019. [Online]. Available: https://doi.org/10.1016/J.COMPGEO.2019.02.022

[2] L. V. Andersen & C. J. C. Jones, "Coupled boundary and finite element analysis of vibration from railway tunnels – A comparison of two- and three-dimensional models," *J. Sound Vib.*, vol. 293, no. 3-5, pp. 611–625, 2006. [Online]. Available: https://doi.org/10.1016/J.JSV.2005.08.044

[3] J. R. Astley, "Numerical acoustical modeling (finite element modeling)," in *Handbook of Noise and Vibration Control*, M. Crocker, Ed., ch. 7, pp. 101–115. New Jersey, U.S.A.: John Wiley & Sons, 2007.

[4] T. Astrauskas & R. Grubliauskas, "Modelling of ground borne vibration induced by road transport," *Sci. Future Lith.*, vol. 9, no. 4, pp. 376–380, 2017. [Online]. Available: https://doi.org/10.3846/mla.2017.1060

[5] J. H. Atkinson, *The Mechanics of Soils and Foundations*, 2nd ed. London, U.K.: Taylor & Francis, 2007.

[6] L. Auersch, "The excitation of ground vibration by rail traffic: Theory of vehicle–track–soil interaction and measurements on high-speed lines," *J. Sound Vib.*, vol. 284, no. 1-2, pp. 103–132, 2005. [Online]. Available: https://doi.org/10.1016/J.JSV.2004.06.017

[7] L. Auersch, "Response to harmonic wave excitation of finite or infinite elastic plates on a homogeneous or layered half-space," *Comput. Geotech.*, vol. 51, pp. 50–59, 2013. [Online]. Available: https://doi.org/10.1016/j.compgeo.2013.02.001

[8] P. K. Banerjee & S. M. Mamoon, "A fundamental solution due to a periodic point force in the interior of an elastic half-space," *Earthq. Eng. Struct. Dyn.*, vol. 19, no. 1, pp. 91–105, 1990. [Online]. Available: https://doi.org/10.1002/eqe.4290190109

[9] V. A. Baranov, "On the calculation of excited vibrations of an embedded foundation (in Russian)," *Voprosy Dynamiki i Prochnocti*, vol. 14, pp. 195–209, 1967.

[10] K.-J. Bathe, *Finite Element Procedures in Engineering Analysis*. New Jersey, U.S.A.: Prentice-Hall, 1982.

[11] K.-J. Bathe & E. L. Wilson, "Stability and accuracy analysis of direct integration methods," *Earthq. Eng. Struct. Dyn.*, vol. 1, no. 3, pp. 283–291, 1972. [Online]. Available: https://doi.org/10.1002/eqe.4290010308

[12] G. Beer, I. M. Smith, & C. Duenser, *The Boundary Element Method with Programming: For Engineers and Scientists*, 1st ed. Berlin, Germany: Springer-Verlag, 2008.

[13] J.-P. Bérenger, "A perfectly matched layer for the absorption of electromagnetic waves," *J. Comput. Phys.*, vol. 114, no. 2, pp. 185–200, 1994. [Online]. Available: https://doi.org/10.1006/jcph.1994.1159

[14] D. E. Beskos, "Wave propagation through ground," in *Boundary Element Techniques in Geomechanics*, G. D. Manolis & T. G. Davies, Eds., ch. 11, pp. 359–406. Elsevier Science, 1993.

[15] P. Bettess & O. C. Zienkiewicz, "Diffraction and refraction of surface waves using finite and infinite elements," *Int. J. Numer. Methods Eng.*, vol. 11, no. 8, pp. 1271–1290, 1977. [Online]. Available: https://doi.org/10.1002/nme.1620110808

[16] X.-C. Bian, W.-F. Jin, & H.-G. Jiang, "Ground-borne vibrations due to dynamic loadings from moving trains in subway tunnels," *J. Zhejiang Univ. Sci. A*, vol. 13, no. 11, pp. 870–876, 2012. [Online]. Available: https://doi.org/10.1631/jzus.A12ISGT5

[17] J. Bielak, K. Loukakis, Y. Hisada, & C. Yoshimura, "Domain reduction method for three-dimensional earthquake modeling in localized regions, Part I: Theory," *Bull. Seismol. Soc. Am.*, vol. 93, no. 2, pp. 817–824, 2003. [Online]. Available: https://doi.org/10.1785/0120010251

[18] D. R. Bland, *Theory of Linear Viscoelasticity*. Oxford, U.K.: Pergamon Press, 1960.

[19] T. Bloch, R. Sacks, & O. Rabinovitch, "Interior models of earthquake damaged buildings for search and rescue," *Adv. Eng. Inf.*, vol. 30, no. 1, pp. 65–76, 2016. [Online]. Available: https://doi.org/10.1016/J.AEI.2015.12.001

[20] C. A. Brebbia & J. Domínguez, *Boundary Elements An Introductory Course*, 2nd ed. Southampton, U.K.: WIT Press, 1994.

[21] British Standards Institution, *Guide to measurement and evaluation of human exposure to whole-body mechanical vibration and repeated shock*. BS 6841:1987, 1987.

[22] British Standards Institution, *Evaluation and measurement for vibration in buildings, Part 2: Guide to damage levels from groundborne vibration*. BS 7385-2:1993, 1993.

[23] British Standards Institution, *Description and measurement of environmental noise, Part 1: Guide to quantities and procedures*. BS 7445-1:2003, 2003.

[24] British Standards Institution, *Guide to evaluation of human exposure to vibration in buildings, Part 1: Vibration sources other than blasting*. BS 6472-1:2008, 2008.

[25] British Standards Institution, *Code of Practice for Foundations*. BS 8004:2015, 2015.

[26] D. Brookes, W. I. Hamad, J. P. Talbot, H. E. M. Hunt, & M. F. M. Hussein, "The dynamic interaction effects of railway tunnels: Crossrail and the Grand Central recording studios," *Proc. Inst. Mech. Eng., Part F: J. Rail Rapid Transit*, vol. 232, no. 2, pp. 542–559, 2018. [Online]. Available: https://doi.org/10.1177/0954409716679446

[27] A. J. Burton & G. F. Miller, "The application of integral equation methods to the numerical solution of some exterior boundary-value problems," *Proc. R. Soc. Lond. A*, vol. 323, no. 1553, pp. 201–210, 1971. [Online]. Available: https://doi.org/10.1098/rspa.1971.0097

[28] R. C. Y. Chin, "Dispersion and Gibbs phenomenon associated with difference approximations to initial boundary-value problems for hyperbolic equations," *J. Comput. Phys.*, vol. 18, no. 3, pp. 233–247, 1975. [Online]. Available: https://doi.org/10.1016/0021-9991(75)90001-7

[29] V. G. Cleante, M. J. Brennan, G. Gatti, & D. J. Thompson, "On the spectrum of rail vibration generated by a passing train," *Procedia Eng.*, vol. 199, pp. 2657–2662, 2017. [Online]. Available: https://doi.org/10.1016/J.PROENG.2017.09.532

[30] R. W. Clough & J. Penzien, *Dynamics of Structures*, 2nd ed. New York, U.S.A.: McGraw-Hill, 1993.

[31] D. Clouteau, M. Arnst, T. M. Al-Hussaini, & G. Degrande, "Freefield vibrations due to dynamic loading on a tunnel embedded in a stratified medium," *J. Sound Vib.*, vol. 283, no. 1-2, pp. 173–199, 2005. [Online]. Available: https://doi.org/10.1016/J.JSV.2004.04.010

[32] D. Clouteau, D. Broc, G. Devésa, V. Guyonvarh, & P. Massin, "Calculation methods of Structure-Soil-Structure Interaction (3SI) for embedded buildings: Application to NUPEC tests," *Soil Dyn. Earthq. Eng.*, vol. 32, no. 1, pp. 129–142, 2012. [Online]. Available: https://doi.org/10.1016/j.soildyn.2011.08.005

[33] D. Clouteau, R. Cottereau, & G. Lombaert, "Dynamics of structures coupled with elastic media – A review of numerical models and methods," *J. Sound Vib.*, vol. 332, no. 10, pp. 2415–2436, 2013. [Online]. Available: https://doi.org/10.1016/J.JSV.2012.10.011

[34] D. Clouteau, M. L. Elhabre, & D. Aubry, "Periodic BEM and FEM-BEM coupling: application to seismic behaviour of very long structures," *Comput. Mech.*, vol. 25, no. 6, pp. 567–577, 2000. [Online]. Available: https://doi.org/10.1007/s004660050504

[35] C. Cobbing, J. Webb, & O. Bewes, "Control of Railway Induced Grounborne Noise and Vibration from the UK's Crossrail Project," Crossrail Learning Legacy, 2018.

[36] H. B. Coda & W. S. Venturini, "On the coupling of 3D BEM and FEM frame model applied to elastodynamic analysis," *Int. J. Solids Struct.*, vol. 36, no. 31-32, pp. 4789–4804, 1999. [Online]. Available: https://doi.org/10.1016/S0020-7683(98)00265-0

[37] H. B. Coda, W. S. Venturini, & M. H. Aliabadi, "A general 3D BEM/FEM coupling applied to elastodynamic continua/frame structures interaction analysis," *Int. J. Numer. Methods Eng.*, vol. 46, no. 5, pp. 695–712, 1999. [Online]. Available: https://doi.org/10.1002/(SICI)1097-0207(19991020)46:5<695::AID-NME692>3.0.CO;2-M

[38] A. Colaço, P. Alves Costa, & D. P. Connolly, "The influence of train properties on railway ground vibrations," *Struct. Infrastruct. Eng.*, vol. 12, no. 5, pp. 517–534, 2015. [Online]. Available: https://doi.org/10.1080/15732479.2015.1025291

[39] D. P. Connolly, G. Kouroussis, O. Laghrouche, C. L. Ho, & M. C. Forde, "Benchmarking railway vibrations – Track, vehicle, ground and building effects," *Constr. Build. Mater.*, vol. 92, pp. 64–81, 2015. [Online]. Available: https://doi.org/10.1016/J.CONBUILDMAT.2014.07.042

[40] D. P. Connolly, G. P. Marecki, G. Kouroussis, I. Thalassinakis, & P. K. Woodward, "The growth of railway ground vibration problems – A review," *Sci. Total Environ.*, vol. 568, pp. 1276–1282, 2016. [Online]. Available: https://doi.org/10.1016/J.SCITOTENV.2015.09.101

[41] M. Costabel, "Principles of boundary element methods," *Comput. Phys. Rep.*, vol. 6, no. 1-6, pp. 243–274, 1987. [Online]. Available: https://doi.org/10.1016/0167-7977(87)90014-1

[42] P. Coulier, *The Vibration Response of Piled Foundations to Inertial and Underground Railway Induced Loadings*, MSc Thesis, KU Leuven, Belgium, 2010.

[43] P. Coulier, G. Degrande, K. A. Kuo, & H. E. M. Hunt, "A comparison of two models for the vibration response of piled foundations to inertial and underground-railway-induced loadings," in *Proc. 17th Int. Congr. Sound Vib. (ICSV17)*, vol. 2, pp. 1512–1519, Cairo, Egypt, 2010.

[44] P. Coulier, G. Lombaert, & G. Degrande, "The influence of source-receiver interaction on the numerical prediction of railway induced vibrations," *J. Sound Vib.*, vol. 333, no. 12, pp. 2520–2538, 2014. [Online]. Available: https://doi.org/10.1016/J.JSV.2014.01.017

[45] S. H. Crandall, "The hysteretic damping model in vibration theory," *Proc. Inst. Mech. Eng., Part C: J. Mech. Eng. Sci.*, vol. 205, no. 1, pp. 23–28, 1991. [Online]. Available: https://doi.org/10.1243/PIME_PROC_1991_205_086_02

[46] L. Cremer, M. Heckl, & B. A. T. Petersson, *Structure-Borne Sound: Structural Vibrations and Sound Radiation at Audio Frequencies*, 3rd ed. Berlin, Germany: Springer-Verlag, 2005.

[47] Crossrail, "Groundborne Noise and Vibration Prediction Validation on DLR Greenwich," Cross London Rail Links Limited, London, U.K., 2004.

[48] D. P. Cryer, *Modelling of Vibration in Buildings with Applications to Base Isolation*, PhD Thesis, University of Cambridge, U.K., 1994.

[49] D. de Domenico, G. Ricciardi, & I. Takewaki, "Design strategies of viscous dampers for seismic protection of building structures: A review," *Soil Dyn. Earthq. Eng.*, vol. 118, pp. 144–165, 2019. [Online]. Available: https://doi.org/10.1016/J.SOILDYN.2018.12.024

[50] G. Degrande, D. Clouteau, R. Othman, M. Arnst, H. Chebli, R. Klein, P. Chatterjee, & B. Janssens, "A numerical model for ground-borne vibrations from underground railway traffic based on a periodic finite element-boundary element formulation," *J. Sound Vib.*, vol. 293, no. 3-5, pp. 645–666, 2006. [Online]. Available: https://doi.org/10.1016/j.jsv.2005.12.023

[51] R. Dobry & G. Gazetas, "Simple method for dynamic stiffness and damping of floating pile groups," *Géotechnique*, vol. 38, no. 4, pp. 557–574, 1988. [Online]. Available: https://doi.org/10.1680/geot.1988.38.4.557

[52] J. Domínguez, *Boundary Elements in Dynamics*. Southampton, U.K.: Elsevier Science, 1993.

[53] C. H. Dowding, *Construction Vibrations*. Essex, U.K.: Pearson Education, 1996.

[54] T. E. Doyle, "Iterative simulation of elastic wave scattering in arbitrary dispersions of spherical particles," *J. Acoust. Soc. Am.*, vol. 119, pp. 2599–2610, 2006. [Online]. Available: https://doi.org/10.1121/1.2184989

[55] T. L. Edirisinghe & J. P. Talbot, "A parametric study of the train-induced vibration of a single pile located near an underground railway tunnel," (in press) *Soil Dyn. Earthq. Eng.*, 2022. [Online]. Available: https://doi.org/10.1016/j.soildyn.2022.107274

[56] T. L. Edirisinghe & J. P. Talbot, "Inertial interaction in pile-groups: A study of the influence of coupling via an iterative wave-scattering approach," *Comput. Geotech.*, vol. 128, pp. 103 804–1–15, 2020. [Online]. Available: https://doi.org/10.1016/j.compgeo.2020.103804

[57] T. L. Edirisinghe & J. P. Talbot, "The significance of source-receiver interaction in the response of piled foundations to ground-borne vibration from underground railways," *J. Sound Vib.*, vol. 506, pp. 116 178–1–18, 2021. [Online]. Available: https://doi.org/10.1016/j.jsv.2021.116178

[58] T. L. Edirisinghe, J. P. Talbot, & M. F. M. Hussein, "Accounting for the influence of the free surface on the vibration response of underground railway tunnels: a new iterative method," in *Proc. Int. Conf. Noise Vib. Eng. (ISMA 2020)*, pp. 2655–2664, Leuven, Belgium, 2020.

[59] European Standard, *Eurocode - Basis of structural design*. EN 1990:2002/A1:2005, 2002.

[60] European Standard, *Eurocode 1: Actions on structures - Part 1-1: General actions - Densities, self-weight,imposed loads for buildings*. EN 1991-1-1:2002, 2002.

[61] European Standard, *Eurocode 7: Geotechnical design - Part 1: General rules*. EN 1997-1:2004, 2004.

[62] K. Fan, G. Gazetas, A. M. Kaynia, E. Kausel, & S. Ahmad, "Kinematic seismic response of single piles and pile groups," *J. Geotech. Eng.*, vol. 117, no. 12, pp. 1860–1879, 1991. [Online]. Available: https://doi.org/10.1061/(ASCE)0733-9410(1991)117:12(1860)

[63] O. Farrell, "From acoustic specification to handover. A practical approach to an effective and robust system for the design and construction of base (vibration) isolated buildings," in *Proc. 24th Int. Congr. Sound Vib. (ICSV24)*, London, U.K., 2017.

[64] J. G. Fikioris & P. C. Waterman, "Multiple scattering of waves. Part II: 'Hole corrections' in the scalar case," *J. Math. Phys.*, vol. 5, no. 10, pp. 1413–1420, 1964. [Online]. Available: https://doi.org/10.1063/1.1704077

[65] J. G. Fikioris & P. C. Waterman, "Multiple scattering of waves. Part III: The electromagnetic case," *J. Quant. Spectrosc. Radiat. Transfer*, vol. 123, pp. 8–16, 2013. [Online]. Available: https://doi.org/10.1016/J.JQSRT.2012.09.007

[66] W. Flügge, *Stresses in Shells*, 2nd ed. Berlin, Germany: Springer-Verlag, 1973. [Online]. Available: https://doi.org/10.1007/978-3-642-88291-3

[67] J. A. Forrest, "Vibration-isolation performance of floating slab track used in underground railways," in *Proc. 5th Int. Congr. Sound Vib. (ICSV5)*, pp. 2665–2672, Adelaide, Australia, 1997.

[68] J. A. Forrest, *Modelling of Ground Vibration from Underground Railways*, PhD Thesis, University of Cambridge, U.K., 1999.

[69] J. A. Forrest & H. E. M. Hunt, "A three-dimensional tunnel model for calculation of train-induced ground vibration," *J. Sound Vib.*, vol. 294, no. 4-5, pp. 678–705, 2006. [Online]. Available: https://doi.org/10.1016/j.jsv.2005.12.032

[70] S. François, M. Schevenels, P. Galvín, G. Lombaert, & G. Degrande, "A 2.5D coupled FE–BE methodology for the dynamic interaction between longitudinally invariant structures and a layered halfspace," *Comput. Methods Appl. Mech. Eng.*, vol. 199, no. 23-24, pp. 1536–1548, 2010. [Online]. Available: https://doi.org/10.1016/J.CMA.2010.01.001

[71] F. Frederich, "Die Gleislage – aus fahrzeugtechnischer Sicht [Effect of track geometry on vehicle performance]," *Zeitschrift für Eisenbahnwesen und Vekehrstechnik – Glasers Annalen*, vol. 108, no. 12, pp. 355–362, 1984.

[72] P. Galvín, S. François, M. Schevenels, E. Bongini, G. Degrande, & G. Lombaert, "A 2.5D coupled FE-BE model for the prediction of railway induced vibrations," *Soil Dyn. Earthq. Eng.*, vol. 30, no. 12, pp. 1500–1512, 2010. [Online]. Available: https://doi.org/10.1016/J.SOILDYN.2010.07.001

[73] G.-Y. Gao, Z.-Y. Li, C. Qiu, & Z.-Q. Yue, "Three-dimensional analysis of rows of piles as passive barriers for ground vibration isolation," *Soil Dyn. Earthq. Eng.*, vol. 26, no. 11, pp. 1015–1027, 2006. [Online]. Available: https://doi.org/10.1016/J.SOILDYN.2006.02.005

[74] G. Gazetas, "Soil dynamics: An overview," in *Dynamic Behaviour of Foundations and Buried Structures: Vol. 3*, P. K. Banerjee & R. Butterfield, Eds., ch. 1, pp. 1–39. Essex, U.K.: Elsevier Science, 1987.

[75] G. Gazetas, "Foundation Vibrations," in *Foundation Engineering Handbook*, 2nd ed., H.-V. Fang, Ed., ch. 15, pp. 553–593. New York, U.S.A.: Van Nostrand Reinhold Co., 1991.

[76] G. Gazetas & R. Dobry, "Horizontal response of piles in layered soils," *J. Geotech. Eng.*, vol. 110, no. 1, pp. 20–40, 1984. [Online]. Available: https://doi.org/10.1061/(ASCE)0733-9410(1984)110:1(20)

[77] G. Gazetas, K. Fan, A. M. Kaynia, & E. Kausel, "Dynamic interaction factors for floating pile groups," *J. Geotech. Eng.*, vol. 117, no. 10, pp. 1531–1548, 1991. [Online]. Available: https://doi.org/10.1061/(ASCE)0733-9410(1991)117:10(1531)

[78] G. Gazetas & N. Makris, "Dynamic pile-soil-pile interaction. Part I: Analysis of axial vibration," *Earthq. Eng. Struct. Dyn.*, vol. 20, no. 2, pp. 115–132, 1991. [Online]. Available: https://doi.org/10.1002/eqe.4290200203

[79] D. C. Gazis, "Three-dimensional investigation of the propagation of waves in hollow circular cylinders. Part I: Analytical foundation," *J. Acoust. Soc. Am.*, vol. 31, no. 5, pp. 568–573, 1959. [Online]. Available: https://doi.org/10.1121/1.1907753

[80] D. C. Gazis, "Three-dimensional investigation of the propagation of waves in hollow circular cylinders. Part II: Numerical results," *J. Acoust. Soc. Am.*, vol. 31, no. 5, pp. 573–578, 1959. [Online]. Available: https://doi.org/10.1121/1.1907754

[81] A. Ghobarah, "Performance-based design in earthquake engineering: State of development," *Eng. Struct.*, vol. 23, no. 8, pp. 878–884, 2001. [Online]. Available: https://doi.org/10.1016/S0141-0296(01)00036-0

[82] K. F. Graff, *Wave Motion in Elastic Solids*. New York, U.S.A.: Dover Publications, 1991.

[83] P. Grootenhuis, "Floating track slab isolation for railways," *J. Sound Vib.*, vol. 51, no. 3, pp. 443–448, 1977. [Online]. Available: https://doi.org/10.1016/S0022-460X(77)80087-4

[84] P. Grootenhuis, "Structural elastomeric bearings and resilient seatings," in *Polymers and polymer composites in construction*, L. C. Hollaway, Ed., ch. 9. London, U.K.: Thomas Telford Publishing, 1990.

[85] S. Gupta, M. F. M. Hussein, G. Degrande, H. E. M. Hunt, & D. Clouteau, "A comparison of two numerical models for the prediction of vibrations from underground railway traffic," *Soil Dyn. Earthq. Eng.*, vol. 27, no. 7, pp. 608–624, 2007. [Online]. Available: https://doi.org/10.1016/j.soildyn.2006.12.007

[86] W. I. Hamad, H. E. M. Hunt, M. F. M. Hussein, & J. P. Talbot, "Tunnel-soil-pile interaction in the prediction of vibration from underground railways: Validation of the sub-models," in *Proc. 9th Eur. Conf. Struct. Dyn. (EURODYN 2014)*, Porto, Portugal, 2014.

[87] W. I. Hamad, H. E. M. Hunt, J. P. Talbot, M. F. M. Hussein, & D. J. Thompson, "The dynamic interaction of twin tunnels embedded in a homogeneous half-space," in *Proc. 5th Int. Conf. Comput. Methods in Struct. Dyn. Earthquake Eng. (COMPDYN 2015)*, pp. 1–13, Crete, Greece, 2015.

[88] W. I. Hamad, E. Ntotsios, H. E. M. Hunt, M. F. M. Hussein, D. J. Thompson, & J. P. Talbot, "Modelling the dynamic pile-soil-pile interaction in a multi-layered half-space," in *Proc. 10th Eur. Congr. Exposition Noise Control Eng. (EuroNoise 2015)*, pp. 1231–1236, Maastricht, Netherlands, 2015.

[89] A. K. Hamid & M. I. Hussein, "Iterative solution to the electromagnetic plane wave scattering by two parallel conducting elliptic cylinders," *J. Electromagn. Waves Appl.*, vol. 17, no. 6, pp. 813–828, 2003. [Online]. Available: https://doi.org/10.1163/156939303322503376

[90] J. Han, X. Xiao, Y. Wu, Z. Wen, & G. Zhao, "Effect of rail corrugation on metro interior noise and its control," *Appl. Acoust.*, vol. 130, pp. 63–70, 2018. [Online]. Available: https://doi.org/10.1016/J.APACOUST.2017.09.007

[91] C. E. Hanson, D. A. Towers, & L. D. Meister, "Transit noise and vibration impact assessment," U.S. Department of Transportation, 2006.

[92] H. Hao, T. C. Ang, & J. Shen, "Building vibration to traffic-induced ground motion," *Build. Environ.*, vol. 36, no. 3, pp. 321–336, 2001. [Online]. Available: https://doi.org/10.1016/S0360-1323%2800%2900010-X

[93] H. M. Hawari & M. H. Murray, "Effects of train characteristics on the rate of deterioration of track roughness," *J. Eng. Mech.*, vol. 134, no. 3, pp. 234–239, 2008. [Online]. Available: https://doi.org/10.1061/(ASCE)0733-9399(2008)134:3(234)

[94] L.-X. He, C. Wu, & J. Li, "Post-earthquake evaluation of damage and residual performance of UHPSFRC piers based on nonlinear model updating," *J. Sound Vib.*, vol. 448, pp. 53–72, 2019. [Online]. Available: https://doi.org/10.1016/J.JSV.2019.02.011

[95] M. J. Heaton & J. P. Talbot, "A power-flow based investigation into the performance of partial base-isolation for mitigating ground-borne noise and vibration in buildings," in *Proc. 22nd Int. Congr. Sound Vib. (ICSV22)*, Florence, Italy, 2015.

[96] M. Heckl, "Measurements of absorption coefficients on plates," *J. Acoust. Soc. Am.*, vol. 34, no. 6, pp. 803–808, 1962. [Online]. Available: https://doi.org/10.1121/1.1918199

[97] M. Heckl, G. Hauck, & R. Wettschureck, "Structure-borne sound and vibration from rail traffic," *J. Sound Vib.*, vol. 193, no. 1, pp. 175–184, 1996. [Online]. Available: https://doi.org/10.1006/JSVI.1996.0257

[98] R. W. Henn, *Practical Guide to Grouting of Underground Structures*. London, U.K.: Thomas Telford Publishing, 1996.

[99] P. Hensen, "The isolation from railway vibration of the BBC Egton Wing, Portland Place, London," in *Proc. 8th Eur. Conf. Noise Control (EuroNoise 2009)*, pp. 3510–3519, Edinburgh, U.K., 2009.

[100] P. Hensen & J. G. Charles, "Vibration isolation of the IMAX Cinema, Waterloo, London," *Proc. Inst. Acoust.*, vol. 22, no. 2, pp. 255–262, 2000.

[101] D. W. Hight, F. McMillan, J. J. M. Powell, R. J. Jardine, & C. P. Allenou, "Some characteristics of London clay," in *Characterisation and Engineering Properties of Natural Soils*, T. S. Tan, K. K. Phoon, D. W. Hight, & S. Leroueil, Eds., vol. 2, pp. 851–907. Tokyo, Japan: Balkema, 2003.

[102] R. Hildebrand, *Countermeasures Against Railway Ground and Track Vibrations*, PhD Thesis, KTH Royal Institute of Technology, Sweden, 2001. [Online]. Available: https://urn.kb.se/resolve?urn=urn:nbn:se:kth:diva-3263

[103] D. M. Hiller & G. I. Crabb, "Groundborne vibration caused by mechanised construction works," Report 429, Transport Research Laboratory, Crowthorne, U.K., 2000.

[104] D. M. Hiller & V. S. Hope, "Groundborne vibration generated by mechanized construction activities," *Proc. Inst. Civ. Eng. Geotech. Eng.*, vol. 131, no. 4, pp. 223–232, 1998. [Online]. Available: https://doi.org/10.1680/igeng.1998.30714

[105] P. Hölscher & V. Hopman, "Test site Regent's Park London. Soil description." Report 381540-104, Version 2, GeoDelft, CONVURT EC-Growth Project G3RD-CT-2000-00381, 2003.

[106] R. A. Hood, R. J. Greer, M. Breslin, & P. R. Williams, "The calculation and assessment of ground-borne noise and perceptible vibration from trains in tunnels," *J. Sound Vib.*, vol. 193, no. 1, pp. 215–225, 1996. [Online]. Available: https://doi.org/10.1006/jsvi.1996.0261

[107] O. Hudaini, "Traffic vibrations in buildings," Construction Technology Update No. 39, National Research Council of Canada, 2000.

[108] H. E. M. Hunt, *Measurement and Modelling of Traffic-Induced Ground Vibration*, PhD Thesis, University of Cambridge, U.K., 1988.

[109] H. E. M. Hunt & M. F. M. Hussein, "Ground-Borne Vibration Transmission from Road and Rail Systems: Prediction and Control," in *Handbook of Noise and Vibration Control*, M. J. Crocker, Ed., ch. 123, pp. 1458–1469. New Jersey, U.S.A.: John Wiley & Sons, 2007. [Online]. Available: https://doi.org/10.1002/9780470209707.ch123

[110] H. E. M. Hunt, M. F. M. Hussein, & W. I. Hamad, "The PiP model and progress in ground vibration from railways," in *Proc. Annu. Conf. Aust. Acoust. Soc.*, Perth, Australia, 2017.

[111] H. E. M. Hunt & J. E. May, "Vibration generated by underground railway trains," in *Proc. 5th Int. Congr. Sound Vib. (ICSV5)*, pp. 2653–2660, Adelaide, Australia, 1997.

[112] M. F. M. Hussein, *Vibration from Underground Railways*, PhD Thesis, University of Cambridge, U.K., 2004. [Online]. Available: https://doi.org/10.17863/CAM.19122

[113] M. F. M. Hussein, S. François, M. Schevenels, H. E. M. Hunt, J. P. Talbot, & G. Degrande, "The fictitious force method for efficient calculation of vibration from a tunnel embedded in a multi-layered half-space," *J. Sound Vib.*, vol. 333, no. 25, pp. 6996–7018, 2014. [Online]. Available: https://doi.org/10.1016/j.jsv.2014.07.020

[114] M. F. M. Hussein, S. Gupta, H. E. M. Hunt, G. Degrande, & J. P. Talbot, "An efficient model for calculating vibration from a railway tunnel buried in a half-space," in *Proc. 13th Int. Congr. Sound Vib. (ICSV13)*, Vienna, Austria, 2006.

[115] M. F. M. Hussein & H. E. M. Hunt, "A power flow method for evaluating vibration from underground railways," *J. Sound Vib.*, vol. 293, no. 3-5, pp. 667–679, 2006. [Online]. Available: https://doi.org/10.1016/j.jsv.2005.12.012

[116] M. F. M. Hussein & H. E. M. Hunt, "PiP: A software for calculating vibration from underground railways," 2013. [Online]. Available: http://pipmodel.eng.cam.ac.uk/PiP.html

[117] M. F. M. Hussein, H. E. M. Hunt, K. A. Kuo, P. Alves Costa, & J. M. de Oliveira Barbosa, "The use of sub-modelling technique to calculate vibration in buildings from underground railways," *Proc. Inst. Mech. Eng., Part F: J. Rail Rapid Transit*, vol. 229, no. 3, pp. 303–314, 2015. [Online]. Available: https://doi.org/10.1177/0954409713511449

[118] M. F. M. Hussein, H. E. M. Hunt, L. Rikse, S. Gupta, G. Degrande, J. P. Talbot, S. François, & M. Schevenels, "Using the PiP model for fast calculation of vibration from a railway tunnel in a multi-layered half-space," in *Proc. 9th Int. Workshop Railway Noise (IWRN9)*, pp. 136–142, Munich, Germany, 2007. [Online]. Available: https://doi.org/10.1007/978-3-540-74893-9_19

[119] S. W. Jacobsz, K. H. Bowers, N. A. Moss, & G. Zanardo, "The effects of tunnelling on piled structures on the CTRL," in *Proc. 5th Int. Conf. Symp. TC28 (ISSMGE)*, pp. 115–121, Amsterdam, Netherlands, 2005.

[120] P. Jean, "A 3D FEM/BEM code for ground–structure interaction: Implementation strategy including the multi-traction problem," *Eng. Anal. Boundary Elem.*, vol. 59, pp. 52–61, 2015. [Online]. Available: https://doi.org/10.1016/J.ENGANABOUND.2015.04.007

[121] P. Jean & M. Villot, "A comparison of 2D, 2.5D and 3D BEM models for the study of railway induced vibrations," in *Proc. 10th Eur. Congr. Exposition Noise Control Eng. (EuroNoise 2015)*, pp. 1243–1247, Maastricht, Netherlands, 2015.

[122] Q. Jin, D. J. Thompson, D. E. J. Lurcock, M. G. R. Toward, & E. Ntotsios, "A 2.5D finite element and boundary element model for the ground vibration from trains in tunnels and validation using measurement data," *J. Sound Vib.*, vol. 422, pp. 373–389, 2018. [Online]. Available: https://doi.org/10.1016/j.jsv.2018.02.019

[123] C. J. C. Jones, "Use of numerical models to determine the effectiveness of anti-vibration systems for railways," *Proc. Inst. Civ. Eng. Transp.*, vol. 105, no. 1, pp. 43–51, 1994. [Online]. Available: https://doi.org/10.1680/itran.1994.25706

[124] C. J. C. Jones & J. R. Block, "Prediction of ground vibration from freight trains," *J. Sound Vib.*, vol. 193, no. 1, pp. 205–213, 1996. [Online]. Available: https://doi.org/10.1006/JSVI.1996.0260

[125] S. Jones, *Ground Vibration from Underground Railways: How Simplifying Assumptions Limit Prediction Accuracy*, PhD Thesis, University of Cambridge, U.K., 2010. [Online]. Available: https://doi.org/10.17863/cam.13982

[126] S. Jones, K. A. Kuo, M. F. M. Hussein, & H. E. M. Hunt, "Prediction uncertainties and inaccuracies resulting from common assumptions in modelling vibration from underground railways," *Proc. Inst. Mech. Eng., Part F: J. Rail Rapid Transit*, vol. 226, no. 5, pp. 501–512, 2012. [Online]. Available: https://doi.org/10.1177/0954409712441744

[127] S. Kaewunruen, A. Aikawa, & A. M. Remennikov, "Vibration attenuation at rail joints through under sleeper pads," *Procedia Eng.*, vol. 189, pp. 193–198, 2017. [Online]. Available: https://doi.org/10.1016/J.PROENG.2017.05.031

[128] A. Karlström, "An analytical model for ground vibrations from accelerating trains," *J. Sound Vib.*, vol. 293, no. 3-5, pp. 587–598, 2006. [Online]. Available: https://doi.org/10.1016/J.JSV.2005.08.038

[129] M. Katou, T. Matsuoka, O. Yoshioka, Y. Sanada, & T. Miyoshi, "Numerical simulation study of ground vibrations using forces from wheels of a running high-speed train," *J. Sound Vib.*, vol. 318, no. 4-5, pp. 830–849, 2008. [Online]. Available: https://doi.org/10.1016/J.JSV.2008.04.053

[130] E. Kausel, "An explicit solution for the Green's functions for dynamic loads in layered media," Research Report R81-13, Department of Civil Engineering, MIT, 1981.

[131] E. Kausel, *Fundamental Solutions in Elastodynamics: A Compendium*. Cambridge, U.K.: Cambridge University Press, 2006. [Online]. Available: https://doi.org/10.1017/CBO9780511546112

[132] A. M. Kaynia, *Dynamic Stiffness and Seismic Response of Pile Groups*, PhD Thesis, Massachusetts Institute of Technology, U.S.A., 1982.

[133] A. M. Kaynia, "Piles," in *Boundary Element Techniques in Geomechanics*, G. D. Manolis & T. G. Davies, Eds., ch. 7, pp. 209–242. London, U.K.: Computational Mechanics, 1993.

[134] A. M. Kaynia & E. Kausel, "Dynamic behaviour of pile groups," in *Proc. 2nd Int. Conf. Numer. Methods Offshore Piling*, pp. 509–532, Austin, Texas, U.S.A., 1982.

[135] A. M. Kaynia, C. Madshus, & P. Zackrisson, "Ground vibration from high-speed trains: prediction and countermeasure," *J. Geotech. Geoenviron. Eng.*, vol. 126, no. 6, pp. 531–537, 2000. [Online]. Available: https://doi.org/10.1061/(ASCE)1090-0241(2000)126:6(531)

[136] O. N. Kirillov & D. E. Pelinovsky, *Nonlinear Physical Systems: Spectral Analysis, Stability and Bifurcations*. New Jersey, U.S.A.: John Wiley & Sons, 2013.

[137] V. Knall, "Railway noise and vibration: effects and criteria," *J. Sound Vib.*, vol. 193, no. 1, pp. 9–20, 1996. [Online]. Available: https://doi.org/10.1006/JSVI.1996.0240

[138] U. G. Köpke, "Transverse vibration of buried pipelines due to internal excitation at a point," *Proc. Inst. Mech. Eng., Part E: J. Process Mech. Eng.*, vol. 207, no. 1, pp. 41–59, 1993. [Online]. Available: https://doi.org/10.1243/PIME_PROC_1993_207_206_02

[139] G. Kouroussis, D. P. Connolly, M. C. Forde, & O. Verlinden, "Train speed calculation using ground vibrations," *Proc. Inst. Mech. Eng., Part F: J. Rail Rapid Transit*, vol. 229, no. 5, pp. 466–483, 2015. [Online]. Available: https://doi.org/10.1177/0954409713515649

[140] G. Kouroussis, D. P. Connolly, & O. Verlinden, "Railway induced ground vibrations – A review of vehicle effects," *Int. J. Rail Transp.*, vol. 2, no. 2, pp. 69–110, 2014. [Online]. Available: https://doi.org/10.1080/23248378.2014.897791

[141] E. Kreyszig, *Advanced Engineering Mathematics*, 10th ed. New Jersey, U.S.A.: John Wiley & Sons, 2014.

[142] V. V. Krylov, A. R. Dawson, M. E. Heelis, & A. C. Collop, "Rail movement and ground waves caused by high-speed trains approaching track-soil critical velocities," *Proc. Inst. Mech. Eng., Part F: J. Rail Rapid Transit*, vol. 214, no. 2, pp. 107–116, 2000. [Online]. Available: https://doi.org/10.1243/0954409001531379

[143] R. L. Kuhlemeyer, "Static and dynamic laterally loaded floating piles," *J. Geotech. Eng. Div.*, vol. 105, no. 2, pp. 289–304, 1979. [Online]. Available: https://doi.org/10.1061/AJGEB6.0000771

[144] R. L. Kuhlemeyer, "Vertical vibration of piles," *J. Geotech. Eng. Div.*, vol. 105, no. 2, pp. 273–287, 1979. [Online]. Available: https://doi.org/10.1061/AJGEB6.0000770

[145] K. A. Kuo, *Vibration from Underground Railways: Considering Piled Foundations and Twin Tunnels*, PhD Thesis, University of Cambridge, U.K., 2010. [Online]. Available: https://doi.org/10.17863/CAM.13999

[146] K. A. Kuo, S. Jones, H. E. M. Hunt, & M. F. M. Hussein, "Applications of PiP: vibration of embedded foundations near a railway tunnel," in *Proc. 7th Eur. Congr. Exposition Noise Control Eng. (EuroNoise 2008)*, Southampton, U.K., 2008.

[147] K. A. Kuo, G. Lombaert, & G. Degrande, "Quantifying dynamic soil-structure interaction for railway induced vibrations," *Procedia Eng.*, vol. 199, pp. 2372–2377, 2017. [Online]. Available: https://doi.org/10.1016/J.PROENG.2017.09.256

[148] K. A. Kuo, M. Papadopoulos, G. Lombaert, & G. Degrande, "The coupling loss of a building subject to railway induced vibrations: Numerical modelling and experimental measurements," *J. Sound Vib.*, vol. 442, pp. 459–481, 2019. [Online]. Available: https://doi.org/10.1016/J.JSV.2018.10.048

[149] H. Kuppelwieser & A. Ziegler, "A tool for predicting vibration and structure-borne noise immissions caused by railways," *J. Sound Vib.*, vol. 193, no. 1, pp. 261–267, 1996. [Online]. Available: https://doi.org/10.1006/jsvi.1996.0266

[150] J. C. Lachat, *A Further Development of the Boundary Integral Equations for the Three-dimensional Helmholtz Equation*, PhD Thesis, University of Southampton, U.K., 1975.

[151] H. Lamb, "On the propagation of tremors over the surface of an elastic solid," *Philos. Trans. R. Soc. A*, vol. 203, no. 359-371, pp. 1–42, 1904. [Online]. Available: https://doi.org/10.1098/rsta.1904.0013

[152] X. Li & J. A. Hudson, "Multiple scattering of elastic waves from a continuous and heterogeneous region," *Geophys. J. Int.*, vol. 126, pp. 845–862, 1996. [Online]. Available: https://doi.org/10.1111/j.1365-246X.1996.tb04707.x

[153] Z. G. Li & T. X. Wu, "Modelling and analysis of force transmission in floating-slab track for railways," *Proc. Inst. Mech. Eng., Part F: J. Rail Rapid Transit*, vol. 222, no. 1, pp. 45–57, 2008. [Online]. Available: https://doi.org/10.1243/09544097JRRT145

[154] G. R. Liu & S. S. Quek Jerry, "A non-reflecting boundary for analyzing wave propagation using the finite element method," *Finite Elem. Anal. Des.*, vol. 39, no. 5-6, pp. 403–417, 2003. [Online]. Available: https://doi.org/10.1016/S0168-874X(02)00081-1

[155] Q. Liu, F. Deng, & Y. He, "Kinematic response of single piles to vertically incident P-waves," *Earthq. Eng. Struct. Dyn.*, vol. 43, no. 6, pp. 871–887, 2014. [Online]. Available: https://doi.org/10.1002/eqe.2377

[156] Y. J. Liu, S. Mukherjee, N. Nishimura, M. Schanz, W. Ye, A. Sutradhar, E. Pan, N. A. Dumont, A. Frangi, & A. Saez, "Recent Advances and Emerging Applications of the Boundary Element Method," *ASME Appl. Mech. Rev.*, vol. 64, no. 3, pp. 030 802–1–38, 2012. [Online]. Available: https://doi.org/10.1115/1.4005491

[157] K. T. Lo, *Measurement and modelling of vibration transmission through piled-foundations*, PhD Thesis, University of Cambridge, U.K., 1994.

[158] G. Lombaert, G. Degrande, B. Vanhauwere, B. Vandeborght, & S. François, "The control of ground-borne vibrations from railway traffic by means of continuous floating slabs," *J. Sound Vib.*, vol. 297, no. 3-5, pp. 946–961, 2006. [Online]. Available: https://doi.org/10.1016/J.JSV.2006.05.013

[159] P. Lopes, P. Alves Costa, M. Ferraz, R. Calçada, & A. Silva Cardoso, "Numerical modeling of vibrations induced by railway traffic in tunnels: From the source to the nearby buildings," *Soil Dyn. Earthq. Eng.*, vol. 61-62, pp. 269–285, 2014. [Online]. Available: https://doi.org/10.1016/J.SOILDYN.2014.02.013

[160] Lord Rayleigh, "On waves propagated along the plane surface of an elastic solid," *Proc. London Math. Soc.*, vol. s1-17, no. 1, pp. 4–11, 1885. [Online]. Available: https://doi.org/10.1112/plms/s1-17.1.4

[161] M. Lou, H. Wang, X. Chen, & Y. Zhai, "Structure-soil-structure interaction: literature review," *Soil Dyn. Earthq. Eng.*, vol. 31, no. 12, pp. 1724–1731, 2011. [Online]. Available: https://doi.org/10.1016/J.SOILDYN.2011.07.008

[162] N. Makris, "Soil-pile interaction during the passage of rayleigh waves: An analytical solution," *Earthq. Eng. Struct. Dyn.*, vol. 23, no. 2, pp. 153–167, 1994. [Online]. Available: https://doi.org/10.1002/eqe.4290230204

[163] N. Makris & D. Badoni, "Seismic response of pile groups under oblique-shear and Rayleigh waves," *Earthq. Eng. Struct. Dyn.*, vol. 24, no. 4, pp. 517–532, 1995. [Online]. Available: https://doi.org/10.1002/eqe.4290240405

[164] N. Makris & G. Gazetas, "Dynamic pile-soil-pile interaction. Part II: Lateral and seismic response," *Earthq. Eng. Struct. Dyn.*, vol. 21, no. 2, pp. 145–162, 1992. [Online]. Available: https://doi.org/10.1002/eqe.4290210204

[165] S. M. Mamoon & S. Ahmad, "Seismic response of piles to obliquely incident SH, SV, and P waves," *J. Geotech. Eng.*, vol. 116, no. 2, pp. 186–204, 1990. [Online]. Available: https://doi.org/10.1061/(ASCE)0733-9410(1990)116:2(186)

[166] S. M. Mamoon, A. M. Kaynia, & P. K. Banerjee, "Frequency Domain Dynamic Analysis of Piles and Pile Groups," *J. Eng. Mech.*, vol. 116, no. 10, pp. 2237–2257, 1990. [Online]. Available: https://doi.org/10.1061/(ASCE)0733-9399(1990)116:10(2237)

[167] J. E. Manning, "Statistical energy analysis," in *Handbook of Noise and Vibration Control*, M. J. Crocker, Ed., ch. 17, pp. 241–254. New Jersey, U.S.A.: John Wiley & Sons, 2007.

[168] K. J. Marfurt, "Accuracy of finite-difference and finite-element modeling of the scalar and elastic wave equations," *Geophysics*, vol. 49, no. 5, pp. 533–549, 1984. [Online]. Available: https://doi.org/10.1190/1.1441689

[169] P. A. Martin, *Multiple Scattering: Interaction of Time-Harmonic Waves with N Obstacles*, ser. Encyclopedia of Mathematics and its Applications. Cambridge, U.K.: Cambridge University Press, 2006. [Online]. Available: https://doi.org/10.1017/CBO9780511735110

[170] MATLAB, "Version 9.4, R2018a," 2018.

[171] M. McNulty, "The use of trial piles in assessments of ground-borne vibration," in *Proc. 24th Int. Congr. Sound Vib. (ICSV24)*, pp. 5619–5626, London, U.K., 2017.

[172] D. J. Mead, *Passive Vibration Control*. New Jersey, U.S.A.: John Wiley & Sons, 1998.

[173] A. V. Metrikine & A. C. W. M. Vrouwenvelder, "Surface ground vibration due to a moving train in a tunnel: two-dimensional model," *J. Sound Vib.*, vol. 234, no. 1, pp. 43–66, 2000. [Online]. Available: https://doi.org/10.1006/JSVI.1999.2853

[174] M. A. Millán & J. Domínguez, "Simplified BEM/FEM model for dynamic analysis of structures on piles and pile groups in viscoelastic and poroelastic soils," *Eng. Anal. Boundary Elem.*, vol. 33, no. 1, pp. 25–34, 2009. [Online]. Available: https://doi.org/10.1016/J.ENGANABOUND.2008.04.003

[175] G. F. Miller & H. Pursey, "On the partition of energy between elastic waves in a semi-infinite solid," *Proc. R. Soc. Lond. A*, vol. 233, no. 1192, pp. 55–69, 1955. [Online]. Available: https://doi.org/10.1098/rspa.1955.0245

[176] A. Mita & J. E. Luco, "Impedance functions and input motions for embedded square foundations," *J. Geotech. Eng.*, vol. 115, no. 4, pp. 491–503, 1989. [Online]. Available: https://doi.org/10.1061/(ASCE)0733-9410(1989)115:4(491)

[177] G. Mylonakis & G. Gazetas, "Vertical vibration and additional distress of grouped piles in layered soil," *Soils Found.*, vol. 38, no. 1, pp. 1–14, 1998. [Online]. Available: https://doi.org/10.3208/sandf.38.1

[178] G. Mylonakis & G. Gazetas, "Kinematic pile response to vertical P-wave seismic excitation," *J. Geotech. Geoenviron. Eng.*, vol. 128, no. 10, pp. 860–868, 2002. [Online]. Available: https://doi.org/10.1061/(ASCE)1090-0241(2002)128:10(860)

[179] F. Naeim & J. M. Kelly, *Design of Seismic Isolated Structures*. New Jersey, U.S.A.: John Wiley & Sons, 1999.

[180] D. E. Newland, *An Introduction to Random Vibrations, Spectral & Wavelet Analysis*, 3rd ed. New York, U.S.A.: Dover Publications, 2005.

[181] D. E. Newland, *Mechanical Vibration Analysis and Computation*, 1st ed. New York, U.S.A.: Dover Publications, 2006.

[182] D. E. Newland & H. E. M. Hunt, "Isolation of buildings from ground vibration: A review of recent progress," *Proc. Inst. Mech. Eng., Part C: J. Mech. Eng. Sci.*, vol. 205, no. 1, pp. 39–52, 1991. [Online]. Available: https://doi.org/10.1243/PIME_PROC_1991_205_090_02

[183] S. L. D. Ng, *Transmission of Ground-Borne Vibration from Surface Railway Trains*, PhD Thesis, University of Cambridge, U.K., 1995.

[184] J. C. O. Nielsen, "Numerical prediction of rail roughness growth on tangent railway tracks," *J. Sound Vib.*, vol. 267, no. 3, pp. 537–548, 2003. [Online]. Available: https://doi.org/10.1016/S0022-460X(03)00713-2

[185] T. Nogami, "Dynamic group effect of multiple piles under vertical vibration," in *Proc. ASCE Eng. Mech. Div. Spec. Conf.*, pp. 750–754, Austin, Texas, U.S.A., 1979.

[186] T. Nogami, "Flexural responses of grouped piles under dynamic loading," *Earthq. Eng. Struct. Dyn.*, vol. 13, no. 3, pp. 321–336, 1985. [Online]. Available: https://doi.org/10.1002/eqe.4290130306

[187] T. Nogami & M. Novak, "Soil-pile interaction in vertical vibration," *Earthq. Eng. Struct. Dyn.*, vol. 4, no. 3, pp. 277–293, 1976. [Online]. Available: https://doi.org/10.1002/eqe.4290040308

[188] M. Novak, "Dynamic stiffness and damping of piles," *Can. Geotech. J.*, vol. 11, no. 4, pp. 574–598, 1974. [Online]. Available: https://doi.org/10.1139/t74-059

[189] M. Novak & R. F. Grigg, "Dynamic experiments with small pile foundations," *Can. Geotech. J.*, vol. 13, no. 4, pp. 372–385, 1976. [Online]. Available: https://doi.org/10.1139/t76-039

[190] M. Novak & J. F. Howell, "Torsional vibrations of pile foundations," *J. Geotech. Eng. Div.*, vol. 103, no. 4, pp. 271–285, 1977. [Online]. Available: https://doi.org/10.1061/AJGEB6.0000400

[191] M. Novak & T. Nogami, "Soil-pile interaction in horizontal vibration," *Earthq. Eng. Struct. Dyn.*, vol. 5, no. 3, pp. 263–281, 1977. [Online]. Available: https://doi.org/10.1002/eqe.4290050305

[192] E. Ntotsios, W. I. Hamad, D. J. Thompson, M. F. M. Hussein, H. E. M. Hunt, & J. P. Talbot, "Predictions of the dynamic response of piled foundations in a multi-layered half-space due to inertial and railway induced loadings," in *Proc. 5th Int. Conf. Comput. Methods Struct. Dyn. Earthq. Eng. (COMPDYN 2015)*, pp. 133–145, Crete, Greece, 2015.

[193] E. Ntotsios, D. J. Thompson, & M. F. M. Hussein, "The effect of track load correlation on ground-borne vibration from railways," *J. Sound Vib.*, vol. 402, pp. 142–163, 2017. [Online]. Available: https://doi.org/10.1016/J.JSV.2017.05.006

[194] C. H. Pang, K. Y. Yong, Y. K. Chow, & J. Wang, "The response of pile foundations subjected to shield tunnelling," in *Proc. 5th Int. Symp. Geotech. Aspects Underground Constr. Soft Ground*, pp. 737–744, Amsterdam, Netherlands, 2006.

[195] E. Peris, J. Woodcock, G. Sica, A. T. Moorhouse, & D. C. Waddington, "Annoyance due to railway vibration at different times of the day," *J. Acoust. Soc. Am.*, vol. 131, no. 2, pp. 191–196, 2012. [Online]. Available: https://doi.org/10.1121/1.3679390

[196] H. G. Poulos, "Analysis of the settlement of pile groups," *Géotechnique*, vol. 18, no. 4, pp. 449–471, 1968. [Online]. Available: https://doi.org/10.1680/geot.1968.18.4.449

[197] H. G. Poulos, "Behaviour of laterally loaded piles. Part II: Pile groups," *J. Soil Mech. Found. Div.*, vol. 97, no. 5, pp. 733–751, 1971. [Online]. Available: https://doi.org/10.1061/JSFEAQ.0001593

[198] H. G. Poulos & E. H. Davis, *Pile Foundation Analysis and Design*. New York, U.S.A.: John Wiley & Sons, 1980.

[199] J. S. Przemieniecki, *Theory of Matrix Structural Analysis*. New York, U.S.A.: Dover Publications, 1985.

[200] S. Rajasekaran, *Structural Dynamics of Earthquake Engineering*. Cambridge, U.K.: Woodhead Publishing, 2009.

[201] J. J. Rego Silva, H. Power, & L. C. Wrobel, "A boundary element method for 3D time-harmonic elastodynamics – Numerical aspects," in *Boundary Elements XV Vol 2 Stress Analysis*, C. A. Brebbia & J. J. Rencis, Eds., vol. 2, pp. 423–439. Southampton, U.K.: WIT Press, 1993.

[202] P. J. Remington, L. G. Kurzweil, & D. A. Towers, "Low-frequency noise and vibration from trains," in *Transportation Noise Reference Book*, P. M. Nelson, Ed., ch. 16. London, U.K.: Butterworth, 1987.

[203] P. Ropars, X. Vuylsteke, & E. Augis, "Vibrations induced by metro in sensitive buildings: experimental and numerical comparisons," in *Proc. 11th Eur. Congr. Exposition Noise Control Eng. (EuroNoise 2018)*, pp. 1381–1386, Crete, Greece, 2018.

[204] T. J. Royston, Y. Yazicioglu, & F. Loth, "Surface response of a viscoelastic medium to subsurface acoustic sources with application to medical diagnosis," *J. Acoust. Soc. Am.*, vol. 113, no. 2, pp. 1109–1121, 2003. [Online]. Available: https://doi.org/10.1121/1.1536153

[205] J. Salvi, F. Pioldi, & E. Rizzi, "Optimum tuned mass dampers under seismic soil-structure interaction," *Soil Dyn. Earthq. Eng.*, vol. 114, pp. 576–597, 2018. [Online]. Available: https://doi.org/10.1016/J.SOILDYN.2018.07.014

[206] G. Sanitate, *A Performance-based Design Framework for Base-isolated Buildings Against Ground-borne Vibration*, PhD Thesis, University of Cambridge, U.K., 2019. [Online]. Available: https://doi.org/10.17863/CAM.48986

[207] G. Sanitate & J. P. Talbot, "A power-flow based investigation into the response of tall buildings to ground-borne vibration," in *Proc. 23rd Int. Congr. Sound Vib. (ICSV23)*, Athens, Greece, 2016.

[208] G. Sanitate & J. P. Talbot, "Soil-structure interaction and the added-building effect: simplified models for assisting with the prediction of ground-borne vibration in buildings," in *Proc. 25th Int. Congr. Sound Vib. (ICSV25)*, Hiroshima, Japan, 2018.

[209] G. Sanitate & J. P. Talbot, "On the plate-like and layer-like response of slab foundations to ground-borne vibration," *Comput. Geotech.*, vol. 114, pp. 103 141–1–13, 2019. [Online]. Available: https://doi.org/10.1016/J.COMPGEO.2019.103141

[210] R. J. Schaefer, "Mechanical properties of rubber," in *Shock and Vibration Handbook*, 5th ed., C. M. Harris & A. G. Piersol, Eds., ch. 33.   New York, U.S.A.: McGraw-Hill, 2002.

[211] M. Schevenels, S. François, & G. Degrande, "EDT: Elastodynamics Toolbox for MATLAB," 2008. [Online]. Available: https://bwk.kuleuven.be/bwm/edt

[212] R. Sen, T. G. Davies, & P. K. Banerjee, "Dynamic analysis of piles and pile groups embedded in homogeneous soils," *Earthq. Eng. Struct. Dyn.*, vol. 13, no. 1, pp. 53–65, 1985. [Online]. Available: https://doi.org/10.1002/eqe.4290130107

[213] X. Sheng, C. J. C. Jones, & D. J. Thompson, "A comparison of a theoretical model for quasi-statically and dynamically induced environmental vibration from trains with measurements," *J. Sound Vib.*, vol. 267, no. 3, pp. 621–635, 2003. [Online]. Available: https://doi.org/10.1016/S0022-460X(03)00728-4

[214] X. Sheng, C. J. C. Jones, & D. J. Thompson, "Modelling ground vibration from railways using wavenumber finite- and boundary-element methods," *Proc. R. Soc. A*, vol. 461, no. 2059, pp. 2043–2070, 2005. [Online]. Available: https://doi.org/10.1098/rspa.2005.1450

[215] M. G. Smith, M. Ögren, J. Ageborg Morsing, & K. Persson Waye, "Effects of ground-borne noise from railway tunnels on sleep: A polysomnographic study," *Build. Environ.*, vol. 149, pp. 288–296, 2019. [Online]. Available: https://doi.org/10.1016/J.BUILDENV.2018.12.009

[216] H. Sucuoğlu & S. Akkar, *Basic Earthquake Engineering: From Seismology to Analysis and Design*.   Berlin, Germany: Springer-Verlag, 2014. [Online]. Available: https://doi.org/10.1007/978-3-319-01026-7

[217] M. R. Svinkin, "Soil and structure vibrations from construction and industrial sources," in *Proc. 6th Int. Conf. Case Hist. Geotech. Eng.*, vol. 8, Arlington, Virginia, U.S.A., 2008.

[218] A. J. B. Tadeu, J. António, & L. Godinho, "Green's function for two-and-a-half dimensional elastodynamic problems in a half-space," *Comput. Mech.*, vol. 27, no. 6, pp. 484–491, 2001. [Online]. Available: https://doi.org/10.1007/s004660100259

[219] A. J. B. Tadeu & E. Kausel, "Green's functions for two-and-a-half-dimensional elastodynamic problems," *J. Eng. Mech.*, vol. 126, no. 10, pp. 1093–1097, 2000. [Online]. Available: https://doi.org/10.1061/(ASCE)0733-9399(2000)126:10(1093)

[220] H. Takemiya, "Simulation of track–ground vibrations due to a high-speed train: The case of X-2000 at Ledsgard," *J. Sound Vib.*, vol. 261, no. 3, pp. 503–526, 2003. [Online]. Available: https://doi.org/10.1016/S0022-460X(02)01007-6

[221] J. P. Talbot, *On the Performance of Base-Isolated Buildings: A Generic Model*, PhD Thesis, University of Cambridge, U.K., 2001. [Online]. Available: https://doi.org/10.17863/CAM.14035

[222] J. P. Talbot, "Base-isolated buildings: towards performance-based design," *Proc. Inst. Civ. Eng. Struct. Build.*, vol. 169, no. 8, pp. 574–582, 2016. [Online]. Available: https://doi.org/10.1680/jstbu.15.00057

[223] J. P. Talbot & H. E. M. Hunt, "A computationally efficient piled-foundation model for studying the effects of ground-borne vibration on buildings," *Proc. Inst. Mech. Eng., Part C: J. Mech. Eng. Sci.*, vol. 217, no. 9, pp. 975–989, 2003. [Online]. Available: https://doi.org/10.1243/095440603322407227

[224] J. P. Talbot & H. E. M. Hunt, "Isolation of buildings from rail-tunnel vibration: A review," *Build. Acoust.*, vol. 10, no. 3, pp. 177–192, 2003. [Online]. Available: https://doi.org/10.1260/135101003322661998

[225] D. J. Thompson, *Railway Noise and Vibration: Mechanisms, Modelling and Means of Control*, 1st ed.   Oxford, U.K.: Elsevier Science, 2010.

[226] D. J. Thompson, T. Wu, & T. Armstrong, "Wheel/rail rolling noise – The effects of non-linearities in the contact zone," in *Proc. 10th Int. Congr. Sound Vib. (ICSV10)*, Stockholm, Sweden, 2003.

[227] R. M. Thornely-Taylor, "The prediction of vibration, groundborne and structure-radiated noise from railways using finite difference methods – Part I - Theory," *Proc. Inst. Acoust.*, vol. 26, no. 2, pp. 69–79, 2004.

[228] S. Timoshenko & J. N. Goodier, *Theory of Elasticity*, 3rd ed.   New York, U.S.A.: McGraw-Hill, 1970.

[229] M. J. Tomlinson & J. Woodward, *Pile Design and Construction Practice*, 6th ed.   London, U.K.: Taylor & Francis, 2015. [Online]. Available: https://doi.org/10.1201/b17526

[230] Transport for London, "Infrastructure protection - Special conditions for outside parties working on or near the railway," Transport for London, London, U.K., 2015.

[231] Transport for London, "Crossrail 2: Information for developers," Transport for London, London, U.K., 2017.

[232] Union Internationale des Transports Publics, "World metro figure - statistics brief," UITP, Brussels, Belgium, 2018.

[233] F. Vicencio & N. A. Alexander, "Dynamic interaction between adjacent buildings through nonlinear soil during earthquakes," *Soil Dyn. Earthq. Eng.*, vol. 108, pp. 130–141, 2018. [Online]. Available: https://doi.org/10.1016/J.SOILDYN.2017.11.031

[234] N. Vincent, P. Bouvet, D. J. Thompson, & P. E. Gautier, "Theoretical optimization of track components to reduce rolling noise," *J. Sound Vib.*, vol. 193, no. 1, pp. 161–171, 1996. [Online]. Available: https://doi.org/10.1006/jsvi.1996.0255

[235] P. C. Vinh & R. W. Ogden, "On formulas for the Rayleigh wave speed," *Wave Motion*, vol. 39, no. 3, pp. 191–197, 2004. [Online]. Available: https://doi.org/10.1016/J.WAVEMOTI.2003.08.004

[236] J. Virieux, "P-SV wave propagation in heterogeneous media: velocity-stress finite-difference method," *Geophysics*, vol. 51, no. 4, pp. 889–901, 1986. [Online]. Available: https://doi.org/10.1190/1.1442147

[237] A. S. Volmir, *Nelineinaya Dinamika Plastinok i Obolochek [Nonlinear Dynamics of Plates and Shells]*.   Moscow, Russia: Nauka, 1972.

[238] A. M. Wahl, *Mechanical Springs*, 2nd ed.   New York, U.S.A.: McGraw-Hill, 1963.

[239] F. Wahl, G. Schmidt, & L. Forrai, "On the significance of antiresonance frequencies in experimental structural analysis," *J. Sound Vib.*, vol. 219, no. 3, pp. 379–394, 1999. [Online]. Available: https://doi.org/10.1006/jsvi.1998.1831

[240] E. Winkler, *Die Lehre von der Elastizität und Festigkeit [The theory of elasticity and strength]*.   Prague, Czech Republic: Dominicus, 1867.

[241] J. P. Wolf & G. R. Darbre, "Dynamic-stiffness matrix of soil by the boundary-element method: embedded foundation," *Earthq. Eng. Struct. Dyn.*, vol. 12, no. 3, pp. 401–416, 1984. [Online]. Available: https://doi.org/10.1002/eqe.4290120308

[242] J. P. Wolf & G. A. von Arx, "Impedance function of a group of vertical piles," in *Proc. ASCE Spec. Conf. Earthquake Eng. Soil Dyn.*, vol. 2, pp. 1024–1041, Pasadena, California, U.S.A., 1978.

[243] H. L. Wong & J. E. Luco, "Tables of impedance functions and input motions for rectangular foundations," Report CE-78-15, University of Southern California, California, U.S.A., 1978.

[244] J. Woodhouse, "Linear damping models for structural vibration," *J. Sound Vib.*, vol. 215, no. 3, pp. 547–569, 1998. [Online]. Available: https://doi.org/10.1006/jsvi.1998.1709

[245] R. D. Woods, "Screening of surface wave in soils," *J. Soil Mech. Found. Div.*, vol. 94, no. 4, pp. 951–980, 1968. [Online]. Available: https://doi.org/10.1061/JSFEAQ.0001180

[246] Q. Xu, Z. Xiao, T. Liu, P. Lou, & X. Song, "Comparison of 2D and 3D prediction models for environmental vibration induced by underground railway with two types of tracks," *Comput. Geotech.*, vol. 68, pp. 169–183, 2015. [Online]. Available: https://doi.org/10.1016/J.COMPGEO.2015.04.011

[247] Y.-B. Yang & H.-H. Hung, "A parametric study of wave barriers for reduction of train-induced vibrations," *Int. J. Numer. Methods Eng.*, vol. 40, no. 20, pp. 3729–3747, 1997. [Online]. Available: https://doi.org/10.1002/(SICI)1097-0207(19971030)40:20<3729::AID-NME236>3.0.CO;2-8

[248] Y.-B. Yang, X. Liang, H.-H. Hung, & Y. Wu, "Comparative study of 2D and 2.5D responses of long underground tunnels to moving train loads," *Soil Dyn. Earthq. Eng.*, vol. 97, pp. 86–100, 2017. [Online]. Available: https://doi.org/10.1016/J.SOILDYN.2017.02.005

[249] C. Yoshimura, J. Bielak, Y. Hisada, & A. Fernández, "Domain reduction method for three-dimensional earthquake modeling in localized regions, Part II: Verification and applications," *Bull. Seismol. Soc. Am.*, vol. 93, no. 2, pp. 825–840, 2003. [Online]. Available: https://doi.org/10.1785/0120010252

[250] Z. Yuan, A. Boström, & Y. Cai, "Benchmark solution for vibrations from a moving point source in a tunnel embedded in a half-space," *J. Sound Vib.*, vol. 387, pp. 177–193, 2017. [Online]. Available: https://doi.org/10.1016/J.JSV.2016.10.016

Appendix A

Fourier Analysis

Fourier analysis is the study of how functions can be decomposed into oscillatory components. This appendix summarises the different Fourier analysis techniques used in this dissertation.

A.1 The Fourier Transform

Consider the continuous function $x(t)$. The Fourier transform of $x(t)$, with respect to the time t-domain, transforms $x(t)$ into the function $X(\omega)$ in the frequency ω-domain [141]:

$$X(\omega) = \int_{-\infty}^{\infty} x(t) \cdot e^{-i\omega t} dt. \tag{A.1}$$

Equivalently, the Fourier transform of the function $y(x)$, with respect to the space x-domain, transforms $y(x)$ into the function $\widetilde{Y}(\xi)$ in the wavenumber ξ-domain:

$$\widetilde{Y}(\xi) = \int_{-\infty}^{\infty} y(x) \cdot e^{-i\xi x} dx. \tag{A.2}$$

In order to transform $X(\omega)$ back into the t-domain, the inverse Fourier transform of $X(\omega)$ is applied with respect to the frequency ω-domain [141]:

$$x(t) = \frac{1}{2\pi} \int_{-\infty}^{\infty} X(\omega) \cdot e^{i\omega t} d\omega. \tag{A.3}$$

Similarly, to transform $\widetilde{Y}(\xi)$ back into the x-domain:

$$y(x) = \frac{1}{2\pi} \int_{-\infty}^{\infty} \widetilde{Y}(\xi) \cdot e^{i\xi x} d\xi. \tag{A.4}$$

It is worth noting that if the continuous function is periodic, Eqs. (A.1)–(A.4) can be evaluated over a finite period of the function rather than from $-\infty$ to ∞.

A.2   Computing the Fourier Transform

The numerical models developed in this dissertation operate by processing digital signals that consist of discrete data points. This means that the Fourier transform of a general signal needs to be evaluated over a finite interval. In this section, two approaches for numerically computing the Fourier transform are described: the discrete Fourier transform and contour integration.

A.2.1   The Discrete Fourier Transform

The discrete Fourier transform (DFT) is a numerical approach used to approximate the Fourier transform of a sampled signal. Consider that the function $y(x)$ is sampled at N discrete points, with equal sample spacing Δx, to obtain the signal $y[m]$, where the integer m denotes each data point from 0 to $N-1$. The DFT of $y[m]$ can be expressed as [141]

$$\widehat{Y}[k] = \sum_{m=0}^{N-1} y[m] e^{-i(2\pi km/N)} \quad \text{for } k = 0, 1, \ldots, (N-1),$$
(A.5)

where the sampled $\widehat{Y}[k]$ is evaluated at discrete wavenumber components $\xi_k = \frac{2\pi k}{N\Delta x}$ of the DFT $\widehat{Y}(\xi)$. It can be shown that $\widehat{Y}(\xi)$ is equivalent to the following expression [141]:

$$\widehat{Y}(\xi) = \frac{1}{\Delta x} \sum_{k=-\infty}^{\infty} \widetilde{Y}\left(\xi - \frac{2\pi k}{\Delta x}\right),$$
(A.6)

where the continuous Fourier transform $\widetilde{Y}(\xi)$ is shifted along the ξ-domain by the sampling wavenumber $2\pi/\Delta x$. Although the Fourier transform is not periodic by definition, Eq. (A.6) shows that the DFT is periodic, which means that Eq. (A.5) computes the DFT using a finite number of sampled values over one period.

In order to obtain a good approximation of the Fourier transform over one DFT period, the x-domain data must be over-sampled. This allows Δx to be small enough to ensure there is sufficient separation between the shifted Fourier transforms in the sum of Eq. (A.6); otherwise, they will overlap. Under-sampling can result in aliasing, which is a form of sampling artefact where high-wavenumber components are falsely mapped onto lower wavenumbers due to the Fourier transforms overlapping. To avoid aliasing, it is necessary to satisfy the Nyquist criterion (or sampling theorem): the sampling wavenumber $2\pi/\Delta x$ must at least be twice the largest ξ-component in the sampled signal to accurately capture all the ξ-components. It follows that the highest ξ-component extracted by the DFT is half the sampling wavenumber, known as the

Nyquist wavenumber $\xi_{Nyquist} = \pi/\Delta x$.

The inverse discrete Fourier transform (IDFT) of $\widehat{Y}[k]$ can be expressed as [141]

$$y[m] = \frac{1}{N} \sum_{k=0}^{N-1} \widehat{Y}[k] e^{i(2\pi km/N)} \quad \text{for } m = 0, 1, \ldots, (N-1). \tag{A.7}$$

A.2.2 Contour Integration

Contour integration is another approach by which the Fourier transform can be computed. This is an analytical method that applies the residue theorem to evaluate the infinite integral along curved paths in a complex plane, referred to as contours.

For convenience, the example provided here demonstrates how contour integration can be applied to find the inverse Fourier transform of the function $F(\xi)$, but a similar approach can also be used to find the Fourier transform. The inverse Fourier transform can be expressed as

$$f(x) = \frac{1}{2\pi} \int_{-\infty}^{\infty} F(\xi) \cdot e^{i\xi x} d\xi. \tag{A.8}$$

In this case, assume that the function $F(\xi) \cdot e^{i\xi x}$ has eight poles, which are its singular points. As shown in Fig. A.1, the integration of $F(\xi) \cdot e^{i\xi x}$ along the real axis from $\xi_a \to -\infty$ to $\xi_b \to \infty$ is equivalent to integrating along the closed-path contour that includes the real axis from ξ_a to ξ_b and the complex semicircle from ξ_b to ξ_a, provided that the integral along the semicircle is zero. The integral along the contour is equivalent to the summation of the residues at the poles of $F(\xi) \cdot e^{i\xi x}$ [141]:

$$\int_{-\infty}^{\infty} F(\xi) \cdot e^{i\xi x} d\xi = 2\pi i \sum_{j=1}^{n} \text{Res}\left(F(\xi) \cdot e^{i\xi x}, \xi_j\right), \tag{A.9}$$

where $\text{Res}\left(F(\xi) \cdot e^{i\xi x}, \xi_j\right)$ is the residue of $F(\xi) \cdot e^{i\xi x}$ at the pole ξ_j and n is the total number of poles enclosed by the contour. By substituting $\xi = re^{i\theta}$, where the complex wavenumber is expressed in polar notation, the integral along the semicircle in Fig. A.1 can be written as

$$\int_{-\infty}^{\infty} F(\xi) \cdot e^{i\xi x} d\xi = \int_{0}^{\pi} F(r^{i\theta}) \cdot re^{i\theta} \cdot e^{(ir\cos\theta - r\sin\theta)x} d\theta. \tag{A.10}$$

The $e^{-irx\sin\theta}$ term in Eq. (A.10) determines whether the integral approaches zero or infinity as $r \to \infty$. In the first and second quadrant of the complex plane, $\sin\theta \geq 0$ and the integral only tends to zero when $x \geq 0$, which means that the closed path illustrated in Fig. A.1a is used. The

contours in the third and fourth quadrants, as shown in Fig. A.1b, are used to solve the integral when $x < 0$. This ensures that the integral along the semicircle contour always tends to zero as $r \to \infty$.

Once a closed-path contour is selected along the complex plane, the contour integral can be replaced by a summation of the residues evaluated at the enclosed poles [141]. If none of the poles lie on the real axis, as represented in Fig. A.1, Eq. (A.8) can be simplified to

$$f(x) = \begin{cases} i \sum_{j=1}^{4} F(\xi_j) \cdot e^{i\xi_j x} & \text{for } x \geq 0, \\ -i \sum_{j=5}^{8} F(\xi_j) \cdot e^{i\xi_j x} & \text{for } x < 0. \end{cases} \tag{A.11}$$

However, if some poles lie on the real axis, the contour path must be modified to include or exclude specific poles on the basis of physical arguments. With regard to wave motion, poles on the real axis represent purely propagating waves due to the $e^{i\xi x}$ term in Eq. (A.11). In the absence of sources at $x \geq 0$, these propagating waves should only travel to the right (i.e., in the direction of increasing x values). Therefore, positive real poles must be excluded when solving the integral for $x \geq 0$, as shown by the small semicircle in Fig. A.2a, because they cause waves to propagate to the left. A similar argument can be applied when there are no sources at $x < 0$.
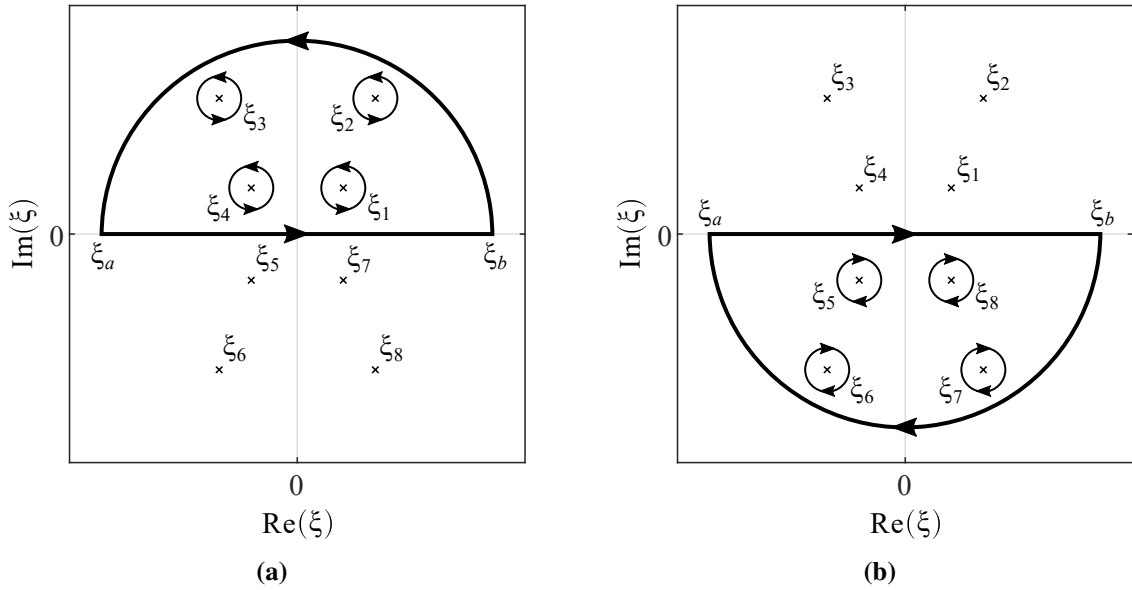
Fig. A.1 The integration of the function $F(\xi)e^{i\xi x}$ along the real axis from $\xi_a \to -\infty$ to $\xi_b \to \infty$ is equivalent to integrating along the closed-path contour that includes the real axis from ξ_a to ξ_b and the complex semicircle from ξ_b to ξ_a when **(a)** $x \geq 0$ and **(b)** $x < 0$. Integrating along the contour is also equivalent to the sum of integrals along the closed paths around the poles ξ_j that lie within the contour.
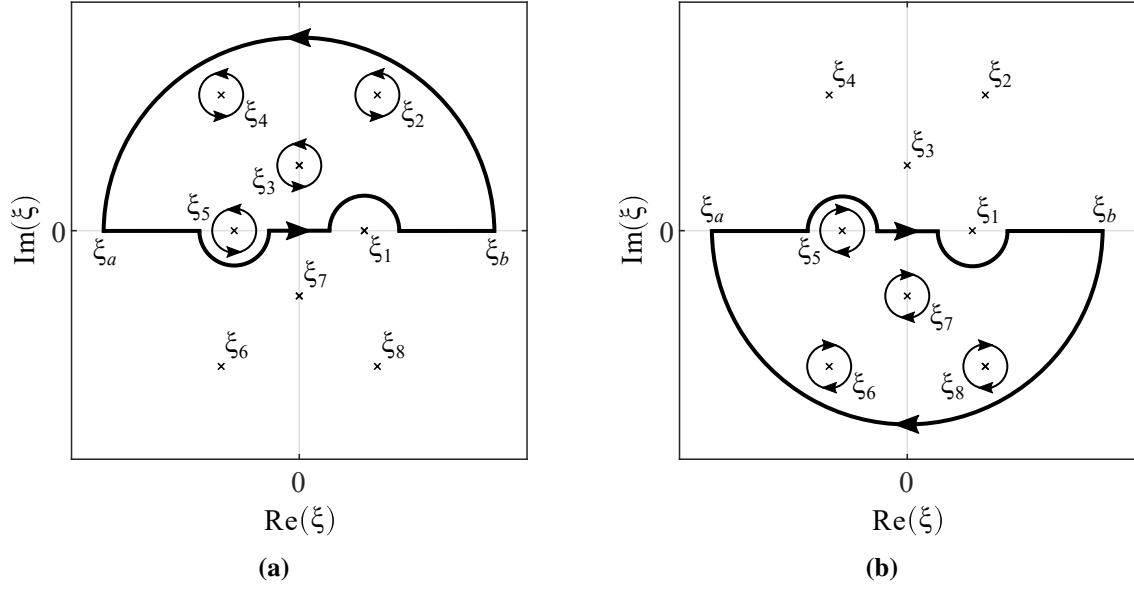
Fig. A.2 The modified contour path when some poles lie on the real axis for **(a)** $x \geq 0$ and **(b)** $x < 0$.

In this case, the same positive real poles must be excluded, as shown in Fig. A.2b, because the purely propagating waves should only travel to the left when $x < 0$.

A.3   The Fourier Series

Consider the continuous function $f(t)$ with period T. By decomposing $f(t)$ into harmonically related sinusoids, its Fourier series can be expressed as [141]

$$f(t) = \sum_{n=0}^{\infty} \left(a_n \cos\left(\frac{2\pi nt}{T}\right) + b_n \sin\left(\frac{2\pi nt}{T}\right) \right), \tag{A.12}$$

where the Fourier series coefficients are

$$a_0 = \frac{1}{T} \int_0^T f(t)dt\,, \tag{A.13}$$

$$b_0 = 0\,, \tag{A.14}$$

$$a_n = \frac{2}{T} \int_0^T f(t) \cdot \cos\left(\frac{2\pi nt}{T}\right) dt \quad \text{for } n \geq 1\,, \tag{A.15}$$

$$b_n = \frac{2}{T} \int_0^T f(t) \cdot \sin\left(\frac{2\pi nt}{T}\right) dt \quad \text{for } n \geq 1\,, \tag{A.16}$$

and the integer n represents the nth harmonic mode.

Now, consider that $f(t)$ is discretised over the interval $[0,T]$ at N evenly spaced points with spacing $\Delta t = T/(N-1)$ to obtain the sampled function $f[k]$, where the integer k denotes each data point from 0 to $N-1$. In this case, the discrete Fourier series, which is related to the DFT described in Appendix A.2.1, can decompose $f[k]$ into a summation of sinusoids [141]:

$$f[k] = \sum_{n=0}^{n_{max}} \left(a_n \cos\left(\frac{2\pi nk}{N-1}\right) + b_n \sin\left(\frac{2\pi nk}{N-1}\right) \right) \quad \text{for } k = 0, 1, \ldots, (N-1), \quad (A.17)$$

where the discrete Fourier series coefficients are

$$a_0 = \frac{1}{N-1}\left(\frac{f[0]}{2} + \sum_{k=1}^{N-2} f[k] + \frac{f[N-1]}{2} \right), \quad (A.18)$$

$$b_0 = 0, \quad (A.19)$$

$$a_n = \frac{2}{N-1}\left(\frac{f[0]}{2} + \sum_{k=1}^{N-2} f[k] \cdot \cos\left(\frac{2\pi nk}{N-1}\right) + \frac{f[N-1]}{2} \right) \quad \text{for } 1 \leq n \leq n_{max}, \quad (A.20)$$

$$b_n = \frac{2}{N-1} \sum_{k=1}^{N-2} f[k] \cdot \sin\left(\frac{2\pi nk}{N-1}\right) \quad \text{for } 1 \leq n \leq n_{max}. \quad (A.21)$$

It is worth noting that the summation in Eq. (A.17) is finite, where the upper bound is the largest mode n_{max} extracted from the sampled data.

In order to avoid sampling errors when computing the coefficients, the following sampling condition must be satisfied:

$$N > 2n_{max} + 1. \quad (A.22)$$

Figure A.3 shows the importance of over-sampling the data. Here, the discrete Fourier series coefficients of the function $y = \cos(4\theta)$ are evaluated using three different data samples over the interval $[-\pi, \pi]$. The coefficients are then used to reconstruct y by computing the summation in Eq. (A.17) up to $n_{max} = 4$. When the data is under-sampled ($N = 6$ or $N = 9$), the discrete Fourier series coefficients do not reconstruct y perfectly because the sampling condition is not satisfied. In contrast, when the coefficients are computed using $N = 12$ points, the function y is accurately reconstructed, as the sampling condition is now satisfied.
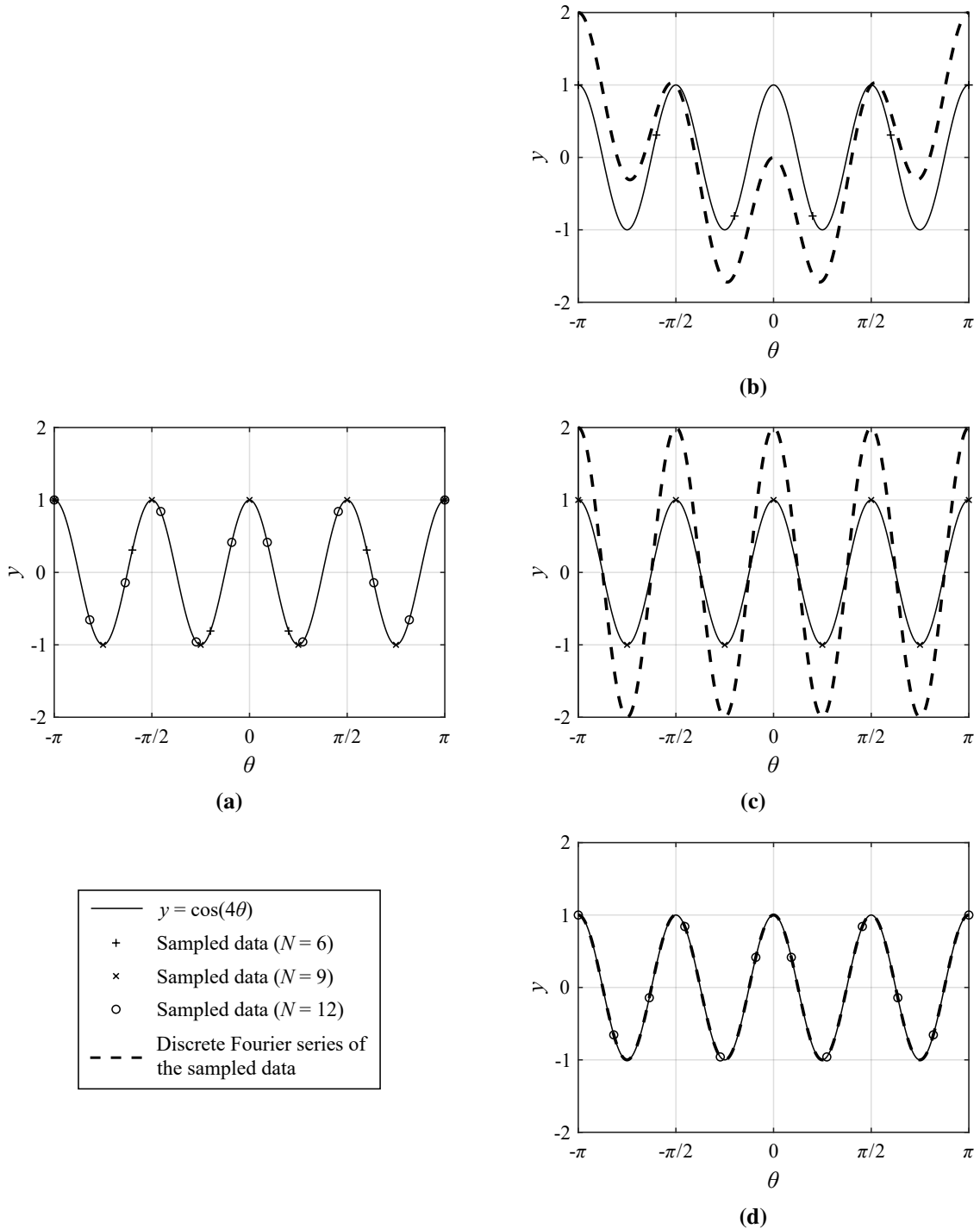
Fig. A.3 Reconstructing the function $y = \cos(4\theta)$ by **(a)** sampling over the interval $[-\pi, \pi]$, and then evaluating the discrete Fourier series coefficients using **(b)** $N = 6$, **(c)** $N = 9$ and **(d)** $N = 12$ points.

Appendix B

The Boundary-Element Method (BEM)

In most fields of engineering, the governing equations for a problem may be represented by a system of boundary integral equations (BIEs). After extensive development work throughout the 1970s, the boundary-element method (BEM) is now the most popular numerical technique for solving BIEs.

This appendix summaries the integral formulation of the BEM, which is used to solve the governing equations of an elastodynamic continuum experiencing steady-state, time-harmonic excitation. There are two different integral formulations that provide equivalent solutions: the direct and indirect approaches. The latter introduces fictitious sources with unknown intensities along the boundary [241], while the former, which is described in this appendix, expresses the integral equations directly in terms of the actual field variables of the problem concerned [20]. In elastodynamics, the field variables are the displacements and tractions.

All the equations in this appendix are derived by assuming the continuum is linear-elastic. Nonetheless, the continuum can also be assumed to display viscoelastic behaviour by applying the viscoelastic correspondence principle [18]: an elastic material property k is replaced by its complex equivalent $k^* = k(1 + i\eta)$, where $i = \sqrt{-1}$ and η is the hysteretic loss factor.

B.1   Integral Transforms

Before describing the BEM, it is important to understand the definition of an integral transform. These transforms can be expressed as a Fredholm integral equation of the first kind [141]:

$$g(x) = \int K(x,s) f(s) \, ds, \tag{B.1}$$

where an input function $f(s)$ is transformed into an output function $g(x)$ by using a specific kernel function or integral kernel $K(x,s)$, relating the variables x and s. The motivation behind this mathematical operation is to 'map' an equation from its original domain, where it might be algebraically unwieldly to solve, to another domain where the algebraic manipulation is far simpler. An example is the Fourier transform, while is detailed in Appendix A.

In linear vibration analysis, differential equations involving ordinary derivatives or partial derivatives need to be solved. One approach for solving them is to derive the Green's function. Given a linear differential operator $\mathcal{L} = \mathcal{L}(x)$ acting over a domain $\Omega \subset \mathbb{R}^n$, a Green's function $G(x,s)$ at the point $s \in \Omega$ is a solution to

$$\mathcal{L} G(x,s) = \delta(x-s), \tag{B.2}$$

where $\delta(x-s)$ is the Dirac delta function translated to the point $x = s$. In order words, $G(x,s)$ inverts $\mathcal{L}$ so that a differential equation $\mathcal{L} f(x) = g(x)$ can be solved:

$$g(x) = \int G(x,s) f(s) \, ds, \tag{B.3}$$

where the integral is analogous to Eq. (B.1). Hence, if a Green's function can be derived for a governing linear differential equation, multiplying and integrating it with an input function $f(s)$ will solve the desired response function $g(x)$ using the linear superposition principle.

B.2   Types of Boundary Conditions

Different boundary conditions can be applied to solve the BIEs. This section discusses three methods for structuring a problem based on its boundary conditions: Dirichlet, Neumann and Cauchy problems [41].

The Dirichlet (first-type) boundary condition specifies the value that a solution needs to take along a finite boundary of the domain, whereas the Neumann (second-type) boundary condition specifies the derivative of the solution along the boundary. Consider the homogeneous, elliptic equation:

$$\nabla^2 y + y = 0, \tag{B.4}$$

where $y(\mathbf{x})$ is a function of the position vector $\mathbf{x}$. Different boundary conditions can be applied onto the boundary Γ of domain Ω, where $y \in \Omega$. A Dirichlet boundary conidtion satisfies:

$$y(\mathbf{x}) = f(\mathbf{x}) \quad \text{for all } \mathbf{x} \subset \Gamma, \tag{B.5}$$

while a Neumann boundary condition satisfies:

$$\frac{\partial y}{\partial \mathbf{n}}(\mathbf{x}) = f(\mathbf{x}) \quad \text{for all } \mathbf{x} \subset \Gamma, \tag{B.6}$$

where $\mathbf{n}$ is the normal unit-vector to Γ, and the function $f \in \Gamma$.

For an elastodynamic problem, a Dirichlet boundary condition specifies the displacement field vector $\mathbf{u}$ along Γ, similar to Eq. (B.5), and the traction field vector $\mathbf{p}$ along Γ is unknown. In contrast, a Neumann boundary condition specifies $\mathbf{p}$ along Γ, similar to Eq. (B.6), and $\mathbf{u}$ along Γ is unknown. This is because the tractions are proportional to the first derivative of the displacements normal to a surface.

A Cauchy boundary condition specifies both a function and its normal derivative on Γ. This corresponds to imposing Dirichlet and Neumann boundary conditions over the sub-boundaries Γ_1 and Γ_2, respectively, where Γ_1 and Γ_2 are free to overlap and $(\Gamma_1 \cup \Gamma_2) \subset \Gamma$. The BIEs in this dissertation are solved as a Cauchy problem by satisfying both the displacement and traction conditions at the same boundary.

B.3   The Dynamic (Betti-Rayleigh) Reciprocity Theorem

Consider a homogeneous, isotropic, linear-elastic body defined by a three-dimensional (3D) domain Ω, with position vector $\mathbf{x} = \{x_1, x_2, x_3\}^{\text{T}}$ in a Cartesian coordinate system, and a two-dimensional (2D) boundary surface Γ. The steady-state, time-harmonic displacement $\mathbf{u}$ of the body at a given angular excitation frequency ω is governed by Navier's equation:

$$(\lambda + \mu)\nabla\nabla\cdot\mathbf{u} + \mu\nabla^2\mathbf{u} + \rho\mathbf{b} = -\omega^2\rho\mathbf{u}, \tag{B.7}$$

where the vector $\mathbf{b}$ denotes the internal body forces per unit mass, ρ is the mass density, and λ and μ are the first and second elastic Lamé constants, respectively. Cauchy boundary conditions are applied onto Γ to specify a particular elastodynamic state, as illustrated in Fig. B.1a.

One method of deriving the BIEs, relating $\mathbf{u}$ and $\mathbf{p}$ on the surface of the body, is to use the dynamic reciprocity theorem. The dynamic reciprocity theorem of elastodynamics, which is an extension of Betti's theorem in elastostatics, relates two arbitrary elastodynamic states of the body in a strong formulation of Navier's equation [52]. The first state includes $\mathbf{u}$ and $\mathbf{b}$ from Eq. (B.7) and the associated tractions $\mathbf{p}$ due to $\mathbf{u}$; the corresponding variables in the second

state are denoted as $\mathbf{u}^*$, $\mathbf{b}^*$ and $\mathbf{p}^*$. For the case of time-harmonic excitation, the reciprocity integral in index notation is

$$\int_\Gamma p_k u_k^* d\Gamma + \int_\Omega \rho b_k u_k^* d\Omega = \int_\Gamma p_k^* u_k d\Gamma + \int_\Omega \rho b_k^* u_k d\Omega. \tag{B.8}$$

The first state represents the problem of interest with applied boundary conditions and the internal body forces can be assumed to be zero ($b_k = 0$) because the problem only considers vibration about an equilibrium position. The second state, which is known as the fundamental solution or Green's function, is the forced response in the $\mathbf{e}_l$ direction at a receiver or integration point $\mathbf{x}_i$ due to a unit-magnitude, time-harmonic point force applied in the $\mathbf{e}_k$ direction at a source or collocation point $\mathbf{x}_j$ (see Fig. B.1b). To apply the reciprocity theorem, both states must be defined for the same body, and it is assumed that Ω is part of an infinite domain.
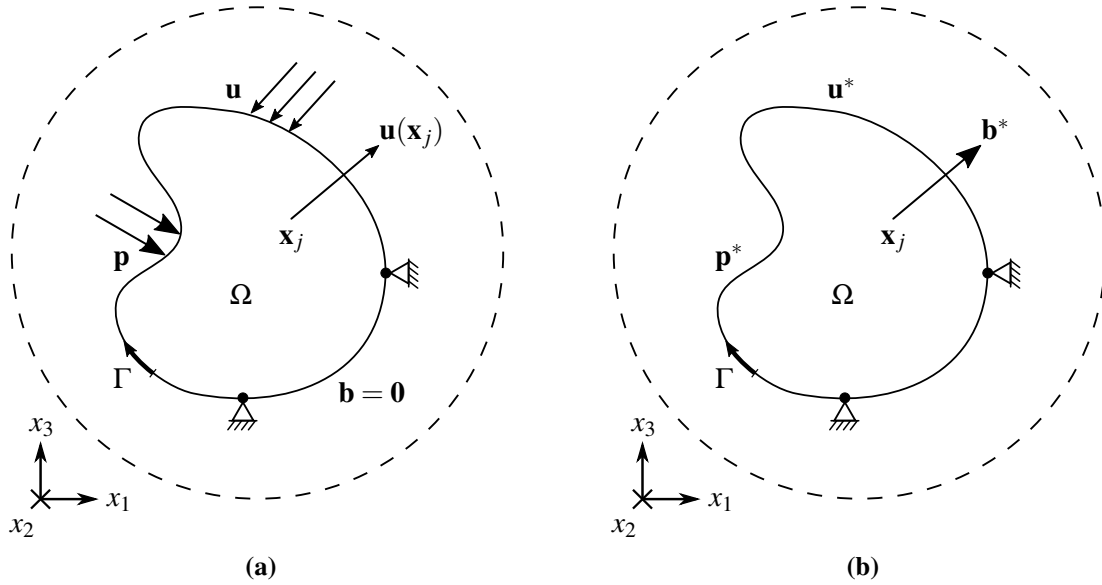
Fig. B.1 Elastodynamic states of a body, with domain Ω and boundary surface Γ, illustrating **(a)** the problem of interest with no body forces ($\mathbf{b} = \mathbf{0}$) and **(b)** the fundamental solution corresponding to a point force $\mathbf{b}^*$ applied at the collocation point $\mathbf{x}_j$. The infinite domain is represented by the dashed circle.

B.4 The Fundamental Solution

It is important to note that different fundamental solutions may suit the problem based on its domain. This appendix describes the Green's functions for a time-harmonic point force applied in a full-space, or infinite domain because they can be written as closed-form, analytical expressions. Therefore, the soil domain is modelled as an homogeneous, isotropic continuum.

The Green's functions for a homogeneous [8] or layered [31] half-space, computed using the ElastoDynamics Toolbox (EDT) [211], are also suitable for modelling elastodynamic problems that contain propagating wave-fields in the soil. Note that when the Green's functions for a full-space are used, the free surface has to be discretised (see Section 3.2). However, this is not the case when using the half-space Green's functions.

The displacement and traction Green's functions are denoted as the second-order tensors (or matrices) u_{lk}^*, and p_{lk}^*, respectively, in index notation. The time-harmonic point force in a linear-elastic full-space can be expressed as a body force:

$$\rho b_k^* = \delta(r)\delta_{lk},\qquad(B.9)$$

where $\delta(r)$ is the 3D Dirac delta function centred at $r = |\mathbf{x}_i - \mathbf{x}_j|$, and δ_{lk} is the Kronecker delta. The explicit expressions for the full-space Green's functions are [52]:

$$u_{lk}^* = \frac{1}{4\pi\rho c_S^2}\left(\psi\delta_{lk} - \chi r_{,l}r_{,k}\right),\qquad(B.10)$$

$$p_{lk}^* = \frac{1}{4\pi}\left[A\left(\frac{\partial r}{\partial n}\delta_{lk} + n_l r_{,k}\right) + B r_{,l}r_{,k}\frac{\partial r}{\partial n} + C r_{,l}n_k\right],\qquad(B.11)$$

where n_l is the normal unit-vector in the $\mathbf{e}_l$ direction. Equations (B.10) and (B.11) are expressed in terms of the following variables:

$$\psi = \frac{e^{-k_S r}}{r}\left(1 + \frac{1}{k_S r} + \frac{1}{k_S^2 r^2}\right) - \frac{e^{-k_P r}}{r}\frac{c_S^2}{c_P^2}\left(1 + \frac{1}{k_P r} + \frac{1}{k_P^2 r^2}\right),\qquad(B.12)$$

$$\chi = \frac{e^{-k_S r}}{r}\left(1 + \frac{3}{k_S r} + \frac{3}{k_S^2 r^2}\right) - \frac{e^{-k_P r}}{r}\frac{c_S^2}{c_P^2}\left(1 + \frac{3}{k_P r} + \frac{3}{k_P^2 r^2}\right),\qquad(B.13)$$

$$A = \frac{d\psi}{dr} - \frac{\chi}{r},\qquad(B.14)$$

$$B = 4\frac{\chi}{r} - 2\frac{d\chi}{dr},\qquad(B.15)$$

$$C = \frac{\lambda}{\mu}\left(\frac{d\psi}{dr} - \frac{d\chi}{dr} - 2\frac{\chi}{r}\right) - 2\frac{\chi}{r},\qquad(B.16)$$

with wavenumbers:

$$k_{P,S} = \frac{i\omega}{c_{P,S}}, \tag{B.17}$$

and phase speeds:

$$c_P = \sqrt{\frac{\lambda + 2\mu}{\rho}}, \tag{B.18}$$

$$c_S = \sqrt{\frac{\mu}{\rho}}, \tag{B.19}$$

where the subscripts 'P' and 'S' denote the variables associated with P- and S-waves in the body Ω. For convenience, the analytical expressions for $\frac{d\psi}{dr}$ and $\frac{d\chi}{dr}$ are not stated here, but the reader can refer to them in [52].

B.5 The Boundary Integral Equation (BIE)

The BIE, which describes the displacement-state at an internal point $\mathbf{y} \in \Omega$, can be derived by substituting Eq. (B.9) into Eq. (B.8) and disregarding the internal body forces about the equilibrium position:

$$u_l(\mathbf{y}, \omega) + \int_\Gamma p_{lk}^*(\mathbf{y}, \mathbf{x}_j, \omega) u_k(\mathbf{x}_j, \omega) d\Gamma = \int_\Gamma u_{lk}^*(\mathbf{y}, \mathbf{x}_j, \omega) p_k(\mathbf{x}_j, \omega) d\Gamma. \tag{B.20}$$

The BIE expresses the displacement $u_l(\mathbf{y}, \omega)$ at $\mathbf{y}$ in terms of the displacement $u_k(\mathbf{x}_j, \omega)$ and traction $p_k(\mathbf{x}_j, \omega)$ at the collocation point $\mathbf{x}_j \in \Gamma$. The field variables u_l, u_k and p_k represent 3×1 column vectors, whereas u_{lk}^* and p_{lk}^* represent 3×3 matrices of the fundamental solutions. Equation (B.20) is valid for both bounded and unbounded domains, as illustrated in Fig. B.2. The ability to model unbounded domains, is one of the advantages of the BEM, as described in Section 2.3.2, because it satisfies the radiation damping condition for elastodynamic waves in an infinite or semi-infinite domain.

Now, consider when the internal point $\mathbf{y}$ moves to the boundary surface Γ to become the integration point $\mathbf{x}_i \in \Gamma$. Note that at the limit when $\mathbf{x}_i$ coincides with $\mathbf{x}_j$, the fundamental solutions and the integral in Eq. (B.20) become singular as $r \to 0$. To avoid these singularities, Domínguez [52] recommends to extend a surface Γ_ε around the sub-domain Ω_ε containing the collocation point $\mathbf{x}_j \in \Omega_\varepsilon$ into a hemisphere of small radius ε, as shown in Fig. B.2. The singular behaviour of the integral is then evaluated at the limit $\varepsilon \to 0$. Further details on the limiting process, which depends on the type of boundary-element and number of dimensions,

can be found in books by Domínguez [52] and Beer et al. [12]. For the special case when Γ is smooth, Eq. (B.20) becomes

$$\frac{1}{2}u_l\left(\mathbf{x}_i,\omega\right)+\int_\Gamma p^*_{lk}\left(\mathbf{x}_i,\mathbf{x}_j,\omega\right)u_k\left(\mathbf{x}_j,\omega\right)d\Gamma=\int_\Gamma u^*_{lk}\left(\mathbf{x}_i,\mathbf{x}_j,\omega\right)p_k\left(\mathbf{x}_j,\omega\right)d\Gamma. \qquad \text{(B.21)}$$

(a)   **(b)**
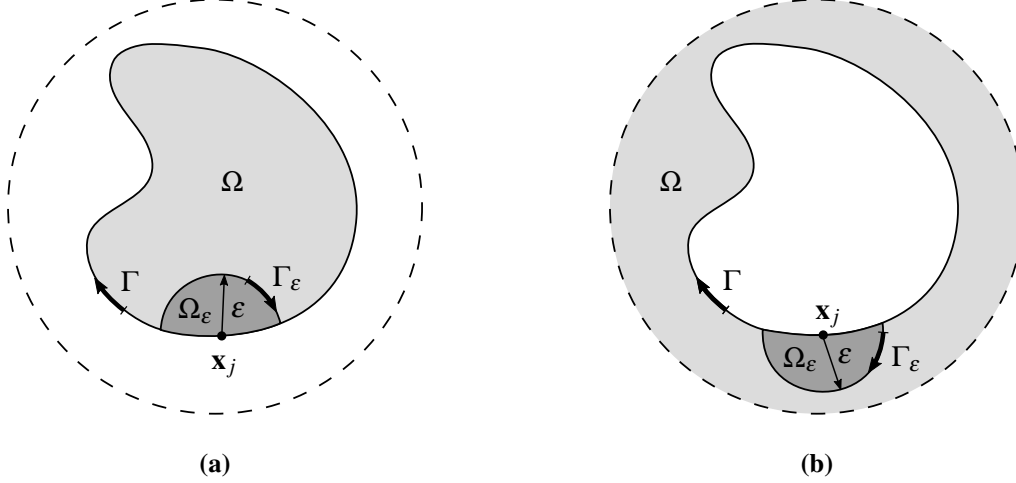
Fig. B.2 The lighter shaded regions illustrate **(a)** a bounded and **(b)** an unbounded domain Ω within an infinite domain, represented using the dashed line. The darker shaded regions show the limiting process applied to avoid singularities when a collocation point $\mathbf{x}_j$ coincides with an integration point $\mathbf{x}_i$.

B.6   Solving the BIEs at the Boundary Surface

By evaluating the integrals in Eq. (B.21) over the boundary surface Γ, with both the integration points $\mathbf{x}_i$ and collocation points $\mathbf{x}_j$, the unknown boundary values at Γ can be calculated. For an elastodynamic problem, the displacement and traction wave-fields represent the boundary values. The techniques used for solving the BIEs at the boundary surface are described in this section.

Numerical integration schemes can approximately compute the BIEs. The best option is to use standard Gauss-Legendre quadrature because of its high degree of precision [141]. In this method, the surface Γ is divided into N elements and the integral is restructured as a summation over n interpolated Gauss points within each element. For example, the integration of a one-dimensional function $g(t)$ over the limit $[t_1, t_2]$ can be approximated as

$$\int_{t_1}^{t_2} g(t)\,dt = \int_{-1}^{1} f(\xi)\frac{dg}{d\xi}d\xi \approx \sum_{p=1}^{n}\frac{dg}{d\xi}f_p w_p, \qquad \text{(B.22)}$$

where ξ is an intrinsic transformed coordinate system with limit $[-1, 1]$, and f_p and w_p are the discrete values of the transformed function and the corresponding weighting functions of each Gauss point p, respectively.

The boundary surface is discretised into smooth, constant, rectangular elements, where the displacement and traction wave-fields at the central node j of each element are denoted by the vectors $\mathbf{u}(\mathbf{x}_j)$ and $\mathbf{p}(\mathbf{x}_j)$, respectively. Although higher-order boundary elements, which vary linearly or quadratically over each element, offer faster convergence, they require more extensive, numerical techniques to evaluate [12]. As $\mathbf{u}$ and $\mathbf{p}$ are assumed to be constant over each element, Eq. (B.21) can be rewritten as

$$
\frac{1}{2}\mathbf{u}(\mathbf{x}_i, \omega) + \sum_{j=1}^{N} \left(\int_{\Gamma_j} \mathbf{p}^*(\mathbf{x}_i, \mathbf{x}_j, \omega) \, d\Gamma_j \right) \mathbf{u}(\mathbf{x}_j, \omega) =
$$
$$
\sum_{j=1}^{N} \left(\int_{\Gamma_j} \mathbf{u}^*(\mathbf{x}_i, \mathbf{x}_j, \omega) \, d\Gamma_j \right) \mathbf{p}(\mathbf{x}_j, \omega) ,
$$

(B.23)

where Γ_j is the surface of each boundary element. Note that the integrals enclosed within the brackets only depend on the Green's functions $\mathbf{u}^*$ and $\mathbf{p}^*$. These integrals are denoted as the $\hat{\mathbf{H}}$ and $\mathbf{G}$ matrices, which means that Eq. (B.23) can be rewritten as

$$
\frac{1}{2}\mathbf{u}(\mathbf{x}_i, \omega) + \sum_{j=1}^{N} \hat{\mathbf{H}}(\mathbf{x}_i, \mathbf{x}_j, \omega) \mathbf{u}(\mathbf{x}_j, \omega) = \sum_{j=1}^{N} \mathbf{G}(\mathbf{x}_i, \mathbf{x}_j, \omega) \mathbf{p}(\mathbf{x}_j, \omega) .
$$

(B.24)

Now assume that the body force expressed in Eq. (B.9) is applied at each of the boundary-element nodes from 1 to N. Thus, Eq. (B.24) can be expressed as N matrix equations:

$$
\sum_{j=1}^{N} \mathbf{H}(\mathbf{x}_i, \mathbf{x}_j, \omega) \mathbf{u}(\mathbf{x}_j, \omega) = \sum_{j=1}^{N} \mathbf{G}(\mathbf{x}_i, \mathbf{x}_j, \omega) \mathbf{p}(\mathbf{x}_j, \omega) \quad \text{for } i = 1, 2, \ldots, N ,
$$

(B.25)

where

$$
\mathbf{H}(\mathbf{x}_i, \mathbf{x}_j, \omega) = \begin{cases} \hat{\mathbf{H}} & \text{if } i \neq j , \\ \hat{\mathbf{H}} + \frac{1}{2}\mathbf{I} & \text{if } i = j . \end{cases}
$$

(B.26)

The N equations in Eq. (B.25) can be grouped into the following matrix equation:

$$
\mathbf{Hu} = \mathbf{Gp} ,
$$

(B.27)

where $\mathbf{H}$ and $\mathbf{G}$ are the $3N \times 3N$ collocation matrices, and the $3N \times 1$ vectors $\mathbf{u}$ and $\mathbf{p}$ are the boundary values. It is important to note that the collocation matrices inherently account for the dynamic coupling between all nodes located on the boundary surface because the fundamental solutions in Eq. (B.23) are used to find the response at all nodes when a body force is applied at each node one-by-one.

Standard Gauss-Legendre quadrature [141] is used to compute the integrals at each element in the collocation matrices. When $i \neq j$, $\mathbf{H}$ can be computed as follows:

$$
\mathbf{H}\left(\mathbf{x}_i, \mathbf{x}_j, \omega\right) = \int_{\Gamma_j} \mathbf{p}^*\left(\mathbf{x}_i, \mathbf{x}_j, \omega\right) d\Gamma_j = \int_{-1}^{1} \int_{-1}^{1} \mathbf{p}^*\left(\mathbf{x}_i, \mathbf{x}_j, \omega\right) |J| d\xi_1 d\xi_2 ,
$$

$$
\approx \sum_{p=1}^{n} \sum_{q=1}^{n} \mathbf{p}^*\left(\xi_p, \xi_q, \omega\right) |J| w_p w_q ,
$$

(B.28)

where $|J|$ is the Jacobian, ξ_p and ξ_q are the transformed coordinates, and w_p and w_q are the corresponding weighting functions at each Gauss point. Talbot [221] suggests that six Gauss points are sufficient to achieve reasonable convergence over the frequency range of interest from 1 to 80 Hz. Figure B.3 illustrates how the global Cartesian coordinates along the boundary surface can be transformed into intrinsic coordinates.

As expressed previously, when $i = j$ (i.e., the points $\mathbf{x}_i$ and $\mathbf{x}_j$ coincide) a limiting process is required to avoid integrating over the singularities. At the limit when $r \to 0$, p_{lk}^* contains a
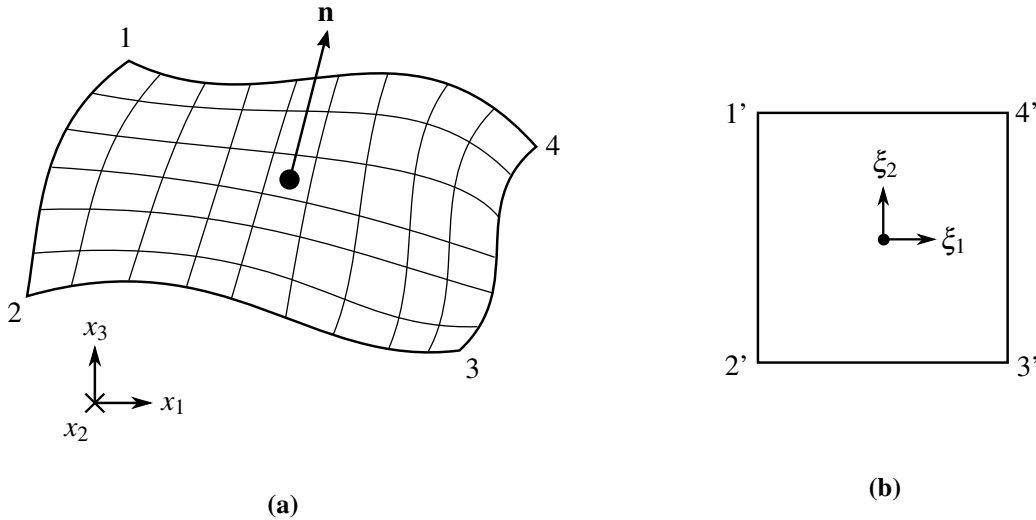
Fig. B.3 Transformation from **(a)** the global Cartesian (x_1, x_2, x_3) coordinate system to **(b)** the intrinsic (ξ_1, ξ_2) coordinate system so that the wave-fields can be numerically integrated over the boundary surface using standard Gauss-Legendre quadrature.

strong singularity of order $1/r^2$ in 3D space. For rectangular elements, computing $\mathbf{H}(\mathbf{x}_i, \mathbf{x}_i, \omega)$ is straightforward: $\mathbf{H}(\mathbf{x}_i, \mathbf{x}_i, \omega) = \frac{1}{2}\mathbf{I}$ [52]. When non-rectangular elements are used instead, computing $\mathbf{H}(\mathbf{x}_i, \mathbf{x}_i, \omega)$ becomes more involved, requiring the consideration of static rigid-body displacements [52].

Calculating $\mathbf{G}(\mathbf{x}_i, \mathbf{x}_i, \omega)$ requires element subdivision, as proposed by Lachat [150], where the element is subdivided into four triangular sub-elements. Each sub-element is treated as a quadrilateral domain, with two of the corners coinciding with the central node of the original element [52]. Thus, the *weak singularity* in u_{lk}^*, which is of order $1/r$ in 3D space, cancels out with the Jacobian $|J|$ as the limit $r \to 0$ is reached. Standard Gauss-Legendre quadrature can then be used to compute the integrals numerically.

When Cauchy boundary conditions, denoted by a vector $\mathbf{f}$, are applied on Γ, Eq. (B.27) can be solved by restating it as the following matrix equation:

$$\mathbf{A}\mathbf{y} = \mathbf{f}, \tag{B.29}$$

where $\mathbf{y}$ is a vector representing the unknown displacement and traction wave-fields, and the matrix $\mathbf{A}$ is a linear combination of $\mathbf{H}$ and $\mathbf{G}$. Equation (B.29) is best solved numerically using Gaussian elimination, as $\mathbf{A}$ is often a fully populated, non-symmetric matrix in elastodynamic problems.

B.7 Solving the BIEs at the Internal Points

Now, consider when the internal point $\mathbf{y} \in \Omega$ also lies on the surface Γ_y of sub-domain Ω_y, where $\Omega_y \subset \Omega$, as shown in Fig. B.4. In this case, the integral equations in the BEM need to be modified so as to find the displacement and traction wave-fields at multiple internal points $\mathbf{y}_i$.

By approximating the integral in Eq. (B.20) using standard Gauss-Legendre quadrature and assuming the wave-fields are uniform at the N collocation nodes located on the boundary surface Γ, the displacement at M internal nodes on the surface Γ_y can be expressed as

$$
\begin{aligned}
u_l(\mathbf{y}_i, \omega) + \sum_{j=1}^{N} \left(\int_{\Gamma_j} p_{lk}^*(\mathbf{y}_i, \mathbf{x}_j, \omega)\, d\Gamma_j \right) u_k(\mathbf{x}_j, \omega) = \\
\sum_{j=1}^{N} \left(\int_{\Gamma_j} u_{lk}^*(\mathbf{y}_i, \mathbf{x}_j, \omega)\, d\Gamma_j \right) p_k(\mathbf{x}_j, \omega) \quad \text{for } i = 1, 2, \ldots, M,
\end{aligned}
\tag{B.30}
$$

where $\mathbf{y}_i$ and $\mathbf{x}_j$ denotes each internal integration point and collocation point, respectively. The
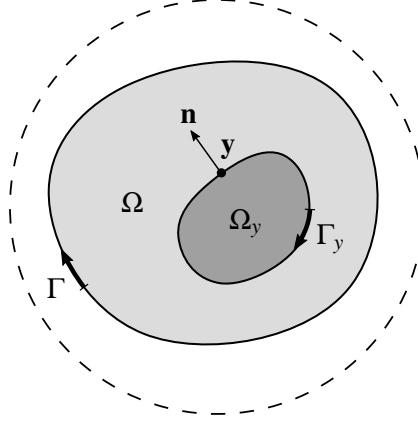
Fig. B.4 A body, with domain Ω (lighter shaded region) and boundary surface Γ, is defined within an infinite domain, represented by the dashed line. The internal point $\mathbf{y} \in \Omega$, with normal unit-vector $\mathbf{n}$, lies on the surface Γ_y separating the sub-domain Ω_y (darker shaded region) from Ω.

distance between each integration and collocation point is $r = \left| \mathbf{y}_i - \mathbf{x}_j \right|$. It is worth noting that the weak and strong singularities in u_{lk}^* and p_{lk}^*, respectively, at the limit when $r \to 0$ do not need to be considered. This is because the integration and collocation points never share the same coordinates, so element subdivision, as detailed in Appendix B.6, is not required.

The integrals enclosed within the brackets in Eq. (B.30) are denoted as the displacement-state collocation matrices $\mathbf{G}_u$ and $\mathbf{H}_u$. Thus, the BIE can be rewritten as

$$\mathbf{u}^{\text{int}}(\mathbf{y}_i, \omega) = \sum_{j=1}^{N} \mathbf{G}_u\left(\mathbf{y}_i, \mathbf{x}_j, \omega\right) \mathbf{p}\left(\mathbf{x}_j, \omega\right) - \sum_{j=1}^{N} \mathbf{H}_u\left(\mathbf{y}_i, \mathbf{x}_j, \omega\right) \mathbf{u}\left(\mathbf{x}_j, \omega\right), \tag{B.31}$$

where the vector $\mathbf{u}^{\text{int}}(\mathbf{y}_i, \omega)$ is the displacement wave-field at each internal node i. Applying Eq. (B.31) to all M internal nodes and performing the summation over the N collocation nodes gives the matrix equation:

$$\mathbf{u}^{\text{int}} = \mathbf{G}_u \mathbf{p} - \mathbf{H}_u \mathbf{u}, \tag{B.32}$$

where the vector $\mathbf{u}^{\text{int}}$ is the displacement wave-field at all M internal nodes within the domain Ω, and the vectors $\mathbf{u}$ and $\mathbf{p}$ are the displacement and traction boundary conditions, respectively, applied at the N nodes on the surface Γ. It should be noted that both $\mathbf{G}_u$ and $\mathbf{H}_u$ are $3M \times 3N$ non-square matrices.

In order to compute the traction wave-field at an internal point $\mathbf{y} \in \Omega_y$, the stress-state at $\mathbf{y}$ needs to be defined. This is done by taking the partial derivatives of Eq. (B.20), with respect to $\mathbf{y}$, and then substituting the resulting equation into the linear-elastic kinematic relationship:

$$\varepsilon_{lm}(\mathbf{y}, \omega) = \frac{1}{2} \left(u_{l,m}(\mathbf{y}, \omega) + u_{m,l}(\mathbf{y}, \omega) \right), \tag{B.33}$$

and the generalised Hooke's Law for an isotropic continuum:

$$\sigma_{lm}(\mathbf{y}, \omega) = \lambda \varepsilon_{kk}(\mathbf{y}, \omega) \delta_{lm} + 2\mu \varepsilon_{lm}(\mathbf{y}, \omega), \tag{B.34}$$

where δ_{lm} is the Kronecker delta, ε_{lm} is the infinitesimal strain tensor, σ_{lm} is the Cauchy stress tensor, and $\varepsilon_{kk} = \varepsilon_{xx} + \varepsilon_{yy} + \varepsilon_{zz}$ is the volumetric strain. Thus, the BIE for the stress-state [201] at $\mathbf{y}$ can be defined as follows:

$$\sigma_{lm}(\mathbf{y}, \omega) + \int_{\Gamma} p^*_{lmk}(\mathbf{y}, \mathbf{x}_j, \omega) u_k(\mathbf{x}_j, \omega) d\Gamma = \int_{\Gamma} u^*_{lmk}(\mathbf{y}, \mathbf{x}_j, \omega) p_k(\mathbf{x}_j, \omega) d\Gamma, \tag{B.35}$$

where u^*_{lmk} and p^*_{lmk} are third-order tensors that represent the stress-state fundamental solutions:

$$u^*_{lmk} = -\frac{1}{4\pi} \left[A \left(r_{,l} \delta_{mk} + r_{,m} \delta_{lk} - r_{,k} \delta_{lm} \right) + B r_{,l} r_{,m} r_{,k} \right], \tag{B.36}$$

$$
\begin{aligned}
p^*_{lmk} = \frac{\rho c_S^2}{4\pi} \Bigg[&-A \frac{2}{r} \left(n_l \delta_{mk} + n_m \delta_{lk} \right) + D \left(r_{,k} \delta_{lm} \frac{\partial r}{\partial n} + r_{,l} r_{,m} n_k \right) + \\
&E \left(\frac{\partial r}{\partial n} \left[r_{,l} \delta_{mk} + r_{,m} \delta_{lk} \right] + r_{,m} r_{,k} n_l + r_{,l} r_{,k} n_m \right) + \\
&F r_{,l} r_{,m} r_{,k} \frac{\partial r}{\partial n} + G n_k \delta_{lm} \Bigg],
\end{aligned}
\tag{B.37}
$$

with the following coefficients:

$$D = 2 \left[\frac{d^2 \psi}{dr^2} - \frac{1}{r} \left(\frac{d\psi}{dr} + \frac{d\chi}{dr} \right) + \frac{\chi}{r^2} \right], \tag{B.38}$$

$$E = -\frac{d^2 \psi}{dr^2} + \frac{1}{r} \left(\frac{d\psi}{dr} + 3 \frac{d\chi}{dr} \right) - 6 \frac{\chi}{r^2}, \tag{B.39}$$

$$F = 4 \left(\frac{3}{2} \frac{d^2 \chi}{dr^2} - \frac{5}{r} \frac{d\chi}{dr} + 7 \frac{\chi}{r^2} \right), \tag{B.40}$$

$$G = -2 \left(\frac{d^2 \psi}{dr^2} + 2 \frac{d^2 \chi}{dr^2} \right). \tag{B.41}$$

The expressions for ψ, χ, A and B are the same as those denoted in Eqs. (B.12)–(B.15), and the derivatives $d^2\psi/dr^2$ and $d^2\chi/dr^2$ are fully expressed by Rego Silva et al. [201].

The stress $\sigma_{lm}(\mathbf{y},\omega)$ in Eq. (B.35) can be converted into the traction $p_l(\mathbf{y},\omega)$ by applying Cauchy's formula, which can be represented as

$$p_l(\mathbf{y},\omega) = \sigma_{lm}(\mathbf{y},\omega)\, n_m(\mathbf{y}),\tag{B.42}$$

where $n_m(\mathbf{y})$ is the normal unit-vector at the surface Γ_y associated with the internal point $\mathbf{y}$, as shown in Fig. B.4. Once Cauchy's formula is applied to Eq. (B.35), standard Gauss-Legendre quadrature can be used to approximate the integrals. Therefore, the traction at M internal nodes on the surface Γ_y can be expressed as

$$
\begin{aligned}
p_l(\mathbf{y}_i,\omega) + \sum_{j=1}^{N}\left(\int_{\Gamma_j} p_{lmk}^*(\mathbf{y}_i,\mathbf{x}_j,\omega)\, n_m(\mathbf{y}_i)\, d\Gamma_j\right) u_k(\mathbf{x}_j,\omega) = \\
\sum_{j=1}^{N}\left(\int_{\Gamma_j} u_{lmk}^*(\mathbf{y}_i,\mathbf{x}_j,\omega)\, n_m(\mathbf{y}_i)\, d\Gamma_j\right) p_k(\mathbf{x}_j,\omega) \quad \text{for } i=1,2,\ldots,M.
\end{aligned}
\tag{B.43}
$$

It is worth noting that both $u_{lmk}^* n_m$ and $p_{lmk}^* n_m$ are second-order tensors. Hence, the integrals enclosed within the brackets in Eq. (B.43) are denoted as the traction-state collocation matrices $\mathbf{G}_p$ and $\mathbf{H}_p$, and the BIE can be rewritten as

$$\mathbf{p}^{\text{int}}(\mathbf{y}_i,\omega) = \sum_{j=1}^{N}\mathbf{G}_p(\mathbf{y}_i,\mathbf{x}_j,\omega)\,\mathbf{p}(\mathbf{x}_j,\omega) - \sum_{j=1}^{N}\mathbf{H}_p(\mathbf{y}_i,\mathbf{x}_j,\omega)\,\mathbf{u}(\mathbf{x}_j,\omega),\tag{B.44}$$

where the vector $\mathbf{p}^{\text{int}}(\mathbf{y}_i,\omega)$ is the traction wave-field at each internal node i. By applying Eq. (B.44) to all M internal nodes and performing the summation over the N collocation nodes, the following matrix equation can be obtained:

$$\mathbf{p}^{\text{int}} = \mathbf{G}_p\mathbf{p} - \mathbf{H}_p\mathbf{u},\tag{B.45}$$

where the vector $\mathbf{p}^{\text{int}}$ is the traction wave-field at all M internal nodes within the domain Ω, and the vectors $\mathbf{u}$ and $\mathbf{p}$ are equivalent to the ones defined in Eq. (B.32). Similar to $\mathbf{G}_u$ and $\mathbf{H}_u$ in Eq. (B.32), $\mathbf{G}_p$ and $\mathbf{H}_p$ are also $3M \times 3N$ non-square matrices.

B.8 A Note on Fictitious Eigenfrequencies

While the BEM is very powerful when applied to unbounded ground-borne vibration problems, it does have some shortcomings due to numerical difficulties. It turns out that the BIEs have a unique solution for the unbounded problem with boundary Γ, except when the excitation frequency coincides with one of the eigenvalues (natural frequencies) of the bounded problem, with the same boundary conditions on Γ [52]. Therefore, fictitious eigenfrequencies may be predicted in the unbounded domain formulation.

There are methods that can eliminate these fictitious eigenfrequencies by using special BEM formulations. An example is the approach used by Burton & Miller [27] when a second integral equation is derived and combined with the original BIE. However, these fictitious eigenfrequencies are not always present; the implementation of full-space Green's functions, in conjunction with a free surface that is appropriately discretised, is one such example [14].

Appendix C

The Iterative Pipe-in-Pipe (PiP) Model

The standard pipe-in-pipe (PiP) model, which simulates a tunnel embedded in a homogeneous, isotropic half-space [114], is a computationally efficient tool that can predict the response of the surrounding soil when the tunnel is excited by train-induced loads. The PiP model originates from a study conducted by Köpke [138] on the vibration of underground pipelines. Köpke applies the thick-walled, cylindrical shell approach used by Gazis [79, 80] to a 'pipe in a pipe'; the inner shell represents a buried pipeline, while the outer shell, which extends to an infinite outer diameter, represents the surrounding soil as a full-space. Hunt & May [111] use Köpke's solution to calculate soil's response around a railway tunnel. Further work conducted by Forrest [68] and Hussein [112] on symmetric and anti-symmetric loading laid the foundation for the current version of the standard PiP model [116].

In this dissertation, the response of the soil is considered when two different time-harmonic modes of excitation are applied within the tunnel. The first mode of excitation is a vertical point force applied at the base of the inner tunnel wall, which is referred to as the tunnel invert. The second mode of excitation is a roughness applied at the wheel-rail interface when a train-track system is coupled to the tunnel invert. Forrest [68] describes in detail how to calculate the soil response when a time-harmonic point force is applied within a tunnel embedded in a full-space.

However, a notable disadvantage of the standard PiP model is that it inaccurately predicts the soil response of shallow tunnels, as it is assumed that the waves reflected at the free surface do not affect the near-field response around the tunnel [113]. Thus, the iterative wave-scattering approach, as described in Section 2.5.1, is applied in this appendix to approximate the dynamic interaction between the ground and the tunnel, such that the near-field response of the tunnel can be modified. The first section presents the components and assumptions of the iterative PiP

model. The following three sections derive the equations of motion for a tunnel embedded in a full-space when it is driven by the passage of a train. In the fifth section, the iterative approach is applied to account for the scattered wave-field that is induced at the outer tunnel wall due to wave interaction. Finally, the expressions for the far-field displacements and tractions in the soil around a tunnel embedded in a half-space are derived in the last two sections.

C.1 Components

When the excitation due to a train is applied at the tunnel invert, the PiP model can be divided into four main components: the train, the track, the tunnel, and the soil. To simplify the derived equations, the train, track and tunnel are assumed to be infinitely long in the longitudinal space x-domain. This section describes the modelling parameters of each component.

C.1.1 Train

The train is assumed to move at constant speed v, and it includes bogies with fixed axle spacing L_a. Since the average speed of underground trains is low, it is reasonable to only account for excitation due to wheel-rail roughness (see Section 2.1.1). It is important to note that the PiP model is only appropriate for predicting the vibration when the train speed is below the critical speed of the track, which is dependent on the track's cut-on frequency (see Section 2.4).

Excitation occurs as the train axles pass over a fixed point on the track at low frequencies below the track's cut-on frequency. Simple train bogie models can capture this by using either a single degree of freedom (SDOF) system, consisting of the unsprung axle mass, or a two DOF system, which accounts for the semi-sprung bogie mass and primary suspension. A parametric study of various train parameters by Colaço et al. [38] showed that the semi-sprung mass has an insignificant effect on the generation of ground-borne vibration. The study also highlighted that the primary suspension effectively decouples the unsprung mass from its bogie at frequencies above 15 Hz. Therefore, an SDOF axle system is used in the PiP model, with M_a denoting the unsprung axle mass.

The governing equations of motion are derived by keeping the train stationary and moving a pull-through roughness at speed v between the axle masses and the track's rails. The roughness accounts for the irregularities along the wheel-rail interface, and it is assumed to be spatially harmonic in the x-domain, with wavelength λ and magnitude Δ in the vertical direction. Thus,

the wheel-rail roughness can be expressed in the space-time (x,t)-domain as $\bar{\Delta}(x,t) = \Delta e^{i\omega t}$, where $\omega = 2\pi v/\lambda$ is the angular excitation frequency. As the axles follow the profile of the pull-through roughness, time-harmonic forces, which oscillate at frequency ω, are applied onto the rails due to the inertia of the axles.

Note that the roughness is typically approximated as a random, stationary process using random vibration analysis, so the spectrum or power-spectral density (PSD) is used to define the variation of the roughness with frequency [180]. The simplest case is to assume the roughness has a white-noise distribution; however, this is physically unrealistic. More realistic roughness spectra are also available; Frederich [71] (paper in German) defines a formula for the PSD of irregularities at the wheel-rail interface, which is dependent on the track unevenness, waviness and train speed, by fitting curves to measured data.

C.1.2 Track

A slab (non-ballasted) track, which consists of two parallel rails mounted via rubber rail pads on a pre-cast or in-situ concrete slab, is coupled to the tunnel invert. Slab tracks provide better service performance and a longer life-span compared to traditional ballasted tracks that are often used for surface railways. In a standard (fixed) slab track, the slab is supported above the tunnel invert by a layer of mortar or self-compacting concrete (SCC), which acts as a bonding agent. At particular locations where track vibration or noise may be of concern, a floating slab track (FST) can be used as an effective countermeasure [158]. Here, the slab is supported by a combination of rubber bearings and springs, as illustrated in Fig. C.1. In practice, the FST's design parameters, such as the slab's natural frequency, need to be carefully selected in order to isolate the motion of the track from the tunnel wall over certain frequencies [153].
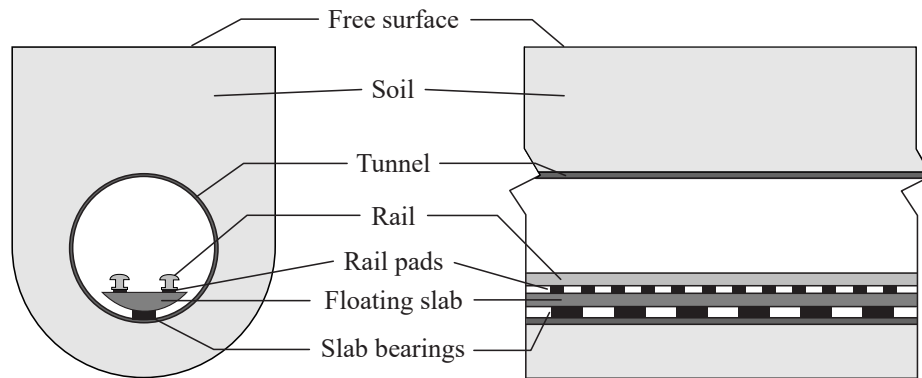
Fig. C.1 Components of the floating slab track (FST) and the underground railway tunnel embedded in a homogeneous half-space.
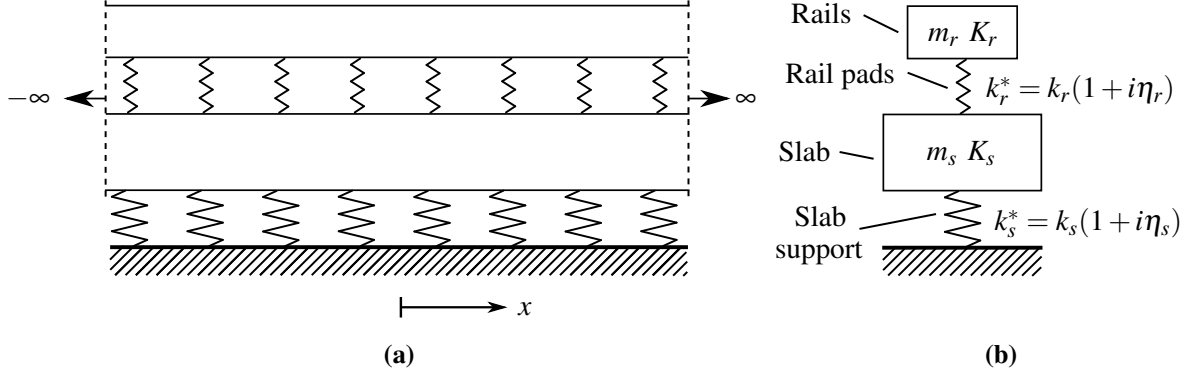
Fig. C.2 (a) Side and **(b)** front views of the two degree of freedom (DOF) system representing an infinite, continuous slab track coupled to the tunnel invert.

The slab and the two rails are modelled as infinite, continuous Euler-Bernoulli beams. It is possible to account for discontinuous slabs, which induce parametric excitation, in the track model [112], but this is not considered in this dissertation because it only has a significant effect on high-speed trains. It is assumed that there is no phase-delay in wheel-rail roughness between the two rails (strongly correlated), so both rails can be combined into a single beam with mass per unit length m_r and bending stiffness $K_r = E_r I_r$. Likewise, the material parameters of the slab are defined as m_s and $K_s = E_s I_s$. Although it is justifiable to assume the rails are strongly correlated at low frequencies (long wavelengths) as the rails follow the track-bed profile, perfect correlation is not observed at high frequencies [225].

The rail pads and slab sub-layer are modelled as uniformly distributed hysteretic springs with stiffness per unit length k and loss factor η. The complex stiffnesses of the rail pads and the slab sub-layer can be expressed as $k_r^* = k_r(1 + i\eta_r)$ and $k_s^* = k_s(1 + i\eta_s)$, respectively, using the viscoelastic correspondence principle [18]. The frequency-independent, hysteretic damping model characterises how the energy dissipated in structural materials depends on the vibration amplitude. In contrast, the viscous damping model assumes the energy dissipated depends on the frequency, which overpredicts the material damping at high frequencies [45]. Based on these considerations, the vertical displacement of a slab track can be captured using the two DOF system illustrated in Fig. C.2.

C.1.3 Tunnel

The tunnel is assumed to behave as a homogeneous, isotropic, linear-elastic continuum that is longitudinally invariant. The governing equations of motion for the tunnel can be found by

either modelling it as a thin-walled, cylindrical shell using shell theory [66, 237], if the wall thickness is small compared to the mean radius, or as a thick-walled, cylindrical shell [82]. Between 1 and 200 Hz, there is good agreement in the dispersion curve characteristics of a free tunnel modelled as a thin-shell and a thick-shell [112]. Since the thin-shell formulation only causes a negligible reduction in computation time compared to the latter approach, and to be consistent with the governing equations for the soil, the tunnel is modelled using the thick-shell formulation. Therefore, the tunnel's circular geometry is described by an inner radius r_{ti} and an outer radius r_{to}.

C.1.4 Soil

The soil surrounding the tunnel is assumed to be a homogeneous, isotropic, linear-viscoelastic continuum in an infinite full-space. As described in Section 2.3.1, material damping in the soil can be captured using a complex shear modulus $G^* = G(1 + i\eta_G)$. The governing equations of motion for the soil are found by modelling it as a thick, cylindrical cavity with an infinite outer radius $r_{so} \to \infty$ and an inner radius $r_{si} = r_{to}$. The soil is assumed to be perfectly bonded to the tunnel along the soil-tunnel interface. However, a study by Jones et al. [126] found that voids at the soil-tunnel interface can cause the vibration predictions to vary by at least 5 dB.

C.2 The Excitation Force at the Rails

In this section, the distributed force at the rails is derived due to motion of the train's axles when a spatially harmonic roughness is applied at the wheel-rail interface.

In order to find the distributed force at the rails, the tunnel invert coupled to the slab sublayer of the two DOF system, shown in Fig. C.2, is modelled as a rigid foundation instead of as an elastic structure. A rigid foundation is used so that the inverse Fourier transform of the rail displacement, with respect to the x-domain, can be expressed analytically, as shown later in Eq. (C.15). The analytical expression for the integral gives an exact solution compared to the numerically computed IDFT (see Appendix A.2.1). Since the rubber rail pads have a relatively lower stiffness compared to the concrete base, modelling the tunnel invert as a rigid foundation will have a negligible effect on the force distribution applied onto the rails.

Consider a time-harmonic, vertical point force $\bar{F}$ applied at $x = 0$ on the rails, as shown in Fig. C.3. The point force, with angular excitation frequency ϖ, is defined in the (x,t)-domain:

$$\bar{F}(x,t) = F_0 \cdot \delta(x) \cdot e^{i\varpi t}, \tag{C.1}$$

where $\delta(x)$ is the Dirac delta function centred at $x = 0$. Equation (C.1) is written using complex notation for convenience, but it is worth noting that only the real part accounts for the physical representation of the force. This complex notation will be used through the remainder of this appendix.

The differential equations for the rails and slab in the (x,t)-domain are

$$K_r\frac{\partial^4 \bar{y}_r}{\partial x^4} + m_r\frac{\partial^2 \bar{y}_r}{\partial t^2} + k_r^*(\bar{y}_r - \bar{y}_s) = F_0 \cdot \delta(x) \cdot e^{i\varpi t}, \tag{C.2}$$

$$K_s\frac{\partial^4 \bar{y}_s}{\partial x^4} + m_s\frac{\partial^2 \bar{y}_s}{\partial t^2} + k_s^*\bar{y}_s - k_r^*(\bar{y}_r - \bar{y}_s) = 0, \tag{C.3}$$

where $\bar{y}_r$ and $\bar{y}_s$ are the displacements along the rails and slab, respectively. Equations (C.2) and (C.3) are transformed into the wavenumber-time (ξ,t)-domain by applying the Fourier transform with respect to the x-domain:

$$K_r\xi^4\check{y}_r + m_r\frac{\partial^2 \check{y}_r}{\partial t^2} + k_r^*(\check{y}_r - \check{y}_s) = F_0 \cdot e^{i\varpi t}, \tag{C.4}$$

$$K_s\xi^4\check{y}_s + m_s\frac{\partial^2 \check{y}_s}{\partial t^2} + k_s^*\check{y}_s - k_r^*(\check{y}_r - \check{y}_s) = 0, \tag{C.5}$$

where the displacements $\check{y}_r$ and $\check{y}_s$ are defined in the (ξ,t)-domain. Equations (C.4) and (C.5) are transformed into the wavenumber-frequency (ξ,ω)-domain by taking the Fourier transform with respect to the t-domain:
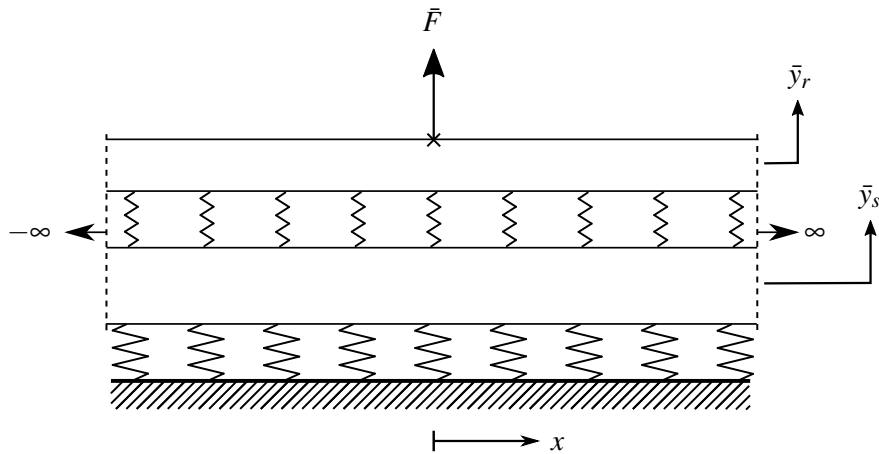
Fig. C.3 The slab track coupled to a rigid foundation is excited at $x = 0$ by a time-harmonic point force $\bar{F}$, which causes the rails and slab to deform by $\bar{y}_r$ and $\bar{y}_s$, respectively, in the space-time (x,t)-domain.

$$K_r\xi^4\widetilde{y}_r - m_r\omega^2\widetilde{y}_r + k_r^*(\widetilde{y}_r - \widetilde{y}_s) = F_0 \cdot 2\pi(\omega - \varpi), \tag{C.6}$$

$$K_s\xi^4\widetilde{y}_s - m_s\omega^2\widetilde{y}_s + k_s^*\widetilde{y}_s - k_r^*(\widetilde{y}_r - \widetilde{y}_s) = 0, \tag{C.7}$$

where the displacements $\widetilde{y}_r$ and $\widetilde{y}_s$ are defined in the (ξ, ω)-domain. Equations (C.6) and (C.7) can be restated as the matrix equation:

$$\mathbf{A}\begin{Bmatrix}\widetilde{y}_r \\ \widetilde{y}_s\end{Bmatrix} = \begin{Bmatrix}F_0 \cdot 2\pi(\omega - \varpi) \\ 0\end{Bmatrix}, \tag{C.8}$$

where the matrix $\mathbf{A}$ is

$$\mathbf{A} = \begin{bmatrix} K_r\xi^4 - m_r\omega^2 + k_r^* & -k_r^* \\ -k_r^* & K_s\xi^4 - m_s\omega^2 + k_r^* + k_s^* \end{bmatrix}. \tag{C.9}$$

Solving for $\widetilde{y}_r$ and $\widetilde{y}_s$ in Eq. (C.8) gives

$$\widetilde{y}_r = F_0 \cdot 2\pi(\omega - \varpi) \cdot \frac{f_2(\xi, \omega)}{f_1(\xi, \omega)}, \tag{C.10}$$

$$\widetilde{y}_s = F_0 \cdot 2\pi(\omega - \varpi) \cdot \frac{k_r^*}{f_1(\xi, \omega)}, \tag{C.11}$$

where $f_1 = |\mathbf{A}|$, $f_2 = K_s\xi^4 - m_s\omega^2 + k_r^* + k_s^*$, and $|\mathbf{A}|$ is the determinant of the matrix $\mathbf{A}$. For convenience, the computation of $\widetilde{y}_s$ are not presented here; nonetheless, the approach detailed below for solving $\widetilde{y}_r$ can also be applied to solve for $\widetilde{y}_s$. Equation (C.10) is transformed into the (ξ, t)-domain by applying the inverse Fourier transform with respect to the ω-domain:

$$\check{y}_r(\xi, t) = F_0 \cdot e^{i\varpi t} \cdot \frac{f_2(\xi, \omega = \varpi)}{f_1(\xi, \omega = \varpi)}. \tag{C.12}$$

Note that the time-harmonic response of a function $\bar{u}$ can be expressed as

$$\bar{u}(x, t) = u(x, \omega = \varpi) \cdot e^{i\varpi t}. \tag{C.13}$$

By taking the inverse Fourier transform of Eq. (C.12) with respect to the ξ-domain and applying Eq. (C.13), the displacement at the rails can be expressed in the space-frequency (x, ω)-domain:

$$y_r(x, \omega) = \frac{F_0}{2\pi} \cdot \int_{-\infty}^{\infty} \frac{f_2(\xi, \omega)}{f_1(\xi, \omega)} \cdot e^{i\xi x} d\xi, \tag{C.14}$$

where $\omega = \varpi$ is implied due to the time-harmonic nature of the excitation. Equation (C.14) can be either solved numerically using the IDFT or analytically using contour integration (see Appendix A.2). In this case, contour integration is used because it avoids the complexity of discretising the ξ-domain when computing the IDFT. The complex function f_1 is an eighth-order polynomial, so the integrand in Eq. (C.14) contains eight complex poles. By applying the residue theorem to find the equivalent contour integral of Eq. (C.14), the analytical expression for y_r/F_0 can be written as

$$
\frac{y_r}{F_0} =
\begin{cases}
\dfrac{i}{K_r K_s} \cdot \displaystyle\sum_{j=1}^{4} \frac{f_2(\xi_j, \omega) \cdot e^{i\xi_j x}}{\Pi_j} = H^+(x, \omega) & \text{for } x \geq 0, \\[4mm]
\dfrac{-i}{K_r K_s} \cdot \displaystyle\sum_{j=5}^{8} \frac{f_2(\xi_j, \omega) \cdot e^{i\xi_j x}}{\Pi_j} = H^-(x, \omega) & \text{for } x < 0,
\end{cases}
\tag{C.15}
$$

where $\Pi_j = (\xi_j - \xi_1)(\xi_j - \xi_2)\ldots(\xi_j - \xi_{j-1})(\xi_j - \xi_{j+1})(\xi_j - \xi_8)$, and H is the displacement frequency-response function (FRF) of the rails due to F_0. The roots of the equation $f_1 = 0$ are denoted as $\xi_1, \xi_2, \xi_3, \xi_4, \xi_5, \xi_6, \xi_7, \xi_8$, with the roots in the first and second quadrants being $\xi_1, \xi_2, \xi_3, \xi_4$ and the roots in the third and fourth quadrants being $\xi_5, \xi_6, \xi_7, \xi_8$.

Due to symmetry in the x-domain and the infinite nature of the slab track and the tunnel, the rail FRF is only dependent on the magnitude of the separation s between the position where the rail displacement y_r is measured and the position where the point force F_0 is applied. Hence, Eq. (C.15) can be rewritten as

$$
y_r = H(s, \omega)F_0 . \tag{C.16}
$$

When a train, modelled using equally spaced unsprung axle masses, is positioned above the track, the deformation of the rails becomes

$$
\mathbf{y}_r = \mathbf{H}_a \mathbf{f}_a , \tag{C.17}
$$

where the vectors $\mathbf{y}_r$ and $\mathbf{f}_a$ describe the rail displacements and dynamic axle loads, respectively, at the contact points between each axle mass and the rail, and $\mathbf{H}_a$ is the rail-axle displacement FRF matrix. Each element in $\mathbf{H}_a$ is determined by the H component at the location of each axle mass. To illustrate the general approach, the rail-axle displacement FRF matrix for a finite number of five axles masses, with regular spacing L_a, is

$$\mathbf{H}_a = \begin{bmatrix} H(0) & H(L_a) & H(2L_a) & H(3L_a) & H(4L_a) \\ H(L_a) & H(0) & H(L_a) & H(2L_a) & H(3L_a) \\ H(2L_a) & H(L_a) & H(0) & H(L_a) & H(2L_a) \\ H(3L_a) & H(2L_a) & H(L_a) & H(0) & H(L_a) \\ H(4L_a) & H(3L_a) & H(2L_a) & H(L_a) & H(0) \end{bmatrix}. \tag{C.18}$$

The frequency ω is omitted from Eq. (C.18) for clarity, but the reader should note that the FRF matrix is expressed in the (x, ω)-domain. This approach can easily be extended to include more axle masses until the response converges for an infinite train. When five masses are considered, the dynamic axle loads at the rail are $\mathbf{f}_a = \left\{ F_{-2L_a}, F_{-L_a}, F_0, F_{L_a}, F_{2L_a} \right\}^{\mathrm{T}}$, as shown in Fig. C.4, where the superscript 'T' denotes the vector transpose. The number of axle masses N_a must be odd, with the central mass located at $x = 0$, to ensure a symmetrical distribution of axle loads in the x-domain.

In Fig. C.4, the train axles are modelled as point masses with unsprung mass M_a and spacing L_a. The vector $\mathbf{y}_r + \mathbf{\Delta}$ describes the vertical displacements of the axles, where $\mathbf{\Delta}$ is the wheel-rail roughness beneath each axle. The governing equation of motion for all the axles is

$$\mathbf{f}_a = \omega^2 M_a (\mathbf{y}_r + \mathbf{\Delta}). \tag{C.19}$$

Substituting Eq. (C.17) into Eq. (C.19) and rearranging the equation gives

$$\mathbf{f}_a = \omega^2 M_a \left[\mathbf{I} - \omega^2 M_a \mathbf{H}_a \right]^{-1} \mathbf{\Delta}, \tag{C.20}$$
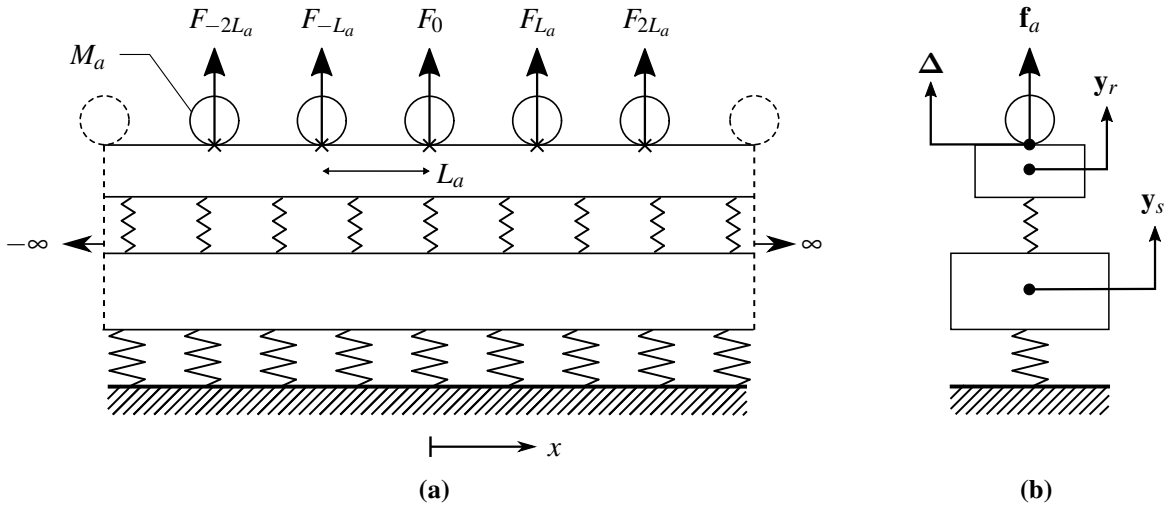
Fig. C.4 (a) Side and (b) front views of the train-track system. The train axles are represented as point masses with unsprung mass M_a and spacing L_a. The dynamic axle loads $\mathbf{f}_a$, the wheel-rail roughness $\mathbf{\Delta}$, and the displacements of the rails $\mathbf{y}_r$ and slab $\mathbf{y}_b$ are described in the space-frequency (x, ω)-domain.

where $\mathbf{I}$ is the $N_a \times N_a$ identity matrix. The distributed force F_b at the rails due to the five axle masses is

$$F_r(x, \omega) = F_{-2L_a} \cdot \delta(x + 2L_a) + F_{-L_a} \cdot \delta(x + L_a) + F_0 \cdot \delta(x) + \ldots$$
$$F_{L_a} \cdot \delta(x - L_a) + F_{2L_a} \cdot \delta(x - 2L_a). \tag{C.21}$$

Equation (C.21) can be generalised for N_a axles:

$$F_r(x, \omega) = \sum_{p=-N_m}^{N_m} F_p \cdot \delta(x - pL_a), \tag{C.22}$$

where $N_m = (N_a - 1)/2$. The distributed force F_r is transformed into the force $\widetilde{F}_r$ in the (ξ, ω)-domain by taking the Fourier transform of Eq. (C.22) with respect to the x-domain. Since each point force F_p is multiplied by a delta function, which is shifted in the x-direction by a multiple of L_a, the Fourier transform simply relates to applying the shifting principle:

$$\widetilde{F}_r(\xi, \omega) = \sum_{p=-N_m}^{N_m} F_p \cdot e^{-i\xi pL_a}. \tag{C.23}$$

C.3 The Driving-Point Response of the Tunnel Invert

In this section, the driving-point displacement FRF of the tunnel invert is derived in the (ξ, ω)-domain. This FRF is defined as the vertical displacement along the invert when a distributed force is applied within a tunnel embedded in a full-space.

C.3.1 Modelling the Excitation at the Tunnel Invert

The tunnel response is defined in the cylindrical (r, θ, x) coordinate system with respect to the radial r-, circumferential θ-, and longitudinal x-directions. Consider a time-harmonic, radial distributed force F_t applied along the x-axis of the tunnel invert, as illustrated in Fig. C.5a. The distributed force, with angular excitation frequency ω, can be defined in the (x, ω)-domain by the inverse Fourier transform:

$$F_t(x, \omega) = \frac{1}{2\pi} \int_{-\infty}^{\infty} \widetilde{F}_t \cdot e^{i\xi x} d\xi, \tag{C.24}$$

where the force $\widetilde{F}_t$ is defined in the (ξ, ω)-domain.
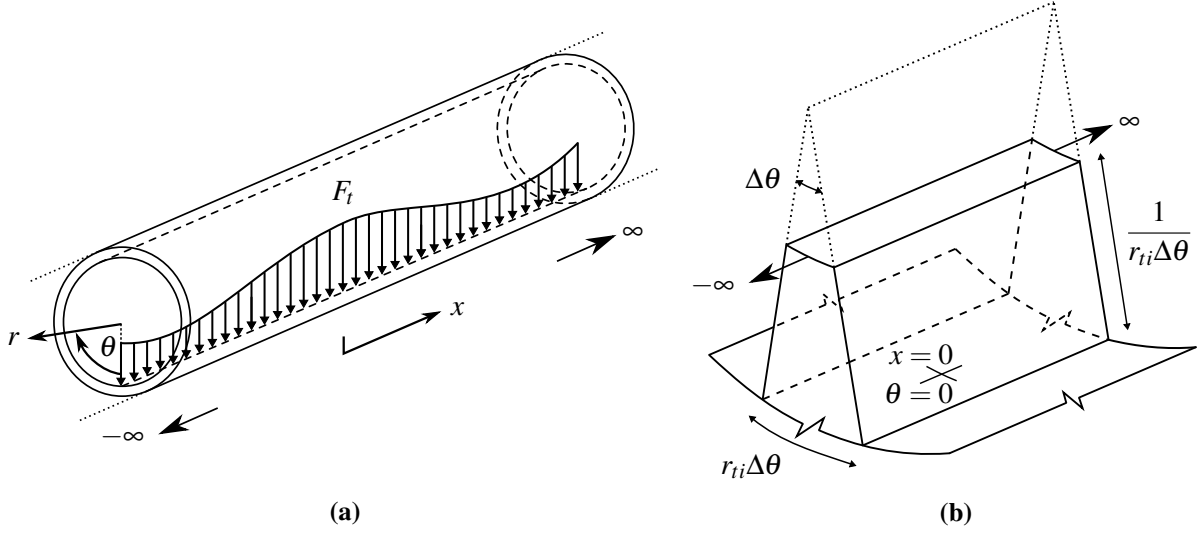
Fig. C.5 Schematic diagram of (a) the distributed force $F_t(x, \omega)$ applied at the tunnel invert can be constructed as (b) an appropriately scaled normal traction acting over an infinitesimal length $r_{ti}\Delta\theta$.

The distributed force can be transformed into a normal traction acting over an infinitesimal length $r_{ti}\Delta\theta$ that is centred at $\theta = 0$, as illustrated in Fig. C.5b. The traction is scaled by a factor of $1/r_{ti}\Delta\theta$ so that it is equal in magnitude to the distributed force. Therefore, the components of the traction wave-field $\mathbf{q} = \{q_r, q_\theta, q_x\}^{\mathrm{T}}$ at the tunnel invert can be expressed as

$$
q_r = \begin{cases} \dfrac{1}{2\pi} \displaystyle\int_{-\infty}^{\infty} \widetilde{F}_t \cdot \dfrac{1}{r_{ti}\Delta\theta} \cdot e^{i\xi x} d\xi & \text{for } \dfrac{-\Delta\theta}{2} < \theta < \dfrac{\Delta\theta}{2}\,, \\[4mm] 0 & \text{otherwise}\,, \end{cases}
$$

$$
q_r \to \dfrac{1}{2\pi} \int_{-\infty}^{\infty} \widetilde{F}_t \cdot \dfrac{\delta(\theta)}{r_{ti}} \cdot e^{i\xi x} d\xi \quad \text{as } \Delta\theta \to 0\,,
$$

$$
q_\theta = q_x = 0\,,
$$

(C.25)

where $\delta(\theta)$ is the Dirac delta function centred at $\theta = 0$, with period 2π. This means the term $\delta(\theta)/r_{ti}$ in Eq. (C.25) can be decomposed into a linear summation of n circumferential ring modes using the Fourier series:

$$
\frac{\delta(\theta)}{r_{ti}} = \frac{1}{\pi r_{ti}} \left(\frac{1}{2} + \sum_{n=1}^{\infty} \cos n\theta \right). \tag{C.26}
$$

The reader is referred to Appendix A.3 for additional details on the Fourier Series. Note that Eq. (C.26) excludes sine terms from the Fourier series because $\delta(\theta)$ is an even, symmetric function about $\theta = 0$. Substituting Eq. (C.26) into Eq. (C.25) gives

$$\mathbf{q}(r,\theta,x,\omega) = \begin{Bmatrix} q_r \\ q_\theta \\ q_x \end{Bmatrix} = \frac{1}{2\pi} \int_{-\infty}^{\infty} \sum_{n=0}^{\infty} \begin{Bmatrix} \widetilde{q}_{rn}\cos n\theta \\ \widetilde{q}_{\theta n}\sin n\theta \\ \widetilde{q}_{xn}\cos n\theta \end{Bmatrix} \cdot e^{i\xi x} d\xi, \tag{C.27}$$

where the components of $\widetilde{\mathbf{q}}_n = \{\widetilde{q}_{rn}, \widetilde{q}_{\theta n}, \widetilde{q}_{xn}\}^{\mathrm{T}}$ in the modal-wavenumber-frequency (n, ξ, ω)-domain are

$$\widetilde{q}_{rn}(n,\xi,\omega) = \begin{cases} \dfrac{\widetilde{F}_t}{2\pi r_{ti}} & \text{for } n = 0, \\[2mm] \dfrac{\widetilde{F}_t}{\pi r_{ti}} & \text{for } n \geq 1, \end{cases} \tag{C.28}$$

$$\widetilde{q}_{\theta n}(n,\xi,\omega) = \widetilde{q}_{xn}(n,\xi,\omega) = 0 \quad \text{for all } n.$$

It should be noted that the traction components in Eq. (C.28) are symmetric about $\theta = 0$ because $\widetilde{F}_t$ only acts in the vertical direction. As n increases, the modal traction wave-field $\widetilde{\mathbf{q}}_n$ decreases in magnitude. Thus, in practice, only a finite number of modes are required to achieve convergence over the frequency range of interest. All the governing equations of motion for the tunnel and surrounding soil in the following two sections are transformed into the (n, ξ, ω)-domain to account for the tunnel's longitudinal invariance and circumferential periodicity. If a unit-magnitude, time-harmonic point force $F_t(x, \omega) = \delta(x)$ is applied at the tunnel invert instead, the equations in the remainder of this appendix can be used to find the soil response by setting $\widetilde{F}_t = 1$ [67].

C.3.2 Modelling the Tunnel and the Soil

Section 2.3.1 describes how Navier's equations for a homogeneous, isotropic continuum can be decomposed into scalar ϕ and vector $\mathbf{H}$ potentials, as shown using Helmholtz decomposition in Eqs. (2.10)–(2.12). In order to solve these equations, the potentials can be expressed in the cylindrical coordinate system, as illustrated in Fig. C.6a, by separation of variables. When the loading at the tunnel invert is symmetrical, the potentials are

$$\phi = f(r) \cdot \cos n\theta \cdot e^{i(\omega t + \xi x)}, \tag{C.29}$$

$$H_r = g_r(r) \cdot \sin n\theta \cdot e^{i(\omega t + \xi x)}, \tag{C.30}$$

$$H_\theta = g_\theta(r) \cdot \cos n\theta \cdot e^{i(\omega t + \xi x)}, \tag{C.31}$$

$$H_x = g_x(r) \cdot \sin n\theta \cdot e^{i(\omega t + \xi x)}. \tag{C.32}$$

Once the expressions in Eqs. (C.29)–(C.32) are substituted into Eqs. (2.11) and (2.12), the general solutions for f, g_r, g_θ and g_x can be evaluated. These expressions are substituted back into Eq. (2.10) to compute the displacement wave-field $\mathbf{u} = \{u_r, u_\theta, u_x\}^T$ of an infinitesimal element, as shown in Fig. C.6b. The linear-elastic kinematic relationship and the generalised Hooke's Law, relating the displacements, strains and stresses in 3D space, are used to evaluate the traction wave-field $\mathbf{p} = \{\sigma_{rr}, \sigma_{r\theta}, \sigma_{rx}\}^T$ at the inner surface of an infinitesimal element, as illustrated in Fig. C.6c. Therefore, the displacement and traction wave-fields for a thick-walled, cylindrical shell can be expressed as the following matrix equations:

$$\mathbf{u}(r, \theta, x, \omega) = \begin{Bmatrix} u_r \\ u_\theta \\ u_x \end{Bmatrix} = \frac{1}{2\pi} \int_{-\infty}^{\infty} \sum_{n=0}^{\infty} \mathbf{S}_1 \widetilde{\mathbf{u}}_{n1} \cdot e^{i\xi x} d\xi, \tag{C.33}$$

$$\mathbf{p}(r, \theta, x, \omega) = \begin{Bmatrix} \sigma_{rr} \\ \sigma_{r\theta} \\ \sigma_{rx} \end{Bmatrix} = \frac{1}{2\pi} \int_{-\infty}^{\infty} \sum_{n=0}^{\infty} \mathbf{S}_1 \widetilde{\mathbf{p}}_{n1} \cdot e^{i\xi x} d\xi, \tag{C.34}$$

where

$$\mathbf{S}_1 = \begin{bmatrix} \cos n\theta & 0 & 0 \\ 0 & \sin n\theta & 0 \\ 0 & 0 & \cos n\theta \end{bmatrix}, \tag{C.35}$$

$$\widetilde{\mathbf{u}}_{n1}(r, n, \xi, \omega) = \begin{Bmatrix} \widetilde{u}_{rn1} \\ \widetilde{u}_{\theta n1} \\ \widetilde{u}_{xn1} \end{Bmatrix} = \widetilde{\mathbf{U}}_1 \widetilde{\mathbf{c}}_1, \tag{C.36}$$

$$\widetilde{\mathbf{p}}_{n1}(r, n, \xi, \omega) = \begin{Bmatrix} \widetilde{\sigma}_{rrn1} \\ \widetilde{\sigma}_{r\theta n1} \\ \widetilde{\sigma}_{rxn1} \end{Bmatrix} = \widetilde{\mathbf{T}}_{r1} \widetilde{\mathbf{c}}_1. \tag{C.37}$$
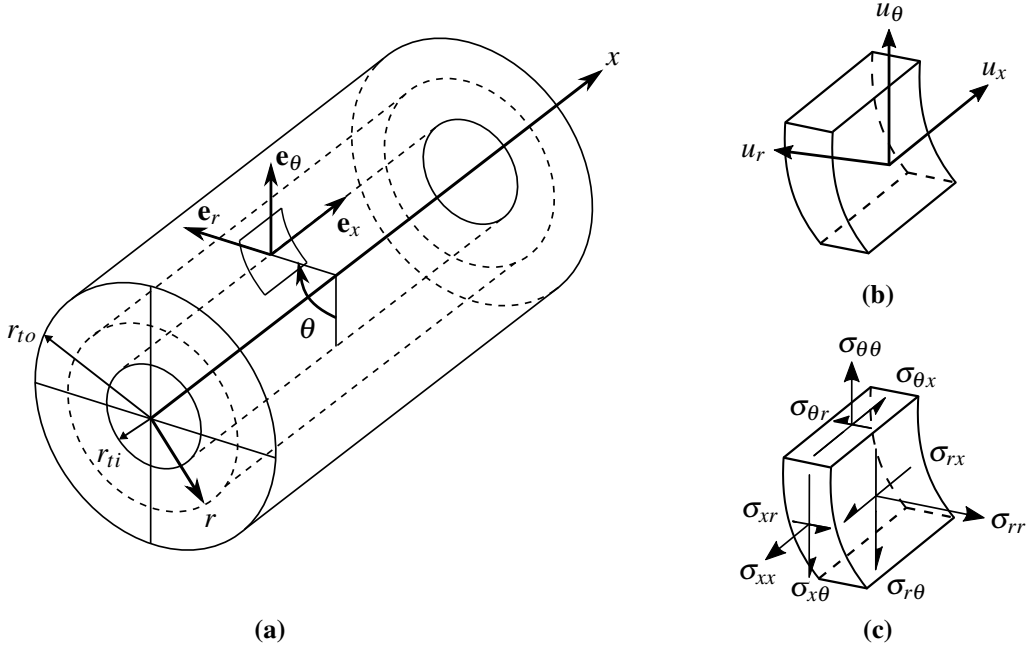
Fig. C.6 Cylindrical (r, θ, x) coordinate system used for an elastic continuum, showing **(a)** the principal directions for an infinitesimal element of radius r and the sign convention applied at the infinitesimal element's inner surface for the **(b)** displacement and **(c)** traction components.

The vector $\widetilde{\mathbf{c}}_1$ denotes the six unique coefficients in the general solutions for f, g_r, g_θ and g_x in Eqs. (C.29)–(C.32). Closed-form, analytical expressions for the 3×6 matrices $\widetilde{\mathbf{U}}_1(r, n, \xi, \omega)$ and $\widetilde{\mathbf{T}}_{r1}(r, n, \xi, \omega)$ are presented in Appendix D. It is important to note that Eqs. (C.33)–(C.37) correspond to symmetric displacement and traction components, denoted by the subscript '1' in the vectors and matrices. The derivation of Eqs. (C.36) and (C.37) is thoroughly presented by Forrest [68], so it is not repeated here.

By evaluating Eqs. (C.36) and (C.37) at particular radii, the modal displacement and traction wave-fields at the inner ($r = r_{ti}$) and outer ($r = r_{to}$) tunnel walls can be found:

$$\widetilde{\mathbf{u}}_{n1,ti}(n, \xi, \omega) = \widetilde{\mathbf{U}}_1 \Big|_{r=r_{ti}} \widetilde{\mathbf{c}}_1 , \tag{C.38}$$

$$\widetilde{\mathbf{p}}_{n1,ti}(n, \xi, \omega) = \widetilde{\mathbf{T}}_{r1} \Big|_{r=r_{ti}} \widetilde{\mathbf{c}}_1 , \tag{C.39}$$

$$\widetilde{\mathbf{u}}_{n1,to}(n, \xi, \omega) = \widetilde{\mathbf{U}}_1 \Big|_{r=r_{to}} \widetilde{\mathbf{c}}_1 , \tag{C.40}$$

$$-\widetilde{\mathbf{p}}_{n1,to}(n, \xi, \omega) = \widetilde{\mathbf{T}}_{r1} \Big|_{r=r_{to}} \widetilde{\mathbf{c}}_1 . \tag{C.41}$$

Note the negative sign in Eq. (C.41) because the tractions at the outer and inner surfaces of an infinitesimal element are equal in magnitude but act in opposite directions.

As described in Appendix C.1.4, the soil is modelled as a thick, cylindrical cavity with an infinite outer radius $r_{so} \to \infty$ and an inner radius $r_{si} = r_{to}$. The radiation boundary condition at infinity requires $\widetilde{\mathbf{u}} \to 0$ and $\widetilde{\mathbf{p}} \to 0$, which reduces the number of coefficients denoted by the vector $\widetilde{\mathbf{b}}_1$ to three. Hence, the modal displacement $\widetilde{\mathbf{u}}_{n1,st}$ and traction $\widetilde{\mathbf{p}}_{n1,st}$ wave-fields at the soil-tunnel interface are

$$\widetilde{\mathbf{u}}_{n1,st}(n,\xi,\omega) = \widetilde{\mathbf{U}}_{m1}\Big|_{r=r_{to}} \widetilde{\mathbf{b}}_1\,, \tag{C.42}$$

$$\widetilde{\mathbf{p}}_{n1,st}(n,\xi,\omega) = \widetilde{\mathbf{T}}_{m1}\Big|_{r=r_{to}} \widetilde{\mathbf{b}}_1\,, \tag{C.43}$$

where the 3×3 matrices $\widetilde{\mathbf{U}}_{m1}(r,n,\xi,\omega)$ and $\widetilde{\mathbf{T}}_{m1}(r,n,\xi,\omega)$ contain the second, fourth and sixth columns of $\widetilde{\mathbf{U}}_1(r,n,\xi,\omega)$ and $\widetilde{\mathbf{T}}_{r1}(r,n,\xi,\omega)$, respectively.

If anti-symmetric loads are applied at the tunnel invert, the general form of the equations will be similar to those given in Eqs. (C.33)–(C.43), but the subscript '2' will be used instead of '1' to denote all the vectors and matrices. Closed-form expressions for the 3×6 matrices $\widetilde{\mathbf{U}}_2(r,n,\xi,\omega)$ and $\widetilde{\mathbf{T}}_{r2}(r,n,\xi,\omega)$ are given in Appendix D, and the matrix $\mathbf{S}_2$ can be found by simply replacing any $\cos n\theta$ terms in Eq. (C.35) with $\sin n\theta$ terms, and vice versa for the $\sin n\theta$ terms.

C.3.3 Coupling at the Soil-Tunnel Interface

Perfect bonding at the soil-tunnel interface means that the displacements must satisfy $\widetilde{\mathbf{u}}_{to} = \widetilde{\mathbf{u}}_{si}$ due to compatibility. Assuming there are also no resultant forces at the soil-tunnel interface, the tractions must satisfy $\widetilde{\mathbf{p}}_{to} = -\widetilde{\mathbf{p}}_{si}$ due to equilibrium. Both of these relationships are imposed to couple the tunnel and soil together. By substituting Eqs. (C.39)–(C.43) into the compatibility and equilibrium relationships, the coefficient vectors $\mathbf{c}_1$ and $\mathbf{b}_1$ can be written as the following matrix equations:

$$
\widetilde{\mathbf{c}}_1 = \begin{bmatrix} \widetilde{\mathbf{T}}_{r1}\Big|_{r=r_{ti}} \\ \widetilde{\mathbf{T}}_{r1}\Big|_{r=r_{to}} - \widetilde{\mathbf{T}}_{m1}\Big|_{r=r_{to}} \widetilde{\mathbf{U}}_{m1}^{-1}\Big|_{r=r_{to}} \widetilde{\mathbf{U}}_1\Big|_{r=r_{to}} \end{bmatrix}^{-1} \left\{ \begin{matrix} \widetilde{\mathbf{p}}_{n1,ti} \\ \mathbf{0} \end{matrix} \right\},
$$

$$
= \begin{bmatrix} \widetilde{\mathbf{C}}_{11} & \widetilde{\mathbf{C}}_{12} \end{bmatrix} \left\{ \begin{matrix} \widetilde{\mathbf{p}}_{n1,ti} \\ \mathbf{0} \end{matrix} \right\} = \widetilde{\mathbf{C}}_{11}\widetilde{\mathbf{q}}_n\,, \tag{C.44}
$$

$$\widetilde{\mathbf{b}}_1 = \widetilde{\mathbf{U}}_{m1}^{-1}\Big|_{r=r_{to}} \widetilde{\mathbf{U}}_1\Big|_{r=r_{to}} \widetilde{\mathbf{c}}_1\,,$$

$$= \widetilde{\mathbf{U}}_{m1}^{-1}\Big|_{r=r_{to}} \widetilde{\mathbf{U}}_1\Big|_{r=r_{to}} \widetilde{\mathbf{C}}_{11}\widetilde{\mathbf{q}}_n\,, \tag{C.45}$$

where $\mathbf{0}$ is a 3×1 vector of zeros, and $\widetilde{\mathbf{C}}_{11}$ and $\widetilde{\mathbf{C}}_{12}$ are 6×3 sub-matrices. Note that $\widetilde{\mathbf{q}}_n = \widetilde{\mathbf{p}}_{n1,ti}$ in Eqs. (C.44) and (C.45).

As described in Appendix C.3.1, the traction wave-field $\widetilde{\mathbf{q}}$ at the tunnel invert due to the force $\widetilde{F}_t$ is purely symmetric, so Eq. (C.28) can be substituted into Eqs. (C.44) and (C.45). Thus, the displacement wave-field $\widetilde{\mathbf{u}}_{ti}$ at the tunnel invert can be found in the (ξ, ω)-domain by computing the Fourier series summation of the symmetric and anti-symmetric displacement wave-fields:

$$\widetilde{\mathbf{u}}_{ti}(\xi,\omega) = \sum_{n=0}^{\infty} \mathbf{S}_1\widetilde{\mathbf{u}}_{n1} + \mathbf{S}_2\widetilde{\mathbf{u}}_{n2} = \sum_{n=0}^{\infty} \mathbf{S}_1 \, \mathbf{U}_1\big|_{r=r_{ti}} \mathbf{C}_{11}\widetilde{\mathbf{q}}_n\,, \tag{C.46}$$

where $\widetilde{\mathbf{u}}_{n2} = \mathbf{0}$ because there is no anti-symmetric loading at the tunnel invert. Since only the radial component of $\widetilde{\mathbf{q}}_n$ is non-zero, the vertical displacement $\widetilde{y}_t$ at the tunnel invert is found by evaluating Eq. (C.46) at $\theta = 0$ to give

$$\widetilde{y}_t = \sum_{n=0}^{\infty} \mathbf{S}_1\big|_{\theta=0} \, \widetilde{\mathbf{U}}_1\big|_{r=r_{ti}} \widetilde{\mathbf{C}}_{11} \left\{ \begin{array}{c} \widetilde{q}_{rn}/\widetilde{F}_t \\ 0 \\ 0 \end{array} \right\} \widetilde{F}_t = \widetilde{H}_t\widetilde{F}_t\,, \tag{C.47}$$

where $\widetilde{H}_t$ is the driving-point displacement FRF of the tunnel invert.

C.4 The Excitation Force at the Tunnel Invert

In this section, the force $\widetilde{F}_t$ that is transferred to the tunnel invert by the track is calculated when the force $\widetilde{F}_r$, derived in Appendix C.2, is applied at the rails. The track and tunnel are coupled by defining the equations of motion in the (ξ, ω)-domain.

Figure C.7 illustrates the same slab track in Fig. C.2, but it is now coupled to an elastic foundation. The track-tunnel system is divided into five sub-structures: the rails, the slab, the tunnel invert, the rail pads, and the slab sub-layer. Coupling forces, denoted by $\widetilde{G}_1$, $\widetilde{G}_2$ and $\widetilde{G}_3$, are imposed between the sub-structures.
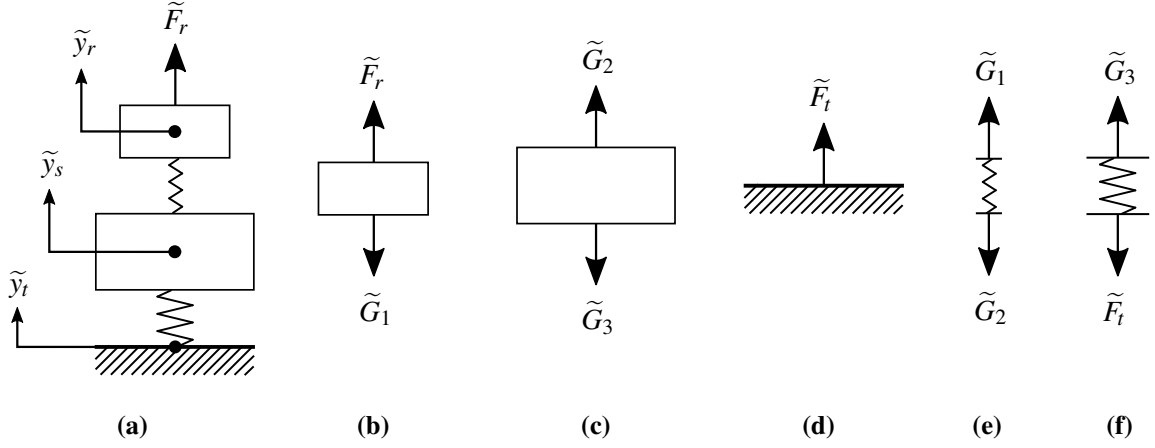
Fig. C.7 Coupling of the five sub-structures in **(a)** the track-tunnel system: **(b)** the rails, **(c)** the slab, **(d)** the tunnel invert, **(e)** the rail pads and **(f)** the slab sub-layer. The displacements and forces are defined in the wavenumber-frequency (ξ, ω)-domain.

To couple the sub-structures together, the displacement FRFs of the tunnel invert, and the beams representing the rails and slab, need to be found. Note that the displacement FRF of the tunnel invert $\widetilde{H}_t$ was derived in the previous section.

Consider a time-harmonic, vertical distributed force $\bar{P}$ applied to an Euler-Bernoulli beam. The following equation describes the beam's undamped motion in the (x,t)-domain [181]:

$$K\frac{\partial^4 \bar{y}}{\partial x^4} + m\frac{\partial^2 \bar{y}}{\partial t^2} = \bar{P}, \tag{C.48}$$

where $\bar{y}$ is the beam's vertical displacement. When the beam is driven at an angular frequency of ω, the displacement and force can be expressed as $\bar{y}(x,t) = \widetilde{y}e^{i(\xi x + \omega t)}$ and $\bar{P}(x,t) = \widetilde{P}e^{i(\xi x + \omega t)}$, respectively. Substituting these expressions into Eq. (C.48) gives

$$K\xi^4\widetilde{y} - m\omega^2\widetilde{y} = \widetilde{P}, \tag{C.49}$$

where both the displacement and force are transformed into the (ξ, ω)-domain. Rearranging Eq. (C.49) results in

$$\widetilde{H}_b = \frac{\widetilde{y}}{\widetilde{P}} = \frac{1}{K\xi^4 - m\omega^2}, \tag{C.50}$$

where $\widetilde{H}_b$ is the displacement FRF of an Euler-Bernoulli beam. Applying Eq. (C.50) to the rails and slab beams gives:

$$\widetilde{H}_r = \frac{1}{K_r\xi^4 - m_r\omega^2}, \tag{C.51}$$

$$\widetilde{H}_s = \frac{1}{K_s \xi^4 - m_s \omega^2}, \tag{C.52}$$

where $\widetilde{H}_r$ and $\widetilde{H}_s$ denote the displacement FRFs of the rails and slab, respectively.

The motion of the rails, slab and tunnel invert are described by the following equations:

$$\widetilde{y}_r = \widetilde{H}_r \left(\widetilde{F}_r - \widetilde{G}_1 \right), \tag{C.53}$$

$$\widetilde{y}_s = \widetilde{H}_s \left(\widetilde{G}_2 - \widetilde{G}_3 \right), \tag{C.54}$$

$$\widetilde{y}_t = \widetilde{H}_t \widetilde{F}_t, \tag{C.55}$$

where $\widetilde{y}_r$, $\widetilde{y}_s$ and $\widetilde{y}_t$ are the displacements at the rails, slab and tunnel invert, respectively. The coupling forces at the rail pads and slab sub-layer satisfy the following equations:

$$\widetilde{G}_1 = \widetilde{G}_2 = k_r^* \left(\widetilde{y}_r - \widetilde{y}_s \right), \tag{C.56}$$

$$\widetilde{G}_3 = \widetilde{F}_t = k_s^* \left(\widetilde{y}_s - \widetilde{y}_t \right). \tag{C.57}$$

Equations (C.53)–(C.57) can be restated as the following matrix equation:

$$\mathbf{B} \begin{Bmatrix} \widetilde{y}_r \\ \widetilde{y}_s \\ \widetilde{y}_t \end{Bmatrix} = \begin{Bmatrix} \widetilde{H}_r \widetilde{F}_r \\ 0 \\ 0 \end{Bmatrix}, \tag{C.58}$$

where the matrix $\mathbf{B}$ is

$$\mathbf{B} = \begin{bmatrix} 1 + \widetilde{H}_r k_r^* & -\widetilde{H}_r k_r^* & 0 \\ -\widetilde{H}_s k_r^* & 1 + \widetilde{H}_s \left(k_s^* + k_r^* \right) & -\widetilde{H}_s k_s^* \\ 0 & -\widetilde{H}_t k_s^* & 1 + \widetilde{H}_t k_s^* \end{bmatrix}. \tag{C.59}$$

Solving Eq. (C.58) gives the following displacement FRFs for the track-tunnel system:

$$\frac{\widetilde{y}_r}{\widetilde{F}_r} = \frac{1}{|\mathbf{B}|} \cdot \widetilde{H}_r \left(1 + \widetilde{H}_s k_r^* + \left(\widetilde{H}_s + \widetilde{H}_t \right) k_s^* + \widetilde{H}_s \widetilde{H}_t k_r^* k_s^* \right), \tag{C.60}$$

$$\frac{\widetilde{y}_s}{\widetilde{F}_r} = \frac{1}{|\mathbf{B}|} \cdot \widetilde{H}_r \widetilde{H}_s k_r^* \left(1 + \widetilde{H}_t k_s^* \right), \tag{C.61}$$

$$\frac{\widetilde{y}_t}{\widetilde{F}_r} = \frac{1}{|\mathbf{B}|} \cdot \widetilde{H}_r \widetilde{H}_s \widetilde{H}_t k_r^* k_s^*, \tag{C.62}$$

where the determinant of $\mathbf{B}$ is

$$|\mathbf{B}| = 1 + \left(\widetilde{H}_r + \widetilde{H}_s\right) k_r^* + \left(\widetilde{H}_s + \widetilde{H}_t\right) k_s^* + \left(\widetilde{H}_r \widetilde{H}_s + \widetilde{H}_r \widetilde{H}_t + \widetilde{H}_s \widetilde{H}_t\right) k_r^* k_s^*. \tag{C.63}$$

Substituting Eq. (C.55) into Eq. (C.62) derives the force transmissibility ratio from the input force $\widetilde{F}_r$ at the rails to the output force $\widetilde{F}_t$ at the tunnel invert:

$$\frac{\widetilde{F}_t}{\widetilde{F}_r} = \frac{1}{|\mathbf{B}|} \cdot \widetilde{H}_r \widetilde{H}_s k_r^* k_s^*. \tag{C.64}$$

By substituting Eq. (C.23) into Eq. (C.64), and the resulting equation into Eq. (C.28), the modal traction wave-field $\widetilde{\mathbf{q}}_n$ at the tunnel invert can be expressed as a function of the wheel-rail roughness vector $\mathbf{\Delta}$ at each axle's position. This expression for $\widetilde{\mathbf{q}}_n$ can be substituted into the coefficient vectors $\widetilde{\mathbf{c}}_1$ and $\widetilde{\mathbf{b}}_1$ in Eqs. (C.44) and (C.45), respectively. Once $\widetilde{\mathbf{c}}_1$ and $\widetilde{\mathbf{b}}_1$ are solved, the following matrix equations can be used to find the modal displacement and traction wave-fields at a radius R from a tunnel in a full-space:

$$\widetilde{\mathbf{u}}_{n1}(r,n,\xi,\omega) = \widetilde{\mathbf{U}}_1\Big|_{r=R} \widetilde{\mathbf{c}}_1 \quad \text{and} \quad \widetilde{\mathbf{p}}_{n1}(r,n,\xi,\omega) = \widetilde{\mathbf{T}}_{r1}\Big|_{r=R} \widetilde{\mathbf{c}}_1, \tag{C.65}$$

if $r_{ti} < R < r_{to}$ (within the tunnel wall), or

$$\widetilde{\mathbf{u}}_{n1}(r,n,\xi,\omega) = \widetilde{\mathbf{U}}_{m1}\Big|_{r=R} \widetilde{\mathbf{b}}_1 \quad \text{and} \quad \widetilde{\mathbf{p}}_{n1}(r,n,\xi,\omega) = \widetilde{\mathbf{T}}_{m1}\Big|_{r=R} \widetilde{\mathbf{b}}_1, \tag{C.66}$$

if $R \geq r_{to}$ (within the soil).

C.5 The Scattered Wave-Fields at the Soil-Tunnel Interface

When the railway tunnel is close to the free surface or other soil-embedded structures, such as foundations, the wave-fields reflected towards the tunnel can induce dynamic coupling. In this section, the iterative wave-scattering approach is used to account for the through-soil coupling between a tunnel and a pile-group; this is done by defining the scattered wave-field at the soil-tunnel interface and revising the tunnel response after each iteration, as detailed in Section 6.1.

Note, the incident wave-fields at the soil-tunnel interface are calculated using the BEM described in Appendix B.7, so the wave-fields are defined in the $(\mathbf{x}, \omega)$-domain, where $\mathbf{x}$ is a

position vector. The wave-fields can be transformed into the (n, ξ, ω)-domain by applying the discrete Fourier transform (DFT), with respect to the x-domain, and then finding the discrete Fourier series coefficients, with respect to the θ-domain (see Section 6.1).

Since the BEM is also defined in the Cartesian (x, y, z) coordinate system, the incident wave-fields need to be transformed into the cylindrical (r, θ, x) coordinate system of the PiP model before the scattered wave-fields can be computed. Given a wave-field $\mathbf{u}' = \{u_x, u_y, u_z\}^{\mathrm{T}}$ in the Cartesian coordinate system, the vector components can be transformed into $\mathbf{u} = \{u_r, u_\theta, u_x\}^{\mathrm{T}}$ in the cylindrical coordinate system using the matrix equation:

$$\mathbf{u} = \mathbf{Q}\mathbf{u}', \tag{C.67}$$

where the 3×3 transformation matrix $\mathbf{Q}$ is

$$\mathbf{Q} = \begin{bmatrix} 0 & \sin\theta & -\cos\theta \\ 0 & \cos\theta & \sin\theta \\ 1 & 0 & 0 \end{bmatrix}. \tag{C.68}$$

Once the incident displacement $\widetilde{\mathbf{u}}_{st}^{\mathrm{inc}}$ and traction $\widetilde{\mathbf{p}}_{st}^{\mathrm{inc}}$ wave-fields at the soil-tunnel interface are found, the waves can excite the outer tunnel wall in addition to the traction wave-field $\widetilde{\mathbf{q}}$ at the tunnel invert, as illustrated in Fig. C.8. Note that the wave-fields reflected by the free surface or the pile-group may contain (anti-)symmetric components, while $\widetilde{\mathbf{q}}$ only contains symmetric components. By decomposing the wave-field at the soil-tunnel interface into an incident wave-
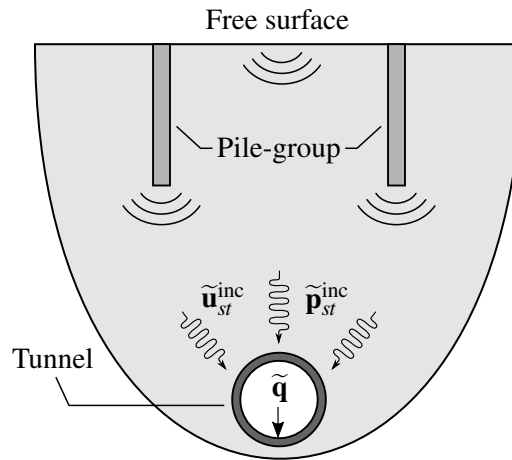

Fig. C.8 Schematic diagram of the incident displacement $\widetilde{\mathbf{u}}_{st}^{\mathrm{inc}}$ and traction $\widetilde{\mathbf{p}}_{st}^{\mathrm{inc}}$ wave-fields at the outer tunnel wall and the traction wave-field $\widetilde{\mathbf{q}}$ at the tunnel invert, which are applied as external excitation on the tunnel in the iterative PiP model.

field and a scattered wave-field, as first described in Section 4.2, Eqs. (C.42) and (C.43) can be rewritten as the following matrix equations:

$$\widetilde{\mathbf{u}}_{n1,st} - \widetilde{\mathbf{u}}_{n1,st}^{\text{inc}} = \widetilde{\mathbf{U}}_{m1}\Big|_{r=r_{to}} \widetilde{\mathbf{b}}_1 , \tag{C.69}$$

$$\widetilde{\mathbf{p}}_{n1,st} - \widetilde{\mathbf{p}}_{n1,st}^{\text{inc}} = \widetilde{\mathbf{T}}_{m1}\Big|_{r=r_{to}} \widetilde{\mathbf{b}}_1 , \tag{C.70}$$

where $\widetilde{\mathbf{u}}_{n1,st} - \widetilde{\mathbf{u}}_{n1,st}^{\text{inc}}$ and $\widetilde{\mathbf{p}}_{n1,st} - \widetilde{\mathbf{p}}_{n1,st}^{\text{inc}}$ are the scattered displacement and traction wave-fields, respectively, due to symmetric loading. Similarly, the following matrix equations express the scattered wave-fields due to anti-symmetric loading:

$$\widetilde{\mathbf{u}}_{n2,st} - \widetilde{\mathbf{u}}_{n2,st}^{\text{inc}} = \widetilde{\mathbf{U}}_{m2}\Big|_{r=r_{to}} \widetilde{\mathbf{b}}_2 , \tag{C.71}$$

$$\widetilde{\mathbf{p}}_{n2,st} - \widetilde{\mathbf{p}}_{n2,st}^{\text{inc}} = \widetilde{\mathbf{T}}_{m2}\Big|_{r=r_{to}} \widetilde{\mathbf{b}}_2 . \tag{C.72}$$

By applying the same coupling procedure detailed in Appendix C.3.3, Eqs. (C.69)–(C.72) for the soil can be rearranged with the governing equations of motion for the tunnel to find the revised coefficient vectors due to symmetric loading:

$$\widetilde{\mathbf{c}}_1 = \begin{bmatrix} \widetilde{\mathbf{C}}_{11} & \widetilde{\mathbf{C}}_{12} \end{bmatrix} \left\{ \begin{array}{c} \widetilde{\mathbf{q}}_n \\ \widetilde{\mathbf{p}}_{n1,st}^{\text{inc}} - \widetilde{\mathbf{T}}_{m1}\Big|_{r=r_{to}} \widetilde{\mathbf{U}}_{m1}^{-1}\Big|_{r=r_{to}} \widetilde{\mathbf{u}}_{n1,st}^{\text{inc}} \end{array} \right\}, \tag{C.73}$$

$$\widetilde{\mathbf{b}}_1 = \widetilde{\mathbf{U}}_{m1}^{-1}\Big|_{r=r_{to}} \left(\widetilde{\mathbf{U}}_1\Big|_{r=r_{to}} \widetilde{\mathbf{c}}_1 - \widetilde{\mathbf{u}}_{n1,st}^{\text{inc}} \right), \tag{C.74}$$

and anti-symmetric loading:

$$\widetilde{\mathbf{c}}_2 = \begin{bmatrix} \widetilde{\mathbf{C}}_{21} & \widetilde{\mathbf{C}}_{22} \end{bmatrix} \left\{ \begin{array}{c} \mathbf{0} \\ \widetilde{\mathbf{p}}_{n2,st}^{\text{inc}} - \widetilde{\mathbf{T}}_{m2}\Big|_{r=r_{to}} \widetilde{\mathbf{U}}_{m2}^{-1}\Big|_{r=r_{to}} \widetilde{\mathbf{u}}_{n2,st}^{\text{inc}} \end{array} \right\}, \tag{C.75}$$

$$\widetilde{\mathbf{b}}_2 = \widetilde{\mathbf{U}}_{m2}^{-1}\Big|_{r=r_{to}} \left(\widetilde{\mathbf{U}}_2\Big|_{r=r_{to}} \widetilde{\mathbf{c}}_2 - \widetilde{\mathbf{u}}_{n2,st}^{\text{inc}} \right). \tag{C.76}$$

Substituting Eqs. (C.73)–(C.76) into Eqs. (C.69)–(C.72) solves the revised response at the soil-tunnel interface during each iteration.

Note, for the first iteration, $\widetilde{\mathbf{u}}_{n1,st}^{\text{inc}} = \widetilde{\mathbf{p}}_{n1,st}^{\text{inc}} = \mathbf{0}$ because the free surface and pile-group have not yet been excited by the railway tunnel. Thus, the tunnel response due to the first iteration is equivalent to response predicted by the standard PiP model for a tunnel in a full-space [69].

C.6 The Fictitious-Force Method

At present, the equations in Appendices C.3–C.5 describe the motion of a tunnel in a full-space. However, for the purpose of modelling the ground-borne vibration of a realistic underground tunnel, it needs to be embedded in a homogeneous, isotropic half-space. Hence, the fictitious-force method [114] is used to find an equivalent set of fictitious line-loads that, when applied in a homogeneous full-space where the tunnel cavity is filled in with soil material, produce the same displacements at the soil-tunnel interface as when the cavity was present. The line-loads are then used to excite a half-space by applying them at the same depth as the tunnel. Figure C.9 summarises the three main steps in the fictitious-force method:

1. calculate the displacement wave-field $\widetilde{\mathbf{u}}_{to}$ at the soil-tunnel interface when the tunnel is excited using the iterative PiP model in a full-space;

2. find the internal source $\widetilde{\mathbf{p}}_{in}$ that produces the same $\widetilde{\mathbf{u}}_{to}$ when applied at the outer surface of a virtual cylinder comprising of the soil material around the tunnel;

3. convert $\widetilde{\mathbf{p}}_{in}$ into an equivalent set of fictitious line-loads $\widetilde{\mathbf{f}}$ that are later applied around the soil-tunnel interface in a homogenous half-space.

When the fictitious-force method is applied, an important assumption is that the near-field displacement of the soil surrounding the tunnel is not influenced by the far-field displacement at the free surface. Hence, the standard PiP model can only make valid predictions of the response when the tunnel is at least two tunnel diameters below the free surface [113]. Nevertheless, the iterative wave-scattering approach described in the prior section can approximate the coupling between the free surface and the tunnel (see Section 6.2).

(a)   (b)   (c)
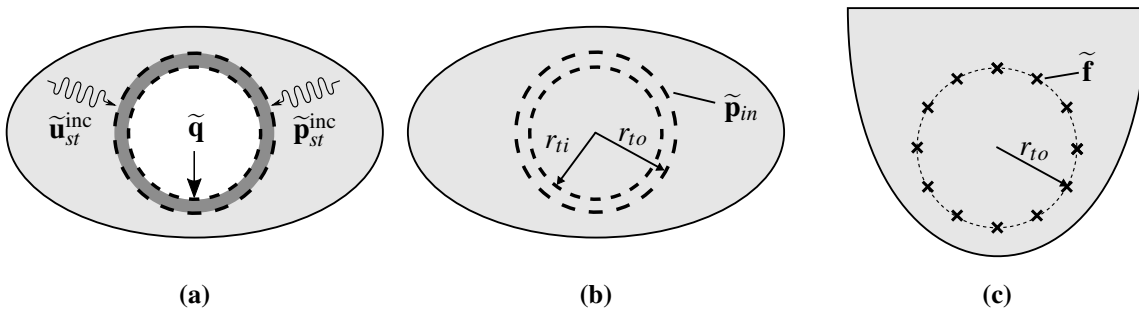
Fig. C.9 The fictitious-force method: **(a)** the excited tunnel embedded in a full-space; **(b)** the internal source $\widetilde{\mathbf{p}}_{in}$ applied onto the outer surface of a virtual cylinder that produce the same tunnel response; and **(c)** the source $\widetilde{\mathbf{p}}_{in}$ is converted into an equivalent set of fictitious line-loads $\widetilde{\mathbf{f}}$ that are later applied around the soil-tunnel interface in a homogenous half-space.

The internal source $\widetilde{\mathbf{p}}_{in}$ is computed by using the elastic continuum formulation described in Appendix C.4 to derive the governing equations of motion for a virtual cylinder with radius $r_{to} = r_{si}$. Given that the displacement and traction wave-fields at $r = 0$ need to be finite, the coefficients of the functions f, g_r, g_θ and g_x in Eqs. (C.29)–(C.32) reduce to three; a detailed explanation for this is provided by Hussein [112]. Therefore, the symmetric displacement and traction wave-fields at the virtual cylinder's surface are

$$\widetilde{\mathbf{u}}_{n1,sc}(n,\xi,\omega) = \left.\widetilde{\mathbf{U}}_{p1}\right|_{r=r_{to}} \widetilde{\mathbf{e}}_1 \,, \tag{C.77}$$

$$-\widetilde{\mathbf{p}}_{n1,sc}(n,\xi,\omega) = \left.\widetilde{\mathbf{T}}_{p1}\right|_{r=r_{to}} \widetilde{\mathbf{e}}_1 \,, \tag{C.78}$$

where the 3×3 matrices $\widetilde{\mathbf{U}}_{p1}(r,n,\xi,\omega)$ and $\widetilde{\mathbf{T}}_{p1}(r,n,\xi,\omega)$ contain the first, third and fifth columns of the matrices $\widetilde{\mathbf{U}}_1(r,n,\xi,\omega)$ and $\widetilde{\mathbf{T}}_{r1}(r,n,\xi,\omega)$, and the vector $\widetilde{\mathbf{e}}_1$ contains the three coefficients. Matrix equations, which are similar to Eqs. (C.77) and (C.78), also exist for the anti-symmetric wave-fields.

At the soil-tunnel interface, the internal source can be expressed as $\widetilde{\mathbf{p}}_{in} = \widetilde{\mathbf{p}}_{sc} + \widetilde{\mathbf{p}}_{st}$ due to equilibrium, and the displacement wave-fields must satisfy $\widetilde{\mathbf{u}}_{st} = \widetilde{\mathbf{u}}_{sc}$ due to compatibility. After some manipulation of Eqs. (C.77) and (C.78), using the compatibility and equilibrium conditions, the symmetric components of the internal source can be expressed as

$$\widetilde{\mathbf{p}}_{n1,in}(n,\xi,\omega) = \widetilde{\mathbf{p}}_{n1,st} - \left.\widetilde{\mathbf{T}}_{p1}\right|_{r=r_{to}} \left.\widetilde{\mathbf{U}}_{p1}\right|_{r=r_{to}}^{-1} \widetilde{\mathbf{u}}_{n1,st} \,. \tag{C.79}$$

Likewise, the anti-symmetric components of the internal source can be expressed as

$$\widetilde{\mathbf{p}}_{n2,in}(n,\xi,\omega) = \widetilde{\mathbf{p}}_{n2,st} - \left.\widetilde{\mathbf{T}}_{p2}\right|_{r=r_{to}} \left.\widetilde{\mathbf{U}}_{p2}\right|_{r=r_{to}}^{-1} \widetilde{\mathbf{u}}_{n2,st} \,. \tag{C.80}$$

The internal source $\widetilde{\mathbf{p}}_{in}$ in the (ξ,ω)-domain is found by taking the Fourier series summation of Eqs. (C.79) and (C.80):

$$\widetilde{\mathbf{p}}_{in}(\xi,\omega) = \sum_{n=0}^{\infty} \mathbf{S}_1 \widetilde{\mathbf{p}}_{n1,in} + \mathbf{S}_2 \widetilde{\mathbf{p}}_{n2,in} \,. \tag{C.81}$$

The internal source is converted into an equivalent set of M equidistant fictitious line-loads, which are located around the soil-tunnel interface in a homogeneous half-space, as shown in Fig. C.10. After applying the inverse of the coordinate transformation in Eq. (C.67) to transform the wave-fields from the cylindrical coordinate system to the Cartesian coordinate system, each fictitious line-load can be expressed in the (ξ,ω)-domain as
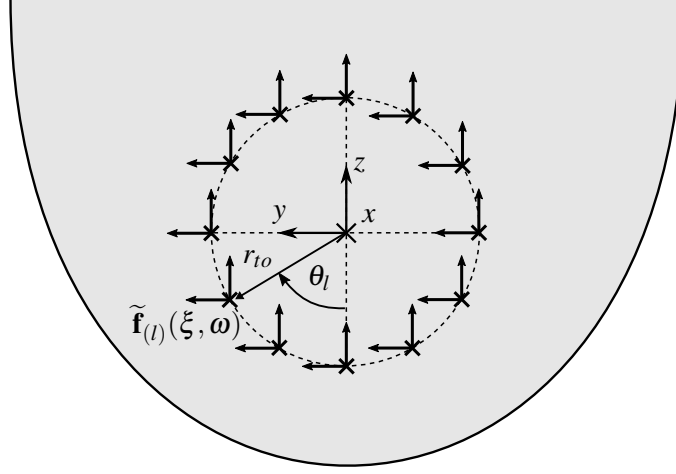
Fig. C.10 The internal source is converted into an equivalent set of fictitious line-loads at $M = 12$ equidistant points around the soil-tunnel interface in a homogeneous half-space.

$$\widetilde{\mathbf{f}}_{(l)}(\xi,\omega) = \left\{ \widetilde{f}_x, \widetilde{f}_y, \widetilde{f}_z \right\}^{\mathrm{T}} \quad \text{for } l = 1, 2, \ldots, M. \tag{C.82}$$

To find the displacement and traction wave-fields in a half-space due to $\widetilde{\mathbf{p}}_{in}$, the fictitious line-loads need to be expressed in the double-wavenumber-frequency (ξ, γ, ω)-domain, where γ is the wavenumber with respect to the space y-domain. Each line-load can be rewritten in the (ξ, y, z, ω)-domain:

$$\widetilde{\mathbf{f}}_{(l)}(\xi, y, z, \omega) = \widetilde{\mathbf{f}}_{(l)}(\xi, \omega) \cdot \delta\left(y - r_{to} \sin\theta_l\right) \cdot \delta\left(z + r_{to} \cos\theta_l\right). \tag{C.83}$$

The y-domain is transformed into the γ-domain by applying the Fourier transform:

$$
\begin{aligned}
\widehat{\mathbf{f}}_{(l)}(\xi, \gamma, z, \omega) &= \int_{-\infty}^{\infty} \widetilde{\mathbf{f}}_{(l)}(\xi, y, z, \omega) \cdot e^{-i\gamma y} dy, \\
&= \int_{-\infty}^{\infty} \widetilde{\mathbf{f}}_{(l)}(\xi, \omega) \cdot \delta\left(y - r_{to} \sin\theta_l\right) \cdot \delta\left(z + r_{to} \cos\theta_l\right) \cdot e^{-i\gamma y} dy, \\
&= \widetilde{\mathbf{f}}_{(l)}(\xi, \omega) \cdot e^{-i\gamma r_{to} \sin\theta_l} \cdot \delta\left(z + r_{to} \cos\theta_l\right).
\end{aligned}
\tag{C.84}
$$

C.7 The Far-Field Displacements and Tractions in the Soil

The far-field displacements induced by the fictitious line-loads in a half-space can be calculated using the two-and-a-half-dimensional (2.5D) Green's functions derived by Tadeu et al. [218] for a homogeneous, isotropic half-space. The half-space Green's functions can be expressed as

$$\widehat{\mathbf{G}}_{u(l)}^{\text{half}}(\xi,\gamma,\omega) = \begin{bmatrix} \widehat{G}_{u_{xx}}^{\text{half}} & \widehat{G}_{u_{xy}}^{\text{half}} & \widehat{G}_{u_{xz}}^{\text{half}} \\ \widehat{G}_{u_{yx}}^{\text{half}} & \widehat{G}_{u_{yy}}^{\text{half}} & \widehat{G}_{u_{yz}}^{\text{half}} \\ \widehat{G}_{u_{zx}}^{\text{half}} & \widehat{G}_{u_{zy}}^{\text{half}} & \widehat{G}_{u_{zz}}^{\text{half}} \end{bmatrix}, \tag{C.85}$$

where $\widehat{\mathbf{G}}_{u(l)}^{\text{half}}$ denotes the 3×3 displacement Green's function matrix for a half-space. Each $\widehat{G}_{u_{ij}}^{\text{half}}$ component in $\widehat{\mathbf{G}}_{u(l)}^{\text{half}}$ is a transfer function that relates the displacement $\widehat{u}_i$ induced in the soil by each fictitious line-load component $\widehat{f}_j$. By taking the sum of all M fictitious line loads around the soil-tunnel interface, the displacement wave-field $\widehat{\mathbf{u}}$ in the soil can be expressed as

$$\widehat{\mathbf{u}}(\xi,\gamma,z,\omega) = \left\{ \widehat{u}_x, \widehat{u}_y, \widehat{u}_z \right\}^{\text{T}} = \sum_{l=1}^{M} \widehat{\mathbf{G}}_{u(l)}^{\text{half}} \, \widehat{\mathbf{f}}_{(l)}. \tag{C.86}$$

In their current form, the half-space Green's functions can only compute the displacement wave-fields in the soil. In order to compute the traction wave-fields, the linear-elastic kinematic relationship and the generalised Hooke's Law, for an isotropic continuum, are used to relate the displacements, strains and stresses together. These respective relationships can be written in index notation:

$$\widehat{\varepsilon}_{ij} = \frac{1}{2} \left(\widehat{u}_{i,j} + \widehat{u}_{j,i} \right), \tag{C.87}$$

$$\widehat{\sigma}_{ij} = \lambda \widehat{\varepsilon}_{kk} \delta_{ij} + 2\mu \widehat{\varepsilon}_{ij}, \tag{C.88}$$

where δ_{ij} is the Kronecker delta, $\widehat{\varepsilon}_{ij}$ is the infinitesimal strain tensor, $\widehat{\sigma}_{ij}$ is the Cauchy stress tensor, $\widehat{\varepsilon}_{kk} = \widehat{\varepsilon}_{xx} + \widehat{\varepsilon}_{yy} + \widehat{\varepsilon}_{zz}$ is the volumetric strain, and λ and μ are the elastic Lamé constants. Therefore, the half-space Green's functions for the stress wave-field can be derived. Similar to Eq. (C.85), these Green's functions can be expressed as

$$\widehat{\mathbf{G}}_{\sigma(l)}^{\text{half}}(\xi,\gamma,\omega) = \begin{bmatrix} \widehat{G}_{\sigma_{xx,x}}^{\text{half}} & \widehat{G}_{\sigma_{xx,y}}^{\text{half}} & \widehat{G}_{\sigma_{xx,z}}^{\text{half}} \\ \widehat{G}_{\sigma_{xy,x}}^{\text{half}} & \widehat{G}_{\sigma_{xy,y}}^{\text{half}} & \widehat{G}_{\sigma_{xy,z}}^{\text{half}} \\ \widehat{G}_{\sigma_{xz,x}}^{\text{half}} & \widehat{G}_{\sigma_{xz,y}}^{\text{half}} & \widehat{G}_{\sigma_{xz,z}}^{\text{half}} \\ \widehat{G}_{\sigma_{yy,x}}^{\text{half}} & \widehat{G}_{\sigma_{yy,y}}^{\text{half}} & \widehat{G}_{\sigma_{yy,z}} \\ \widehat{G}_{\sigma_{yz,x}}^{\text{half}} & \widehat{G}_{\sigma_{yz,y}}^{\text{half}} & \widehat{G}_{\sigma_{yz,z}}^{\text{half}} \\ \widehat{G}_{\sigma_{zz,x}}^{\text{half}} & \widehat{G}_{\sigma_{zz,y}}^{\text{half}} & \widehat{G}_{\sigma_{zz,z}}^{\text{half}} \end{bmatrix}, \tag{C.89}$$

where $\widehat{\mathbf{G}}_{\sigma(l)}^{\text{half}}$ denotes the 6×3 stress Green's function matrix for a half-space. Each $\widehat{G}_{\sigma_{ij,k}}^{\text{half}}$ component in $\widehat{\mathbf{G}}_{\sigma(l)}^{\text{half}}$ is a transfer function that relates the stress $\widehat{\sigma}_{ij}$ induced in the soil by each fictitious line-load component $\widehat{f}_j$. Thus, the stress wave-fields in the soil can be expressed as

$$\left\{\widehat{\sigma}_{xx}, \widehat{\sigma}_{xy}, \widehat{\sigma}_{xz}, \widehat{\sigma}_{yy}, \widehat{\sigma}_{yz}, \widehat{\sigma}_{zz}\right\}^{\text{T}} = \sum_{l=1}^{M} \widehat{\mathbf{G}}_{\sigma(l)}^{\text{half}} \, \widehat{\mathbf{f}}_{(l)}. \tag{C.90}$$

Only the six stress wave-fields in Eq. (C.90) are required to populate the Cauchy stress tensor $\widehat{\sigma}$ because it is reasonable to assume that there is no net moment acting on the soil. This makes the tensor symmetric ($\widehat{\sigma}_{ij} = \widehat{\sigma}_{ji}$) due to conservation of angular momentum:

$$\widehat{\sigma}(\xi, \gamma, z, \omega) = \begin{bmatrix} \widehat{\sigma}_{xx} & \widehat{\sigma}_{xy} & \widehat{\sigma}_{xz} \\ \widehat{\sigma}_{xy} & \widehat{\sigma}_{yy} & \widehat{\sigma}_{yz} \\ \widehat{\sigma}_{xz} & \widehat{\sigma}_{yz} & \widehat{\sigma}_{zz} \end{bmatrix}. \tag{C.91}$$

The traction wave-field $\widehat{\mathbf{p}}$ in the soil can then be evaluated by applying Cauchy's formula:

$$\widehat{\mathbf{p}}(\xi, \gamma, z, \omega) = \left\{\widehat{p}_x, \widehat{p}_y, \widehat{p}_z\right\}^{\text{T}} = \widehat{\sigma}\mathbf{n}(\mathbf{x}), \tag{C.92}$$

where $\mathbf{n}$ denotes the normal unit-vector to a surface centred at position vector $\mathbf{x} = \{x, y, z\}^{\text{T}}$ in the half-space.

In order to calculate the wave-fields in the space-frequency $(\mathbf{x}, \omega)$-domain, the inverse Fourier transform is performed twice with respect to each wavenumber domain. For example, the following integrals are used to compute the displacement wave-field:

$$\widetilde{\mathbf{u}}(\xi, y, z, \omega) = \frac{1}{2\pi} \int_{-\infty}^{\infty} \widehat{\mathbf{u}}(\xi, \gamma, z, \omega) \cdot e^{i\gamma y} d\gamma, \tag{C.93}$$

$$\mathbf{u}(\mathbf{x}, \omega) = \frac{1}{2\pi} \int_{-\infty}^{\infty} \widetilde{\mathbf{u}}(\xi, y, z, \omega) \cdot e^{i\xi x} d\xi. \tag{C.94}$$

A similar set of integrals to Eqs. (C.93) and (C.94) are used to compute the traction wave-field $\mathbf{p}(\mathbf{x}, \omega)$. These integrals can be used in either the iterative or standard PiP models.

In particular for the standard PiP model, the integrals can be simplified if each j component of $\mathbf{u}$ and $\mathbf{p}$, denoted as u_j and p_j, has specific properties, such as being odd or even functions. By applying Euler's formula, Eqs. (C.93) and (C.94) can be rewritten as the following integrals:

$$\widetilde{u}_j(\xi, y, z, \omega) = \frac{1}{2\pi} \int_0^\infty \left(\widehat{u}_j(\xi, \gamma, z, \omega) + \widehat{u}_j(\xi, -\gamma, z, \omega) \right) \cdot \cos(\gamma y) d\gamma$$

$$+ \frac{i}{2\pi} \int_0^\infty \left(\widehat{u}_j(\xi, \gamma, z, \omega) + \widehat{u}_j(\xi, -\gamma, z, \omega) \right) \cdot \sin(\gamma y) d\gamma, \tag{C.95}$$

$$u_j(\mathbf{x}, \omega) = \frac{1}{2\pi} \int_0^\infty \left(\widetilde{u}_j(\xi, y, z, \omega) + \widetilde{u}_j(-\xi, y, z, \omega) \right) \cdot \cos(\xi x) d\xi$$

$$+ \frac{i}{2\pi} \int_0^\infty \left(\widetilde{u}_j(\xi, y, z, \omega) + \widetilde{u}_j(-\xi, y, z, \omega) \right) \cdot \sin(\xi x) d\xi. \tag{C.96}$$

Table C.1 summarises the (anti-)symmetry arguments of the function $u_j(\mathbf{x}, \omega)$ on the xy-plane; the same arguments also apply for the function $p_j(\mathbf{x}, \omega)$. If the functions $u_j(\mathbf{x}, \omega)$ and $p_j(\mathbf{x}, \omega)$ are even with respect to the space x- and y-domains, the sine terms in Eqs. (C.95) and (C.96) must be zero. Conversely, if the functions are odd, the cosine terms will be zero. It is important to note that these (anti-)symmetric arguments are only true for the standard PiP model because, in this case, the tunnel is excited by a symmetric traction distribution at the tunnel invert. By applying the arguments in Table C.1, each displacement wave-field component $u_j(\mathbf{x}, \omega)$ can be reduced to the following integrals:

$$u_x(\mathbf{x}, \omega) = \frac{1}{\pi^2} \int_0^\infty \int_0^\infty \widehat{u}_x(\xi, \gamma, z, \omega) \cdot i \sin(\xi x) \cdot \cos(\gamma y) d\xi d\gamma, \tag{C.97}$$

$$u_y(\mathbf{x}, \omega) = \frac{1}{\pi^2} \int_0^\infty \int_0^\infty \widehat{u}_y(\xi, \gamma, z, \omega) \cdot \cos(\xi x) \cdot i \sin(\gamma y) d\xi d\gamma, \tag{C.98}$$

$$u_z(\mathbf{x}, \omega) = \frac{1}{\pi^2} \int_0^\infty \int_0^\infty \widehat{u}_z(\xi, \gamma, z, \omega) \cdot \cos(\xi x) \cdot \cos(\gamma y) d\xi d\gamma. \tag{C.99}$$

A similar set of integrals can be used to compute each traction wave-field component $p_j(\mathbf{x}, \omega)$. Note that only the positive ξ and γ wavenumbers are used in these integrals, which improves the computational efficiency of the standard PiP formulation.

	(x, y, z)	$(-x, y, z)$	$(x, -y, z)$	$(-x, -y, z)$
u_x	$+$	$-$	$+$	$-$
u_y	$+$	$+$	$-$	$-$
u_z	$+$	$+$	$+$	$+$

Table C.1 (Anti-)symmetry arguments for each displacement wave-field component $u_j(\mathbf{x}, \omega)$ in the soil.

Appendix D

Matrices for an Elastic Continuum

The closed-form, analytical expressions of the matrices that determine the displacement and traction components for an elastic continuum are outlined in this appendix. In the equations below, $\alpha^2 = \xi^2 - \frac{\omega^2}{c_P^2}$, $\beta^2 = \xi^2 - \frac{\omega^2}{c_S^2}$, and I_n and K_n are modified n^{th} order Bessel functions of the first and second kinds, respectively. The first and second elastic Lamé constants are λ and μ, respectively. The phase speeds of P-waves and S-waves in the elastic medium are c_P and c_S, respectively. The angular frequency is ω, and ξ is the longitudinal wavenumber.

The elements of the matrices $\widetilde{\mathbf{U}}_1$ and $\widetilde{\mathbf{U}}_2$, which determine the displacement components of an elastic continuum with cylindrical geometry, are

$$u_{11} = \frac{n}{r} I_n(\alpha r) + \alpha I_{n+1}(\alpha r) \,,$$

$$u_{12} = \frac{n}{r} K_n(\alpha r) - \alpha K_{n+1}(\alpha r) \,,$$

$$u_{13} = i\xi I_{n+1}(\beta r) \,,$$

$$u_{14} = i\xi K_{n+1}(\beta r) \,,$$

$$u_{15} = \frac{n}{r} I_n(\beta r) \,,$$

$$u_{16} = \frac{n}{r} K_n(\beta r) \,,$$

$$u_{21} = -\frac{n}{r} I_n(\alpha r) \,,$$

$$u_{22} = -\frac{n}{r} K_n(\alpha r) \,,$$

$$u_{23} = i\xi I_{n+1}(\beta r) \,,$$

$$u_{24} = i\xi K_{n+1}(\beta r) \,,$$

$$u_{25} = -\frac{n}{r} I_n(\beta r) - \beta I_{n+1}(\beta r),$$

$$u_{26} = -\frac{n}{r} K_n(\beta r) + \beta K_{n+1}(\beta r),$$

$$u_{31} = i\xi I_n(\alpha r),$$

$$u_{32} = i\xi K_n(\alpha r),$$

$$u_{33} = -\beta I_n(\beta r),$$

$$u_{34} = \beta K_n(\beta r),$$

$$u_{35} = 0,$$

$$u_{36} = 0.$$

For symmetric loading, the matrix $\widetilde{\mathbf{U}}_1$ is given by

$$\widetilde{\mathbf{U}}_1(r,n,\xi,\omega) = \begin{bmatrix} u_{11} & u_{12} & u_{13} & u_{14} & u_{15} & u_{16} \\ u_{21} & u_{22} & u_{23} & u_{24} & u_{25} & u_{26} \\ u_{31} & u_{32} & u_{33} & u_{34} & u_{35} & u_{36} \end{bmatrix}. \tag{D.1}$$

For anti-symmetric loading, the matrix $\widetilde{\mathbf{U}}_2$ is given by

$$\widetilde{\mathbf{U}}_2(r,n,\xi,\omega) = \begin{bmatrix} u_{11} & u_{12} & -u_{13} & -u_{14} & -u_{15} & -u_{16} \\ -u_{21} & -u_{22} & u_{23} & u_{24} & u_{25} & u_{26} \\ u_{31} & u_{32} & -u_{33} & -u_{34} & -u_{35} & -u_{36} \end{bmatrix}. \tag{D.2}$$

The elements of the matrices $\widetilde{\mathbf{T}}_{r1}$ and $\widetilde{\mathbf{T}}_{r2}$, which determine the traction components of an elastic continuum with cylindrical geometry, are

$$t_{11} = \left(2\mu \frac{(n^2 - n)}{r^2} - \lambda \xi^2 + (\lambda + 2\mu) \alpha^2 \right) I_n(\alpha r) - 2\mu \frac{\alpha}{r} I_{n+1}(\alpha r),$$

$$t_{12} = \left(2\mu \frac{(n^2 - n)}{r^2} - \lambda \xi^2 + (\lambda + 2\mu) \alpha^2 \right) K_n(\alpha r) + 2\mu \frac{\alpha}{r} K_{n+1}(\alpha r),$$

$$t_{13} = 2\mu i\xi \beta I_n(\beta r) - 2\mu i\xi \frac{(n+1)}{r} I_{n+1}(\beta r),$$

$$t_{14} = -2\mu i\xi \beta K_n(\beta r) - 2\mu i\xi \frac{(n+1)}{r} K_{n+1}(\beta r),$$

$$t_{15} = 2\mu \frac{(n^2 - n)}{r^2} I_n(\beta r) + 2\mu \frac{n}{r} \beta I_{n+1}(\beta r),$$

$$t_{16} = 2\mu \frac{(n^2 - n)}{r^2} K_n(\beta r) - 2\mu \frac{n}{r} \beta K_{n+1}(\beta r),$$

$$t_{21} = -2\mu \frac{(n^2 - n)}{r^2} I_n(\alpha r) - 2\mu \frac{n}{r} \alpha I_{n+1}(\alpha r),$$

$$t_{22} = -2\mu \frac{(n^2 - n)}{r^2} K_n(\alpha r) + 2\mu \frac{n}{r} \alpha K_{n+1}(\alpha r),$$

$$t_{23} = \mu i \xi \beta I_n(\beta r) - 2\mu i \xi \frac{(n+1)}{r} I_{n+1}(\beta r),$$

$$t_{24} = -\mu i \xi \beta K_n(\beta r) - 2\mu i \xi \frac{(n+1)}{r} K_{n+1}(\beta r),$$

$$t_{25} = \left(-2\mu \frac{(n^2 - n)}{r^2} - \mu \beta^2 \right) I_n(\beta r) + 2\mu \frac{\beta}{r} I_{n+1}(\beta r),$$

$$t_{26} = \left(-2\mu \frac{(n^2 - n)}{r^2} - \mu \beta^2 \right) K_n(\beta r) - 2\mu \frac{\beta}{r} K_{n+1}(\beta r),$$

$$t_{31} = 2\mu i \xi I_n(\alpha r) + 2\mu i \xi \alpha I_{n+1}(\alpha r),$$

$$t_{32} = 2\mu i \xi K_n(\alpha r) - 2\mu i \xi \alpha K_{n+1}(\alpha r),$$

$$t_{33} = -\mu \frac{n}{r} \beta I_n(\beta r) - \mu(\xi^2 + \beta^2) I_{n+1}(\beta r),$$

$$t_{34} = \mu \frac{n}{r} \beta K_n(\beta r) - \mu(\xi^2 + \beta^2) K_{n+1}(\beta r),$$

$$t_{35} = \mu i \xi \frac{n}{r} I_n(\beta r),$$

$$t_{36} = \mu i \xi \frac{n}{r} K_n(\beta r).$$

For symmetric loading, the matrix $\widetilde{\mathbf{T}}_{r1}$ is given by

$$\widetilde{\mathbf{T}}_{r1}(r, n, \xi, \omega) = \begin{bmatrix} t_{11} & t_{12} & t_{13} & t_{14} & t_{15} & t_{16} \\ t_{21} & t_{22} & t_{23} & t_{24} & t_{25} & t_{26} \\ t_{31} & t_{32} & t_{33} & t_{34} & t_{35} & t_{36} \end{bmatrix}. \tag{D.3}$$

For anti-symmetric loading, the matrix $\widetilde{\mathbf{T}}_{r2}$ is given by

$$\widetilde{\mathbf{T}}_{r2}(r, n, \xi, \omega) = \begin{bmatrix} t_{11} & t_{12} & -t_{13} & -t_{14} & -t_{15} & -t_{16} \\ -t_{21} & -t_{22} & t_{23} & t_{24} & t_{25} & t_{26} \\ t_{31} & t_{32} & -t_{33} & -t_{34} & -t_{35} & -t_{36} \end{bmatrix}. \tag{D.4}$$